Development of Photoswitchable Charge-Transfer Materials with Photochromic Spirooxazines: from Molecular Systems to Surfaces

by

Aiko Kurimoto

B.Sc., University of Victoria, 2011

A Dissertation Submitted in Partial Fulfillment
of the Requirements for the Degree of

DOCTOR OF PHILOSOPHY

in the Department of Chemistry

Supervisory Committee

Development of Photoswitchable Charge-Transfer Materials
with Photochromic Spirooxazines: from Molecular Systems to Surfaces

by

Aiko Kurimoto
BSc., University of Victoria, 2011

Supervisory Committee

Dr. Natia L. Frank, (Department of Chemistry)
Supervisor

Dr. David J. Berg (Department of Chemistry)
Departmental Member

Dr. Peter Wan (Department of Chemistry)
Departmental Member

Dr. Byoung-Chul Choi (Department of Physics and Astronomy)
Outside Member

Abstract

Supervisory Committee
Dr. Natia L. Frank, (Department of Chemistry)
Supervisor
Dr. David J. Berg (Department of Chemistry)
Departmental Member
Dr. Peter Wan (Department of Chemistry)
Departmental Member
Dr. Byoung-Chul Choi (Department of Physics and Astronomy)
Outside Member

Optical modulation of the physical properties of materials is important for future development of optical memories and switches, optoelectronics, and smart surfaces. Incorporation of an optically bistable photochromic compound into an electronically bifunctional material is a promising strategy for a development of photoswitchable materials. Photochromic spirooxazine ligands undergo light-induced ring-opening and closure between the closed-spirooxazine (SO) and open-photomerocynanine (PMC) forms. The structural reorganization leads to accompanying changes in electronic structure which can lead to a change in the oxidation/reduction potentials and spin state of a bound metal center. Changes in the ligand field about a metal center in turn can lead to "non-classical" photoinduced magnetic (PIM) effects. The "non-classical" PIM effect is an effect that occurs through ligand-centered processes via the metal center, rather than direct excitation at the metal center. The structural change of the photochromic compounds also results in a change in the frontier orbital energies and donor-acceptor character, which may lead to optically-gated charge-transfer and energy-transfer processes.

In this dissertation, the structural factors that govern thermal relaxation of spirooxazines, as optical control units, was investigated toward controlling the photostationary states of this important class of photochromes. The electronic structure of the PMC form of azahomoadamantyl-based spirooxazines was found to control the thermal coloration/decoloration rates of photochromic spirooxazines. A significant charge-separated character of the PMC form was correlated with the slow thermal coloration/decoloration rates in spirooxazines. This concept was then extended to an investigation of the effect of Lewis-acidic metal complexation. Solution study of the charge-separated character of the PMC form via metal complexation of the photochromic

spirooxazines supported the correlation between the charge-separated character of the PMC form and the rate of the thermal coloration/decoloration. The studies provide a potential pathway for modulating PMC thermal relaxation rates through optimization of the structure of the spirooxazines and metal complexation. The studies were then extended to an investigation of the photomodulation of charge-transfer processes in cobalt multinuclear clusters by photoisomerization of photochromic spirooxazines. Incorporation of optically bistable phenanthroline-spirooxazine ligands into a magnetically bistable cobalt-dioxolene valence tautomeric cluster resulted in large magnetic moments in the solid and solution states. This study suggests that the redox-isomeric behavior of the cobalt dioxolenes can be coupled to isomerization of the photochromic ligand in the solution state when the π-acceptor ability of the photochromic ligands align with the direction of charge transfer of the cobalt dioxolene components. The potential of these cobalt multinuclear clusters to enhance the relaxivity of water in MRI for biological imaging was investigated. A cobalt tetranuclear cluster was prepared and found to exhibit high magnetic moments in solution at room temperature, and large relaxivities relative to commercially available gadolinium based MRI contrast agents. Lastly, the photomodulation of ionic doping of graphene organic field-effect transistors (OFETs) by photochromic spirooxazines was investigated. The electron donor or acceptor nature of the photochromic isomers modulates the direction and magnitude of ionic doping of graphene, and in turn the gate voltages of graphene OFETs, leading to optical modulation of OFET gate voltages for data processing and memory technologies.

Table of Contents

List of Tables

List of Figures

List of Schemes

List of Numbered Compounds

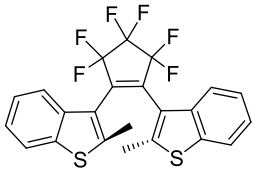

1.1

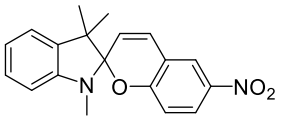

1.2

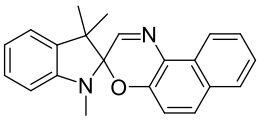

1.3

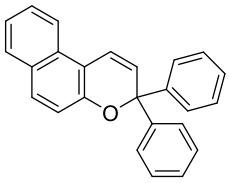

1.4

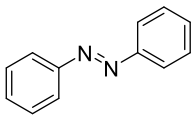

1.5

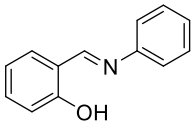

1.6

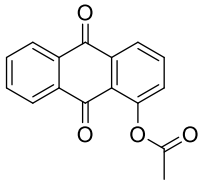

1.7

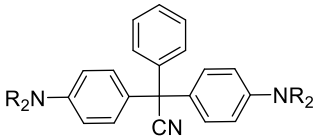

1.8

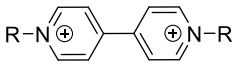

1.9

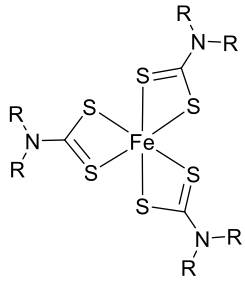

R = C_4H_9
C_3H_7
$C_{16}H_{33}$

1.10

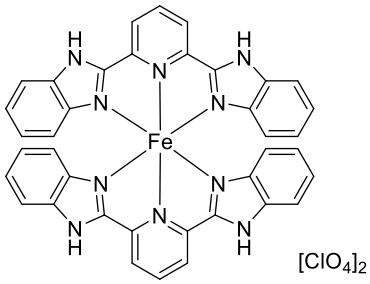

$[ClO_4]_2$

1.11

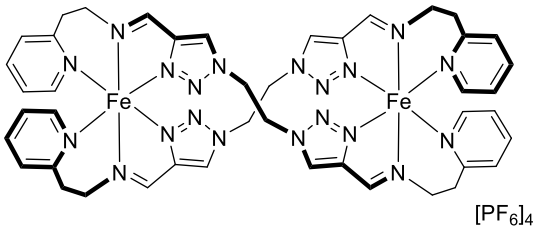

$[PF_6]_4$

1.12

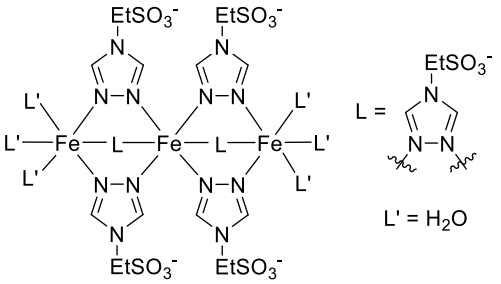

L =

L' = H_2O

1.13

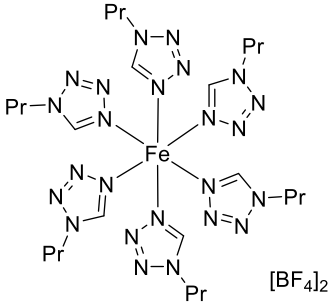

$[BF_4]_2$

1.14

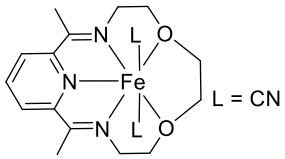

L = CN

1.15

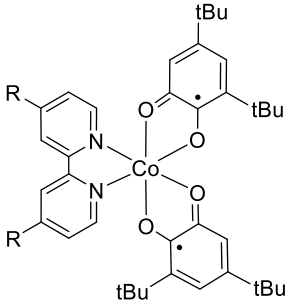

R = H **1.16**
Ph **1.17**
CH_3 **1.18**

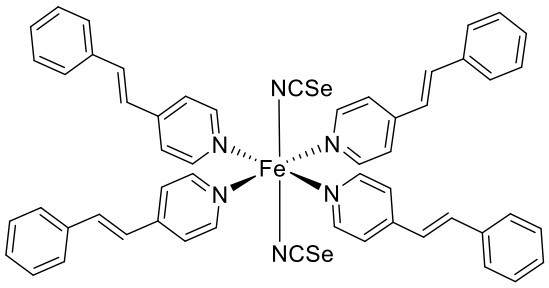

1.19

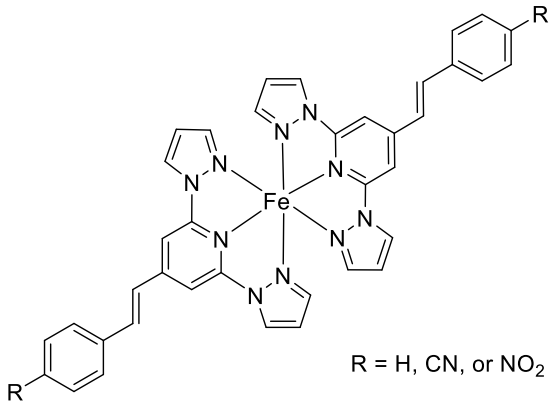

1.20

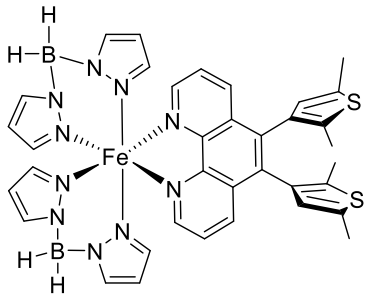

1.21

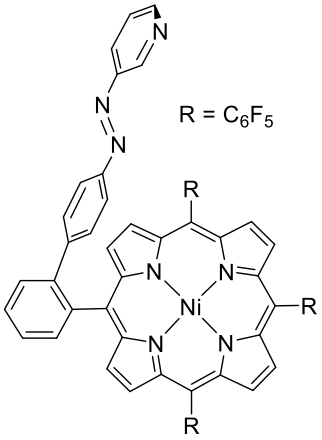

1.22

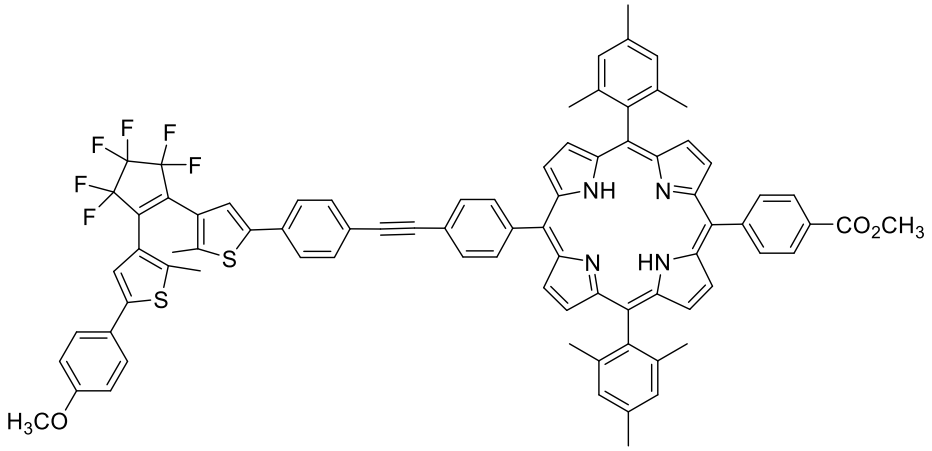

1.23

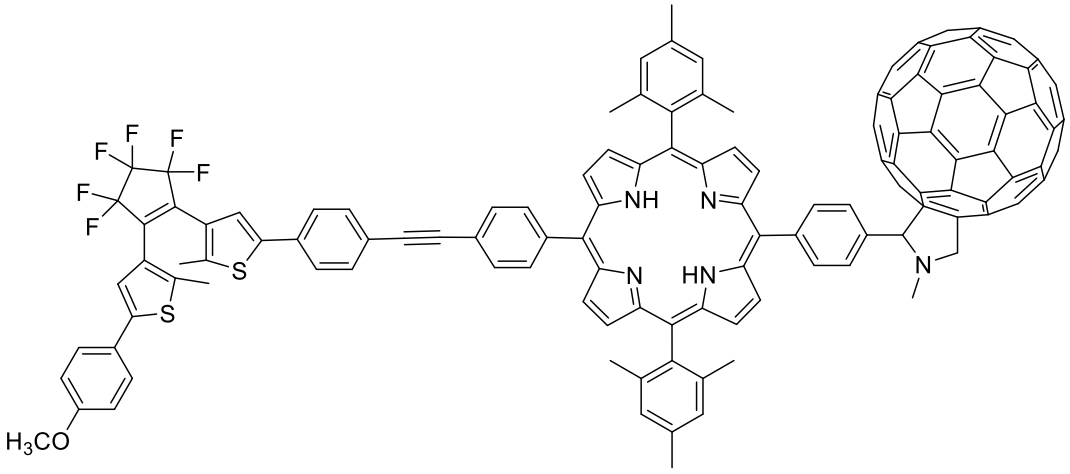

1.24

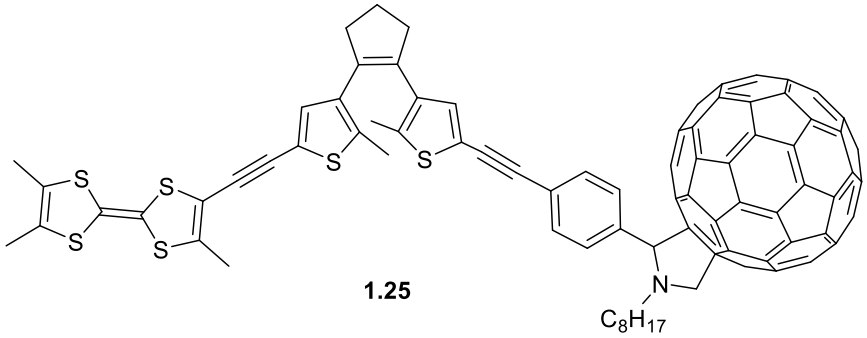

1.25

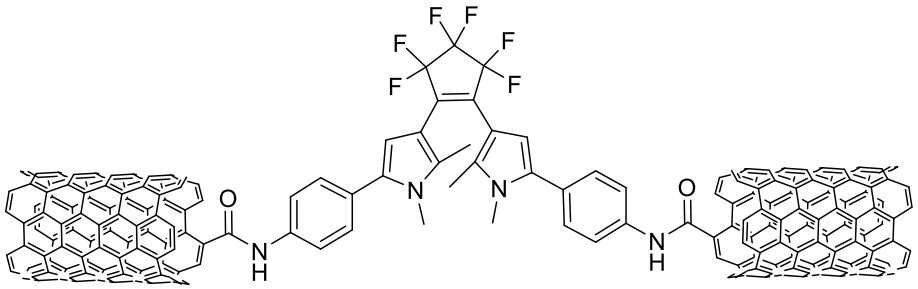

1.26

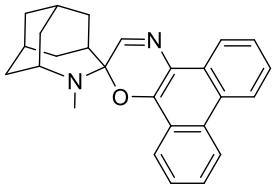

2.1

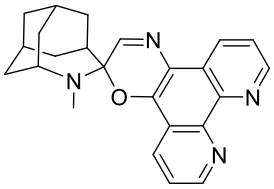

2.2

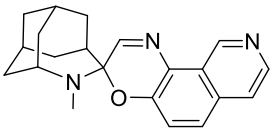

2.3

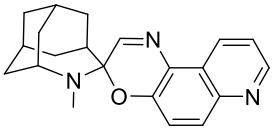

2.4

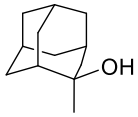

2.5

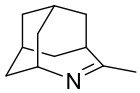

2.6

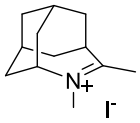

2.7

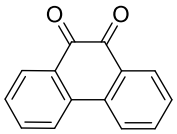

2.8

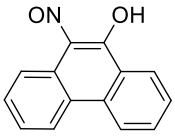

2.9

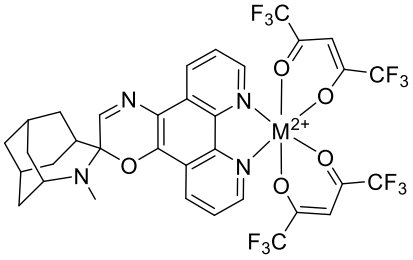

M = Mn(II) **3.1a**, Co(II) **3.1b**, Ni(II) **3.1c**

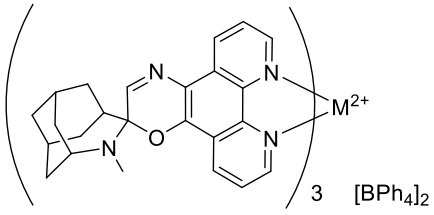

M = Mn(II) **3.2a**, Fe(II) **3.2b**, Co(II) **3.2c**

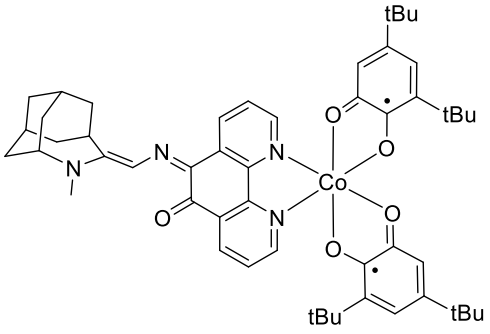

4.1

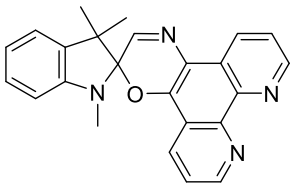

4.2

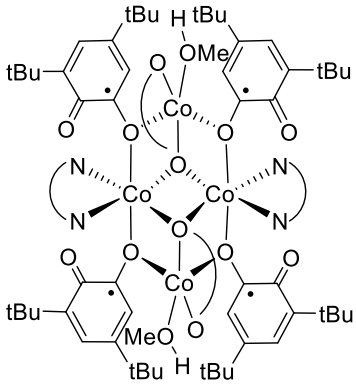

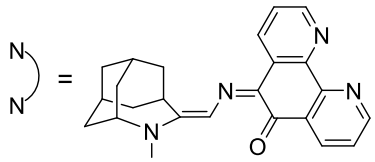

4.3

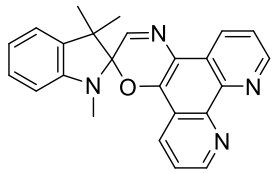

4.4

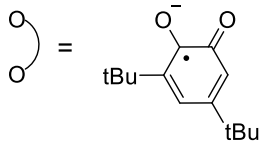

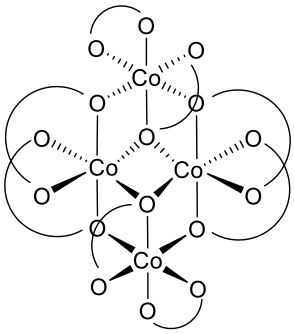

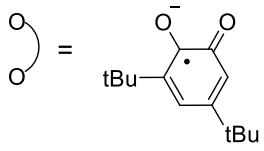

5.1

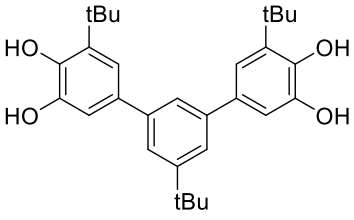

7.1

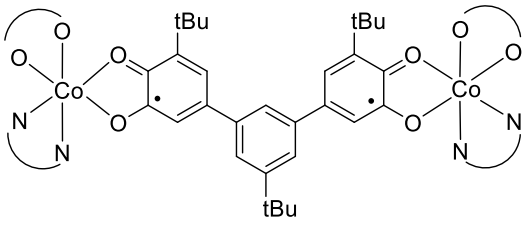

7.2

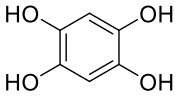

7.3

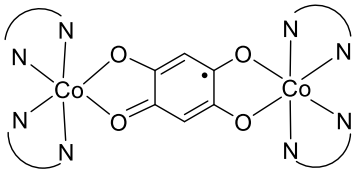

7.4

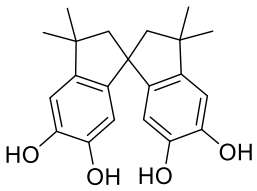

7.5

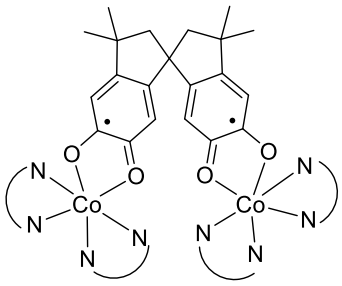

7.6

List of Abbreviations

^{1}H	proton
^{13}C	carbon-thirteen
^{19}F	fluorine-nineteen
0D	zero-dimensional
1D	one-dimensional
2D	two-dimensional
2,2'-bpy	2,2'-bipyridine
3,5-dbsq	3,5-di-*t*-butyl semiquinone
3,5-dbdiox	3,5-di-*t*-butyl dioxolene
6-31+G(d,p)	split-valence basis set with diffuse and polarization functions
6-311+G(d,p)	triple split-valence basis set with diffuse and polarization function
a	crystallographic lattice constant
A	acceptor, absorbance
A*	acceptor excited state
$A^{\bullet-}$	acceptor radical anion
A_o	initial absorbance
a_o	calculated molecular volume
AFM	antiferromagnetic
AIQSO	spiro[azahomoadamantane-isoquinolinoxazine]
anal. calcd	analytically calculated
APSO	spiro[azahomoadamantane-phenanthrolinoxazine]
APESO	spiro[azahomoadamantane-phenantherenoxazine]
aq	aqueous
AQSO	spiro[azahomoadamantane-quinolinoxazine]
a.u.	arbitrary units
ax	axial
$A/\hbar$	hyperfine coupling constant between the paramagnetic ion and proton nucleus
b	crystallographic lattice constant
B3LYP	Becke-style 3-parameter DFT with Lee-Yang-Parr correlation functional
BF_4^-	tetrafluoroborate
BLA	bond-length alternation
BPh_4^-	tetraphenylborate
bpy	bipyridine
BQ	benzoquinone
br	broad
btphen	5,6-bis(2,5-dimethyl-3-thienyl)-1,10-phenanthroline
bu	butyl
bzimpy	2,6-bis(benzimidazol-2-yl)pyridine

c	crystallographic lattice constant
C_{60}	Buckminsterfullerene
Can. Micro.	Canadian Microanalytical Services
Cat^{2-}	catecholate
CCC	*cis-cis-cis*
CCD	charge-coupled device
CCT	*cis-cis-trans*
CH_2Cl_2	dichloromethane
cm	centimeter
cm^{-1}	wavenumber
CNM	carbon-based nanomaterial
CNT	carbon nanotube
CO	carbonyl
CS	Curie spin
CT	charge transfer
CTC	*cis-trans-cis*
CTCST	charge-transfer-coupled spin transition
CTIST	charge-transfer-induced spin transition
CTT	*cis-trans-trans*
CV	cyclic voltammogram
d	doublet
D	debye, donor
D*	donor excited state
$D^{\bullet+}$	donor radical cation
D-A	donor-acceptor
DAE	diarylethene
DD	dipole-dipole
deg	degree
DFT	density functional theory
diox	dioxolene
DMSO	dimethylsulfoxide
Dq	differential of quanta
DTBQ	di-*tert*-butyl-*ortho*-quinone
e^-	electron
E_a	activation energy
E_{a1}	activation energy for SO → PMC thermal isomerization
E_{a2}	activation energy for PMC → SO thermal isomerization
EA	elemental analysis
EDG	electron-donating group
E_F	Fermi energy

emu	electromagnetic unit
eq	equatorial
equiv.	equivalents
ESI-MS	electrospray ionization mass spectrometry
E_T	Dimroth–Reichardt solvent polarity scale
E_T^N	normalized Dimroth–Reichardt solvent polarity scale
Et_2O	diethyl ether
Et_3N	trimethylamine
EtOAc	ethyl acetate
EtOH	ethanol
eV	electron-volt
EWG	electron-withdrawing group
expt.	experimental
FET	field-effect transistor
FRET	Förster resonance energy transfer, fluorescence resonance energy transfer
fs	femtoseconds
FT-IR	Fourier transform infrared
^{F}TPP	tetrakis(pentafluorophenyl)porphyrinato
FW	formula weight
g	gaseous
g	gram, g-factor
GBCA	Gadolinium-based contrast agent
h	hour
h	crystallographic index, Planck constant
hfac	hexafluoroacetylacetonate
HOMO	highest occupied molecular orbital
hs	high spin
hν	photon energy
Hz	hertz
IPSO	spiro[indoline-phenanthrolinoxazine]
I_{SD}	source-drain current
IVCT	intervalence charge transfer
J	NMR coupling constant
k	rate constant, crystallographic index
K	Kelvin
k_1	rate constant for SO → PMC thermal isomerization
k_2	rate constant for PMC → SO thermal isomerization
k_B	Boltzmann constant
k_BT	thermal energy
k_{ex}	water exchange rate

k_{obs}	observed rate constant for thermal back reaction
K_T	thermal equilibrium constant
kV	kilovolt
l	crystallographic index
L	ancillary ligand
LD-CISSS	light-driven coordination-induced spin-state switching
LD-LISC	ligand-driven light-induced spin-crossover
LFER	linear free energy relationship
LIESST	light-induced excited-spin-state trapping
LMCT	ligand-to-metal charge transfer
ls	low spin
LUMO	lowest unoccupied molecular orbital
m	multiplet
m	mass of paramagnetic solute in 1.00 mL solvent (Evan's method)
M	molarity, molecular ion, metal
max	maximum
Me	methyl
MeO	methoxide
MeOH	methanol
mg	milligram
MHz	megahertz
min	minutes
mL	milliliter
MLCT	metal-to-ligand charge transfer
MLG	multi-layer graphene
mm	millimeter
mmol	mmol
MO	molecular orbital
mol	mol
MRI	magnetic resonance imaging
mSAM	mixed self-assembled monolayer
*M*t	intensity of the detected magnetization
mV	millivolt
mW	milliwatt
M_{xy}	transverse magnetization
M_z	longitudinal magnetization
m/z	mass-to-charge ratio
NEXAFS	Near Edge X-Ray Absorption Fine Structure
NIR	near infrared
NLO	nonlinear optics

nm	nanometer
NMR	nuclear magnetic resonance
NN	diimine ligand
NOESY	nuclear overhauser effect spectroscopy
NP	nanoparticle
NSF	nephrogenic systemic fibrosis
o	ortho
Oe	Oersted
OFET	organic field-effect transistor
P	porphyrin
P	pressure
PB	Prussian Blue
PBA	Prussian Blue Analogue
PES	potential energy surface
PFBT	poly[(9,9-dioctylfluorenyl-2,7-diyl)-*co*-(1,4-benzo-{2,10-3}-thiadiazole)]
Ph	phenyl
phen	phenanthroline
PIM	photoinduced magnetic
PMC	photomerocyanine
PMMA	poly(methyl methacrylate)
ppm	parts per million
ps	picoseconds
PSS	photostationary state
PISCES	photoisomerization-induced spin-charge excited states
ptz	1-propyltetrazole
pz	1-pyrazolyl
q	magnitude of charge, number of coordinated water molecules
R	*R*-factor
r_1	longitudinal relaxivity
r_2	transverse relaxivity
r^{IS}	relaxivity arising from the inner-sphere water
r_{MH}	ion-proton distance
r^{OS}	relaxivity arising from the outer-sphere water
r^{SS}	relaxivity arising from the second-sphere water
r^{obs}	observed relaxivity
RDS	rate-determining step
r.t.	room temperature
s	singlet, strong
S	total spin quantum number
S_0	singlet ground state

S_1	singlet excited state
SC	scalar
SCO	spin-crossover
sh	shoulder
SLG	single-layer graphene
SO	spirooxazine
^{1}SO*	singlet excited state of spirooxazines
SP	spiropyran
$SQ^{\bullet-}$	semiquinone
SQUID	superconducting quantum interference device
stpy	styrylpyridine
SWCNT	single-walled carbon nanotube
t	triplet
t	*tert*
T	temperature
T_1	longitudinal relaxation time
$T_{1/2}$	transition temperature
T_2	transverse relaxation time
*T*c	critical temperature
T_{LIESST}	magnetization relaxation temperature of LIESST effect
T_{relax}	magnetization relaxation temperature
TCT	*trans-cis-trans*
TCC	*trans-cis-cis*
THF	tetrahydrofuran
TS	transition state
TTC	*trans-trans-cis*
TTT	*trans-trans-trans*
$\Phi_{A\rightarrow B}$	quantum yield for A → B photoisomerization
$\Phi_{B\rightarrow A}$	quantum yield for B → A photoisomerization
Φ_{CS}	quantum yield for charge sepration
$\Phi_{PMC\rightarrow SP}$	quantum yield for PMC → SO photoisomerization
$\Phi_{SO\rightarrow PMC}$	quantum yield for SO → PMC photoisomerization
v	very
V	volt, vibronic transition
V_{GS}	source-gate voltage
Vis	visible
V_{SD}	source-drain voltage
VT	variable temperature
V_{th}	threshold voltage
w	weak

wR_2	weighted *R*-factor
x	cartesian axis
XRD	X-ray diffraction
y	cartesian axis
z	cartesian axis
Z	number of asymmetric units per crystallographic unit cell
α	crystallographic lattice constant, torsional angle
β	crystallographic lattice constant, torsional angle
γ	crystallographic lattice constant, torsional angle
γ_H	proton magnetogyric ratio
δ	chemical shift
ε	dielectric constant, extinction coefficient
θ	theta (range for crystallographic data collection)
λ	wavelength
λ_{exc}	excitation wavelength
λ_{max}	maximum wavelength of absorption peak
μ	dipole moment
μ_0	permittivity of vacuum
μ_B	Bohr magneton
μM	micromolar
ν	operating frequency of NMR spectrometer, vibrational state
ρ_{calc}	calculated density
ρ_0	density of pure solvent (Evan‘s method)
ρ	density of solvent-containing solute (Evan‘s method)
Π	spin-pairing energy
σ	estimated standard deviation
τ	lifetime
τ_m	lifetime of water in a MRI contrast agent complex
χ_{g0}	gram magnetic susceptibility of solvent (Evan‘s method)
χ_g	gram magnetic susceptibility of sample (Evan‘s method)
χT	magnetic moment
χ_mT	molar magnetic moment
χ_m	molar susceptibility
χ_d	diamagnetic susceptibility
ω_H	Larmor precession frequency of protons
Δ	thermal energy
ΔE_{H-L}	energy difference between high spin and low spin
ΔG^o	Gibbs free energy
$\Delta G^{\ddagger}$	activation energy
ΔH	change in enthalpy

Δ_{oct}	ligand field strength
ΔS	change in entropy
Δv	resonance shift between solute-containing solvent and reference solvent
°	degree
°C	degree Celsius
Å	angstrom

Acknowledgements

First, I must thank my supervisor, Natia, for all of her endless support and encouragement. Over my degree, she has allowed me to grow as a scientist in every possible aspects. I have never met anybody who is a more scientifically knowledgeable person than her, and I doubt I will meet many people like her in the future. I thank her for passing along a little drop of the knowledge over the years, and making me proud of myself being a stronger and confident person. I would also like to thank to all of the Frank group member in the past and present. In particular, I would like to thank to Julia and Tom. I would not able to do the graphene project without Julia's considerable help, and I always learned something new from talking with Tom. I also thank the many UVic faculty and staff. Thank you to my committee members, Dave, Peter, and BC, for being extremely patient and supportive. I would also like to thank Andrew and Shubha for always being so helpful with constant instrument breakdown and making my life a lot easier. Huge thank you to Chris for helping me running complicated NMR experiments and explaining me about NMR over and over.

I must thank to all my friends in UVic Chemistry who put up with my everyday research tantrum and supported me in every way possible. First, I would like to thank all Hicks group members for being such enjoyable office mates. Particularly, thank to Dillon for always feeding me, cheering me up, and being there for me. I could always count on you. Thank you also to Genny, who is one of the most knowledgeable grad students I have ever met. She always had insightful answers for both chemistry and life-related questions. I also thank to Corey for delighting me with his dad jokes. I also would like to thank to Rhonda who I can never thank enough for providing continuous encouragement. She always taught me how much I have grown over years and how to be proud of myself. I also must thank to Alok, Karol, Natasha, Roman, and Graham who put up with my thesis crisis and kept me going with their endless support and love for last several months. I could not accomplish this without you all. This friendship I built in grad school is as invaluable as this degree, and I will forever be grateful all of you. Lastly, I thank to my family, who let me make this huge decision to come to Canada. I will always be thankful for their support.

Dedication

To my mother

Chapter 1. Introduction: Photochromic Photoswitchable Materials from Molecular Systems to Nanomaterials

In the last decade, great strides toward the development of multifunctional materials have been made. One of the most important classes of the multifunctional materials is a photoswitchable material which interconverts between two states in response to optical stimuli and is of interest for technologies ranging from optically-induced electronics and data storages to functional coatings. The distinct photoinduced states can be accompanied by changes in physical properties such as conductivity, optical properties, and magnetic properties allowing for optical control over multiple physical properties of the system, simultaneously. Optical modulation of the physical properties of molecular systems has been studied extensively over the last several decades. Recent investigations into optically modulated functional materials have been extended beyond molecular systems into areas such as supramolecular chemistry, nanoparticles, and surfaces.

This thesis describes the development of photoswitchable organic-inorganic hybrids and surfaces with an emphasis on optical gating of charge-transfer processes leading to the modulation of magnetic and electrical properties by utilizing photochromic spirooxazines as optical control units. First, we will discuss the photochromic compounds and their critical physical properties to be considered.

1.1. Photochromic Compounds: Optical Control Units

The first photochromic behavior was reported by Fritzsche in 1867.[1] Fritzche found that an orange-colored solution of tetracene was bleached by daylight and underwent regeneration of its color in the dark. Since then, interest in photochromic compounds grew substantially as a need of technologies for photoswitchable applications (optically controlled electronics, data storages, and functional coatings) increased over the decades. A photochrome is a compound which undergoes a reversible photochemical reaction with different wavelengths to generate two forms A and B. The forms A and B must have different absorption spectra, and either one state or both typically absorb in the visible light region. The color change by a photochemical reaction from one state to another, led to the origin of the word "photochromic" (Figure 1.1a). Irradiation with $h\nu_1$ leads to excitation of, in this case, the more thermodynamically stable form A, from the singlet ground state (S_0) to the singlet excited state (S_1), followed by photoisomerization to the photostationary state B (Figure 1.1b). The back reaction can occur thermally after cessation of the irradiation (T-type photochromism) or photochemically by irradiation by a different wavelength $h\nu_2$ (P-type photochromism).[2] In T-type photochromic molecules, the photogenerated state B is thermally stable and returns to state A, with a rate dependent on the energy barrier of thermal relaxation ($\Delta G^{\ddagger}$) to the ground state. In P-type photochromes, thermal relaxation to state A does not occur spontaneously after removal of optical stimuli, and conversion to state A requires an alternate wavelength of light.

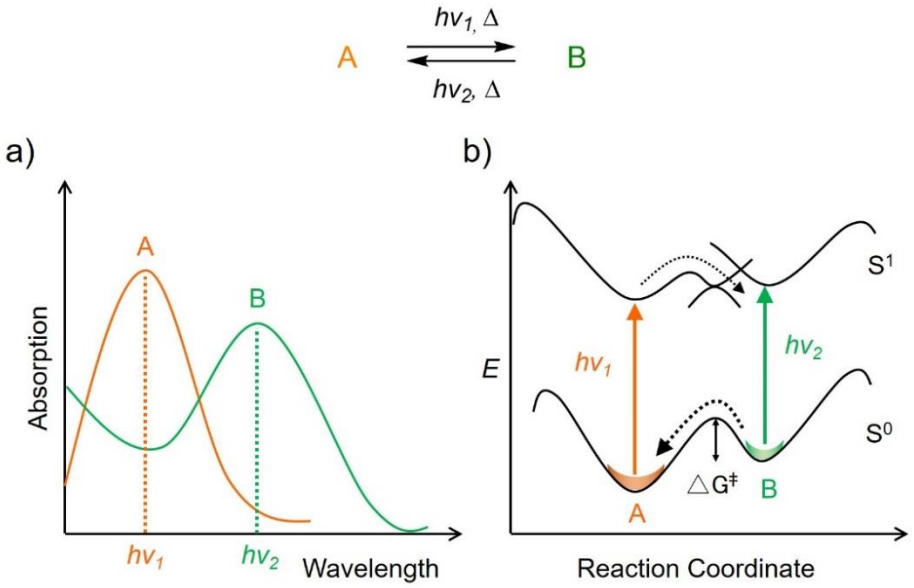

Figure 1.1. Photoisomerization and thermal relaxation between the A and B states is shown, with schematic absorption spectra (a), and the potential energy diagram for interconversion for a typical photochromic system (b).

1.1.1 Photochrome Classes

Photoisomerization can take place in several types of mechanistic reactions, as shown in Figure 1.2 which illustrates some of the important classes of organic photochromes and their photochemical reactions. Some photochromes such as furylfulgides,[3] diarylethenes **1.1**,[4,5] spiropyrans **1.2**,[6,7] spirooxazines **1.3**,[8] and chromenes **1.4**[9] undergo electrocyclization. *Cis-trans* (*E/Z*) isomerizations occur in stilbenes,[10] azobenzenes **1.5**,[11] thioindigos[12] as well as retinal proteins.[13] Photoinduced intramolecular hydrogen transfer can be found in anils **1.6**,[14] and benzylpyridines[15], while intramolecular group transfer occurs in polycyclic quinones **1.7**.[16] Dissociation processes and electron transfer are found in triarylmethanes **1.8**,[17] triarylimidazole dimers,[18] tetrachloronaphthalenes,[19] perchlorotoluene,[19] nitrosodimers,[20] and viologens **1.9**,[21] respectively.

Pericyclic reactions

Diarylethenes

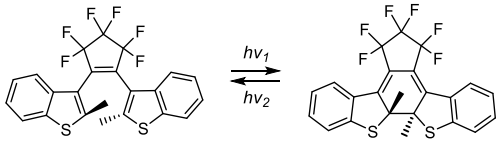

1.1

Spiropyrans

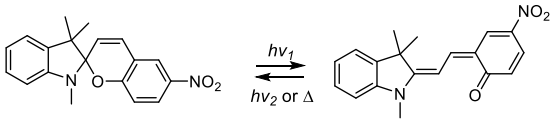

1.2

Spirooxazines

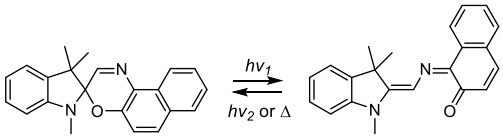

1.3

Chromenes

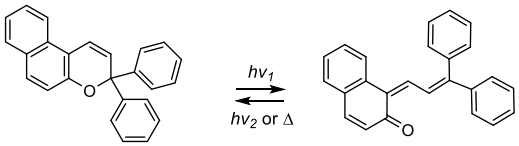

1.4

Cis-trans isomerization

Azobenzenes

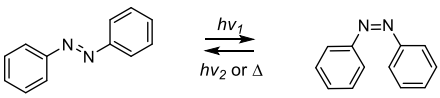

1.5

Intramolecular hydrogen transfer

Anils

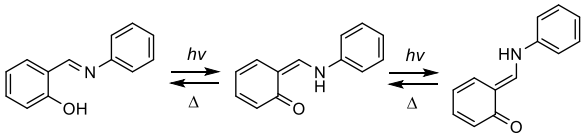

1.6

Intramolecular group transfer

Polycyclic quinones

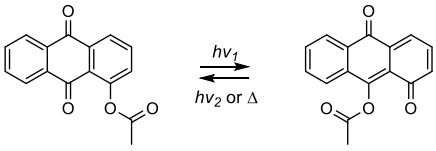

1.7

Dissociation

Triarylmethanes

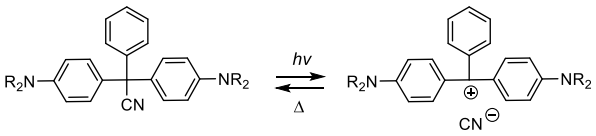

1.8

Electron tranfer

Viologens

1.9

Figure 1.2. Classes of organic photochromic compounds and their photochemical reactions.

1.1.2 Photochromic Spirooxazines and Their Important Physical Properties

Spirooxazines are a subclass of photochromes that exhibit extremely high fatigue-resistance,[22] a change in both nonlinear and linear optical properties with isomerization[23] and the ability to undergo photoisomerization in the solid state.[24-29] Absorbance of UV light (λ_{max} ~ 350 nm) in the closed spirooxazine (SO) form induces C–O bond cleavage, followed by isomerization to give the open photomerocyanine (PMC) form with a characteristic absorbance at λ_{max} ~ 600 nm (Figure 1.3). Visible light-induced ring-closure can occur by excitation of the PMC π–π* transition or by thermal relaxation along the ground state potential energy surface.[2,22,30] Reversible photoisomerization between the closed (SO) form, which is often the ground state, and the open (PMC) form can occur both photochemically and thermally, leading to T-type photochromism.

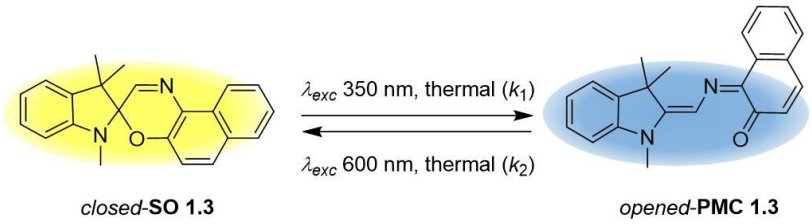

Figure 1.3. Photoisomerization and thermal relaxation processes in spirooxazines.

The important properties for the use of photochromic spirooxazines as optical control units for photoswitching materials are (i) the position of thermal equilibrium (*i.e.*, K_T = [state A]/[state B] = k_1/k_2.), (ii) the extent of fatigue-resistance, (iii) photoresponsivity (or quantum yield), and (iv) the rate of thermal relaxation from the photostationary state to the thermal equilibrium state. The thermal equilibrium is dependent on the relative thermodynamic stability of the two isomers A (colorless) and B (colored). Positive photochromism exists when the colorless form A is the more stable state, and

photoisomerization to the metastable colored form B occurs by irradiation with a shorter wavelength of light (UV, where $h\nu_1 < h\nu_2$). Negative photochromism, on the other hand, implies that the colored form B is the thermodynamically stable form, which can photoisomerize to the metastable colorless form A by irradiation with a longer wavelength light (visible light, $h\nu_2$). The development of negative photochromes has received a great deal of attention due to their potential for practical applications in the areas of biological and organic electronics. One of the main advantages is that lower energy visible light irradiation is utilized to induce photoisomerization, which is more biocompatible than UV light, and avoids the rapid photodegradation associated with repetitive UV light irradiation required by most photochromes. Though some examples of negative photochromes in azobenzenes,[31] acylhydrazones,[32] imidazole,[33-35] anils,[36,37] spiropyrans[38-44] and spirooxazines.[45,46] have been reported, molecular design for the development of negative photochromes remains a challenge.

In the negative photochromic spirooxazines, the thermodynamically stable form is the open (photomerocyanine: PMC) form. The shift in equilibrium between the open-form (PMC) and the metastable closed-form (SO) is strongly dependent on the nature of the substitution pattern,[39,42] and dielectric of the surrounding medium.[38,41,47,48] In general, electron-withdrawing groups on the oxazine moiety or electron-donating group on the amine moiety lead to greater charge separation due to partial stabilization of the developing charges, resulting in the stabilization of the PMC form.[8,49] Likewise, polar environments lead to greater charge separation and a corresponding shift in equilibrium toward the PMC form. Lewis-acid metal complexation can also result in greater charge separation by pulling more electron density from the oxazine moiety and stabilization of the PMC form.[40]

Photochromes are often characterized by their photoresponsivity, which empirically is the % change in color (A/A_o) (often also called the "colorability" in the older literature) of the photochrome upon irradiation. As the photoresponsivity is dependent on solvent, concentration, and power of light irradiation, the quantum yield is a more appropriate parameter to consider. The quantum yield of photoisomerization is defined as the efficiency of the photochromic change with respect to the amount of photons absorbed, which is the quantum yield ($\Phi_{A\rightarrow B}$ and/or $\Phi_{B\rightarrow A}$). To have efficient conversion from one form to another, the quantum yield should be high.

An understanding of the mechanism of photoisomerization in spirooxazines would allow optimization of the photoresponsivities of these systems. Fully elucidating the photochemical process for isomerization from the SO to the PMC form is extremely challenging, however, due to the existence of eight possible PMC isomers that can be formed via photoisomerization (Figure 1.4).

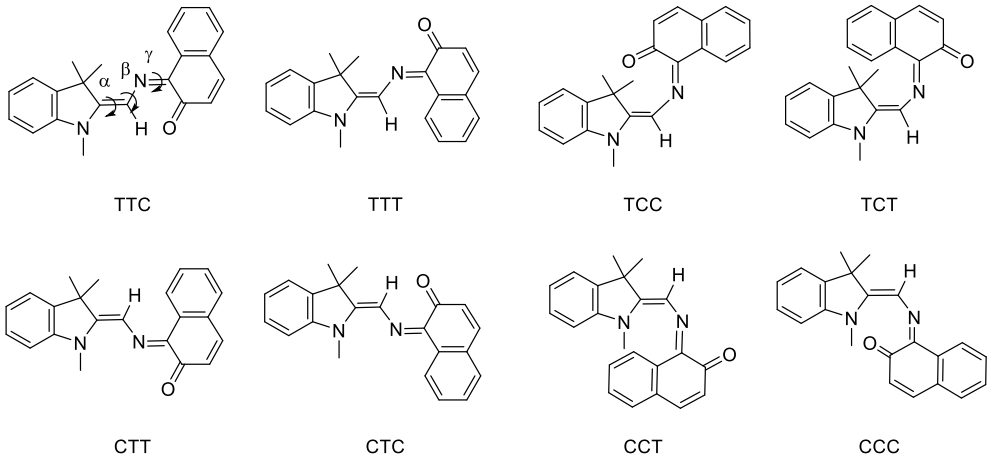

Figure 1.4. The eight possible PMC isomers formed by isomerization about the azomethine backbone.

Spirooxazines undergo a 6e- electrocyclization/reversion process, which according to the Woodward-Hoffman rules for pericyclic reactions is thermally allowed through a disrotatory process, and photochemically allowed through a conrotatory ring-closure/opening process. The first step of the photochromic reaction of spirooxazines is the dissociation of a C-O bond when the molecule occupies an electronic excited state, the exact nature of which depends on substitution pattern. The primary photochemical process that determines the mechanism of the photochromic behavior of spirooxazines has been studied by stationary,[49-51] and laser flash[52-54] (nano-, pico-, femtosecond) photolysis. UV light irradiation of spirooxazines generates a singlet excited state ($SO \rightarrow {}^1SO^*$) localized on the oxazine moiety, which undergoes transformation to the primary photoproduct with a lifetime of 100–300 fs (CCC and TCC intermediate) and subsequently rearranges in a few tens of picoseconds into the more stable merocyanine species (TTC or CTC).[50,52,53,55,56] For unsubstituted spirooxazines, a slower secondary transition process proceeds on the picosecond timescale to give the stable merocyanine TTC or CTC exclusively on the singlet potential energy surface. Conversely, for some nitro-substituted spirooxazines, a major channel of the photochemical reaction is through the triplet state.[57-59] Utilizing nanosecond transient absorption spectroscopy, formation of a transient triplet state was detected, and its subsequent relaxation to the ground state was determined to be 15 μs,[58,59] consistent with the triplet-state mechanism of nitro-substituted spiropyrans.[55] Generally speaking, introduction of an EDG on the indolyl moiety or an EWG on the oxazine moiety leads to reduction in the photocoloration quantum yield ($\Phi_{SO \rightarrow MC}$ = 0.106–0.137 in toluene)[49] as compared to that of unsubstituted indolino-naphthospirooxazines **1.3** ($\Phi_{SO \rightarrow MC}$ = 0.23 in toluene).[60] Computational studies suggested that this is primarily due

to the D-A type substitution pattern which increases the population of the S_1 state after $S_0 \rightarrow S_2$ excitation through conical intersection. While passing through the conical intersection, some molecules go on the potential energy surface (PES) of the S_1 state which may subsequently relax to the ground state SO form.[61] The photocoloration quantum yield also increases with a longer C(spiro)–O bond length.[62] As photocoloration occurs via C–O bond cleavage; a higher photocoloration quantum yield correlates with increased C–O bond length as these longer, weaker bonds are more susceptible to photolysis.[62]

While the mechanism and structural correlation of the photocoloration processes (SO→PMC) has been extensively studied, the photodecoloration (PMC→SO) process has not been fully explored due to the challenges associated with developing negative photochromes. However, femtosecond transient absorption spectroscopy of spiropyrans suggests that the photoexcitation of the merocyanine form leads to the first singlet excited state formed from a higher-energy excited state with a lifetime in the range of 10–100 ps[63-65] and subsequent formation of the SP form.[66] The singlet manifold was found to be predominant, and no evidence for triplet-state transients was observed.[67]

Another important property of photochromic compounds is the fatigue resistance during photoisomerization, which is arbitrarily defined as the percentage of intact photochromic material remaining after 1000 photoisomerization cycles. Photochromic reactions are always accompanied by rearrangement of chemical bonds, and this rearrangement may lead to undesirable side reactions which can reduce the number of cycles of photochromic reactions. Spirooxazines are characterized by their high tolerance to photodegradation as compared to the broader family of spiropyrans. The high fatigue resistance of the spirooxazines is because the majority of spirooxazines undergo

photoisomerization via the singlet manifold exclusively. Excitation involving the triplet manifold facilitates the formation of singlet molecular oxygen from the triplet excited state and thus a greater possibility of photodegradation via oxidation by singlet oxygen. Electronic effects of the substituents on spirooxazines showed that the introduction of an electron-donating group (EDG) onto the indolyl moiety improves the fatigue resistance, with exemplary molecules showing no degradation after 1000 cycles. Conversely, the introduction of electron-withdrawing groups (EWG) diminishes it, presumably due to the destabilization of the metastable open-form or involvement of triplet excited state.[39,68-70]

Lastly, modulation of the rate of thermal back reaction, which relates to the thermal stability of the photogenerated isomer, is important for practical applications. The ability to achieve (i) fast thermal relaxation rates for optical coating applications or (ii) slow (or irreversible, P-type) thermal reaction for memory applications is critical for practical applications. Modulation of the thermal back reaction involves tuning the height of the energy barrier ($\Delta G^{\ddagger}$) from the photogenerated form to the thermodynamically stable form. This in turn requires an understanding of mechanism for thermal relaxation. A major challenge in designing experiments to determine the mechanism of thermal isomerization of the spirooxazine/spiropyran class of photochromes arises from the very short lifetimes of the metastable PMC form. The pathway for spirooxazine thermal relaxation between the SO and the PMC form has been proposed computationally to go through either a rotation pathway or an inversion pathway; however, currently there is no experimental evidence to support either pathway. Investigation of the thermal coloration/decoloration pathway of spirooxazines via experiment and computation is discussed in Chapter 2.

1.2. Optical Switching of Magnetic Properties in Organic-Metal Hybrid Materials

One strategy for the development of multifunctional materials relies on electronically bistable systems in which the relative stability of two states can be switched by external stimuli. An important subclass of multifunctional materials exhibit photoinduced magnetic (PIM) effects in which the magnetization of a material can be changed by light irradiation leading to change in the magnitude of magnetization, coercivity, or magnetic ordering. Light-induced changes in magnetic ordering are particularly important for potential applications in memory and data storage technologies in which data is "written" with light, but "read" magnetically.[71] Light modulation of magnetic properties at the molecular level has been demonstrated via metal-to-metal charge transfer processes in Prussian blue analogues,[72,73] photo-induced spin-crossover in spin-transition complexes,[72,74-76] and photo-induced valence tautomerism in mixed valent metal complexes.[77] However, the lifetime of the photomagnetic states is dictated by the short lifetime of metal-centered excited states, with rapid thermal magnetization relaxation to the ground state occurring at cryogenic temperatures. As such, observation of photomagnetic effects at room temperature in the solid state remains a significant challenge.

The incorporation of photochromic ligands as optical switching units into organic-metal hybrid materials is a promising strategy to induce long magnetization relaxation times via a ligand-centered excited state rather than a metal-centered excited state. Photochromic molecules undergo photoinduced isomerization between two metastable states that differ in electronic structure, allowing effective optical modulation of electrical, redox, magnetic, and optical properties of bound transition-metal complexes. In principle, two approaches can be taken toward this end, i) modulation of the ligand field at the metal

center, and ii) optical modulation of the coordination environment of the metal center. In this section, an overview of recent results toward increasing the operating temperature for photoinduced magnetic effects in molecular systems is discussed.

1.2.1. Prussian Blue Analogues (PBAs)

Prussian Blue (PB) is a mixed-valent Fe(II)-Fe(III) bimetallic cyanide with a generalized formula of $Fe(III)_4[Fe(II)(CN)_6]_3 \cdot xH_2O$, where x=14-17. An intense blue color gives rise to its use as a pigment ("Tunrnbull's Blue" or "Paris Blue") since the first report in 1710 by Frisch.[78] Prussian blue exhibits a cubic framework constructed from hexacoordinate Fe(II)–C–N-Fe(III) sequences, and various site defects associated with solvation and the presence of other cations such as Na^+, Ca^{++}, etc. The magnetic properties became of great interest in the early '80s with the discovery of long-range ferromagnetic ordering with a Curie temperature T_c of 5.6 K.[79] The low magnetic ordering temperature (T_c) is due to weak magnetic exchange coupling between two high-spin d_5 Fe(III) metals ions via superexchange through the low-spin d_6 Fe(II) center (10.17 A). An increase in exchange coupling could be achieved by substituting iron centers with different paramagnetic metal ions to give rise to bimetallic cyano-bridged structural motifs called Prussian Blue Analogues (PBAs). In PBAs, a cubic $M_a[M'(CN)_6]_b$ framework is constructed from octahedral $[M'(CN)_6]^{a-}$ complexes linked via nitrogen-coordinated octahedral M^{b+} centers (Figure 1.5). Depending on the stoichiometry M'/M and the respective oxidation states, the PBA framework can also contain cationic counterions such as Na^+, K^+, Rb^+, and Cs^+, located in the cavity of the cubic framework or $[M'(CN)_6]^{a-}$

vacancies when a > b. In a presence of the vacancies, bound water molecule occupies the available coordination site on M. In an effort to fully exploit the PBAs, several series of compounds with various transition metals were investigated. Among all, PBAs with vanadium and chromium were found to have the highest magnetic ordering temperatures such as T_c = 315–376 K in $KV[Cr(CN)_6]\cdot xH_2O$,[80,81] and T_c = 240 K in $[Cr_5(CN)_{12}]\cdot 2.8H_2O$.[80,82]

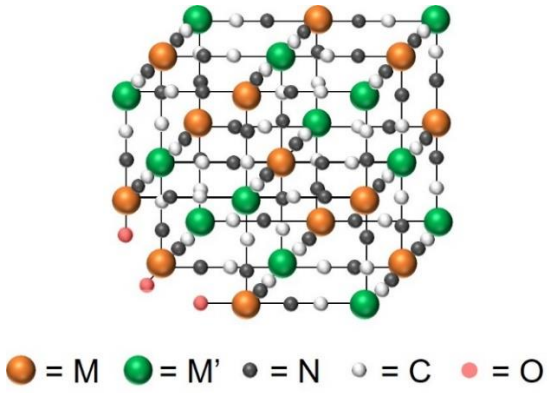

Figure 1.5. Schematic representation of PBAs network.

The first photomagnetic effect in molecular systems was reported in $K_{0.2}Co(II)_{1.4}[Fe(III)(CN)_6]_2\cdot H_2O$ by Sato in 1996.[83] Irradiation with red light (λ_{exc} = 660 nm) at 5 K led to an enhancement of magnetization due to a photoinduced metal-to-metal charge transfer process from Fe(II) to Co(III). Light irradiation therefore induced a change in magnetization due to conversion from a diamagnetic *ls*-Co(III)Fe(II) configuration (S = 0) to a paramagnetic *hs*-Co(II)Fe(III) configuration (S = 1/2 for *ls*-Fe(III) and S = 3/2 for *hs*-Co(II)) accompanied with a spin transition of the Co center (Figure 1.6). The sample relaxes back to the original state when it was heated to 150 K, demonstrating that the magnetization can be modulated under light irradiation, and the initial properties can be

restored by thermal treatment. Due to the different electronic distributions of the cobalt center (*hs* or *ls*), and charge transfer process accompanied by a spin transition at the cobalt center the process is called charge-transfer-induced spin transition (CTIST)[84] or charge-transfer-coupled spin transition (CTCST)[85] depending on whether the spin transition process is "induced" by CT or occurs simultaneously is "coupled" with CT. The nature of the photomagnetic effect is postulated to involve vacancies in which water or solvent molecules are responsible for fine tuning between retaining diamagnetic nature of the Co centers and the flexibility for the contraction and expansion of crystal lattice as a result of electron transfer and consequential structural reorganization.[72,83,86] A larger degree of hydration around the Co center induces a weak ligand field, thus stabilizing the *hs*-Co(II)Fe(III) species which does not undergo the photoinduced charge transfer under red light irradiation. However, the total absence of a solvation results in an extremely rigid structure not amenable to structural reorganization, and therefore does not exhibit photomagnetic effects. Although the degree of vacancies can be modified by the nature and the quantity of the monocationic counterions, the distribution of vacancies and defects of the network are inhomogeneous throughout the material. The inhomogeneity results in a distribution of local environments around the cobalt centers and distribution of charge transfer processes that coexist with inactive diamagnetic or paramagnetic Fe–CN–Co pairs. The inconsistent reproducibility of the photomagnetic behavior of the high dimension PBAs led to increased research effort on the implementation of the photomagnetic process in lower dimensional systems. The discrete fragments of extended three-dimensional structures of PBA derivatives such as cubes and cages,[72,87-90] chains,[91,92] and squares[93-96] all showed a well-defined environment of the cobalt coordination sphere that favors a full

charge transfer in the system. However, the magnetization relaxation temperature (T_{relax}) of the photoinduced state is still low (<120 K) in the systems studied to date due to the short lifetime of metal-centered excited states, making it difficult to integrate them into practical applications.

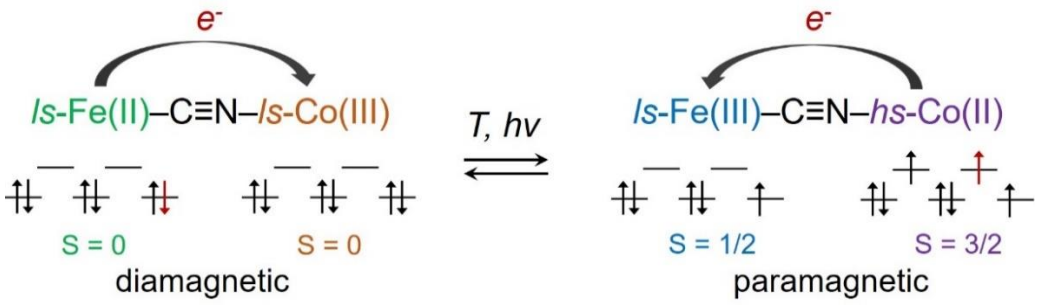

Figure 1.6. Metal-to-metal charge transfer coupled spin transition in Prussian Blue Analogues.

1.2.2. Spin-crossover Complexes

Spin-crossover is the most common spin-state switching mechanism for metal complexes and was first observed in Fe(III)tris(dithiocarbamate) (**1.10**) in 1931.[97] The phenomenon involves a reversible transition between two metastable spin-states by rearrangement of *d* electrons from lower lying orbitals (t_{2g} in octahedral geometry) to the higher lying orbitals (e_g in octahedral geometry), which results in conversion from a low-spin (*ls*) to high-spin (*hs*) state (Figure 1.7). In order to exhibit spin-crossover behavior, (i) the spin-paring energy Π needs to sit between the splitting parameters (10 *Dq*) for *ls* and *hs* states, and (ii) the energy difference between the states (ΔE_{H-L}) need to be on the order of magnitude of the thermal energy (k_BT) to obtain thermal spin transition.[98] At a given temperature, if the energy between two sets of *d* orbitals (ligand field strength, Δ_{oct}) is

greater than the energy that it would take to pair up the electrons (spin-pairing energy), the low-spin state will be populated. Contrarily, if the Δ_{oct} is less than the spin-paring energy, the high-spin state will be populated. Since the e_g subset exhibits antibonding character, the population and depopulation of the e_g orbital leads to a change in metal-to-ligand bond distance r(M-L); hence, spin-crossover is accompanied by large changes in r(M-L) between *ls* and *hs* state such as Δr(M-L) of 0.2, 0.15, and 0.10 Å for Fe(II), Fe(III), and Co(II), respectively.[98]

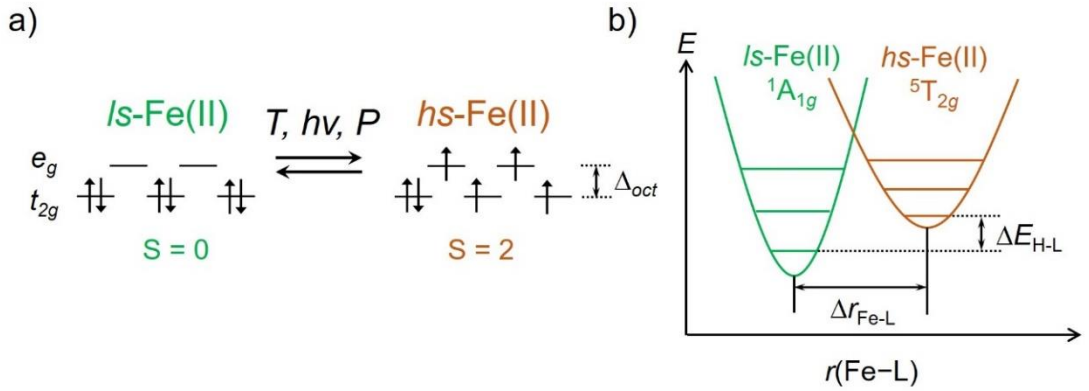

Figure 1.7. Spin-crossover process between a low-spin (*ls*) and high spin (*hs*) Fe(II) state in Fe(II) complexes (a), the reaction coordinate (Fe−L) corresponding to stretching of the metal−ligand bond, ΔE_{H-L}, and the energy difference between the low-spin and high-spin states (b).

To date, more than a thousand transition metal spin-crossover complexes (d_4-d_7) have been studied, 90 % of which are iron complexes.[99] Observations of thermally induced spin-crossover from low spin to high spin with a transition temperature ($T_{1/2}$) above room temperature and an abrupt spin transition require strong cooperative interactions in the solid state. Boca demonstrated an abrupt spin-crossover of $[Fe(II)(bzimpy)_2](ClO_4)_2 \cdot 0.25H_2O$ (bzimpy = 2,6-bis(benzimidazol-2-yl)pyridine) (**1.11**,

Figure 1.8) with $T_{1/2}$ = 403 K and a hysteresis of 12 K due to a perfect π-stacking of the ligand-based benzimidazole rings.[100] More recently, Hagiwara reported $[Fe(II)_2(L)_2](PF_6)_4 \cdot 5H_2O \cdot MeCN]$ (L = 1,1'-(1,2-ethanediyl)bis-1,2,3-triazol-4-yl-methylideneamino-2-ethylpyridine) (**1.12**, Figure 1.8) with a $T_{1/2}$ = 432 K and a hysteresis of 11 K arising from a double helicate structure.[101] $[Fe(II)_3(\mu\text{-}L)_6(H_2O)_6]$ (L = 4-(1,2,4-triazol-4-yl)ethanesulfonate) (**1.13**, Figure 1.8) with $T_{1/2}$ = 351 K and a hysteresis of 14 K was found in studies of a multi-bridged structure.[102] This abrupt switching above 300 K makes spin-crossover complexes very desirable as switching device applications in which a small external thermal perturbation leads to a large "readout" (magnetization) effect.

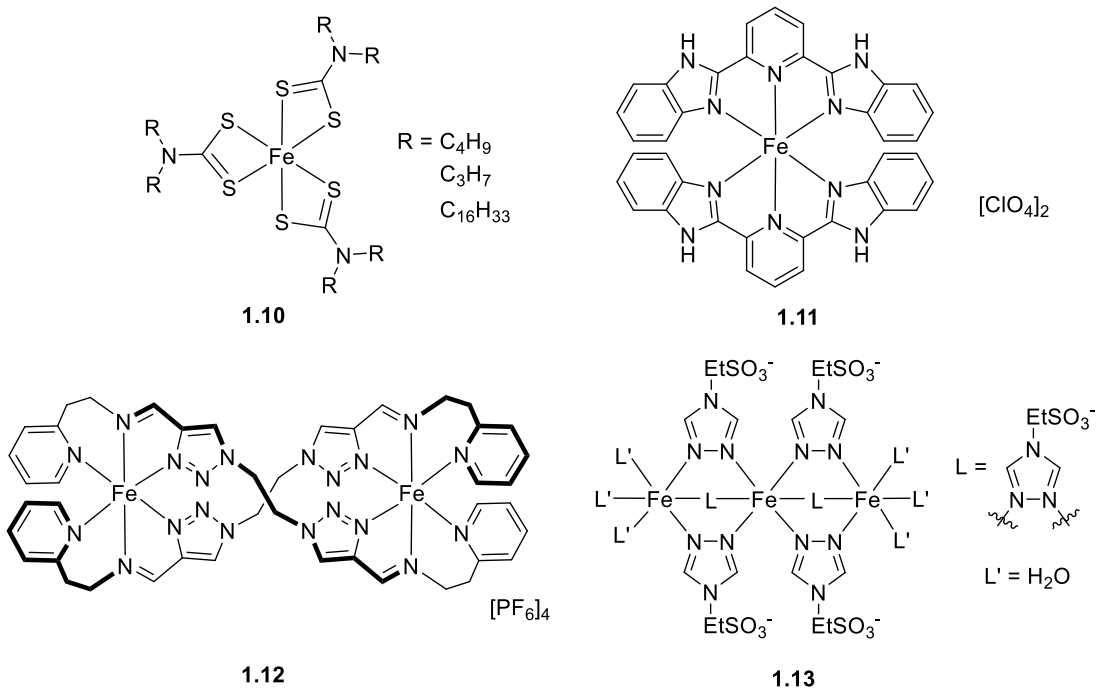

Figure 1.8. Structures of spin-crossover complexes **1.10**–**1.13**.

Spin-crossover can be initiated by light or thermal energy. Light-Induced Excited Spin-State Trapping (LIESST) was first observed in $Fe(II)(ptz)_6(BF_4)_2$ (ptz = 1-

propyltetrazole) (**1.14**, Figure 1.9) by Decurtins and Gütlich in 1984.[103,104] Irradiation of the low spin-state into the Fe(II) *d*-*d* transition with λ_{exc} = 514.5 nm at a temperature below 50 K leads to a spin-allowed $^1A_{1g} \rightarrow {}^1T_{1g}$ transition, followed by double intersystem crossing through the intermediate spin-state $^3T_{2g}$ to a $^5T_{2g}$ pentet state, which is a long-lived metastable high-spin state (Figure 1.10). The original low-spin state can be restored by red light (λ_{exc} = 820 nm) irradiation.[105] The discovery of the LIESST effect represented an important advancement in the study of the dynamics of spin-crossover processes in the solid state, showing that the ground state equilibrium could be perturbed by direct light excitation. Since then, the number of Fe(II) spin-crossover complexes observed to undergo the LIESST effect has increased considerably. However, the lifetime of the metastable high-spin state is still short (minutes to hours below 20 K), resulting in the magnetization relaxation temperature (T_{LIESST}) of the photo-induced state remaining as low as 50 K.[75] The highest relaxation temperature of 130 K was found in $[Fe(II)(L)(CN)_2]\cdot H_2O$, where L is a Schiff-base macrocyclic ligand (**1.15**, Figure 1.9), by Hayami in 2001.[106]

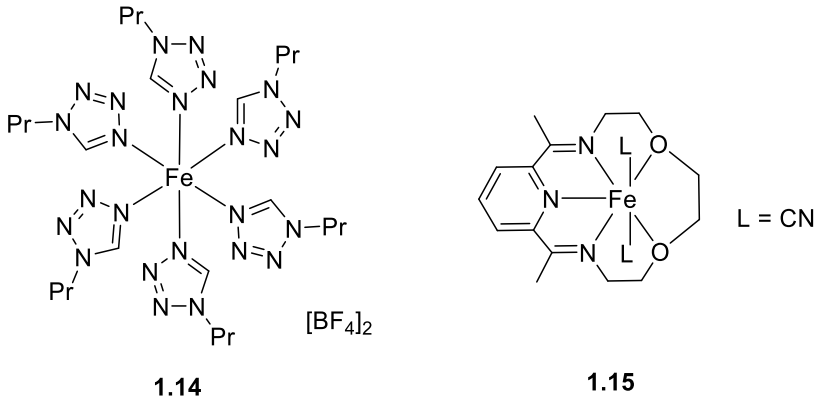

1.14 **1.15**

Figure 1.9. Structures of LIESST complexes **1.14** and **1.15**.

The strength of the ligand field is thought to dictate the nature of the lifetime of the excited state. Hauser demonstrated that the lifetime $\tau_{H\text{-}L}{}^0$ (*i.e.* the low temperature tunneling rate $k_{H\text{-}L}{}^0 = (\tau_{H\text{-}L}{}^0)$ of the LIESST state) is inversely correlated with the energy difference $\Delta E_{H-L}{}^0$ between the lowest vibronic energy levels of the *hs* and *ls* states involved, which is called the 'inverse energy law.[107] The energy gap $\Delta E_{H-L}{}^0$ increases with increasing ligand field strength, and the lifetime of the metastable state is expected to be reduced with increasing energy gap. Létard investigated 60 spin-crossover complexes and showed that the thermal transition temperature ($T_{1/2}$) inversely correlates with the magnetization temperature (T_{LIESST}) in agreement with the inverse energy law.[108] Despite the enormous amount of work reported, the LIESST is still only observable below 50 K.[108]

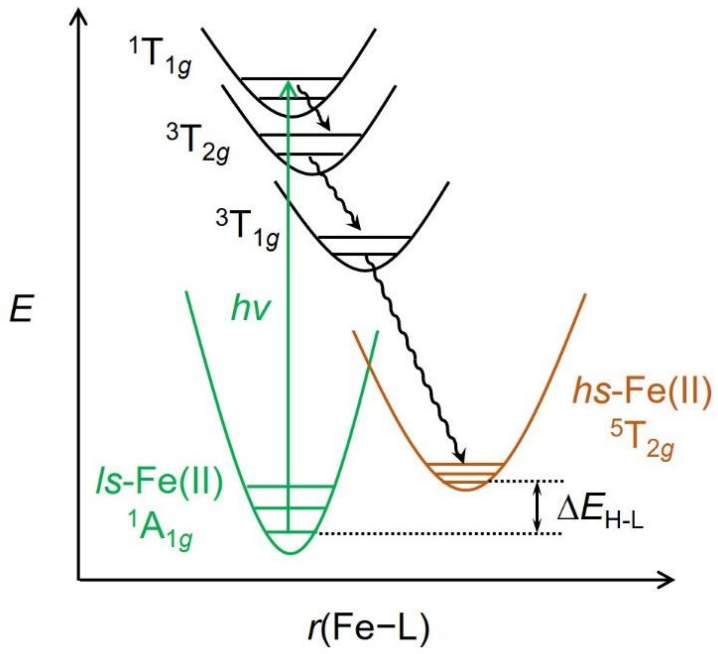

Figure 1.10. The process of light-induced spin crossover (LISSET).

1.2.3. Valence Tautomeric Complexes

Another important class in molecular photomagnetism is the "valence tautomeric" complexes which involve an intramolecular charge transfer between a redox-active ligand and a redox-active metal center. The charge-transfer process is accompanied by a spin transition, giving rise to an equilibrium between two different redox isomers. Although the term valence tautomerism has been used historically, first coined by Peirpont and Hendrickson,[109] we prefer the term "redox isomerism", as there is no movement of nuclei (typically required of tautomeric equilibria). Redox isomerism has been observed in numerous complexes with metals including V,[110] Mn,[111,112] Fe,[113,114] Ni,[115,116] and Cu[117,118]; and with a variety of redox-active ligands such as *o*-dioxolenes, *o*-diimines, and o-amino-phenolates. However, octahedral cobalt complexes with *o*-dioxolene ligands have been the most well-studied class of redox-isomeric complexes. The first report of a redox-isomeric transition was made for [Co(2,2'-bpy)(3,5-dbsq)(3,5-dbdiox)] where 3,5-dbsq = 3,5-di-*t*-butyl semiquinone, 3,5-dbdiox = 3,5-di-*t*-butyl dioxolene, and 2,2'-bpy = 2,2'-bipyridine (**1.16**, Figure 1.12).[109] Redox isomerism in cobalt dioxolenes involves a cobalt-based spin transition accompanied by intramolecular charge transfer. With external stimuli such as heat, light, or pressure, ligand-to-metal charge transfer (LMCT) occurs from a diamagnetic catecholate (Cat^{2-}) ligand coordinated to a *ls*-Co(III) center with S = 0, resulting in a *hs*-Co(II) (S = 3/2) with a paramagnetic semiquinone ($SQ^{\bullet-}$) ligand (S = ½) (Figure 1.11) Antiferromagnetic exchange between the paramagnetic *hs*-Co(II) center and $SQ^{\bullet-}$ ligand leads to a lower observed magnetic moment than the spin–only value. The thermally induced redox isomerism process in cobalt dioxolenes is entropically driven, arising from

the large entropy gain due to formation of a higher density of vibrational states and spin-state degeneracy in the *hs*-Co(II)($SQ^{\bullet-}$) state.[77]

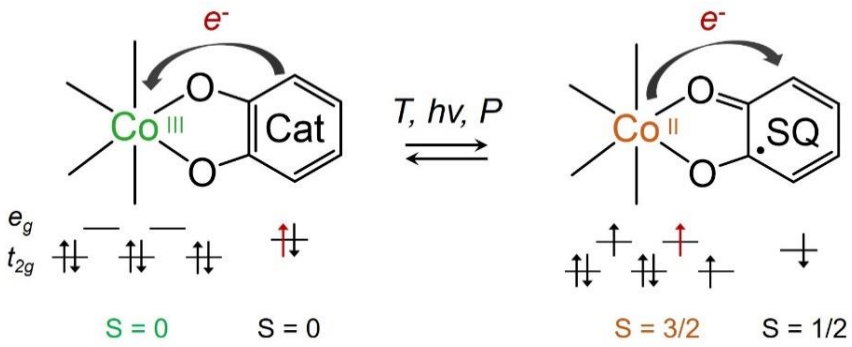

Figure 1.11. Charge transfer between the cobalt center and *o*-dioxolene ligand accompanied by spin transition.

Similar to Prussian blue analogues and spin-crossover complexes, increasing the critical temperature ($T_{1/2}$) has been the biggest challenge for redox-isomeric complexes. The $T_{1/2}$ is defined as the temperature at which equal populations of the two isomeric forms co-exist.[77] The $T_{1/2}$ values for the cobalt-dioxolene complexes are in the range of 100–390 K,[77,119] in which the $T_{1/2}$ correlates linearly with the reduction potential of the ancillary diimine ligand.[120,121] The greater the π-acceptor ability of the diimine ligand, the more the ligand stabilizes the *hs*-Co(II) form over the *ls*-Co(III) state, leading to a lower $T_{1/2}$.

Cobalt dioxolene complexes that exhibit thermally induced redox-isomeric transitions often display a photoinduced transition as well. A photoinduced redox-isomeric transition was first reported in 1995 by Adams for [Co(N_2L)(3,5-dbsq)(3,5-dbdiox)] where N_2L = 4,4'-diphenyl-2,2'-bipyridine (**1.17**, Figure 1.12) and 4,4-dimethyl-2,2'-bipyridine (**1.18**, Figure 1.12).[122] The excitation of the ligand-to-metal charge transfer band of *ls*-

Co(III)(Cat^{2-}) by green light irradiation (λ_{exc} = 532 nm) results in a LMCT excited state, which relaxes to the transient metastable *hs*-Co(II)($SQ^{\bullet-}$) species. Typical lifetimes of the photoinduced redox isomer are in the range of 1-2 nanoseconds, with Arrhenius-like behavior due to the presence of an activation energy between two redox isomers. The low activation energy leads to a low 'effective T_{LIESST}' in the range of 38–80 K.[77] Even in the low-temperature relaxation regime, the lifetime of photoinduced redox isomer is typically in the range of 10^4–10^5 seconds which is significantly shorter than spin-crossover complexes.

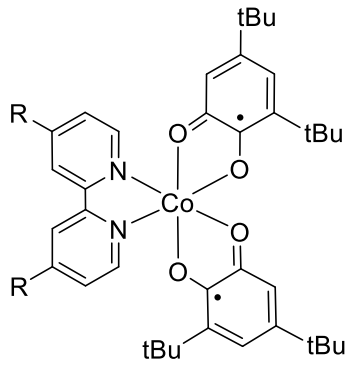

R = H **1.16**
Ph **1.17**
CH_3 **1.18**

Figure 1.12. Structures of redox-isomeric complexes **1.16**–**1.18**.

Although enormous research effort has led to the development of different classes of photomagnetic organic-metal hybrids, the observation of photomagnetic effects at room temperature in the solid state remains the single biggest challenge due to the short lifetime of the metal-centered excited state in these systems. An alternative strategy to modulating the magnetization of organic-metal hybrids is to generate ligand-centered excited states that modulate the metal center indirectly, a "nonclassical" photomagnetic effect (an effect that occurs through ligand-centered processes via the metal center, rather than direct

reactivity at the metal center ("classical" photomagnetic effects). In principle, two approaches can be taken to this end, i) modulation of the ligand field at the metal center, and ii) a change in ligand coordination about the metal center. In the next section, these two classes of ligand-centered photomagnetic molecular systems are discussed.

1.2.4. Ligand-centered Photomagnetic Complexes: LD-LISC and LD-CISSS

A Ligand-Driven Light Induced Spin Change (LD-LISC) process is a subclass of the spin-crossover complexes, utilizing a change in ligand field strength by photoisomerization of a ligand to affect the spin equilibrium between *low*-spin and *high*-spin states.[123] In a system exhibiting LD-LISC, one isomer of the ligand induces a stronger ligand field and stabilize the *ls*-state whereas the other isomer generates a weaker ligand field and stabilize the *hs*-state. Hence, photoisomerization between the two isomers can in principle trigger spin-crossover at the coordinated metal center. The first observation of LD-LISC was reported by Boillot in Fe(II)(4-styrylpyridine)$_4$(NCBPh$_3$)$_2$, in which the *trans*-styrylpyridine (Stpy) complex undergoes a thermally-induced spin-crossover (S = 2 → S = 0) with transition temperature ($T_{1/2}$) of 190 K whereas the *cis*-Stpy maintains *hs*-character at temperatures between 2 and 300 K .[123] UV light irradiation (λ_{exc} = 322 nm) led to photoisomerization of the *trans*-Stpy to the *cis*-Stpy in solution. In this case, the initial *trans*-Stpy isomer is more planar and thus a better π-acceptor, which stabilizes the *ls*-Fe(II) state. Contrarily, the photogenerated *cis*-isomer is non-planar and thus a poorer π-acceptor, which leads to stabilization of the *hs*-Fe(II) state. Electronic absorption spectroscopic studies in cellulose acetate thin-films at 140 K showed photoisomerization of Stpy in thin-films; however, no direct observation of changes in magnetization were reported, which

would support photoisomerization-induced spin-crossover behavior. The direct observation of the change in magnetization of Fe(II)(Stpy)$_4$(NCSe)$_2$ (**1.19,** Figure 1.13) embedded in PMMA at 130 K was reported by Boillot in 2009.[124] UV light irradiation (λ_{exc} = 355 nm) leads to reversible *trans*-to-*cis* isomerization accompanied by a spin-transition from *ls*-Fe(II) to *hs*-Fe(II).

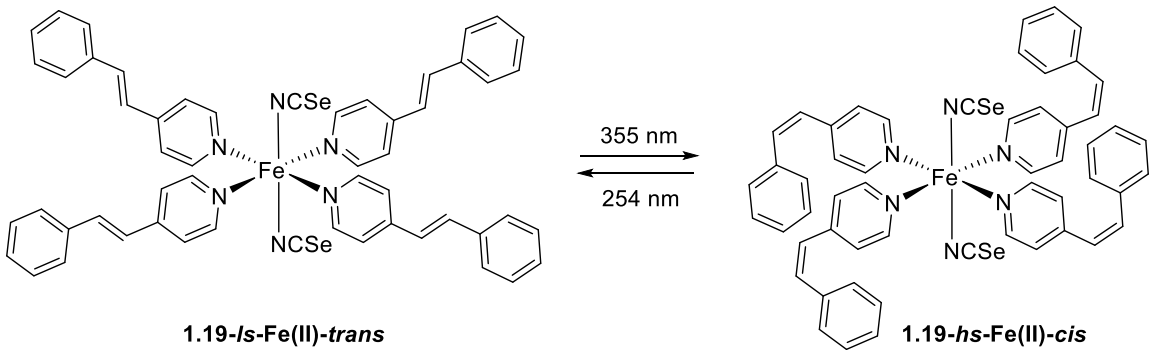

Figure 1.13. LD-LISC of Fe(II)(Stpy)$_4$(NCSe) (**1.19**).

A direct observation of LD-LISC in crystals and solid samples is often challenging due to structural rearrangement requiring relatively large void space. An irreversible LD-LISC was observed in a microcrystalline sample of a [Fe(II)(2,6-*di*(1*H*-pyrazol-1-yl)-4-styrylpyridine)$_2$](BF$_4$)$_2$ (**1.20**, Figure 1.14). Visible light irradiation ($\lambda_{exc} \geq 420$ nm) at room temperature resulted in a conversion of *hs*-Fe(II) to *ls*-Fe(II) of up to 15 %; however it required 150 hours of irradiation to achieve the maximum conversion and the spin crossover process was found to be irreversible.[125]

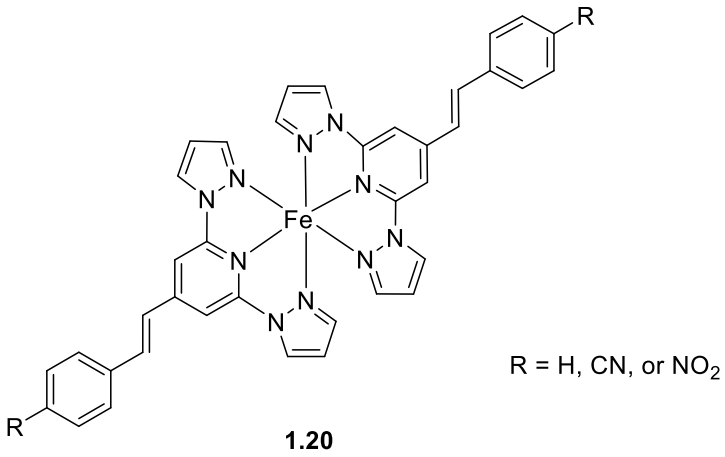

1.20

Figure 1.14. Structure of LD-LISC complex **1.20**.

The biggest challenge in the LD-LISC systems is the relatively small modulation in ligand field by photoisomerization of styrypyridine, which makes quantitative photoswitching between low-spin and high-spin-states difficult. To achieve a larger change in electronic structure, different classes of photochromic ligands have also been incorporated into LD-LISC systems. Incorporation of diarylethenes into LD-LISC in $[Fe(H_2B(pz)_2)_2(btphen)]$ where pz =1-pyrazolyl and btphen = 5,6-bis(2,5-dimethyl-3-thienyl)-1,10-phenanthroline $[Fe(bpz)_2(btphen)]\cdot H_2O$ (**1.21**, Figure 1.15) has been investigated.[126,127] Diarylethenes undergo photocyclization/cycloreversion between open and closed-ring forms. Nihei *et al.* and Milek *et al*. have demonstrated that a reversible photoisomerization-induced spin transition between *hs*-Fe(II)(open) ↔ *ls*-Fe(II)(closed) in a microcrystalline sample (5 K)[127] and in solution (300 K).[126] The non-planar geometry of the open-ring diarylethenes ligand stabilizes the *hs*-Fe(II) state while the more planar geometry of the closed-ring isomer stabilizes the *ls*-Fe(II), leading to a spin-crossover in the system. More recently, a reversible photoisomerization-induced spin transition between

hs-Fe(II)(open) ↔ *ls*-Fe(II)(closed) was observed in the same system in the solid state at room temperature by NEXAFS spectroscopy, demonstrating UV-light irradiation induced 32 % *hs*-Fe(II) to *ls*-Fe(II) conversion.[128] The percent conversion of the spin-state is consistent with the photocyclization conversion of the diarylethenes unit, suggesting the spin-transition is induced by the photoisomerization of the diarylethenes ligand. However, the slow switching speed (min to hours), low photoresponsivity ($\Phi_{o\rightarrow c} < 0.5$),[129] and small changes in ligand field leads to challenges for the induction of greater spin-state conversions in diarylethene-based LD-LISC systems.

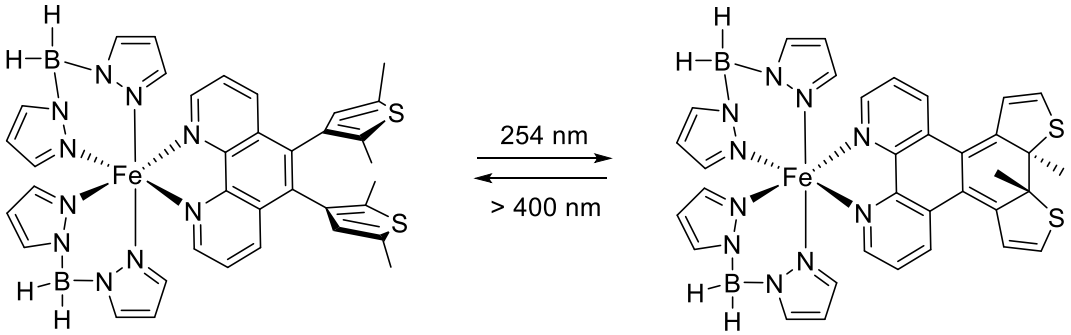

Figure 1.15. LD-LISC of $[Fe(bpz)_2(btphen)]\cdot H_2O$ (**1.21**).

Another class of LD-LISC is Light-Driven Coordination-Induced Spin-State Switching (LD-CISSS), which is based on utilizing a photochromic ligand to modulate the spin-state of a first-row transition metal center via coordination number.[130,131] In contrast to LD-LISC, the photoisomerization of the ligand in the LD-CISSS causes ligand dissociation/association from the metal center, which in turn gives rise to a change in spin state. Consequently, the spin-state conversion in most LD-LISC processes is relatively low,

whereas LD-CISSS has the potential to provide greater conversion, depending on the extent of "reaction" induced by photoisomerization of the ligand. LD-CISSS was first developed for an azopyridine-functionalized four-coordinate square planar Ni(II) complex [Ni(II)(^{F}TPP)] where ^{F}TPP = tetrakis(pentafluorophenyl)porphyrinato (**1.22**, Figure 1.16) by Herges in 2011.[130,131] In this system, a photochromic azopyridine, capable of photodissociation, is covalently linked to a Ni(II) porphyrin complex. The *trans* azopyridine isomer possesses a geometry such that the pyridine nitrogen of azopyridine is too remote to coordinate to the Ni, leading to a four-coordinate *ls*-Ni(II) complex (S = 0, diamagnetic).[130,131] Photoisomerization of the *cis*-isomer by visible light irradiation (λ_{exc} = 500 nm) leads to azopyridine coordination to the Ni center and a change in coordination number to a pentacoordinate square-pyramidal *hs*-Ni(II) or hexacoordinate *hs*-Ni(II) octahedral complex. In addition, coordination by free pyridine in solution occurs in order to stabilize the *hs*-Ni(II) complex. In solution, photoswitching between diamagnetic *ls*-Ni(II) and paramagnetic *hs*-Ni(II) can occur, resulting in 48 % photoconversion.[132] Structural modification through the introduction of electron-donating groups into the coordinating pyridine results in increased photoconversion of the spin-state up to 85 %.[132] However, one serious limitation of the LD-CISSS is that the process requires additional coordination by free pyridine in solution, and therefore can only occur in the solution state, limiting its use in practical applications.

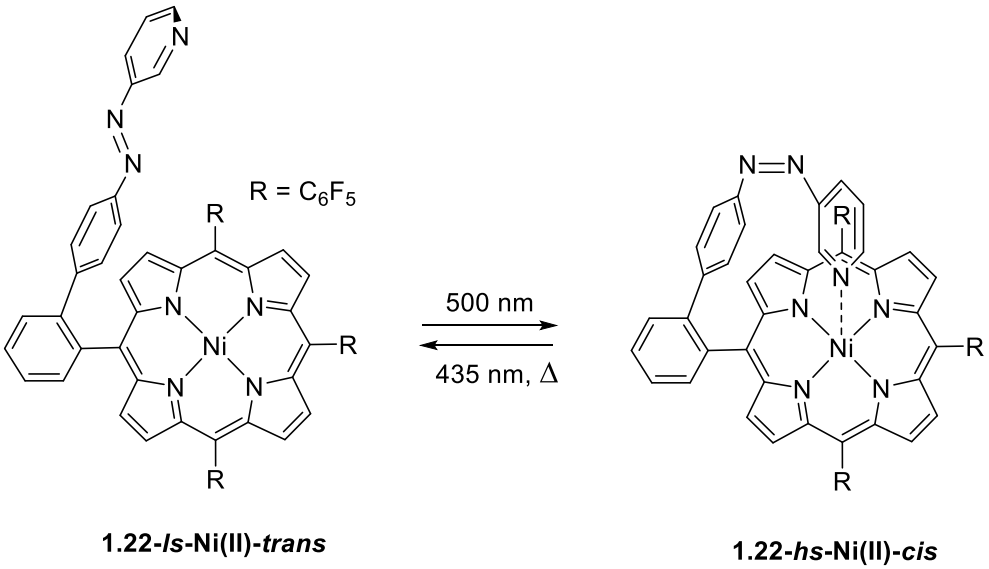

Figure 1.16. LD-CISSS of [Ni(II)(^{F}TPP)] (**1.22**).

1.3. Optical Switching of Energy and Electron Transfer Processes in Large Systems

Photochromic compounds may be used as optical control units to induce changes in fluorescence or electrical conductivity by serving either as an electron/energy donor or acceptor component. When a molecule is exposed to light with appropriate energy, a single photon will be absorbed to generate an excited state which can undergo various processes including non-radiative decay to the ground state, singlet-singlet emission (fluorescence), and intersystem crossing to a triplet excited state followed by non-radiative or radiative (phosphorescence) relaxation process. In a bimolecular process, the excited state can also undergo electron transfer with a neighboring molecule $D^* + A \rightarrow D^{\bullet+} + A^{-\bullet}$. This photoinduced electron transfer (PET) is a common process that can lead to quenching of fluorescence.

If the acceptor is a photochromic compound, the change in geometry and electronic structure accompanying photoisomerization gives rise to different driving forces (ΔG) for electron transfer of the two isomers. The difference in electron transfer driving force is due to changes in redox potentials with photoisomerization. In cases in which electron transfer and fluorescence from an excited state are competing processes, photoisomerization can lead to modulation of the fluorescence intensity of the donor. Quenching the singlet excited state of the fluorophore via electron transfer to one of the photoisomers can result in the efficient suppression of the fluorescence emission. Contrarily, the other photochromic state may not lead to electron transfer from the fluorophore, and the emission is retained. Therefore, control over the redox potentials of one or both of a donor-acceptor pair enables one to use light to induce or suppress electron transfer processes, which in turn can be used to modulate fluorescence intensity.

Fluorescence quenching can also be induced by a Förster energy transfer (EnT) or a singlet-singlet energy transfer process. For example, if a donor fluorophore (D) absorbs a photon to generate the singlet excited state ($D \rightarrow D^*$), the emission energy of the excited state D* can be transferred to a neighboring acceptor (A). If the excited state of the acceptor can only decay by nonradiative decay, then the EnT process results in an overall quenching of emission form the D. While the electron transfer processes from the donor to acceptor rely on the relative redox potentials of the donor/acceptor pair, the energy transfer process requires energy matching. The emission spectrum of D* and the absorbance spectrum of the acceptor (A) needs to have good spectral overlap in order for energy transfer processes to be efficient. The process is illustrated as $^1D^* + A \rightarrow D + {}^1A^*$. In the case where the acceptor is a photochromic compound, the change in geometry and electronic structure

accompanying photoisomerization leads to different absorption spectra of the two photoisomers. If photoisomer 1 has better spectral overlap with the emission spectrum of fluorophore D than photoisomer 2, then generation of photoisomer 1 leads to energy transfer to the photoisomer, and then either radiative or nonradiative decay from the excited state of photoisomer 1. The local excitation of a fluorophore donor therefore can result in energy transfer to one of the isomers having better spectral overlap with the emission spectrum of the D*, leading to quenching of the singlet excited state of the fluorophore. Contrarily, the other photochromic state with poor spectral overlap does not result in energy transfer from the donor fluorophore, leading to fluorescence of the fluorophore donor. Hence, tuning of the absorption spectra of the two photochromic isomers allows one to integrate photoisomerization induced or suppressed energy transfer processes into a fluorescence donor-acceptor system.

Energy and electron transfer processes can be modulated intramolecularly or intermolecularly by operation of a photochromic switch. In intramolecular processes, the photochromic component and its complementary donor/acceptor are integrated within the same molecular skeleton. Conversely, in intermolecular processes, the donor and acceptor interact within a supramolecular assembly using non-covalent interactions such as π–π stacking, hydrophobic, van der Waals, and/or electrostatic interactions. The approach allows one to optically control the electron/energy transfer processes not only in small molecules but also larger systems such as nanoparticles,[133,134] metal nanocrystals,[135] conjugated polymers,[136-138] and carbon nanomaterials. Further discussion will be focused around the incorporation of the photochromic compounds into nanoparticles and carbon nanomaterials which are relevant to this thesis.

1.3.1. Charge Transfer Processes in Photochromic Carbon Nanomaterials

The ability to photomodulate electronic properties in molecular conjugated and 2D systems (surfaces) has been investigated over the last 10 years. Carbon-based nanomaterials (CNMs) are sp^2-hybrid carbon networks such as fullerenes (0D), carbon nanotubes (CNTs, 1D) and graphene (2D). CNMs have become increasingly attractive materials due to their remarkable electronic and conducting properties, arising from long-range π-conjugation. Functionalization of CNMs can be achieved through either covalent or non-covalent approaches. Covalent functionalization of CNMs modifies the electronic structure directly by adding atoms into the lattice and disrupting conjugation.[139] Noncovalent modification of carbon-based nanomaterials typically utilizes physical adsorption of dopants on the surface of the carbon-based nanomaterials via π–π stacking, hydrophobic, van der Waals, and or electrostatic interactions.[139] As compared to covalent functionalization, noncovalent functionalization only mildly perturbs the electronic structure of the carbon-based nanomaterials, allowing modification of their electronic properties via ionic doping without introducing sp^3 carbon defects into the lattice.

Functionalization of the CNMs with photochromic compounds would allow for photomodulation of their fundamental optoelectronic properties such as charge generation, transfer, and recombination; properties which make CNMs highly desirable for potential applications in molecular junctions,[140-143] field-effect transistors,[144-146] and optical memories.[147] Modulation of charge transfer/separation has been observed in a photochrome-functionalized fullerene intramolecular D-A system arising from the electron-acceptor character of fullerenes and their derivatives. In these systems, a donor and an acceptor pair are covalently linked via a bridging photochromic unit. Liddele *et al*.

synthesized a diarylethene-porphyrin dyad (DAE-P) **1.23** (Figure 1.17), which demonstrated photoinduced intramolecular energy transfer controlled by the state of the diarylethene moiety.[148] When DAE is in an open form (DAEo), excitation of the porphyrin (λ_{exc} = 550 nm) led the porphyrin to fluoresce with an emission band at 650 nm in methyltetrahydrofuran, to give the "ON" state. UV light irradiation (λ_{exc} = 350 nm) leads to photoisomerization of the diarylethene from the open (DAEo) to the closed form (DAEc). The closed form of DAE exhibits a broad absorption band at 600 nm which overlaps with the porphyrin emission band. The spectral overlap of the absorption band of DAEc and the emission band of the porphyrin resulted in quenching of the porphyrin exited state via singlet-singlet energy transfer to give the "OFF" state.[148] Incorporation of another acceptor component fullerene into the diarylethene-porphyrin dyad (DAE-P) resulted in a diarylethene-porphyrin-fullerene (C_{60}) triad (DAE-P-C_{60}) **1.24**. In this system, the triad did not show significant porphyrin fluorescence with either the open or closed form isomers of DAE giving 'OFF' states. When DAE is in the open form (DAEo), the excited state of the porphyrin (λ_{exc} = 550 nm) is quenched via electron transfer from porphyrin to C_{60} to yield a charge-separated DAEo-$P^{\bullet+}$-$C_{60}^{-\bullet}$ species (Φ_{cs} = 1).[148] When DAE is in the closed form, DAEc quenches the porphyrin singlet excited state via singlet–singlet energy transfer as was seen in the DAE-P dyad **1.23**. The quenching of the porphyrin excited state through energy transfer to the DAEc competes with the electron transfer process to C_{60}. However, the energy transfer process to the DAEc is faster (2.3 ps) than the electron-transfer process (23 ps), precluding significant electron transfer (Φ_{cs} = 0.09). This study demonstrates the potential for the use of photochromes as optical control units for photomodulation of the different fluorescence quenching pathways.[148]

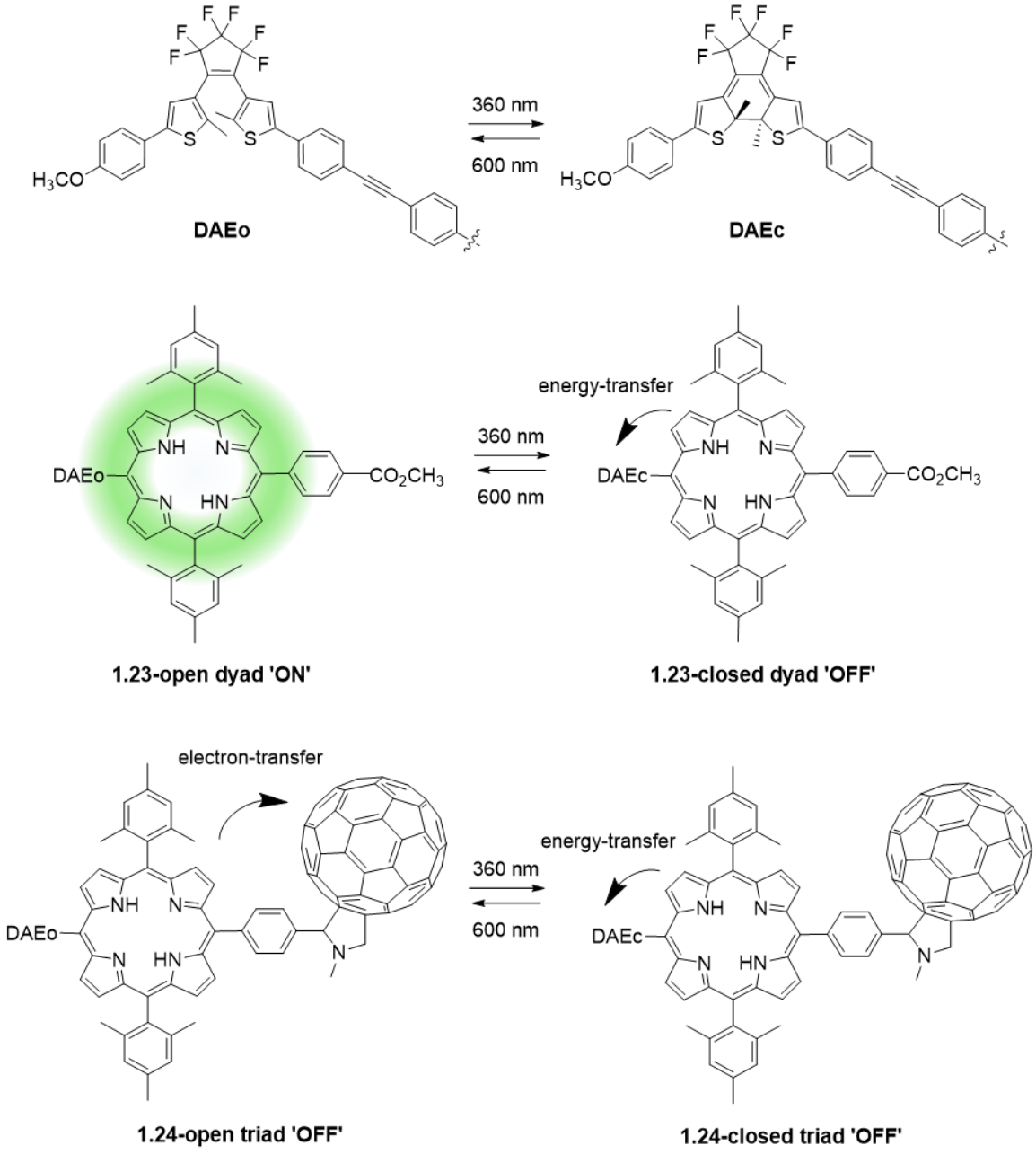

Figure 1.17. Intramolecular charge transfer process of diarylethene-porphyrin dyad (DAE-P) (**1.23**) and diarylethene-porphyrin-fullerene (C_{60}) triad (DAE-P-C_{60}) (**1.24**).

Moreover, the lifetime of the charge-separated species can be modulated by photoisomerization of the photochromic linker. Castellanos *et al*. synthesized a tetrathiafulvalene-diarylethene-fullerene (C_{60}) triad (TTF-DAE-C_{60}) **1.25**. When DAE is

in the open-form, excitation of the TTF donor resulted in the generation of charge-separated species $TTF^{\bullet+}$-DAEo-$C_{60}^{-\bullet}$ with a lifetime of 54.4 ns in THF. When DAE is in the closed form, excitation of the TTF also led to a generation of the charge-separation species $TTF^{\bullet+}$-DAEc-$C_{60}^{-\bullet}$ with a shorter lifetime of 1.1 ns.[149] The decreased lifetime of the $TTF^{\bullet+}$-DAEc-$C_{60}^{-\bullet}$ species is attributed to the structural difference in isomers of the DAE resulting in different relaxation mechanisms. When DAE is the open-form, the $TTF^{\bullet+}$-DAEo-$C_{60}^{-\bullet}$ species is more likely to undergo a tunneling mechanism with no participation of the non-conjugated bridging unit.[149] When DAE is in the closed-form, $TTF^{\bullet+}$-DAEc-$C_{60}^{-\bullet}$ undergoes fast decay which is attributed to the extended π-conjugation throughout the ring-closed bridging unit. This study demonstrates that the lifetime of the charge-separated species can be modulated by the photochromic bridge that dictates the electronic coupling between the donor and acceptor.

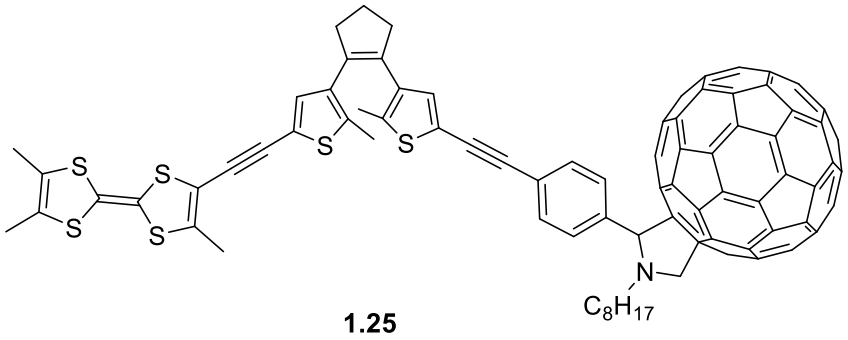

1.25

Figure 1.18. Structure of photochromic charge-transfer complex **1.25**.

Modulation of electron transfer processes by photoisomerization of a photochromic component can also be detected by changes in electrical conductivity. Bridging CNMs with photochromic compounds can be used to create photoswitchable molecular junctions. The

use of CNMs as electrodes has advantages, such as extraordinary and tunable electronic properties, and chemical compatibility that enables more stable covalent contacts to metal electrodes to be made. The conductivity of an electrode-molecule-electrode junction is governed by the structure and energies of the three components at their interface, as well as by the ability of a molecular linker to transport charges. Both of these properties depend on electron donor-acceptor ability. Hence, structural changes accompanied by modulation of the electronic structure and redox potentials (HOMO/LUMO) of the photochromic unit via photoisomerization can potentially result in significant changes in the electron transport properties of a molecular junction. Whalley *et al.* prepared a sample of single-walled carbon nanotubes (SWCNTs) bridged by diarylethenes (DAE) via amide formation (**1.26**, Figure 1.19).[143] Reversible photomodulation of the charge transport through the SWCNT was observed with a 25-fold increase in conductance from the open to the closed-form. Larger conductance was found in the closed-form attributed to the completely π-conjugated current path along the molecule. In the open-form, on the other hand, the current path is broken up into two decoupled system, leading to smaller conductance.[143]

Graphene can also be used to form molecular junction electrodes via point-contact arrays. Narrow gaps can be patterned by lithography processes using carboxylic acid terminal groups to generate point-contact arrays. In this system, azobenzene was used as the photochromic bridging component, which was linked via amide tethering to a graphene point-contact array. Photoisomerization of azobenzene from the *trans*-to-*cis* isomer resulted in a 1.5 fold decrease in conductance. The decrease in conductance is due to the *cis* form having a larger HOMO-LUMO energy gap and/or poorer energy level alignment with the Fermi level of the graphene electrode.[150]

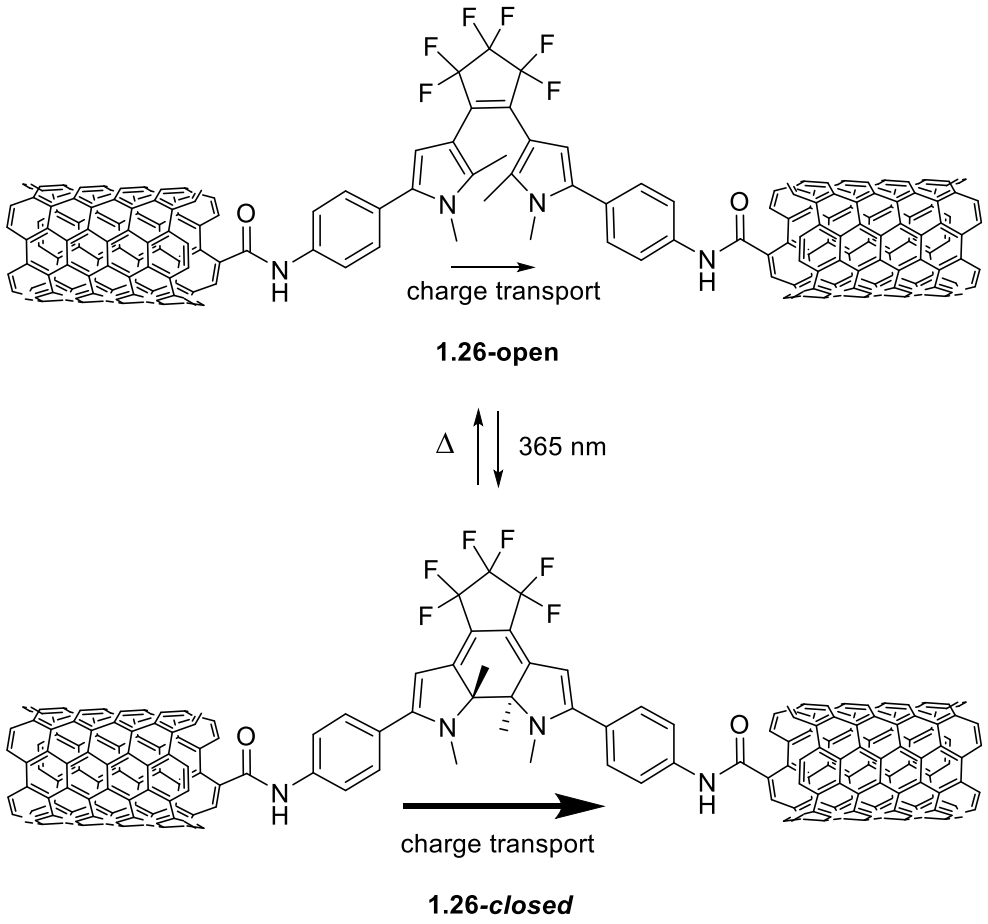

Figure 1.19. Molecular junction of single-walled carbon nanotubes (SWCNTs) bridged by diarylethene (**1.26**).

Utilizing a photochromic linkage to the CNMs molecular junction allows photomodulation of the charge transport properties of CNMs 'directly' and at the 'single molecule level' by regulating/opening the charge transport through photoisomerization of the photochromic component. On the other hand, the charge transport properties of the CNMs may be more 'indirectly' and 'macroscopically' modulated by controlling the electronic structure of the CNMs by differential ionic doping associated with the donor-acceptor ability of photochromic isomers. In principle, the redox potential (estimated by HOMO/LUMO energy levels) of the two isomers are different, which give rise to

differences in electron donor/acceptor ability and consequently in magnitude and/or direction of ionic doping to the CNM substrate. This type of photomodulation of charge transport properties is often used for CNM-based field-effect transistors. The conventional FETs rely on electrical gating to modulate transport of one type of charge carrier in the semiconducting material. However, the integration of photoresponsive components into a FET allows for the development of a bi-functional device; that is, a device which is capable of responding to two independent stimuli. The effective optical gating of the ionic doping of CNMs will be discussed in chapter 6.

1.3.2 Fluorescence Resonance Energy Transfer (FRET) in Photochromic Nanoparticles

Incorporation of photochromic materials onto the surface of NPs draws particular attention on account of its potential ability to optically modulate the chemical and physical properties of NPs. Nanoparticles (NPs) are defined as solid colloidal particles ranging in size from 1 to 100 nm and have attracted considerable interest in recent years for their diverse applications such as drug delivery[151,152], imaging and sensing[153-155], catalysis[156,157], energy[158,159] and electronic applications.[160] This is largely due to their unique size-dependent chemical and physical properties which bridge between the atomic/molecular level and bulk materials. NPs possess unique optical properties, and fluorescent nanoparticles (NPs) are of great interest for imaging applications[153-155] due to their high intrinsic sensitivity and fatigue resistance. Photoswitchable fluorescent NPs is an emerging area in not only imaging,[161,162] but also data processing, and storage applications[163,164] due to their spatiotemporal controllability of fluorescent intensity.[165] Particularly, the large

surface to volume ratio of NPs provides an opportunity to functionalize the surface of NPs with photochromes, which makes possible the design of systems able to modulate the emission intensity (quenching) of a nearby fluorescent NPs by light. This process occurs via fluorescence resonance energy transfer (FRET) from the fluorescent NPs to the acceptor photochromes. In photochromic FRET, the thermally stable form of the photochrome may or may not quench the NP emission, leading to a resting state of "OFF" or "ON" depending on the spectral overlap and energy matching between photochrome state and NP. Irradiation converts the photochrome to its photostationary form which can act either as an efficient fluorescent quencher via FRET leading to an "OFF" state, or as a poorer energy quencher, leading to an "ON" state (Figure 1.20). As a result, the excitation energy of the fluorophore NPs can be absorbed by the proximal photochrome with an accompanying loss of fluorescent intensity of the NPs that can be modulated by controlling the form of the photochrome. The challenge of the photochromic NPs is to achieve maximum efficiency of fluorescence quenching and to design the system such that emission is turned "ON" with grating, rather than turned "OFF".

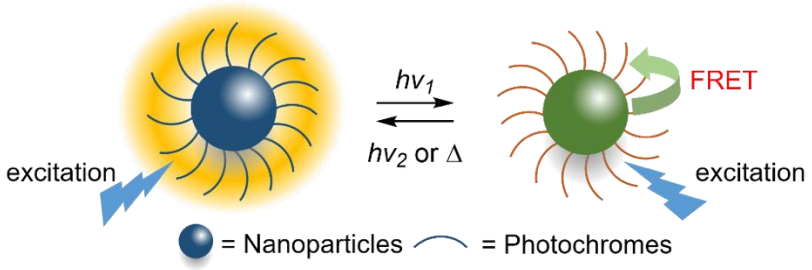

Figure 1.20. Photoswitchable FRET of Photochromes Functionalized NPs.

Diaz *et al.* demonstrated that CdSe/CsS/ZnS core-shell-shell nanoparticles functionalized with diarylethenes anchored by poly(isobutylene-alt-maleic anhydride) exhibited maximum quenching of the fluorescence of NPs 38 ± 2% upon photoisomerization of the diarylethene from the open to the closed form.[166] This relatively large quenching ratio is attributed to the high photoresponsivity of the diarylethene, leading to preferential cycloreversion of the diarylethene on the NPs surface and/or a more favorable orientation to induce FRET processes.[166] Wachtveitl *et al.* reported even higher quenching efficiency in diarylethene functionalized Cd/Se NPs where the diarylethene is attached to the surface of NPs via an adamantyl-based tripodal linker functionalized with three carboxylate anchoring groups.[167] This system showed strong fluorescence in the diarylethene open-form and quenching in the closed-form, with an efficiency of approximately 80 %.[167] FRET can also be reversed to provide off-on fluorescence switching rather than on-off photoswitching, which has advantage of greater sensitivity in detector applications and an increase in fluorescence from a zero background as opposed to a decrease in fluorescence from an initially strong signal.[168] Previous work in our group in collaboration with Zhang *et al.* describes preparation of a spirooxazine-doped conjugated polymer (PFBT) nanoparticles where the PFBT is poly[(9,9-dioctylfluorenyl-2,7-diyl)-*co*-(1,4-benzo-{2,10-3}-thiadiazole)].[133] The spirooxazine-doped conjugated polymer nanoparticles (CPNs) switched their fluorescence reversibly from dark to bright by photoisomerization of the spirooxazines.[133] The open-PMC form of an azahomoadamantyl-based spirooxazine is the thermodynamically stable form, which undergoes energy transfer from CPNs, leading to fluorescent quenching (off state). Visible light irradiation results in photoisomerization to the closed-SO form, thereby shutting down

energy transfer processes and resulting in emission of an “ON” state. In this system, FRET from the CPNs caused excitation of the PMC leading to an unusual amplified conversion to the SO form. This amplified FRET enables reversible modulation of fluorescence intensity with efficiency exceeding 80 %.[133]

1.4. Scope of Thesis

This thesis describes the design of spirooxazine-based photoswitchable materials that exhibit charge-transfer processes accompanied by modulation of magnetic properties and electrical conducting properties. The class of photochromes used in this work, the spirooxazines have many appealing features for optically gating materials properties, but suffer from the formation of a photostationary state. One can therefore never achieve 100% of the open or closed form, as one can in the diarylethenes for example. Chapter 2 describes work aimed at understanding the thermal isomerization pathway of spirooxazines and factors that may lead to control of the thermal isomerization barrier height. Experimental studies to support a rotation pathway are provided via an analysis of a series of azahomoadamantyl-based spirooxazines using 2D ^{1}H NMR spectroscopy, vibronic analysis of the PMC π–π^* electronic absorption band, solvatochromism, and solid state bond-length alternation (BLA) analysis. Experimental and computational analyses were performed to fully elucidate the effects of the charge-separated character of the PMC form on the rate of thermal coloration/decoloration. This study provides experimental evidence for a preferential relaxation pathway, insight into thermal coloration/decoloration pathways in spirooxazines, and develops useful design principles for controlling the thermal isomerization rate in engineered photochromic materials. Chapter 3 presents the effects of

metal complexation of the photochromic spirooxazines. The Lewis acidic nature of the metal center and ancillary ligand enhance the charge-separated character of the PMC form, which correlates with the rate of thermal coloration/decoloration. We provide evidence to suggest that the nature of the metal center and the ancillary ligand have a strong influence on the electronic structure of the PMC form, thereby providing a potential pathway for modulating PMC thermal relaxation rates through metal complexation. Chapter 4 describes the integration of optically bistable phenanthroline-spirooxazine ligands into magnetically bistable cobalt-dioxolene redox-isomeric tetranuclear clusters. A photochromic cobalt dioxolene tetranuclear clusters are prepared and investigated spectroscopically. The complexes exhibit a large magnetic moment in both the solid state and solution state at room temperature. The thermally induced redox-isomeric behavior of the cobalt dioxolenes and isomerization of the photochromic ligand in the solution state suggest that the incorporation of the photochromic ligand into magnetically bistable multinuclear clusters may be an effective approach towards achieving a large changes in magnetization. Most importantly, this study revealed an essential factor for the development of photomagnetic materials: an equilibrium of the distinct electronic states which exhibit charge transfer processes that are strongly coupled to the photochromic ligand. The large magnetization at room temperature in the optically bistable photochromic cobalt dioxolene clusters introduces the potential for photoswitching of large magnetization, which is highly desirable for the development of photoswitchable magnetic materials. The magnetism of the system, however, is quite complex, and analysis relied on deconvoluting the magnetic behavior of the parent cobalt dioxolene cluster. The large magnetization of the parent cluster suggested that it may in fact be interesting as a contrast agent for MRI. Chapter 5

presents the first example of molecular cobalt-based MRI contrast agent displaying high relaxivities. This work demonstrates the proof-of-principle by which a cluster comprised of metal and redox-active ligands can lead to a large magnetic moment and therefore a large T_1 and T_2 relaxation. The resultant cobalt cluster provides a platform for future development of molecular non-gadolinium based MRI contrast agents. Chapter 6 describes photomodulation through ionic doping of noncovalently-functionalized graphene field effect transistors. Electronic transport and Raman measurements reveal ionic doping of graphene can be optically modulated by the electron donor or acceptor nature of the photochromic isomers. This study demonstrates a solid-state visible light induced optically gated spirooxazine-graphene transistor which does not rely on an anchoring moiety to achieve photoisomerization. The resultant photoswitchable graphene-OFET provides an opportunity for future development of bi-functional quaternary memory devices which can be gated both electrically and optically. Lastly, Chapter 7 summarizes the work and outlines several avenues for further exploration of spirooxazine-based photoswitchable materials.

Chapter 2. Modulating Photostationary States in Photochromic Spirooxazines: A Mechanistic Study

2.1. Introduction

Current designs of sensors, gates, and switches require functional materials that exhibit a measurable response to external stimuli and environment. Gating of optical and electronic properties with light, pressure, heat, dielectric, or microenvironment has been achieved by using chromogenic materials that undergo changes in color with temperature (thermochromism),[169-172] light (photochromism),[173-176] solvation (solvatochromism),[177-179] and pressure (piezochromism)[180-184]. T-type photochromes undergo thermally reversible photoinduced isomerization between closed and open-forms, in which one form exists as the ground state and the other as a higher energy metastable state. If thermal isomerization pathways between the two forms exist, the system is bistable in which the relative population of the two states, open and closed, can be perturbed by external stimuli (heat, light, pressure, dielectric). T-type photochromes have been used as a switching element in an enormous range of applications including multistate NLO switches,[185-187] sol-gel nanophotonics[188] optode sensors,[189] photoaddressable displays,[190] photorheological fluids,[191] displays,[192] control of ionic permselectivity,[193] photoresponsive papers,[194] phase change materials,[38] metal ion detection,[195] solvent polarity indicators,[196] molecular motors,[197] fluorescence switching,[198,199] FRET switching,[200,201] molecular logic gates,[202,203] data storage,[204,205] pharmacology,[206-212] and catalysis.[213]

In determining the choice of photochrome and microenvironment (e.g., solvent, matrix) for a given application, absorbance/emission characteristics of the colored form,

colorability, thermal relaxation kinetics, positive vs. negative photochromism, the effect of external stimuli on the equilibria between closed and open-forms, and fatigue resistance are critical parameters. The ability to achieve either (i) fast switching rates in polymeric materials for optical coatings or (ii) slow (or irreversible) thermal relaxation for memory/switching applications remains, however, a significant challenge. While some pharmacological[214] and holographic applications require long relaxation times or thermal irreversibility, the manufacturing of photoprotective coatings[215] requires rapid thermal coloration and decoloration relaxation kinetics to return the system to its ground state quickly.

Spirooxazines are a subclass of photochromes that exhibit extremely high fatigue resistance,[22] a change in both nonlinear and linear optical properties with isomerization[23] and ability to undergo photoisomerization in the solid state.[24-29] Absorbance of UV irradiation ($\lambda_{max} \approx 350$ nm) in the closed spirooxazine (SO) form induces C–O bond cleavage, typically via the singlet excited state, followed by isomerization to give the open photomerocyanine (PMC) form with a characteristic absorbance at $\lambda_{max} \approx 600$ nm (Figure 2.1). Visible-light-induced ring-closure generates the closed-SO form via excitation of the PMC π–π^* transition ($\lambda_{exc} \approx 600$ nm). The ring-closure can also occur by thermal relaxation along the ground state potential energy surface.[2,22,30] Reversible photoisomerization between the closed (SO) form, which is often the ground state, and the open (PMC) form can therefore occur both photochemically and thermally, leading to T-type photochromism.

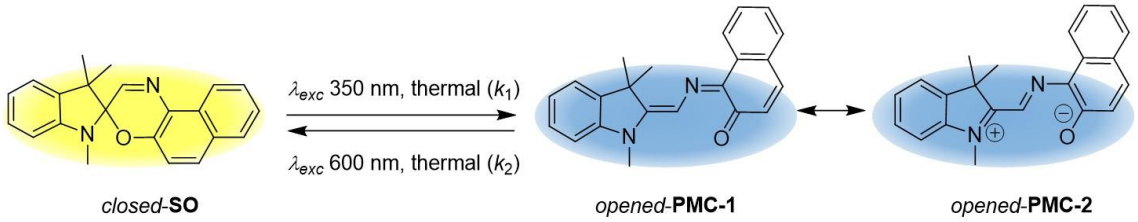

Figure 2.1. Photoisomerization and thermal relaxation processes in spirooxazines.

Subtle changes in the electronic structure and stability of the SO and PMC forms are dominated by the degree of charge separation and polarizability in the ground and excited states.[2,16,24] This, in turn, is dictated by the relative contributions of the neutral (PMC-1) and charge-separated (PMC-2) resonance forms to the ground-state electronic structure of the PMC form (Figure 2.1). The PMC form is structurally similar to merocyanines, in which the degree of neutral or charge-separated character is strongly dependent on the nature of the substitution pattern and dielectric of the medium.[46,216] Electron-withdrawing groups on the oxazine moiety or electron-donating groups on the amine moiety leads to greater charge separation due to partial stabilization of the developing charges.[8,49] Azahomoadamantyl substitution significantly enhances the charge separation and stability of the PMC form (negative photochromism, Figure 2.2), which allows for investigation of its structure by solution-state spectroscopy and X-ray diffraction techniques.[46] Polar environments lead to greater charge-separated character (PMC-2), whereas non-polar solvents stabilize the neutral form (PMC-1).[46]

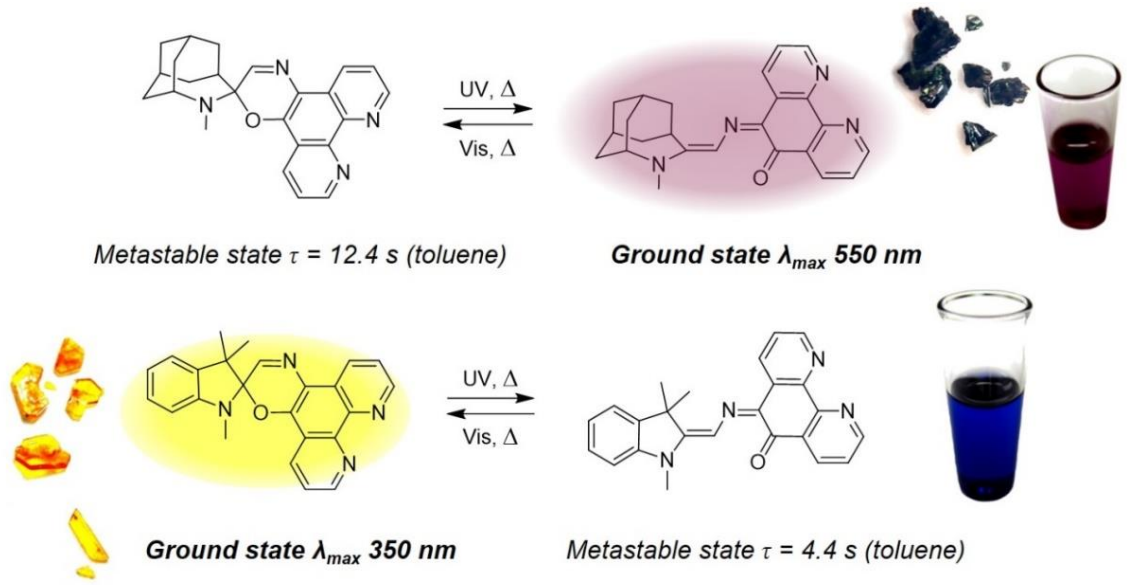

Figure 2.2. Positive vs. negative photochromism in azahomoadamantyl- and indoly-based spirooxazines.

The effect of structure on thermal coloration/decoloration rates is not well understood, primarily due to lack of structural information of the PMC form.[46] Controversy exists over the mechanism for SO–PMC thermal isomerization which is in part complicated by the existence of eight possible PMC isomers (Figure 2.3). Computational and spectroscopic studies suggest that the TTC (*trans*-*trans*-*cis*) isomer is the most stable conformation in both the solution and solid states.[217-220] In addition, the barriers to isomerization are quite high, leading to very little interconversion between isomers at ambient temperatures.[24,217,221,218,219,46,222] Mechanistic studies therefore must account for formation of the TTC isomer as the dominant form. Computational studies have identified two distinct thermal isomerization pathways in the spiropyran-spirooxazine class.[216,221] In spiropyrans, thermal isomerization from the metastable merocyanine to the SO ground state can follow a two-step rotation pathway in which *trans*-to-*cis* isomerization at the C-

N β-bond occurs (Scheme 2.1) followed by C–O bond formation to give the SO isomer.[216] The pathway for spirooxazine thermal relaxation from the PMC to the SO form has been proposed to go through either a rotation pathway or an inversion pathway (Scheme 2.1).[221] The three-step inversion pathway involves *cis*-to-*trans* isomerization at the γ-bond to generate a TTT isomer, followed by inversion at the central nitrogen and C–O bond formation to give the SO form (Scheme 2.1) Other possible pathways have been suggested based on computational studies, but require much higher activation energies or lead to high energy isomers, and are therefore less likely to occur in situ.[221]

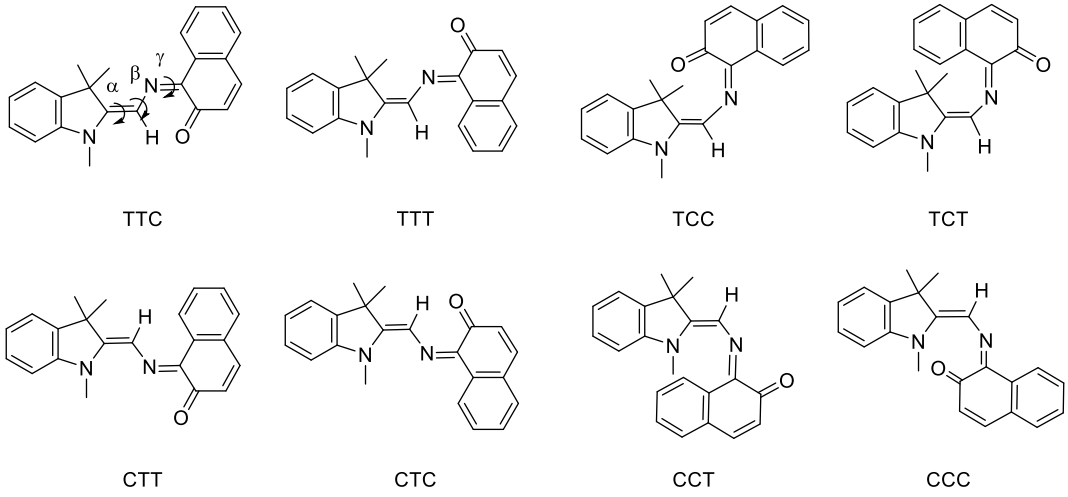

Figure 2.3. The eight possible PMC isomers formed by isomerization about the azomethine backbone.

Scheme 2.1. Possible thermal isomerization pathways.

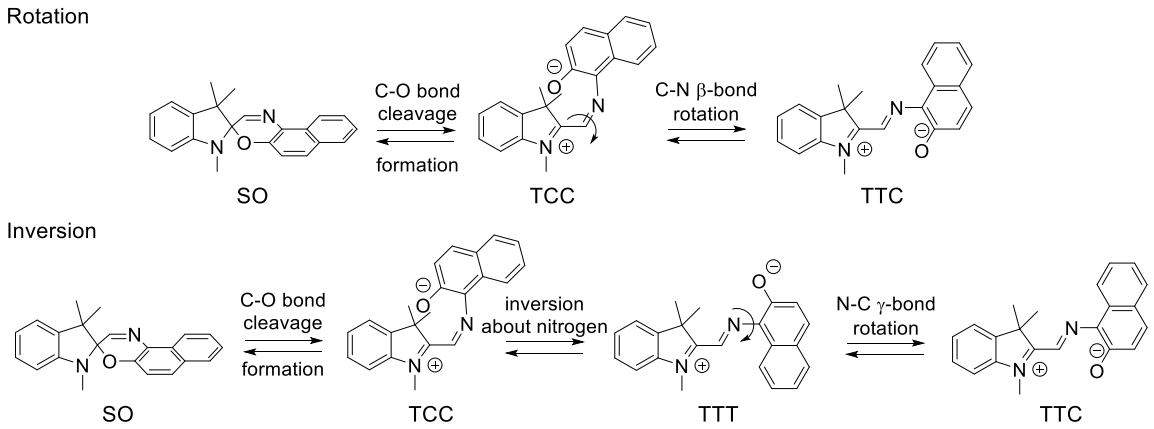

Challenges in designing experimental studies to determine the mechanism of thermal isomerization in the spirooxazine/spiropyran class of photochromes arises from the very short lifetime of the metastable PMC form. We have developed a series of negative photochromic spirooxazines, in which the PMC form is the ground state and the SO form is a metastable state, with a lifetime on the order of seconds. The reversal of ground and metastable states in the series allows for structural investigation of the parameters that dictate thermal reversion barriers, ultimately leading to a greater understanding of the thermal isomerization mechanism. Here we present a spectroscopic, structural, and theoretical investigation of the thermal relaxation rates of a series of photochromic spirooxazines as a function of the structure of the PMC and SO forms, in which a correlation between the thermal rates of coloration and the electronic structure of the PMC form is found. Investigation of four structurally similar azahomoadamantyl based spirooxazines, APESO (spiro[azahomoadamantane-phenanthrenoxazine]) (**2.1**), APSO (spiro[azahomoadamantane-phenanthrolinoxazine]) (**2.2**), AIQSO (spiro[azahomoadamantane-isoquinolinoxazine]) (**2.3**), and AQSO

(spiro[azahomoadamantane-quinolinoxazine]) (**2.4**) reveals vastly different thermal relaxation kinetics (Figure 2.4). The kinetics are correlated to ground state structural parameters in the PMC form as determined by spectroscopic, X-ray crystallographic, and computational analysis. The analyses suggest the degree of charge-separated *vs.* neutral character varies along the series, with charge-separated character linearly correlated to slower thermal coloration kinetics. The results are found to be consistent with the β-rotation pathway, and the effect of structure and medium on stabilizing/destabilizing intermediates along the pathway are discussed. This study provides new insight into the structural factors that govern thermal relaxation rates in spirooxazines for targeted utility in switching materials, photoresponsive coatings, optical data processing and data storage applications.

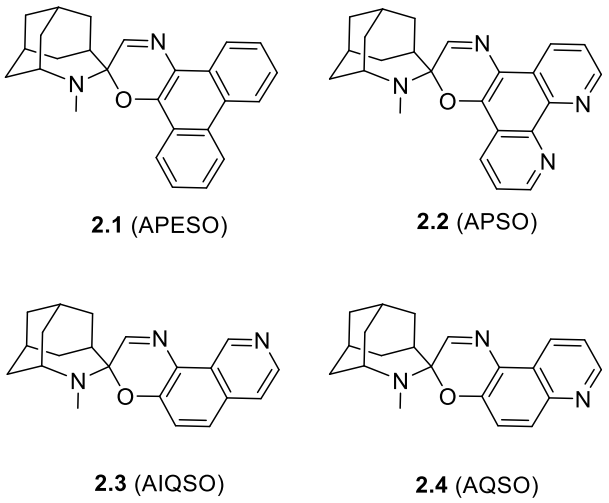

Figure 2.4. Structures of azahomoadamantyl-based spirooxazines.

2.2. Results and Discussion

2.2.1. Synthesis of Spirooxazines

Spirooxazines **2.1**–**2.4** were prepared as an equilibrium mixture of closed-SO and open-PMC forms, the equilibrium constant of which is dependent on the structure of the photochrome. The generalized synthetic methodology involved base-promoted condensation of *o*-hydroxy-nitroso-arenes with 5-methyl-4-azahomoadamantyl-4-enium iodide to yield the final spirooxazines in reasonable yield (Scheme 1).[46] The azahomoadamantyl-4-enium salt was prepared from commercially available 2-methyladamant-2-ol (**2.5**) via a Curtius–Hoffman nitrene insertion reaction to give 5-methyl-4-azahomoadamant-4-ene (**2.6**) in nearly quantitative yield. Methylation of the imine **2.6** with methyl iodide gave 4,5-dimethyl-4-azahomoadamant-4-enium iodide (**2.7**) in high yield (87%). The functionalized arene 5-hydroxy-6-nitroso-phenanthrene (**2.9**) was prepared from condensation of commercially available 9,10-phenanthrenedione (**2.8**) with hydroxylamine. Treatment of 4,5-dimethyl-4-azahomoadamant-4-enium iodide (**2.7**) with trimethylamine at 0 °C leads to generation of the enamine *in situ* which then undergoes condensation with functionalized phenanthrene **2.9** to give the spiro[azahomoadamantyl-phenanthrene]oxazine **2.1** as a green polycrystalline solid (59 % yield, Scheme 2.2).

Scheme 2.2. Synthesis of spiro[azahomoadamantane-phenanthrenoxazine] (APESO, **2.1**).

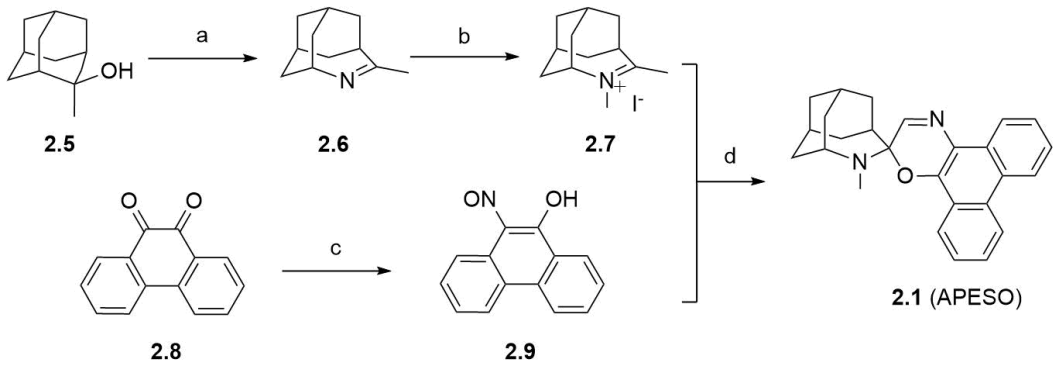

Conditions and Reagents. (a) sodium azide, methanesulfonic acid, CH_2Cl_2, 7 hrs, 95 %; (b) methyl iodide, CH_2Cl_2, 12 hrs, 87 %; (c) sodium nitrite, HCl/H_2O, reflux, 3 hr, 77%; (d) triethylamine, CH_2Cl_2, 0°C to reflux, 6 hrs, 59 %.

2.2.2. Solution-State Isomerization Properties

Thermal Equilibrium: Reversible thermal isomerization between the SO and PMC forms along the ground state potential energy surface in spirooxazines leads to an equilibrium that is dependent on structure, temperature, solvent, and the dielectric of the medium.[46] The thermal equilibrium constant, K_T (K_T = [PMC]/[SO]), of spirooxazines **2.1**–**2.4** were obtained by solution state ^{1}H NMR spectroscopy in a range of solvents of differing polarity (toluene-d_8, THF-d_8, CD_2Cl_2, acetone-d_6, DMSO-d_6, and methanol-d_4) at 300 K (Table 2.1). The azomethine proton resonance differs significantly for the PMC ($\delta \approx 10$ ppm) and SO ($\delta \approx 8$ ppm) forms allowing determination of K_T under a given set of conditions.(Table 2.1). The effects of structure on K_T are consistent with known structure correlations for spirooxazines in which electron withdrawing effects in the oxazine moiety stabilize the PMC form. In a given solvent, the thermal equilibria across the series **2.1**–**2.4** increase by 1–2 orders of magnitude, from the quinoline derivatives **2.3** and **2.4** (~ 0.01–0.1) to the phenanthryl derivatives **2.1** and **2.2** (1–25). The stability of the PMC isomer is

greater in the phenanthryl derivatives relative to the quinoline derivatives due to stabilization of the PMC form by larger aromatics.

Table 2.1. Thermal equilibrium constants K_T and $\Delta G^o_{PMC\text{-}SO}$ (kcal·mol^{-1})) as a function of solvent at 300 K.[a]

Solvent	2.1	2.2	2.3	2.4
Toluene	0.22 (0.9)	1.2 (-0.11)	<0.01 (2.7)	<0.01 (2.7)
THF	0.38 (0.6)	2.7 (-0.59)	<0.01 (2.7)	<0.01 (2.7)
CH_2Cl_2	1.4 (-0.2)	11 (-1.4)	0.11 (1.3)	0.03 (2.1)
Acetone	1.2 (-0.11)	8.4 (-1.3)	0.03 (2.1)	0.02 (2.3)
DMSO	3.8 (-0.79)	20 (-1.7)	0.35 (0.63)	0.53 (0.38)
MeOH	2.9 (-0.63)	25 (-1.9)	0.87 (0.083)	0.71 (0.20)

[a] K_T = [PMC]/[SO]. The K_T was determined by azomethine proton resonance of the PMC ($\delta \approx 10$ ppm) and SO ($\delta \approx 8$ ppm) form by ^{1}H NMR spectroscopy in a concentration of ~10^{-2} M.

The effect of solvent polarity on K_T is consistent with known effects of dielectric on stabilization of the PMC form in the larger family of spirooxazines and spiropyrans.[46,218] An increase in dielectric of the medium stabilizes the PMC over the SO form due to the charge-separated nature of the PMC form. For the quinoline derivatives **2.3** and **2.4,** in nonpolar solvents such as pentane and toluene, the thermal equilibrium lies toward the SO isomer, whereas for **2.1** and **2.2**, the equilibrium lies toward the PMC form. Within a given solvent series, an increase in solvent polarity leads to greater concentration of the PMC form. For example, the equilibrium constant K_T for **2.1** increase from 0.22 (18% PMC) in toluene to 3.8 (79% PMC) in DMSO.

Temperature dependent equilibrium constants of compound **2.1**–**2.4** in THF-d_8 were obtained in the temperature range 293–323 K by ^{1}H NMR spectroscopy to determine

the enthalpy and entropy of the thermal isomerization process. While spirooxazine **2.2** reveals a general temperature independence of the equilibria from 293–323 K, with a slight increase in PMC form with increasing temperature for spirooxazine **2.1,** no changes in the SO form occurs with increasing temperature for **2.3** and **2.4** (Table 2.2). A van't Hoff plot provides information about the temperature dependence of the equilibrium constant. A van't Hoff plot of the temperature dependence of K_T (Figure 2.5) supported that SO → PMC thermal isomerization is an endothermic reaction for spirooxazine **2.1** but exothermic reaction for spirooxazine **2.2** in THF. A positive change in enthalpy (ΔH^o) was found for **2.1** while a negative ΔH^o was found for **2.2** (Table 2.3). The positive change in enthalpy implies the reaction is endothermic, and the negative change in enthalpy indicates the reaction is exothermic. The entropic contributions (ΔS^o) were significantly small for both **2.1** and **2.2**, indicating the enthalphic contribution governs the thermodynamic stability of the SO and PMC form. Both enthalphic and entropic van't Hoff parameters of **2.3** and **2.4** were very small. Determination of van't Hoff parameters for the spirooxazines **2.3** and **2.4** suggests an extremely small temperature dependence of the thermal equilibrium constants, consistent with non-observed changes in concentration of the PMC form within the detection limit for ^{1}H NMR spectroscopy (< 5%).

Table 2.2. Temperature dependent equilibrium constants K_T ($\Delta G^o_{PMC\text{-}SO}$ (kcal·mol^{-1})) in THF-d_8.[a]

Temperature	2.1	2.2	2.3[b]	2.4[b]
293.15	0.37 (-0.58)	2.78 (0.60)	<0.01(2.7)	<0.01
298.15	0.38 (-0.57)	2.70 (0.59)	<0.01	<0.01
303.15	0.38 (-0.58)	2.50 (0.55)	<0.01	<0.01
308.15	0.39 (-0.58)	2.50 (0.56)	<0.01	<0.01
313.15	0.39 (-0.59)	2.33 (0.53)	<0.01	<0.01
323.15	0.42 (-0.56)	2.13 (0.49)	<0.01	<0.01

[a] K_T = [PMC]/[SO]. The K_T was determined by azomethine proton resonance of the PMC ($\delta \approx 10$ ppm) and SO ($\delta \approx 8$ ppm) form by ^{1}H NMR spectroscopy in a concentration of ~10^{-2} M. [b] The concentration of the PMC form was below the limit of detection for ^{1}H NMR (< 5 %).

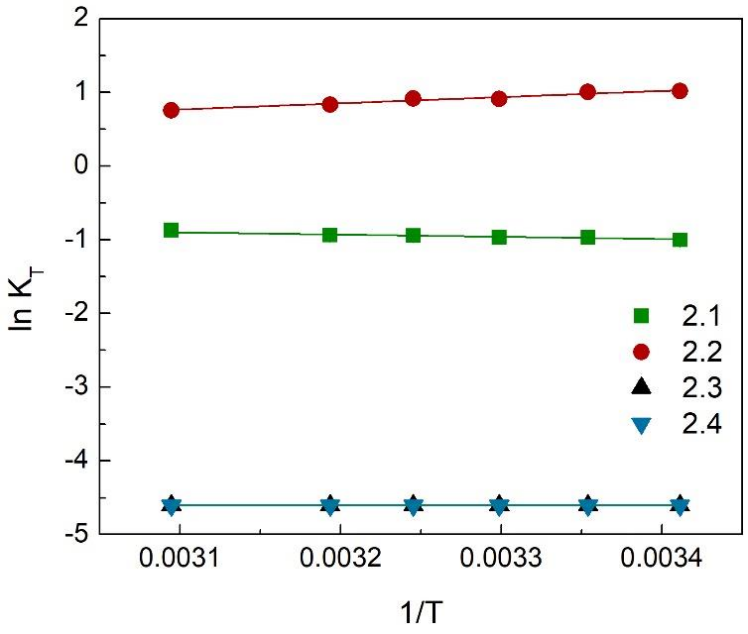

Figure 2.5. Temperature dependence of thermal equilibrium constant fit to a Van't Hoff expression for compounds **2.1**–**2.4**.

Table 2.3. Van't Hoff parameters ΔH^{o} (kcal·mol^{-1}) and ΔS^{o} (kcal·mol^{-1}·K^{-1}).[a]

	2.1	**2.2**	**2.3**	**2.4**
ΔH^{o}/ kcal·mol^{-1}	0.59 ± 0.03	-1.7 ± 0.1	(9.6 ± 0.5)×10^{-15}	(9.6 ± 0.5)×10^{-15}
ΔS^{o}/ cal·mol^{-1}·K^{-1}	0.042 ± 0.002	-3.7 ± 0.2	-9.2 ± 0.5	-9.2 ± 0.5

[a] Standard errors are determined by linear least squares regression.

Kinetics of thermal relaxation: The photochromic and thermal relaxation process of compounds **2.1**–**2.4** differs depending on the structure and medium. For the quinoline derivatives **2.3** and **2.4,** in nonpolar solvents such as pentane and toluene, the thermal equilibrium lies toward the SO isomer. UV light irradiation ($\lambda_{exc} \approx 350$ nm) can then induce SO → PMC conversion and the generation of a photostationary state due to competition between the forward photochemical ring-opening and thermal ring-closure processes. Thermal reversion to the original SO/PMC equilibrium proceeds in the absence of light, and the process of irradiation/thermal relaxation can be repeated over several photocycles. For the phenanthryl derivatives **2.1** and **2.2** however, the thermal equilibrium lies far toward the PMC isomer, and UV irradiation leads to an irreversible UV-induced photodecomposition in these solvents. Visible irradiation (multiline $\lambda_{exc} \approx$ 513–568 nm) of the open-form however leads to a photoinduced isomerization to the SO form to, again, a photostationary state, with thermal reversion to the open-form in the absence of light excitation. As with the quinoline derivatives, light-induced/thermal cycling can occur due to the reversibility of the processes.

The kinetics of thermal isomerization from the visible-light-induced photostationary states of **2.1**–**2.4** were monitored by electronic absorption spectroscopy. Continuous irradiation with a multiline source (Spectra-Physics Stabilite mixed gas Ar-Kr ion laser operating at 100–300 mW at $\lambda_{exc} \approx$ 513–568 nm) induces photoisomerization to

the SO form, as demonstrated by a decrease in the π–π* absorption band at $\lambda_{max} \approx 554$ nm ($\varepsilon \approx 50000\ M^{-1}\ cm^{-1}$) (Figure 2.6). The thermodynamically stable form of the spirooxazines **2.3** and **2.4** are the SO form in both non-polar and polar solvents. The visible-light-induced SO → PMC photoisomerizations for **2.3** and **2.4** could however be monitored in more concentrated solutions (10^{-4} M), in which the absorbance band of the PMC form could be observed. The thermal relaxation rate constants for SO → PMC (coloration, k_1) and PMC → SO conversion (decoloration k_2) (Figure 2.6) were calculated from $k_{obs} = k_1 + k_2$ and K_T = [PMC]/[SO] = k_1/k_2.[51] The kinetics of thermal coloration and decoloration conversion follows monoexponential kinetics in all cases, and are summarized in Table 2.4 as a function of solvent polarity.

Table 2.4. Thermal coloration (k_1) and decoloration (k_2) rate constants [$s^{-1} \times 10^{-3}$] of **2.1**–**2.4** in several solvents at 300 K.[a]

Solvent		**2.1**	**2.2**	**2.3**	**2.4**
Toluene	k_1	230 ± 20	82 ± 5	0.046 ± 0.001	0.074 ± 0.001
	k_2	1100 ± 100	68 ± 5	4.6 ± 0.1	7.5 ± 0.1
THF	k_1	119 ± 3	41 ± 3	0.057 ± 0.001	0.092 ± 0.009
	k_2	330 ± 10	15 ± 2	2.8 ± 0.1	4.6 ± 0.5
CH_2Cl_2	k_1	220 ± 10	51 ± 1 [b]	0.26 ± 0.03	0.032 ± 0.5
	k_2	160 ± 10	4.7 ± 0.1 [b]	2.4 ± 0.3	1.1 ± 0.2
Acetone	k_1	150 ± 20	42 ± 1 [b]	0.035 ± 0.003	0.035 ± 0.002
	k_2	120 ± 20	5.1 ± 0.1 [b]	1.2 ± 0.1	1.8 ± 0.1
DMSO	k_1	180 ± 10	70 ± 1 [b]	0.41 ± 0.3	0.48 ± 0.03
	k_2	48 ± 3	3.5 ± 0.1 [b]	1.2 ± 0.1	0.91 ± 0.06
MeOH	k_1	340 ± 10	8.7± 0.1 [b]	0.069 ± 0.005	0.058 ± 0.001 [c]
	k_2	120 ± 10	0.35 ± 0.01 [b]	0.080 ± 0.008	0.072 ± 0.001 [c]

[a] Determined by UV/Vis spectroscopy in a sample concentration of 10^{-4}–10^{-5} M. Experimental errors of the thermal relaxation constant are determined from 3 independent runs. [b] Ref [223]. [c] Ref [224].

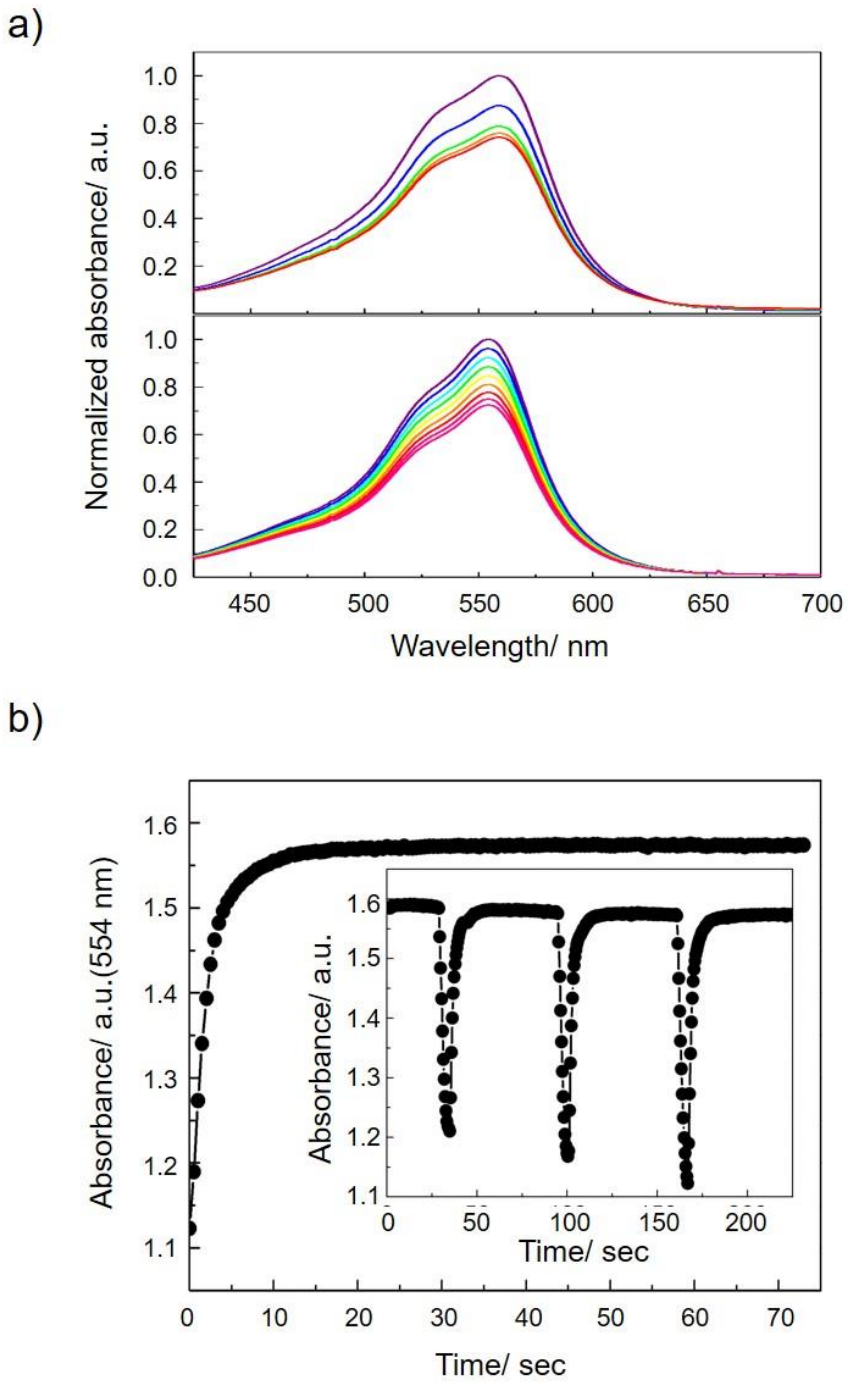

Figure 2.6. Electronic absorption spectrum of **2.1** (top), and **2.2** (bottom) with steady-state visible light irradiation (multiline λ_{exc} = 514–568 nm) in toluene at 298 K in toluene (a). Kinetics of thermal relaxation of **2.1** following visible irradiation measured as time-dependent absorbance intensity (0.5 second intervals), and three cycles of light irradiation/thermal relaxation as a function of time (inset) (b).

The rate constants for coloration (k_1) and decoloration (k_2) in a given solvent are sensitive to both oxazine substitution and amine functionality. The rate constants of coloration (k_1) and decoloration (k_2) are 2–3 orders of magnitude higher for the phenanthryl derivatives than the quinolyl derivatives and in general an order of magnitude higher for the phenanthrene derivative **2.1** relative to the phenanthroline derivative **2.2**. This suggests that the effects of substitution at the oxazine moiety on the rates of ring opening are substantial. In addition, the coloration rate constants (k_1) do not exhibit a significant solvent polarity dependence whereas the decoloration rate constants (k_2) do, and decrease with increasing solvent polarity for all of the compounds studied (Figure 2.7). This suggests an increase in the energy barrier to thermally-induced ring closure in more polar solvents.

The temperature dependence of the thermal relaxation rate constants was measured for **2.1**–**2.4** in THF. The activation parameters of thermal coloration (SO → PMC, E_{a1}) and decoloration (SO → PMC E_{a2}) for **2.1**–**2.4** were obtained from fitting of the data to the Arrhenius equation (Figure 2.8, Table 2.5, Equation 2.1). The thermal coloration (k_1) and decoloration (k_2) rate constants were calculated from $k_{obs} = k_1 + k_2$ and K_T = [PMC]/[SO] = k_1/k_2.[51] To determine E_{a1} and E_{a2}, k_1 and k_2 were corrected by K_T as determined at each temperature (293 K–313 K) to allow fitting of the Arrhenius equation.

$$k_i = Aexp\left(\frac{-E_{ai}}{RT}\right) \qquad Equation\ 2.1$$

$$lnk_i = \frac{-E_{ai}}{R}\left(\frac{1}{T}\right) + ln(A)$$

From a plot lnk_i (i = 1 or 2) as a function of 1/T where R is the gas constant, the activation energies for thermal coloration (E_{a1}) and decoloration (E_{a2}) processes were extracted.

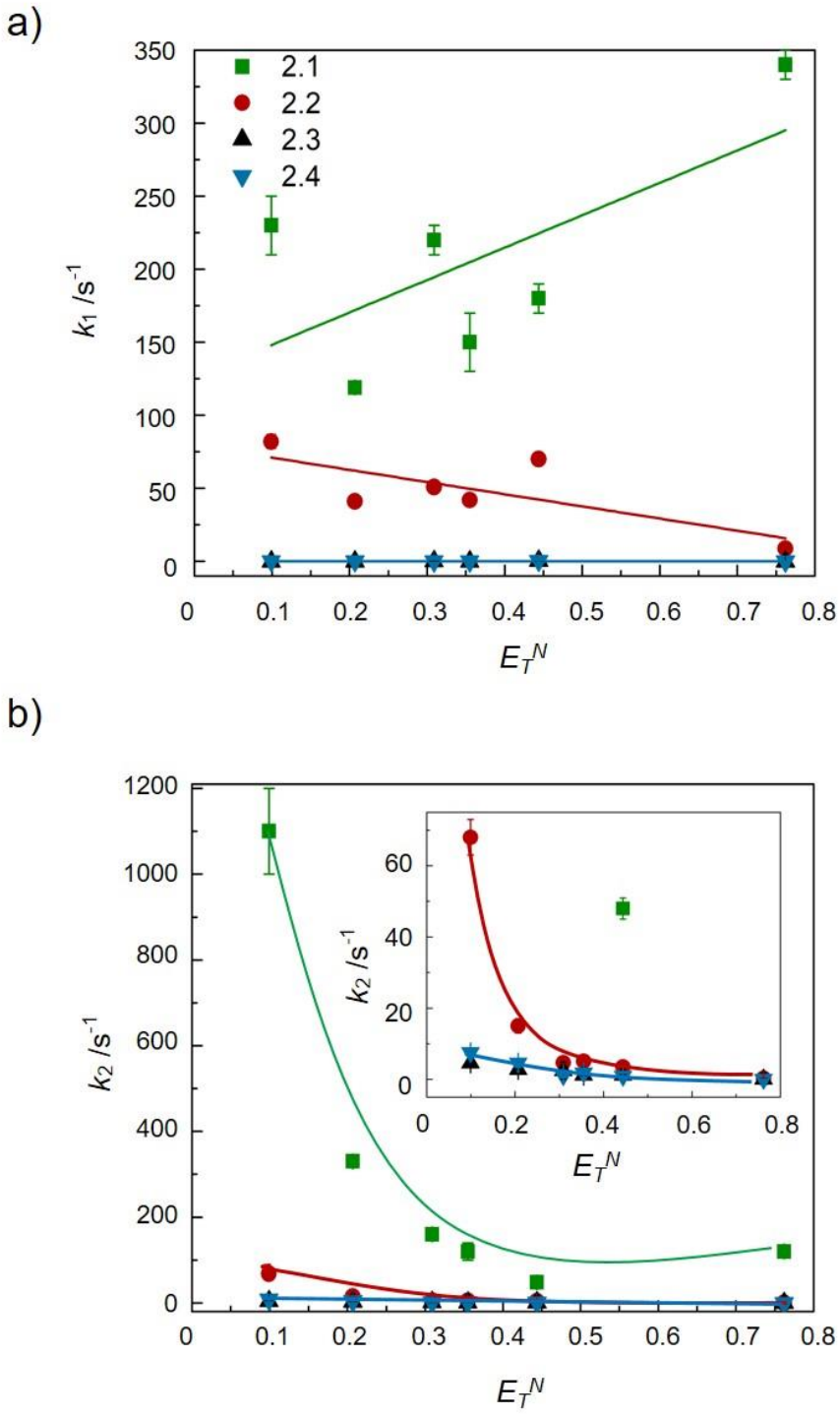

Figure 2.7. Correlation plots of Dimroth-Reichardt E_T^N solvent polarity scale *vs*. thermal coloration rate constant k_1 (a), and decoloration rate constant k_2 (b) of **2.1**–**2.4** at 300 K.

Table 2.5. Activation Energies (kcal·mol^{-1}) for thermal coloration SO → PMC (E_{a1}) and decoloration PMC → SO (E_{a2}) of compound **2.1**–**2.4**.[a]

	2.1	**2.2**	**2.3**	**2.4**
E_{a1} /kcal·mol^{-1}	21.9 ± 0.4	22.2 ± 0.3	23.4 ± 0.5	23.8 ± 0.3
E_{a2} /kcal·mol^{-1}	21.4 ± 0.3	23.9 ± 0.4	23.4 ± 0.5	23.8 ± 0.3

[a] Determined by UV/Vis spectroscopy in a sample concentration of 10^{-4}–10^{-5} M in THF and from fitting the data to the Arrhenius equation. Standard errors are determined by linear least squares regression.

In general, the activation energies for both coloration and decoloration are larger in the quinoline derivatives **2.3** and **2.4** than in **2.1** and **2.2** suggesting a higher barrier for thermal isomerization in **2.3** and **2.4**. If one compares the relative rates of coloration and decoloration in the series, one finds differences for the forward and reverse in **2.1** and **2.2** but not in **2.3** and **2.4**. The activation energy for thermal coloration (E_{a1}) of **2.1** was found to be 0.5 kcal·mol^{-1} higher than that for decoloration (E_{a2}) whereas the E_{a2} of **2.2** was found to be 1.7 kcal·mol^{-1} higher than E_{a1} (Table 2.5). This may be due to the stabilization of the PMC form of **2.2** leading to higher E_{a2} than E_{a1}. However, the E_{a1} and E_{a2} of spirooxazines **2.3** and **2.4** are found to be identical. Since the thermal coloration rate constants were found to be significantly higher than decoloration rate constants ($k_1 << k_2$) for **2.3** and **2.4**, the activation energy of SO → PMC (coloration, E_{a1}) was expected to be higher than PMC → SO (decoloration, E_{a2}). This discrepancy arose from an error associated with the determination of temperature dependent equilibrium constant (K_T) by ^{1}H NMR spectroscopy. As K_T is determined by ^{1}H NMR integration which is only accurate to within ± 5 %, the thermal equilibrium values obtained for **2.3** and **2.4** (< 0.1) are within the margin of error (Table 2.2). In theory, an error of 5 % in K_T could lead to error in E_{a1} by as much as ~10 kcal·mol^{-1} for **2.3** and **2.4**. This could possibly explain the observed discrepancy in values.

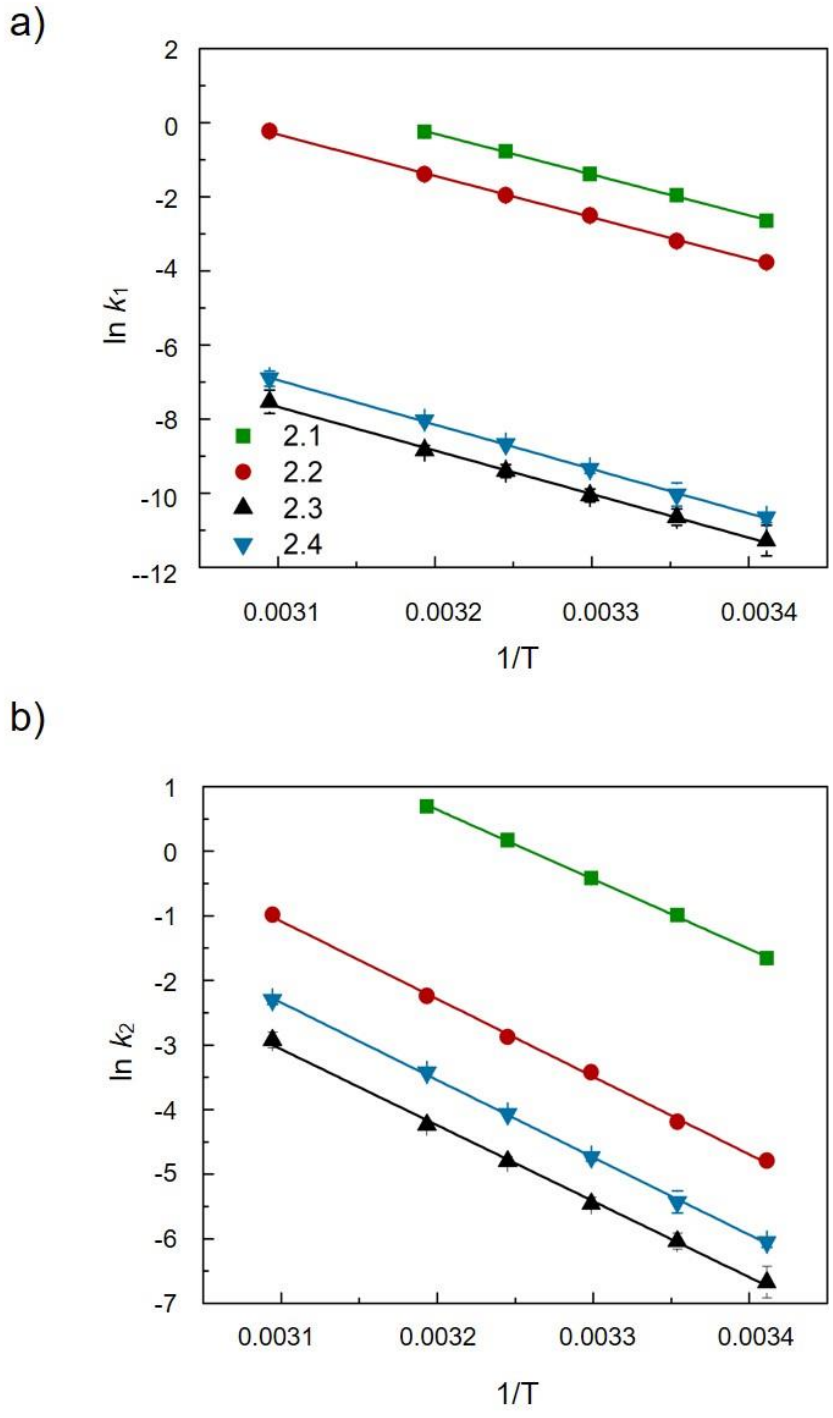

Figure 2.8. Temperature dependence of thermal SO → PMC isomerization (a), PMC→SO (b) fit to an Arrhenius expression for compounds **2.1**–**2.4**.

The enthalpic and entropic activation parameters were determined by fitting the data to the Eyring equation (Equation 2.2, Figure 2.9, Table 2.6)

$$k_i = \frac{k_B T}{h} exp\left(\frac{-\Delta H_i^{\ddagger}}{RT}\right) exp\left(\frac{\Delta S_i^{\ddagger}}{R}\right) \qquad Equation\ 2.2$$

$$ln\left(\frac{k_i}{T}\right) = \frac{-\Delta H_i^{\ddagger}}{R}\frac{1}{T} + ln\left(\frac{k_B}{h}\right) + \frac{\Delta S_i^{\ddagger}}{R}$$

From a plot 1/T as a function of ln(k_i/T) (i = 1 or 2) where R is a gas constant, k_B is a Boltzmann constant, and h is a Planck constant, the enthalpic contributions $\Delta H^{\ddagger}_i$ and entropic contributions $\Delta S^{\ddagger}_i$ for thermal coloration and decoloration process were determined. The activation parameters reveal that the enthalpic contributions dominate the barrier to both thermal coloration and decoloration processes for **2.1**–**2.4** (Table 2.6). The highest enthalpic contribution for thermal coloration ($\Delta H_1^{\ddagger}$) and decoloration ($\Delta H_2^{\ddagger}$) were found for **2.3** and **2.4** and the lowest for **2.1**, which is consistent with the highest activation energies found in **2.3** and **2.4**. The negative entropy of the decoloration ($\Delta S_2^{\ddagger}$) found for **2.3** and **2.4** may be due to solvent reorganization around the PMC form suggesting greater charge-separated character in the PMC forms of **2.3** and **2.4**.

Table 2.6. Enthalpic ($\Delta H^{\ddagger}$) and entropic ($\Delta S^{\ddagger}$) contributions (kcal·mol^{-1}) to the activation energies of SO → PMC (E_{a1}) and PMC → SO (E_{a2}) isomerization.[a]

	2.1	**2.2**	**2.3**	**2.4**
$\Delta H_1^{\ddagger}$ / kcal·mol^{-1}	21.3 ± 0.4	21.5 ± 0.3	22.8 ± 0.5	23.2 ± 0.3
$\Delta S_1^{\ddagger}$ / cal·mol^{-1}·K^{-1}	8.9 ± 0.2	7.7 ± 0.1	-3.3 ± 0.1	-0.57 ± 0.01
$\Delta H_2^{\ddagger}$ / kcal·mol^{-1}	20.8 ± 0.3	23.3 ± 0.4	22.8 ± 0.5	23.2 ± 0.3
$\Delta S_2^{\ddagger}$ / cal·mol^{-1}·K^{-1}	9.9 ± 0.2	11.4 ± 0.3	5.8 ± 0.2	8.6 ± 0.1

[a] Determined by UV/Vis spectroscopy in a sample concentration of 10^{-4}–10^{-5} M and from fitting the data to the Erying equation. Standard errors are determined by linear least squares regression.

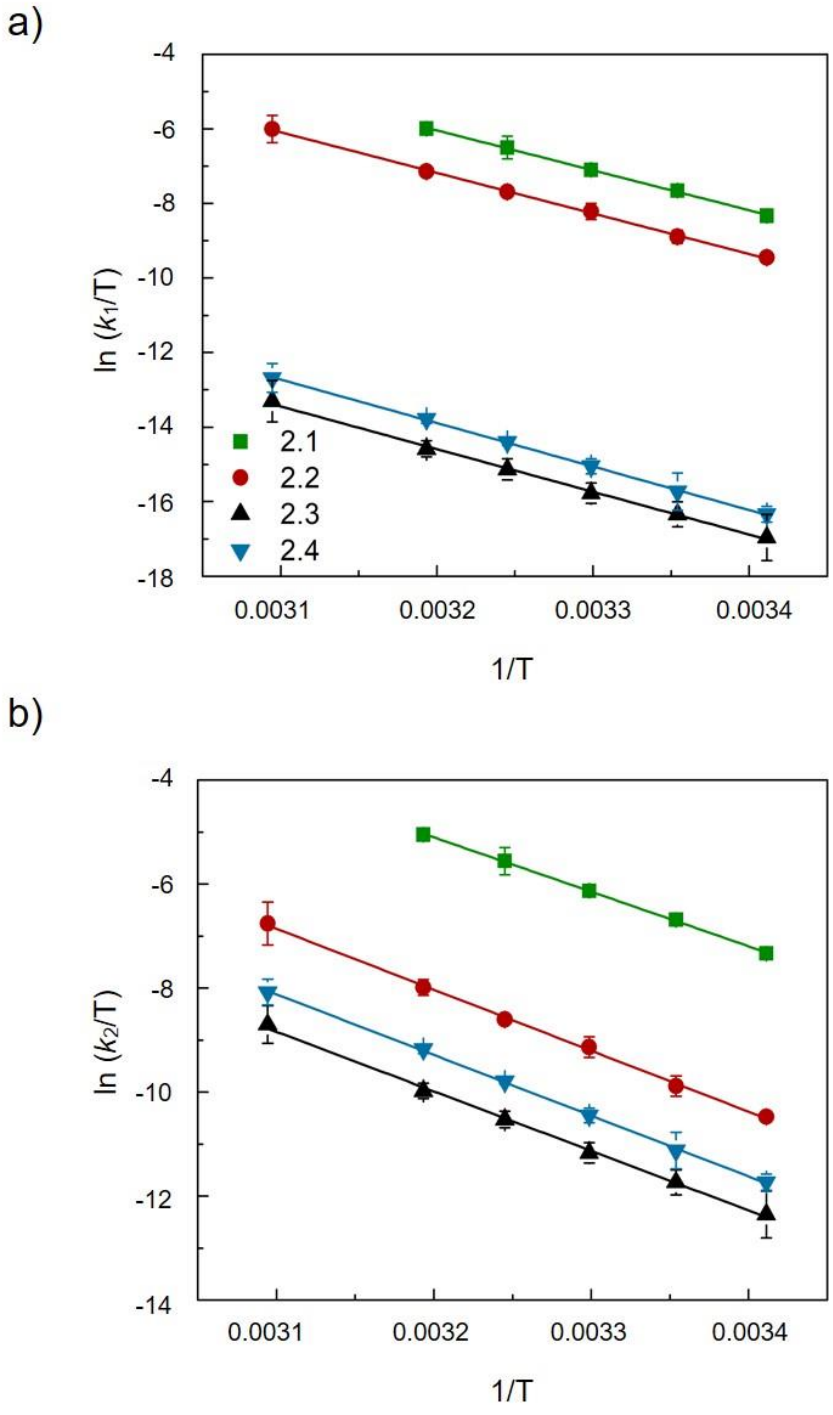

Figure 2.9. Temperature dependence of thermal SO → PMC coloration (a), thermal PMC → SO decoloration (b) fit to an Eyring expression for compounds **2.1**–**2.4**.

First principles suggest that as the PMC form is stabilized relative to the SO form, thermal relaxation (SO → PMC) should become faster. A preliminary examination of the energy relationship between $\Delta G^{o}_{(PMC\text{-}SO)}$ and the rate of thermal SO → PMC relaxation (k_1) for the series of spirooxazines reveals surprisingly no such correlation (Figure 2.10). The absence of a simple linear free energy relationships (LFER) between ground state PMC and SO energies $\Delta G^{o}_{(PMC\text{-}SO)}$ and kinetics for isomerization suggests that the ground state PMC form (generally the TTC isomer) may not be the isomer involved in the rate-determining step for SO → PMC thermal relaxation.

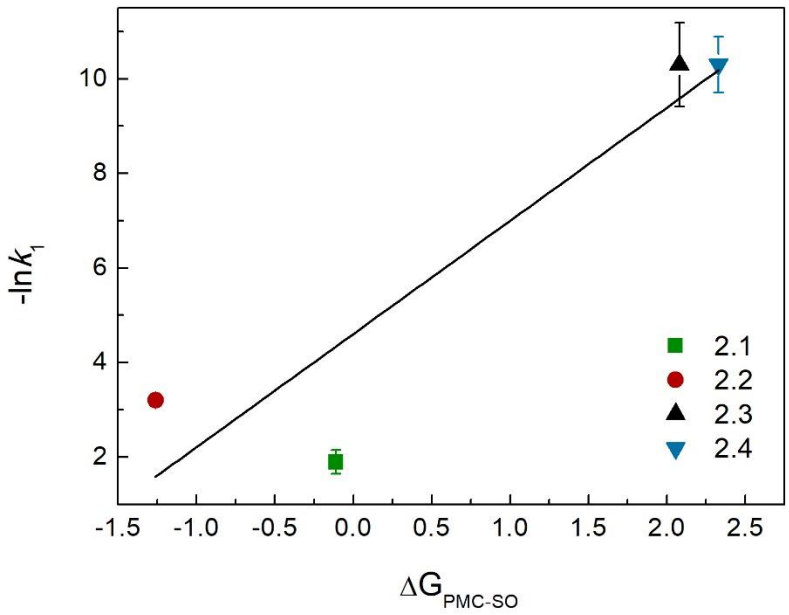

Figure 2.10. The plot of ΔG^{o} against $-\ln k_1$ (observed thermal SO → PMC coloration rate) of **2.1**–**2.4** in acetone.

In the rotation pathway, the rate-determining step involves *cis*-to-*trans* isomerization at the C-N β-bond from the TCC isomer to the TTC isomer. An increase in C-N single bond character would lead to a decrease in the activation energy for C-N β-bond rotation. This suggests that greater contribution of neutral character (PMC-1) in the

PMC form would lead to faster thermal coloration kinetics. Conversely, in the inversion pathway, the rate determining step is a *trans*-to-*cis* isomerization at the γ-bond in which single bond character of the C-N γ-bond would lead to a decrease in the activation energy for the thermal coloration. A greater contribution of charge-separated character (PMC-2) to the PMC electronic structure would then exhibit faster thermal coloration kinetics. It was reasoned that analysis of the electronic structure of the PMC form would, therefore, provide insight into the structural factors governing thermal coloration in the series.

2.2.3. Structure of the PMC form in Solution

Absorption of visible light induces cleavage of the C–O bond and a possible $2^3 = 8$ PMC isomers (Figure 2.3) formed by rotation about the central conjugated backbone comprised of the C–C (α), C–N (β), and N–C (γ) bonds. Transoids (*trans* with respect to C–N (β), TTC, TTT, CTC, CTT) are about 10 kcal·mol^{-1}more stable than the cissoids due to steric hindrance.[221] Ambiguities exist as to whether the PMC isomer distribution in the solid state is that which exists in solution for any given spirooxazine, making solution state methods important for correlation with solution state kinetics. Each transoid exhibits different through-space interactions between the azomethine proton and neighboring protons, allowing determination of the equilibrium distribution of isomers in solution by ^{1}H NMR. Investigation of both the through-space proton-proton interactions (red contours) and the existence of chemical exchange between the SO and PMC form in solution (black contours) was carried out by two-dimensional NOESY spectra of **2.1** in $CDCl_3$ at 298 K (Figure 2.12). The TTC isomeric structure of **2.1** was supported by the presence of through-space proton-proton interactions between two phenanthrene protons (H-22 and H-26, δ

8.16 and δ 8.24), the N-methyl (H-1, δ 3.46) and the bridgehead methine proton (H-6, δ 3.68), and two bridgehead methine and methylene protons (H-6 and H-7, δ 3.68 and δ 1.80) as shown in Figure 2.11. The presence of through-space proton-proton interactions between the azomethine (H-3, δ 9.82) and N-methyl proton (H-1, δ 3.46) suggests that the TTC isomer is the dominant form under these conditions. An intensity of NOE is inversely proportional to r^6 (where r is the direct distance between protons), and the maximum detectable NOE proton-proton distance r is approximately 5 Å.[225] The presence of CTT and TTT isomers would give rise to cross-peaks between the azomethine (H-3) and phenanthroline (H-19) protons (Figure 2.11). An optimized geometry of the TTT isomer (B3LYP/6-31G+(d,p)) suggests that distance between the azomethine (H-3) and phenanthroline (H-19) protons is 2.02 Å, which is significantly less than the detectable distance (5 Å). Similarly, the CTC would exhibit cross-peaks between the bridgehead (H-10) and azomethine (H-3) protons (Figure 2.12); however, neither of which is observed.

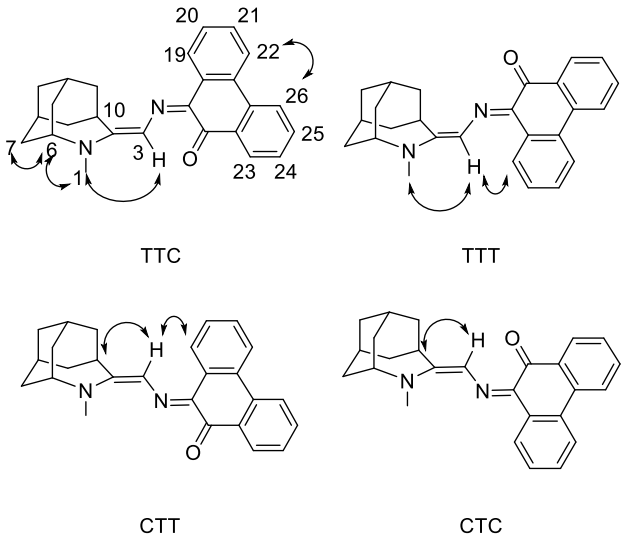

Figure 2.11. Structures of the transoids showing proton labels and NOE cross-peaks correlations.

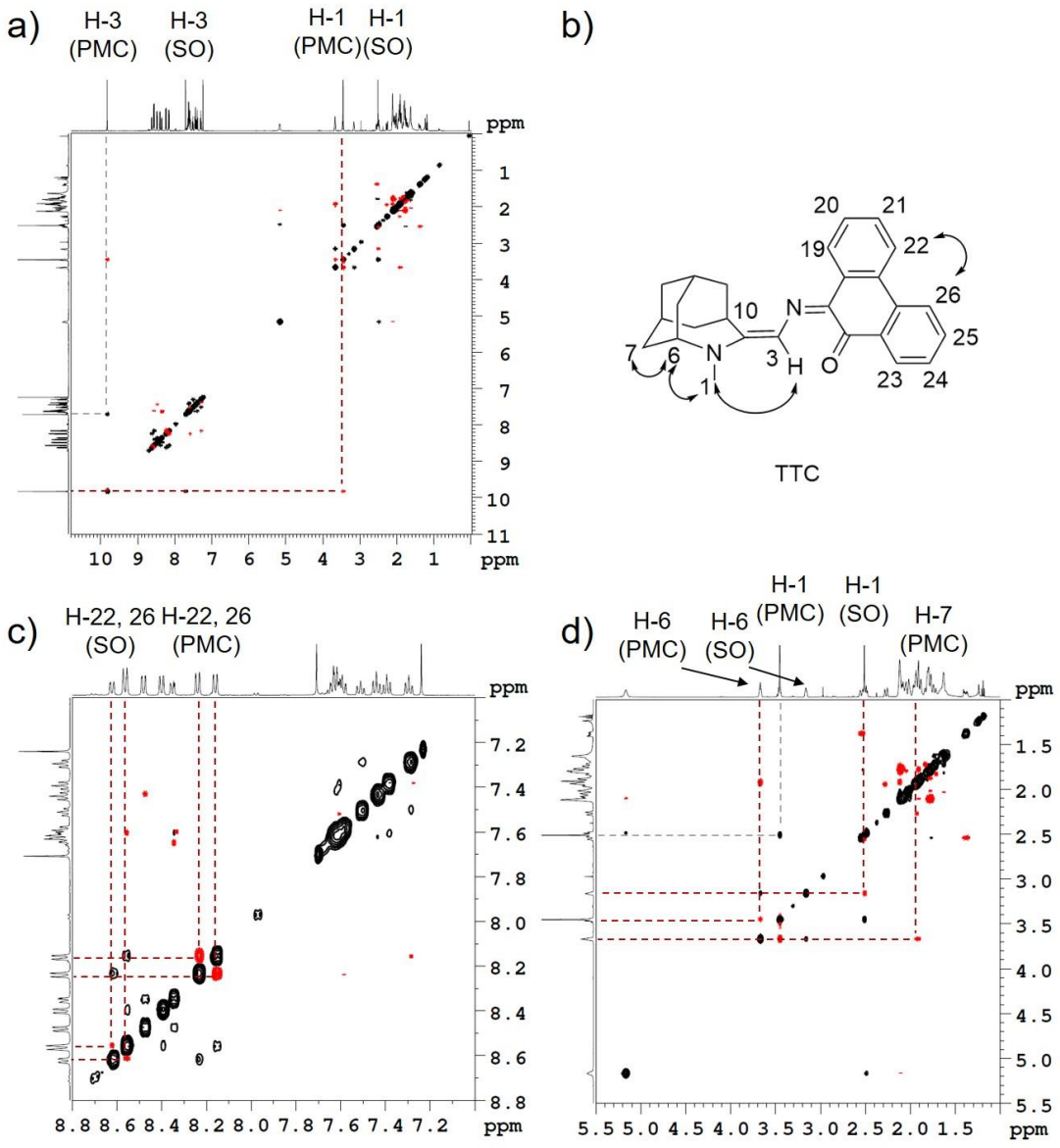

Figure 2.12. ^{1}H NMR NOESY spectra of spirooxazine **2.1** in $CDCl_3$ at 300 K. Full NOESY spectrum of **2.1** (a), structure of the TTC form showing proton labels and NOE cross-peak correlations (b), NOESY of the aromatic region (8.8-7.2 ppm) (c), and NOESY of the aliphatic region (5.5-1.0 ppm) (d).

The presence of NOE cross-peaks between azomethine resonances in the PMC (H-3, δ 9.82) and SO form (H-3, δ 7.71) indicates the presence of chemical exchange between PMC and SO forms. NOE cross-peaks between N-methyl protons of the PMC (H-1, δ 3.46)

and SO (H-1, δ 2.51) also support chemical exchange between the SO form and the TTC PMC isomer. Previous computational studies suggest the barrier for TTT→TTC (*trans*-to-*cis* isomerization at γ-bond) is relatively high (~ 30 kcal/mol),[221] If thermal isomerization from the SO to the PMC took place via an inversion pathway, one would expect to observe a reasonable concentration of the TTT form in solution. The absence of cross-peaks assignable to the TTT isomer by NOESY suggests that thermal relaxation of **2.1** does not likely go through an inversion pathway.

2.2.4. Effect of the Medium and Vibronic Analysis of the PMC Form

The nature of the solvatochromic response and analysis of vibronic structure associated with the PMC π–π* electronic transition provides insight into the degree of charge separation of the ground state PMC form in solution.[46] The solvatochromism of **2.1–2.4** was examined in a series of solvents, and the λ_{max} of the PMC form was correlated with the normalized Dimroth-Reichardt E_T^N solvent polarity scale,[226] which accounts for solvation effects arising from both nonspecific (e.g., dipole–dipole, induced dipole–induced dipole, etc.) and specific solvent interactions (e.g., hydrogen bonding, nucleophilicity). This scale has often been used to evaluate the solvatochromism of merocyanines and has been found to correlate with the degree of charge separation.[227,228] The dielectric constant, which is the ratio of the permittivity of a solvent to that of vacuum describes the ability of a solvent to effectively screen electric charge and does not account for specific solvent interactions. Since the electronic structure of the photomerocyanines can be perturbed by both nonspecific and specific solvent interactions, the normalized

Dimroth-Reichardt E_T^N solvent polarity scale was chosen to evaluate solvation effects of photomerocyanines.

The direction of solvatochromism (negative or positive) provides information regarding the relative degree of charge separation in the ground and excited state of a given chromophore.[229,230] In positive solvatochromism, higher polarity solvents induce a bathochromic shift in the π–π* absorption band, as is observed for compound **2.1** (Δ λ_{max} of 6 nm, Table 2.7, Figure 2.13) indicating that the excited state has a higher dipole moment than the ground state. Negative solvatochromism (hypsochromic shift in π–π*) is observed for **2.3** and **2.4** (Δ λ_{max} of 25 and 23 nm, respectively, Table 2.7, Figure 2.13) due to a higher dipole moment in the ground state relative to the excited state. A smaller solvatochromic response observed for **2.2**, consistent with a fully delocalized structure (Table 2.7, Figure 2.13).

Table 2.7. λ_{max} and % peak area of three subbands v_0, v_1, v_2, and I_{ref} of **2.1**–**2.4** in selected solvents.

2.1										
		Expt.	v_1		v_2		v_3			I_{ref}
Solvent	E_T^N	λ_{max} /nm	λ_{max} /nm	% Area	λ_{max} /nm	% Area	λ_{max} /nm	% Area	R^2	
Toluene	0.099	559	565	33	533	41	480	26	0.998	1.24
THF	0.207	559	563	36	532	37	478	27	0.999	1.03
CH_2Cl_2	0.309	563	567	47	535	40	458	13	0.998	0.85
Acetone	0.355	564	562	42	531	41	469	17	0.998	0.98
DMF	0.386	562	565	46	534	41	463	13	0.998	0.89
DMSO	0.444	565	567	48	536	41	457	11	0.998	0.85
CH_3CN	0.460	558	561	45	530	42	462	13	0.998	0.93
MeOH	0.762	564	567	48	534	43	430	9	0.998	0.90

2.2

		Expt.	ν_1		ν_2		ν_3			
Solvent	E_T^N	λ_{max} /nm	λ_{max} /nm	% Area	λ_{max} /nm	% Area	λ_{max} /nm	% Area	R^2	I_{ref}
Toluene	0.099	554	558	47	527	40	481	13	0.996	0.85
THF	0.207	553	555	53	524	37	476	10	0.994	0.70
CH_2Cl_2	0.309	554	562	55	530	38	472	7	0.995	0.69
Acetone	0.355	550	552	57	521	36	461	7	0.994	0.63
DMF	0.386	552	553	54	523	35	451	11	0.998	0.65
DMSO	0.444	552	555	61	524	31	442	8	0.996	0.51
CH_3CN	0.460	547	549	58	519	35	447	7	0.998	0.60
MeOH	0.762	527	544	48	518	37	418	15	0.991	0.77

2.3

		Expt.	ν_1		ν_2		ν_3			
Solvent	E_T^N	λ_{max} /nm	λ_{max} /nm	% Area	λ_{max} /nm	% Area	λ_{max} /nm	% Area	R^2	I_{ref}
Toluene	0.099	577	581	40	546	40	502	20	0.999	1.00
THF	0.207	573	577	40	542	29	503	31	0.999	0.73
CH_2Cl_2	0.309	572	576	47	542	33	493	20	0.999	0.70
Acetone	0.355	569	571	49	538	33	495	18	0.999	0.67
DMF	0.386	569	571	49	539	34	490	17	0.999	0.76
DMSO	0.444	568	571	45	539	33	480	22	0.999	0.73
CH_3CN	0.460	564	568	47	536	33	487	20	0.999	0.70
MeOH	0.762	552	558	42	529	46	447	12	0.999	1.09

2.4

		Expt.	ν_1		ν_2		ν_3			
Solvent	E_T^N	λ_{max} /nm	λ_{max} /nm	% Area	λ_{max} /nm	% Area	λ_{max} /nm	% Area	R^2	I_{ref}
Toluene	0.099	565	572	28	536	37	488	35	0.999	1.32
THF	0.207	563	567	38	534	40	495	22	0.999	1.05
CH_2Cl_2	0.309	563	567	45	534	39	489	16	0.998	0.87
Acetone	0.355	558	563	33	531	39	442	28	0.999	1.18
DMF	0.386	559	563	43	532	36	483	21	0.999	0.84
DMSO	0.444	559	562	37	533	44	441	19	0.999	1.19
CH_3CN	0.460	555	560	41	529	36	481	23	0.999	0.88
MeOH	0.762	542	549	38	521	47	447	15	0.999	1.24

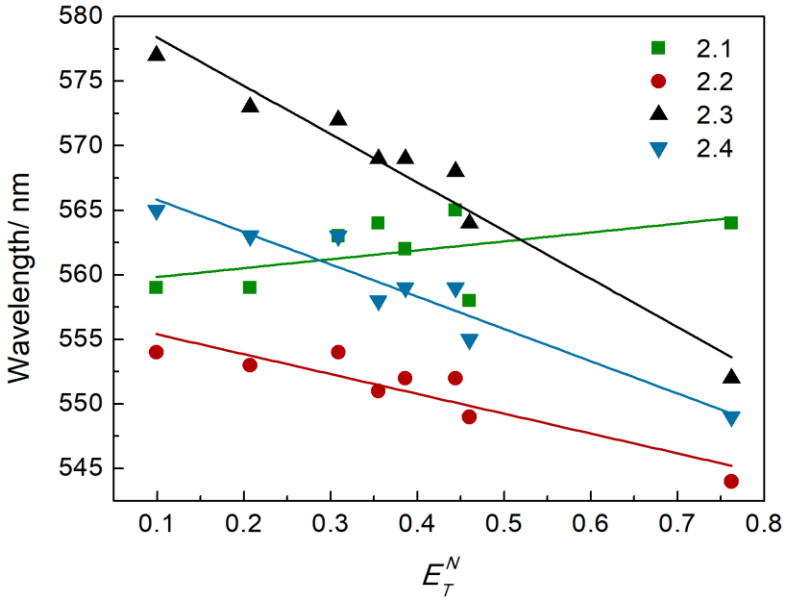

Figure 2.13. Solvatochromism plot. λ_{max} of π–π* absorption band as a function of Dimroth-Reichardt E_T^N solvent polarity scale in selected solvents of **2.1**–**2.4**.

Vibronic structure gives insight into the relative geometries of the ground and excited states reflected by the relative intensities of the vibronic bands of the π–π* transition. The vibronic progression commonly observed for the π–π* charge transfer band of merocyanines for the lowest energy transition ($v_0 \rightarrow v'_0$ (V_0)) and higher energy transitions ($v_0 \rightarrow v'_1$ (V_1), $v_0 \rightarrow v'_2$ (V_2) etc.)) is attributed to symmetric C=C bond stretching modes.[231] The electronic absorption spectra of spirooxazine and spiropyran-based photomerocyanines exhibit a similar vibronic progression.[232,233] The relative intensities of the V(0), V(1), and V(2) provide insight into the degree of bond localization of the PMC form in solution.[46] If the change in geometry is small between the ground and excited state, by the Frank-Condon principle, the electronic transition from the ground to the excited state results in a large overlap integral of vibrational wavefunctions between the lowest vibrational level in the ground (v_0) and excited (v'_0) states. The transition

probabilities of a given vibrational level are proportional to the square of the overlap integrals, the Frank-Condon factor. A vibronic transition band with a large Frank-Condon factor will exhibit a strong intensity relative to the other vibronic subbands. For merocyanines, if a delocalized conjugated structure for the ground state exists, there are equal contributions from neutral and charge-separated resonance structures, and small changes in electronic structure occur upon a population of the excited state. Hence, a large Frank Condon factor would be found, with the V(0) band exhibiting the strongest intensity relative to the other vibronic subbands (i.e., V(1) and V(2)). Conversely, a more localized electronic structure in the ground state (either neutral or charge-separated) would give rise to a small Frank Condon factor leading to a decrease in intensity of the V(0) band relative to the other subbands.

Compounds **2.1**–**2.4** exhibit vibronic progressions centered at $\lambda_{max} \approx 550$ nm with vibronic transitions separated by 30–50 nm (Figure 2.14, Table 2.7). The PMC π-π^* absorption bands of **2.1**–**2.4** were deconvoluted into three transitions by Lorentzian functions to give a lowest energy band, assigned to the V(0) transition, a mid-energy band V(1), and a high energy band assigned to the V(2) transition. The peak areas of V(0), V(1), and V(2) of **2.1**, **2.2**,[46] and **2.3**, **2.4** were plotted as a function of solvent polarity using the normalized Dimroth-Reichardt E_T^N solvent polarity scale[226], and the plots of **2.1** and **2.2** are shown in Figure 2.14. In both compound **2.1** and **2.2**, V(0) exhibits maxima with regard to solvent polarity, suggesting a more delocalized structure in high polarity solvents for **2.1**, and medium polarity solvents for **2.2**. The relative intensity of the ratio ((I_{ref}) = V(1)/V(0)) subbands reflects the degree of delocalization as a function of structure and solvent polarity, in which higher I_{ref} values correspond to greater bond localization (either

in the neutral or charge-separated state). The I_{ref} values of **2.1**–**2.4** are plotted as a function of normalized Dimroth-Reichardt E_T^N solvent polarity scale (Figure 2.14d). The PMC forms of **2.1** and **2.2** become increasingly delocalized (low I_{ref}) with higher solvent polarity (up to $E_T^N = 0.45$), whereas I_{ref} for **2.3** and **2.4** exhibit inflection points at $E_T^N = 0.3$, with some deviation in acetone ($E_T^N = 0.36$) and DMSO ($E_T^N = 0.44$) perhaps due to specific solvent interactions (nucleophlicity). Analysis of I_{ref} reveals that spirooxazine **2.2** has the most delocalized ground state (smallest I_{ref} among **2.1**–**2.4**) in the series of solvents. The vibronic band analysis observed is consistent with the solvatochromism suggesting a more neutral character in **2.1**, delocalized character in **2.2,** and greater charge-separated character of **2.3** and **2.4** in solution.

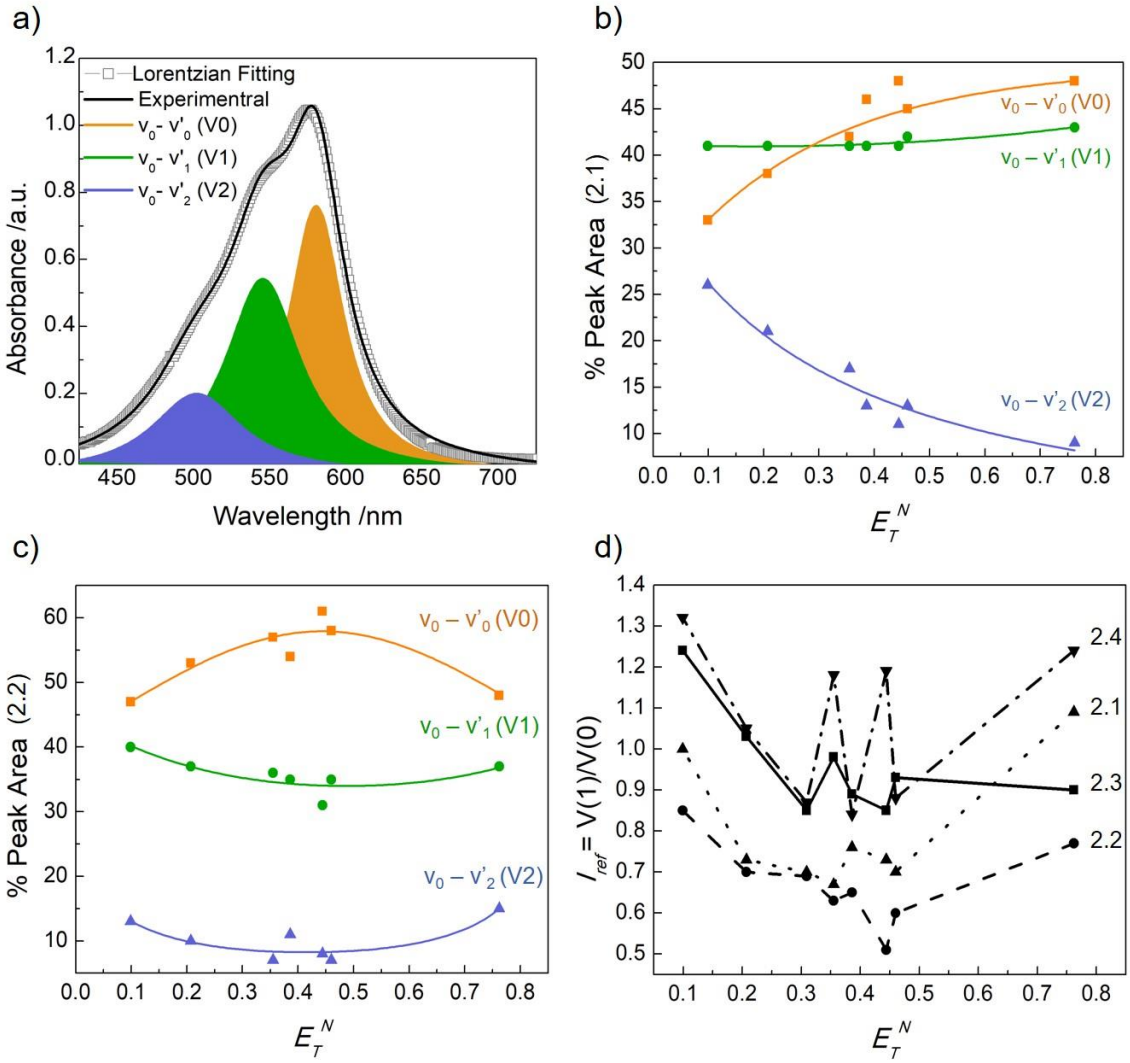

Figure 2.14. Deconvoluted PMC π–π* electronic absorption band of **2.1** in toluene at 298 K using Lorentzian function (orange: V(0), green: V(1), blue: V(2), □: sum of V(0), V(1). and V(2) bands, black: original absorption band) (a). Relative peak areas of V(0), V(1) and V(2) as a function of the Dimroth-Reichardt E_T^N solvent polarity scale in selected solvents of **2.1** (b), and **2.2** (c). Relative intensity I_{ref} (V(1)/V(0)) against as a function of the Dimroth-Reichardt E_T^N solvent polarity (■solid line: **2.1**, ●dashed line: **2.2**, ▲dashed line: **2.3**, ▼dashed line: **2.4**) (d).

2.2.5. Structural Analysis of PMC Form in the Solid State

The degree of charge-separated character for the PMC form in the solid state was investigated through X-ray diffraction techniques. Single crystals of spirooxazine **2.1**

suitable for single crystal X-ray diffraction were obtained by slow evaporation from ethyl acetate. Spirooxazine **2.1** crystallizes in a monoclinic crystal system, $P2_1/c$ space group with Z = 4 molecules in the unit cell. The molecules form dimers due to π–π edge-to-face interactions between phenanthrene rings with a large interplanar separation of 4.55 Å. These dimers further assemble into chains along the *b*-axis (Figure 2.15). The molecular structure of **2.1** reveals crystallization in the open PMC form with a TTC geometry. The X-ray diffraction analysis of **2.2** (PMC), **2.3** (PMC), and **2.4** (SO) have been previously reported[46] and selected experimental bond lengths along the azomethine bridge for these spirooxazines along with **2.1** are tabulated in Table 2.8.

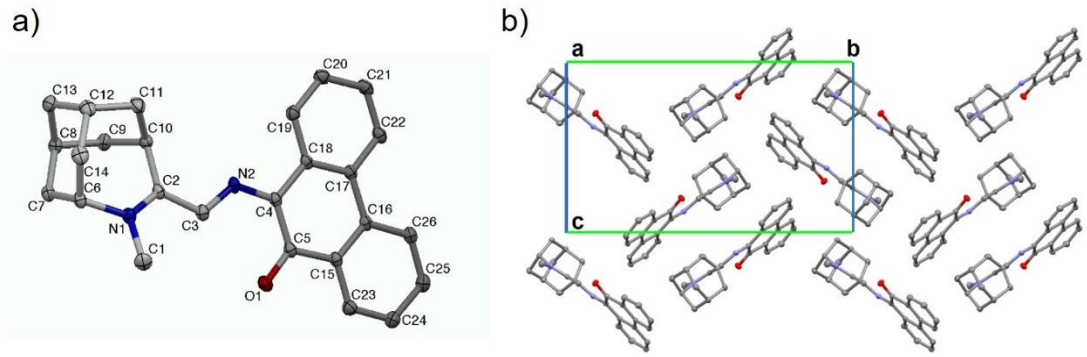

Figure 2.15. Molecular structure of **2.1** with thermal ellipsoids shown at the 50% probability level (a) and crystal packing along the *a*-axis (b).

In order to evaluate the magnitude of charge separation in the PMC form of **2.1**–**2.3**, a modified bond length alternation (BLA) analysis based on experimental (XRD) geometries was carried out. The BLA parameter is defined by the average bond length between alternating carbon-carbon bonds in donor-acceptor polyenes[234] and in general correlates with the degree of localization in π-conjugated polyenes. As the valence-bond wavefunction for the ground state electronic structure is a linear combination of neutral

and charge-separated forms, a positive BLA implies a larger contribution from the neutral form while a negative BLA suggests a larger contribution from the charge-separated form. Equal contributions from both neutral and charge-separated resonance forms give rise to BLA = 0.[235] The BLA calculations were modified to include carbon heteroatom bonding according to equation 2.3. Here we denote N(1)–C(2), C(2)–C(3), C(3)–N(2), N(2)–C(4), C(4)–C(5), C(5)–O(1) as BL1, BL2, BL3, BL4, BL5, BL6, respectively (Figure 2.16).

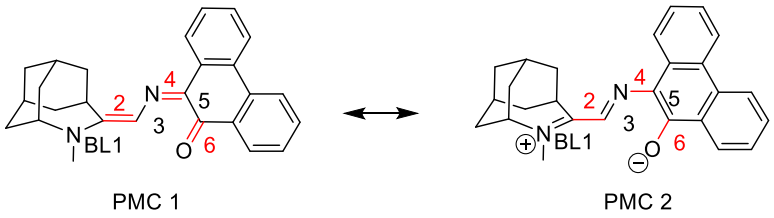

$$BLA = [(BL1 + BL3 + BL5) / 3] - [(BL2 + BL4 + BL6) / 3] \qquad \text{(Equation 2.3)}$$

Figure 2.16. Bond labeling of the neutral (PMC-1) and charge-separated (PMC-2) form for BLA.

Table 2.8. Experimental and Predicted Bond lengths with Calculated BLA of **2.1**–**2.3**, PMC-1 and PMC-2.

	2.1[a]	**2.2**[b]	**2.3**[b]	PMC-1[c]	PMC-2[c]
C(1)–N(1)	1.469(1)	1.478(5)	1.485(9)	1.469(14)	1.485(9)
N(1)–C(2)	1.335(1)	1.327(2)	1.337(9)	1.355(14)	1.316(9)
C(2)–C(3)	1.424(1)	1.427(2)	1.445(9)	1.360(20)	1.460(15)
C(3)–N(2)	1.332(1)	1.326(2)	1.319(8)	1.376(11)	1.279(8)
N(2)–C(4)	1.340(1)	1.346(2)	1.374(8)	1.279(8)	1.376(11)
C(4)–C(5)	1.456(1)	1.442(2)	1.447(11)	1.478(11)	1.364(14)
C(5)–O(1)	1.251(1)	1.249(2)	1.266(10)	1.222(13)	1.362(15)
BLA	0.036	0.024	0.006	0.116	-0.080

[a] Formula: C26H26N2O. FW: 382.49 g·mol^{-1}. Crystal system: monoclinic. Space group: $P2_1/c$ (no. 14). a: 9.1082(3) Å. b: 19.1136(7) Å. c: 11.4675(4) Å. $\alpha = 90°$. $\beta = 99.715(1)°$ $\gamma = 90°$. V: 1967.8(1) Å^3. $Z = 4$. ρcalc = 1.291 g·cm^{-3}. μ = 0.79 cm^{-1}. T: 90(1) K. λ: 0.71073 Å. R_1: 0.048. wR_2: 0.117. $R_1 = \Sigma||Fo| - |Fc|| / \Sigma|Fo|$. $wR_2 = [\Sigma(w(Fo^2 - Fc^2)^2) / \Sigma w(Fo^2)^2]^{1/2}$; $w = 1/[\sigma^2(Fo)^2 + (0.0648P)^2 + 0.6419P]$. [b] From reference[46]. [c] PMC-1 is the canonical neutral form, and PMC-2 is the canonical charge separated form with bond lengths taken from analysis of the crystallographic database; see ref[236]

BLAs of the canonical neutral (PMC-1) and charge-separated (PMC-2) forms utilizing bond lengths extracted from the Cambridge Crystallographic Database[236] were calculated, in which BLA > 0 for the neutral form and BLA < 0 for the charge-separated form, consistent with the trends found in general for π-conjugated polyenes.[234] The positive BLA values obtained for **2.1**–**2.3** (0.036, 0.024, and 0.006, respectively) suggest that the ground state electronic structures of **2.1**–**2.3** have a larger contribution from the neutral form. The contribution of the neutral form to the PMC structure in the ground state decreases along the series as **2.1** > **2.2** > **2.3** (Table 2.8), in which **2.1** has the greatest neutral character. An absence of electronegative nitrogen atom in the phenanthrene in **2.1** decreases the electron-withdrawing character of the oxazine moiety in **2.1** as compared to **2.2** and **2.3**. The more electron-rich oxazine in **2.1,** therefore, leads to less charge separation between an electron rich amine moiety and oxazine in the open-form.

2.2.6. Computational Studies

In order to understand the effects of structure and solvent on the kinetic parameters for thermal relaxation in the series, computations were carried out to model the effects of both on the thermal isomerization pathway. Two pathways have been proposed for the thermal ring opening and closure process: a rotation and an inversion pathway.[221] The rotation pathway requires two steps: C–O bond cleavage from the SO form to a TCC/CCC isomer followed by a *cis*-to-*trans* isomerization at the C–N *β*-bond to give the TTC/CTC isomers. The inversion pathway, on the other hand, involves C–O bond cleavage from the SO form to a TCC/CCC isomer and inversion at the central nitrogen to give the TTT/CTT isomers, followed by *trans*-to-*cis* isomerization at the γ-bond to generate the TTC/CTC

isomers. Previous computational studies suggest that energy barrier of the TTT/CTT → TTC/CTC *trans*-to-*cis* isomerization at the γ-bond is relatively high (~ 30 kcal·mol^{-1}). It's unlikely, therefore, that formation of the TTT/CTT isomers by thermal ring-opening would be followed by *cis-to-trans* isomerization to the TTC/CTC isomers.[221] Experimental evidence for the presence or absence of PMC isomers before and after thermal isomerization can be gleaned from spectroscopy. By ^{1}H NMR or XRD analysis, we observe only the TTC isomer and find no evidence for the presence of the TTT or CTT isomers. In addition, thermal relaxation processes follow monoexponential kinetics and not biphasic,[221] suggesting that spirooxazines **2.1**–**2.4** undergo thermal ring-opening via a single rotation pathway process. This is consistent with other spirooxazines and spiropyrans, in which the rotation pathway is proposed to be the dominant pathway computationally.[216,221,237,238] The rotation pathway can in principle generate two isomers, the TTC and CTC isomers. However, since the only distinction between forming the TTC *vs*. CTC is initial C–O bond cleavage to give either the S or R enantiomer of the spirooxazine, it is difficult to distinguish chirality of opening in the systems investigated in the absence of chiral resolution.

Geometry optimizations of the SO, TTC, and TCC forms for **2.1**–**2.4** were performed at the DFT/B3LYP level with the 6-31+G(d,p) basis set. The free energy difference (ΔG^o) for SO → PMC for the series **2.1**–**2.4** suggests that in all, the PMC form is more stable than the SO form (-4.8 kcal·mol^{-1}, -5.8 kcal·mol^{-1}, -2.1 kcal·mol^{-1}, and -1.5 kcal·mol^{-1} for **2.1–2.4**, respectively), with the energy difference being larger in **2.1** and **2.2** than in **2.3** and **2.4** (Table 2.9, Figure 2.17). Experimentally, however, the SO forms for **2.3** and **2.4** were found to be more stable than the PMC by 2–3 kcal·mol^{-1} in non-polar

solvents and within 1 kcal·mol^{-1} in polar solvents (Table 2.1). Computations performed with larger basis sets (i.e., 6-311+G (d,p) and the inclusion of solvation via the Onsager model did not lead to better agreement between the computational and experimental results. This is presumably due to the known tendency of DFT to preferentially stabilize delocalized π-conjugated systems over localized π-systems[239] which would lead to over-stabilization of the PMC form. The intermediate TCC forms for **2.1**–**2.4** and were found to be significantly higher in energy than the SO (8–12 kcal·mol^{-1}) and TTC forms (12–13 kcal·mol^{-1}) which is consistent with the TCC form being an intermediate along the PMC potential energy surface, and not a ground state.

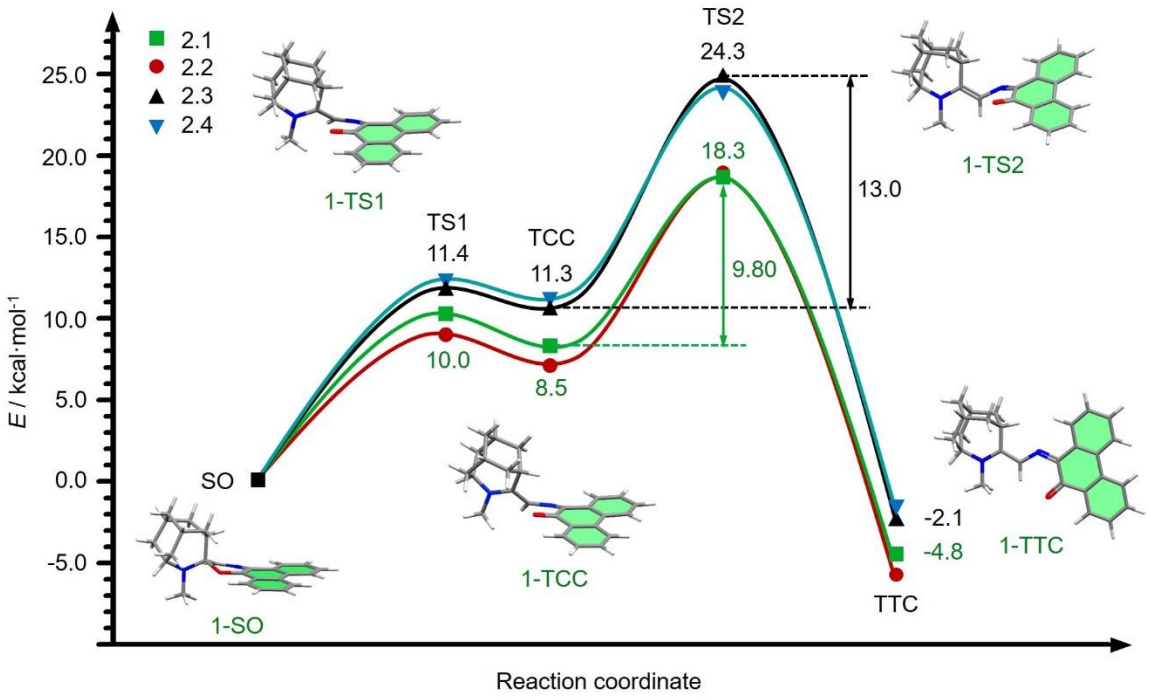

Figure 2.17. Ground state potential energy profile for the thermal coloration and decoloration of **2.1**–**2.4**. (B3LYP/6-31+G(d,p)).

Table 2.9. Relative energies (kcal·mol^{-1}) of optimized structures of the SO, TTC, TTC isomers and TS relative to the SO form of **2.1**–**2.4**.[a]

	SO	TS1	TCC	TS2	TTC
2.1	0	10.0	8.5	18.3	-4.8
2.2	0	8.8	7.6	18.4	-5.8
2.3	0	11.4	11.3	24.3	-2.1
2.4	0	11.8	11.8	23.9	-1.5

[a] DFT/B3LYP/6-31+G(d,p) without solvation using the Onsager model.

The optimized geometries of the TCC, and TTC forms allow computational prediction of the degree of bond length alternation (BLA) analysis and in turn, the degree of D-A charge separation in spirooxazines in **2.1**–**2.4**. The BLA parameters calculated for the optimized structures of the TTC forms for **2.1**–**2.4** were all found to be positive (0.21, 0.20, 0.20, and 0.20, respectively, Table 2.10), and larger than those obtained experimentally in the solid state by XRD analysis. The BLA analysis suggests that the computational geometries are more localized than the experimental geometries perhaps due either to challenges in DFT modeling of electronic structures of charge-separated systems,[240] or the extreme sensitivity of PMC structures to the dielectric of the medium, which may differ in the crystalline state *vs.* gas phase. The TTC form of **2.1** was predicted to have the least charge-separated character along the series, which is consistent with the experimental BLA parameters. The BLA parameter calculated for the optimized structure of the TCC forms for **2.1**–**2.4** were also all found to be positive (0.19, 0.17, 0.12 and 0.12, respectively, Table 2.10), suggesting less D-A character in the TCC form as well. The BLA analysis of the computational geometries of the TTC and TCC for **2.1**–**2.4** suggests that the degree of charge-separated character in the TTC is correlated with the D-A character of the TCC. In both the TTC and TCC, compounds **2.3** and **2.4** have the greatest D-A character

while compound **2.1** has the least. The trend is supported within error by the computational dipole moments of the series. The largest dipole moments for the TCC and TTC forms were found in compound **2.2,** while the smallest dipole moments were found in **2.1**. Unexpectedly, the dipole moments of the TCC and TTC forms in **2.3** and **2.4** were smaller than **2.2**, even though the charge-separated character of the PMC form in **2.3** and **2.4** were significant. The discrepancy may be due to the contribution of distance between point charges to the dipole moment, in which the dipole moment $\mu = q \times \mathrm{d}$, where q is the magnitude of charges, and d is the center-to-center distance between point charges. A smaller effective distance between the positively-charged azahomoadamantyl and negatively-charged quinolyl-oxazine moiety in **2.3** and **2.4** is predicted, based on molecular geometry, which, assuming similar magnitudes of "point" charge (q) would lead to an effective decrease in the dipole moment, relative to **2.2**. Overall, computational analysis of the PMC-TTC forms, as metastable states, provides significant insight into the D-A character of both ground state structures and intermediates along the thermal isomerization pathway.

Table 2.10. Dipole moment of optimized structures (BLA) of 2.1–2.4 in Debye.[a]

	Dipole moment					BLA	
	SO	TS1	TCC	TS2	TTC	TCC	TTC
2.1	3.0	7.4	5.1	2.0	6.1	0.19	0.21
2.2	6.1	11.2	9.3	1.9	9.9	0.17	0.20
2.3	5.5	8.7	7.7	2.6	6.5	0.12	0.20
2.4	4.1	9.0	8.3	2.0	9.0	0.12	0.20

[a] DFT/B3LYP/6-31+G(d,p) without solvation using the Onsager model.

Geometry optimization of the transition states for the thermal SO → TCC (TS1) and TCC → TTC (TS2) coloration process of spirooxazines **2.1**–**2.4** were performed at the

DFT/B3LYP level with 6-31+G (d,p) basis set using a quadratic synchronous transit approach[241] (QST2 for **2.1** and **2.2** and QST3 for **2.3** and **2.4**). For the series **2.1**–**2.4**, the *cis*-to-*trans* isomerization at the C–N *β*-bond from the TCC isomer to the TTC isomer was found to be the rate limiting step for thermal SO → PMC (k_1) and PMC → SO relaxation process (k_2). The activation energies for C-O bond cleavage (TS1) for the series **2.1**–**2.4** were found to be smaller (10.0, 8.8, 11.4, and 11.8 kcal·mol^{-1}, respectively) than the activation energies for *cis*-to-*trans* isomerization (TS2) in energy (18.3, 18.4, 24.3, and 23.9 kcal·mol^{-1}, respectively, Table 2.9). A larger activation energy for TS2 over TS1 was found for the series **2.1**–**2.4** for both the thermal SO → PMC and PMC → SO relaxation processes. The TS2 of **2.3** and **2.4** (24.3 and 23.9 kcal·mol^{-1}, respectively) were found to be higher than **2.1** and **2.2 (**18.3 and 18.4 kcal·mol^{-1}, respectively) which is consistent with the kinetic data. The larger TS2 energy suggests that *cis*-to-*trans* isomerization at the C–N *β*-bond from the TCC isomer to the TTC isomer is rate limiting step for both thermal SO → PMC (k_1) and PMC → SO relaxation process (k_2) shown in Figure 2.17. The similarity for the TS2 energies for both compounds **2.1** and **2.2** are surprising, as both the TCC and TTC isomers differ in structure and energy between the two spirooxazines. This may be due to the poor reproducibility of multiconfigurational structures with single configurational DFT, and the tendency of DFT to over-delocalize conjugated structures.[239]

2.2.7. Structural Correlation of the Spirooxazines in Solution and Solid States with Thermal Relaxation Rates

A preliminary examination of the energy relationship between $\Delta G_{(PMC\text{-}SO)}$ and the rate of thermal SO → PMC relaxation (k_1) for the series of spirooxazines reveals that a

simple linear free energy relationship (LFER) between the ground state energies of the PMC-TTC and SO structures and rate of thermal isomerization between those forms does not hold for the spirooxazines **2.1**–**2.4**. Due to the general instability of the PMC in the spirooxazine/spiropyran class, the relationship of $\Delta G_{(PMC\text{-}SO)}$ to (k_1) and (k_2) has not been determined for any other spirooxazine or spiropyran, so it's not clear whether the lack of LFER in this case is specific to this series of compounds, or is a general phenomenon. The lack of a LFER however suggests that the TTC isomer may not be the isomer involved in the rate-determining step for SO → PMC thermal relaxation pathway. Computational studies suggest that the rate-determining step of the rotation pathway is the *cis*-to-*trans* isomerization at the C–N β-bond from the TCC isomer to the TTC isomer. Based on the Hammond postulate, the TCC isomer will dictate the energy barrier for thermal isomerization. In the rotation pathway, the initial C–O bond cleavage step is endothermic implying the energy and structure of TS1 are dictated by the energy and structure of the TCC form (Figure 2.17). The following *cis*-to-*trans* isomerization step (TS2) is however exothermic, suggesting that the energy and structure of the TS2 are also dictated by the TCC form. Hence, the structure and energy of the TCC form governs the activation energies for both TS1 and TS2, and in turn the SO → PMC (coloration) and PMC → SO (decoloration) thermal isomerization pathways.

Both solid state and solution state analysis suggest that the PMC has less charge separated character in **2.1**, relative to spirooxazines **2.2**–**2.4**, and it is observed that **2.1** also has the fastest rate of thermal relaxation. This suggests that a correlation between rates of thermal isomerization and the degree of bond length alternation in the open PMC form may exist. Figure 2.18 shows a correlation of the BLA parameters of the TTC forms for **2.1**–**2.3**

with k_1 and k_2 in a series of solvents. In general, the rates of thermal relaxation in both directions (k_1 and k_2) increase as the BLA increases, and the correlation is independent of the solvent polarity (Figure 2.18). The correlation of rates (k_1 and k_2) and BLA holds for both the TTC and TCC isomers, as shown in Figure 2.19a, for TTC forms for **2.1**–**2.3**. A similar correlation was found for the computationally derived BLA parameters of the TCC form and the rates of thermal isomerization. Lastly, a linear correlation of the magnitude of BLA with the slope of the solvatochromism (Figure 2.20) indicates that the degree of charge-separated character in the PMC form correlates with the bond length alternation parameters, which in turn is correlated with the rate. Thus, the D-A character of both the TTC and TCC, which are dictated by structure and solvent, correlates linearly with rate of thermal relaxation.

If the *cis*-to-*trans* isomerization at the C–N β-bond is the RDS, as computational studies suggest, the thermal coloration rate (k_1) is dictated by both TS1 and TS2 while the thermal decoloration rate (k_2) is dictated by only TS2. An increase in dielectric will result in an increase of the charge-separated character of the TTC isomers of **2.1**–**2.4**, and a concomitant change in energy of the TTC form. The charge-separated character of the TCC intermediate is expected to become greater as well, which would affect the structure and energy of TS1 and TS2 as a function of solvent polarity. Conversely, the thermal decoloration rate (k_2) is predominantly dictated by TS2 (Figure 2.17). A decrease in thermal decoloration kinetics (k_2) with increasing solvent polarity is consistent with increasing the charge-separated character of the TCC isomer and in turn the C–N double bond character of the TCC intermediate, which leads to slower thermal coloration rates in more polar media.

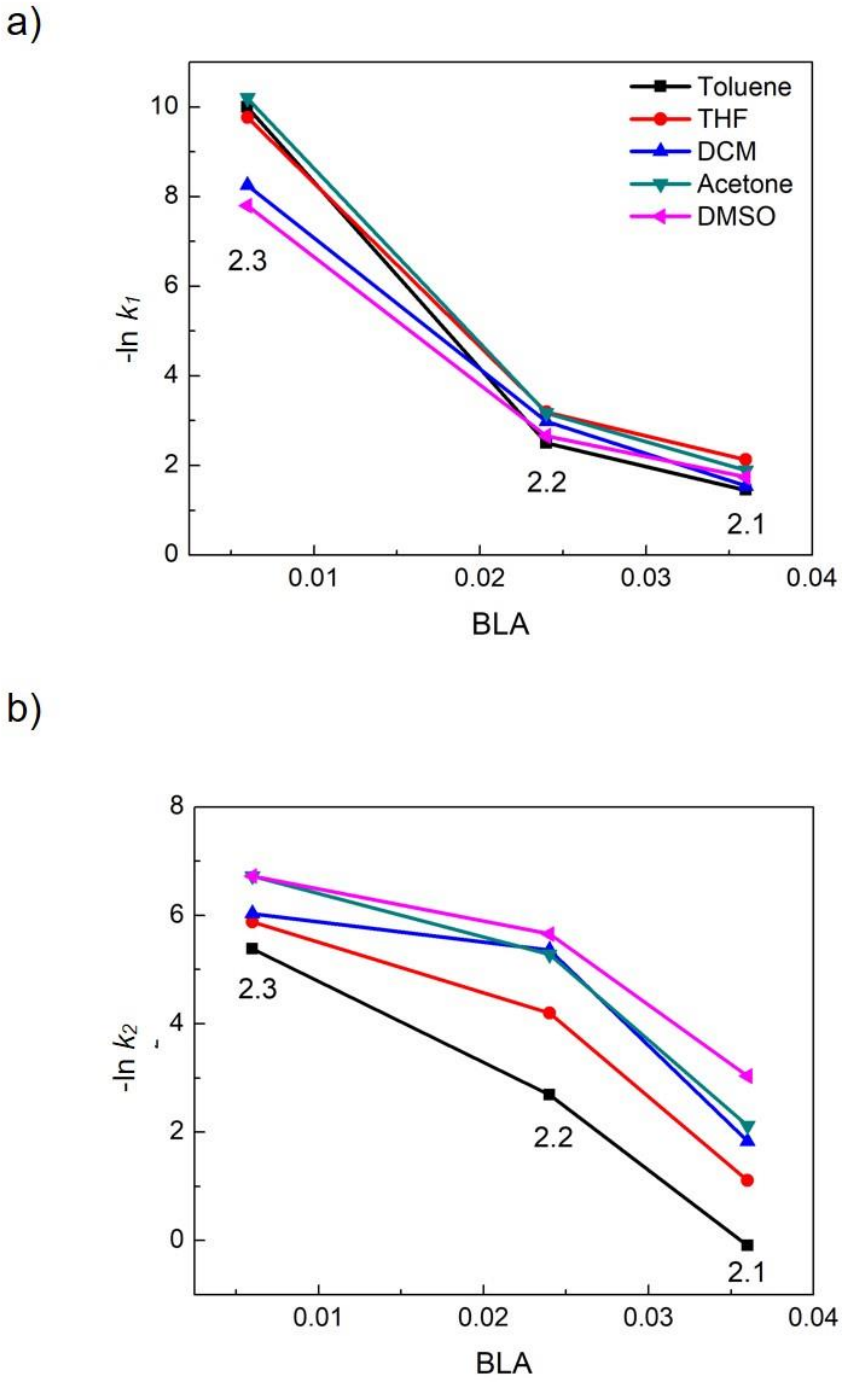

Figure 2.18. Correlation of structural parameter BLA and thermal coloration rates k_1 (a), thermal decoloration rates k_2 in a series of solvents (b).

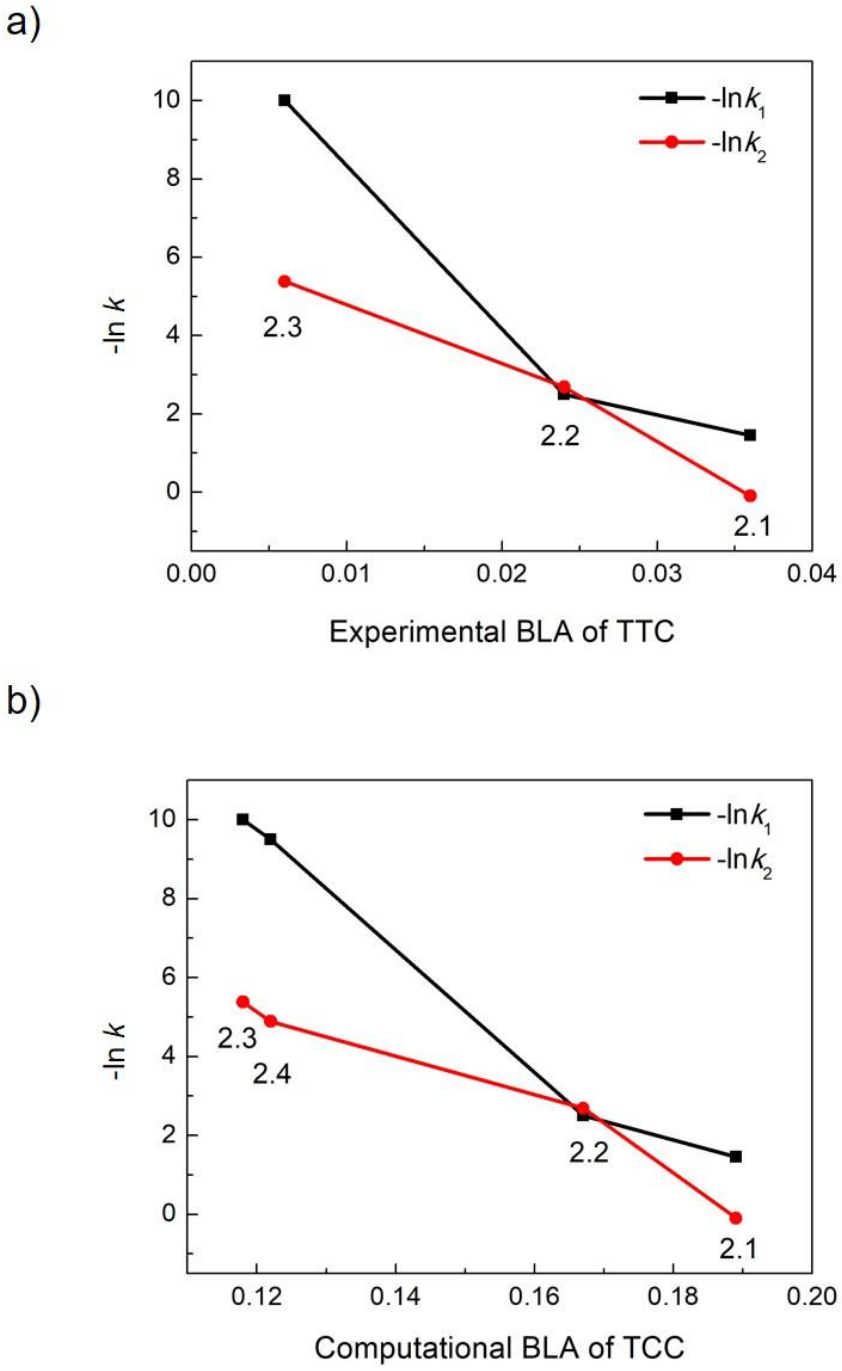

Figure 2.19. Correlation of thermal coloration rates k_1 and thermal decoloration rates k_2 in toluene with experimental BLA parameters of the TTC isomer (a), and optimized geometry of the TCC isomers of a series **2.1**–**2.4** (b).

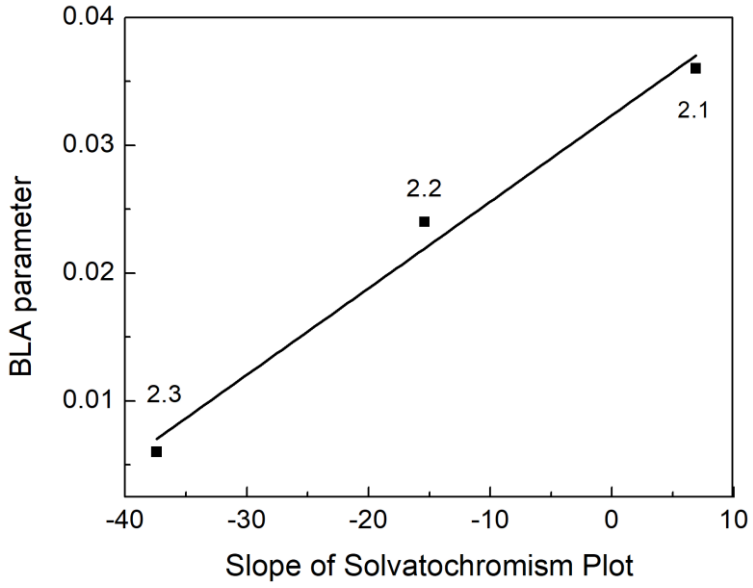

Figure 2.20. BLA of **2.1**–**2.3** as a function of the slope of solvatochromism plot.

Analysis of the electronic structures of the PMC form by spectroscopic techniques in association with computational analysis supports that the spirooxazines **2.1**–**2.4** undergo a rotation pathway. In light of the spectroscopic data, an increase in C–N single bond character (Figure 2.21) would lead to a decrease in the activation energy for C–N β-bond rotation (TS2), which is found to be the rate-determining step. Poor D-A character (neutral, PMC-1) would lead to faster thermal coloration kinetics, as is observed in compound **2.1**. Greater D-A character (charge-separated, PMC-2) of the PMC electronic structure would lead to slower thermal coloration kinetics, as is observed for compound **2.3** and **2.4**. The TS2 is governed by the electronic structure and the energy of the TCC intermediate, and in support of this argument, a linear correlation between the D-A character of the TTC and TCC isomers and the thermal relaxation kinetics is indeed found.

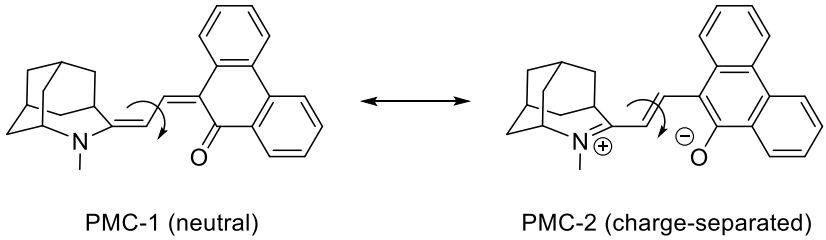

Figure 2.21. β-bond rotation in the PMC-1 (neutral) and PMC-2 (charge-separated) from.

Both computation and structural correlation studies support the hypothesis that a greater charge-separated character (D-A character) in the PMC form leads to slower coloration kinetics in the series of spirooxazines. The BLA parameters obtained by computation are consistent with the experimental results, suggesting that the donor-acceptor character of the PMC form can reasonably be estimated by the geometry optimized structures of TCC and TTC. This becomes valuable in the greater class of spiropyrans and spirooxazines in which the PMC form is metastable and cannot be characterized structurally by experiment. The computational study also suggests that the TCC form governs the activation energies for the thermal coloration as well as thermal decoloration. The structural dependency of thermal coloration (k_1) and decoloration (k_2) can be estimated computationally by calculating BLA of the TCC form and its donor-acceptor ability.

2.3. Conclusions

Spirooxazines are an important class of photochromes that exhibit unusually high fatigue resistance, high photoresponsivities, exquisite sensitivity to the environment, and both positive and negative photochromism. Knowledge of the structural parameters that

dictate the thermal isomerization barrier allows the control of the switching rates of photochromic spirooxazines for a wide range of applications from single molecule memory to switching materials in biology. Analysis of the bond length alternation (BLA) parameters in the solid state, along with vibronic analysis and solvatochromism of the PMC band reveal that the structure of the PMC form dictates the rates of thermal relaxation. A correlation of BLA analysis, vibronic coupling, and solvatochromism with the rate of thermal coloration, suggest that greater D-A charge-separated character of the spirooxazines leads to slower thermal coloration rates. The correlations found in this work support the rotation pathway as the dominant pathway. Greater charge-separated (D-A) character leads to greater double bond character at β-bond resulting in slower *cis*-to-*trans* isomerization (the rate-determining step) and slower thermal relaxation. Conversely, greater quinoidal or neutral character, as estimated by the BLA, leads to faster thermal relaxation kinetics. This study suggests that perturbation of the electronic structure of spirooxazines towards either more charge-separated or neutral character in the ground state allows modulation of the rate-determining step of thermal coloration, providing insight into the design principles necessary for controlling thermal relaxation rates in spirooxazines at the molecular level. Such parameters can be determined computationally in cases where the experimental structures are not known, making this correlation extremely valuable as a predictive tool. Given the high fatigue resistance, rapid and robust photochemical conversions of the spirooxazines, such structural principles for improving the class of photochromes are critical for development of switching materials in materials and biological applications.

2.4. Experimental and Theoretical Methods

2.4.1. Synthesis of Spirooxazines

All reagents were purchased from commercial sources and used without further purification unless otherwise specified. Spectroscopic-grade CH_2Cl_2 was acquired from an MBraun solvent purification system. Triethylamine was dried over and distilled from KOH. Compounds **2.2**–**2.4** were synthesized according to previously reported methods[46] and characterized by ^1H, ^{13}C NMR and IR spectroscopy.

Spiro[azahomoadamantane-phenanthreneoxazine] (APESO, 2.1). Triethylamine (0.98 mL, 7.03 mmol) was added to a solution of 5-methyl-4-azahomoadamant-4-enium iodide[46] (**2.7**) (1.061 g, 3.48 mmol) in CH_2Cl_2 (150 mL), and the solution was stirred at 0 °C for 20 minutes. Hydroxy-nitroso-phenanthrene (**2.9**) (777 mg, 3.48 mmol) and molecular sieves were added, and the solution was allowed to warm r.t. and heated to reflux in the absence of light for five hours. The solution was cooled, filtered, and the solvent removed *en vacuo*. The compound was purified by silica gel column chromatography with EtOAc as eluent to give 600 mg (59 %) of a polycrystalline solid. ^1H NMR (300 MHz, $CDCl_3$) PMC form: δ 9.82 (s, 1H), 8.48 (dd, *J* = 7.5, 1.5 Hz, 1H), 8.40 (dd, *J* = 9.0, 3.0 Hz, 1H), 8.24 (br d, *J* = 6.0, 1H), 8.16 (br d, *J* = 6.0, 1H), 7.44 (ddd, *J* = 9.0, 3.0, 3.0, 1H), 7.39 (ddd, *J* = 6.0, 6.0, 3.0 Hz, 1H), 7.29 (ddd, *J* = 9.0, 9.0, 1.5 Hz), 5.17 (br s, 1H), 3.68 (quintet, *J* = 2.1 Hz, 1H) , 3.45 (s, 3H); SO form: δ 8.62 (m, 1H), 8.57 (m, 2H), 8.35 (m, 1H), 7.51 (ddd, *J* = 9.0, 9.0, 3.0 Hz, 1H), 7.71 (s, 1H), 3.16 (br t, *J* = 5.1 Hz, 1H), 2.51 (s, 3H), 2.59–2.41 (m, 1H), 2.27 (m, 1H), 1.39 (d of sept, *J* = 13.5, 2.6 Hz, 1H) ppm; PMC + SO: δ 7.66–7.57 [m, 1H (PMC), 3H (SO)], 2.16–1.57 [m, 12H (PMC), 10H (SO)]. ^{13}C NMR (300 MHz, δ, $CDCl_3$) PMC and SO forms: 177.2 (C), 176.7

(C), 157.2 (CH), 136.3 (C), 135.3 (C), 133.2 (C), 131.2 (CH), 131.1 (C), 130.5 (C), 130.3 (C), 127.9 (CH), 127.2 (CH), 127.1 (C), 126.8 (C), 126.7 (CH), 126.5 (CH), 126.1 (C), 125.3 (C), 124.8 (CH), 124.3 (CH), 123.8 (CH), 123.7 (CH), 122.7 (CH), 122.6 (CH), 122.5 (CH/CH_3), 122.4 (CH), 122.3 (CH), 122.1 (CH), 120.3 (C), 94.3 (C), 76.6 (C), 63.8 (CH), 58.8 (CH), 42.7 (CH), 40.1 (CH_2), 39.6 (CH), 38.0 (CH), 36.2 (CH_2), 34.4 (CH_2), 33.4 (CH_2). 32.8 (CH_2), 30.3 (CH_2), 30.1 (CH_2), 26.9 (CH/CH_3), 26.9 (CH/CH_3). FT/IR (cm^{-1}, KBr): 3062 (w, sp^2 C–H), 2906 (s, sp^3 C–H), 2845 (m, sp^3 C–H), 1547 (s, C=N), 1441 (s, CH_2), 1418 (s, CH_3), 1228 (s, C–O), 1094 (s, C–N), 757 (m, sp^2 C–H), 726 (m, sp^2 C–H). EI-MS: *m*/*z* (%) 382 (25) [M]+, 163 (100). Anal. Calcd for $C_{26}H_{26}N_2O$: C, 81.64; H, 6.85; N, 7.32. Found: C, 81.58; H, 6.83, N, 7.16. Cyclic Voltammetry PMC form: a reversible process with half potential $E_{1/2}$ = -1.30 V (ΔE_p = 0.065 V, i_a/i_c = 1.28); SO form: a quasirreversible reduction process with an anodic peak potential E_{pa} = -0.55 V.

5-Methyl-4-azahomoadamant-4-ene (2.6). ^{1}H NMR (300 MHz, δ, $CDCl_3$): 3.95 (quintet, *J* = 3.0 Hz, 1H), 2.54 (septet, *J* = 2.4 Hz, 1H), 2.04 (quintet, *J* = 2.6 Hz, 2H), 1.97 (s, 3H), 1.76–1.68 (m, 6H), 1.66–1.58 (m, 4H,) ppm. ^{13}C NMR (300 MHz, $CDCl_3$): 178.5 (C), 54.5 (CH), 40.7 (CH), 35.6 (CH_2), 33.2 (CH_2), 30.9 (CH_2), 29.5 (CH), 27.9 (CH_2) ppm. FT/IR (cm^{-1}, KBr): 2909 (m, sp^3 C–H), 2831 (m, sp^3 C–H), 1666 (s, C=N), 1436 (s, CH_3), 1101 (s, C–N).

5-Methyl-4-azahomoadamant-4-enium Iodide (2.7) ^{1}H NMR (300 MHz, δ, $CDCl_3$): 4.20 (tt, *J* = 6.0, 3.0 Hz, 1H), 3.87 (s, 3H), 3.15 (t, *J* = 6.2 Hz, 1H), 2.83 (s, 3H), 2.43 (t, *J* = 4.2 Hz, 1H), 2.38 (t, *J* = 4.6 Hz, 1H), 2.30 (s, 1H), 2.25 (t, *J* = 3.0 Hz, 1H), 2.19 (quintet, *J* = 3.0 Hz, 2H), 1.98–1.74 (m, 6H) ppm. ^{13}C NMR (300 MHz, $CDCl_3$): 196.3 (C), 67.0 (CH), 48.4 (CH), 41.6 (CH/CH_3) 32.6 (CH_2), 30.0 (CH_2), 28.7 (CH), 27.8

(CH_2), 24.6 (CH_3) ppm. FT/IR (cm^{-1}, KBr): 2918 (m, sp^3 C–H), 2883 (m, sp^3 C–H), 2849 (m, sp^3 C–H), 1664 (s, C=N), 1416 (s, CH_3), 1107 (s, C–N).

5-hydroxy-6-nitroso-phenanthrene (2.9) ^{1}H NMR ($CDCl_3$, 300 MHz): δ 8.36 (ddd, J = 14.1, 8.0, 0.6 Hz, 2H), 8.16 (br d, J = 8.3 Hz, 1H), 8.09 (br d, J = 8.0 Hz, 1H), 7.77 (ddd, J = 8.2, 7.3, 1.5 Hz, 1H), 7.55–7.41 (m, 3H) ppm.

2.4.2. Spectroscopic Methods

Electronic absorption spectra were recorded on an Agilent 8453 spectrophotometer equipped with a photodiode array and Peltier temperature control. Sample solutions (concentration of 10^{-4} M–10^{-5} M) were prepared under inert conditions in degassed spectroscopic grade solvents. All experiments were carried out at 298 K in the dark, with continuous stirring. Excitation experiments were carried out via multiline irradiation (514, 532, 568 nm) with a Spectra-Physics Stabilite 2018 mixed gas Ar-Kr ion laser, and directed to the sample via with a Newport liquid light guide. The power at the sample was measured with a Spectra-Physics 407A power meter with typical powers of 100–300 mW. The rates of thermal relaxation were determined in the absence of light by following the intensity of the PMC π–π^* absorption band ($\lambda_{max} \approx 555$ nm) with 0.5 second interval after generation of the photostationary state. Each data set was fit to the monoexponential function by linear least square analysis. Multiple cycles (3 or more) were averaged to give the final rate constants. ^{1}H NMR spectra were acquired with Brucker AC 300 spectrometer and Bruker AVANCE 500 spectrometer in a series of solvents at 300 K and spectra were calibrated to the residual solvent peaks. Two-dimensional NOESY NMR was recorded on 500 MHz Bruker AVANCE 500 spectrometer in $CDCl_3$ at 300 K. FT-IR spectra were acquired as

KBr pellets with a Perkin Elmer Spectrum One spectrometer. The EI mass spectrum of **2.1** was recorded with a double focusing mass spectrometer (Kratos MS-50) coupled with a MASPEC data system by mass spectroscopy center (UBC). Elemental analysis was performed by Canadian Microanalysis Services.

2.4.3. Computational Methods

Geometry optimization calculations of the SO, TCC, TTC form of **2.1**–**2.4** were performed using density functional theory (DFT) with the hybrid Becke-style three-parameter exchange functional[242] and the Lee-Yang-Parr correlation functional (B3LYP)[243] using a 6-31+G(d,p) basis set with the Gaussian 09 software package.[244] The optimizations for structures **2.1**–**2.3** were performed using a starting geometry from X-ray diffraction analysis atomic coordinates. The optimization for structure **2.4** was performed using a modified X-ray diffraction analysis atomic coordinates of **2.3** as a starting geometry. Solvent effects were modeled in H_2O ($\varepsilon = 78.39$) using the Onsager model with a_0 values of 5.97 Å (SO) and 5.88 Å (PMC) for **2.1** and 5.99 Å (SO) and 5.95 Å (PMC) for **2.2** as determined by a volume calculation in Gaussian. Stability and frequency calculations were performed on all optimized geometries obtained from gas-phase calculations, and structures were found to be minima on the potential energy surfaces. Transition states of **2.1** and **2.2** were calculated using quadratic synchronous transit approach (QST2),[241,245] and transition states of **2.3**–**2.4** were calculated using QST3).[245]

2.4.4. X-ray Crystallography

X-ray crystallographic data of **2.1** was collected and solved by Brian O. Patrick (UBC). A purple prism crystal of $C_{26}H_{26}N_2O$ having approximate dimensions of 0.28 x 0.34 x 0.36 mm was mounted on a glass fiber. All measurements were made on a Bruker DUO APEX II diffractometer with graphite monochromated Mo-Kα radiation. The data were collected at a temperature of -183.0 $\pm$ 0.1 °C to a maximum 2θ value of 60.1°. Data were collected in a series of ϕ and ω scans in 0.50° oscillations with 3.0-second exposures. The crystal-to-detector distance was 40.00 mm. Of the 34928 reflections that were collected, 5751 were unique (R_{int} = 0.020); equivalent reflections were merged. Data were collected and integrated using the Bruker SAINT software package.[246] The linear absorption coefficient, μ, for Mo-Kα radiation is 0.79 cm^{-1}. Data were corrected for absorption effects using the multi-scan technique (SADABS),[247] with minimum and maximum transmission coefficients of 0.914 and 0.978, respectively. The data were corrected for Lorentz and polarization effects. The structure was solved by direct methods.[248] All non-hydrogen atoms were refined anisotropically. All hydrogen atoms were placed in calculated positions. The final cycle of full-matrix least-squares refinement $\Sigma w(F_o^2 - F_c^2)^2$ on F^2 was based on 5751 reflections and 263 variable parameters and converged (largest parameter shift was 0.00 times its esd) with unweighted and weighted agreement factors of $R_1 = \Sigma \, ||F_o| - |F_c|| \, / \, \Sigma \, |F_o| = 0.048$ and $wR_2 = [\Sigma(w(F_o^2 - F_c^2)^2)/\Sigma w(F_o^2)^2]^{1/2} = 0.117$. The standard deviation of an observation of unit weight $\{[\Sigma w(F_o^2 - F_c^2)^2/(N_o - N_v)]^{1/2}$ where N_o is the number of observations and N_v is the number of variables was 1.03. The weighting scheme was based on counting statistics. The

maximum and minimum peaks on the final difference Fourier map corresponded to 0.48 and –0.18 e^-/Å,[248] respectively. Neutral atom scattering factors were taken from Cromer and Waber.[249] Anomalous dispersion effects were included in F_{calc};[250] the values for Δf' and Δf" were those of Creagh and McAuley.[251] The values for the mass attenuation coefficients are those of Creagh and Hubbell.[252] All refinements were performed using the SHELXL-97[253] via the WinGX interface[254]

Chapter 3. The Effect of Metal Complexation on the Photochromic Properties of Spirooxazines

3.1. Introduction

Photochromic compounds are those that can undergo a reversible reaction between two states in response to external stimuli such as light exposure, leading to concomitant changes in molecular structure, electronic structure and optical properties. This concept allows for the design of light-induced molecular switches and even more complex systems such as logic gates.[203,255-257] For practical applications, it is crucial to maintain the most critical photochromic properties such as high fatigue resistance, fast switching speed, and desirable (slow/irreversible) thermal relaxation rates at ambient temperatures. Although improvements have been made in increasing fatigue resistance (thermal and photostability) and switching speeds (photochemical processes), the modulation of thermal relaxation rates in most photochromes remains a challenge.

Among the molecular classes of photochromic compounds, spirooxazines are perhaps the most heavily utilized in practical applications due to their high colorability and fatigue resistance. The incorporation of spirooxazines into transition metal coordination complexes is a powerful strategy for the development of photoswitchable multifunctional materials that allow optical modulation of electrical or magnetic properties.[258] Photoinduced or thermal isomerization leads to two metastable states, a closed spirooxazine (SO) and photomerocyanine (PMC) form, which have significantly different electronic structures. This difference in electronic structure alters the ligand field around ligand-bound transition metals, leading to changes in the electronic structure, redox

properties, and spin state of the transition metal center. Coordination of a metal center by a photochromic ligand results in not only in changes about the metal center but also significant modulation of the electronic structure of the spirooxazine ligands and their photochromic properties. We have previously reported a series of metal-spirooxazine $[M(IPSO)_3]^{2+}$ complexes (IPSO = spiro[indoline-phenanthrolinoxazine], M = Co(II), Ni(II), Mn(II), Fe(II), Fe(III), Cu(II), Zn(II)) that exist as non-transient species due to metal complexation of the phenanthroline moiety of a spirooxazine ligand.[258,259] Metal complexation gives rise to extremely large photochromic responses relative to the parent spirooxazine, and leads to a significant stabilization of the PMC form. In addition, a decrease in thermal fading rates and an increase in photoresponsivity of up to an order of magnitude were observed for some metal complexes.[259] This proof-of-principle study demonstrated that metal complexation is an effective method to tune the photoresponsivity and thermal equilibrium state (K_T =[PMC]/[SO]) of spirooxazines. However, the effect of metal complexation is dependent on both electronic and structural character of the metal center and photochrome. It was therefore of interest to examine the effect of metal complexation with a Lewis acidic metal center (M = Mn(II), Co(II), Ni(II), Fe(II)) to provide insight into how the nature of metals and ancillary ligands affects the photochromic properties of spirooxazine-metal complexes.

Herein, we report the investigation of the effects of metal complexation in a series of azahomoadamantyl-phenanthroline spirooxazines (**2.2**). The azahomoadamantyl spirooxazines are a series of photochromes that exhibit negative photochromism, in which the PMC form is the ground state and the closed SO form is the metastable state. As metal complexation was found previously to stabilize the PMC form of indolylspirooxazines,[259]

it was reasoned that greater stabilization of the PMC form may be induced by metal complexation perhaps leading to >90% of the open PMC form. In addition, as greater photoresponsivity was observed with metal complexation of IPSO,[258] the combination of increased photoresponsivity and shift toward the open form may lead to an effective strategy for increasing photocolorability in spirooxazines.

A series of metal complexes in which three photochromes are bound to a single metal center $M(APSO)_3(BPh_4)_2$ **3.2** where M = Mn(II) **3.2a**, Fe(II) **3.2b**, Co(II) **3.2c** were investigated to determine the effect of metal complexation on the photochromic properties of azahomoadamantyl-based spirooxazine **2.2** in comparison to indolyl-based spirooxazine. In addition, the effect of ancillary ligands on the Lewis acidity, and in turn photochromic properties of the photochromic ligand **2.2** was investigated through a series of $M(APSO)(hfac)_2$ complexes **3.1** where M = Mn(II) **3.1a**, Co(II) **3.1b**, Ni(II) **3.1c** (Figure 3.1). The investigations were carried out through synthesis and optical spectroscopy to characterize the effects of metal complexation on spirooxazine colorabilities.

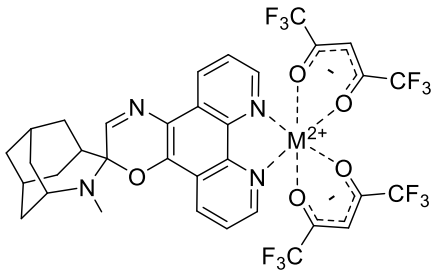

M = Mn(II) **3.1a**, Co(II) **3.1b**, Ni(II) **3.1c**

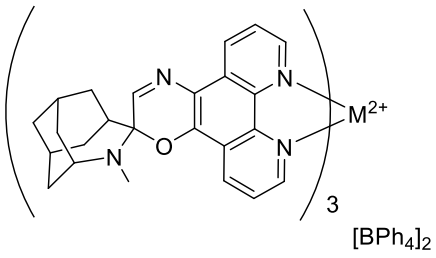

M = Mn(II) **3.2a**, Fe(II) **3.2b**, Co(II) **3.2c**

Figure 3.1. Structure of $M(APSO)(hfac)_2$ **3.1** where M = Mn(II) **3.1a**, Co(II) **3.1b**, Ni(II) **3.1c**, and $M(APSO)_3(BPh_4)_2$ **3.2** where M = Mn(II) **3.2a**, Fe(II) **3.2b**, Co(II) **3.2c**.

3.2. Results and Discussion

3.2.1. Synthesis of the M(APSO)(hfac)$_2$ and M(APSO)$_3$(BPh$_4$)$_2$

The M(APSO)(hfac)$_2$ series **3.1(a-c)** were synthesized by complexation of one equivalent of the spirooxazine **2.2** with one equivalent of M(hfac)$_2$ in degassed methanol. A purple precipitate formed which was isolated and washed with H_2O and THF to yield a dark purple powder in all cases. The composition was confirmed by elemental analysis and ESI-mass spectroscopy, which was consistent with a metal center with one bound spirooxazine **2.2** and two hfac ligands. Mass spectroscopy of spirooxazine complexes typically lead to fragmentation and disproportionation, making mass spectral analysis complicated. [M(APSO)$_2$(hfac)] type of fragments is typically seen as neutral M(APSO) complexes, which is either the charge rearrangement product or the oxidation product resulting from high oxygen sensitivity of the complex in solution.[260] The M(APSO)$_3$(BPh$_4$)$_2$ **3.2(a–c)** were synthesized by complexation of three equivalents of spirooxazine **2.2** with MCl_2 in degassed methanol, followed by precipitation with a methanol solution of two equivalent of $NaBPh_4$. The precipitate was isolated and was washed with H_2O and diethyl ether to yield a purple powder. The composition was confirmed by elemental analysis and ESI-mass spectroscopy, which was consistent with three spirooxazines bound to a metal center. The elemental analysis suggested a large amount of residual water present in the sample presumably due to the hygroscopic nature of the ligand. Attempts to crystallize both complexes **3.1(a–c)** and **3.2(a–c)** in non-polar or polar solvents resulted in the formation of crystalline aggregates that exhibited birefringence typical of spirooxazine aggregates, attributed to the zwitterionic character of the PMC form,[259] but which did not allow structural characterization by single crystal XRD.

3.2.2. Effect of Metal Complexation on the Thermal Equilibrium of 2.2

A thermal equilibrium exists between the SO and PMC forms that is dependent on temperature, solvent, and dielectric of the medium (Figure 3.2).[46] The thermal equilibrium constant K_T (K_T = [PMC]/[SO]) was obtained for the parent spirooxazine **2.2** in THF-d_8 at 298 K from the ^{1}H NMR spectrum. Determination of the thermal equilibrium constant was carried out using the integration for the azomethine proton of the PMC and SO forms, which have chemical shifts of 9.55 ppm and 7.65 ppm, respectively. Using the relative integrations, a thermal equilibrium constant of K_T = 2.7 (73 % PMC) was found. This indicates that the PMC isomer is substantially more stable than the SO isomer of the parent spirooxazine in THF, in contrast to all other known photochromic spirooxazines. Attempts to determine the thermal equilibrium constants of the metal complexes **3.1(a–c)** were made using the same techniques as those used for the parent ligands. However, the presence of unpaired spins in the paramagnetic transition metal centers led to very complicated ^{1}H NMR spectra. Assignments were made difficult due to the paramagnetic shifting and broadening, especially for the Mn complex **3.1a**. Since the number of unpaired electrons on the metal centers decreases as Mn (S = 5/2) > Co (S = 3/2) > Ni (S=1), the order of the paramagnetic shift is expected to be Mn > Co > Ni, leading to the greatest paramagnetic shifts and broadening in the manganese complex, as is observed. Tentative assignment could be made by comparison to the parent ligand. The thermal equilibrium constants for parent spirooxazine **2.2** and the series of M(APSO)(hfac)$_2$ **3.1(a–c)** are shown in Table 3.1. The equilibrium constants (K_T) for **3.1(a–c)** in THF-d_8 were found to be greater than 25 (95% PMC) which is 95 ± 5% based on the detection limit of ^{1}H NMR by integration. The equilibrium constants K_T of the M(APSO)(hfac)$_2$ **3.1(a–c)** were also recorded in toluene-

d_8 to determine whether any differences in K_T would be observed across the series of metal complexes in a less polar solvent. The equilibrium constants K_T in toluene-d_8 for Mn(APSO)(hfac)$_2$ **3.1a**, Co(APSO)(hfac)$_2$ **3.1b**, Ni(APSO)(hfac)$_2$ **3.1c**, were found to be 20.2 (95% PMC form), 11.3 (91% PMC form), and 9.15 (90% PMC form), respectively. The K_T observed in toluene-d_8 were smaller than that observed in THF-d_8, which is due to the less polar solvent stabilizing the SO form. In both the polar and nonpolar solvents, the PMC form was found to be stabilized by one order of magnitude relative to parent spirooxazine **2.2** across the series of metal complexes. The effects of metal complexation on the thermal equilibrium constant can be explained by the perturbation of electronic structure upon metal complexation. Since steric effects are expected to be relatively insignificant for the spirooxazine framework relative to a simple phenanthroline ligand, electronic effects arising from the Lewis acidity and π-back bonding ability of the metal center are most likely the dominant contributions.[261-263] For a given row and oxidation state, the Lewis acidity decreases with increasing atomic number (across a periodic row) whereas π-back bonding ability increases. A Lewis acidic metal center would be expected to withdraw electron density from the oxazine moiety, leading to an increase in charge-separated character and stabilization of the PMC form. Conversely, π-back bonding increases electron density on the oxazine moiety, leading to destabilization of the PMC form. The ancillary ligand (hfac$^-$) is also Lewis acidic which decreases electron density on the metal center, further decreasing the π-back bonding ability of the metal. An increase in K_T upon metal complexation indicates that the Lewis acidity of the metal center dominates the perturbation of electronic structure in the series of M(APSO)(hfac)$_2$ **3.1(a–c)**. Greater Lewis acidic metal centers (Mn > Co > Ni) lead to a larger K_T values, indicating greater

stabilization of the PMC form. A significant destabilization of the PMC form was reported in a Ru(IPSO)(bipy)$_2$ complex due to the strong π-back bonding ability of the metal center which was enhanced by the bipyridine ancillary ligands, suggesting a large dependence on both the nature of the metal center and the ancillary ligand.[264] A relatively small stabilization of the PMC form (K_T = 4) was observed in Co(APSO)(3,5-DTBQ)$_2$ relative to the parent spirooxazine **2.2**, also suggesting the important role of ancillary ligand.[260] No azomethine resonance of the SO form was observed in MeOD, suggesting that metal coordination stabilizes the PMC form to such an extent that the complex is nearly 100% in the PMC form in MeOD. This is consistent with what we expected, as it is known that the equilibrium constant may vary as a function of solvent, similar to the metal-IPSO complexes.[259]

The presence of coordination enantiomers (Δ vs. Λ) in addition to four different isomers (i.e. M(PMC)$_3$, M(PMC)$_2$(SO), M((PMC)(SO)$_2$, M(SO)$_3$) resulted in extremely complicated ^{1}H NMR spectra for the M(APSO)$_3$(BPh$_4$)$_2$ **3.2(a–c)** and K_T cannot be easily determined. However, ^{1}H NMR spectrum of Fe(APSO)$_3$(BPh$_4$)$_2$ is less complicated than the Mn and Co complexes due to the presence of a diamagnetic *ls*-Fe(II) metal center. Qualitative interpretation of the ^{1}H NMR spectrum suggests that the major isomer on the metal is the PMC isomer which is consistent with the greater polarizing ability of the metal center on the PMC form.

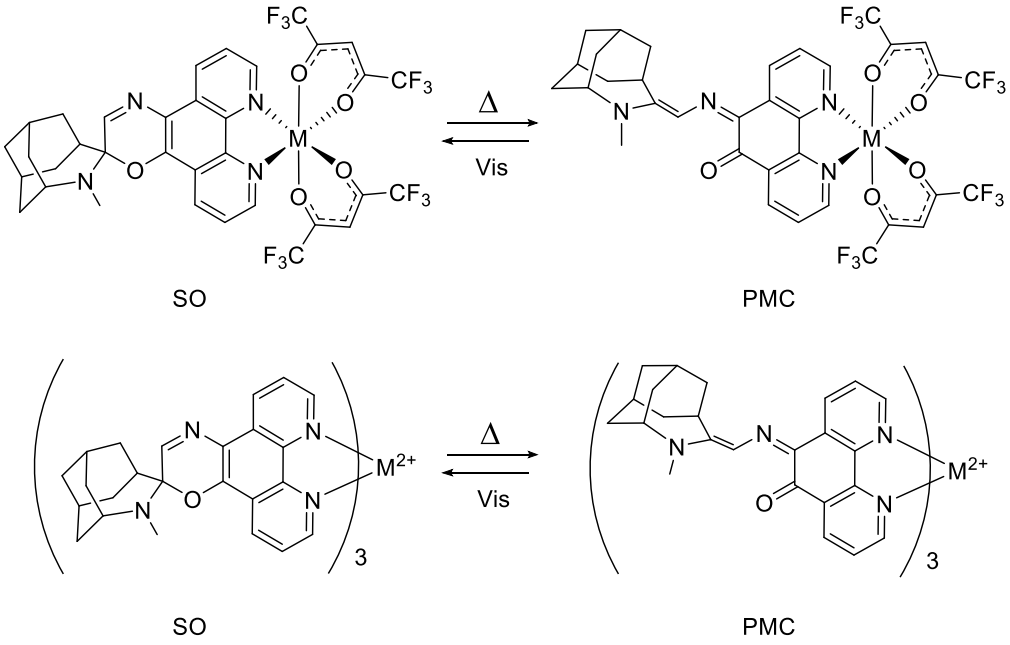

Figure 3.2. Thermal and Photoisomerization of the M(APSO)(hfac)$_2$ **3.1(a–c)** and M(APSO)$_3$(BPh$_4$)$_2$ **3.2(a–c)**.

Table 3.1. Thermal equilibrium constants (K_T) of **2.2** and M(APSO)(hfac)$_2$ **3.1(a–c)** in THF, toluene, MeOH at 298 K.[a]

Solvent	**2.2**	**Mn 3.1a**	**Co 3.1b**	**Ni 3.1c**
THF	2.7	> 20 [b]	> 20 [b]	> 20 [b]
Toluene	1.2	> 20 [b]	11.3	9.1
MeOH	25	> 20 [b]	> 20 [b]	> 20 [b]

[a] K_T = [PMC]/[SO]. The K_T was determined by azomethine proton resonance of the PMC ($\delta \approx$ 10–12 ppm) and SO ($\delta \approx$ 8–10 ppm) form by ^{1}H NMR spectroscopy in a concentration of ~10^{-2} M. [b] The concentration of the SO form was below the limit of detection for ^{1}H NMR (< 5 %).

3.2.3. Effect of the Metal Complexation on the Optical Properties of 2.2

The electronic absorption spectroscopy of the M(APSO)(hfac)$_2$ **3.1(a–c)** and M(APSO)$_3$(BPh$_4$)$_2$ **3.2(a–c)** suggests that metal complexation of the spirooxazine leads to a large perturbation of the HOMO-LUMO gap, resulting in a hypsochromic shift of optical

transitions. The electronic absorption spectra of the parent spirooxazine **2.2** shows a large absorption at $\lambda_{max} \approx 553$ nm in THF, assigned to a π–π* transition of the PMC form. Both **3.1(a–c)** and **3.2(a–c)** also show a large absorption at $\lambda_{max} \approx 547$ nm and ≈ 550 nm, respectively (Figure 3.3). Relative to the parent ligand **2.2**, a small hypsochromic shift of 6 nm for **3.1(a–c)** and 1 ~ 3 nm for **3.2a** and **3.2c** were observed upon metal complexation for all metals except $Fe(APSO)_3(BPh_4)$ **3.2b** which exhibited a ~ 10 nm bathochromic shift.

Orbital analysis of a series of spirooxazine $Mo(CO)_4$ complexes suggests that upon metal complexation, the LUMO+1 of the PMC form metal complex increases in energy, while the HOMO decreases, leading to a larger "HOMO-LUMO" gap in the metal complex and a hypsochromic shift in the electronic absorption spectrum.[265] The smaller shift in **3.1(a–c)** and **3.2(a–c)** relative to the $Mo(CO)_4$ spirooxazine complexes (hypsochromic shift of 9 nm) may be due to weaker mixing between the metal fragment orbitals with the LUMO+1 spirooxazine orbitals. The broad band shape of the Fe complex **3.2b** may be due to the presence of several transitions, which may indicate the presence of an MLCT (Fe(II) → phen) band underneath of the π–π* band, which typically appears at $\lambda_{max} \approx 510$ nm in acidic water.[266] In addition, the MLCT band corresponding to a (Fe(III) → phen) appears at $\lambda_{max} \approx 591$ nm suggesting the possible existence of a mixture of both Fe(II) and Fe(III) oxidation states due to possible oxidation of Fe(II) in solution by oxygen.

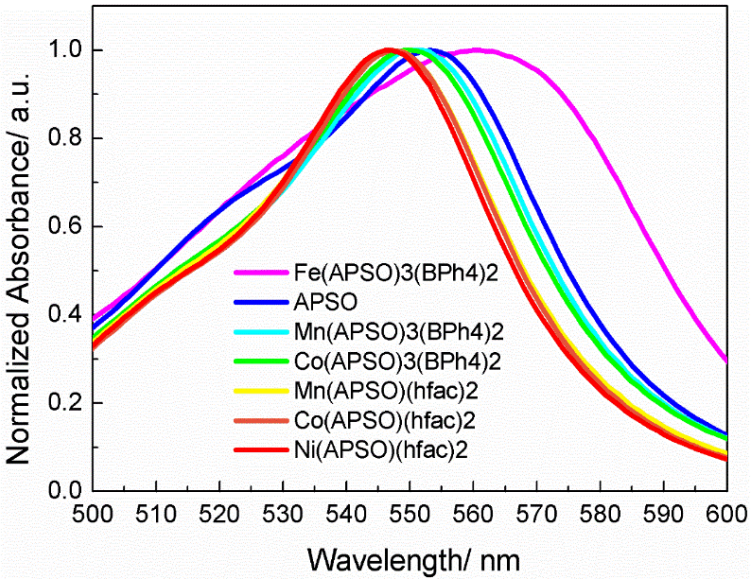

Figure 3.3. λ_{max} of M(APSO)(hfac)$_2$ **3.1(a–c)** and M(APSO)$_3$(BPh$_4$)$_2$ **3.2(a–c)** in THF.

3.2.4. The Effect of Metal Complexation on the Photochromic Properties and Thermal Coloration Kinetics of 2.2

The photochemical and thermal isomerization processes between SO and PMC forms may be monitored by following the absorbance of the PMC π–π* band at ~550 nm in THF which is proportional to the PMC concentration in solution. (Figure 3.4) The response of the photochromic metal complexes to steady state UV and visible light irradiation was followed by UV-Vis spectroscopy ($\lambda_{max} \approx 550$ nm) in THF as a function of time. Both complexes **3.1(a–c)** and **3.2(a–c)** display reversible and photoinduced isomerization upon steady-state visible irradiation. A decrease in intensity of the π–π* absorption band with visible light irradiation is due to SO formation and regeneration of the PMC form in the dark due to thermal SO → PMC conversion. Extremely high

photoresponsivities were observed for both **3.1(a–c)** and **3.2(a–c)** relative to the parent spirooxazine **2.2**.

The photostability of M(APSO)$(hfac)_2$ **3.1(a–c)** was solvent dependent. Whereas relatively high photostability was observed with no photodegradation over the course of 150 irradiation cycles with high power (100 mW) in MeOH, nearly 100 % degradation over the course of 20 irradiation cycles were observed in toluene and THF. The solvent dependence may be due to stabilization of the PMC form by polar solvents, towards effectively ~100% PMC form. Visible irradiation would then lead to decomposition of the PMC form, as photoisomerization to the SO form does not occur. The reason for this is not clear. The photostability of the M$(APSO)_3(BPh_4)_2$ complexes **3.2(a–c)** was similar to that of M(APSO)$(hfac)_2$. Nearly 100 % photodegradation over the course of 25 irradiation cycles under visible-light irradiation (100 mW) in THF was observed.

UV irradiation of compounds **3.1(a–c)** resulted in an irreversible decrease in absorbance at ~550 nm due to decomposition of the parent spirooxazine, rather than isomerization from the SO to PMC form. As metal coordination stabilizes the PMC form, the concentration of the SO form is < 5 %. UV irradiation of the PMC form then leads to light-induced decomposition of the PMC form, rather than photoisomerization as the dominant pathway.

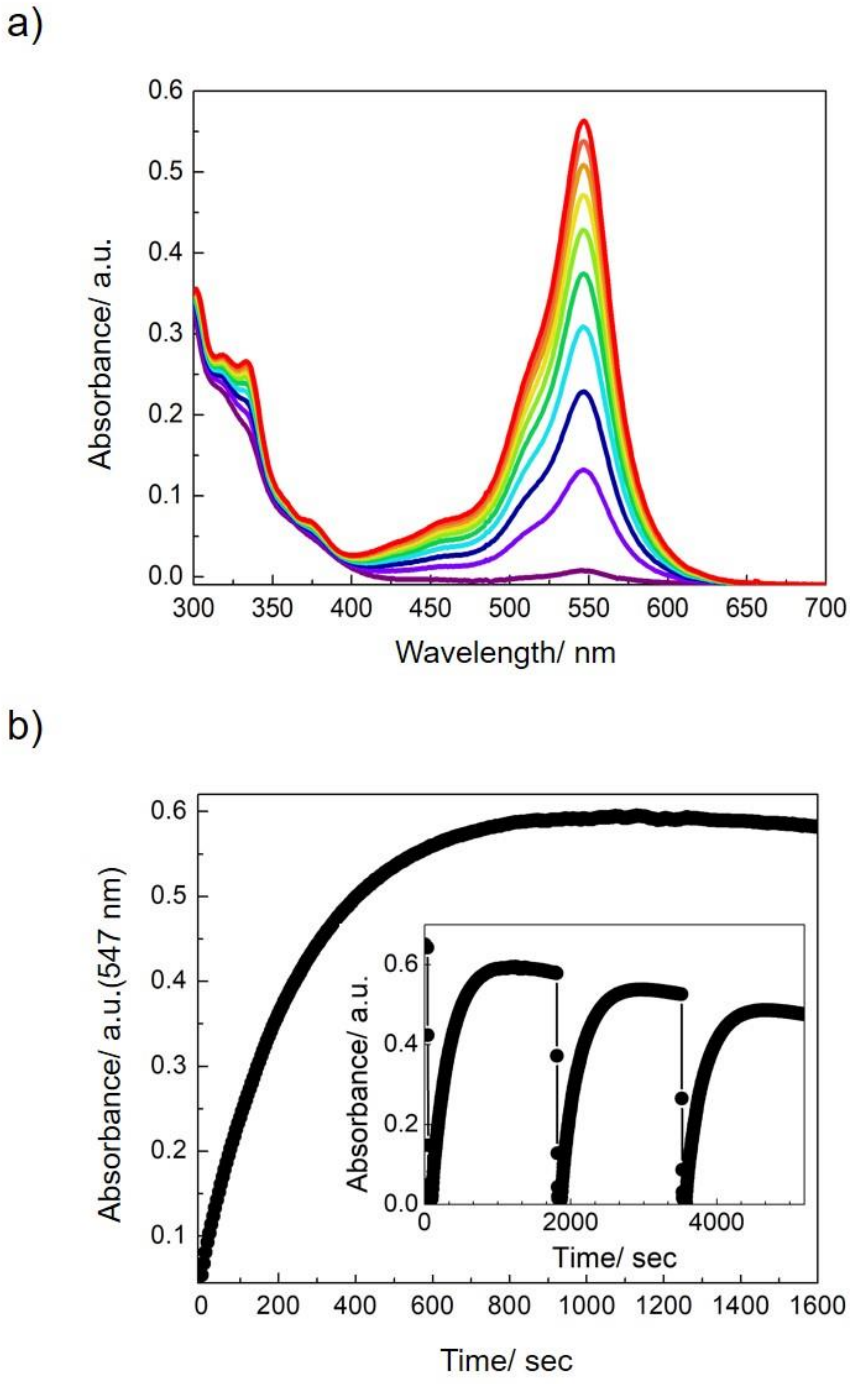

Figure 3.4. Electronic absorption spectrum of Ni(APSO)(hfac)$_2$ **3.1c** in THF over time in the absence of light after visible light irradiation (a), kinetic trace of thermal relaxation followed by the changes in absorbance at 547 nm in absence of light in THF at 298 K (b), and kinetic trace of absorbance intensity at π–π^* λ_{max} at 547 nm over three irradiation cycles (inset).

The first order rate constants for thermal relaxation (k_t) from the visible-light induced photostationary states were measured in **3.1(a–c)** and **3.2(a–c)** in THF (Table 3.2). Upon metal complexation of the parent spirooxazine **2.2**, a decrease in k_t by one order of magnitude is observed for both **3.1(a–c)** and **3.2(a–c)**. A decrease in the thermal relaxation rates to the PMC form is consistent with a stabilization of the PMC form due to metal coordination. The Lewis acidity of the metal center stabilizes the charge-separated zwitterionic form of the PMC, which suggests that stabilization of the zwitterionic form of the PMC form decreases the rate of thermal relaxation, consistent with the findings in Chapter 2. The Lewis acidic ancillary ligand, hfac, may also contribute to a decrease in the thermal relaxation rate. The thermal relaxation rates of M(APSO)$(hfac)_2$ **3.1(a–c)** in toluene were measured in order to evaluate the effect of ancillary ligands. The rate constants of all M(APSO)$(hfac)_2$ complexes were found to be ~ 3×10^{-3} s^{-1} (Table 3.3) in toluene. In comparison, the rate constant of Co(APSO)$(SQ)_2$ was reported to be 1.2×10^{-2} s^{-1} which is an order of magnitude larger than Co(APSO)$(hfac)_2$.[260] This supports the argument that Lewis acidic hfac ligands enhance the stabilization of the charge-separated form, thereby leading to the slower thermal coloration relative to that observed for the more electron-rich semiquinone ancillary ligands.

The thermal coloration kinetics were found to be better fit to a biexponential function than with a monoexponential function, which suggests the presence of at least two different thermal relaxation rates. The relaxation kinetics for thermal coloration of M(APSO)$(hfac)_2$ **3.1(a–c)** and M$(APSO)_3(BPh_4)_2$ **3.2(a-c)** were fit to a biexponential function where k_{t1} and k_{t2} are two components of the observed thermal relaxation (Table 3.2). The presence of two relaxation processes in **3.1(a–c)** and **3.2(a–c)** may be due to

chemically and environmentally inequivalent spirooxazines. In **3.1(a–c)**, since only one ligand **2.2** is bound to the metal center, it is possible that the two rates can be assigned to monomeric and aggregated metal complexes in solution, leading to different chemical environments. The rate constants of the secondary process of **3.1(a–c)** (4.9, 8 and, 13×10^{-3} s^{-1} for Mn, Co, Ni, respectively) are smaller than that of the parent spirooxazine **2.2** (56×10^{-3} s^{-1}), suggesting that decomplexation is not responsible for the biexponential kinetics observed. However, we cannot unambiguously rule out the possibility of free ligand due to the relatively large standard error (up to 40 % for k_{t1}) associated with the rate constants. For the $M(APSO)_3(BPh_4)_2$ **3.2(a–c)**, the biexponential kinetics likely arise from the presence of chemically inequivalent spirooxazines and electronic coupling between three photochromic ligands. Each photochromic ligand can have two coordination enantiomers (Δ vs. Λ) which can also have three different forms (PMC or SO) (i.e., $M(PMC)_3$, $M(PMC)_2(SO)$, $M((PMC)(SO)_2)$ or $M(SO)_3$). The eight isomers may contribute to different thermal relaxation rates in addition to any intermolecular aggregation that may occur. Moreover, photoisomerization of one ligand in the complex from the PMC to SO form may lead to a change in the ligand field about the metal center. The change in ligand field may change the electronic structure of the metal complex, which may lead to a change in the SO/PMC equilibrium constant (K_T) for the other two photochromic ligands, as well as thermal relaxation rates. Thus, the biexponential kinetics may also be a result of some degree of electronic coupling between photochromic ligands resulting in different thermal relaxation kinetics.

Table 3.2. Thermal coloration rates of M(APSO)(hfac)$_2$ **3.1(a–c)** and M(APSO)$_3$(BPh$_4$)$_2$ **3.2(a–c)** in THF.[a]

	2.2	**Mn 3.1a**	**Co 3.1b**	**Ni 3.1c**
k_{t1} /s^{-1} 10^{-3}	56 ± 4	6.6 ± 0.5	3.9 ± 0.1	3.7 ± 0.07
k_{t2} /s^{-1} 10^{-3}		4.9 ± 3.4	8 ± 19	13 ± 36
		Mn 3.2a	**Fe, 3.2b**	**Co 3.2c**
k_{t1} /s^{-1} 10^{-3}		8 ± 3	6.7 ± 0.5	5 ± 2
k_{t2} /s^{-1} 10^{-3}		13 ± 22	24 ± 4	5 ± 2

[a] Determined by UV/Vis spectroscopy in a sample concentration of 10^{-5}–10^{-6} M. Experimental errors of the thermal relaxation constant are determined from 3 independent runs.

Table 3.3. Thermal coloration rates of M(APSO)(hfac)$_2$ **3.1(a–c)** in a series of solvents.[a]

Solvent		**2.2**	**Mn 3.1a**	**Co 3.1b**	**Ni 3.1c**
THF	k_{t1} /s^{-1} 10^{-3}	56 ± 4	6.6 ± 0.5	3.9 ± 0.1	3.70 ± 0.07
	k_{t2} /s^{-1} 10^{-3}		4.9 ± 3.4	8 ± 19	13 ± 36
Toluene	k_t /s^{-1} 10^{-3}	150 ± 10	3.6 ± 0.1	3.1 ± 0.2	2.9 ± 0.2
MeOH	k_t /s^{-1} 10^{-3}	90 ± 1	16.2 ± 0.6	18.4 ± 0.3	14 ± 3

[a] Determined by UV/Vis spectroscopy in a sample concentration of 10^{-5}–10^{-6}. Experimental errors of the thermal relaxation constant are determined from 3 independent runs.

3.3. Conclusion

A series of metal complexes of an azahomoadamantyl-phenanthroline spirooxazine was synthesized. The spirooxazine ligand is bound to a series of first row transitions metals either exclusively (M(APSO)$_3$(BPh)$_2$ where M = Mn(II) **3.2a**, Fe(II) **3.2b**, Co(II) **3.2c** or with ancillary ligands (M(APSO)(hfac)$_2$ where M = Mn(II) **3.1a**, Co(II) **3.1b**, Ni(II) **3.1c**. The optical properties of the complexes were investigated toward understanding the effect of metal complexation on the photochromic properties of the negative photochromic spirooxazine class. Metal complexation results in a greater stabilization of the PMC form and decreased rates of thermal relaxation in these metal complexes by as much as an order of magnitude relative to the parent spirooxazine. This suggests that the Lewis acidic nature

of the metal center enhances charge separation in the PMC form, which in turn decreases the rate of thermal relaxation. The effect of the ancillary ligand was found to depend on the nature of the ligand. The hfac ligands significantly enhance the Lewis acidity of the metal center and induce charge separation of PMC form. This suggests that the nature of the metal center and the ancillary ligand have a great impact on the electronic structure of the PMC form, leading to the observed changes in the rates of thermal relaxation. Metal complexation can therefore be used as an effective strategy for modulating both the thermal equilibrium and thermal relaxation rates in photochromic spirooxazines.

3.4. Experimental

3.4.1. Synthesis

Reactions were performed under inert atmosphere (N_2) using standard Schlenk techniques. Methanol was distilled over CaH_2 under inert atmosphere (Ar) and degassed by three freeze-pump-thaw cycles prior to use. ^{1}H NMR spectroscopy was carried out on a 500 MHz Bruker AVANCE500 spectrometer in THF-d_8 at 300 K. ^{19}F NMR spectroscopy was performed on 300 MHz Bruker spectrometer in $CDCl_3$. FT-IR spectrum was acquired as KBr pellet with a Perkin-Elmer Spectrum One FTIR spectrometer. Mass spectra were collected by Jingwei Luo (UVic) using a Micromass Q-Tof II mass spectrometer in positive ion mode using pneumatically assisted electrospray ionization: capillary voltage, 3000 V; extraction voltage, 0 V; Source temperature, 90°C; desolvation temperature, 180°C; cone gas flow, 200 L/h; desolvation gas flow, 50 L/h; collision voltage, 8 V (for MS experiments); MCP voltage, 2200 V. Elemental analysis was performed by Microanalysis center (UBC).

M(APSO)(hfac)$_2$ 3.1(a–c). A solution of 0.040g (0.104 mmol) of spirooxazine **2.2** in 1.5 mL MeOH was added to a solution of M(hfac)$_2$ (M = Co, Mn, Ni) (0.104 mmol) in 1.5 mL MeOH. The reaction mixture was stirred for 1 hour at 22° C and left to stand overnight in the absence of light, which led to the formation of a dark purple precipitate. The precipitate was filtered and washed with H_2O and THF to yield a dark purple powder. **Mn(APSO)(hfac)$_2$ 3.1a** Yield: 44 mg, 50 %. FT/IR (cm^{-1}, KBr): 3300-3500 (br, O-H), 1647 (s, C=O), 1256 (s, C–O), 1204 (m, C–F), 1144 (s, C–F). Anal. Calcd for $C_{34}H_{26}N_4O_5F_{12}$ Mn: C, 47.85; H, 3.07; N, 6.56. Found: C, 48.13; H, 3.16, N, 6.26. ESI-MS: m/z (%) 646.0143 [Mn(APSO)(hfac)]$^+$, 1030.1462 [Mn(APSO)$_2$(hfac)]$^+$. **Co(APSO)(hfac)$_2$ 3.1b** Yield: 22 mg, 24 %. FT/IR (cm$_{-1}$, KBr): 3300-3500 (br, O-H), 1640 (s, C=O), 1254 (s, C–O), 1206 (s, C–F), 1144 (s, C–F). Anal. Calcd for $C_{34}H_{26}N_4O_5F_{12}Co$: C, 47.62; H, 3.06; N, 6.53. Found: C, 47.27; H, 3.08, N, 6.31. ESI-MS: m/z (%) 649.9603 [Co(APSO)(hfac)]$^+$, 1034.1093 [Co(APSO)$_2$(hfac)]$^+$. **Ni(APSO)(hfac)$_2$ 3.1c** Yield: 25 mg, 28 %. FT/IR (cm^{-1}, KBr): 3300-3500 (br, O-H), 1643 (s, C=O), 1258 (s, C–O), 1206 (s, C–F), 1142 (s, C–F). Anal. Calcd for $C_{34}H_{26}N_4O_5F_{12}Ni$: C, 47.64; H, 3.06; N, 6.54. Found: C, 46.29; H, 3.06, N, 6.34. ESI-MS: m/z (%) 648.9543 [Ni(APSO)(hfac)]$^+$, 1033.3691 [Ni(APSO)$_2$(hfac)]$^+$.

M(APSO)$_3$(BPh$_4$)$_2$ 3.2(a–c). 0.0095 g (0.048 mmol) of $MCl_2 \cdot xH_2O$ (M = Mn, Fe, Co) was added to a solution of 0.055 g (0.15 mmol) of the spirooxazine **2.2** in 5 mL methanol. $NaBPh_4$ (0.0328 g) in 5 mL methanol was added to the solution. For Fe complex, one equivalent of ascorbic acid (0.0084 g) was added to prevent oxidation of Fe(II)Cl_2 upon reaction. The reaction mixture was stirred for 1 hour at room temperature and left to stand overnight leading to the formation of a dark purple precipitate. The precipitate was

filtered and washed with H_2O and diethyl ether to yield purple powder. **$Mn(APSO)_3\cdot(BPh_4)_2\cdot 11H_2O$ 3.2a** Yield: 62 mg, 63 %. FT/IR (cm^{-1}, KBr): 3300-3700 (br. O-H), 2913 (s, sp^3 C–H), 2864 (s, sp^3 C–H). 1599 (m, C=N), 1455 (s, CH_2), 1421 (s, CH_3), 1223 (s, C–O), 1098 (s, C–N), 744 (m, sp^2 C–H), 700 (m, sp^2 C–H). Anal. Calcd for $C_{120}H_{134}B_2N_{12}O_{14}Mn$: C, 70.48; H, 6.60; N, 8.22. Found: C, 69.85; H, 5.80, N, 9.68. ESI-MS: m/z (%) 603.7664 $[Mn(APSO)_3]^{++}$. **$Fe(APSO)_3\cdot(BPh_4)_2\cdot 2H_2O$ 3.2b** Yield: 42 mg, 46 %. FT/IR (cm^{-1}, KBr): 3300-3700 (br. O–H), 2913 (s, sp^3 C–H), 2864 (s, sp^3 C–H). 1599 (m, C=N), 1455 (s, CH_2), 1421 (s, CH_3), 1223 (s, C–O), 1098 (s, C–N), 744 (m, sp^2 C–H), 700 (m, sp^2 C–H). Anal. Calcd for $C_{120}H_{116}B_2N_{12}O_5Fe$: C, 76.51; H, 6.21; N, 8.92. Found: C, 76.28; H, 5.92; N, 8.80. ESI-MS: m/z (%) 604.2615 $[Fe(APSO)_3]^{++}$. **$Co(APSO)_3\cdot(BPh_4)_2\cdot 7H_2O$ 3.2c** Yield: 43 mg, 45 %. FT/IR (cm_{-1}, KBr): 3300-3700 (br. O-H), 2917 (s, sp^3 C-H), 2869 (s, sp^3 C-H). 1599 (m, C=N), 1455 (s, CH_2), 1416 (s, CH_3), 1223 (s, C–O), 1098 (s, C–N), 744 (m, sp^2 C–H), 703 (m, sp^2 C–H). Anal. Calcd for $C_{120}H_{126}B_2N_{12}O_{10}Co$: C, 72.91; H, 6.42; N, 8.50. Found: C, 73.07; H, 5.85, N, 8.66. ESI-MS: m/z (%) 605.7582 $[Co(APSO)_3]^{++}$.

3.4.2. Spectroscopic Methods

Electronic absorption spectra were recorded on an Agilent 8453 spectrophotometer equipped with a photodiode array and Peltier temperature control. Sample solutions (concentration of 10^{-5} M–10^{-6} M) were prepared under inert conditions in degassed spectroscopic grade solvents. All experiments were carried out at 298 K in the dark, with continuous stirring. Excitation experiments were carried out via multiline irradiation (514, 532, 568 nm) with a Spectra-Physics Stabilite 2018 mixed gas Ar-Kr ion laser, and directed

to the sample via with a Newport liquid light guide. The power at the sample was measured with a Spectra-Physics 407A power meter with typical powers of 100 mW. The rates of thermal relaxation were determined in the absence of light by following the intensity of the PMC π–π* absorption ($\lambda_{max} \approx 547$ nm) with a five-second interval after generation of the photostationary state. Multiple cycles (>3) were used for fitting of data, which was found to be the best fit to a biexponential rate function with linear least-squares methods. Typical fitting to the biexponential function is shown in Figure 3.5.

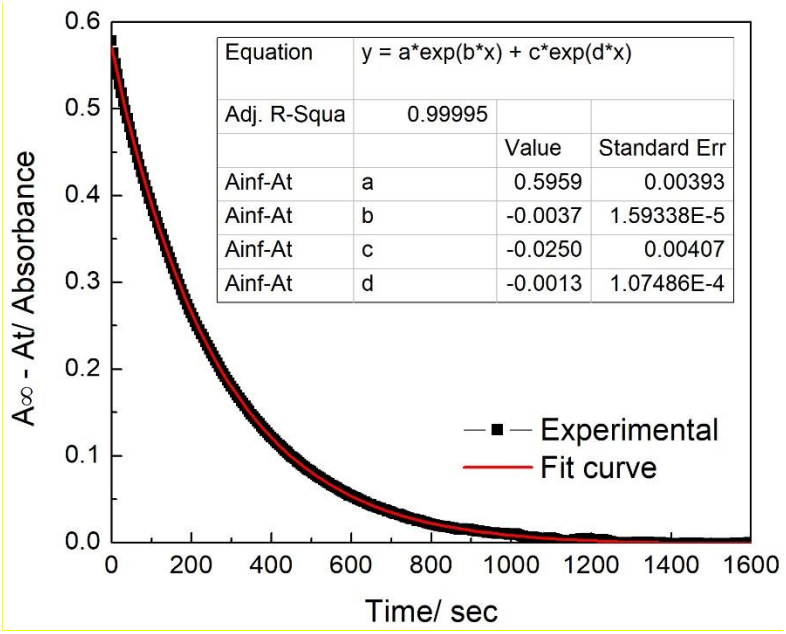

Figure 3.5. Kinetic trace of thermal relaxation of Ni(APSO)(hfac)$_2$ **3.1c** followed by the changes in absorbance at 547 nm in the absence of light after irradiation. THF solution at 298 K, with a biexponential fit of the data shown (red line).

Chapter 4. Investigation of Photochromism-Induced Redox Isomerism in Tetranuclear Cobalt Complexes

4.1. Introduction

Optically switchable magnetic materials interconvert between two spin states upon application of an optical stimulus.[267-269] The interconversion between two spin states induces changes in magnetization, coercivity, or magnetic ordering, all of which may be used to store information. Since the first example of photoinduced magnetic effect was reported,[83] significant progress in different classes of compounds, which exhibit photoinduced magnetic effects, has been made to date, such as Prussian blue analogues,[72,88-90] chains and polymers,[91,92] squares,[94,95,96] and spin crossover complexes.[76,270,271] However, the lifetime of these systems is often dictated by the rapid thermal relaxation of the metal-centered excited state to the ground state, and direct observation of the photoinduced magnetic effect in the solid state at ambient temperature remains a challenge.

Our strategy towards the development of photomagnetic materials involves the incorporation of photochromic ligands into a class of electronically bistable metal complexes, thereby allowing for longer lifetimes of the ligand-centered magnetization excited state. Cobalt dioxolene complexes are valence redox-isomeric complexes which reversibly interconvert between two distinct electronic and spin states, the *ls*-Co(III) and *hs*-Co(II) states.[77,111] The conversion occurs via a combination of intramolecular charge transfer (CT) and spin transition processes between a redox-active cobalt center Co(II)/Co(III) and a redox-active ligand 3,5-DTBQ $Cat^{2-}/SQ^{\bullet-}$ (DTBQ = di-*tert*-butyl-

ortho-quinone, Cat^{2-} = catecholate, $SQ^{\bullet-}$ = semiquinone). [77,111,120] The conversion leads to two distinct states *hs*-Co(II)$(SQ^{\bullet-})_2$ and *ls*-Co(III)$(SQ^{\bullet-})(Cat^{2-})$ which differ in electronic and spin states and display profoundly different spectroscopic and magnetic properties. In order to gain optical control over the electronic bistability of cobalt dioxolene complexes, we incorporated photochromic ligands into the complex that can interconvert between two stable isomers.

Photochromic spirooxazines undergo reversible photoisomerization between a closed (spirooxazine SO) form and an open (photomerocyanine PMC) form.[2,22,30] UV light irradiation of the SO form at $\lambda_{max} \approx 350$ nm induces C–O bond cleavage via a singlet excited state to give the photomerocyanine (PMC) form with $\lambda_{max} \approx 600$ nm. Visible-light induced ring closure can occur by excitation of the π–π^* transition of the PMC form or thermal relaxation along the ground state potential energy surface.[22,30,272] The transition temperature ($T_{1/2}$) for a thermally-induced charge transfer coupled spin transition (CTCST) is linearly correlated with the reduction potential of the ancillary ligand for Co(3,5-DTBQ)$_2$(NN) compounds.[273] Redox-isomeric behavior may therefore be modulated by a change in ligand field associated with an ancillary photochromic ligand. The closed SO form was found to be a better π–acceptor (by 0.3 eV) and is expected to preferentially stabilize electron-rich metal centers.[265] It is predicted therefore that the SO form would stabilize the Co(II) state over the Co(III) state. The distinct electronic structure provided by the different redox potential of the SO and PMC forms provides the potential for photoswitching of the driving force for the charge transfer processes between the redox-active metal center and ligand.

We have recently shown that photoisomerization-induced spin-charge excited states (PISCES) can arise to give photoinduced magnetic effects of Co(APSO)(3,5-DTBQ)$_2$ (**4.1**) (APSO = spiro[azahomoadamantyl-phenanthrolinoxazine] (**2.2**)) at room temperature in both the solution and the solid-state. Modulation of cobalt dioxolene electronic states via spirooxazine ligand photoisomerization leads to a four-state system with thermal equilibration between the [open(PMC)/closed(SO)] and [*ls*-Co(III)/*hs*-Co(II)] states.[260] In this system, the ground state is a Co(III)-PMC state. Visible light irradiation at 298 K causes photoisomerization from the PMC form to the closed (SO) form. This induces a transition to the *hs*-Co(II) state, consistent with the ability of the SO form to stabilize the lower oxidation state. Spectral changes in visible/NIR transitions are accompanied by changes in magnetization with a relaxation rate of $k \sim 0.1\ s^{-1}$ at 300 K.[260] This is the first observation of the photomagnetic effect at room temperature in the thin film state, representing the first possible step towards harnessing the photomagnetic effect for memory applications. However, the change in magnetization upon photoisomerization in this system is still small due to the presence of only one redox-active metal center. A greater change in magnetization may be desirable for practical applications in which large changes in magnetization are induced optically.

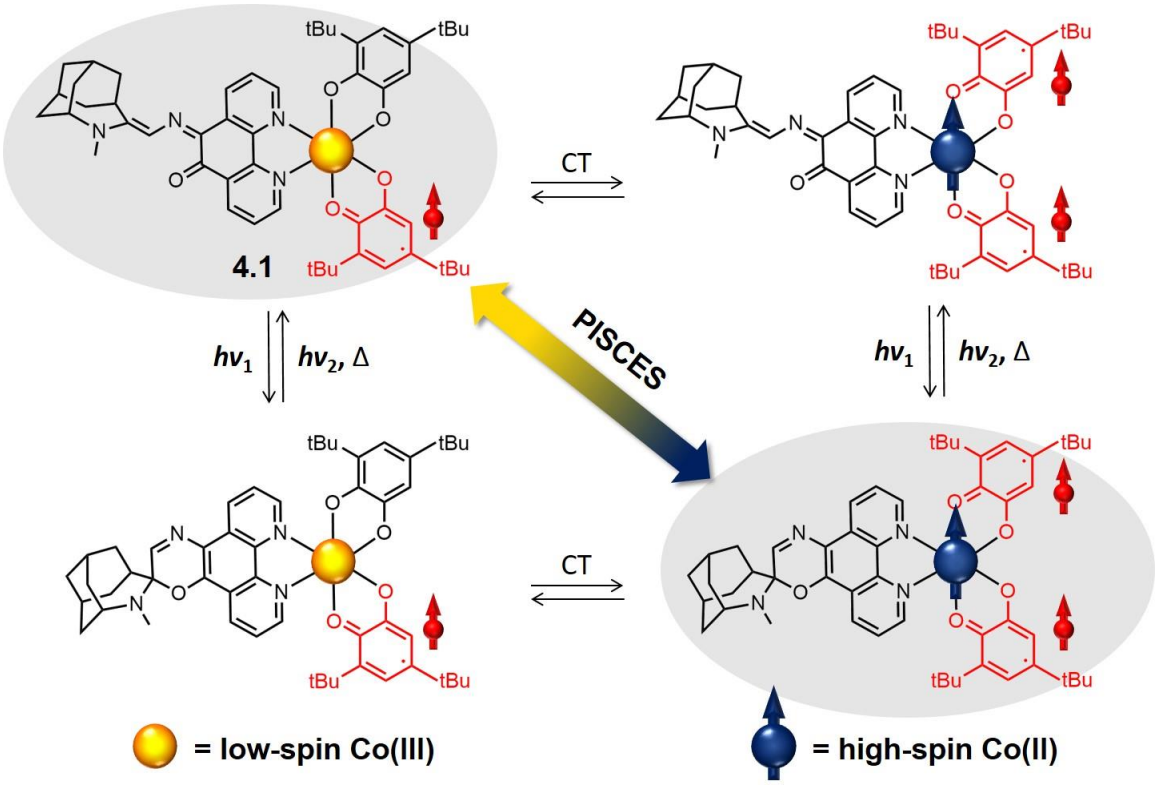

Figure 4.1. Schematic representation of the photoisomerization-induced spin-charge excited states (PISCES) observed in Co(APSO)(3,5-DTBQ)$_2$ (**4.1**).[260]

In this study, we investigate the effect of a photochromic spirooxazine ligand in a tetranuclear cobalt dioxolene cluster with multiple redox-active metal centers. During the preparation of the photochromic mononuclear complexes, a photochromic tetranuclear cobalt cluster containing the APSO ligand (**2.2**) was isolated and structurally characterized.[223] The cluster was photochromic and exhibited redox-isomeric behaviour had not been determined however, as the cluster had not been characterized spectroscopically. This work describes an investigation into the effect of (i) the redox-isomeric behaviour of multiple redox active metal centers on the thermal behaviour, and (ii) the effect of photochromic ligand structure on the ability to optically switch the spin

and charge state of the metal centers. Two different photochromic ligands, APSO **2.2** and IPSO (spiro[indoline-phenanthrolinoxazine]) (**4.2**) were incorporated into tetranuclear cobalt clusters to give $Co_4(APSO)_2(3,5\text{-}DBSQ)_6(MeOH)_2$ (**4.3**) and $Co_4(APSO)_2(3,5\text{-}DBSQ)_6(MeOH)_2$ (**4.4**). In each of the clusters, the cobalt centers can exist in either the *ls*-Co(III) or *hs*-Co(II) oxidation states (Figure 4.2), and the photochromic ligands, of which there are two bound to the cobalt cluster, can exist in either the closed SO or open PMC states. The oxidation state of the four cobalt centers is examined by X-ray crystallographic analysis, bond valence sum (BVS) analysis, and magnetization experiments. The redox-isomeric behavior in solution and in solid state was investigated spectroscopically. Finally, the results of the photochromic studies of the clusters were combined with the magnetization and spectroscopic data in order to propose a rationale for the effects of the equilibrium of distinct electronic states on the exhibition of the PISCES effect. This study provides insight into the structural principles that dictate the generalizability of using the PISCES effect to optically gate magnetic states in metal complexes. This study outlines a promising new strategy for the incorporation of photoisomerization induced redox-isomeric processes into clusters for the purposes of modulating magnetization at room temperature.

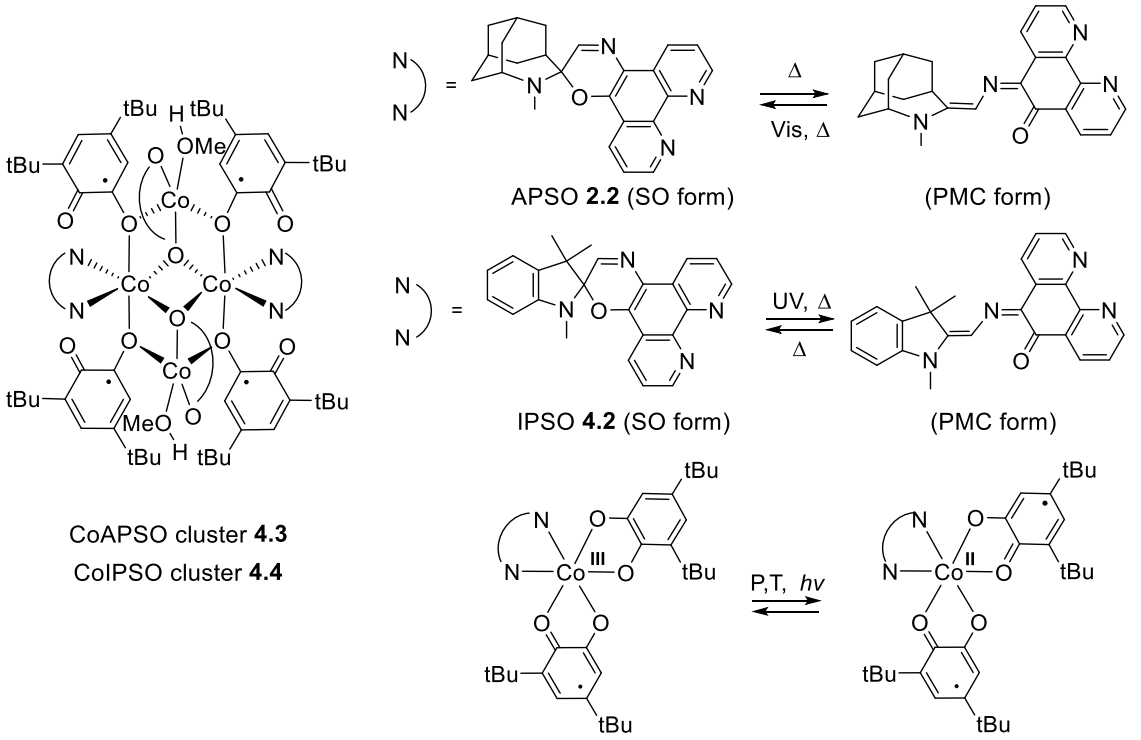

Figure 4.2. Structure of the tetranuclear complexes **4.3** and **4.4**.

4.2. Results and Discussion

4.2.1. Synthesis

The tetranuclear complexes **4.3** and **4.4** were prepared by stoichiometric addition of $Co_2(CO)_8$ dissolved in methanol to a stirred mixture of 3,5-DTBQ (DTBQ = di-*tert*-butyl-*ortho*-quinone) and the photochromic ligands APSO **2.2** or IPSO **2.2** in methanol. The photochromic ligands **2.2**[46] and **4.2**[205] were synthesized according to a previously reported method. Oxidation of the cobalt(0) octacarbonyl complex by benzoquinone and dissociation of the CO ligands occurs to give the clusters, which then may undergo ligand displacement with the photochromes to give clusters **4.3** and **4.4**. The solution was stirred for one hour at room temperature and left overnight in the absence of light to yield needle-shaped dark purple for **4.3** (41 % yield) and dark-blue crystals of **4.4** (45% yield).

Elemental analysis for **4.3** gave calculated analysis for $C_{134}H_{178}Co_4N_8O_{16}\cdot 2CH_3OH$: C, 66.49; H, 7.63; N, 4.56 and found: C, 64.10; H, 7.55; N, 4.69. It was noted that the while agreement for both H and N was within 0.12 and 0.13 %, the analysis for C is low by 2.3 %. The low carbon content found may be due to the presence of water as was found for the parent $Co_4(SQ)_8$ cluster (Chapter 5). Including four water in the lattice gives a calculated elemental analysis for $C_{134}H_{178}Co_4N_8O_{16}\cdot 2(CH_3OH)\cdot 4(H_2O)$: C, 64.65; H, 7.65; N, 4.43, which leads to better agreement between the theoretical and experimental values within an experimental error of ~0.4 % for C, H, and N. Elemental analysis for **4.4** crystals were consistent with the formula for the complex with two methanol solvent molecules in the lattice, which gave calculated analysis for $C_{136}H_{174}Co_4N_8O_{18}$: C, 66.82; H, 7.17; N, 4.58 and found: C, 66.32; H, 7.32; N, 4.52. Attempts to obtain ESI-mass spectrometry for the clusters did not show a molecular ion peak for the whole molecule or fragments, which may be due to the air sensitivity of the clusters. ^{1}H NMR analysis of the clusters is extremely complicated due to the combination of multiple paramagnetic cobalt centers, multiple dioxolene/semiquinone ligands and two photochromic ligands which can take either the open or closed-form. Therefore, EA and IR were used to characterize the structures, along with single crystal XRD.

4.2.2. Structural Analysis of the Photochromic Cobalt Clusters in the Solid State

Structural analysis carried out at 90 K by single crystal X-ray crystallography revealed the structure of the tetranuclear complexes **4.3** and **4.4** as $Co_4(II)(SQ^{\bullet -})_4(Cat^{2-})_2(PMC\text{-}APSO)_2(MeOH)_2$ and $Co_4(II)(SQ^{\bullet -})_4(Cat^{2-})_2(SO\text{-}IPSO)_2(MeOH)_2$, respectively. The crystal structure of **4.3** was previously reported in the dissertation of Michelle Paquette.[223]

The molecular structure of **4.3** is shown in Figure 4.3, and selected bond lengths and angles are shown in Table 4.1 for comparison to the structure of **4.4**.

The tetranuclear complex **4.3** contains two hexacoordinate cobalt centers (Co1, Co1') and two pentacoordinate cobalt centers (Co2, Co2') in a coplanar arrangement. The core cobalt centers bind to six dioxolene ligands and two APSO ligands **2.2** with a coordination geometry similar to that found in Co_4(3,5-DTBQ)$_8$ **5.1** as reported by Buchanan *et al*.[274] The APSO ligands were found to exist predominantly in the open form, which is consistent with the negative-photochromic nature of the ligand. The hexacoordinate cobalt centers (Co1, Co1') are found in nearly octahedral coordination geometries and bind to two nitrogen atoms (N1, N2) from the APSO ligand **2.2**, and two μ_2 (O3, O5) and the μ_3 (O7) bridging oxygen atoms from the dioxolene ligands. The pentacoordinate cobalt centers (Co2, Co2') on the other hand exist in a distorted trigonal bipyramidal geometry. The Co2 and Co2' coordinate to a μ_3 (O4) bridging and a MeO/MeOH ligand in the axial position and two μ_2 (O3, O5) and a terminal (O6) oxygen atom in the equatorial position. The bond angles of the Co2 and Co2' with the coordinated atoms on the equatorial position are relatively distorted from 120º (O3–Co2–O5 = 115.8º, O3–Co2–O6 = 108.7º, O6–Co2–O5 = 131.1º).

While the geometry of the core for **4.3** is similar to that of Co_4(3,5-DTBQ)$_8$ complex **5.1**, the coordination environment is not the same. In the Co_4(3,5-DTBQ)$_8$ complex, all four cobalt centers are hexacoordinate whereas Co2 and Co2'in **4.3** are pentacoordinate and coordinate to the MeO/MeOH ligand instead of the dioxolene ligand. In addition, all dioxolene ligands in the Co_4(3,5-DTBQ)$_8$ are chelating while four of the dioxolene ligands in **4.3** are non-chelating. Instead, the APSO ligand **2.2** replaces the four

available coordination sites of the cobalt centers. This core structure is very similar to that of cobalt bicubane analogues consisting of four cobalt centers, the coordination geometry of which are octahedral and distorted trigonal bipyramid.[275-277]

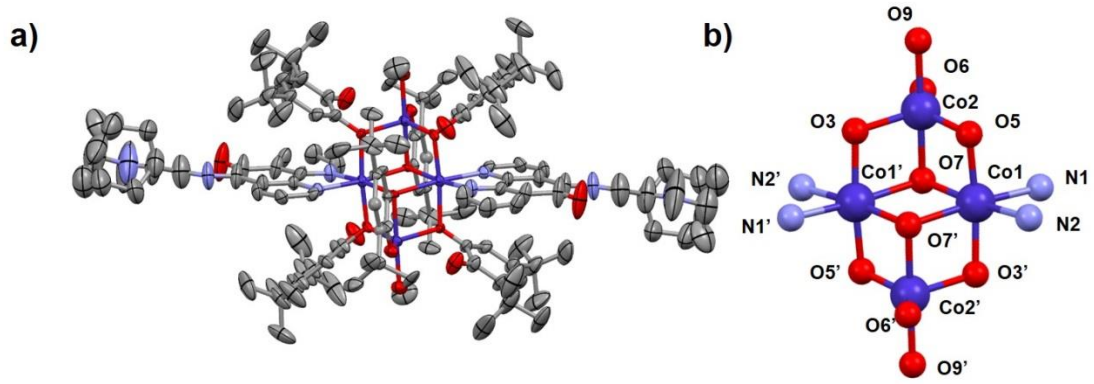

Figure 4.3. Molecular structure of $Co_4(3,5\text{-DTBQ})_6(APSO)_2(MeOH)_2 \cdot 2MeOH$ (**4.3**) (a). Ellipsoids shown at the 33% probability level. Core of the molecular structure of **4.3** (b).[223]

The tetranuclear complex **4.4** was crystallized in the orthorhombic *Pbca* space group with a half-molecule in the asymmetric unit, four molecules per unit cell. The structure was disordered across a mirror plane, resulting in poor refinement factors ($R_1 = 0.1925$, w$R_2 = 0.3290$). The poor refinement factors are predominantly attributed to the photochromic ligands existing in equilibrium between two isomers. The molecular structure of **4.4** is shown in Figure 4.4. Similar to **4.3**, the tetranuclear complex **4.4** contains two hexacoordinate (Co1, Co1') and two pentacoordinate cobalt centers (Co2, Co2') in a coplanar arrangement. The core cobalt centers bind to six dioxolene ligands and two IPSO ligands **4.2**. The IPSO ligands crystallize in the closed-form, which is consistent with the positive-photochromic nature of the IPSO ligand **4.2**.

The tetranuclear complex **4.4** crystallizes with significant disorder as reflected in the large refinement factors (R_1: 0.1945, wR_2: 0.3778). Besides positional disorder typical of *t*-butyl groups, a disorder in the position of the Co2–OHMe fragment is subsequently coupled with the disorder about the coordinating C–O (C40–O5 and C53–O7) bonds in two of the $SQ^{\bullet-}$ ligands. In addition, the IPSO ligands exists as a mixture of both the closed and open forms, as determined by ^{1}H NMR, which introduces significant disorder of the ligand structure. The closed form is prevalent, with the coordinated phenanthroline moiety common to the two forms. The enlarged ellipsoids of the indolyl fragment strongly suggest significant thermal motion or an averaging of multiple orientations of the indolyl fragment. Refinement of the site occupancy of this fragment suggests the crystal consists of approximately 74% closed form in this orientation. The open form of the ligand is virtually indiscernible. Attempts to fit the electron density map to multiple possible isomers of the PMC form did not lead to improved fit. Electron density consistent with an extra X–CH_3 group bound to the azomethine carbon of the closed form results in a better fit to the electron density map. One possibility is that while the complex crystallizes with the photochrome in the SO form, it is known from UV-Vis in solution and the color of the crystals that the open form is present in a roughly 20% mixture of open/closed. It is possible that the low resolution data observed is due to the disorder caused by the presence of both open and closed forms in the lattice, making structural modeling of the photochromic moiety difficult. Certainly, if functionalization of the azomethine backbone took place, the photochrome would no longer be photochromic, and as will be discussed later, the samples are all

photochromic. For these reasons, the additional X–CH_3 group is attributed to extra electron density due to disorder and low resolution XRD data. However, functionalization of some portion of the sample cannot be unambiguously ruled out. Examples of structurally similar spiropyrans show that functionalization of the azomethine carbon with O–CH_3 while the azomethine C–N bond maintains double bond character leads to photochromic derivatives.[278] Elemental analysis suggests that if partial functionalization of the photochrome takes place, the X–CH_3 moiety must be a methoxy group (-O–CH_3), and that one of the methanol molecules attributed to solvent in the lattice may instead be covalently bound. The bond length of the azomethine N3–C13 was found to be 1.36(2) Å, which is significantly longer than the N=C bond of the free IPSO ligand (1.2809(11) Å) suggesting that perhaps some degree of functionalization of the ligand *in situ* may have taken place.[46]

The geometry of **4.4** is very similar to that of the structure of **4.3** (Figure 4.4). The hexacoordinate cobalt centers (Co1, Co1') are found to exist in octahedral coordination geometries due to binding to two nitrogen atoms (N1, N2) from the IPSO ligand with two μ_2 (O3, O5) and a μ_3 (O7) bridging oxygen atoms from the dioxolene ligands. The pentacoordinate cobalt centers (Co2, Co2') exist in distorted trigonal bipyramidal geometries. The Co2/Co2' metal centers are axially bound by a μ_3 (O7) bridging and a MeO/MeOH ligand, and equatorially by two μ_2-oxygens (O3, O5) and a terminal (O6) oxygen. The O9–Co2–O7 angle is nearly 180° at 177.5(4)° while the three bond angles associated with equatorially coordinated atoms is about 120° (O3–Co2–O5 113.9(3) °, O3–Co2–O5 121.6(4) °, and O5–Co2–

O6 120.1(4)°). The nearly 120° equatorial bond angles suggest a less distorted trigonal bipyramidal geometry than that of **4.3**.

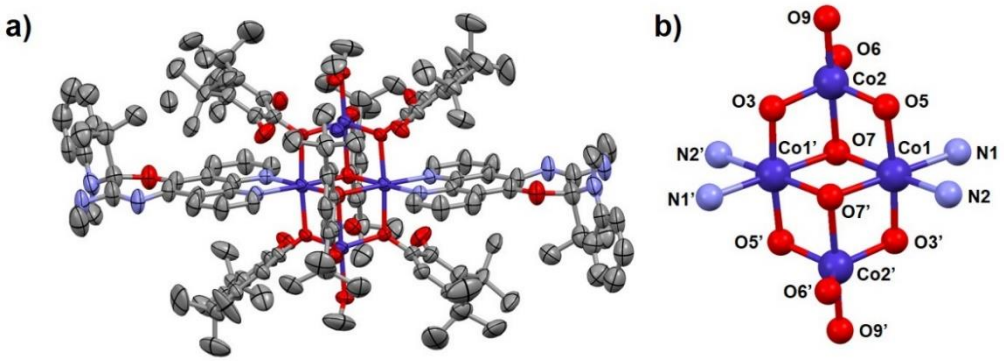

Figure 4.4. Molecular structure of Co_4(3,5-DTBQ)$_6$(IPSO)$_2$(MeOH)$_2$ (**4.4**) (a). Ellipsoids shown at the 20% probability level. Core of the molecular structure of **4.4** (b).

Table 4.1. Selected Bond Lengths (Å) and bond angles (º) for 4.3 [a] and 4.4.[b]

Bond Length	**4.3**	**4.4**
Co1'–O3	2.070 (4)	2.069 (7)
Co1'–O7	2.158 (7)	2.114 (6)
Co1'–O7'	2.175 (4)	2.082 (7)
Co1'–O5'	2.070 (4)	2.096 (7)
Co1'–N1'	2.128 (7)	2.141 (6)
Co1'–N2'	2.143 (8)	2.121 (5)
Co2–O3	1.975 (4)	1.906 (8)
Co2–O5	1.930 (9)	1.949 (7)
Co2–O7	2.168 (6)	2.283 (8)
Co2–O6	1.898 (5)	1.913 (11)
Co2–O9	2.086 (10)	2.109 (10)
Bond Angle	CoAPSO **4.3**	CoIPSO **4.4**
O9–Co2–O7	176.1	177.5 (4)
O3–Co2–O5	115.8	113.9 (3)
O3–Co2–O6	108.7	121.6 (4)
O6–Co2–O5	131.1	120.1 (4)

[a] Ref.[223] [b] Formula: $C_{136}H_{178}Co_4N_9O_{18}$. FW: 2462.58 g·mol^{-1}. Crystal system: orthorhombic. Space group: *Pbca* (no. 61). *a*: 15.9002(9) Å. *b*: 28.7289(15) Å. *c*: 29.3550(16) Å.$\alpha = \beta = \gamma = 90°$. *V*: 13409.2(13) Å^3. $Z = 4$. ρcalc = 1.220 g·cm^{-3}. $\mu = 4.325$ cm^{-1}. *T*: 90(2) K. λ: 1.54178 Å. GooF: 1.285. R_1: 0.1945. wR_2: 0.3778. $R_1 = \Sigma||Fo| - |Fc|| / \Sigma|Fo|$. $wR_2 = [\Sigma(w(Fo^2 - Fc^2)^2) / \Sigma w(Fo^2)^2]^{1/2}$

The geometries of the cobalt-dioxolene complexes differ considerably between the *hs*-Co(II)/*ls*-Co(III) states allowing determination of the oxidation states of the cobalt centers based on Co–O and Co–N bond lengths. In general, the Co–O and Co–N bond length in *hs*-Co(II) hexacoordinate complexes are expected to be 0.10-0.20 Å longer than that in the *ls*-Co(III) complexes. In the *hs*-Co(II) complexes, the antibonding (e_g*) type orbitals are populated, leading to longer ligand-metal bond lengths. Typical Co–O bond lengths for the *hs*-Co(II) and *ls*-Co(III) centers found in similar systems [Co(3,5-DTBQ)$_2$(phen)],[120] and [Co$_4$(3,5-DTBQ)$_8$][274] are 2.02–2.18 Å and 1.86–1.92 Å, respectively. For the tetranuclear complex **4.3**, the Co–O bond lengths of the hexacoordinate cobalt centers (Co1, Co1') were found to be 2.070 (4) Å, 2.158 (7) Å, 2.175 (4) Å, and 2.070 (4) Å for Co1'–O3, Co1'–O7, Co1'–O7', and Co1'–O5, respectively. All the Co–O bond lengths found in the Co1 and Co1' fall within the range expected for a *hs*-Co(II) species. Similarly, the Co–N bond lengths of the Co1 and Co1' were 2.128 (7) Å and 2.143 (8) Å, for Co1–N1 and Co1–N2, respectively. The Co–N bond lengths of *hs*-Co(II) and *ls*-Co(III) complexes are typically found in the range of 2.13–2.14 Å[120] and 1.93–1.96 Å,[120,223] respectively. Both Co–O and Co–N bond lengths suggest the hexacoordinate cobalt centers (Co1, Co1') are *hs*-Co(II) state. Contrarily, the Co–O bond lengths of the pentacoordinate cobalt centers (Co2, Co2') were found to be relatively shorter than Co1 and Co1' (1.975 (4), 1.898 (5), 2.168 (6), and 1.930 (9) for Co2–O3, Co2–O6, Co2–O7, and Co2–O5, respectively). Unlike hexacoordinate cobalt complexes, examples of pentacoordinate Co(3,5-DTBQ) complexes are very limited, and only *hs*-Co(II) complexes have been reported.,[279-281] The Co–O bond lengths for the *hs*-Co(II) centers in pentacoordinate cobalt-dioxolene complexes with distorted trigonal bipyramid

geometry were found to be within the range of 1.87–2.05 Å,[279-281] which is significantly shorter than *hs*-Co(II)–O bond lengths found in hexacoordinate cobalt dioxolene complexes. A pentacoordinate bridging Co–(μ_2-O) bond was found to be longer (~2.15 Å) than the terminal Co–O bond which is consistent with the Co–(μ_3-O) bond length of the complex **4.3** being longer than Co–(μ_2-O) and terminal Co–O bond lengths.[281] The Co–O bond lengths for the Co2 and Co2' centers fall within the range expected for the pentacoordinate *hs*-Co(II) species. Despite the fact that the reported pentacoordinate cobalt dioxolene complexes have different ancillary ligands (hydrotris(cumenylmethyl-pyrazolyl)borate,[279] phenyltris-((tert-butylthio)methyl)borate,[280] or t(BuCOO)$_4$(NEt$_3$)$_2$,[281] they are all donor ligands and the oxidation states of the Co2 and Co2' centers are assigned as *hs*-Co(II). Therefore, all four cobalt centers of **4.3** are likely *hs*-Co(II) at 90 K. The relatively long non-bridging Co–O bond length (2.086 (10) Å) of the MeO/MeOH ligand suggests that the methoxy ligand is likely protonated. Therefore, the electronic structure of the complex **4.3** at 90 K is assigned as $Co_4(II)(SQ^{\bullet-})_4(Cat^{2-})_2$(PMC-APSO)$_2$(MeOH)$_2$.

Bond length analysis of the tetranuclear complex **4.4** suggests that the assignment of cobalt oxidation and spin state in **4.4** is very similar to that of **4.3**. The Co–O bond lengths of the hexacoordinate cobalt centers (Co1, Co1') were found to be 2.065(7) Å, 2.113(6) Å, 2.081(7) Å, and 2.094 (7) Å for Co1'–O3, Co1'–O7, Co1'–O7', and Co1'–O5, respectively. The Co–N bond lengths of the Co1 and Co1' are 2.122(5) Å and 2.141(6) Å, for Co1–N1 and Co1–N2, respectively. The Co1–O and Co1–N bond lengths all fall within the range expected for a *hs*-Co(II) species, suggesting that the hexacoordinate cobalt centers (Co1, Co1') are in the *hs*-Co(II) state. Similarly, the Co–O bond lengths of the pentacoordinate cobalt centers (Co2,

Co2') were found to be 1.910(7), 1.917(11), 2.289(8), and 1.961(7) for Co2–O3, Co2–O6, Co2–O7, and Co2–O5, respectively. The Co–O bond lengths for the Co2 and Co2' centers also fall within the range expected for a pentacoordinate *hs*-Co(II) species. Hence, all four cobalt centers of **4.4** are assigned as *hs*-Co(II) at 90 K. The long Co–O bond lengths (2.113(10) Å) of the MeO/MeOH ligand suggests the methoxy ligands are protonated. Therefore, the electronic structure of **4.4** at 90 K is assigned as $Co_4(II)(SQ^{\bullet -})_4(Cat^{2-})_2(SO\text{-}IPSO)_2(MeOH)_2$.

A bond valence sum (BVS) analysis of the tetranuclear complexes **4.3** and **4.4** supports the assignment of all cobalt centers existing in the *hs*-Co-(II). The BVS analysis was performed using parameters from experimentally determined bond lengths and angles.[282] The bond valence states of the Co1/Co1' and Co2/Co2' centers were determined to be 1.9 and 2.1, respectively, in **4.3** and 2.0 and 2.1, in **4.4**, respectively, suggesting that all of the cobalt centers are in the +2 oxidation state.

Assignment of the oxidation state based on bond valence sum analysis assumes that the experimental error in the bond lengths of interest is within the error associated with BVS assigned oxidation states.[283] The differences in Co–O bond lengths (0.05–0.20 Å) of the Co(II)/Co(III) forms for the parent analogue phen-derivative are greater than the experimentally determined 2σ values (0.008–0.022 Å) for **4.3** and **4.4**, supporting the validity of using BVS analysis for assignment of the oxidation state in the tetranuclear complexes **4.3** and **4.4**. The caveat however, is that bond valence sum analysis was originally formulated for localized metal centers.[282] The bond valence states of cobalt in the parent analogues *hs*-Co(II)(3,5-$DTSQ^{\bullet -}$)$_2$(phen) and *ls*-Co(III)(3,5-$DTSQ^{\bullet -}$)(3,5-$DTCat^{2-}$)(phen) were reported as 2.3 and 3.7, respectively, consistent with a +2 and + 3

oxidation state in cobalt complexes. In addition, the bond valence state of the structurally similar *ls*-Co(III)(APSO)(3,5-DTSQ$^{\bullet-}$)(3,5-DTCat^{2-}) was reported as 3.2,[260] consistent with a +3 oxidation state. The bond valence sum analysis therefore leads to a reasonable prediction of the metal-centered oxidation state, despite its mixed-valent character. The tetranuclear complexes are most likely mixed-valent (Co(II)-Co(III)) to some extent, which gives rise to their electronic bistability. Nevertheless, it is assumed here that the degree of mixed-valency is small relative to the charge localization at 90 K, and the good agreement with known bond lengths suggests that the assignment of *hs*-Co(II) for all four cobalt centers in both tetranuclear complexes **4.3** and **4.4** is valid.

4.2.3. Structural Analysis of the Photochromic Cobalt Clusters in Solution State

In general, redox-isomeric cobalt dioxolene complexes undergo a change in oxidation/spin state from the *ls*-Co(III) to the *hs*-Co(II) with increasing temperature in an entropically-driven process. The population of the *hs*-Co(II) state at high temperature is due to the greater entropic contributions to the Gibbs free energy of the *hs*-Co(II) than the *ls*-Co(III) species.[120] Likewise, the photochromic ligand can thermally isomerize between the PMC and SO states, either of which can be the ground state in a given complex. Two possible oxidation states of the cobalt center (*hs*-Co(II) vs. *ls*-Co(III)) for four metal centers and two possible isomeric states of the two photochromic ligands (PMC vs. SO) results in thirty-six (6^2) possible states of the Co clusters (Figure 4.5).

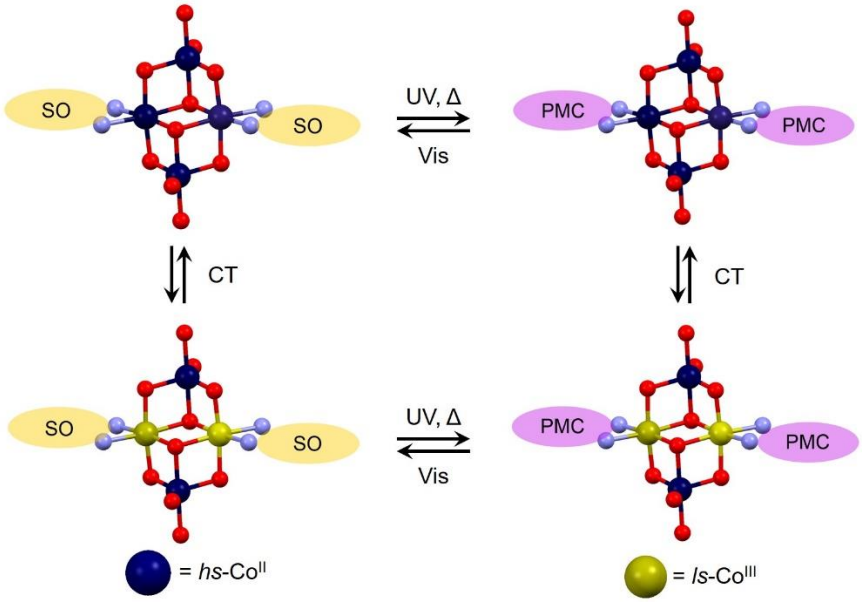

Figure 4.5. Four of the many possible states for the tetranuclear complexes **4.3** and **4.4**.

Characteristic spectral features typically seen in this class of redox-isomeric Co(3,5-DTBQ)$_2$ complexes contains information about the oxidation state of the cobalt centers. The distinct spectroscopic features arise from the presence of different redox isomers. The electronic absorption spectrum of the Co(3,5-DTBQ)$_2$(NN)$_2$ complex - typically shows a broad absorption band at $\lambda_{max} \approx 765$ nm with a shoulder at $\lambda_{max} \approx 640$ nm corresponding to a metal-to-ligand *hs*-Co(II) → $SQ^{\bullet-}$ charge-transfer (MLCT) band of the Co(II) state.[120] A decrease in intensity of the MLCT band along with an appearance of a new band at ≈ 600 nm, characteristic of the *ls*-Co(III), was observed for the parent as with decreasing temperature (295 K to 210 K).[120] At low temperature (210 K), the dominant spectral characteristic is the band at ≈ 600 nm, suggesting greater population of the Co(III) form. The change in electronic absorption spectrum with temperature is therefore informative in assigning the *hs*-Co(II) or *ls*-Co(III) state.[120] In addition, a broad band at

$\lambda_{max} \approx 2500$ nm is observed at low temperature arising from either a $Cat^{2-} \rightarrow$ *ls*-Co(III) charge transfer.

Variable-temperature electronic absorption spectroscopy of the tetranuclear complexes **4.3** and **4.4** suggest that thermal conversion of the photochromic ligand is strongly coupled with the metal-ligand charge transfer processes to give Co(III)(Cat^{2-}) ↔ *hs*-Co(II)($SQ^{\bullet-}$) interconversion. Variable-temperature electronic absorption spectroscopy was measured to determine the positions of thermal equilibrium for the Co(II)/Co(III) and SO/PMC equilibria processes as function of temperature. Variable-temperature electronic absorption spectra of **4.3** in toluene are shown in Figure 4.6a. At 293 K, the electronic absorption spectrum of **4.3** exhibits a prominent PMC π–π* band with a λ_{max} of 555 nm, similar to the free ligand (554 nm). The spectrum also shows a broad absorption band at ($\lambda_{max} \approx 770$ nm) assigned to the *hs*-Co(II) → $SQ^{\bullet-}$ MLCT transition. Closer inspection of the spectrum of **4.3** at 293 K (Figure 4.6b) shows two broad bands which can be deconvoluted to a transition at $\lambda_{max} \approx 770$ nm and $\lambda_{max} \approx 1050$ nm. The two bands may be due to MLCT transitions associated with the two different photochromic states to give an SO-*hs*-Co(II) → $SQ^{\bullet-}$ and PMC-*hs*-Co(II) → $SQ^{\bullet-}$ transition. No bands in the NIR region were observed at 293 K suggesting a low population of the Co(III) state at 293 K. The presence of the MLCT band and absence of the LMCT band with the intense PMC π–π* band suggests that PMC-*hs*-Co(II) is the dominant state of **4.3** at 293 K in solution, which is consistent with single crystal XRD analysis. A small population of Co(III) in solution at 293 K however cannot not be ruled out, as the absorption bands are weak and of low intensity for this state.

An increase in temperature from 293 K to 333 K results in a small decrease in intensity of the PMC π–π* band, due to conversion to the SO form with increasing temperature. This is consistent with the greater thermodynamic stability of the PMC form in **2.2**, and a thermally-induced isomerization from PMC → SO form. Contrarily, the broad MLCT band with a λ_{max} of 770 nm increases slightly at higher temperatures with an isosbestic point at 570 nm, indicative of redox isomerization from the *ls*-Co(III) to *hs*-Co(II) states. The slight increase in population of the *hs*-Co(II) state at high temperature is attributed to formation of the SO form, which is predicted to stabilize the *hs*-Co(II) state. The closed SO form is a better π–acceptor (by 0.3 eV) and is therefore expected to preferentially stabilize the more electron-rich Co(II) metal center,[265] which would lead to an increase in population of the *hs*-Co(II) form at high temperature. Variable-temperature spectroscopic studies of **4.3** suggests that the dominant form in solution at 293 K is the PMC-*hs*-Co(II) state and that redox and thermochromic isomerism between the PMC-*ls*-Co(III) and SO-*hs*-Co(II) states occurs with increasing temperature, though to a small extent. The small change in Co oxidation/spin state observed in **4.3** is attributed to the fact that the dominant species in solution at 293 K is the PMC-Co(II) state, with only a very small population of the Co(III) state under these conditions. Conversion from the PMC to SO form therefore leads to only a very small increase in population of the Co(II) state. It does however suggest that the predicted directionality of change for photochrome state and redox isomerism is correct.

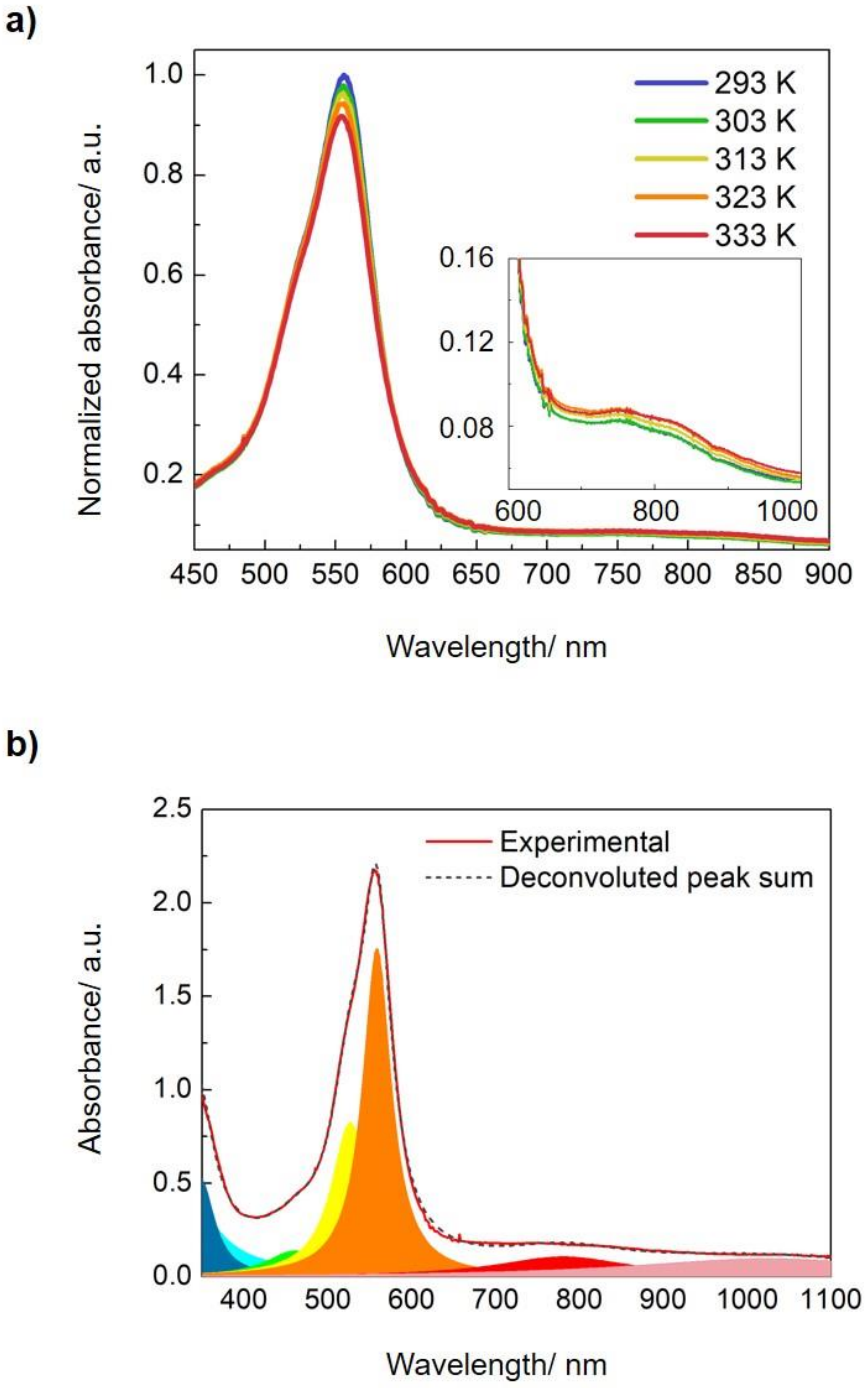

Figure 4.6. Electronic absorption spectrum of **4.3** (a) from 293 – 333 K in toluene [1×10^{-4} M] and (b) deconvoluted electronic absorption band in toluene at 298 K using Lorentzian function (grey dash: sum of deconvoluted peaks, red: original absorption band).

It is this observation that led to the hypothesis that initiated preparation of the tetranuclear complex **4.4**. We hypothesized that if one were to generate a cluster in which the dominant state at room temperature were the SO-Co(II) state, conversion to the PMC form would lead to conversion to the Co(III) state, leading to a larger change in redox isomers with optical gating. As the indolyl-spirooxazines exist in the SO form in the ground state, incorporation of an indolyl-phenanthroline ligand (IPSO) into the tetranuclear complexes would lead to a larger change in redox isomerism with light or temperature than that observed in **4.3**.

Variable-temperature electronic absorption spectroscopy of the tetranuclear complex **4.4** shows that thermal conversion of the photochromic ligand leads to charge transfer processes between the *ls*-Co(III)(Cat^{2-}) and *hs*-Co(II)($SQ^{\bullet-}$) states. Variable-temperature electronic absorption spectra of **4.4** in toluene are shown in Figure 4.7a. At 293 K, the electronic absorption spectrum of **4.4** exhibits a prominent PMC π–π* absorption band with λ_{max} = 593 nm, which is bathochromically shifted from that of the free ligand (583 nm).[46] Similar to **4.3**, the spectrum also shows a broad absorption band ($\lambda_{max} \approx$ 750 nm) corresponding to the *hs*-Co(II) → $SQ^{\bullet-}$ MLCT band. A deconvoluted spectrum of **4.4** at 293 K (Figure 4.7b) also shows two broad transitions at $\lambda_{max} \approx$ 770 nm and $\lambda_{max} \approx$ 1050 nm, which may be associated with the two states of the photochrome isomers to give a transition *hs*-Co(II)(SO) → $SQ^{\bullet-}$ and *hs*-Co(II)(PMC) → $SQ^{\bullet-}$. Investigation of the NIR region in a thin film at 300 K reveals the absence of a Cat^{2-} → *ls*-Co(III) LMCT band at 2500 nm suggesting a negligible concentration of the *ls*-Co(III) at 300 K. The presence of the MLCT band and absence of the LMCT band suggest that the *hs*-Co(II) is the dominant form of **4.4** at 293 K in solution and in the solid state.

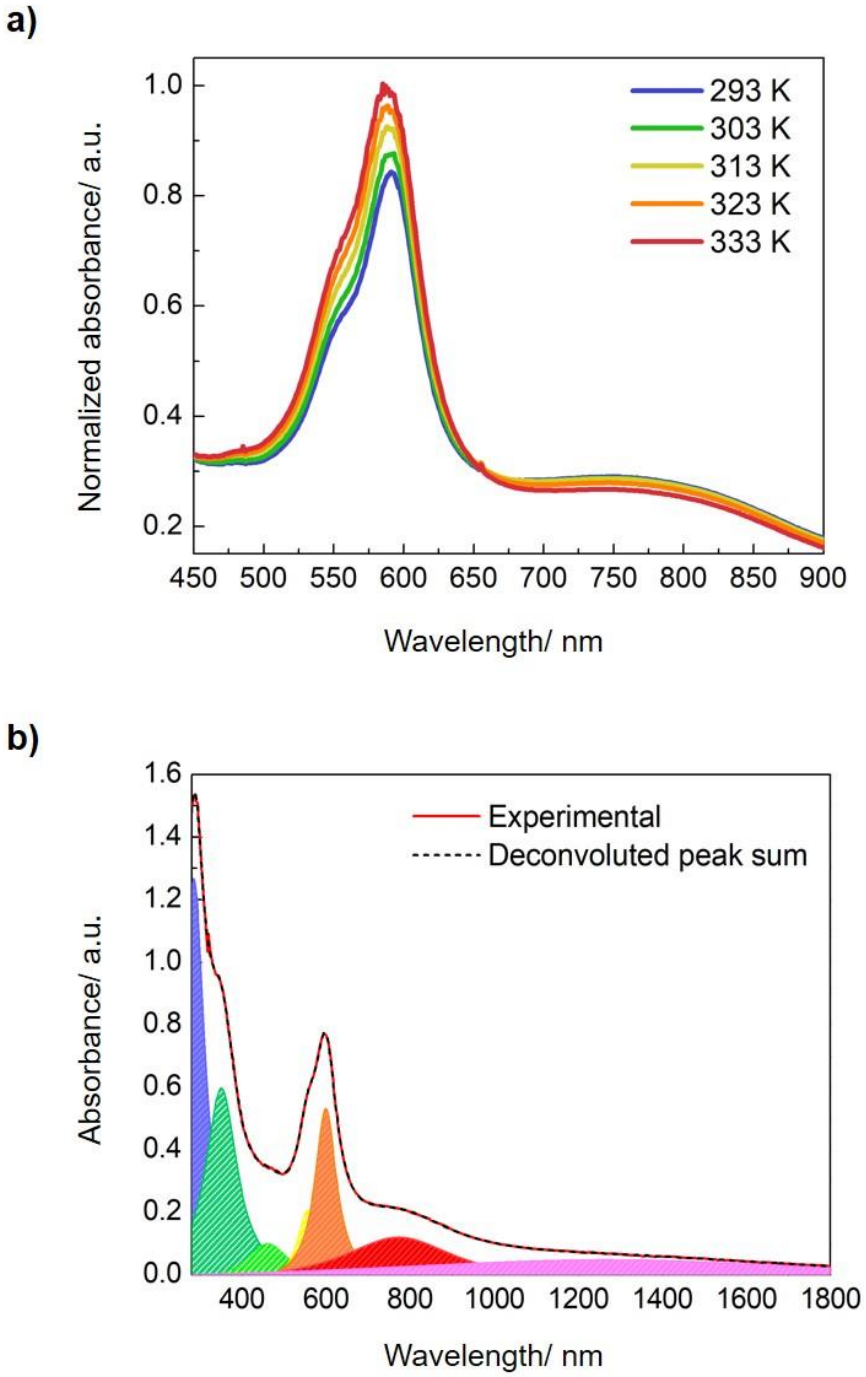

Figure 4.7. Electronic absorption spectrum of **4.4** (a) from 293 – 333 K in toluene [1×10^{-4} M] and (b) deconvoluted electronic absorption band in toluene at 298 K using Lorentzian function (grey dash: sum of deconvoluted peaks, red: original absorption band).

An increase in temperature from 293 K to 333 K resulted in an increase in the intensity of the PMC π–π* band, indicative of the greater thermodynamic stability of the SO form in solution. This is contrary to **4.3**, in which the thermodynamically stable form of the photochrome is the open PMC form. Investigation of the electronic absorption spectra of **4.4** in the thin film with decreasing temperature (300 K to 150 K) revealed no change presumably due an increase in the barrier to thermal isomerization in constrained media. With regard to the metal-centered transitions, observation of a broad MLCT band at $\lambda_{max} \approx 750$ nm was observed which decreased reversibly with increasing temperature from 293 K to 333 K (isosbestic point at 660 nm). The decrease in the MLCT band with increasing temperature is indicative of an increase in population of the $Cat^{2-} \rightarrow$ *ls*-Co(III) state at higher temperatures. Surprisingly, the MLCT band decreased with decreasing temperature as well, from 300 K to 150 K in the thin film (Figure 4.8), suggesting depopulation of the *hs*-Co(II) state via a thermally driven isomerization to the *ls*-Co(III)$\rightarrow Cat^{2-}$ charge transfer state. The question arises, how can conversion to the Co(III) state occur with increasing *and* decreasing temperature, as this would require opposite thermodynamic processes to give the same final state of the metal center.

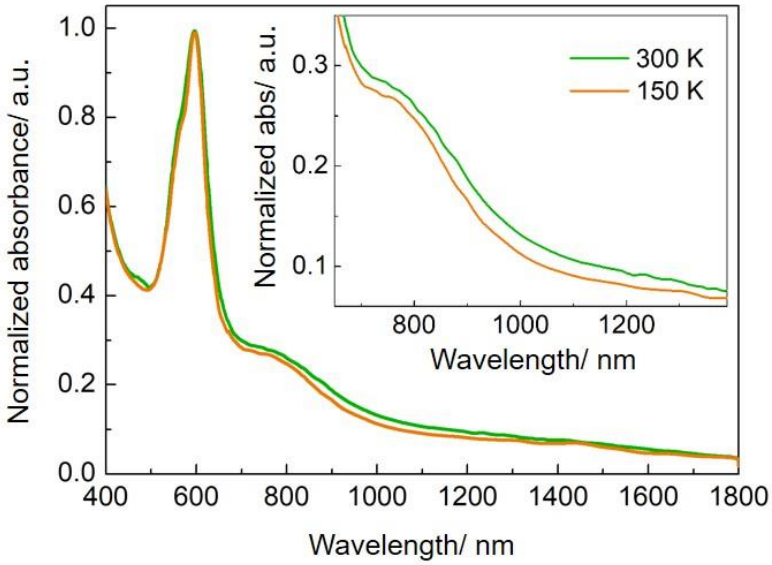

Figure 4.8. Electronic absorption spectrum of **4.4** at 300 and 150 K in thin film prepared by spin coating under Ar.

As was seen in the complex **4.3**, and all other known cobalt-dioxolene complexes,[77,111,120] the *hs*-Co(II) species is preferentially stabilized at higher temperatures due to entropic contributions. The conversion to the *ls*-Co(III) state with decreasing temperature is in agreement. It is noted here that photochrome isomerization was not observed on going to lower temperatures in the thin film state. This suggests that the behaviour of **4.4** upon decreasing temperature is wholly dictated by the thermal redox isomerism process observed in the greater class of cobalt dioxolenes. Upon increasing temperature however, the reverse of this process is observed, wherein an *increase* in the Co(III) state is observed on going from 295 to 333 K. It is also noted that thermal isomerization of the photochrome from the SO to the PMC state *is* observed. This suggests that the high temperature behaviour is dictated by the thermal equilibrium of the photochrome, and suggests strong coupling between the photochrome state and metal-centered oxidation/spin state.

Earlier work suggested that the closed SO form would function as a better π–acceptor (by 0.3 eV) and would preferentially stabilize the electron-rich Co(II) over the Co(III) oxidation state.[265] Contrarily, the PMC state should stabilize the Co(III) state. Therefore, thermal conversion from the SO to the PMC form at high temperatures, which was only observed in solution, should induce a charge-transfer coupled spin-transition process from the *hs*-Co(II)$SQ^{\bullet-}$ to the *ls*-Co(III)Cat^{2-} state, as was observed. This data provides critical evidence for strong coupling between the photochrome state and metal-centered oxidation/spin state, suggesting that the state of the photochrome can induce charge transfer processes in the cobalt-dioxolenes.

Overall, variable-temperature spectroscopic studies of the tetranuclear complexes **4.3** and **4.4** suggest that the multicentered clusters are dominated by the PMC and *hs*-Co(II) or SO-*hs*-Co(II) in solution and the thin film states at 293 K, respectively. The tetranuclear complexes **4.3** and **4.4** undergo redox isomerism between the SO-*hs*-Co(II) and PMC-*ls*-Co(III) states, in which the charge-transfer process is dictated by the thermal equilibrium of the photochromic ligands. The strong coupling between the SO and PMC thermal isomerization and redox-isomeric process in these systems results in the photochrome state effectively overcoming the entropic contributions to the charge-transfer coupled spin transition process.

4.2.4. Magnetic Properties of the Photochromic Cobalt Clusters

Temperature-dependent DC magnetization measurements of polycrystalline samples of **4.3** and **4.4** were performed from 300 K to 2 K at 10,000 Oe to determine

the ground state spin states and spin state transition temperatures for the two complexes. The magnetic moment (χT) per tetranuclear cluster at 300 K for **4.3** and **4.4** were found to be 9.5 and 9.9 emu·K·mol^{-1}, respectively (Figure 4.9). The magnetic moment of the clusters at 300 K is consistent with the spin-only value for four magnetically isolated isotropic *hs*-Co(II) centers (S = 3/2, g = 2) with four magnetically isolated SQ$^{\bullet-}$ ligands (S = 1/2, g = 2) to give a moment of 9 emu·K·mol^{-1}. Similar magnetic moments (10.20–12.22 emu·K·mol^{-1}) at 300 K were reported in the Co(II)$_4$ bicubane clusters which consists of two hexacoordinate and two pentacoordinate trigonal bipyramidal cobalt centers.[275-277] The slightly smaller magnetic moment found in **4.3** and **4.4** relative to other cobalt bicubane analogous may be due to the presence of weak antiferromagnetic exchange interactions between the cobalt centers and SQ$^{\bullet-}$ ligands.

A gradual decrease in the magnetic moment of **4.3** from 300 K to 2 K is observed with a transition temperature $T_{1/2}$ at ≈ 25 K (Figure 4.9a) that indicates depopulation of the *hs*-Co(II) state with decreasing temperature. Similarly, a gradual decrease in magnetic moment of **4.4** from 300 K to 2 K with transition temperature $T_{1/2}$ at ≈14 K (Figure 4.9b) implies similar behavior. Both complexes therefore show gradual transitions to the *ls*-Co(III) state with decreasing temperature due to redox isomerism. The presence of a gradual rather than abrupt transition may be due to the presence of four cobalt centers per cluster, each of which may be electronically coupled, leading to different "transition temperatures" for each cobalt center in the cluster. Each center then undergoes a transition via a change in Boltzmann population of states, rather than exhibiting any cooperativity.

The transition temperature of the bulk sample then becomes the superposition of these individual transition temperatures, leading to a gradual, rather than abrupt transition.

Analysis of the magnetic moment at low temperature provides information about the ground state spin state. In a cluster of uncoupled *hs*-Co(II) centers, the combined effect of a distorted octahedral ligand field and spin-orbit coupling produces six Kramer's doublets with energy splitting on the order of 100–200 cm^{-1}.[284] Hence, each Co(II) center can be described by an effective spin ½ Hamiltonian at low temperature, where only the ground state Kramer's doublet is thermally populated. The magnetic moments at low temperature (2 K) of the tetranuclear complexes **4.3** and **4.4** were found to be 2.6 and 3.0 $emu \cdot K \cdot mol^{-1}$, respectively, indicating that the complexes exhibit similar electronic structures at low temperature as well as at room temperature. The moments of **4.3** and **4.4** are both slightly larger than the χT value (1.5 $emu \cdot K \cdot mol^{-1}$) of two uncoupled Co(II) centers (S = 1/2, $g = 2$) and two $SQ^{\bullet-}$ ligands (S = 1/2, $g = 2$). The deviation of the magnetic moments of the complexes **4.3** and **4.4** from a spin-only formalism may be due to the large *g*-value, zero-field splitting, and spin-orbit coupling present in cobalt centers. Overall, the magnetic behavior from 300 K to 2 K suggests that there is charge transfer coupled spin transition process in both clusters from a *hs*-$Co_4(II)(SQ^{\bullet-})_4(Cat^{2-})_2$ to a *ls*-$Co_2(II)Co_2(III)(SQ^{\bullet-})_2(Cat^{2-})_4$ state.

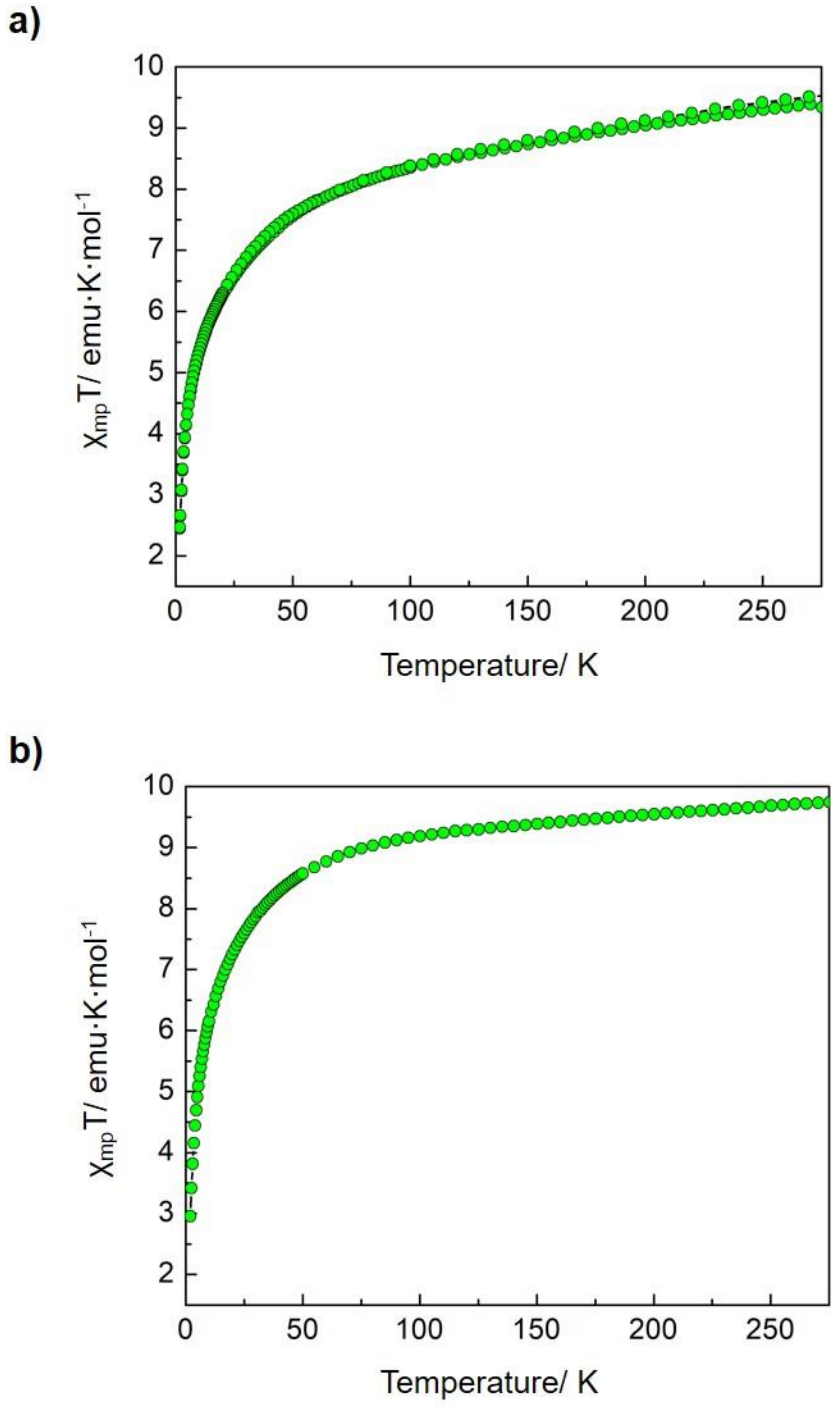

Figure 4.9. DC Magnetization 2–300 K at 10,000 Oe measured with MPMS of **4.3** (a), and **4.4** (b).

Modelling of the magnetic behaviour of the tetranuclear complexes **4.3** and **4.4** as a function of temperature requires an understanding of the contributions of magnetic exchange interactions, spin-orbit coupling and *g*-anisotropy to the bulk magnetic behaviour, which for these clusters is extremely complicated. In model tetranuclear bicubane cobalt clusters, two types of Co–Co exchange interactions have been described, Co1–O7–Co1' (J_1) and Co1–O3–Co2 (J_2) shown in Figure 4.10.[275] Here, we assume that metal-metal magnetic exchange interactions between Co2 and Co2' are negligible due to the large internuclear distance between the Co2 and Co2'centers, which was found to be 5.17 Å in **4.3** and **4.4**, well-outside the sum of van der Waal's radii for two cobalt centers (400 pm, 4 Å).[285] The magnitude and sign of exchange interactions J_1 and J_2 may be estimated by the inner Co–O–Co (α, J_1) and outer Co–O–Co (β, J_2) bond angles. In general, small Co–O–Co angles favour ferromagnetic (FM) interactions (< 110°) due to orbital orthogonality between the metal d-orbitals and bridging oxygen ligand orbitals. At larger angles, significant orbital overlap occurs, and as a consequence, antiferromagnetic (AFM) interactions dominate, with the transition between FM and AFM interactions occurring at angles close to 107°.[275,286-288] The angle α between Co1 and Co1' in complexes **4.3** and **4.4** is 107.1 and 108.2°, respectively, which is at the minimum in the magnetic exchange curve, and suggests the presence of weak FM or AFM interactions. In analogous cobalt bicubane clusters, the angle α is somewhat smaller (~97.49° to 99.74°).[275,276,289-292] However, the observed magnetic properties of the analogous clusters were not always FM as expected, suggesting the magnetic behaviour of the cobalt clusters is a function of both the coupling between Co1/Co1'

and Co2/Co1 as reflected by both α and β.[275] Thus, it is possible, based on geometry that weak or negligible FM exchange interactions may exist between Co1 and Co1'. The angle β of **4.3** and **4.4** were found to be 99.8–103.5° and 100.8–100.5°, respectively, leading to a tentative assignment of weak FM interactions between Co1 and Co2. Typically AFM exchange interactions are observed between the $SQ^{\bullet-}$ ligand and *hs*-Co(II) center in simple mononuclear cobalt dioxolenes,[120], which would suggest AFM metal-ligand interactions in the tetranuclear complexes.

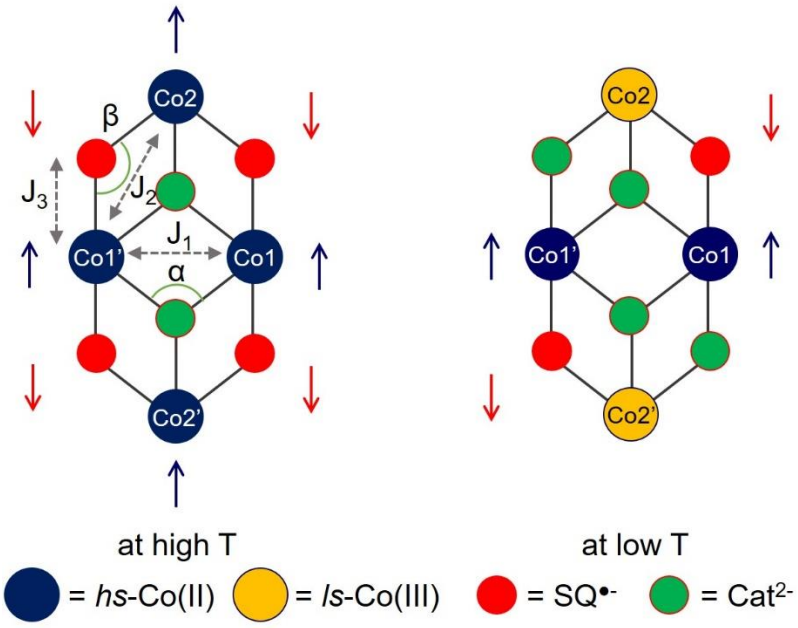

Figure 4.10. Schematic representation of the possible exchange interactions in clusters **4.3** and **4.4** in the limiting high temperature and low temperature structures.

The model of possible metal-metal and metal-ligand exchange interactions for **4.3** and **4.4** at 300 K and 2 K are shown in Figure 4.10. As temperature decreases, charge transfer from the *hs*-Co(II) center to $SQ^{\bullet-}$ ligand is likely to occur, which leaves two FM coupled *hs*-Co(II) (effective S =1/2) and two bridging $SQ^{\bullet-}$ ligands

(S = 1/2) weakly antiferromagnetically coupled to the cobalt centers. Therefore, the *hs*-$Co_4(II)(SQ^{\bullet-})_4(Cat^{2-})_2$ and *ls*-$Co_2(II)Co_2(III)(SQ^{\bullet-})_2(Cat^{2-})_4$ are the best representations of the electronic structure of both **4.3** and **4.4** at 300 K and 2 K.

Solution-state magnetization experiments support the presence of intracluster ferromagnetic exchanges between metal centers. ^{1}H NMR spectroscopy utilizing Evan's method was performed to determine the magnetic moment (χT) of **4.3** and **4.4** in CD_2Cl_2 as a function of temperature from 300 K to 200 K (Figure 4.11). The magnetic moments (χT) of **4.3** and **4.4** at 300 K in CD_2Cl_2 were found to be 14.7 and 16.1 emu·K·mol^{-1}, respectively. The magnetic moments (χT) in solution are significantly higher than the moments in the solid state (9.5 and 9.9 emu·K·mol^{-1}). The increased magnetic moment found in solution may provide additional support for the presence of intracluster ferromagnetic exchange interactions. For the high-temperature model, comprised of four FM coupled Co(II) centers (S = 1/2, g = 2) and four AFM coupled $SQ^{\bullet-}$ ligands (S = 1/2, g = 2) the theoretical magnetic moment is 10 emu·K·mol^{-1}. The experimental values of 14.7 and 16.1 emu·K·mol^{-1} are significantly larger than the theoretical spin-only value, perhaps due to g-anisotropy and spin-orbit coupling, each of which leads to an increase in the observed magnetic moment for *hs*-Co(II) above the spin-only value (χT = 2.76–3.38 emu·K·mol^{-1} per *hs*-Co center in a octahedral complex).[293] The lower moment in the solid state can then be explained by intercluster magnetic dipole-dipole interactions which would lead to a decrease in the overall magnetic moment of the bulk sample due to antiparallel alignment of nearest neighbour clusters.

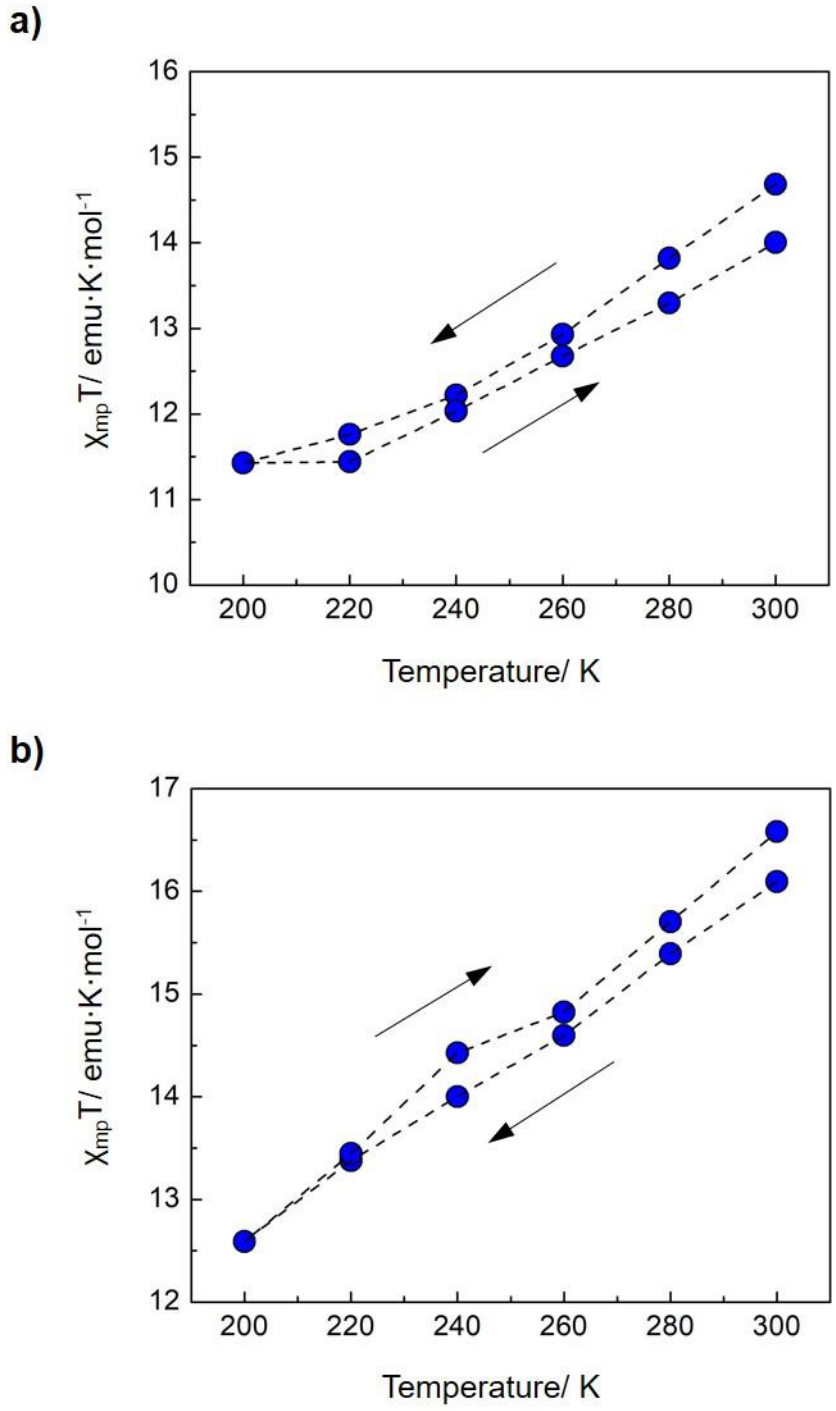

Figure 4.11. Temperature dependence of the magnetic moment (χT) for **4.3** (a) and **4.4** (b) in CD_2Cl_2 (200–300 K) as determined by Evan's method with a 500 MHz spectrometer.

A decrease in temperature from 300 K to 200 K in solution results in a gradual decrease in magnetic moment of **4.3** from 14.7 to 11.4 emu·K·mol^{-1} (Figure 4.11a). Similarly, a gradual decrease in magnetic moment of **4.4** from 16.1 to 12.6 emu·K·mol^{-1} was observed under the same conditions (Figure 4.11b). The decrease in magnetic moment is due to depopulation of the *hs*-Co(II) species, which is consistent with a gradual charge transfer coupled spin transition process, as is observed in solid-state magnetization experiments. A relatively small thermal hysteresis of 10 K was observed from 200K to 300K, for both **4.3** and **4.4**, which may be due to structural changes that are slow relative to the NMR timescale. A possible source of the thermal hysteresis observed may be slow interconversion of the photochromic ligands in frozen solutions. A coupling between ligand state and metal center would then lead to a coupling of photochrome interconversion and metal-centered magnetic state, as is observed. A difference in the direction of hysteresis between the **4.3** and **4.4** clusters is also observed. A descent in temperature results in a decrease in magnetic moment after heating to 300K for **4.3** (14.7 to 14.0 emu·K·mol^{-1} at 300 K) (Figure 4.11a). In complex **4.3**, as the temperature is decreased, the equilibrium shifts to the more thermodynamically stable PMC form, which preferentially stabilizes the *ls*-Co(III) state, leading to a decrease in magnetic moment. Since the thermal interconversion rate from the PMC to SO form would be slower at low temperature in solution, reversion back to the SO form does not occur reversibly on the NMR timescale, and a lower magnetic moment is observed upon increasing temperature to 300 K. Conversely, for complex **4.4**, an increase in the magnetic moment was observed after temperature descent (16.1 to 16.6 emu·K·mol^{-}

^{1} at 300 K, Figure 4.11b). In complex **4.4**, as the temperature decreases, the equilibrium shifts to the SO form, which preferentially stabilizes the *hs*-Co(II) state. Due to the slow thermal interconversion between the SO and PMC forms at low temperature, the SO-*hs*-Co(II) form is effectively trapped, leading to a greater magnetic moment observed with increasing temperature. These observations are consistent with the spectroscopic results and suggest strong coupling between the photochromic ligands and the cobalt-dioxolenes.

4.2.5. Photochromic properties of the Photochromic Cobalt Clusters

Visible light irradiation of the tetranuclear complexes **4.3** and **4.4** further support electronic coupling between the photochromic ligands and the cobalt dioxolene charge-transfer processes. Irradiation of **4.3** in toluene at 300 K with a mixed-gas Ar-Kr laser (multiline $\lambda_{exc} \approx$ 513–568 nm, 100 mW) leads to photoinduced isomerization to the SO form as observed by a decrease in intensity of the PMC π–π^* band at 555 nm. (Figure 4.12). Thermal relaxation to the PMC form occurs in the absence of light with first-order kinetics and a biexponential rate constants of $k_1 = 0.015$ s^{-1} (89 %) and $k_2 = 0.003$ s^{-1} (11 %). The rates of thermal reversion in **4.3** are one to two orders of magnitude slower than the thermal relaxation rates of the parent APSO spirooxazine ligand **2.2** ($k_{obs} = 0.15$ s^{-1}).[46] Biexponential kinetics may result from a thermal relaxation of the two distinct APSO ligands in the complex, or possibly from the photochromes existing in two different environments due to aggregation. In an effort to determine whether aggregation takes place, a preliminary study of the effect of concentration on the electronic absorption spectra was carried out in toluene. No evidence for aggregation was found as evidenced by no

change in the absorption spectra as a function of concentration in the range examined (10^{-4} M to 10^{-6} M).

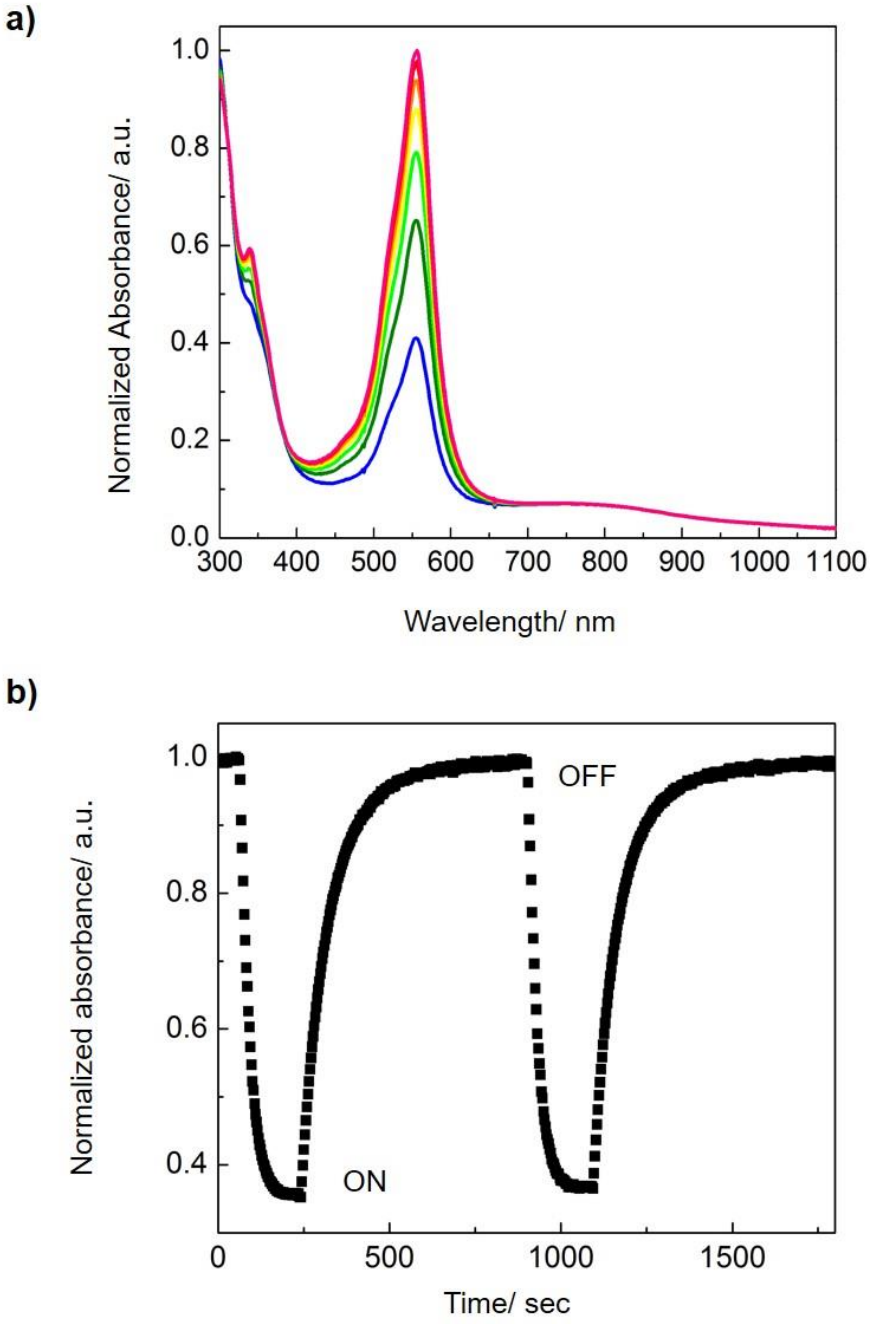

Figure 4.12. Electronic absorption spectrum of **4.3** (a) and kinetic trace (b) of absorbance intensity at λ_{max} = 555 nm in absence of light following visible light irradiation (λ_{exc} = 513–568 nm) in toluene at 298 K.

Visible light-irradiation of **4.3** in solution and the thin film state suggest that the complex **4.3** does not exhibit photoisomerization-induced charge transfer processes. Evidence for a PISCES process in the parent mononuclear complex **4.1** was found by changes in the metal centered transitions as a function of change in the PMC/SO equilibrium. Irradiation of the parent mononuclear complex **4.1** in toluene with visible light led to an increase in intensity of the MLCT band at ≈ 770 nm with concomitant decrease in the PMC π–π* band and an isosbestic point at 700 nm, evidence for a photoisomerization of the APSO-PMC to the SO form accompanied by conversion to the *hs*-Co(II) state.[260] Visible light irradiation of **4.3** in solution and the thin film at 300 K did not lead to any observable changes in the intensity of the *hs*-Co(II) → $SQ^{\bullet-}$ MLCT band at 770 nm (Figure 4.12a), even though photoisomerization to the SO form does take place. As no changes were observed in the MLCT band upon visible light irradiation, it was concluded that **4.3** does not convert to the *hs*-Co(II) upon photoisomerization, and therefore does not exhibit a PISCES process to any observable extent.

An analysis of the lack of observation of a PISCES process in **4.3** leads to insight into the structural factors that govern the process. The PISCES process relies on the ability of the system to exist in (i) at least two distinct states that are close in energy (electronic bistability), and (ii) two optical states that differ in ligand field effects (optical bistability). Once this has been established, two structural factors then become important, (iii) which state is most populated under a given set of conditions, and (iv) the directionality of change in thermal equilibrium with regard to a particular perturbation or stimulus. In order to exhibit a PISCES process, all four requirements (i-iv) must be met. In complex **4.3**, the dominant state at 300 K is the PMC-*hs*-Co(II) state. With changing temperature or light,

both electronic and optical bistability are observed. However, as the system switches to an SO state with visible light irradiation, and there is very little Co(III) present at 300 K in solution, little change in the metal centered oxidation/spin state is observed. It was therefore reasoned that a photochrome which sits in the SO form at 300 K may exhibit the PISCES process.

UV Irradiation of the complex **4.4** in toluene at 300 K with a mixed-gas Ar-Kr laser (multiline $\lambda_{exc} \approx 333.6–363.8$ nm, 30 mW) leads to a photoinduced isomerization to the PMC form as observed as a decrease in intensity of the PMC π–π* band at 593 nm (Figure 4.13). The relatively small changes in intensity of the PMC π–π* band observed is due to the low photoresponsivity of the IPSO ligand. Thermal relaxation to the SO form occurs with first-order kinetics and a biexponential rate constant of $k_1 = 0.13\ s^{-1}$ (41 %) and $k_2 = 0.02\ s^{-1}$ (59 %), which are within an order of magnitude of the thermal relaxation rates in the parent IPSO ligand in toluene ($k_{obs} = 0.23$ s-1).[46]

UV light-irradiation of **4.4** revealed that the photochromic behavior was strongly coupled with redox-isomeric processes, which is consistent with variable-temperature spectroscopic studies. UV light induced photoisomerization in **4.3** also leads to a decrease in intensity of the MLCT band at ≈ 750 nm and an isosbestic point at ≈ 630 nm, between the PMC π–π* band and MLCT band. The spectral changes are indicative of photoisomerization from the IPSO-SO to the PMC form inducing conversion to the *ls*-Co(III) state. Photoisomerization to the PMC form, which exhibits less π-acceptor ability, leads to stabilization of the *ls*-Co(III) state and charge transfer from *hs*-Co(II)$SQ^{\bullet -}$ → *ls*-Co(III)Cat^{2-}. The accompanied changes of the photochromic and redox-isomeric process are consistent with the variable-temperature spectroscopic studies. The photoisomerization

induced charge transfer process, PISCES, is observed in **4.4** due to all of the requirements for a PISCES process being met.

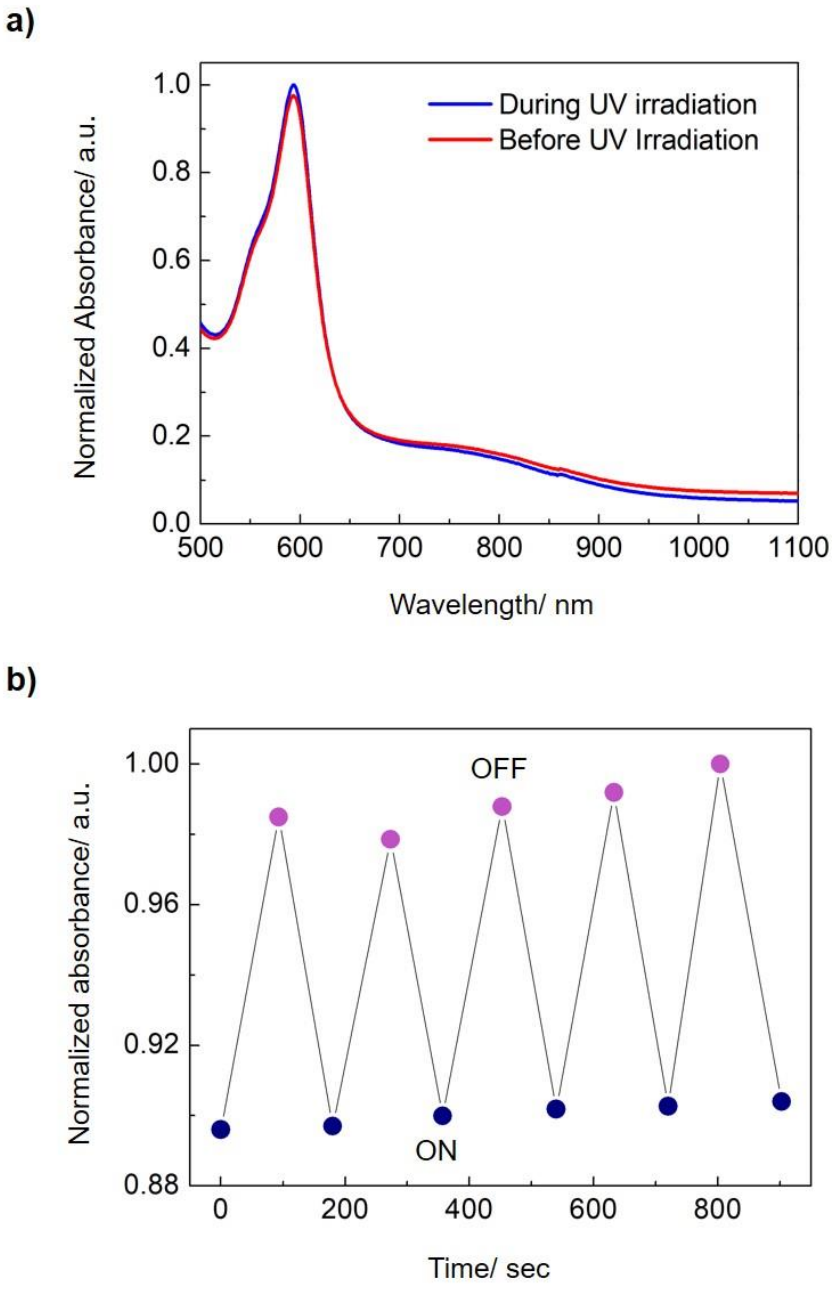

Figure 4.13. Electronic absorption spectrum of **4.4** (a) and kinetic trace (b) of absorbance intensity at λ_{max} = 593 nm in absence of light following UV light irradiation (λ_{exc} = 333.6–363.8 nm) in toluene at 298 K.

In order to for there to be strong coupling between photochromic and redox states, the direction of the change in ligand field upon photoisomerization needs to be aligned to stabilize the desired redox/spin state of the cobalt centers. XRD structure analysis, variable-temperature electronic absorption spectroscopy, and solution and solid state magnetization experiments suggest that the electronic structures of the tetranuclear complexes are *hs*-$Co_4(II)(SQ^{\bullet-})_4(Cat^{2-})_2(MeOH)_2$ at 90 K and 300 K. The difference between the two complexes is the thermodynamically stable isomer of the photochromic ligands (SO vs. PMC). Previous studies have shown that the SO form is a strong π-acceptor ligand and stabilizes the *hs*-Co(II) state.[260,265] For the complex **4.3**, photoisomerization from PMC to the SO form by visible light irradiation leads to an increase in π-acceptor character of the photochromic ligand, which stabilizes the *hs*-Co(II) state. However, the cobalt centers in **4.3** are already in favor of the *hs*-Co(II) state at 300 K. Therefore, the *ls*-Co(III)/*hs*-Co(II) equilibrium would not shift by conversion of the APSO ligand **2.2** to the SO state. The generation of the SO form via photoisomerization consequently impedes the stabilization of the *ls*-Co(III) form, and the driving force for charge transfer from *hs*-Co(II)→$SQ^{\bullet-}$ is lost. On the other hand, photoisomerization of **4.4** from the SO to PMC form decreases the π-acceptor character of the IPSO ligand, which leads to stabilization of the *ls*-Co(III) species and a shift in the metal centered equilibrium from *hs*-Co(II) to *ls*-Co(III).

4.3. Conclusion

We have synthesized two photochromic redox-isomeric cobalt tetranuclear complexes possessing multiple distinct electronic states. X-ray crystallographic analysis, solution and solid-state magnetic properties, and variable-temperature electronic

absorption studies indicate that the dominant forms of the tetranuclear complexes **4.3** and **4.4** at room temperature are *hs*-$Co_4(II)(SQ^{\bullet-})_4(Cat^{2-})_2(PMC)_2(MeOH)_2$ state and *hs*-$Co_4(II)(SQ^{\bullet-})_4(Cat^{2-})_2(SO)_2(MeOH)_2$, respectively. The magnetic properties and variable-temperature electronic absorption studies suggest that **4.3** undergoes thermally-induced redox-isomeric behavior, which may be coupled with the thermally-induced conversion of the APSO ligands **2.2**. The complex **4.4**, however, shows the presence of strong coupling in the complexes between the change in ligand field of the photochromic ligands and redox-isomeric behavior of the cobalt dioxolenes in solution. The photochromic behavior of the complexes with a large magnetic moment suggests that there is potential for the integration of the PISCES effect into multinuclear complexes. The complex **4.3** did not exhibit a photoisomerization-induced redox isomerization process. The greater π-acceptor ability of the SO form generated via photoisomerization impedes stabilization of the *ls*-Co(III) and the driving force for the charge transfer critical to the PISCES process is lost. The complex **4.4** on the other hand exhibits a photoisomerization-induced redox isomerization due to the generation of the PMC form which stabilizes the *ls*-Co(III) species.

The strategy to incorporate photochromic ligands into a multinuclear complex exhibiting a large magnetic moment can also be extended to the development of the photoswitchable MRI contrast agents. Modulating the contrast in an MRI agent is important for interventional radiology, which is catheter-based surgery under imaging control. The conventional way of controlling the contrast is obtained by administering additional contrast agents, which can be harmful. Optical switching of the contrast agents has an advantage of avoiding multiple injections. The photochromic tetranuclear complexes described in this work may be suitable candidates for use as photoswitchable

MRI contrast agents if they possess large T_1 and T_2 relaxivities. To this end, we will investigate the parent cobalt dioxolene tetranuclear complex in Chapter 5 to determine whether the parent tetranuclear cobalt tetranuclear complex exhibits the large relaxivities necessary to be an effective MRI contrast agent, as the first step the development of the photoswitching MRI contrast agents.

4.4. Experimental

4.4.1. Synthesis of the tetranuclear complexes

All reagents were purchased from commercial sources and used without further purification. Reactions were performed under inert atmosphere (N_2) using standard Schlenk techniques. The tetranuclear complexes **4.3** and **4.4** are not very stable in the solid state in the air and are highly oxygen sensitive in solution, which makes it crucial that handling in solution be done under inert conditions. All solvents were spectroscopic-grade, dry, and deoxygenated. MeOH and toluene were dried over CaH_2, distilled under argon, and freeze-pump-thawed. ^{1}H NMR spectroscopy was carried out on 500 MHz Bruker AVANCE500 spectrometer at 300 K. FT-IR spectrum was acquired as KBr pellet with a Perkin-Elmer Spectrum One FTIR spectrometer. Elemental analyses were performed by Canadian Microanalytical Services. The photochromic ligands APSO **2.2** and IPSO **4.2** were prepared according to published procedure.[223]

Co_4(3,5-DTBQ)$_2$(APSO)$_2$(MeOH)$_2$·2MeOH (4.3). $Co_2(CO)_8$ (0.1 mmol, 0.034 g) in MeOH (3.5 mL) was added slowly over 10 min to stirred mixture of APSO **2.2** (0.1 mmol, 0.038 g) and 3,5-DTBQ (0.3 mmol, 0.066 g) in MeOH (4 mL). The reaction mixture was stirred for 1 h and left to stand for an additional 12 hr. Dark purple microcrystalline

solids were formed, which were isolated by filtration through filter stick, washed with MeOH (2 × 2 mL) and dried under vacuum to yield dark purple solids in 41 % yield. Anal. Calcd for $C_{134}H_{178}Co_4N_8O_{16}\cdot 2CH_3OH$: C, 66.49; H, 7.63; N, 4.56. Found: C, 64.10; H, 7.55; N, 4.69. FT-IR (KBr, cm-1): v 3444 (s), 2955 (vs), 2903 (s), 2864(s), 1749 (w), 1712(w), 1602 (m), 1579 (m), 1556 (w), 1458 (m), 1414 (s), 1353 (m), 1318 (w), 1243 (w), 1226 (s), 1127 (s), 1098 (m), 1064 (w), 1035 (w), 1012 (w), 982 (w), 963 (w), 906 (w), 881 (w), 826 (w), 806 (w), 746 (m), 732 (w), 652 (w), 602 (w), 493 (w).

$[Co_4(IPSO)_2(3,5\text{-}DTBQ)_6(MeOH)_2]$ (4.4). $Co_2(CO)_8$ (0.1 mmol, 0.034 g) in MeOH (3.5 mL) was added slowly over 10 min to stirred mixture of IPSO **4.2** (0.1 mmol, 0.038 g) and 3,5-DTBQ (0.3 mmol, 0.066 g) in MeOH (4 mL). The reaction mixture was stirred for 1 h and left to stand for an additional 12 hr. Dark blue microcrystalline solids were formed, which were isolated by filtration, washed with MeOH (2 × 2 mL) and dried under vacuum to yield dark blue solids in 45 % yield. Anal. Calcd for $C_{136}H_{174}Co_4N_8O_{18}$: C, 66.82; H, 7.17; N, 4.58. Found: C, 66.32; H, 7.32; N, 4.52. FT-IR (KBr, cm^{-1}): v 3439 (s), 2951 (vs), 2903 (s), 2864(s), 1609 (m), 1583 (m), 1481 (s), 1457 (s), 1417 (s), 1383 (m), 1356 (m), 1303 (s), 1259(m), 1248 (m), 1199 (w), 1168 (w), 1110 (m), 1088 (w), 1059 (w), 1018 (m), 968 (m), 929 (m), 908 (w), 876 (w), 857 (w), 826 (w), 806 (w), 775 (w), 744 (m), 732 (m), 669 (w), 657 (w), 599 (w), 554 (w), 515(w), 495 (w).

4.4.2. X-ray Crystallography

X-ray crystallographic data was collected and solved by Brian O. Patrick (UBC). Single blue irregular-shaped crystals were obtained by recrystallization from methanol. A suitable crystal (0.44×0.19×0.15) mm^3 was selected and mounted on a mylar loop in oil on

a Bruker APEX II area detector diffractometer. The crystal was kept at T = 90(2) K during data collection. Using Olex2,[294] the structure was solved with the XM structure solution program,[295] using the Dual Space solution method. The model was refined with version 2017/1 of XL,[296] using Least Squares minimization.

4.4.3. Spectroscopic methods

Variable-temperature NIR spectroscopy of the complexes in the low-temperature regime (150 K and 300 K) was performed with a Perkin Elmer (PE) Lambda 1050 spectrophotometer, while temperature control was achieved using an Oxford OptistatCF continuous-flow static-exchange-gas cryostat system fitted with inner sapphire windows and middle and outer infrasil quartz windows. A thin film was prepared by solution deposition from a 10^{-3} M solution in toluene in argon atmosphere glove box. Variable-temperature electronic absorption spectroscopy of the complexes **4.3** and **4.4** in high-temperature regime (293 – 333 K) was carried out with an Agilent photodiode array with Peltier temperature control unit. A 10^{-4} M solution was prepared in toluene in argon atmosphere glove box and transferred to a long-stemmed quartz cuvette sealed under argon. Spectra were acquired in increments from 293 to 333 K for high-temperature regime with ~30 min of equilibration at each temperature.

4.4.4. Solid-state magnetic measurements

DC-SQUID measurements on samples of the complexes **4.3** and **4.4** were obtained from 2–320 K with a Quantum Design magnetic property measurement system at a field of 10,000 Oe. Powder samples of 15 mg were weighed into gelules, sealed with Kapton

tape, and inserted into straw tubes. The diamagnetic moment of the samples was calculated using Pascal's constants for atomic diamagnetic contributions to obtain a correction of -1.529×10^{-3} and -1.449×10^{-3} emu·K·mol^{-1} for the complexes **4.3** and **4.4**, respectively. The sample was corrected for the diamagnetic susceptibility of the gelule and insertion tube (-1.9×10^{-8} emu·K·mol^{-1}) which is negligible relative to the sample magnetization. The molar magnetic moment (χT_m) was determined assuming a molecular formula derived from elemental analysis.

4.4.5. Solution-state magnetic measurements: Evan's method

In an inert atmosphere argon glove box, the complexes **4.3** and **4.4** (0.4 mg) was dissolved quantitatively in CD_2Cl_2 (1.00 mL), and the solution was transferred to a 5-mm NMR tube fitted with a coaxial insert tube and filled with CD_2Cl_2. Spectra were acquired on a Bruker AVANCE 500 MHz NMR spectrometer between 200 and 300 K at 20 K intervals for variable temperature magnetic measurements. The solutions were allowed to equilibrate for 30 min at each temperature step. Evan's method was used to determine the solution-state magnetic susceptibility of the sample by monitoring the frequency shift of the $CHDCl_2$ proton resonance. The gram magnetic susceptibility of the sample, χ_g, was calculated with equation 4.1,[297-299]

$$\chi_g = -\frac{3\Delta\nu}{4\pi m\nu} + \chi_{g0} + \chi_{g0}\frac{\rho_0 - \rho_s}{m} \qquad \text{Equation4.1}$$

where $\Delta\nu$ (Hz) is the shift between the resonances for the solute-containing solvent and the reference solvent, ν (Hz) is the operating frequency of the NMR spectrometer, m is the mass (g) of paramagnetic solute in 1.00 mL of solvent, χ_{g0} is the gram magnetic

susceptibility of the solvent, ρ_0 is the density of the pure solvent, and ρ_s is the density of the solute-containing solvent. The *m* value was corrected for the change in solvent density at each temperature.[300] The temperature-dependent density of the solvent was approximated by applying the very nearly linear behaviour of the density of CH_2Cl_2 between 200 and 300 K[301] to the density of CD_2Cl_2 at 298 K (1.362 g/mL). The second and third terms in equation 1 were neglected.[302] The molar susceptibilities, χ_M, were calculated from the χ_g values and were subsequently corrected for the diamagnetic contribution of the complex, χ_d (same as those used for the solid-state magnetic measurements; *vide infra*), to obtain the paramagnetic contribution to the molar magnetic moment, $\chi_M T$.

4.4.6. Laser Irradiation Experiments

Solution-state electronic absorption irradiation experiments were performed on an Agilent spectrophotometer. Sample solutions (concentration of 10^{-4} M) were prepared under inert conditions in degassed spectroscopic grade toluene. All experiments were carried out at 298 K in the dark, with continuous stirring. Excitation experiments of the **4.3** were carried out via visible light irradiation (multiline $\lambda_{exc} \approx$ 513–568 nm, 100 mW) with a Spectra-Physics Stabilite 2018 mixed gas Ar-Kr ion laser, and directed to the sample via with a Newport liquid light guide. The power at the sample was measured with a Spectra-Physics 407A power meter with typical powers of 100 mW. The rates of thermal relaxation were determined in the absence of light by following the intensity of the PMC π-π* absorption band ($\lambda_{max} \approx$ 555 nm) with three-second interval after generation of the photostationary state. Each data set was fit to the biexponential function by linear least square analysis. Multiple cycles (3 or more) were averaged to give the final rate constants. Similarly,

Excitation experiments of **4.4** were carried out via UV irradiation (λ_{exc} = 333.6–363.8 nm) with a Spectra-Physics Stabilite 2018 mixed gas Ar-Kr ion laser and directed to the sample via with a Newport liquid light guide. The power at the sample was measured with a Spectra-Physics 407A power meter with typical powers of 30 mW. The rates of thermal relaxation were determined in the absence of light by following the intensity of the PMC π-π^* absorption band ($\lambda_{max} \approx$ 595 nm) with 0.5-second interval after generation of the photostationary state. Each data set was fit to the biexponential function by linear least squares analysis. Multiple cycles (3 or more) were averaged to give the final rate constants.

Chapter 5. Tetranuclear Bicubane Cobalt Complexes as Redox Active MRI Contrast Agents

5.1. Introduction

Magnetic resonance imaging (MRI) is a powerful diagnostic imaging technique that provides insight into differences in proton density, rates of water diffusion, and chemical shift in biological tissues.[303-305] For clinical imaging, MRI is used to measure differences in the magnetic relaxation rates of protons, which have a nuclear spin of ½, in water. In general, the relaxation rates of water show some contrast in different biological tissues due to differences in chemical environments (lipids vs. blood *etc.*), and these differences in relaxation rates give rise to contrast in an MRI image. From a diagnostic perspective, it is most important to observe significant contrast between diseased and healthy tissues in order to facilitate a more detailed medical diagnosis. MRI offers significant advantages over other types of diagnostic imaging techniques in that (i) it is a non-invasive technique, (ii) high spatial resolution (~ 100 μm), and (iii) rapid in vivo acquisition of images.[304-307] However, MRI traditionally suffers from decreased sensitivity as compared to other techniques. Magnetic resonance sensitivity is proportional to the net magnetization arising from the relative population ($N_{parallel}/N_{anti\text{-}parallel}$) of spins aligned parallel and antiparallel to an external applied field. The relative spin population for protons in a 1 T field at 300 K is 0.999992, which indicates a nearly equal population of the two states and therefore an intrinsically low sensitivity.[308,309] Improving the sensitivity of MRI techniques represents a major challenge for the development of next-generation MRI- based diagnostic imaging techniques.[304,307]

Biological MRI targets the thermal magnetic relaxation kinetics of hydrogen nuclei (S = 1/2) in water. Differential water concentrations exist in differ tissue types (blood, fat, muscle, bone, etc). In order to improve MRI sensitivity, MRI contrast agents are therefore employed to alter the properties of water protons in their local environment thereby providing contrast based on bodily distribution.[303-305] MRI contrast agents are usually paramagnetic, superparamagnetic, or ferromagnetic compounds that catalytically shorten the relaxation times of bulk water protons.[304,310-312] MRI contrast agents can be divided into two categories; those that change T_1, the longitudinal (or spin-lattice) relaxation time, and those that affect T_2, the transverse (or spin-spin) relaxation time. In the presence of an external magnetic field (B_0), protons precess along or against the direction of the magnetic field (z-axis, Figure 5.1a) at a rate proportional to the gyromagnetic ratio (γ). When an initial radio frequency (RF) is applied, the net magnetization is tipped from the longitudinal (z) axis into the transverse (x-y) plane (Figure 5.1b). The T_1 and T_2 relaxation times reflect the time in which the net magnetization relaxes back from this excited state to the resting state. The transverse magnetization (T_2) describes the decay of the transverse (x-y) component of the net magnetization (M_{xy}) due to coupling to the environment or bath, and is called the spin-spin relaxation time. The longitudinal relaxation time (T_1) describes relaxation back to the z-component of net magnetization (M_z) through coupling to the environment via spin-lattice relaxation processes.

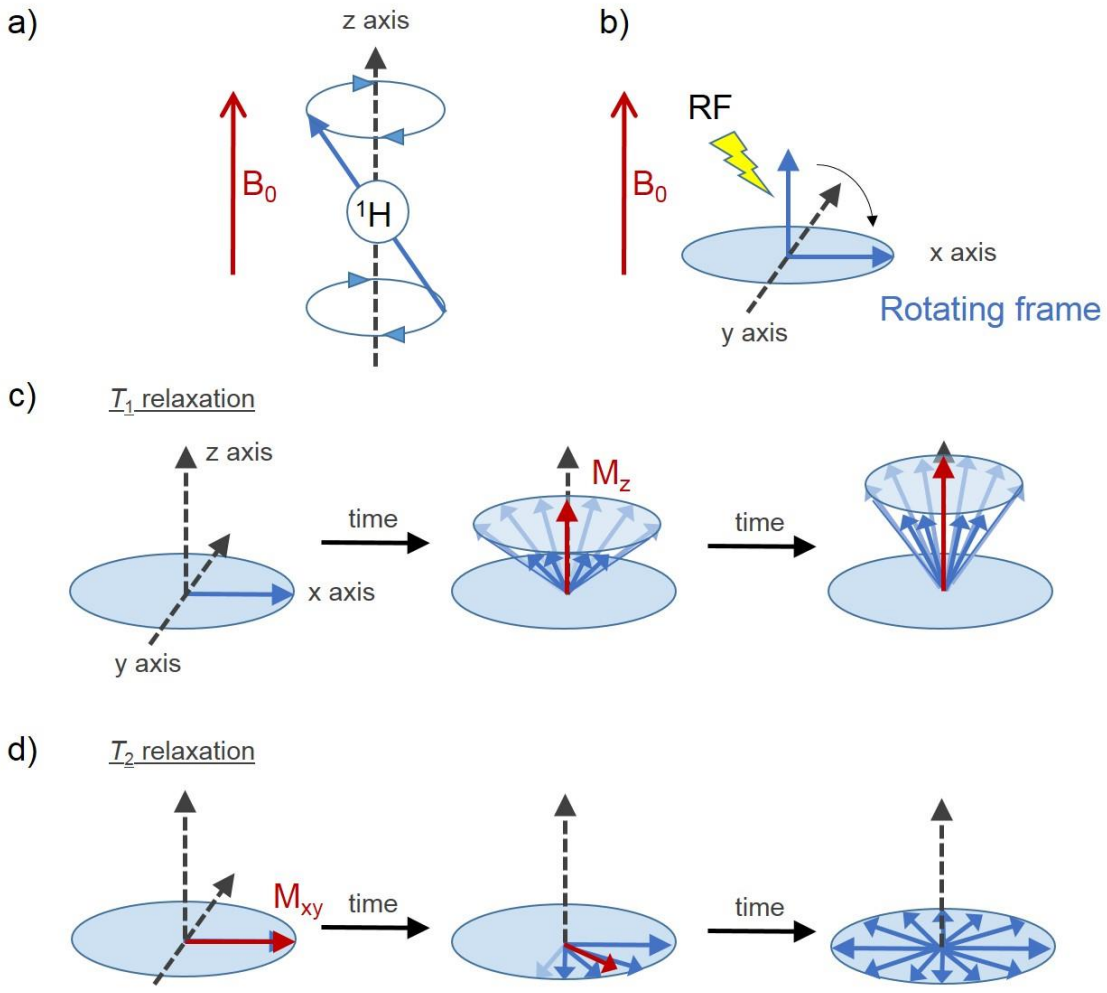

Figure 5.1. A conceptual overview of a proton in an external magnetic field (a), upon exposure to radio frequency (b), T_1 recovery (c) and T_2 decay (d).

All contrast agents decrease both T_1 and T_2; however while T_1 contrast agents increase the longitudinal relaxation rate ($1/T_1$) by roughly the same amount as the transverse relaxation rate ($1/T_2$), T_2 contrast agents increase the transverse relaxation rate profoundly.[304] The ability of a contrast agent to enhance a relaxation rate is represented quantitatively as the relaxivity r_1 and r_2, where the subscript refers to either the longitudinal ($1/T_1$) or the transverse relaxation rate ($1/T_2$). Relaxivities are changes in the relaxation

rates after the introduction of the contrast agents ($\Delta(1/T_{1,2})$) normalized to the concentration of contrast agent.

Most commonly used T_2 contrast agents are metal-oxide nanoparticles (NPs) such as ferrites[310,313] which are most commonly used for imaging enhancement of liver, kidney, and prostate cancers. Despite the fact that the many NP-based T_2 contrast agents are approved for clinical use, the vast majority of contrast-enhanced clinical tests are performed with Gd-based T_1 contrast agents (GBCAs).[304,311] GBCAs consist of a chelate complex of a Gd(III) ion which is shielded from solvent exposure by a high-affinity chelation ligand and is therefore considered safe and well-tolerated. Gadolinium (III) is an important metal ion for the development of contrast agents due to its large magnetic moment of 7.94 μ_B,[304,311] which increases the relaxation rates of protons in water, leading to significant enhancement in MRI contrast images. GBCAs have often been used to enhance contrast of blood vessels in MR angiography brain tumor imaging. However, studies suggest exposure to GBCAs may cause development of nephrogenic systemic fibrosis (NSF) in patients with renal impairments.[314-317] NSF is a potentially fatal disease involving fibrosis of the skin and internal organs. Studies have suggested that severe renal impairment increases the risk for the failure of clearance of GBCAs by kidney and consequently an accumulation of dissociated free Gd(III).[314,316,317] Although it is believed that exposure to GBCAs may cause an accumulation of dissociated Gd(III) in patients with severe renal dysfunction, a deposition of Gd(III) in the brain of patients, who experience renal impairment previously exposed to linear chelate type GBCAs, have been reported.[318-321] The study suggests that the relatively low stability of linear chelate type GBCAs may be responsible for the dissociation of Gd(III) from the GBCAs and deposition in brain

tissue.[319-321] In light of the known toxicities of free Gd(III), the potential risk from clinical use of GBCA needs to be considered and replacing GBCAs with different metal-based MRI contrast agents is of interest.

In order to develop the next generation, non-Gd containing metal-based MRI contrast agents, we need first to consider how MRI contrast agents exert their effects. Paramagnetic relaxation enhancement of a solvent arises from two components, inner-sphere and outer-sphere relaxation. Inner-sphere relaxation occurs via solvent molecule directly coordinated to the paramagnetic metal ion, while outer-sphere relaxation occurs in the second coordination sphere and beyond.[322] The total enhancement defined as relaxivity (r_i^{obs}) is a sum of all inner- (r_i^{IS}), second- (r_i^{SS}), and outer-sphere relaxation (r_i^{OS}) processes, where 1 or 2 refer to the longitudinal or transverse relaxation, respectively, as shown in equation 5.1.

$$r_i^{obs} = r_i^{IS} + r_i^{SS} + r_i^{OS}; i = 1,2 \qquad \text{Equation 5.1}$$

An increase in inner-sphere relaxation induces both T_1 and T_2 relaxation enhancement. Relaxivity arising from inner-sphere water (r_i^{IS}) is expressed as a function of q, where q is the number of coordinated water molecules, T_{im} which is the relaxation time (T_1 or T_2) of the protons in water bound to the metal center in the inner sphere, and τ_m , which is the lifetime of water in the complex (the reciprocal of the water exchange rate k_{ex}), and [H_2O] is the concentration of water in mM (Equation 5.2).[322]

$$r_i^{IS} = \frac{q/[\mathrm{H_2O}]}{(T_{im} + \tau_m)}; i = 1,2 \qquad \text{Equation 5.2}$$

An increase in q or a decrease in T_{im} or τ_m will increase the relaxivity. If $T_{im} > \tau_m$, the relaxivity r_1 and r_2 arising from inner-sphere relaxation will depend mostly on T_1 or T_2, which is observed for the first generation of MRI contrast agents.[304]

Paramagnetic relaxation enhancement has three different mechanistic contributions, (i) dipole-dipole (DD) coupling between the paramagnetic metal ion and water proton, (ii) scalar (SC) relaxation, and (iii) Curie spin (CS) relaxation.[322-325] At an operating field of >1.5 T, T_{1m} relaxation has a contribution from only dipole-dipole coupling whereas T_{2m} relaxation has contributions from all three mechanisms. T_{1m} and T_{2m} relaxations are expressed by the Solomon-Bloembergen-Morgan equations 5.3–5.7.[322,326]

$$\frac{1}{T_{1m}} = \frac{1}{T_1^{DD}} = \frac{2}{15}\left(\frac{\mu_0}{4\pi}\right)\frac{\gamma_H^2 g_e^2 \mu_B^2 S(S+1)}{r_{MH}^6}\left[\frac{3\tau_c}{1+\omega_H^2\tau_{c1}^2}\right] \qquad \text{Equation 5.3}$$

$$\frac{1}{T_{2m}} = \frac{1}{T_2^{DD}} + \frac{1}{T_2^{SC}} + \frac{1}{T_2^{CS}} \qquad \text{Equation 5.4}$$

$$\frac{1}{T_2^{DD}} = \frac{1}{15}\left(\frac{\mu_0}{4\pi}\right)\frac{\gamma_H^2 g_e^2 \mu_B^2 S(S+1)}{r_{MH}^6}\left[4\tau_c + \frac{3\tau_c}{1+\omega_H^2\tau_c^2}\right] \qquad \text{Equation 5.5}$$

$$\frac{1}{T_2^{SC}} = \frac{1}{3}\left(\frac{A}{\hbar}\right)S(S+1)[\tau_{SC}] \qquad \text{Equation 5.6}$$

$$\frac{1}{T_2^{CS}} = \frac{1}{5}\left(\frac{\mu_0}{4\pi}\right)^2\frac{\omega_H^2 g_e^2 \mu_B^4 S^2(S+1)^2}{(3k_BT)^2 r_{MH}^6}[4\tau_{CS}] \qquad \text{Equation 5.7}$$

where μ_0 is the permittivity of vacuum, γ_H is the proton magnetogyric ratio, g_e is the electronic g-factor, μ_B is the Bohr magneton, S is the spin quantum number of the contrast agent, r_{MH} is the ion-proton distance, ω_H is the Larmor frequency of the proton, $A/\hbar$ is the

hyperfine coupling constant between the paramagnetic metal center and proton nucleus, k_B is the Boltzmann constant, and T is temperature in Kelvin. The correlation time τ_c can arise from three processes such as water exchange (τ_m), rotational motion (τ_R) and longitudinal relaxation time of unpaired electrons (T_{1e}). Dipole-dipole coupling relaxation has all three contributions though τ_m dominates at high field. The τ_m and T_{1e} contribute to scalar relaxation and τ_m and τ_R contributes to Curie spin relaxation.

The relaxivity of water protons in the second coordination sphere have the same fundamental contributions as that shown for inner sphere relaxation (equation 5.8), and T'_{im} (relaxation time of the solvent arising from second coordination sphere) can be expressed in the same manner as T_{im} (equations 5.3–5.7).[322] Relaxivity arising from the second coordination sphere water (r_i^{SS}) is expressed as shown in equation 5.8.

$$r_i^{SS} = \frac{q'/[\mathrm{H_2O}]}{(T'_{im} + \tau'_m)}; i = 1,2 \qquad \text{Equation 5.8}$$

While the inner and second coordination sphere relaxivities depend on the number of coordinated water molecules (q), the relaxation rate (T_1 or T_2) of the protons in water bound to the metal center, and the lifetime of water in the complex (τ_m), the outer-sphere contribution to the relaxivity is dominated by the diffusion time of water and a distance of closest approach. Optimization of the diffusion time of water and the distance of closest approach is difficult.[322] The observed relaxivity (r_i^{obs}) is a sum of all inner- (r_i^{IS}), second- (r_i^{SS}), and outer-sphere relaxation (r_i^{OS}) as shown in equation 5.1. Therefore, an increase in inner- (r_i^{IS}) and second- (r_i^{SS}) sphere relaxivity are targeted to obtain high observed relaxivity.

In order to achieve high inner (r_i^{IS}) and second (r_i^{SS}) coordination sphere relaxivity, the parameters in equations 5.2 and 5.8 can be optimized. One can think that a complex which has a large spin quantum number S may decrease the T_{im} for both inner- and second-sphere relaxation and as a result, increase the relaxivity r_1 and r_2. This is indeed why Gd (S = 7/2) has been used so extensively as an MRI contrast agent, as its magnetic moment is 7.94 μ_B. Although many first-row transition metals can exist in a high spin state, not many first-row transition metal based MRI contrast agents have been clinically approved, with the exception of Mn-based (Teslascan and LumenHance) and iron-oxide NPs (Feridex, Resovist, Sinerem).[313,327]

Recent studies have begun to consider *hs*-Co(II) (S = 3/2) which may have a sufficient magnetic moment to induce significant paramagnetic relaxation enhancement. Extensive studies of magnetic CoFeO nanoparticles,[328-331] CoPt nanoparticles,[332] nanocubes,[333] and nanoplates[334] have been reported for T_2-weighted MRI contrast agents. NPs are generally considered to be optimal MRI contrast agents due to their high magnetic moments which leads to high contrast, a variety of nanosized dimensions and shape allowing different biodistribution, and the ability for targeted imaging by surface functionalization and conjugation with biological and targeting probes.[310] Co NPs are reported to have a much higher saturation magnetization value than iron-oxide NPs at room temperature, suggesting a high potential to be used as contrast agents.[335] However, there are some drawbacks for NPs-based MRI contrast agents. For biological imaging applications, the hydrodynamic size of nanoparticles should be kept to below 50 nm, which introduces limitations to the extent of surface functionalization. Larger NPs have short circulation times due to their rapid excretion by the liver and are subject to nonspecific

uptake.[310,336] Moreover, an excessively large magnetic moment can cause magnetic-susceptibility artifacts on the image which distort the background image.[337] Examples of Co-based small-molecule MRI contrast agents are very limited due to the low magnetic moment relative to NPs-based contrast agents. Yang *et al.* and Chen *et al.* synthesized triaza-macrocyclic Co(II) complexes which exhibit r_1 of 2.79 $mM^{-1}s$-^{1} and 2.71 $mM^{-1}s^{-1}$ at 1.5 T, respectively.[338] Frank *et al.* reported cobalt dichloride-N-acetyl cysteine (C4) contrast agents with r_1 and r_2 values at 1.5 T and 3.0 T ranging from 0.1 to 0.4 $mM^{-1}s^{-1}$.[339] New *et al*. demonstrated a dynamic redox-responsive cobalt tris(2-pyridylmethyl)amine (TPA) contrast agent that modulates its r_1 and r_2 upon reduction from 0 to 0.0607 $mM^{-1}s^{-1}$ and 0.239 mM-1s^{-1} at 9.4 T.[340] The Gd-based contrast agents typically shows r_1 and r_2 values in the range from 3 to 5 $mM^{-1}s^{-1}$ at 1.5 T and 3.0 T,[341] suggesting that Co-based small molecule MRI contrast agents with properties comparable to Gd-based contrast agents remain a challenge.

A potential strategy to incorporate first row transition metals into MRI contrast agents may involve intermediate structures between single ion complexes, which have low magnetic moments, and NPs, which have higher moments, but suffer from the disadvantages mentioned above: multinuclear clusters. The tetranuclear cobalt complex, $[Co_4(3,5\text{-DTBQ})_8]$ (**5.1**) was first synthesized by Pierpont in 1979.[274] Solid state magnetic studies revealed that the complex **5.1** has a very high magnetic moment (4.75 μ_B per $Co(SQ^{\bullet -})_2$ at 298 K)[274] due to the presence of four *hs*-Co(II) centers and eight redox-active 3,5-*di*-*t*-butyl-*o*-benzoquinone ligands (3,5-DTBQ). The DTBQ can exist in the partially reduced form, a radical anion semiquinone ($SQ^{\bullet -1}$) or in the fully reduced oxidation state, a dianion catecholate (Cat^{-2}) via a charge-transfer with the Co centers. In the semiquinone

state, additional spins contribute to the overall electronic structure, further increasing the magnetic moment, depending on the sign and magnitude of magnetic exchange within the cluster. Intracluster ferromagnetic exchange interactions between Co-Co, Co-L, and/or L-L would increase the total molecular magnetic moment. Depending on how water interacts with the tetranuclear complex, and whether there is direct ligation of water to a cobalt center, or whether only second- and outer-sphere paramagnetic relaxation effects take place, the increased moment could result in unusually large relaxivities. Hence, investigation of **5.1** (Figure 5.2) is of interest as a proof-of-concept for utilizing multinuclear cobalt clusters as MRI agents. The presence of multiple redox-active Co centers and DTBQ ligands is predicted to lead to high r_1 and r_2 relaxivities, which may provide a platform for future development of molecular non-GBCAs.

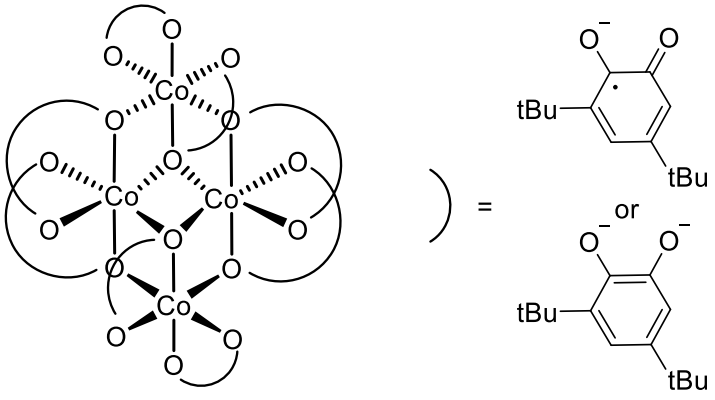

Figure 5.2. Structure of the tetranuclear cobalt complex **5.1**.

5.2. Results and Discussion

5.2.1. Synthesis of the Tetranuclear Cobalt Complex 5.1

The title tetranuclear cobalt complex **5.1** was prepared according to the previously reported method[274] and characterized by ^{1}H NMR, IR, and mass spectroscopy. ^{1}H NMR and ESI-mass spectra of **5.1** suggest that the complex **5.1** retains the general structure, but water possibly replaces one of the Co–O bonds of the dioxolene ligands in the solution state. ^{1}H NMR signals at -20.3, -11.3, 11.0, and 38.7 ppm integrating to 18 protons each are assigned to two sets of *t*-butyl groups (Figure 5.3). Singlets at 0.7, 1.1, 1.3, and 1.5 ppm integrating to nine protons each are assigned as individual *t*-butyl groups (Figure 5.3). A singlet at -18.2 ppm (integration 36) corresponds to four *t*-butyl groups (Figure 5.2). In total, a presence of 16 *t*-butyl groups is consistent with the structure of **5.1**. Downfield and upfield shifts for the t-butyl signals correspond to paramagnetic relaxation due to coordination to the paramagnetic *hs*-Co(II) centers and radical-anion semiquinone ligands. Since the complex **5.1** possesses C*i* symmetry, eight sets of signals corresponding to the *t*-butyl groups are expected, however, more sets were found presumably due to desymmetrization by water coordination in solution. The ring protons of the semiquinone radical anions were not assigned due to the strong paramagnetic relaxation effects which leads to significant broadening and decreases in intensity. The mass spectroscopic analysis led to observation of fragments at 1772 $[Co_3(DTBQ)_7(H_2O)_3]^+$ and 1550 $[Co_3(DTBQ)_6(H_2O)_3]^+$ consistent with water coordination, presumably due to ligand exchange with the catecholate/semiquinone ligands.

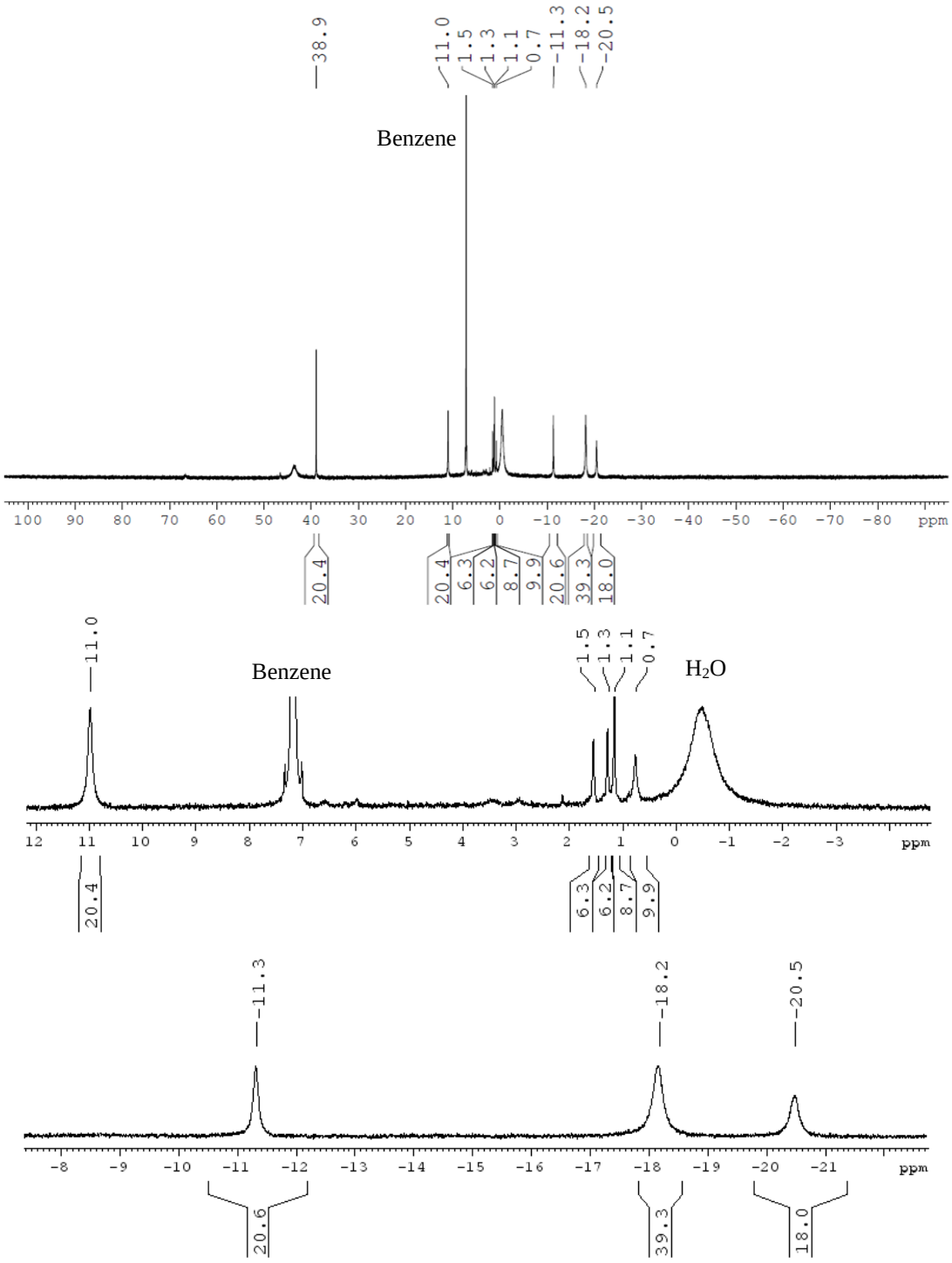

Figure 5.3. ^{1}H NMR spectrum of the tetranuclear cobalt complex **5.1** in benzene-d_6 at 300 K.

5.2.2. Structural Analysis of the Tetranuclear Cobalt Complex 5.1 in Solid State

Structural analysis by single crystal X-ray crystallography revealed that the structure of **5.1** is *hs*-Co_4(II)$(SQ)_8$. The oxidation states of **5.1** were investigated through bond length and bond valence sum analysis based on crystallographic data previously collected at 100 K by Pierpont.[274] The structural geometries of the Co(II)/Co(III) and Cat^{-2}/$SQ^{\bullet-}$ oxidation states in the cobalt dioxolenes is distinctively different, allowing for determination of the oxidation states by analysis of Co–O bond lengths. Two sets of hexacoordinate cobalt centers, Co1/Co1' and Co2/Co2' form a coplanar arrangement through binding to eight dioxolene ligands (Figure 5.4). The selected bond lengths are tabulated in Table 5.1. The Co–O bond lengths of a complex consisting of both *hs*-Co(II) from *ls*-Co(III) can be used to assign the oxidation and spin states of the cobalt centers in 5.1.[342] Typical Co–O length of *hs*-Co(II) and *ls*-Co(III) found in a similar system ($Co(diox)_2(phen)$) are 2.04-2.07 Å and 1.86-1.87 Å, respectively.[120] The *hs*-Co(II)–O length is expected to be 0.10-0.20 Å longer than the *ls*-Co(III) due to electron filling of the antibonding (e_g*) orbitals in the *hs*-Co(II) state. Nearly all of the μ_2-bridging and non-bridging Co–O lengths in the complex **5.1** (2.030–2.093 Å) fall within the range expected for *hs*-Co(II) complexes whereas the μ_3-bridging Co-O lengths (2.133–2.264 Å) were found to be slightly longer. The slight deviation is presumably due to the electron density of the μ_3-bridging alkoxo being shared by multiple cobalt centers or/and being in a more sterically hindered environment. Overall, bond length analysis of the C–O bonds suggests that the oxidation state of both Co1/Co1' and Co2/Co2' are *hs*-Co(II) at 100 K.

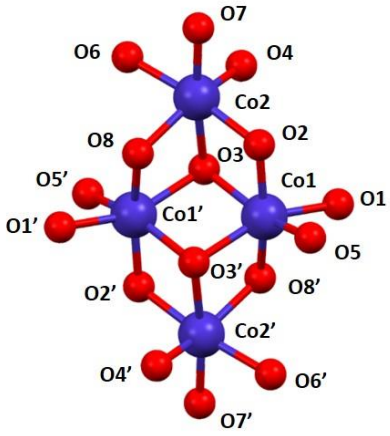

Figure 5.4. Core of molecular structure of the tetranuclear cobalt complex **5.1**.[274]

Table 5.1. Selected Bond Lengths (Å) for the tetranuclear cobalt complex **5.1**.[a]

	Bond Length (Å)		Bond Length (Å)
Co1–O1	2.0426 (8)	Co2- O4	2.0928 (6)
Co1–O2	2.038 (1)	Co2- O2	2.0747 (7)
Co1–O3	2.1753 (6)	Co2- O3	2.264 (1)
Co1–O3'	2.1332 (8)	Co1- O7	2.020 (1)
Co1–O5	2.043 (1)	Co1- O6	2.034 (1)
Co1–O8	2.030 (1)	Co1- O8	2.0928 (6)

[a] ref[274]

A bond-valence sum (BVS) analysis using parameters from Brown and Alterman.[282] also supports the assignment of *hs*-Co(II) for all four cobalt centers in **5.1**. The BVS values for cobalt centers of a *hs*-Co(II)(3,5–$DTSQ^{\bullet-}$)$_2$(phen) and *ls*-Co(III)(3,5–$DTSQ^{\bullet-}$)(3,5–$DTCat^{2-}$)(phen) were determined by using previously reported bond lengths[120] and found to be 2.3 and 3.7, respectively. The distinct difference between the BVS values of *hs*-Co(II)(3,5–$DTSQ^{\bullet-}$)$_2$(phen) and *ls*-Co(III)(3,5–$DTSQ^{\bullet-}$)(3,5–$DTCat^{2-}$)(phen) was used to assign the oxidation states of the cobalt centers in **5.1**. The BVS values for Co1/Co1' and Co2/Co2'of **5.1** were determined to be 2.2 and 2.3, respectively, which

suggest the oxidation states of Co1/Co1' and Co2/Co2' are more likely to be *hs*-Co(II) than *ls*-Co(III) at 100 K. Both valence bond sum and bond length analysis therefore support that the assignment of oxidation and spin state of the Co1/Co1' and Co2/Co2' as *hs*-Co(II) at 100 K.

5.2.3. Electronic Structure of the Tetranuclear Cobalt Complex 5.1 in Solution State

Variable temperature electronic absorption spectroscopy suggests that **5.1** undergoes a thermally induced redox-isomeric behavior between *ls*-Co(III)(Cat^{2-}) → *hs*-Co(II)($SQ^{\bullet-}$). Cobalt dioxolenes complexes undergo a charge transfer coupled spin transition process, often termed valence tautomerism[120] between a *ls*-Co(III)(Cat^{2-}) → *hs*-Co(II)($SQ^{\bullet-}$) with external stimuli. As discussed in Chapter 4, this class of redox-isomeric Co(3,5-DTBQ)$_2$ complexes are known to show very distinct spectroscopic features: an MLCT band at $\lambda_{max} \approx 760$ nm corresponding to a *hs*-Co(II) → $SQ^{\bullet-1}$ and an LMCT band in the NIR at $\lambda_{max} \approx 2500$ nm corresponding to a Cat^{-2} → *ls*-Co(III) transition. Variable-temperature electronic absorption spectra of **5.1** in dichloroethene are shown in Figure 5.5, which show a broad absorption band at $\lambda_{max} \approx 750$ nm which corresponds to population of the *hs*-Co(II) → $SQ^{\bullet-}$ state. The presence of the MLCT band at $\lambda_{max} \approx 750$ nm suggests that the oxidation state of the cobalt centers at 293 K is *hs*-Co(II)$_4$(Cat^{-2})$_8$. Raising the temperature from 293 K to 323 K resulted in an increased intensity of the MLCT band at 750 nm, indicating a greater population of the *hs*-Co(II) state. The intensity of the MLCT band did not change at temperatures above 323 K, which may be because the population of *hs*-Co(II) state has reached saturation at 323 K. The presence of *hs*-Co(II) as a dominant form in the high-temperature regime is consistent with the crystal structure analysis. The

absence of the LMCT (IVCT) band at 2500 nm is also consistent with the population of *hs*-Co(II) in the high-temperature regime.

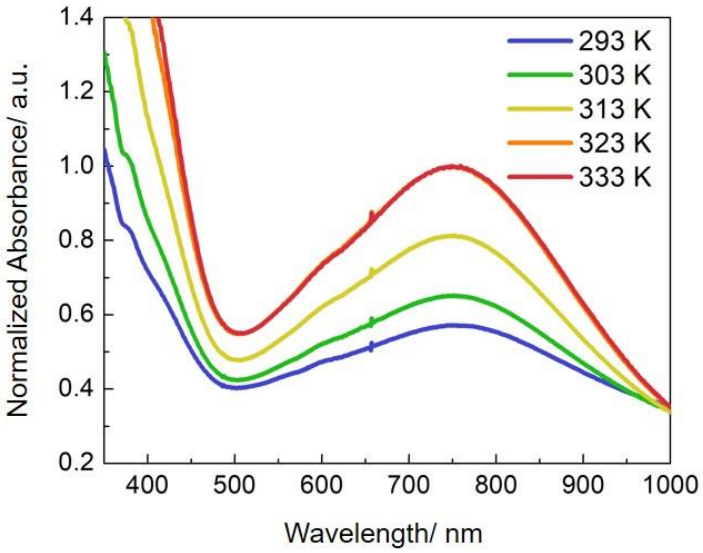

Figure 5.5. Electronic absorption spectrum of the tetranuclear cobalt complex **5.1** from 293–333 K in dichloroethene [1×10^{-4} M].

Concentration-dependent electronic absorption spectroscopy was performed to examine any changes in ligand coordination or aggregation associated with the presence of water in benzene. The absorption spectra for **5.1** were measured in the concentration range from 0.26 mM to 0.086 mM in 100% anhydrous benzene (Figure 5.6a) and 10 mM H_2O benzene (Figure 5.6b). An increase in the concentration of **5.1** in benzene resulted in a small bathochromic shift (2 nm) of the λ_{max} of the MLCT band without an observable change in the band shape. In the presence of 10 mM water, an increase in the concentration of **5.1** showed a larger (7 nm) bathochromic shift with development of a shoulder at ≈ 610 nm. The bathochromic shift of the MLCT band and the change in the band shape at higher concentration are consistent with aggregation or a change in the coordination sphere in the presence of water. The former can be caused by the hydrophobic nature of the *t*-butyl

groups, which form a hydrophobic belt around the cobalt cluster which may facilitate aggregation in water-saturated benzene. Meanwhile, the latter can be caused by the water exchange with the $SQ^{\bullet-}$ ligand leading to a change in the coordination sphere of the complex **5.1** which would also be consistent with ^{1}H NMR and mass spectroscopy analysis.

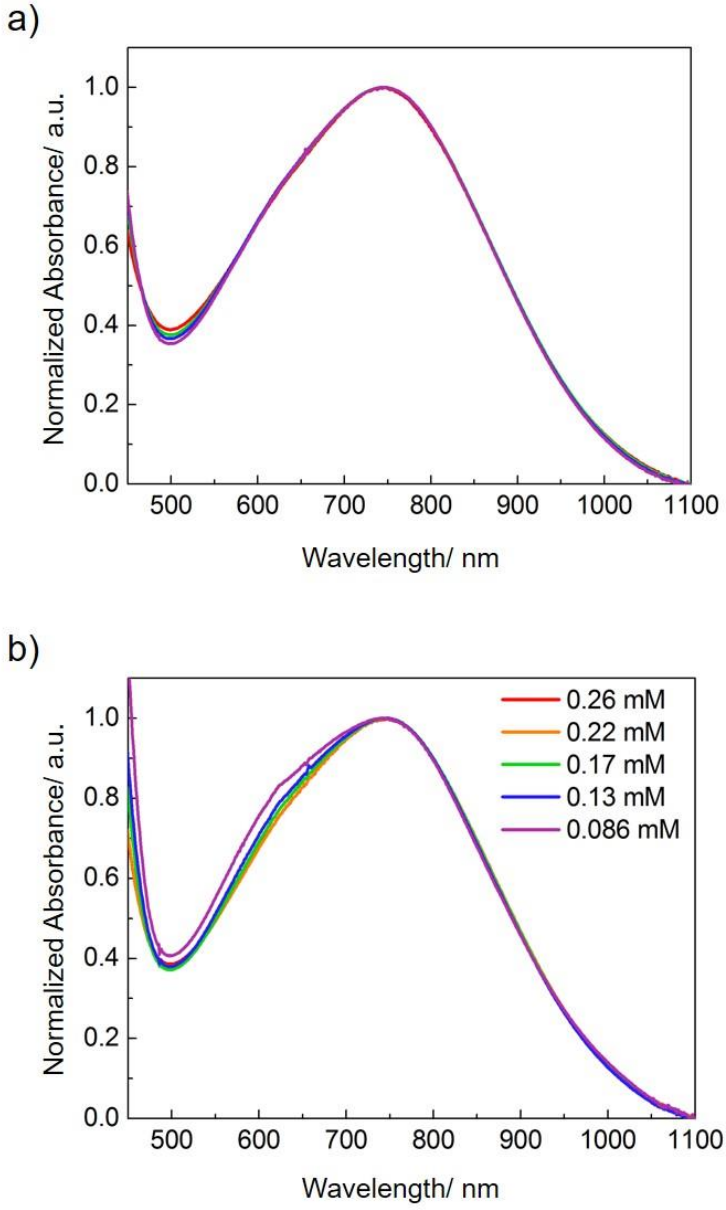

Figure 5.6. Electronic absorption spectrum of the tetranuclear cobalt complex **5.1** in benzene (a) and 10 mM H_2O/benzene (b) in the concentration range [0.26 m M–0.086 mM].

5.2.4. Magnetic Properties of the Tetranuclear Cobalt Cluster in Solid State and Solution State

DC magnetization measurements both in solution and the solid state suggests that the electronic structure of **5.1** at 300 K is *hs*-Co_4(II)($SQ^{\bullet -}$)$_8$. Variable temperature DC magnetization measurements were carried out to determine the ground state magnetic state and charge transfer behavior in both solution and the solid state. In the solution state, the clusters are fairly-well separated, and as such, magnetic properties are dominated by intramolecular exchange and single-ion effects. In the solid state, the bulk magnetic properties are dictated by both intramolecular and intermolecular magnetic interactions. ^{1}H NMR spectroscopy using Evan's Method was carried out in order to determine the magnetic moment (χT) of **5.1** in CD_2Cl_2 in the temperature range 300 K to 200 K. At 300 K the magnetic moment was found to be 21.4 emu·K·mol^{-1}, significantly larger than the spin-only value of 9 emu·K·mol^{-1} (g = 2) for four *hs*-Co_4(II) (S = 3/2) and four semiquinone ligands (S = ½). Experimentally-derived magnetic moments associated with octahedrally coordinated *hs*-Co(II) centers of 2.76–3.38 emu·K·mol^{-1}[293] are due to contributions from spin-orbit coupling (100 cm^{-1}), zero field splitting, and g-anisotropy, all of which lead to an increase in magnetic moment above the spin–only value for *hs*-Co(II). Using these values for the Co(II) centers however only suggests a magnetic moment of 11.04–13.52 emu·K·mol^{-1}, still significantly smaller than that observed experimentally. While Evan's method is known to lead to some degree of error in estimating magnetic moments due to assumptions made in the diamagnetic correction of solvent, it would not lead to an error by a factor of two in the magnetic moment. Another possible explanation for the high magnetic moment would be ferromagnetic interactions between ligand and metal centers, or between metal centers in the complex. Temperature dependent behavior should however support

this. A decrease in temperature from 300 K to 200 K resulted in a gradual decrease in the magnetic moment from 21.4 to 18.0 emu·K·mol^{-1} due to the depopulation of the *hs*-Co(II) species. A thermal hysteresis of 20 K was observed in the solution-state magnetization measurement, which suggests that the cobalt cluster exhibits structural changes that are cooperative with effective intracluster magnetic exchange interactions.

Temperature-dependent DC magnetization measurements of the polycrystalline sample were performed from 300 K to 2 K to determine the magnetic behavior of the cluster in the solid state. At 300 K, the magnetic moment (χT) was found to be smaller than in solution, 15.5 emu·K·mol^{-1} but still higher than the expected spin-only value (9 emu·K·mol^{-1}). The lower magnetic moment found in the solid state sample over that in solution at 300 K (21.4 vs. 15.5 emu·K·mol^{-1}) may be due to the presence of intercluster magnetic dipole-dipole interactions, as was observed for the photochromic cobalt tetranuclear clusters in Chapter 4. A small thermal hysteresis of 10 K in the sample suggests some small degree of cooperativity possibly leading to a decrease in the magnetic moment of the bulk sample compared to that of magnetically isolated clusters in the solution state. A very gradual decrease in the magnetic moment from 325 K to 2 K occurs with a limiting moment of 2.16 emu·K·mol^{-1}at 2 K, consistent with depopulation of the *hs*-Co(II). Similar to the photochromic tetranuclear cluster in Chapter 4, the distorted octahedral ligand field and spin-orbit orbit coupling results in six Kramer's doublets where only the ground state is populated at low temperature. Consequently, each Co(II) center in **5.1** can be described by an effective spin ½ Hamiltonian at low temperature. The magnetic moment (2.16 emu·K·mol^{-1}) at 2 K is consistent with a χT value (2.25 emu·K·mol^{-1}) of two uncoupled Co(II) centers (S = 1/2, g = 2) and four SQ$^{\bullet-}$ ligands (S = 1/2, g = 2). Overall, the magnetic

behavior from 325 K to 2 K suggests that a charge transfer coupled spin transition process from a *hs*-$Co_4(II)(SQ^{\bullet-})_8$ to a *ls*-$Co_2(II)Co_2(III)(SQ^{\bullet-})_4(Cat^{2-})_4$ state occurs. The solution-state and bulk magnetization measurements suggest a presence of intracluster ferromagnetic exchange and intercluster dipole exchange in **5.1** at 300 K.

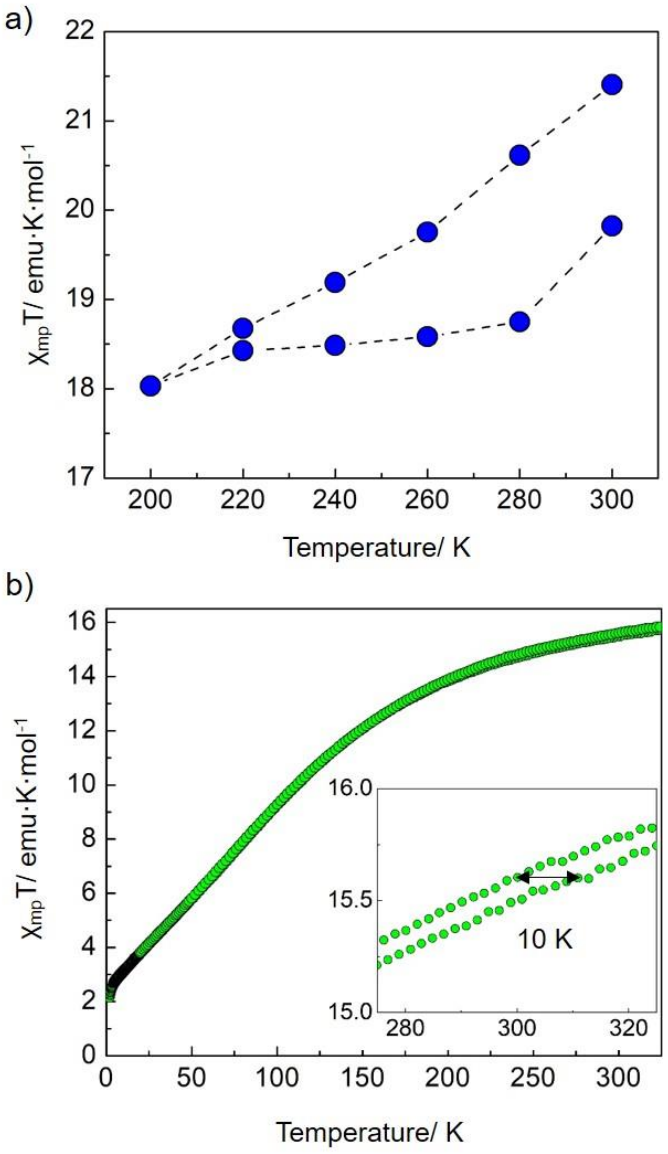

Figure 5.7. Temperature dependence of the magnetic moment (χT) in CD_2Cl_2 (200 – 300 K) as determined by Evan‘s method on a 500 MHz NMR spectrometer (a), DC Magnetization of **5.1** in the solid state in the temperature range 2–325 K with an external applied field of 10,000 Oe (b).

5.2.5. Relaxivity r_1 an r_2 Studies

The longitudinal relaxivity (r_1) and transverse relaxivity (r_2) of the tetranuclear cobalt complex **5.1** were determined by measuring the changes in T_1 and T_2 of water in the presence and absence of **5.1** by NMR spectroscopy. The T_1 and T_2 relaxation times of water at several concentrations of complex from 0 mM (blank) to 0.5 mM were measured on a 500 MHz Bruker AVANCE spectrometer. The T_1 was determined by the inversion recovery method. Integration of water peak as a function of delay time τ was fitted to equation 5.9 to determine T_1 at various concentrations of **5.1** (Figure 5.8a)

$$M_t = M_0\left(1 - 2Ae^{-\frac{\tau}{T_1}}\right) \qquad \text{Equation 5.9}$$

M_t is the intensity of the detected magnetization, and M_0 is equilibrium magnetization. Since the intensity of the detected magnetization of water proton is proportional to the integration of the water proton resonance, integration of normalized water peak was fitted to the equation as a function of delay time to determine T_1.

Similarly, the value of T_2 was determined by the Carr-Purcell-Meiboom-Gill (CPMG) method. Integration of the water peak as a function of total echo time [τ-180° pulse- τ]$_n$ was fitted to equation 5.10 to determine T_2 at various concentrations of **5.1** (Figure 5.8b).

$$M_t = M_0 e^{-\frac{\tau}{T_2}} \qquad \text{Equation 5.10}$$

An increase in concentration of **5.1** resulted in an increase in both longitude and transverse relaxation rates, which indicated the complex **5.1** shortens both T_1 and T_2

relaxation time. The observed shortening in the relaxation rate is consistent with the high magnetic moment of **5.1** in solution.

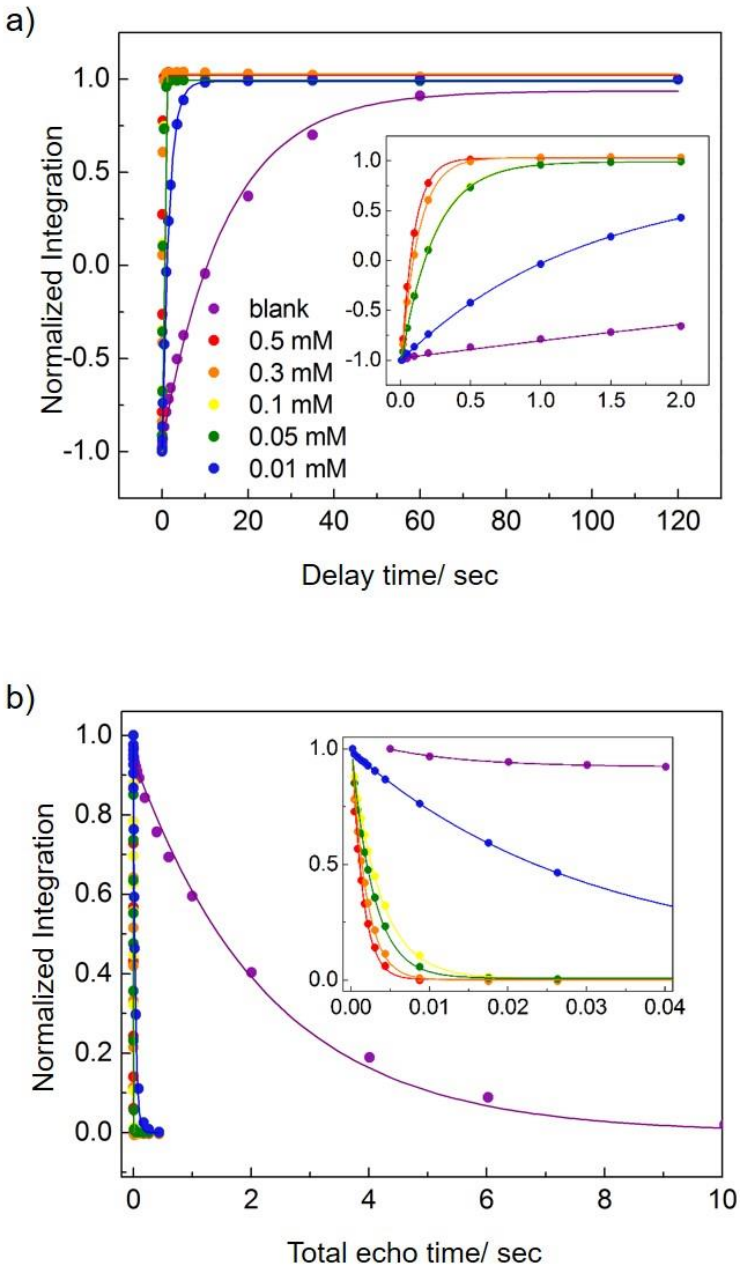

Figure 5.8. Fitted curve of normalized integration of H_2O for determination of T_1 (a) and T_2 (b) of H_2O in different concentration of the tetranuclear cobalt complex **5.1** in benzene measured with 500 Hz NMR spectrometer (Bruker) at 300 K.

In order to evaluate the effect of **5.1** on the relaxation times T_1 and T_2 the relaxivities r_1 and r_2 were determined by fitting to equation 5.11 in which the inverse of the relaxation time T_1 and T_2 are linearly correlated with the concentration of contrast agent.

$$\frac{1}{T_{1,2}} - \frac{1}{T_{dia}} = r_{1,2}[c] \qquad \text{Equation 5.11}$$

The relaxivities r_1 and r_2 of **5.1** were obtained from the slope of the plot of the concentration of the complex against a change in the difference of the inverse of T_1 and T_2 from that of the intrinsic T_1 and T_2 without the contrast agent denoted as T_{dia} (Figure 5.9a and 5.9b). According to this equation, a linear correlation between $T_{1,2}$ and concentration of the cluster is expected. However, a non-linear relationship for $1/T_1$ and $1/T_2$ was observed in which two distinct linear regions, one at low concentration range (0 to 0.1 mM) and the other in the high concentration range (0.1 mM to 0.5 mM) give rise to differential relaxivities. The estimated relaxivity r_1 in the low concentration regime was found to be 52 $mM^{-1}s^{-1}$ whereas r_1 in the high concentration regime was found to be 15 $mM^{-1}s^{-1}$. Both values are an order of magnitude higher than the clinically used T_1 contrast agent, such as Magnevist (GdDTPA, 4.5 $mM^{-1}s^{-1}$ at 1.5 T). The relaxivity r_2 in the low concentration regime was found to be 4100 $mM^{-1}s^{-1}$ while r_2 in high concentration regime was found to be 1300 $mM^{-1}s^{-1}$ which are both an order of magnitude larger than the commonly used T_2 contrast agent Feridex (Fe_2O_3,104 $mM^{-1}s^{-1}$ at 1.5 T). It should be noted that the magnetic field of 500 MHz ^{1}H NMR spectrometer is 11.4 T, and both r_1 and r_2 are field dependent. In fact, r_1 decreases as the magnetic field increases, implying that even higher r_1 value is expected at 1.5 T as compared with the commercially available T_1 contrast agents.[322] Conversely, r_2 increases as the magnetic field increases, implying that lower r_2 value is

expected at 1.5 T.[322] However, the difference between the r_2 value at 1.5 T and 9.4 T is a factor of two.[322] Hence, even after we take into account the field dependency, observed r_1 and r_2 values were still extremely high. The large relaxivities r_1 and r_2 are the result of the large magnetic moment of **5.1**.

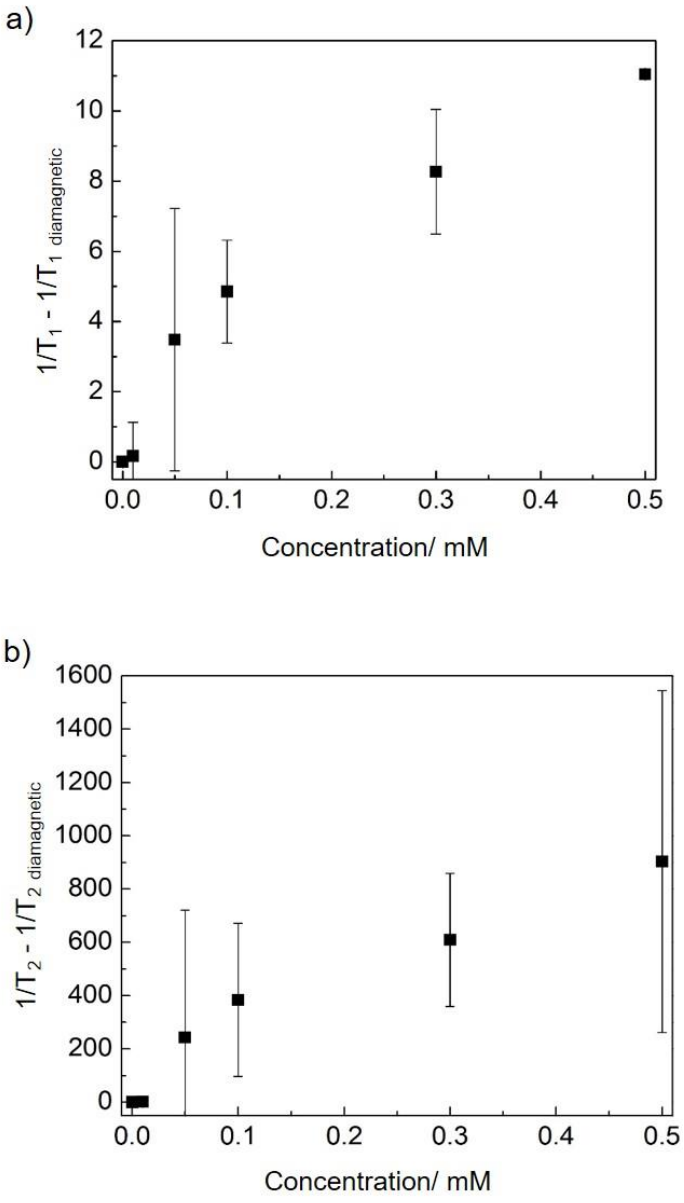

Figure 5.9. The relaxivity r_1 (a) and r_2 (b) of the tetranuclear cobalt complex **5.1** in H_2O saturated benzene measured with 500 Hz NMR spectrometer (Bruker) at 300 K.

Non-linear correlations of T_1 and T_2 with the concentration of contrast agent and a decrease in relaxivities in the high concentration range often arise from oversimplified linear models which do not take into account other variables such as diffusion through biological compartments of interest (such as water diffusion into and out of the cell), pH, temperature, and magnetic field strength.[322,343,344] Dalal *et al*. reported a nonlinear relaxivity for an Fe_8 cluster which showed two distinct linear regions in the low and high concentration ranges. The Fe_8 cluster reaches magnetic saturation in solution, and the smaller relaxivity observed at higher concentrations is attributed to magnetic dipole-dipole interactions between Fe_8 clusters which would lead to an overall magnetic moment per mol. The solution and solid state magnetism studies of **5.1** suggested the presence of magnetic dipole interactions in the solid state, and electronic absorption spectroscopy provided evidence for aggregation at higher concentrations. Therefore, the non-linear relaxivity of the cobalt cluster is likely caused by the intercluster dipole-dipole interactions induced by aggregation at higher concentrations, which would reduce the magnetic moment per mol. The change in the coordination sphere of **5.1** would also change the number of water molecules coordinated to cobalt, which would also lead to a change in relaxivities.

In order to determine if the nonlinear behavior of the relaxivities relate to the magnetic moment, concentration-dependent Evan's Method analyses of the complex **5.1** in either benzene-d_6 or 10 mM H_2O in benzene-d_6 was performed (Table 5.2). In 0.5% H_2O in benzene-d_6, the magnetic moment (χT) decreased by ~3 $emu \cdot K^{-1} \cdot mol^{-1}$ as the concentration of the cobalt cluster increased from from 0.1 mM to 0.3 mM. A decrease in the magnetic moment (χT) that correlates with the decrease in relaxivities found in the high

concentration range suggests the presence of aggregation-induced intercluster dipole coupling as the origin of the nonlinear behaviour. Moreover, the χT values found in 10 mM H_2O in benzene-d_6 were 15-30% smaller than that in benzene at all concentrations, which may indicate that water saturation facilitates the aggregation and/or water ligation causes semiquinone dissociation, which in turn may decrease the magnetic moment per mol, therefore the relaxivities.

Table 5.2. Magnetic moment χT determined of the tetranuclear cobalt complex **5.1** in the different concentration in benzene-d_6 and water saturated benzene-d_6.[a]

	0.5 mM	0.3 mM	0.1 mM	0.08 mM
χT in benzene-d_6	12.5	15.2	15.1	14.5
χT in H_2O/benzene-d_6	10.4	10.6	13.8	N/D[b]

[a] Determined by ^{1}H NMR at 300 K. [b] benzene peaks with **5.1** and without **5.1** could not be resolved.

Even though the cluster exhibits nonlinear behaviour, the extremely high relaxivities suggest that multinuclear cobalt clusters may provide a promising strategy for developing first row transition metal MRI contrast agents. For practical applications, the solubility of the cluster in water needs to be improved, which could be carried out by functionalizing the dioxolene ligands to reduce hydrophobicity. This reduction in hydrophobicity will likely prevent aggregation and perhaps result in a cluster with an even larger magnetic moment, and larger relaxivity.

5.3. Conclusions

In conclusion, we have demonstrated that the tetranuclear cobalt complex Co_4(3,5-DRBQ)$_8$ **5.1** exhibits significantly large r_1 and r_2 relaxivities in water-saturated benzene as a result of the intrinsically high magnetic moment of the cluster. Nonlinear behavior of the

relaxivities is observed, which may be caused by aggregation-induced dipole coupling and/or a change in the coordination sphere of the cluster. This is the first example of molecular cobalt-based MRI contrast agent displaying high relaxivities.

5.4. Experimental

5.4.1. Synthesis of the Tetranuclear Cobalt Complex 5.1

Reactions were performed under inert atmosphere (N_2) using standard Schlenk techniques. The complex **5.1** was prepared as previously described with all handling carried out under inert atmosphere.[274] All solvents were spectroscopic-grade, dry, and deoxygenated. CH_2Cl_2 was dried over CaH_2, distilled under argon, and freeze-pump-thaw degassed. ^{1}H NMR spectroscopy was carried out on a 500 MHz Bruker AVANCE500 spectrometer in benzene-d_6 at 300 K. FT-IR spectroscopy was carried out on samples prepared as KBr pellets and measured with a Perkin-Elmer Spectrum One FTIR spectrometer. Mass spectra were collected using a Micromass Q-Tof II mass spectrometer in positive-ion mode using pneumatically-assisted electrospray ionization.

Co_4(3,5-DTBQ) (5.1) Yield: 1.75 g, 77 %. ^{1}H NMR (500 MHz, benzene-d_6) only t-butyl groups were assigned due to complexity arising from **5.1** being paramagnetic ^{1}H NMR: δ -20.3 (s, 18H), δ -18.2 (s, 36H), δ -11.3 (s, 18H), δ 0.7 (s, 9H), δ 1.1 (s, 9H), δ 1.3 (s, 9H), δ 1.5 (s, 9H), δ 11.0 (s, 18 H), δ 38.9 (s, 18 H). FT/IR (cm^{-1}, KBr): 3300 (vw, O-H), 301 (w, sp^2 C–H), 2953 (s, sp^3 C–H), 2907 (m, sp^3 C–H), 2868 (m, sp^3 C–H), 1582 (s, C=C), 1471 (s, C–O) 1450 (s, C–O), 1357 (m, C–O), 1243 (w, C–C) 1095 (m,) 1027 (m,), 1228 (s, C–O), 1094 (s, C–O), 986 (m, sp^2 C–H), 908 (m, sp^2 C–H), 876 (m, sp^2 C–H), 862 (m, sp^2 C–H), 827 (m, sp^2 C–H), 495 (w, Co–O). ESI-MS: m/z (%) 1772 [$Co_3(DTBQ)_7(H_2O)_3$]

$^{+}$, 1550 $[Co_3(DTBQ)_6(H_2O)_3]^{+}$, 998 $[Co_2(DTBQ)_4]^{+}$. Anal. Calcd for $C_{112}H_{160}O_{16}Co_4 \cdot H_2O$: C, 66.72; H, 8.10; O, 13.49; Co, 11.69, Found: C, 66.71; H, 8.86; O, 13.52; Co, 12.00.

5.4.2. Electron Absorption Spectroscopy

Variable-temperature UV/Vis/NIR spectroscopy of **5.1** in the temperature range 200 K–300 K was performed with a Perkin Elmer (PE) Lambda 1050 spectrophotometer, and Oxford OptistatCF continuous-flow static-exchange-gas cryostat system fitted with inner sapphire windows and middle and outer infrasil quartz windows. A 10^{-4} M solution was prepared in CH_2Cl_2 under inert conditions and transferred to a long-stemmed quartz cuvette sealed under argon. Variable-temperature UV/Vis spectroscopy at temperatures 293-333 K was carried out in dichloroethane and recorded with an Agilent photodiode array with Peltier temperature control unit. Spectra were acquired in 10 K increments from 293 to 333 K for high-temperature regime with ~30 min of equilibration at each temperature.

5.4.3. Solid-State Magnetic Measurements

DC-SQUID measurements on samples of **5.1** were obtained from 2–325 K with a Quantum Design Magnetic Property Measurement System XL-5 at a field of 10,000 Oe. The diamagnetic correction of the samples was calculated using Pascal's constants for atomic diamagnetic contributions to obtain a correction of -1.286×10^{-3} emu·K·mol^{-1} for the complex **5.1**. The sample was corrected for the diamagnetic susceptibility of the gelule and insertion tube (-2.4×10^{-7} emu·K·mol^{-1}) which is negligible relative to the sample magnetization at 1 Tesla.

5.4.4. Solution-State Magnetic Measurements: Evan's Method

In an inert atmosphere argon glove box, the complex **5.1** (0.4 mg) was dissolved quantitatively in CD_2Cl_2 (1.00 mL), and the solution was transferred to a 5-mm NMR tube fitted with a coaxial insert tube and filled with CD_2Cl_2. For variable concentration magnetic measurements, 5.3 mg of **5.1** was dissolved in benzene-d_6 or 10 mM H_2O in benzene-d_6 to make up a stock solution (0.5 mM). Serial dilution was performed to prepare sample solutions of concentration from 0.5 to 0.08 mM. Spectra were acquired with a Bruker AVANCE 500 MHz NMR spectrometer between 200 and 300 K at 20 K intervals for variable temperature magnetic measurements and 300 K for the variable concentration magnetic measurements. Evan's method was used to determine the solution-state magnetic susceptibility of the sample by monitoring the frequency shift of the $CHDCl_2$ proton resonance for the variable temperature magnetic measurements and C_6HD_5 for the variable concentration magnetic measurements. The gram magnetic susceptibility of the sample, χ_g, was calculated with equation 5.12,[297-299]

$$\chi_g = -\frac{3\Delta\nu}{4\pi m\nu} + \chi_{g0} + \chi_{g0}\frac{\rho_0 - \rho_s}{m} \qquad \text{Equation 5.12}$$

where $\Delta\nu$ (Hz) is the shift between the resonances for the solute-containing solvent and the reference solvent, ν (Hz) is the operating frequency of the NMR spectrometer, m is the mass (g) of paramagnetic solute in 1.00 mL of solvent, χ_{g0} is the gram magnetic susceptibility of the solvent, ρ_0 is the density of the pure solvent, and ρ_s is the density of the solute-containing solvent. The m value was corrected for the change in solvent density at each temperature.[300] The temperature-dependent density of the solvent was approximated by applying the very nearly linear behavior of the density of CH_2Cl_2

between 200 and 300 K[301] to the density of CD_2Cl_2 at 298 K (1.362 g/mL). The second and third terms in equation 5.12 were neglected.[302] The molar susceptibilities, χ_M, were calculated from the χ_g values and were subsequently corrected for the diamagnetic contribution of the complex, χ_d (same as those used for the solid-state magnetic measurements; *vide infra*), to obtain the paramagnetic contribution to the molar magnetic moment, $\chi_M T$.

5.4.5. Relaxivity Measurements

Relaxivities of the tetranuclear cobalt complex **5.1** were determined by nuclear magnetic resonance (NMR) spectroscopy. Longitudinal (T_1) and transverse relaxation times (T_2) of water with a various concentration of **5.1** (0 mM, 0.01 mM, 0.05 mM, 0.1 mM, 0.3 mM and 0.5 mM) were measured. 10 mM concentration of H_2O in benzene-d_6 was prepared by saturating 99.6 % atom D benzene with deionized H_2O. The concentration was determined by relative integration of H_2O and benzene peak which is consistent with literature values (33 – 36 mM)[345]. The 10 mM H_2O in benzene-d_6 was further degassed by three cycles of freeze-pump-thaw and brought into an argon atmosphere glove box. A control sample (blank) and a series of different concentration of **5.1** in 10 mM H_2O in benzene-d_6 were prepared and transferred to J Young NMR tubes in the argon atmosphere glove box. ^{1}H NMR spectra were acquired with 500 MHz Bruker AVANCE 500 spectrometer at 300 K. H_2O resonances were observed at 0.3 to -0.1 ppm. The value of T_1 was determined by the inversion recovery method utilizing a two pulse sequence: a 180° pulse followed by a 90° pulse after different inversion recovery times τ (0.01, 0.02, 0.05,

0.1, 0.2, 0.5, 1, 2, 3.5, 5, 10, 20, 35, 60, 120 sec). Integration of water peak as a function of delay time τ was fitted to equation 5.9 to determine T_1 at various concentrations of **5.1**.

$$M_t = M_0\left(1 - 2Ae^{-\frac{\tau}{T_1}}\right) \qquad \text{Equation 5.9}$$

Where M_t is the intensity of the detected magnetization and M_0 is equilibrium magnetization.

Similarly, the value of T_2 was determined by the Carr-Purcell-Meiboom-Gill (CPMG) method: 90° pulse followed by a 180° pulse after fixed delay time τ. Another delay time is applied after 180° pulse before the acquisition. This sequence (τ-180° pulse-τ) was repeated multiple times n (0, 2, 4, 6, 8, 10, 14, 20, 40, 80, 120, 200, 400, 800. 1200, 2000). Integration of the water peak as a function of total echo time $[\tau\text{-}180°\text{ pulse-}\tau]_n$ was fitted to equation 5.10 to determine T_2.

$$M_t = M_0 e^{-\frac{\tau}{T_2}} \qquad \text{Equation 5.10}$$

$1/T_1$ and $1/T_2$ were plotted as a function of concentration of **5.1** to determine relativity r_1 and r_2 modeled by equation (5.11).

$$\frac{1}{T_{1,2}} - \frac{1}{T_{dia}} = r_{1,2}[c] \qquad \text{Equation 5.11}$$

Chapter 6. Optical Modulation of Gate Voltage in Graphene OFETs

6.1. Introduction

The demand for an increase in transistor density per chip has resulted in the incessant miniaturization of transistor size and generations of more complex integrated circuit designs. The desire for transistor size reduction and increased transistor density have created both a "memory" and a "power" wall, fueling the search for new gating devices with fundamentally different physics from that of field-effect transistors (FETs).[346,347] Standard FETs are mono-functional devices that rely on electrical gating (field-effects) to modulate charge transport of one type of charge carrier (electron or hole) in a semiconducting material to give a binary signal. The integration of secondary functional materials orthogonal to the electrical gating such as optical gating allows four discrete signals to be generated, instead of two, which can vastly increase the memory density without increasing transistor density. A development of an electrically and optically gated bifunctional FETs may be a great candidate for an ultra-high memory density data processing/storage (Figure 6.1).

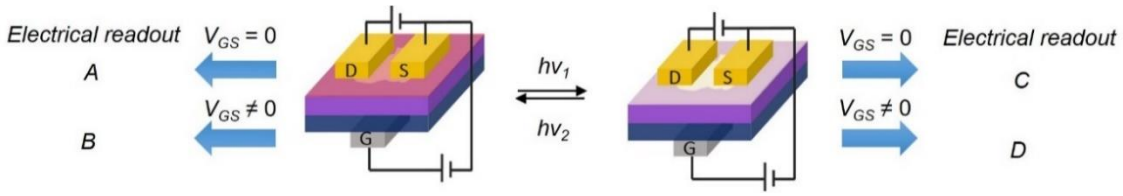

Figure 6.1. Schematic representation of an electrically and optically gated bifunctional graphene-OFET.

Graphene, a two-dimensional polymer of carbon atoms arranged in a hexagonal lattice, is considered a primary candidate for next-generation electronics due to its high electrical and thermal conductivity, high charge mobility, mechanical integrity, and ability to generate quantum Hall effects.[348-350] As a result, there is intense interest in developing methods of exerting control over the electronic properties of graphene. Some success has been found through confining graphene sheets into one-dimensional nanoribbons[351-354] nanomesh structures,[355-357] by exerting mechanical strain[358-361] or lattice strain,[362] or by applying a perpendicular bias to bilayer graphene.[363-365] Other methods are chemical modification of the graphene sheet via covalent bonding to dopants[139,366,367] or substitutional doping in which carbon atoms in the lattice are replaced by boron or nitrogen atoms.[368,369] All of the above methods, however, result in disruption to the 2D graphene lattice to the detriment of the electronic properties of the material. Noncovalent doping has thus emerged as the most effective way to modify the Fermi level of a graphene device without decreasing the charge mobility or otherwise negatively impacting electronic transport.[139,370,371] Electron-poor (p-type) dopants result in a hole injection to graphene decreasing the Fermi level below the Dirac point, and in turn, providing p-type conduction in graphene (Figure 6.2).[370,371] Conversely, electron-rich (n-type) dopants inject electrons to graphene which causes the graphene Fermi level to rise above the Dirac point, providing n-type conduction in the graphene (Figure 6.2).[370,371] The gate voltage of graphene can, therefore, be modulated by changes in ionic doping effects.

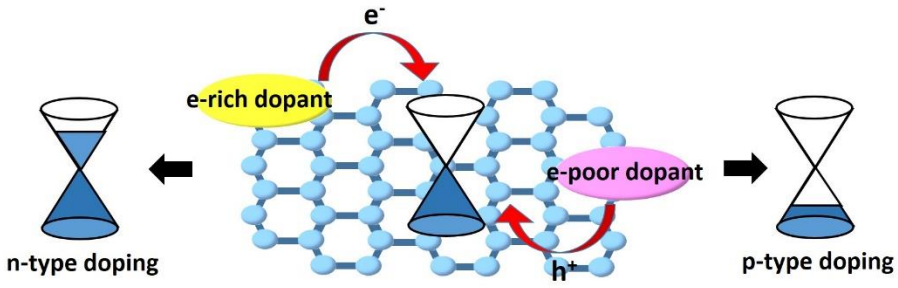

Figure 6.2. n-type and p-type ionic doping of graphene

The ionic doping effect may be modulated by coupling graphene OFETs with photochromic materials. Photochromic compounds undergo photoinduced isomerization between two metastable states that differ in electronic and optical properties due to changes in electronic structure upon photoisomerization. The noncovalent doping of graphene by a photochromic compound may, therefore, provide a route to optically modulate the gate voltage (V_g) of graphene organic field-effect transistors (OFETs).

Among classes of photochromic compounds, the spirooxazines have been heavily utilized in optical applications due to their high colorability and fatigue resistance.[2,22] Spirooxazines undergo reversible photoisomerization between a closed (spirooxazine SO) form and open (photomerocyanine PMC) form (Figure 6.3). UV light irradiation of the SO form with $\lambda_{max} \approx 350$ nm induces C–O bond cleavage via a singlet excited state to give the photomerocyanine (PMC) form with $\lambda_{max} \approx 600$ nm. Visible light induced ring-closure can occur by excitation of the π–π^* transition of the PMC form or thermal relaxation along the potential energy surface.[2,22,30] The photoisomerization of spirooxazines induces changes in electronic structure which leads to a shift in the oxidation/reduction potentials and

donor/acceptor ability of the spirooxazines, which may allow effective optical modulation of the direction and magnitude of ionic doping of graphene.

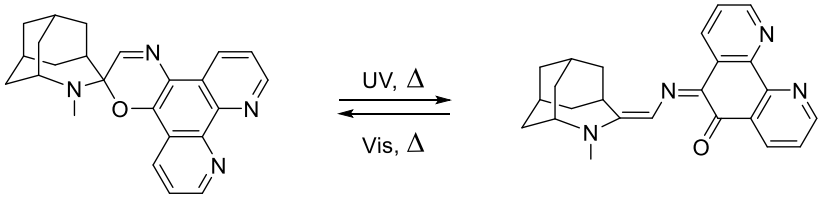

Figure 6.3. Photoisomerization and thermal relaxation of the azahomoadamantyl-based spirooxazines **2.2**.

In order for optically modulated doping to function, the photochrome must be able to photoisomerize on a graphene surface. While extensive studies of photochromic compounds in solution have been carried out, studies on the photoisomerization of photochromic compounds on surfaces are very limited due to difficulties with light-induced structural changes occurring in constrained media and in the absence of solvation. Nevertheless, this is one of the most important directions in the field as functionalization of surfaces becomes more important to functionalized device architectures. Previous investigations of optically gated solid state graphene transistors have employed a perylene-based functional group to noncovalently anchor the photochromic molecule to the surface, leaving the photochromic moiety relatively free to isomerize.[144,372] Jang *et al*. reported reversible optical modulation of the Dirac point of graphene functionalized with pyrene-modified spiropyrans.[371] Functionalization with spiropyrans (SP) resulted in n-doping of graphene, and the photoisomerization from the SP form to PMC form led to a shift of the Dirac point of 6.5 V upon UV irradiation for 30 min.[371] The mechanism of change in ionic doping as a function of photoisomerization state however was not articulated.[371] Peimyoo

et al. reported the photoswitching of an azobenzene directly adsorbed to the graphene surface, with a small change (~ 2V) in threshold voltage by photoisomerization presumably due to a small structural change upon isomerization.[373] Moreover, all reported examples of photoisomerization driven doping of graphene were induced by UV light irradiation. Since pristine graphene has an absorption band ~ 270 nm, UV light irradiation may introduce complications arising from photoexcitation of graphene itself.

We have synthesized an azahomoadamantyl-based spirooxazine which photoisomerizes in the thin film and single crystalline phase[24] making it an excellent candidate for the investigation of photoisomerization processes on surfaces. Moreover, these photochromic compounds exhibit negative photochromism, which allows the use of visible light to induce photoisomerization instead of the more typical UV light. A use of visible light prevents the complication of photoexcitation of electrons in graphene, as graphene does not have significant absorption in the visible region. Visible light is lower in energy and therefore minimizes the rapid photodegradation of organic materials. In addition, longer wavelengths used by optical recording media (600 nm) allow integration of negative photochromes into more complex device architectures.

In this chapter, we investigate the noncovalent functionalization of graphene by a photochromic azahomoadamantyl-based spirooxazine **2.2** (Figure 6.3). The optical modulation of ionic doping of graphene is examined by Raman and electronic absorption spectroscopy accompanied by electron transport measurements. The study demonstrates a solid-state device optically gated with visible light via a spirooxazine-graphene transistor with the largest reported changes in gate voltage upon photoisomerization. The resultant photoswitchable OFET is advantageous in that spatial and temporal resolution can be used

in principle, leading to greater possible control over transistor and integrated circuit architectures. Moreover, the integration of a photoresponsive substrate as a secondary functional material that possesses two states that differ in the electronic structure into a graphene-FET would lead to a bifunctional device that is capable of responding to two orthogonal stimuli – electric field and light – to create a quaternary signal system: four bits instead of two per transistor, for data encoding and processing.

6.2. Results and Discussion

6.2.1. Device Fabrication

A simple graphene OFET architecture was prepared as shown in Figure 6.4. On the top surface of a layer of dielectric silicon dioxide (SiO_2) sit two electrodes, a source, and drain, with a graphene channel running between them. The SiO_2 layer itself sits on top of a p-doped silicon substrate which functions as a back gate. A voltage is applied between the source and drain, and the current between source and drain measured. The measured current is proportional to the conductivity of the graphene channel. By applying a voltage between the back-gate and source electrodes, an electric field is generated which modulates the conductivity of the graphene channel by varying the Fermi level of the graphene.

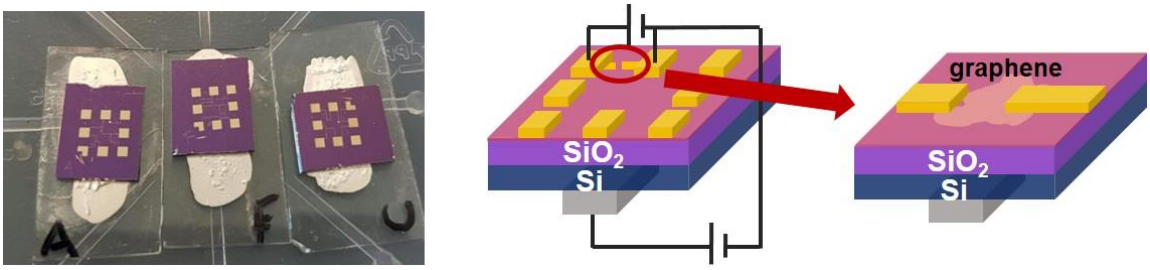

Figure 6.4. Schematic of spirooxazine-functionalized graphene-OFETs.

Preparation of spirooxazine **2.2**-functionalized graphene-OFETs consisted of five steps. The process involves i) optical lithography to deposit a large gold electrode on the silicon wafer, ii) graphene transfer to the wafer, iii) locating and identifying graphene by optical microscopy and Raman spectroscopy, iv) electron-beam lithography (EBL) to pattern gold electrodes that make contact with graphene channel, and v) solution deposition of the spirooxazine (Figure 6.5) onto the graphene substrate.

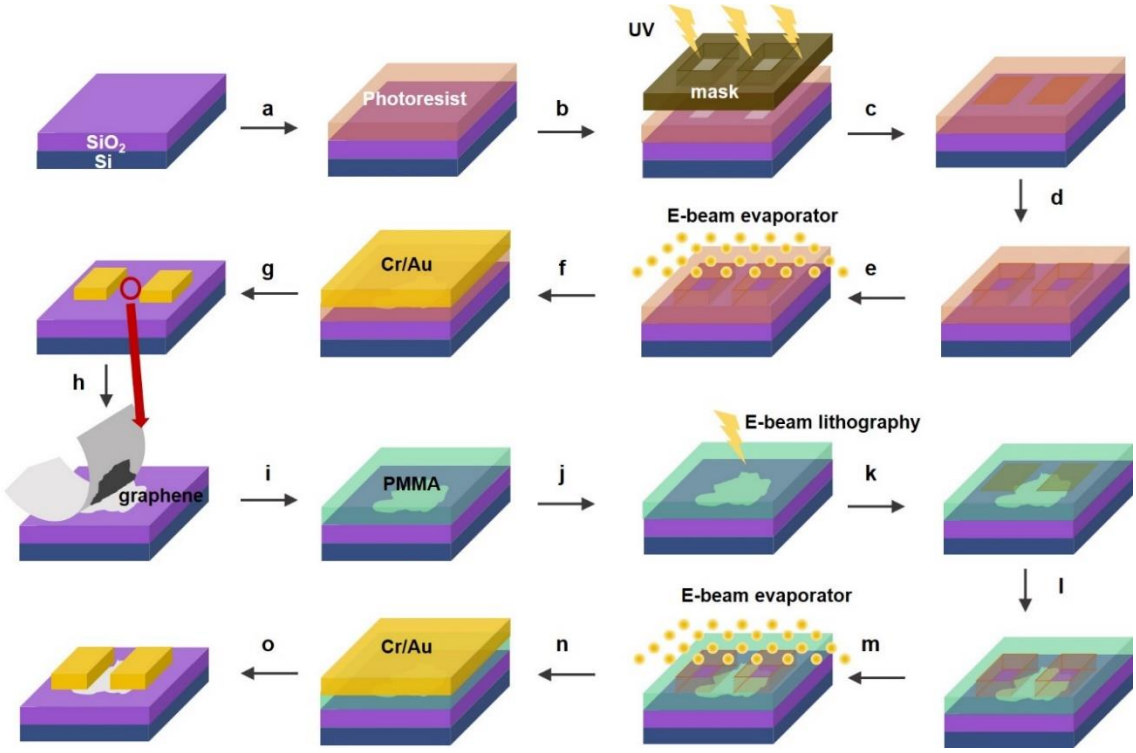

Figure 6.5. Flowchart of graphene-OFET device fabrication.

The graphene-OFETs were prepared by the following procedure. First, optical lithography was performed to deposit large gold electrodes. An AZ5214e photoresist was spin-coated onto the Si substrate with ~1.4 μm thickness at 4000 rpm (Figure 6.5a). The

substrate is a silicon wafer p-doped with boron (a resistivity of 0.005 – 0.020 Ω·cm) with a 280 nm layer of SiO_2 coating, which serves as a back gate. The spin-coated wafer was annealed on a hot plate at 85 °C for 60 s. The optical mask used (100 nm Cr/glass) had a platform design composed of eight external pads measuring 1 × 1 mm, making up a 5 × 5 mm total patterned area. Inside these large electrodes, a 20 × 20 grid of 10 μm squares was used as a finer alignment for locating graphene. The wafer was then positioned on a mask aligner with the optical mask placed on top and was exposed to UV light for 15 s (Figure 6.5b). The wafer was soaked in AZ300MIF developer for 100 s (Figure 6.5c), then rinsed with DI water to stop development, and blown dry with nitrogen gas (Figure 6.5d). The electron-beam (e-beam) evaporator was used to deposit 5 nm of chromium, which served as an adhesion layer, followed by 100 nm of gold (Figure 6.5e). The remaining unexposed resists as well as the top layer of gold (Figure 6.5f), were removed by sonication in acetone then isopropanol for 15 min, leaving the gold pattern transferred onto the silicon wafer (Figure 6.5g). Graphene was then transferred onto the patterned wafer by mechanical exfoliation. Scotch tape was used to remove several layers of pyrolytic graphite (HOPG) and then repeatedly folded onto itself until it had a uniform gray appearance and was no longer reflective and shiny. The tape was applied on the wafer and left to sit before being slowly removed (Figure 6.5 h).

Optical microscopy and Raman spectroscopy were used to locate and confirm the thickness of the graphene. On a 280 nm silicon-oxide substrate, single-layer graphene (SLG) has a faint purple color, which is distinguishable from the dark purple color of multi-layer graphene (MLG) (Figure 6.6). The colors are resultant of the resonance of the optical frequencies within the cavity of silicon dioxide. Raman spectroscopy was used to further

confirm the number of graphene layers. Generally, graphene shows two pronounced peaks, a G band at ~1580 cm^{-1} and a 2D band at ~ 2700 cm^{-1}. The G band is attributed to bond-stretching of sp^2 carbons while the 2D band is associated with the breathing modes of sp^2 carbons in the ring.[374] The number of graphene layers was quantified by the relative intensity and bandwidth of the G and 2D bands. The relative intensity of the G and 2D bands for single layer graphene (SLG) is roughly 1:4. An increase in the number of graphene layers changes the shape and intensity of the 2D band, leading to a broader and less intense band.[374,375] Hence, the ratio of the two bands increases in multilayer graphene (MLG). [375]

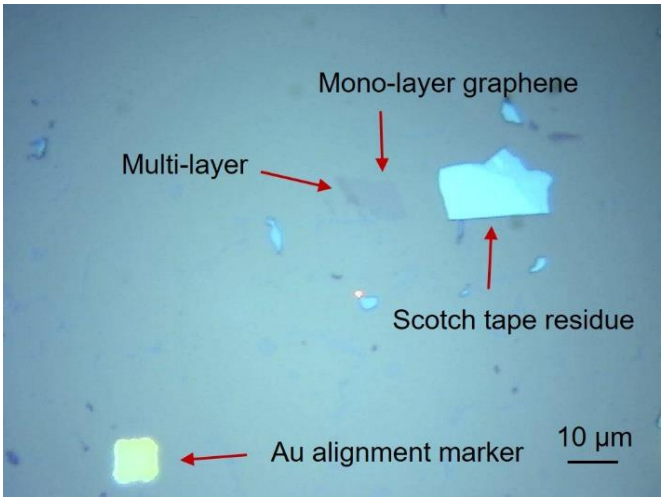

Figure 6.6. Optical microscopic image of mono-layer and multi-layer graphene on the silicon wafer.

A graphene-deposited wafer was then spin-coated with a dual layer of poly(methyl methacrylate) PMMA of differing average molecular weights (495 kDa and 950 kDa) with roughly 200 nm layer of 4 % PMMA 950 on top of a 350 nm thickness of a 6 % PMMA 495 layer (Figure 6.5i). The wafer was then baked for one minute after the first layer was

applied and five minutes after the second layer was applied. A pattern of fine electrodes with contacts to the mono-layer graphene channel was designed using Raith50 CAD software, which was then written on the PMMA-coated wafer by electron beam lithography (Figure 6.5j). The wafer was then developed by soaking for 50 s in 1:3 MIBK:isopropanol (Figure 6.5k) and rinsing with isopropanol before being nitrogen blow dry (Figure 6.5l). The 5 nm of chromium and 100 nm of gold was deposited through the use of an e-beam evaporator (Figure 6.5m, n), followed by removal of excess gold through soaking in acetone for several hours (Figure 6.5o). The final fine structure making contact with the graphene channel is shown in Figure 6.7. Finally, spirooxazine **2.2** was deposited on the substrate by solution deposition (10^{-6} M in methylcyclohexane) for 5 min, followed by rinsing in methylcyclohexane. Silver paint was used to make the back-gate contact.

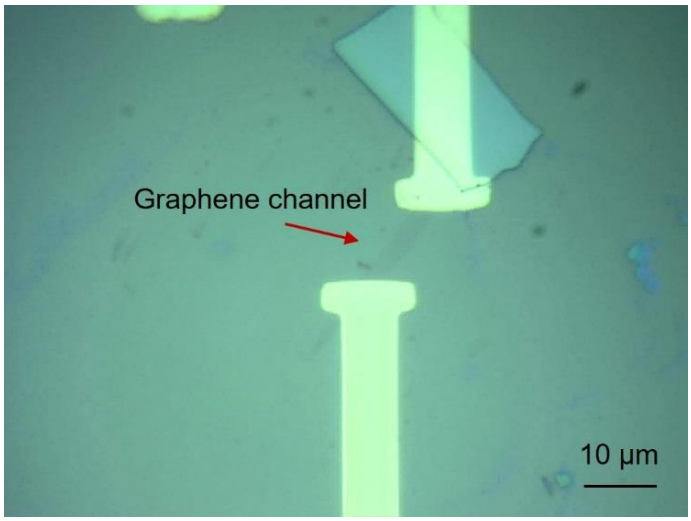

Figure 6.7. Optical microscope image of a graphene channel with Au electrode on top of a silicon wafer.

6.2.2. Atomic Force Microscopy

Tapping atomic force microscopy (TAFM) was carried out on the spirooxazine-functionalized devices to determine the device architecture and thickness of the spirooxazine layer to gain insight into the structure of the solution-deposited thin film. Figure 6.8a shows a tapping AFM image of a device in which electrodes were properly attached to single-layer graphene. Single-layer graphene after solution deposition of spirooxazine **2.2** and topographic profile across the piece of functionalized graphene is shown in the Figure 6.8b and 6.8c. The step height from SiO_2 to functionalized graphene was found to be 4–5 nm (Figure 6.8b). The film was observed to be 5 nm thick for the first ~ 250 nm from the edge of the graphene and 4 nm thick in the center of the device. Previous studies reported the thickness of mechanically exfoliated graphene as in the range of 0.4–1.7 nm[350,376-378] on Si/SiO_2, measured by AFM. An atomically thin film of single layer graphene would be expected to be 0.34 nm.[378] The discrepancy between predicted and observed thickness of SLG is attributed to a gap and puddles between the graphene and SiO_2 substrate.[376,378,379] Assuming a thickness of graphene of 1.1 nm, the observed thickness of 3.3–4.6 nm suggests a spirooxazine thin film comprised of 2–3 monolayers of **2.2**, depending on the orientation of the molecule at the surface. The increased thickness around the graphene edges suggests that deposition occurs preferentially at the dangling bonds of the edge states before proceeding to the interior of the surface. This is consistent with a number of studies of gas-phase deposition of organic molecules on graphene which preferentially deposit at step edges.

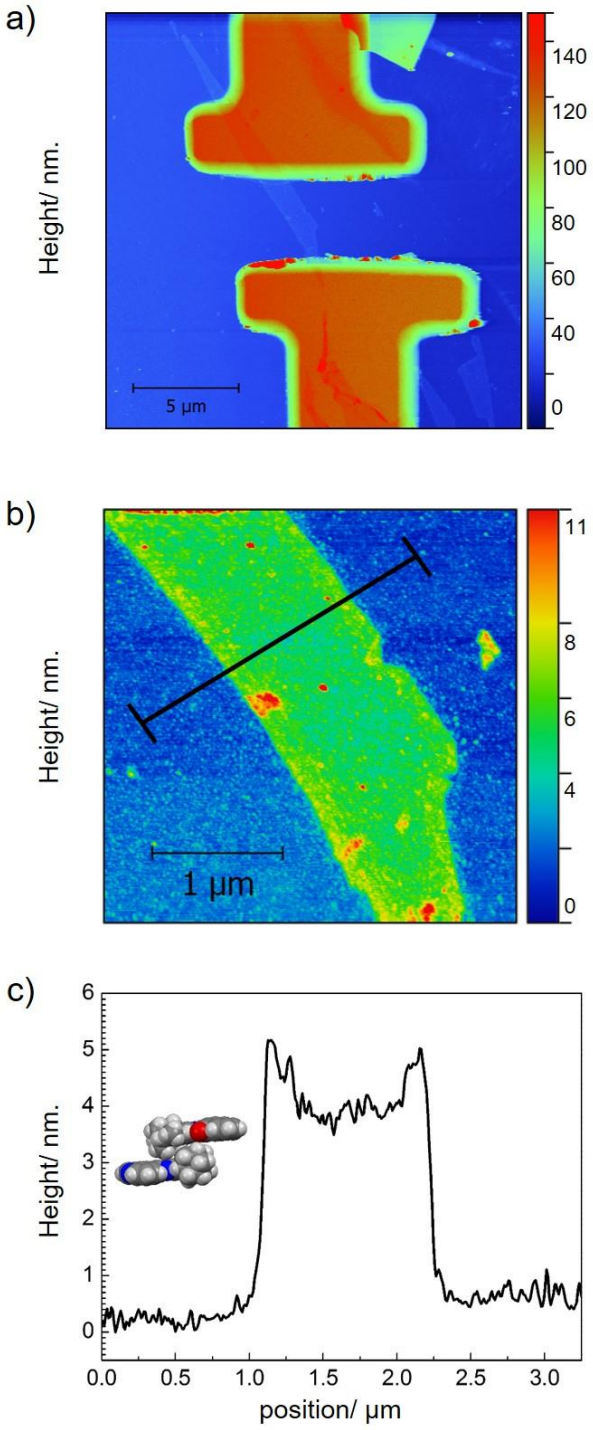

Figure 6.8. Tapping AFM image of single-layer graphene attached to Au electrodes after solution deposition of **2.2** (a), single-layer graphene region of image (b), topographic profile across the top face of functionalized graphene (c); (inset) dimension of typical spirooxazine **2.2** dimer from XRD (Height 10 Å × Length 18 Å × Width 8 Å).

6.2.3. Photochromic Properties of APSO 2.2 on graphene

Model studies of photoisomerization of spirooxazine **2.2** on CVD graphene on quartz reveals that **2.2** undergoes reversible photoisomerization on a graphene surface. Spirooxazine **2.2** was solution deposited on CVD-grown graphene on quartz by soaking in 10^{-5} M solution for 48 hrs in the absence of light. The electronic absorption spectrum of **2.2** deposited graphene on quartz showed the absorption band at $\lambda_{max} \approx 269$ nm and a band at $\lambda_{max} \approx 569$ nm in addition due to π–π* transition of the spirooxazine **2.2** (Figure 6.9a). The electronic absorption spectrum of CVD-grown graphene on quartz shows a distinct absorption band at $\lambda_{max} \approx 270$ nm due to the exciton shifted van Hove singularity in the graphene density of states[380] but no absorption band in the visible region (Figure 6.9a).

The photochromic behavior of **2.2** on graphene was investigated in the presence and absence of visible-light irradiation by electronic absorption spectroscopy. Spirooxazine **2.2** on graphene exhibits both thermally reversible and photoinduced isomerization by steady-state irradiation ($\lambda_{exc} = 513$ nm). Visible light irradiation leads to a decrease in intensity of the π–π* band at 569 nm (Figure 6.9b) due to an increase in concentration of SO form and no change in intensity at 269 nm, indicating visible light irradiation leads to photoisomerization of the spirooxazine **2.2**. Formation of a photostationary state and thermal relaxation to the most stable PMC form occurs with regeneration of the intensity of the π–π* band at 569 nm (Figure 6.9c,d). The rate of thermal relaxation (k_t) for spirooxazine **2.2** on graphene was determined by the monitoring the π–π* absorption band intensity as a function of time following steady-state irradiation. The data was fit to a biexponential plus linear rate function by linear least-square methods. Thermal relaxation rates were found to be $k_{t1} = (2.7 \pm 0.1) \times 10^{-2}$ s^{-1}(48 %) and $k_{t2} = (7.4 \pm$

0.7) × 10^{-3} s^{-1} (52 %). The second component, k_{t2} exhibits an order of magnitude slower relaxation than the first component, $k_{t1,}$ which suggests that one process may be attributed to crystallization and/or aggregation of spirooxazine **2.2** on the graphene surface, which would give rise to the more constrained environment for thermal isomerization. The first component k_{t1} was an order of magnitude slower than the rate of spirooxazine **2.2** in toluene (k_t = 15 ± 1 × 10^{-2} s^{-1}). This suggests that photoisomerization on surfaces is slower than in solution, which may be due to a lack of solvent necessary to stabilize the transition states and intermediates to relaxation. Although photoisomerization in thin film/crystalline phase has been observed, van der Waals interactions between the solute and graphene may lead to an additional barrier to photoswitching. Spirooxazine moieties of the azahomoadamantyl-based spirooxazines are expected to have strong interactions with graphene via π–π interactions of the oxazine and graphene surface. However, the azahomoadamantyl group itself is expected to have relatively small van der Waals interactions with graphene due to its sphere-like morphology. As van der Waals interactions are dependent on the contact surface area, azahomoadamantyl groups decrease contact surface area and are therefore expected to decrease van der Waals interactions relative to the planar spirooxazines. Moreover, the huge azahomoadamantyl group is expected to provide more free volume for structural change upon photoisomerization due to its topology, which may explain why the spirooxazine **2.2** is capable of photoisomerizing on a graphene surface.

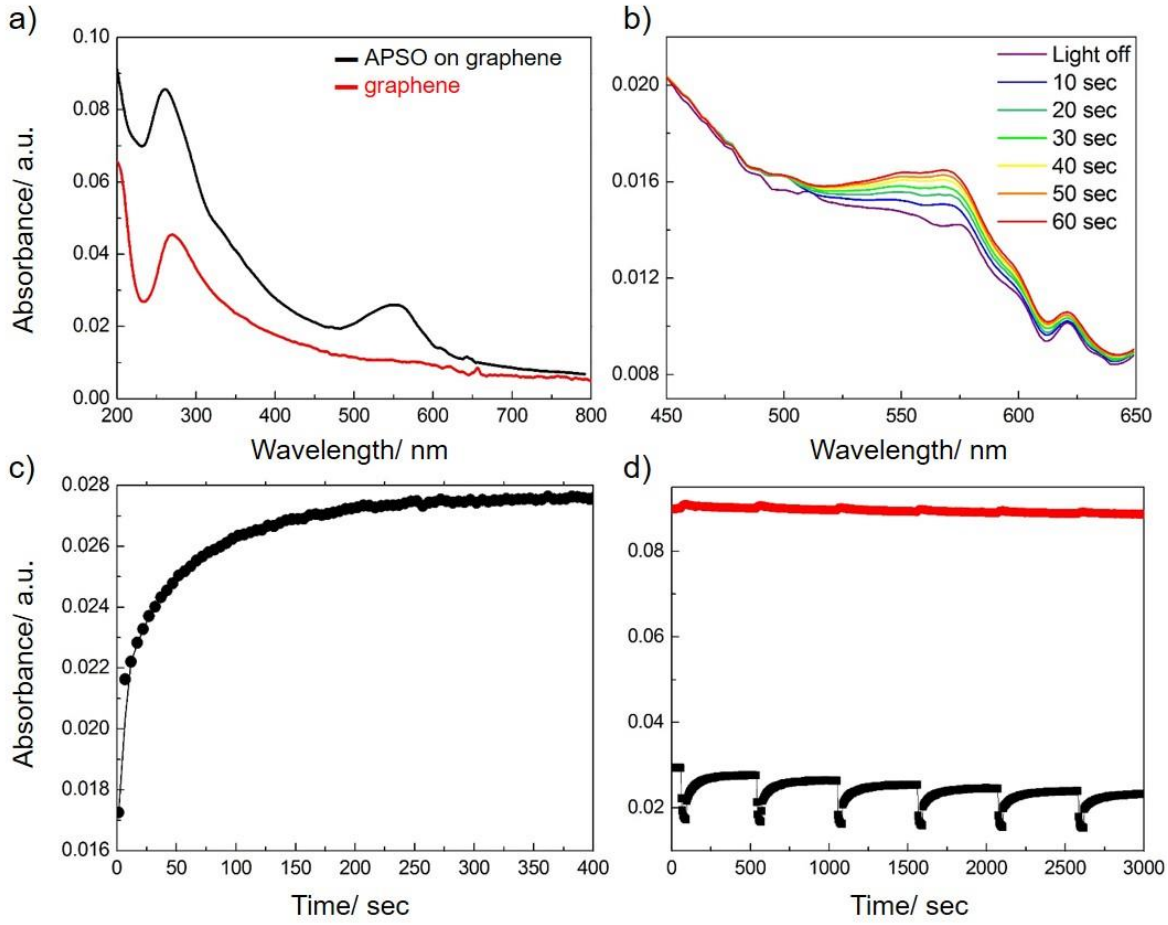

Figure 6.9. Electronic absorption spectra of the spirooxazine **2.2** on graphene/quartz substrate and graphene/quartz, (a), thermal relaxation upon steady state visible light irradiation ($\lambda_{exc} \approx$ 513–568 nm, 100 mW) (b), kinetic trace of absorption intensity (at 569 nm) after formation of the photostationary state (c), and kinetic trace of absorption intensity at 569 nm and 269 nm over 6 irradiation cycles (d).

6.2.4. Raman Spectroscopy

Following deposition of the spirooxazine **2.2** on graphene, Raman spectroscopy was carried out in order to evaluate the covalent or noncovalent nature of the solution-based functionalization. Raman spectroscopy is useful in determining the degree and nature of modifications of the electronic structure of graphene upon noncovalent and covalent

functionalization. Graphene shows two distinct peaks, a G band at ≈ 1580 cm^{-1} and a 2D band at ≈ 2700 cm^{-1}, both of which shift with ionic doping.[381] Another distinct band, the D band at ≈ 1350 cm^{-1} is associated with edge and defect states and its intensity is commonly used to quantify the extent of disruption to the graphene lattice by covalent modification.[382] The absence of the D band in the Raman spectrum after the deposition of spirooxazine **2.2** implies that the molecules are noncovalently bound and that the graphene π-structure remains largely unperturbed (Figure 6.10a). Since covalent bonding disrupts the π-orbital structure of the graphene, it leads to the emergence of the Raman D peak at 1350 cm^{-1}, which is absent in this case.

The Raman spectroscopic analysis of the functionalized graphene substrate also reveals that spirooxazine functionalization results in n-type ionic doping (electron injection into graphene, rather than hole injection). Deposition of the spirooxazine **2.2** resulted in a small shift in energy of the G band to lower energy, and a shift of the 2 D band to higher energy. The direction of G and 2D band shifts (higher or lower energy) are informative in terms of the type of doping. While p-doping causes a shift to higher energy for both the G and 2D bands, n-doping results in a divergence of shifts. (i.e., lower energy shifts for the G band and shift to higher energy for the 2 D band).[383] The nature of the shifts observed in the spirooxazine graphene substrate are consistent with n-doping of graphene by spirooxazine **2.2**. Recent studies have shown that graphene is influenced by both strain and charge puddles on the SiO_2 substrate and that this can also affect Raman peak frequencies in localized regions.[384] For this reason, Raman mapping has become a more accurate and popular method of monitoring changes due to functionalization.

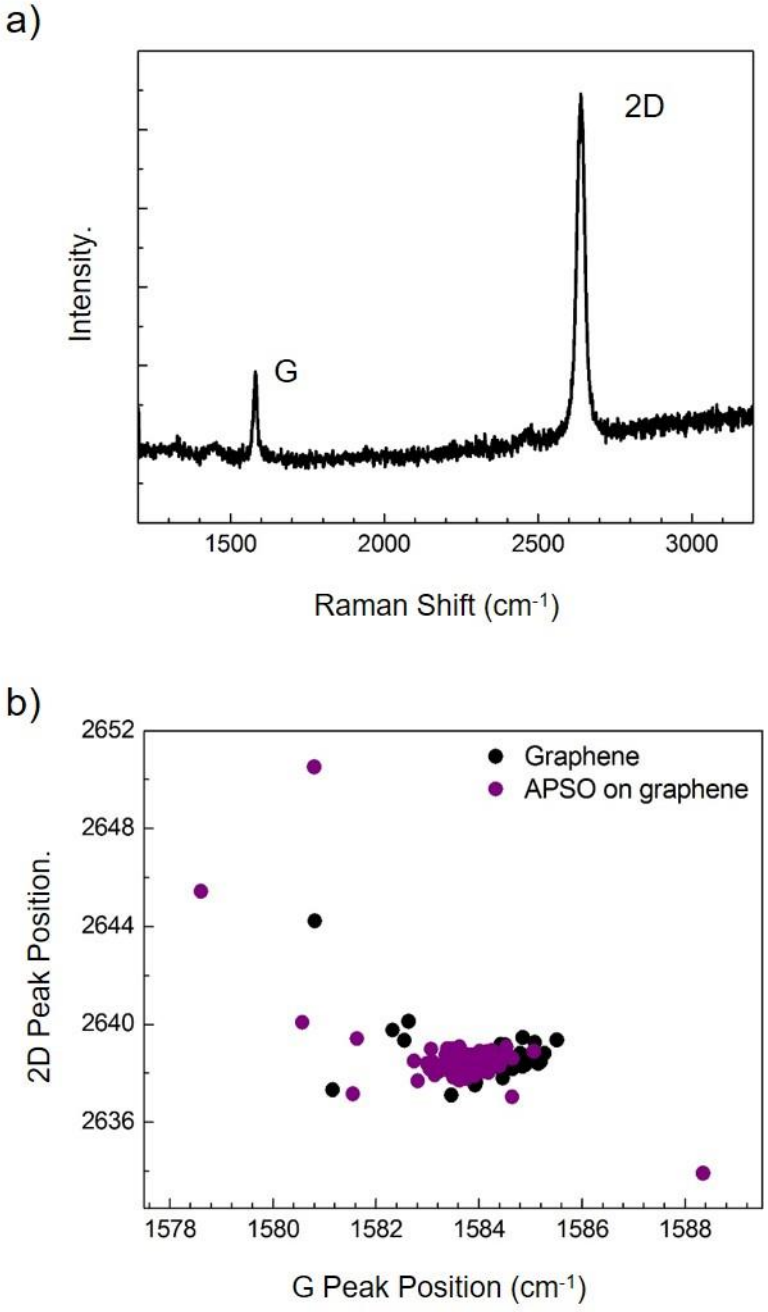

Figure 6.10. Raman spectrum of graphene functionalized with **2.2** (a), Raman mapping analysis of graphene before (black) and after (purple) functionalization with the spirooxazine **2.2** (b).

Raman mapping analysis was carried out on unfunctionalized and functionalized substrates in order to correct for effects present in the unfunctionalized substrate. Seventy-two spectra were collected in an 8 × 9 grid of 600 nm squares of unfunctionalized graphene and the 2D peak frequency of each was plotted as a function of the G peak frequency. The measurement and analysis were repeated a second time following solution deposition of spirooxazine **2.2** on the graphene, Figure 6.10b. There is a clear shift in the G peak toward lower wavenumber, suggesting that spirooxazine **2.2** induces n-type electronic doping of graphene.

6.2.5. Electronic Transport Measurements

Electronic transport measurements revealed that photoisomerization of the spirooxazine **2.2** leads to significant modulation of the ionic doping of graphene in graphene OFETs. Three-point transport measurements, in which the source-drain voltage (V_{SD}) was maintained at 200 mV while the source-gate voltage (V_{GS}) was varied from 0 to 37 V, were performed to determine the ionic doping properties of the spirooxazine **2.2** in the presence and absence of irradiation (Figure 6.11). Prior to functionalization, both devices had a source-drain current (I_{SD}) minimum at $V_{GS} > 0$. This positive value for the threshold voltage (V_{th}) is indicative of p-doping in the unfunctionalized devices and is commonly attributed to oxidative doping due to oxygen and water vapor on the graphene surface as well as the functional groups of the SiO_2 substrate.[350,385] For simplicity, V_{GS} of pristine graphene was corrected to 0 V. Deposition of the spirooxazine **2.2** on the graphene-OFETs resulted in a shift of the threshold voltage (V_{sh}) from 0 V to -19 V. This large negative shift is indicative of electron donation of the adsorbent which leads to n-doping

of the graphene and an increase in the Fermi level (Figure 6.12b). The observation of a negative shift in threshold voltage (V_{th}) is consistent with the Raman mapping analysis. Irradiation of visible light (λ_{exc} = 532 nm, 30 mWatt) led to a positive shift in the threshold voltage V_{sh} to -10 V which suggests that the SO form is either more p-doping or less n-doping than the PMC form (Figure 6.11b).

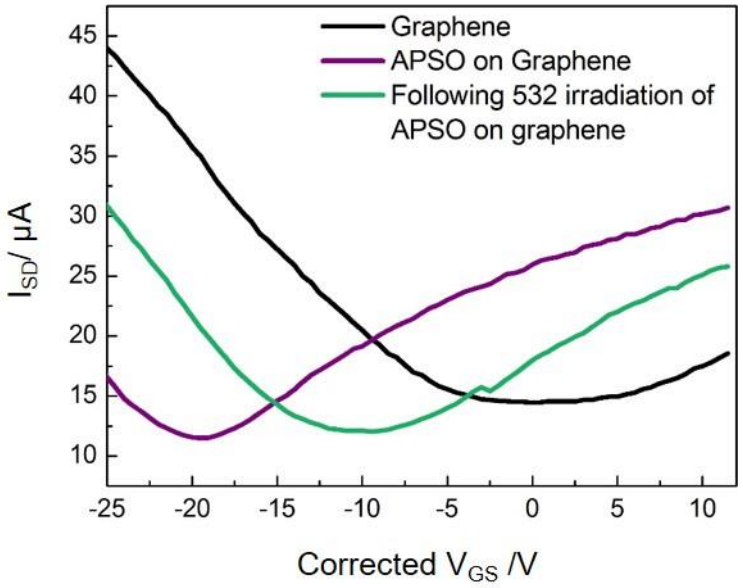

Figure 6.11. Electronic transport measurements of pristine graphene (black), graphene after functionalization with the spirooxazine **2.2** (purple), after irradiation with green light (green).

In order to determine the direction of change in ionic doping upon photoisomerization, an analysis of the frontier molecular orbitals, the HOMO/LUMO energies in comparison to the work function of graphene, was carried out. Experimental values were obtained from measurements of the electrochemical potentials of spirooxazine **2.2** by cyclic voltammetry in acetonitrile, as was carried out previously.[265] The direction of ionic doping between dopants and graphene is determined by the HOMO and LUMO

energy levels of the dopant relative to the Fermi level of graphene.[386,387] The Fermi level of the graphene can be quantitatively described as a workfunction, which is the energy necessary to remove an electron at the Fermi level relative to vacuum.[388] When the HOMO of the dopant is above the Fermi level of graphene, electron transfer from the dopant to the graphene will occur (n-type doping).[386,387] Conversely, when the LUMO of the dopant is below the Fermi level of graphene, electron transfer from the graphene to the dopant will take place (p-type doping).[386,387] Figure 6.12a shows the absolute electrode potentials of the PMC and SO forms relative to vacuum, derived from electrochemical measurement and corrected for solvent and electrode configuration.[389,390] The HOMO energies of the PMC and SO forms of **2.2** are found to both be lower in energy than the workfunction of graphene, at -5.27 eV and -5.54 eV, respectively, so n-type doping would be energetically unfavorable. The LUMO energies of the photochrome are both higher in energy than the workfunction of graphene, so p-type doping would also be unfavorable. Overall, the HOMO energies are closer to the graphene workfunction than the LUMO energies, therefore, dominant n-type doping would be predicted for both forms, as is observed. The HOMO of the PMC form is closer to the work function of graphene on SiO_2 (-4.5 eV)[391] with a gap of ~0.77eV, which would lead to the n-type doping. Upon ring closure, and formation of the closed SO form, the HOMO energy moves down to 1.04 eV lower in energy than graphene. N-type ionic doping would therefore be less favorable, and a decrease in doping would occur upon ring closure, as is observed. The ionic doping process of the closed form is more thermodynamically unfavorable (a more uphill process) than for the open PMC form of the photochrome. Therefore, electron donation from the PMC form to graphene would be expected and is indeed consistent with the n-doping observed by

electron transport measurements and Raman mapping analysis. Likewise, the HOMO of the SO form is closer to the workfunction of graphene than the LUMO. Hence, the SO form also acts as an electron donor to graphene but is weaker than the PMC form due to greater energetic mismatching between the HOMO and the graphene workfunction, weaker n-doping occurs.

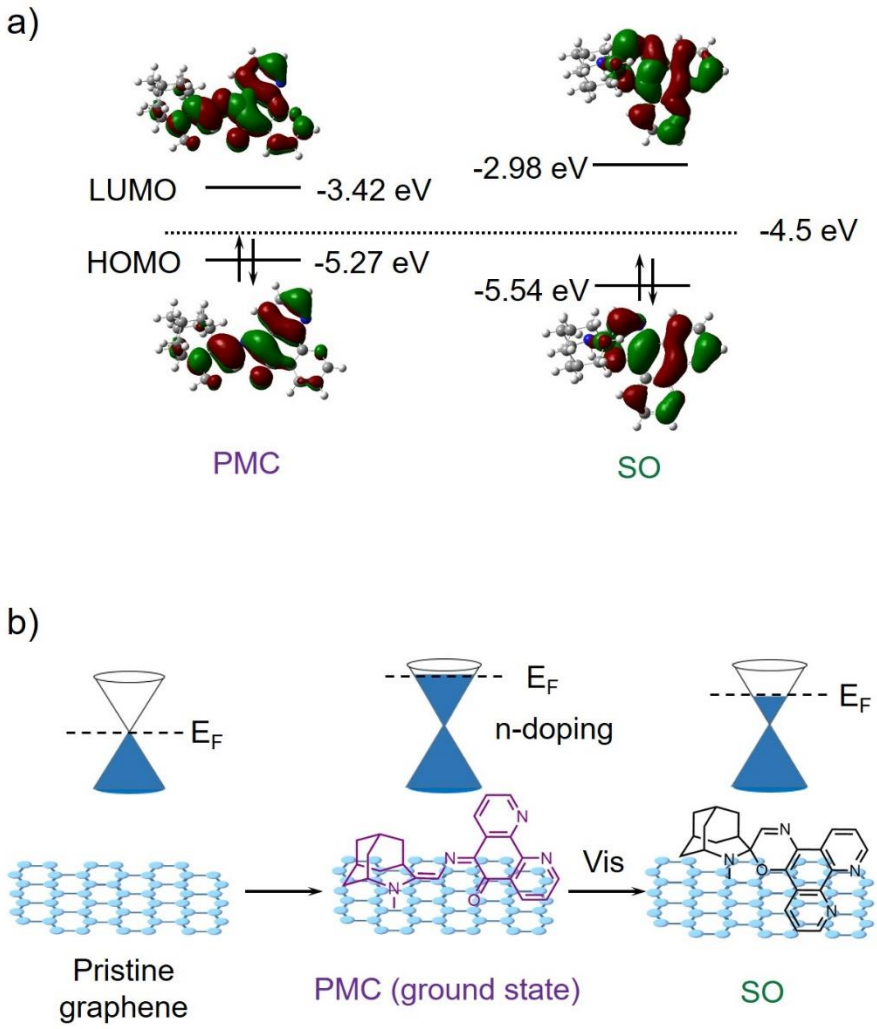

Figure 6.12. Energy levels of the open and closed forms of the spirooxazine **2.2** relative to the graphene work function as determined by cyclic voltammetry and corrected to absolute electrode potential (a), and molecular orbitals are generated by DFT/B3LYP/6-311G+(d,p) (b).

After 20 minutes of darkness to promote thermal relaxation back to the PMC form, the device was re-measured but showed no change in transport properties. It is possible that the irradiation led to decomposition of the molecule on the surface, therefore, preventing further photoisomerization. Alternatively, it may be that 20 minutes is insufficient time to allow the molecules adsorbed to the graphene surface to thermally isomerize back to the PMC form. Future work will investigate the kinetics of light irradiation and thermal relaxation cycles to determine whether the system is irreversible or just exhibits slow thermal relaxation kinetics. Electronic absorption spectroscopy suggests that irradiation/thermal relaxation cycling on a graphene surface does occur, but with a lower fatigue resistance than in solution.

6.3. Conclusion

In conclusion, we have demonstrated optical gating of graphene-OFETs occurs by solution deposition of a photochromic substrate on the surface via noncovalent functionalization. Visible light induces photoisomerization from the PMC to the SO form on graphene OFETs, which leads to a change in electron donor/acceptor ability of the photochrome and ionic doping of graphene. Photoisomerization leads to a decrease in n-type ionic doping, and a positive shift in threshold voltage of 10 volts, demonstrating the first proof-of-principle study of direct visible light induced optical gating of graphene OFETs. This work supports the concept of integrating optical bistability into electronic bistability of OFETs to generate bifunctional quaternary OFETs. Electrical and optical gating of these devices would lead to an increase in memory density without increasing transistor density for high-density data processing and storage devices.

6.4. Experimental

6.4.1. Synthesis

APSO was synthesized according to previously reported methods.[46]

6.4.2. Electronic Absorption Spectroscopy.

Electronic absorption spectra were recorded on an Agilent 8453 spectrophotometer. Sample solutions (concentration of 10^{-5} M) was prepared in degassed spectroscopic grade toluene. CVD monolayer graphene on a quartz substrate (1"×1", graphene supermarket) was soaked in the sample solution for two days in dark and rinsed with toluene prior to use. All experiments were carried out at 298 K in the dark. Irradiation experiments were carried out via multiline irradiation (457 – 647 nm) with a Spectra-Physics Stabilite 2018 mixed gas Ar-Kr ion laser and directed to the sample via with a Newport liquid light guide. The power at the sample was measured with a Spectra-Physics 407A power meter with typical powers of 100 mW. The rates of thermal relaxation were determined in the absence of light by following the intensity of the PMC π–π^* absorption band (λ_{max} = 569 nm) with 5 seconds interval after generation of the photostationary state. The data set was fit to the biexponential function by linear least square analysis. Six cycles were averaged to give the final rate constants.

6.4.3. Graphene-OFET Device Fabrication.

Si substrate with a 280 nm layer of SiO_2 was cut into 1cm × 1 cm. The silicon is a highly p-doped (boron) silicon wafer with a resistivity of 0.005 – 0.020 Ω·cm and serves as a back gate. Photoresist AZ5214e was purchased from Microchemical GmbH. Photoresist developer AZ300MIF was purchased from AZ Electronic Materials. Single-

layer graphene was mechanically exfoliated from pyrolytic graphite (Grade ZYA, Momentive Performance Materials Quartz, Inc.) onto the Si substrate. For electrodes that make contact with graphene, writing patterns were designed using Raith50 CAD software using the optical microscopy images and position data. Electron beam lithography (EBL) was used to pattern the electrodes with an accelerating voltage of 30 keV and a beam current of 1.3 nA with 100 μm write field.

6.4.4. Atomic Force Microscopy

AFM measurements were carried out by Julia Bobak. AFM was carried out on an Agilent 5500 AFM in tapping mode using silicon tips with a force constant of 40 N/m and a resonance frequency of 190 kHz (Ted Pella, TAP190-G). The spirooxazine **2.2** was deposited on the substrate by solution deposition (10^{-6} M in methylcyclohexane) for 5 min, followed by rinsing in methylcyclohexane prior to use.

6.4.5. Raman Spectroscopy

Raman map spectra were collected with a help of Julia Bobak. Raman map spectra were collected every 600 nm over the graphene surface using a micro-Raman spectrometer (inVia, Renishaw, Inc.) with 632.8 nm excitation source, the laser power of approximately 5 mW and a 15 s exposure time. The laser spot size was about 1 μm. Electrical data for the device was obtained using a Keithley 4200 Source Measure Unit in standard field effect transistor configuration under ambient conditions at room temperature. The spirooxazine **2.2** was deposited on the substrate by solution deposition (10^{-6} M in methylcyclohexane) for 5 min, followed by rinsing in methylcyclohexane prior to use.

6.4.6. Electron Transport Measurements

Electron transport measurements were carried out at ambient temperature using a standard 3-pin probe station setup with a Keithley 4200 Source Measure Unit. First, a voltage is applied between the source and drain, while the current through the graphene is measured to observe if the graphene exhibits ohmic contact. For the three-point transport measurements, a voltage is applied at the source, and a current is measured at the drain, but the source voltage is kept constant (V_{SD} = 200 mV) while the second voltage, applied to the back gate, is varied (V_{GS} = 0 to 37 V). For irradiation, a green laser pointer (λ_{exc} 532 nm, 30 mWatt) was hand-held while three point measurements were performed.

Chapter 7. Conclusion and Future Work

Toward the goal of developing new photoswitchable multifunctional materials, this thesis has examined the spirooxazine-based optical gating of charge-transfer processes to modulate magnetic properties and electrical conductivities in OFETs. The thesis covers four main studies, i) an investigation of the mechanism of thermal relaxation in spirooxazines towards modulation of their thermal relaxation rates, ii) the coupling of optically bistable photochromes into an electronically bistable tetranuclear cobalt cluster, iii) the evaluation of a tetranuclear cobalt cluster to enhance the T_1 and T_2 relaxivities for use as an MRI contrast agent, and iv) an analysis of optical gating of the electronic structure of graphene in graphene OFETs.

We first addressed the necessary structural principles for the improvement of photochromes for use as optical control units of photoswitching multifunctional materials. The documented high fatigue resistance of the spirooxazines, in addition to their ability to undergo rapid and robust photochemical conversions, led us to investigate the structural principles of this family of photochromes to determine their suitability for use as optical control units. Chapter 2 presented the importance of the donor-acceptor character to controlling the switching rates of photochromic spirooxazines. Knowledge of the structural parameters that dictate the thermal isomerization barrier allows for the modulation of the thermal coloration/decoloration rates of photochromic spirooxazines. Analysis of a series of azahomoadamantyl-based spirooxazines suggests a correlation between the charge-separated character of the PMC form with the thermal relaxation rates. Experimental and computational analyses support the rotation pathway as the likely relaxation mechanism.

This study provides, for the first time, useful design principles for controlling the thermal isomerization rate in this class of photochromic materials. Insight into the structural factors that govern photostationary states in spirooxazines is critical for a wide range of applications from switching to sensor and data-processing technologies. Chapter 3 presented the effects of metal complexation of the photochromic spirooxazines to support the correlation between the charge-separated character of the PMC form and the rate of the thermal coloration/decoloration found in Chapter 2. The Lewis acidic nature of the metal center and ancillary ligand enhances the charge-separated character of the PMC form, which leads to decreased rates of thermal coloration/decoloration. We provided evidence to suggest that the nature of the metal center and the ancillary ligand have a strong influence on the electronic structure of the PMC form. This work thereby provides a potential pathway for modulating PMC thermal relaxation rates through metal complexation.

The second aspect of this thesis focused on the photomodulation of charge-transfer process in an organic-metal hybrid by photoisomerization of photochromic spirooxazines. The strategy to the development of photomagnetic materials through the integration of optically bistable photochromic ligands into an electronically bistable metal complex was extended to multinuclear cobalt clusters. The ability to structurally control the system is an important step towards providing a platform for future materials design activities. Chapter 4 described the integration of optically bistable phenanthroline-spirooxazine ligands into a magnetically bistable cobalt-dioxolene valence tautomeric cluster. Photochromic cobalt dioxolene clusters exhibited large magnetic moments in the solid and solution states at room temperature. This study suggested that the redox-isomeric behavior of the cobalt dioxolenes can be coupled to isomerization of the photochromic ligand in the solution state.

In this way, the incorporation of a photochromic ligand into magnetically bistable multinuclear clusters is a potentially effective approach towards achieving a large change in magnetization. Most importantly, this study provided an examination of the equilibrium between a multitude of distinct electronic states which are essential factors for coupling between optical bistability and electronic bistability of the cobalt dioxolenes. It was determined that the change in the π-acceptor ability of the photochromic ligands needs to align with the direction of charge transfer of the cobalt dioxolene components in order to achieve photoisomerization-coupled charge transfer. This study therefore provides insight into the design principles necessary for the development of optically bistable photochromic cobalt dioxolene clusters, with the potential for photoswitching of large magnetizations.

The third aspect of the thesis focused on exploiting a new direction for the utilization of the photomagnetic materials. The photochromic clusters investigated in chapter 4 have the potential to enhance the relaxivity of water due to their high magnetic moment in solution at room temperature in a fashion which may be photomodulated. This work lays the groundwork for the development of photoswitching MRI contrast agents. Chapter 5 presented the first example of molecular cobalt-based MRI contrast agent displaying high relaxivities. This work demonstrated the proof-of-principle by which a cluster comprised of metal and redox-active ligands can lead to a large magnetic moment and large changes in relaxivities associated with T_1 and T_2. The resultant cobalt-cluster MRI contrast agent provides a platform for future development of molecular non-gadolinium based MRI contrast agents. The photomodulation of T_1 and T_2 relaxivities of the photochromic clusters discussed in Chapter 5 may be the subject of future investigation.

The last section of this thesis focused on the photomodulation of the electrical conductivity of organic field-effect transistors (OFETs) by utilizing photochromic spirooxazines. This work also emphasizes the unique ability of the photochromic spirooxazines to photoisomerize in the solid state and thereby induce ionic doping of surfaces, essential to utilizing the system in practical applications. Chapter 6 described photomodulation of ionic doping of noncovalently-functionalized graphene field effect transistors. Electronic transport and Raman measurements revealed that the electron donor or acceptor nature of the photochromic isomers could modulate the ionic doping of graphene. This study demonstrated a visible-light gated spirooxazine-graphene transistor that leads to changes of 10 V in gate voltage and does not rely on an anchoring moiety to achieve photoisomerization. The resultant photoswitchable OFET is advantageous in that spatial and temporal resolution of doping could in principle be achieved, leading to greater control over the transistor and integrated circuit architectures. Furthermore, the photoswitchable graphene-OFET provides an opportunity for the future development of optically- and electrically-gated bi-functional quaternary memory devices with potentially increased transistor density.

Future work could involve the photomodulation of magnetic properties by photoisomerization of the photochromic spirooxazines. As discussed in chapter 4, this work demonstrated that the optical bistability of the photochromic spirooxazines could be incorporated into a large cluster which exhibits large magnetic moments. The photochromic cobalt tetranuclear complex **4.4** exhibited a photoisomerization coupled charge transfer process. However, irradiation experiments showed the change in charge transfer process observed spectroscopically was very small. This may be due to two

reasons: i) low photoresponsivity associated with the nature of the photochromic ligand **4.2**, and ii) low spin-transition temperature ($T_{1/2}$) of the complex **4.4**. The first issue results in a small percentage of photochromic ligands isomerizing and inducing a small change in the ligand field around the metal. The second issue may arise from the ligand field strength of the photochromic ligands. In a mononuclear cobalt dioxolene redox-isomeric complex, the transition temperature linearly correlates with the reduction potential of the diimine ligands. The transition temperature expected for the states of **2.2** and **4.2** was estimated by correcting the experimental reduction potentials for the ΔE between the LUMO and LUMO+1 extracted from DFT calculations.[260] The estimated $T_{1/2}$ values for both **2.2** and **4.2** fall on either side of room temperature. In fact, the transition temperature of the photochromic cobalt monomeric complex **4.1** was found to be 325 K experimentally.[260] This gives rise to the question: why were the transition temperatures of the tetranuclear complex **4.3** and **4.4** so much lower than that observed for the monomer **4.1**. One approach would be to synthesize a class of cobalt bicubane tetranuclear complexes in which a series of diimine ligands differing in reduction potential (phenanthroline and bipyridine derivatives) are incorporated. Investigation of a relationship between redox potentials of the diimine ligands and $T_{1/2}$ values of the resulting tetranuclear complex will provide some insight into whether such a relationship holds in the clusters, and if so whether prediction can lead to an increase in the $T_{1/2}$.

Another approach one could take towards increasing the magnitude of the redox isomerism transition would be to design a complex in which each metal center coordinates to a photochromic ligand. In such a system, the change in ligand field induced by photoisomerization of each of the ligands may have a greater effect on the metal centers.

One may simply imagine adding photochromic ligands to the Co2/Co2' coordination site; however, structural engineering of the coordination site on the existing complexes **4.3** and **4.4** may be challenging.

Dinuclear cobalt dioxolene complexes may be promising candidates for the design of complexes in which each cobalt coordinate site is bound to a photochromic ligand. Several examples of dinuclear cobalt dioxolene complexes have been reported. The dinuclear cobalt dioxolene complexes typically employ bridging bidentate dioxolene ligands to coordinate to two cobalt centers. Bodnar and Beni *et al*, synthesized a cobalt-polydioxolene polymer from dioxolene ligand 3,5-bis(3',4'-dihydroxy-5'-*t*-butylphenyl)-1-*t*-butylbenzene (**7.1**) and 1,10-phenanthroline. The resultant dinuclear cobalt dioxolene polymer undergoes thermally-induced redox isomerism *ls*-Co(III)-(Cat^{2-}-Ph-$SQ^{\bullet-}$)-*ls*-Co(III) ↔ *hs*-Co(II)-($SQ^{\bullet-}$-Ph-$SQ^{\bullet-}$)-*hs*-Co(II).[392,393] The polymer showed an abrupt spin transition from *hs*-Co(II) → *ls*-Co(III) with the transition temperature ($T_{1/2}$) of the polymer ~ 300 K.[393] Replacing the phenanthroline with photochromic ligands **2.2** and **4.2** may be a route toward a polymeric structure **7.2**, in which stoichiometric control could prevent polymerization to give a more discrete structure. Carbonera, Tao, and Li *et al*., reported a dinuclear cobalt dioxolenes with 2,5-dihydroxy-1,4-benzoquinone (H_2DHBQ, **7.3**) as a bis-bidentate bridging ligand. The ancillary ligands are used either 7,7,12,14,14-hexamethyl-1,4,8,11-tetraazacyclotetradecane (L = cth)[394] or tris(2-pyridylmethyl)amine (L = tpa)[395,396] as tetradentate blocking ligands to prevent polymerization. The H_2DHBQ cobalt dioxolene complexes undergo a thermally-induced redox-isomeric transition between *ls*-Co(III)-($SQ^{\bullet-}$)-*ls*-Co(III) ↔ *ls*-Co(III)-(BQ)-*hs*-Co(II) with a transition temperature of 175 K[394] and 304–308 K,[395,396] depending on the blocking ligands.

Replacing the blocking ligands with photochromic ligands **2.2** and **4.2** may lead to the formation of dinuclear photochromic cobalt dioxolene complexes **7.4**. Alley *et al*, synthesized a family of dinuclear cobalt complexes **7.6** with 3,3,3',3'-tetramethyl-1,1'-spirobis(indane-5,5',6,6'-tetrol) (spiroH_4, **7.5**) and tpa ligand as blocking ligands.[397] The complexes underwent a thermally induced two-step redox isomerism from the *ls*-Co(III)-(spiro$^{Cat-Cat}$)-*ls*-Co(III) state through a mixed *hs*-Co(II)-(spiro^{SQ-Cat})-*ls*-Co(III) state (100–300 K) to a *hs*-Co(II)-(spiro^{SQ-SQ})-*hs*-Co(II) state (300–355 K).[397] Although the transition observed was not as abrupt as that in the other two types of bridging ligands, incorporation of **2.2** and **4.2** would still be interesting, especially in this type of dinuclear cobalt dioxolene complexes. These complexes exhibit the greatest magnetic moment at room temperature since all redox-active metal centers and ligands are in the paramagnetic state at room temperature. The paramagnetic cobalt centers and dioxolene ligands undergo a complete thermal transition to the diamagnetic state at low temperature, suggesting that large changes in magnetization by photomodulation of the ligand field strength may be possible.

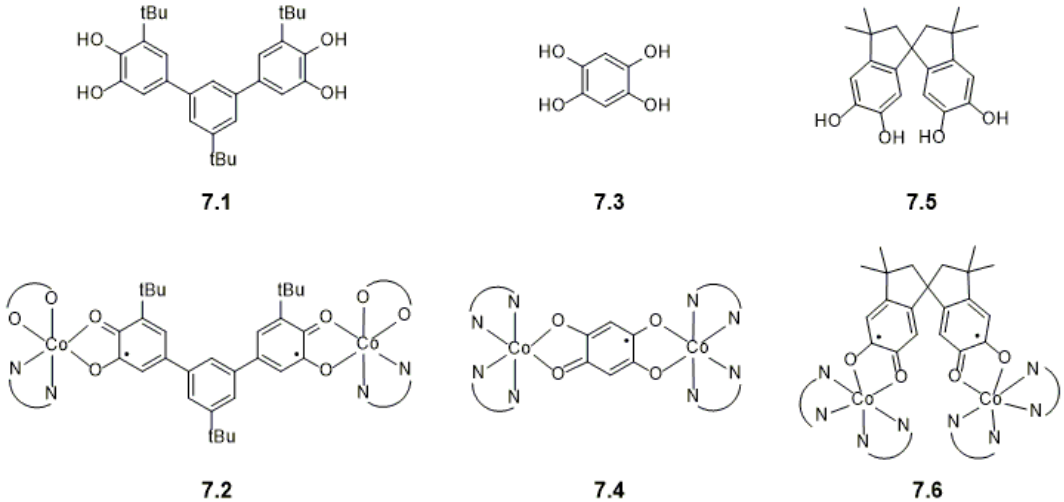

Figure 7.1. Dinuclear valence tautomeric complexes and bidentate bridging ligands.

Another avenue we could take to induce large changes in the magnetic moment of a complex through photoisomerization would be to incorporate photochromes into magnetic nanoparticles (NPs). Magnetic NPs are a class of NPs with magnetic properties that can be manipulated through the application of an external magnetic field. Magnetic NPs have been an active field of research since Brown and Neel introduced the concept of a magnetic single-domain particle.[398,399] The definition of a magnetic single-domain particle implies that the size of the nanoparticle is on the order of a single magnetic domain for a given material. The atoms of the core in a single-domain particle exhibit three dimensional order via magnetic exchange interactions that results in a significant remanence (residual magnetic moment at zero field) and coercivity (the field required to bring the magnetization of the sample back to zero).[400] When the size of the nanoparticle decreases, typically below ~50 nm, the surface to volume ratio increases, and there is a greater number of site defects relative to the internally atoms which are exchange coupled. The decrease in exchange interactions decreases the exchange energy of the nanoparticle such that the exchange energy is on the order of thermal energy k_BT at a given temperature. A temperatures below the blocking temperature, exchange coupling results in a bulk magnetic moment. At temperatures below the blocking temperature, (T_B) there is some degree of exchange coupling, which at temperatures above the blocking temperature, spontaneous reorientation of spins in the core occurs, leading to superparamagnetic behavior.[401] Such individual NPs have a large constant magnetic moment and behave like a giant paramagnetic atom with a fast response to applied magnetic fields with negligible remanence and coercivity.[400] Incorporation of photochromic compounds into the magnetic

NPs may lead to photoinduced magnetic effects with the potential to modulate the large magnetic moment from NPs at room temperature.[402]

Sato *et al*., reported the incorporation of photochromic compounds into magnetic NPs.[403] They prepared iron oxide (γ-Fe_2O_3) decorated with mixed self-assembled monolayers (mSAM) of *n*-octylamine and azobenzene. A reversible increase in magnetization (~10 %) was observed with UV irradiation due to a *trans-cis* isomerization, both at room temperature and below its blocking temperature (5 K, $T_B \approx 15$ K). While the mechanism by which the azobenzene switching affects the magnetization remains unclear, it has been suggested that isomerization-induced changes in either the electrostatic field around the NPs, due to a change in dipole of *cis*-azobenzene, or in the ligand fields of the surface iron atoms could be responsible. Similarly, ferromagnetic NPs are also of interest due to their large stable magnetic moment. Suda *et al.* synthesized FePt alloy nanoparticles functionalized with mSAM azobenzene. They reported that the surface-modified NPs retained typical magnetization curves featuring hysteresis although values of coercivity and remanence were decreased by a factor of ~8 and ~4, respectively.[404] Reversible UV induced *trans-cis* photoisomerization led to an increase in the magnetization value (~ 10%) at room temperature.[404] Computational studies suggest that the magnetization of Fe NPs can be modulated by at least 50 % through photoisomerization of azobenzene at room temperature. *Ab initio* calculations predict that an infinite planar Fe monolayer mimicking the surface of nanoparticles exhibits strong ferromagnetic exchange interactions and experiences a large modulation of exchange interaction parameters (up to 50%) due to *trans-cis* photoisomerization.[405] If the change in dipole moment is responsible for the modulation of the magnetic moment of NPs, spirooxazines may be a suitable substitute as

they exhibit greater changes in dipole than azobenzenes upon isomerization. If isomerization-induced changes in either the electrostatic field around the NPs due to a change in dipole of *cis*-azobenzene or in the ligand fields of the surface iron atoms are responsible for the modulation of magnetization of the NPs as speculated, incorporation of the APSO **2.2** and IPSO **4.2** may result in large change in magnetization. This suggests a photoisomerization induced modification of magnetic properties of NPs are potentially a promising strategy for the design of materials with the intrinsic ability to photomodulate the magnetic moment.

Bibliography

(1) Fritzsche, J.: *Comptes Rendus Acad. Sci., Paris* **1867**, *69*, 1035.

(2) Dürr, H. B.-L., Henri.: *Photochromism: molecules and system*; Elsevier: Amsterdam; Boston:, 1990; Vol. 40.

(3) Yokoyama, Y.: Fulgides for memories and switches. *Chemical Reviews* **2000**, *100*, 1717-1739.

(4) Pu, S.-Z.; Sun, Q.; Fan, C.-B.; Wang, R.-J.; Liu, G.: Recent advances in diarylethene-based multi-responsive molecular switches. *Journal of Materials Chemistry C* **2016**, *4*, 3075-3093.

(5) Tian, H.; Yang, S. J.: Recent progresses on diarylethene based photochromic switches. *Chemical Society Reviews* **2004**, *33*, 85-97.

(6) Klajn, R.: Spiropyran-based dynamic materials. *Chemical Society Reviews* **2014**, *43*, 148-184.

(7) Zhang, G. F.; Chen, T.; Li, C.; Gong, W. L.; Aldred, M. P.; Zhu, M. Q.: Spiropyran-Based Molecular Photoswitches. *Chinese J Org Chem* **2013**, *33*, 927-942.

(8) Minkin, V. I.: Photo-, Thermo-, Solvato-, and Electrochromic Spiroheterocyclic Compounds. *Chemical Reviews* **2004**, *104*, 2751-2776.

(9) Lenoble, C.; Becker, R. S.: Photophysics, Photochemistry and Kinetics of Photochromic 2h-Pyrans and Chromenes. *Journal of Photochemistry* **1986**, *33*, 187-197.

(10) Waldeck, D. H.: Photoisomerization Dynamics of Stilbenes. *Chemical Reviews* **1991**, *91*, 415-436.

(11) Bandara, H. M. D.; Burdette, S. C.: Photoisomerization in different classes of azobenzene. *Chemical Society Reviews* **2012**, *41*, 1809-1825.

(12) Ross, D. L.: Photochromic Indigoids .3. A Photochromic Element Based on Cis-Trans Photoisomerization of a Thioindigo Dye. *Appl Optics* **1971**, *10*, 571-&.

(13) Kirchberg, K.; Kim, T. Y.; Haase, S.; Alexiev, U.: Functional interaction structures of the photochromic retinal protein rhodopsin. *Photochemical & Photobiological Sciences* **2010**, *9*, 226-233.

(14) Hadjoudis, E.; Chatziefthimiou, S. D.; Mavridis, I. M.: Anils: Photochromism by H-transfer. *Curr Org Chem* **2009**, *13*, 269-286.

(15) Corval, A.; Kuldova, K.; Eichen, Y.; Pikramenou, Z.; Lehn, J. M.; Trommsdorff, H. P.: Photochromism and thermochromism driven by intramolecular proton transfer in dinitrobenzylpyridine compounds. *J Phys Chem-Us* **1996**, *100*, 19315-19320.

(16) Crano, J. C.; Guglielmetti, R. J.: *Organic photochromic and thermochromic compounds*; Kluwer Academic Publishers: New York, 2002.

(17) Geiger, M. W.; Turro, N. J.; Waddell, W. H.: Triarylmethane Dye Photochromism - Spectroscopy and Photochemistry of Brilliant Green Leucocyanide. *Photochemistry and Photobiology* **1977**, *25*, 15-20.

(18) Tanaseichuk, B. S.: Triarylimidazole Radicals and Their Dimers. *Khim Geterotsikl+* **1972**, 1299-+.

(19) Bouas-Laurent, H.; Dürr, H.: *Organic photochromism (IUPAC Technical Report)*, 2001; Vol. 73.

(20) Simunic-Meznaric, V.; Mestrovic, E.; Tomisic, V.; Zgela, M.; Vikic-Topic, D.; Cicak, H.; Novak, P.; Vancik, H.: Nitrosobenzene library: A model for studying selectivity in the solid state nitroso-azodioxide dimerization. *Croat Chem Acta* **2005**, *78*, 511-518.

(21) Nanasawa, M.: *Photochromism by Electron Transfer: 'Photochromic Viologens'*, 2002.

(22) Berkovic, G.; Krongauz, V.; Weiss, V.: Spiropyrans and Spirooxazines for Memories and Switches. *Chemical Reviews* **2000**, *100*, 1741-1754.

(23) Guerchais, V.; Ordronneau, L.; Le Bozec, H.: Recent developments in the field of metal complexes containing photochromic ligands: Modulation of linear and nonlinear optical properties. *Coordination Chemistry Reviews* **2010**, *254*, 2533-2545.

(24) Patel, D. G.; Benedict, J. B.; Kopelman, R. A.; Frank, N. L.: Photochromism of a spirooxazine in the single crystalline phase. *Chemical Communications* **2005**, *0*, 2208-2210.

(25) Schaudel, B.; Guermeur, C.; Sanchez, C.; Nakatani, K.; Delaire, J. A.: Spirooxazine- and spiropyran-doped hybrid organic-inorganic matrices with very fast photochromic responses. *Journal of Materials Chemistry* **1997**, *7*, 61-65.

(26) Kim, K.-J.; Lee, J. H.; Jang, S.-W.; Kim, H. D.; Song, J.-W.; Kang, S.-W.: The micro-optic mach-zehnder interferometry: Application to the UV sensors. In *2006 Ieee Sensors, Vols 1-3*; Ieee: New York, 2006; pp 185-+.

(27) Gentili, P. L.; Nocchetti, M.; Miliani, C.; Favaro, G.: Unexpected chromogenic properties of 1,3,3-trimethylspiro(indoline-2,3 '-[3H]naphtho [2,1-b][1,4]oxazine) in the solid phase: photochromism, piezochromism and acidichromism. *New J. Chem.* **2004**, *28*, 379-386.

(28) Frolova, L. A.; Troshin, P. A.; Susarova, D. K.; Kulikov, A. V.; Sanina, N. A.; Aldoshin, S. M.: Photoswitchable organic field-effect transistors and memory elements comprising an interfacial photochromic layer. *Chemical Communications* **2015**, *51*, 6130-6132.

(29) Andersson, N.; Alberius, P.; Ortegren, J.; Lindgren, M.; Bergstrom, L.: Photochromic mesostructured silica pigments dispersed in latex films. *Journal of Materials Chemistry* **2005**, *15*, 3507-3513.

(30) Kobatake, S.; Irie, M.: 8 Photochromism. *Annual Reports Section "C" (Physical Chemistry)* **2003**, *99*, 277-313.

(31) Hemmer, J. R.; Poelma, S. O.; Treat, N.; Page, Z. A.; Dolinski, N. D.; Diaz, Y. J.; Tomlinson, W.; Clark, K. D.; Hooper, J. P.; Hawker, C. J.; de Alaniz, J. R.: Tunable Visible and Near Infrared Photoswitches. *Journal of the American Chemical Society* **2016**, *138*, 13960-13966.

(32) van Dijken, D. J.; Kovaricek, P.; Ihrig, S. P.; Hecht, S.: Acylhydrazones as Widely Tunable Photoswitches. *Journal of the American Chemical Society* **2015**, *137*, 14982-14991.

(33) Yamaguchi, T.; Hatano, S.; Abe, J.: Multistate Photochromism of 1-Phenylnaphthalene-Bridged Imidazole Dimer That Has Three Colorless Isomers and Two Colored Isomers. *Journal of Physical Chemistry A* **2014**, *118*, 134-143.

(34) Hatano, S.; Horino, T.; Tokita, A.; Oshima, T.; Abe, J.: Unusual Negative Photochromism via a Short-Lived Imidazolyl Radical of 1,1 '-Binaphthyl-Bridged Imidazole Dimer. *Journal of the American Chemical Society* **2013**, *135*, 3164-3172.

(35) Yamaguchi, T.; Kobayashi, Y.; Abe, J.: Fast Negative Photochromism of 1,1 '-Binaphthyl-Bridged Phenoxyl-Imidazolyl Radical Complex. *Journal of the American Chemical Society* **2016**, *138*, 906-913.

(36) Safin, D. A.; Bolte, M.; Garcia, Y.: Solid-state photochromism and thermochromism of N-salicylidene pyrene derivatives. *Crystengcomm* **2014**, *16*, 8786-8793.

(37) Safin, D. A.; Bolte, M.; Garcia, Y.: Photoreversible solid state negative photochromism of N-(3,5-dichlorosalicylidene)-1-aminopyrene. *Crystengcomm* **2014**, *16*, 5524-5526.

(38) Julia-Lopez, A.; Hernando, J.; Ruiz-Molina, D.; Gonzalez-Monje, P.; Sedo, J.; Roscini, C.: Temperature-Controlled Switchable Photochromism in Solid Materials. *Angew. Chem.-Int. Edit.* **2016**, *55*, 15044-15048.

(39) Gao, H. Q.; Guo, T. Q.; Chen, Y.; Kong, Y. Y.; Peng, Z. H.: Reversible negative photochromic sulfo-substituted spiropyrans. *J Mol Struct* **2016**, *1123*, 426-432.

(40) Rostovtseva, I. A.; Chernyshev, A. V.; Tkachev, V. V.; Aldoshin, S. M.; Voloshin, N. A.; Metelitsa, A. V.; Makarova, N. I.; Minkin, V. I.: Spiropyrans and spirooxazines. *Russ Chem Bull* **2015**, *64*, 677-682.

(41) Tian, W.; Tian, J.: An insight into the solvent effect on photo-, solvato-chromism of spiropyran through the perspective of intermolecular interactions. *Dyes and Pigments* **2014**, *105*, 66-74.

(42) Sugahara, A.; Tanaka, N.; Okazawa, A.; Matsushita, N.; Kojima, N.: Photochromic Property of Anionic Spiropyran with Sulfonate-substituted Indoline Moiety. *Chem Lett* **2014**, *43*, 281-283.

(43) Wang, W.; Hu, J.; Zheng, M. M.; Zheng, L.; Wang, H.; Zhang, Y.: Multi-responsive supramolecular hydrogels based on merocyanine-peptide conjugates. *Org Biomol Chem* **2015**, *13*, 11492-11498.

(44) Mardaleishvili, I. R.; Kol'tsova, L. S.; Zaichenko, N. L.; Shienok, A. I.; Levin, P. P.; Tatikolov, A. S.: Peculiarities of photochromism and luminescence of dinitrosubstituted hydroxyazomethinespiropyran. *High Energ Chem+* **2015**, *49*, 30-35.

(45) Barachevsky, V. A.: Negative photochromism in organic systems. *Review Journal of Chemistry* **2017**, *7*, 334-371.

(46) Patel, D. G.; Paquette, M. M.; Kopelman, R. A.; Kaminsky, W.; Ferguson, M. J.; Frank, N. L.: A solution- and solid-state investigation of medium effects on charge separation in metastable photomerocyanines. *Journal of the American Chemical Society* **2010**, *132*, 12568-12586.

(47) Piard, J.: Influence of the Solvent on the Thermal Back Reaction of One Spiropyran. *J Chem Educ* **2014**, *91*, 2105-2111.

(48) Kinashi, K.; Nakamura, S.; Imamura, M.; Ishida, K.; Ueda, Y.: The mechanism for negative photochromism of spiropyran in silica. *Journal of Physical Organic Chemistry* **2012**, *25*, 462-466.

(49) Metelitsa, A. V.; Lokshin, V.; Micheau, J. C.; Samat, A.; Guglielmetti, R.; Minkin, V. I.: Photochromism and solvatochromism of push-pull or pull-push spiroindolinenaphthoxazines. *Physical Chemistry Chemical Physics* **2002**, *4*, 4340-4345.

(50) Glebov, E. M.; Vorobyev, D. Y.; Grivin, V. P.; Plyusnin, V. F.; Metelitsa, A. V.; Voloshin, N. A.; Minkin, V. I.; Micheau, J. C.: Photochemistry of phenanthroline-containing spirooxazines in a low-temperature methanol matrix. *Chemical Physics* **2006**, *323*, 490-500.

(51) Metelitsa, A. V.; Micheau, J. C.; Voloshin, N. A.; Voloshina, E. N.; Minkin, V. I.: Kinetic and Thermodynamic Investigations of the Photochromism and Solvatochromism of Semipermanent Merocyanines. *The Journal of Physical Chemistry A* **2001**, *105*, 8417-8422.

(52) Tamai, N.; Miyasaka, H.: Ultrafast Dynamics of Photochromic Systems. *Chemical Reviews* **2000**, *100*, 1875-1890.

(53) Antipin, S. A.; Petrukhin, A. N.; Gostev, F. E.; Marevtsev, V. S.; Titov, A. A.; Barachevsky, V. A.; Strokach, Y. P.; Sarkisov, O. M.: Femtosecond transient absorption spectroscopy of non-substituted photochromic spirocompounds. *Chemical Physics Letters* **2000**, *331*, 378-386.

(54) Chibisov, A. K.; Marevtsev, V. S.; Görner, H.: Photochromism of nitrospironaphthoxazines and spiroanthroxazine. *Journal of Photochemistry and Photobiology A: Chemistry* **2003**, *159*, 233-239.

(55) Minkin, V. I.: Light-controlled molecular switches based on bistable spirocyclic organic and coordination compounds. *Russian Chemical Reviews* **2013**, *82*, 1-26.

(56) Buntinx, G.; Poizat, O.; Foley, S.; Sliwa, M.; Aloise, S.; Lokshin, V.; Samat, A.: Sub-picosecond transient absorption spectroscopy of substituted photochromic spironaphthoxazine compounds. *Dyes and Pigments* **2011**, *89*, 305-312.

(57) Alfimov, M. V.; Balakin, A. V.; Gromov, S. P.; Zaushitsyn, Y. V.; Fedorova, O. A.; Koroteev, N. I.; Pakulev, A. V.; Resnyanskii, A. Y.; Shkurinov, A. P.: Femtosecond spectrochronography of the reverse photochromic transition in derivatives of spiro compounds. *Russ J Phys Chem+* **1999**, *73*, 1685-1694.

(58) Kellmann, A.; Tfibel, F.; Guglielmetti, R.: Effect of Substituents on the Photochromism of a Spiro[Indoline-Naphthoxazine] under Laser Excitation. *Journal of Photochemistry and Photobiology a-Chemistry* **1995**, *91*, 131-136.

(59) Horspool, W. M.; Lenci, F.: *CRC Handbook of Organic Photochemistry and Photobiology, Volumes 1 & 2, Second Edition*; CRC Press, 2003.

(60) Wilkinson, F.; Hobley, J.; Naftaly, M.: Photochromism of Spiro-Naphthoxazines - Molar Absorption-Coefficients and Quantum Efficiencies. *J Chem Soc Faraday T* **1992**, *88*, 1511-1517.

(61) Metelitsa, A. V.; Dorogan, I. V.; Buntinx, G.; Poizat, O.; Lokshin, V. A.; Minkin, V. I.: The role of charge transfer states in deactivation of the electronic excitation energy of spirooxazines. *Dokl Chem* **2011**, *441*, 338-342.

(62) Kholmanskii, A. S.; Kirill, M. D.: The Photochemistry and Photophysics of Spiropyrans. *Russian Chemical Reviews* **1987**, *56*, 136.

(63) Buback, J.; Nuernberger, P.; Kullmann, M.; Langhojer, F.; Schmidt, R.; Wurthner, F.; Brixner, T.: Ring-Closure and Isomerization Capabilities of Spiropyran-Derived Merocyanine Isomers. *Journal of Physical Chemistry A* **2011**, *115*, 3924-3935.

(64) Nuernberger, P.; Ruetzel, S.; Brixner, T.: Multidimensional Electronic Spectroscopy of Photochemical Reactions. *Angew. Chem.-Int. Edit.* **2015**, *54*, 11368-11386.

(65) Kohl-Landgraf, J.; Braun, M.; Ozcoban, C.; Goncalves, D. P. N.; Heckel, A.; Wachtveitl, J.: Ultrafast Dynamics of a Spiropyran in Water. *Journal of the American Chemical Society* **2012**, *134*, 14070-14077.

(66) Kumpulainen, T.; Lang, B.; Rosspeintner, A.; Vauthey, E.: Ultrafast Elementary Photochemical Processes of Organic Molecules in Liquid Solution. *Chemical Reviews* **2017**, *117*, 10826-10939.

(67) Hobley, J.; Pfeifer-Fukumura, U.; Bletz, M.; Asahi, T.; Masuhara, H.; Fukumura, H.: Ultrafast photo-dynamics of a reversible photochromic spiropyran. *Journal of Physical Chemistry A* **2002**, *106*, 2265-2270.

(68) Deniz, E.; Tomasulo, M.; Sortino, S.; Raymo, F. M.: Substituent Effects on the Photochromism of Bichromophoric Oxazines. *Journal of Physical Chemistry C* **2009**, *113*, 8491-8497.

(69) Gautron, R.: Photochromism of Indolinospiropyrans .4. Study of Degradation by Physical Methods . Relationship with Structure. *B Soc Chim Fr* **1968**, 3190-&.

(70) Voiciuk, V.; Redeckas, K.; Martynaitis, V.; Steponaviciute, R.; Sackus, A.; Vengris, M.: Improving the photochromic properties of indolo[2,1-b][1,3]benzoxazines with phenylic substituents. *Journal of Photochemistry and Photobiology a-Chemistry* **2014**, *278*, 60-68.

(71) Kumar, K. S.; Ruben, M.: Emerging trends in spin crossover (SCO) based functional materials and devices. *Coordination Chemistry Reviews* **2017**, *346*, 176-205.

(72) Aguila, D.; Prado, Y.; Koumousi, E. S.; Mathoniere, C.; Clerac, R.: Switchable Fe/Co Prussian blue networks and molecular analogues. *Chemical Society Reviews* **2016**, *45*, 203-224.

(73) Ohkoshi, S. I.; Tokoro, H.: Photomagnetism in Cyano-Bridged Bimetal Assemblies. *Accounts of Chemical Research* **2012**, *45*, 1749-1758.

(74) Bousseksou, A.; Molnar, G.; Salmon, L.; Nicolazzi, W.: Molecular spin crossover phenomenon: recent achievements and prospects. *Chemical Society Reviews* **2011**, *40*, 3313-3335.

(75) Gutlich, P.; Gaspar, A. B.; Garcia, Y.: Spin state switching in iron coordination compounds. *Beilstein J Org Chem* **2013**, *9*, 342-391.

(76) Sato, O.: Dynamic molecular crystals with switchable physical properties. *Nat. Chem.* **2016**, *8*, 644-656.

(77) Tezgerevska, T.; Alley, K. G.; Boskovic, C.: Valence tautomerism in metal complexes: Stimulated and reversible intramolecular electron transfer between metal centers and organic ligands. *Coordination Chemistry Reviews* **2014**, *268*, 23-40.

(78) Frisch, J. L.: Notitia Coerulei Berolinensis nuper inventi. *Miscellanea Berolinensia ad Incrementum Scientiarum* **1710**, *1*, 377-378.

(79) Herren, F.; Fischer, P.; Ludi, A.; Halg, W.: Neutron-Diffraction Study of Prussian Blue, Fe4[Fe(Cn)6]3.Xh2o - Location of Water-Molecules and Long-Range Magnetic Order. *Inorganic Chemistry* **1980**, *19*, 956-959.

(80) Ferlay, S.; Mallah, T.; Ouahes, R.; Veillet, P.; Verdaguer, M.: A ROOM-TEMPERATURE ORGANOMETALLIC MAGNET BASED ON PRUSSIAN BLUE. *Nature* **1995**, *378*, 701-703.

(81) Holmes, S. M.; Girolami, G. S.: Sol-gel synthesis of KVII[Cr-III(CN)(6)]center dot 2H(2)O: A crystalline molecule-based magnet with a magnetic ordering temperature above 100 degrees C. *Journal of the American Chemical Society* **1999**, *121*, 5593-5594.

(82) Mallah, T.; Thiebaut, S.; Verdaguer, M.; Veillet, P.: HIGH-T(C) MOLECULAR-BASED MAGNETS - FERRIMAGNETIC MIXED-VALENCE CHROMIUM(III)-CHROMIUM(II) CYANIDES WITH T(C) AT 240-KELVIN AND 190-KELVIN. *Science* **1993**, *262*, 1554-1557.

(83) Sato, O.; Iyoda, T.; Fujishima, A.; Hashimoto, K.: Photoinduced Magnetization of a Cobalt-Iron Cyanide. *Science* **1996**, *272*, 704-705.

(84) Shimamoto, N.; Ohkoshi, S.; Sato, O.; Hashimoto, K.: Control of charge-transfer-induced spin transition temperature on cobalt-iron Prussian blue analogues. *Inorganic Chemistry* **2002**, *41*, 678-684.

(85) Newton, G. N.; Nihei, M.; Oshio, H.: Cyanide-Bridged Molecular Squares - The Building Units of Prussian Blue. *European Journal of Inorganic Chemistry* **2011**, 3031-3042.

(86) Sato, O.; Einaga, Y.; Fujishima, A.; Hashimoto, K.: Photoinduced Long-Range Magnetic Ordering of a Cobalt-Iron Cyanide. *Inorg Chem* **1999**, *38*, 4405-4412.

(87) Li, D.; Clerac, R.; Roubeau, O.; Harte, E.; Mathoniere, C.; Bris, R. L.; Holmes, S. M.: Magnetic and optical bistability driven by thermally and photoinduced intramolecular electron transfer in a molecular cobalt-iron prussian blue analogue. *J Am Chem Soc* **2008**, *130*, 252-8.

(88) Kang, S.; Zheng, H.; Liu, T.; Hamachi, K.; Kanegawa, S.; Sugimoto, K.; Shiota, Y.; Hayami, S.; Mito, M.; Nakamura, T.; Nakano, M.; Baker, M. L.; Nojiri, H.; Yoshizawa, K.; Duan, C.; Sato, O.: A ferromagnetically coupled Fe-42 cyanide-bridged nanocage. *Nature Communications* **2015**, *6*.

(89) Pinkowicz, D.; Southerland, H.; Wang, X.-Y.; Dunbar, K. R.: Record Antiferromagnetic Coupling for a 3d/4d Cyanide-Bridged Compound. *Journal of the American Chemical Society* **2014**, *136*, 9922-9924.

(90) Chorazy, S.; Stanek, J. J.; Nogas, W.; Majcher, A. M.; Rams, M.; Koziel, M.; Juszynska-Galazka, E.; Nakabayashi, K.; Ohkoshi, S.; Sieklucka, B.; Podgajny, R.: Tuning of Charge Transfer Assisted Phase Transition and Slow Magnetic Relaxation Functionalities in {Fe9-xCox W(CN)(8) (6)} (x=0-9) Molecular Solid Solution. *Journal of the American Chemical Society* **2016**, *138*, 1635-1646.

(91) Risset, O. N.; Quintero, P. A.; Brinzari, T. V.; Andrus, M. J.; Lufaso, M. W.; Meisel, M. W.; Talham, D. R.: Light-Induced Changes in Magnetism in a Coordination Polymer Heterostructure, Rb0.24Co[Fe(CN)6]0.74@K0.10Co[Cr(CN)6]0.70·nH2O and the Role of the Shell Thickness on the Properties of Both Core and Shell. *Journal of the American Chemical Society* **2014**, *136*, 15660-15669.

(92) Zhang, K.; Kang, S.; Yao, Z. S.; Nakamura, K.; Yamamoto, T.; Einaga, Y.; Azuma, N.; Miyazaki, Y.; Nakano, M.; Kanegawa, S.; Sato, O.: Charge-Transfer Phase Transition of a Cyanide-Bridged Fe-II/Fe-III Coordination Polymer. *Angew. Chem.-Int. Edit.* **2016**, *55*, 6047-6050.

(93) Zhang, Y.; Li, D.; Clerac, R.; Kalisz, M.; Mathoniere, C.; Holmes, S. M.: Reversible thermally and photoinduced electron transfer in a cyano-bridged {Fe(2)Co(2)} square complex. *Angew Chem Int Ed Engl* **2010**, *49*, 3752-6.

(94) Koumousi, E. S.; Jeon, I.-R.; Gao, Q.; Dechambenoit, P.; Woodruff, D. N.; Merzeau, P.; Buisson, L.; Jia, X.; Li, D.; Volatron, F.; Mathonière, C.; Clérac, R.: Metal-to-Metal Electron Transfer in Co/Fe Prussian Blue Molecular Analogues: The Ultimate Miniaturization. *Journal of the American Chemical Society* **2014**, *136*, 15461-15464.

(95) Zhang, Y.-Z.; Ferko, P.; Siretanu, D.; Ababei, R.; Rath, N. P.; Shaw, M. J.; Clérac, R.; Mathonière, C.; Holmes, S. M.: Thermochromic and Photoresponsive Cyanometalate Fe/Co Squares: Toward Control of the Electron Transfer Temperature. *Journal of the American Chemical Society* **2014**, *136*, 16854-16864.

(96) Garnier, D.; Jimenez, J. R.; Li, Y.; von Bardeleben, J.; Journaux, Y.; Augenstein, T.; Moos, E. M. B.; Gamer, M. T.; Breher, F.; Lescouezec, R.: K subset of{ Fe-II(Tp)(CN)(3) (4) Co-III((pz)Tp) (3) Co-II((pz)Tp) }: a neutral soluble model complex of photomagnetic Prussian blue analogues. *Chem. Sci.* **2016**, *7*, 4825-4831.

(97) Cambi, L.; Szegö, L.: Über die magnetische Susceptibilität der komplexen Verbindungen. *Berichte der deutschen chemischen Gesellschaft (A and B Series)* **1931**, *64*, 2591-2598.

(98) Real, J. A.; Gaspar, A. B.; Munoz, M. C.: Thermal, pressure and light switchable spin-crossover materials. *Dalton Trans* **2005**, 2062-79.

(99) Minkin, V. I.; Starikov, A. G.: Intramolecular spin state switching mechanisms of transition metal complexes. *Russ Chem Bull* **2015**, *64*, 475-497.

(100) Boca, R.; Boca, M.; Dlhan, L.; Falk, K.; Fuess, H.; Haase, W.; Jarosciak, R.; Papankova, B.; Renz, F.; Vrbova, M.; Werner, R.: Strong cooperativeness in the mononuclear iron(II) derivative exhibiting an abrupt spin transition above 400 K. *Inorganic Chemistry* **2001**, *40*, 3025-3033.

(101) Hagiwara, H.; Tanaka, T.; Hora, S.: Synthesis, structure, and spin crossover above room temperature of a mononuclear and related dinuclear double helicate iron(ii) complexes. *Dalton Trans* **2016**, *45*, 17132-17140.

(102) Gomez, V.; Benet-Buchholz, J.; Martin, E.; Galan-Mascaros, J. R.: Hysteretic Spin Crossover above Room Temperature and Magnetic Coupling in Trinuclear Transition-Metal Complexes with Anionic 1,2,4-Triazole Ligands. *Chemistry-a European Journal* **2014**, *20*, 5369-5379.

(103) Decurtins, S.; Gutlich, P.; Kohler, C. P.; Spiering, H.; Hauser, A.: Light-Induced Excited Spin State Trapping in a Transition-Metal Complex - the Hexa-1-Propyltetrazole-Iron (Ii) Tetrafluoroborate Spin-Crossover System. *Chemical Physics Letters* **1984**, *105*, 1-4.

(104) Decurtins, S.; Gutlich, P.; Hasselbach, K. M.; Hauser, A.; Spiering, H.: Light-Induced Excited-Spin-State Trapping in Iron(Ii) Spin-Crossover Systems - Optical Spectroscopic and Magnetic-Susceptibility Study. *Inorganic Chemistry* **1985**, *24*, 2174-2178.

(105) Gütlich, P.; Hauser, A.; Spiering, H.: Thermal and Optical Switching of Iron(II) Complexes. *Angewandte Chemie International Edition in English* **1994**, *33*, 2024-2054.

(106) Hayami, S.; Gu, Z.; Einaga, Y.; Kobayasi, Y.; Ishikawa, Y.; Yamada, Y.; Fujishima, A.; Sato, O.: A novel LIESST iron(II) complex exhibiting a high relaxation temperature. *Inorganic Chemistry* **2001**, *40*, 3240-+.

(107) Hauser, A.: Intersystem Crossing in Fe(Ii) Coordination-Compounds. *Coordination Chemistry Reviews* **1991**, *111*, 275-290.

(108) Letard, J. F.: Photomagnetism of iron(II) spin crossover complexes - the T(LIESST) approach. *Journal of Materials Chemistry* **2006**, *16*, 2550-2559.

(109) Buchanan, R. M.; Pierpont, C. G.: Tautomeric Catecholate-Semiquinone Interconversion Via Metal-Ligand Electron-Transfer - Structural, Spectral, and Magnetic-Properties of (3,5-Di-Tert-Butylcatecholato)-(3,5-Di-Tert-Butylsemiquinone)(Bipyridyl)Cobalt(Iii), a Complex Containing Mixed-Valence Organic-Ligands. *Journal of the American Chemical Society* **1980**, *102*, 4951-4957.

(110) Drouza, C.; Vlasiou, M.; Keramidas, A. D.: Vanadium(IV/V)-p-dioxolene temperature induced electron transfer associated with ligation/deligation of solvent molecules. *Dalton Trans.* **2013**, *42*, 11831-11840.

(111) Hendrickson, D. N.; Pierpont, C. G.: Valence Tautomeric Transition Metal Complexes. In *Spin Crossover in Transition Metal Compounds II*; Gütlich, P., Goodwin, H. A., Eds.; Springer Berlin Heidelberg: Berlin, Heidelberg, 2004; pp 63-95.

(112) Lannes, A.; Suffren, Y.; Tommasino, J. B.; Chiriac, R.; Toche, F.; Khrouz, L.; Molton, F.; Duboc, C.; Kieffer, I.; Hazemann, J. L.; Reber, C.; Hauser, A.; Luneau, D.: Room Temperature Magnetic Switchability Assisted by Hysteretic Valence Tautomerism in a Layered Two-Dimensional Manganese Radical Coordination Framework. *Journal of the American Chemical Society* **2016**, *138*, 16493-16501.

(113) Shaikh, N.; Goswami, S.; Panja, A.; Wang, X. Y.; Gao, S.; Butcher, R. J.; Banerjee, P.: New route to the mixed valence semiquinone-catecholate based mononuclear Fe-III and catecholate based dinuclear Mn-III complexes: First experimental evidence of valence tautomerism in an iron complex. *Inorganic Chemistry* **2004**, *43*, 5908-5918.

(114) Scheja, A.; Baabe, D.; Menzel, D.; Pietzonka, C.; Schweyen, P.; Broring, M.: Spin Crossover and Valence Tautomerism in Neutral Homoleptic Iron Complexes of Bis(pyridylimino)isoindolines. *Chemistry-a European Journal* **2015**, *21*, 14196-14204.

(115) Ohtsu, H.; Tanaka, K.: Chemical control of valence tautomerism of nickel(II) semiquinone and nickel(III) catecholate states. *Angew. Chem.-Int. Edit.* **2004**, *43*, 6301-6303.

(116) Doistau, B.; Benda, L.; Cantin, J. L.; Chamoreau, L. M.; Ruiz, E.; Marvaud, V.; Hasenknopf, B.; Vives, G.: Six States Switching of Redox-Active Molecular Tweezers by

Three Orthogonal Stimuli. *Journal of the American Chemical Society* **2017**, *139*, 9213-9220.

(117) Kundu, N.; Maity, M.; Chatterjee, P. B.; Teat, S. J.; Endo, A.; Chaudhury, M.: Reporting a Unique Example of Electronic Bistability Observed in the Form of Valence Tautomerism with a Copper(II) Helicate of a Redox-Active Nitrogenous Heterocyclic Ligand. *Journal of the American Chemical Society* **2011**, *133*, 20104-20107.

(118) Wiesner, S.; Wagner, A.; Kaifer, E.; Himmel, H. J.: A Valence Tautomeric Dinuclear Copper Tetrakisguanidine Complex. *Chemistry-a European Journal* **2016**, *22*, 10438-10445.

(119) Bin-Salamon, S.; Brewer, S.; Franzen, S.; Feldheim, D. L.; Lappi, S.; Shultz, D. A.: Supramolecular control of valence-tautomeric equilibrium on nanometer-scale gold clusters. *Journal of the American Chemical Society* **2005**, *127*, 5328-5329.

(120) Adams, D. M.; Dei, A.; Rheingold, A. L.; Hendrickson, D. N.: BISTABILITY IN THE CO(II)(SEMIQUINONATE)2 TO CO(III)(CATECHOLATE)(SEMIQUINONATE) VALENCE-TAUTOMERIC CONVERSION. *Journal of the American Chemical Society* **1993**, *115*, 8221-8229.

(121) Shultz, D. A.: Valence Tautomerism in Dioxolene Complexes of Cobalt. In *Magnetism: Molecules to Materials*; Wiley-VCH Verlag GmbH & Co. KGaA, 2003; pp 281-306.

(122) Adams, D. M.; Li, B. L.; Simon, J. D.; Hendrickson, D. N.: Photoinduced Valence Tautomerism in Cobalt Complexes Containing Semiquinone Anion as Ligand - Dynamics of the High-Spin [Coii(3,5-Dtbsq)(2)] to Low-Spin [Co-Iii(3,5-Dtbsq)(3,5-Dtbcat)] Interconversion. *Angew Chem Int Edit* **1995**, *34*, 1481-1483.

(123) Boillot, M. L.; Roux, C.; Audiere, J. P.; Dausse, A.; Zarembowitch, J.: Ligand-driven light-induced spin change in transition-metal complexes: Selection of an appropriate system and first evidence of the effect, in Fe-II(4-styrylpyridine)(4)(NCBPh(3))(2). *Inorganic Chemistry* **1996**, *35*, 3975-3980.

(124) Boillot, M. L.; Pillet, S.; Tissot, A.; Riviere, E.; Claiser, N.; Lecomte, C.: Ligand-Driven Light-Induced Spin Change Activity and Bidirectional Photomagnetism of Styrylpyridine Iron(II) Complexes in Polymeric Media. *Inorganic Chemistry* **2009**, *48*, 4729-4736.

(125) Takahashi, K.; Hasegawa, Y.; Sakamoto, R.; Nishikawa, M.; Kume, S.; Nishibori, E.; Nishihara, H.: Solid-State Ligand-Driven Light-Induced Spin Change at Ambient Temperatures in Bis(dipyrazolylstyrylpyridine)iron(II) Complexes. *Inorganic Chemistry* **2012**, *51*, 5188-5198.

(126) Milek, M.; Heinemann, F. W.; Khusniyarov, M. M.: Spin Crossover Meets Diarylethenes: Efficient Photoswitching of Magnetic Properties in Solution at Room Temperature. *Inorganic Chemistry* **2013**, *52*, 11585-11592.

(127) Nihei, M.; Suzuki, Y.; Kimura, N.; Kera, Y.; Oshio, H.: Bidirectional Photomagnetic Conversions in a Spin-Crossover Complex with a Diarylethene Moiety. *Chemistry-a European Journal* **2013**, *19*, 6946-6949.

(128) Rosner, B.; Milek, M.; Witt, A.; Gobaut, B.; Torelli, P.; Fink, R. H.; Khusniyarov, M. M.: Reversible Photoswitching of a Spin-Crossover Molecular Complex in the Solid State at Room Temperature. *Angew. Chem.-Int. Edit.* **2015**, *54*, 12976-12980.

(129) Irie, M.; Fulcaminato, T.; Matsuda, K.; Kobatake, S.: Photochromism of Diarylethene Molecules and Crystals: Memories, Switches, and Actuators. *Chemical Reviews* **2014**, *114*, 12174-12277.

(130) Venkataramani, S.; Jana, U.; Dommaschk, M.; Sonnichsen, F. D.; Tuczek, F.; Herges, R.: Magnetic Bistability of Molecules in Homogeneous Solution at Room Temperature. *Science* **2011**, *331*, 445-448.

(131) Thies, S.; Sell, H.; Schutt, C.; Bornholdt, C.; Nather, C.; Tuczek, F.; Herges, R.: Light-Induced Spin Change by Photodissociable External Ligands: A New Principle for Magnetic Switching of Molecules. *Journal of the American Chemical Society* **2011**, *133*, 16243-16250.

(132) Dommaschk, M.; Peters, M.; Gutzeit, F.; Schutt, C.; Nather, C.; Sonnichsen, F. D.; Tiwar, S.; Riedel, C.; Boretius, S.; Herges, R.: Photoswitchable Magnetic Resonance Imaging Contrast by Improved Light-Driven Coordination-Induced Spin State Switch. *Journal of the American Chemical Society* **2015**, *137*, 7552-7555.

(133) Zhang, X. Z.; Chamberlayne, C. F.; Kurimoto, A.; Frank, N. L.; Harbron, E. J.: Visible light photoswitching of conjugated polymer nanoparticle fluorescence. *Chemical Communications* **2016**, *52*, 4144-4147.

(134) Zhang, Y. L.; Zhang, K. Q.; Wang, J.; Tian, Z. Y.; Li, A. D. Q.: Photoswitchable fluorescent nanoparticles and their emerging applications. *Nanoscale* **2015**, *7*, 19342-19357.

(135) Liao, B.; Chen, J. A.; Huang, H. W.; Li, X. F.; He, B. Q.: Gold nanocluster-based light-controlled fluorescence molecular switch. *Journal of Materials Chemistry* **2011**, *21*, 5867-5869.

(136) Chan, Y. H.; Gallina, M. E.; Zhang, X. J.; Wu, I. C.; Jin, Y. H.; Sun, W.; Chiu, D. T.: Reversible Photoswitching of Spiropyran-Conjugated Semiconducting Polymer Dots. *Anal Chem* **2012**, *84*, 9431-9438.

(137) Chen, J.; Wang, D. P.; Turshatov, A.; Munoz-Espi, R.; Ziener, U.; Koynov, K.; Landfester, K.: One-pot fabrication of amphiphilic photoswitchable thiophene-based fluorescent polymer dots. *Polym Chem-Uk* **2013**, *4*, 773-781.

(138) Harbron, E. J.: Fluorescence Intensity Modulation in Photochromic Conjugated Polymer Systems. *Isr. J. Chem.* **2013**, *53*, 256-266.

(139) Georgakilas, V.; Otyepka, M.; Bourlinos, A. B.; Chandra, V.; Kim, N.; Kemp, K. C.; Hobza, P.; Zboril, R.; Kim, K. S.: Functionalization of Graphene: Covalent and Non-Covalent Approaches, Derivatives and Applications. *Chemical Reviews* **2012**, *112*, 6156-6214.

(140) Jia, C. C.; Guo, X. F.: Molecule-electrode interfaces in molecular electronic devices. *Chemical Society Reviews* **2013**, *42*, 5642-5660.

(141) Kumar, S.; van Herpt, J. T.; Gengler, R. Y. N.; Feringa, B.; Rudolf, P.; Chiechi, R. C.: Mixed Monolayers of Spiropyrans Maximize Tunneling Conductance Switching by Photoisomerization at the Molecule-Electrode Interface in EGaln Junctions. *Journal of the American Chemical Society* **2016**, *138*, 12519-12526.

(142) Xiang, D.; Wang, X. L.; Jia, C. C.; Lee, T.; Guo, X. F.: Molecular-Scale Electronics: From Concept to Function. *Chemical Reviews* **2016**, *116*, 4318-4440.

(143) Jia, C. C.; Migliore, A.; Xin, N.; Huang, S. Y.; Wang, J. Y.; Yang, Q.; Wang, S. P.; Chen, H. L.; Wang, D. M.; Feng, B. Y.; Liu, Z. R.; Zhang, G. Y.; Qu, D. H.; Tian, H.; Ratner, M. A.; Xu, H. Q.; Nitzan, A.; Guo, X. F.: Covalently bonded single-molecule junctions with stable and reversible photoswitched conductivity. *Science* **2016**, *352*, 1443-1445.

(144) Kim, M.; Safron, N. S.; Huang, C. H.; Arnold, M. S.; Gopalan, P.: Light-Driven Reversible Modulation of Doping in Graphene. *Nano Lett.* **2012**, *12*, 182-187.

(145) Zhao, Y. C.; Huang, C. S.; Kim, M.; Wong, B. M.; Leonard, F.; Gopalan, P.; Eriksson, M. A.: Functionalization of Single-Wall Carbon Nanotubes with Chromophores of Opposite Internal Dipole Orientation. *Acs Applied Materials & Interfaces* **2013**, *5*, 9355-9361.

(146) Borjesson, K.; Herder, M.; Grubert, L.; Duong, D. T.; Salleo, A.; Hecht, S.; Orgiu, E.; Samori, P.: Optically switchable transistors comprising a hybrid photochromic molecule/n-type organic active layer. *Journal of Materials Chemistry C* **2015**, *3*, 4156-4161.

(147) Tsujioka, T.; Yamamoto, K.: Elemental isomerization processes for a photochromic diarylethene film based on carrier injection toward all-electrically operable organic memory. *Japanese Journal of Applied Physics* **2016**, *55*.

(148) Liddell, P. A.; Kodis, G.; Moore, A. L.; Moore, T. A.; Gust, D.: Photonic switching of photoinduced electron transfer in a dithienylethene-porphyrin-fullerene triad molecule. *Journal of the American Chemical Society* **2002**, *124*, 7668-7669.

(149) Castellanos, S.; Vieira, A. A.; Illescas, B. M.; Sacchetti, V.; Schubert, C.; Moreno, J.; Guldi, D. M.; Hecht, S.; Martin, N.: Gating Charge Recombination Rates through Dynamic Bridges in Tetrathiafulvalene-Fullerene Architectures. *Angew. Chem.-Int. Edit.* **2013**, *52*, 13985-13990.

(150) Cao, Y.; Dong, S. H.; Liu, S.; Liu, Z. F.; Guo, X. F.: Toward Functional Molecular Devices Based on GrapheneMolecule Junctions. *Angew. Chem.-Int. Edit.* **2013**, *52*, 3906-3910.

(151) Parveen, S.; Misra, R.; Sahoo, S. K.: Nanoparticles: a boon to drug delivery, therapeutics, diagnostics and imaging. *Nanomedicine-Nanotechnology Biology and Medicine* **2012**, *8*, 147-166.

(152) Xu, Z. P.; Zeng, Q. H.; Lu, G. Q.; Yu, A. B.: Inorganic nanoparticles as carriers for efficient cellular delivery. *Chemical Engineering Science* **2006**, *61*, 1027-1040.

(153) Padmanabhan, P.; Kumar, A.; Kumar, S.; Chaudhary, R. K.; Gulyas, B.: Nanoparticles in practice for molecular-imaging applications: An overview. *Acta Biomaterialia* **2016**, *41*, 1-16.

(154) Key, J.; Leary, J. F.: Nanoparticles for multimodal in vivo imaging in nanomedicine. *International Journal of Nanomedicine* **2014**, *9*, 711-726.

(155) Medintz, I. L.; Uyeda, H. T.; Goldman, E. R.; Mattoussi, H.: Quantum dot bioconjugates for imaging, labelling and sensing. *Nature Materials* **2005**, *4*, 435-446.

(156) Daniel, M. C.; Astruc, D.: Gold nanoparticles: Assembly, supramolecular chemistry, quantum-size-related properties, and applications toward biology, catalysis, and nanotechnology. *Chemical Reviews* **2004**, *104*, 293-346.

(157) Astruc, D.; Lu, F.; Aranzaes, J. R.: Nanoparticles as recyclable catalysts: The frontier between homogeneous and heterogeneous catalysis. *Angew. Chem.-Int. Edit.* **2005**, *44*, 7852-7872.

(158) Gratzel, M.: Dye-sensitized solar cells. *Journal of Photochemistry and Photobiology C-Photochemistry Reviews* **2003**, *4*, 145-153.

(159) Kamat, P. V.: Meeting the clean energy demand: Nanostructure architectures for solar energy conversion. *Journal of Physical Chemistry C* **2007**, *111*, 2834-2860.

(160) Shipway, A. N.; Katz, E.; Willner, I.: Nanoparticle arrays on surfaces for electronic, optical, and sensor applications. *ChemPhysChem* **2000**, *1*, 18-52.

(161) Nelson, A. J.; Hess, S. T.: Localization microscopy: mapping cellular dynamics with single molecules. *J. Microsc.*. **2014**, *254*, 1-8.

(162) Cusido, J.; Impellizzeri, S.; Raymo, F. M.: Molecular strategies to read and write at the nanoscale with far-field optics. *Nanoscale* **2011**, *3*, 59-70.

(163) Gust, D.; Moore, T. A.; Moore, A. L.: Molecular switches controlled by light. *Chemical Communications* **2006**, 1169-1178.

(164) Gust, D.; Andreasson, J.; Pischel, U.; Moore, T. A.; Moore, A. L.: Data and signal processing using photochromic molecules. *Chemical Communications* **2012**, *48*, 1947-1957.

(165) van de Linde, S.; Sauer, M.: How to switch a fluorophore: from undesired blinking to controlled photoswitching. *Chemical Society Reviews* **2014**, *43*, 1076-1087.

(166) Díaz, S. A.; Gillanders, F.; Jares-Erijman, E. A.; Jovin, T. M.: Photoswitchable semiconductor nanocrystals with self-regulating photochromic Förster resonance energy transfer acceptors. *Nature Communications* **2015**, *6*, 6036.

(167) Dworak, L.; Reuss, A. J.; Zastrow, M.; Ruck-Braun, K.; Wachtveitl, J.: Discrimination between FRET and non-FRET quenching in a photochromic CdSe quantum dot/dithienylethene dye system. *Nanoscale* **2014**, *6*, 14200-14203.

(168) Alvarez, A.; Costa-Fernández, J. M.; Pereiro, R.; Sanz-Medel, A.; Salinas-Castillo, A.: Fluorescent conjugated polymers for chemical and biochemical sensing. *TrAC Trends in Analytical Chemistry* **2011**, *30*, 1513-1525.

(169) Avella-Oliver, M.; Morais, S.; Puchades, R.; Maquieira, A.: Towards photochromic and thermochromic biosensing. *Trac-Trends Anal. Chem.* **2016**, *79*, 37-45.

(170) Seeboth, A.; Loetzsch, D.; Ruhmann, R.; Muehling, O.: Thermochromic Polymers-Function by Design. *Chemical Reviews* **2014**, *114*, 3037-3068.

(171) Wang, Y.; Runnerstrom, E. L.; Milliron, D. J.: Switchable Materials for Smart Windows. In *Annual Review of Chemical and Biomolecular Engineering, Vol 7*; Prausnitz, J. M., Ed.; Annual Reviews: Palo Alto, 2016; Vol. 7; pp 283-304.

(172) Sun, C.; Wang, M.-S.; Li, P.-X.; Guo, G.-C.: Conductance Switch of a Bromoplumbate Bistable Semiconductor by Electron-Transfer Thermochromism. *Angew. Chem.-Int. Edit.* **2017**, *56*, 554-558.

(173) Bisoyi, H. K.; Li, Q.: Light -Driven Liquid Crystalline Materials: From Photo -Induced Phase Transitions and Property Modulations to Applications. *Chemical Reviews* **2016**, *116*, 15089-15166.

(174) Mukhopadhyay, A.; Moorthy, J. N.: Phenomenon to functions: Photochromism of diarylpyrans, spectrokinetic properties and functional materials. *Journal of Photochemistry and Photobiology C-Photochemistry Reviews* **2016**, *29*, 73-106.

(175) Parrot, A.; Bernard, A.; Jacquart, A.; Serapian, S. A.; Bo, C.; Derat, E.; Oms, O.; Dolbecq, A.; Proust, A.; Metivier, R.; Mialane, P.; Izzet, G.: Photochromism and Dual-Color Fluorescence in a Polyoxometalate-Benzospiropyran Molecular Switch. *Angew. Chem.-Int. Edit.* **2017**, *56*, 4872-4876.

(176) Beaujean, P.; Bondu, F.; Plaquet, A.; Garcia-Amoros, J.; Cusido, J.; Raymo, F. M.; Castet, F.; Rodriguez, V.; Champagne, B.: Oxazines: A New Class of Second-Order Nonlinear Optical Switches. *Journal of the American Chemical Society* **2016**, *138*, 5052-5062.

(177) Klymchenko, A. S.: Solvatochromic and Fluorogenic Dyes as Environment-Sensitive Probes: Design and Biological Applications. *Accounts of Chemical Research* **2017**, *50*, 366-375.

(178) Benedetti, E.; Kocsis, L. S.; Brummond, K. M.: Synthesis and Photophysical Properties of a Series of Cyclopenta[b]naphthalene Solvatochromic Fluorophores. *Journal of the American Chemical Society* **2012**, *134*, 12418-12421.

(179) Larsen, B. A.; Deria, P.; Holt, J. M.; Stanton, I. N.; Heben, M. J.; Therien, M. J.; Blackburn, J. L.: Effect of Solvent Polarity and Electrophilicity on Quantum Yields and Solvatochromic Shifts of Single-Walled Carbon Nanotube Photoluminescence. *Journal of the American Chemical Society* **2012**, *134*, 12485-12491.

(180) Xue, P.; Ding, J.; Wang, P.; Lu, R.: Recent progress in the mechanochromism of phosphorescent organic molecules and metal complexes. *Journal of Materials Chemistry C* **2016**, *4*, 6688-6706.

(181) Bai, L.; Bose, P.; Gao, Q.; Li, Y.; Ganguly, R.; Zhao, Y.: Halogen-Assisted Piezochromic Supramolecular Assemblies for Versatile Haptic Memory. *Journal of the American Chemical Society* **2017**, *139*, 436-441.

(182) Sui, Q.; Ren, X.-T.; Dai, Y.-X.; Wang, K.; Li, W.-T.; Gong, T.; Fang, J.-J.; Zou, B.; Gao, E.-Q.; Wang, L.: Piezochromism and hydrochromism through electron transfer: new stories for viologen materials. *Chem. Sci.* **2017**, *8*, 2758-2768.

(183) Xu, B.; Mu, Y.; Mao, Z.; Xie, Z.; Wu, H.; Zhang, Y.; Jin, C.; Chi, Z.; Liu, S.; Xu, J.; Wu, Y.-C.; Lu, P.-Y.; Lien, A.; Bryce, M. R.: Achieving remarkable mechanochromism and white-light emission with thermally activated delayed fluorescence through the molecular heredity principle. *Chem. Sci.* **2016**, *7*, 2201-2206.

(184) Toma, O.; Allain, M.; Meinardi, F.; Forni, A.; Botta, C.; Mercier, N.: Bismuth-Based Coordination Polymers with Efficient Aggregation-Induced Phosphorescence and Reversible Mechanochromic Luminescence. *Angew. Chem.-Int. Edit.* **2016**, *55*, 7998-8002.

(185) Yuan, J. Y.; Yuan, Y. Z.; Tian, X. H.; Sun, J. Y.; Ge, Y.: Spirooxazine-Fulgide Biphotochromic Molecular Switches with Nonlinear Optical Responses across Four States. *Journal of Physical Chemistry C* **2016**, *120*, 14840-14853.

(186) Boixel, J.; Guerchais, V.; Le Bozec, H.; Jacquemin, D.; Amar, A.; Boucekkine, A.; Colombo, A.; Dragonetti, C.; Marinotto, D.; Roberto, D.; Righetto, S.; De Angelis, R.: Second-Order NLO Switches from Molecules to Polymer Films Based on Photochromic Cyclometalated Platinum(II) Complexes. *Journal of the American Chemical Society* **2014**, *136*, 5367-5375.

(187) Li, P.-X.; Wang, M.-S.; Zhang, M.-J.; Lin, C.-S.; Cai, L.-Z.; Guo, S.-P.; Guo, G.-C.: Electron-Transfer Photochromism To Switch Bulk Second-Order Nonlinear Optical Properties with High Contrast. *Angewandte Chemie International Edition* **2014**, *53*, 11529-11531.

(188) Lebeau, B.; Sanchez, C.: Sol-gel derived hybrid inorganic-organic nanocomposites for optics. *Current Opinion in Solid State & Materials Science* **1999**, *4*, 11-23.

(189) Xie, X.; Mistlberger, G.; Bakker, E.: Reversible Photodynamic Chloride-Selective Sensor Based on Photochromic Spiropyran. *Journal of the American Chemical Society* **2012**, *134*, 16929-16932.

(190) Bisoyi, H. K.; Li, Q.: Light-Directing Chiral Liquid Crystal Nanostructures: From 1D to 3D. *Accounts of Chemical Research* **2014**, *47*, 3184-3195.

(191) Lee, H.-Y.; Diehn, K. K.; Sun, K.; Chen, T.; Raghavan, S. R.: Reversible Photorheological Fluids Based on Spiropyran-Doped Reverse Micelles. *Journal of the American Chemical Society* **2011**, *133*, 8461-8463.

(192) Kitagawa, D.; Yamashita, I.; Kobatake, S.: Control of Surface Wettability and Photomicropatterning with a Polymorphic Diarylethene Crystal upon Photoirradiation. *Chemistry-a European Journal* **2011**, *17*, 9825-9831.

(193) Krohm, F.; Kind, J.; Savka, R.; Janssen, M. A.; Herold, D.; Plenio, H.; Thiele, C. M.; Andrieu-Brunsen, A.: Photochromic spiropyran- and spirooxazine-homopolymers in mesoporous thin films by surface initiated ROMP. *Journal of Materials Chemistry C* **2016**, *4*, 4067-4076.

(194) Abdollahi, A.; Rad, J. K.; Mahdavian, A. R.: Stimuli-responsive cellulose modified by epoxy-functionalized polymer nanoparticles with photochromic and solvatochromic properties. *Carbohydrate Polymers* **2016**, *150*, 131-138.

(195) Ye, J. T.; Wang, L.; Wang, H. Q.; Chen, Z. Z.; Qiu, Y. Q.; Xie, H. M.: Spirooxazine molecular switches with nonlinear optical responses as selective cation sensors. *Rsc Advances* **2017**, *7*, 642-650.

(196) Nordhaus, M. A.; Krongauz, V. V.; Hai, T. T.: Synthesis of solvatochromic merocyanine dyes and their immobilization to polymers. *Journal of Applied Polymer Science* **2017**, *134*.

(197) Thomas, R.; Yoshida, Y.; Akasaka, T.; Tamaoki, N.: Influence of a Change in Helical Twisting Power of Photoresponsive Chiral Dopants on Rotational Manipulation of Micro-Objects on the Surface of Chiral Nematic Liquid Crystalline Films. *Chemistry-a European Journal* **2012**, *18*, 12337-12348.

(198) Cusido, J.; Battal, M.; Deniz, E.; Yildiz, I.; Sortino, S.; Raymo, F. M.: Fast Fluorescence Switching within Hydrophilic Supramolecular Assemblies. *Chemistry-a European Journal* **2012**, *18*, 10399-10407.

(199) Jacquart, A.; Williams, R. M.; Brouwer, A. M.; Ishow, E.: Decoupling Fluorescence and Photochromism in Bifunctional Azo Derivatives for Bulk Emissive Structures. *Chemistry-a European Journal* **2012**, *18*, 3706-3720.

(200) Kim, S.; Yoon, S.-J.; Park, S. Y.: Highly Fluorescent Chameleon Nanoparticles and Polymer Films: Multicomponent Organic Systems that Combine FRET and Photochromic Switching. *Journal of the American Chemical Society* **2012**, *134*, 12091-12097.

(201) May, F.; Peter, M.; Huetten, A.; Prodi, L.; Mattay, J.: Synthesis and Characterization of Photoswitchable Fluorescent SiO2 Nanoparticles. *Chemistry-a European Journal* **2012**, *18*, 814-821.

(202) Remon, P.; Hammarson, M.; Li, S.; Kahnt, A.; Pischel, U.; Andreasson, J.: Molecular Implementation of Sequential and Reversible Logic Through Photochromic Energy Transfer Switching. *Chemistry-a European Journal* **2011**, *17*, 6492-6500.

(203) Copley, G.; Gillmore, J. G.; Crisman, J.; Kodis, G.; Gray, C. L.; Cherry, B. R.; Sherman, B. D.; Liddell, P. A.; Paquette, M. M.; Kelbauskas, L.; Frank, N. L.; Moore, A. L.; Moore, T. A.; Gust, D.: Modulating Short Wavelength Fluorescence with Long Wavelength Light. *Journal of the American Chemical Society* **2014**, *136*, 11994-12003.

(204) Audorff, H.; Walker, R.; Kador, L.; Schmidt, H.-W.: Holographic Investigations of Azobenzene-Containing Low-Molecular-Weight Compounds in Pure Materials and Binary Blends with Polystyrene. *Chemistry-a European Journal* **2011**, *17*, 12722-12728.

(205) Paquette, M. M.; Kopelman, R. A.; Beitler, E.; Frank, N. L.: Incorporating optical bistability into a magnetically bistable system: a photochromic redox isomeric complex. *Chemical Communications* **2009**, *0*, 5424-5426.

(206) Broichhagen, J.; Jurastow, I.; Iwan, K.; Kummer, W.; Trauner, D.: Optical Control of Acetylcholinesterase with a Tacrine Switch. *Angewandte Chemie International Edition* **2014**, *53*, 7657-7660.

(207) Velema, W. A.; Szymanski, W.; Feringa, B. L.: Photopharmacology: Beyond Proof of Principle. *Journal of the American Chemical Society* **2014**, *136*, 2178-2191.

(208) Stein, M.; Middendorp, S. J.; Carta, V.; Pejo, E.; Raines, D. E.; Forman, S. A.; Sigel, E.; Trauner, D.: Azo-Propofols: Photochromic Potentiators of GABAA Receptors. *Angewandte Chemie International Edition* **2012**, *51*, 10500-10504.

(209) Izquierdo-Serra, M.; Gascón-Moya, M.; Hirtz, J. J.; Pittolo, S.; Poskanzer, K. E.; Ferrer, È.; Alibés, R.; Busqué, F.; Yuste, R.; Hernando, J.; Gorostiza, P.: Two-Photon Neuronal and Astrocytic Stimulation with Azobenzene-Based Photoswitches. *Journal of the American Chemical Society* **2014**, *136*, 8693-8701.

(210) Tochitsky, I.; Banghart, M. R.; Mourot, A.; Yao, J. Z.; Gaub, B.; Kramer, R. H.; Trauner, D.: Optochemical control of genetically engineered neuronal nicotinic acetylcholine receptors. *Nat Chem* **2012**, *4*, 105-111.

(211) Stawski, P.; Sumser, M.; Trauner, D.: A Photochromic Agonist of AMPA Receptors. *Angew. Chem.-Int. Edit.* **2012**, *51*, 5748-5751.

(212) Han, M. X.; Michel, R.; He, B.; Chen, Y. S.; Stalke, D.; John, M.; Clever, G. H.: Light-Triggered Guest Uptake and Release by a Photochromic Coordination Cage. *Angew. Chem.-Int. Edit.* **2013**, *52*, 1319-1323.

(213) Xie, X. J.; Bakker, E.: Photoelectric Conversion Based on Proton-Coupled Electron Transfer Reactions. *Journal of the American Chemical Society* **2014**, *136*, 7857-7860.

(214) Sadovski, O.; Beharry, A. A.; Zhang, F.; Woolley, G. A.: Spectral Tuning of Azobenzene Photoswitches for Biological Applications. *Angewandte Chemie International Edition* **2009**, *48*, 1484-1486.

(215) Corns, S. N.; Partington, S. M.; Towns, A. D.: Industrial organic photochromic dyes. *Coloration Technology* **2009**, *125*, 249-261.

(216) Sheng, Y.; Leszczynski, J.; Garcia, A. A.; Rosario, R.; Gust, D.; Springer, J.: Comprehensive Theoretical Study of the Conversion Reactions of Spiropyrans: Substituent and Solvent Effects. *The Journal of Physical Chemistry B* **2004**, *108*, 16233-16243.

(217) Nakamura, S.; Uchida, K.; Murakami, A.; Irie, M.: Ab initio MO and proton NMR NOE studies of photochromic spironaphthoxazine. *The Journal of Organic Chemistry* **1993**, *58*, 5543-5545.

(218) Perrier, A. l.; Maurel, F. o.; Perpète, E. A.; Wathelet, V. r.; Jacquemin, D.: Spectral Properties of Spirooxazine Photochromes: TD-DFT Insights. *The Journal of Physical Chemistry A* **2009**, *113*, 13004-13012.

(219) Delbaere, S.; Bochu, C.; Azaroual, N.; Buntinx, G.; Vermeersch, G.: NMR studies of the structure of the photoinduced forms of photochromic spironaphthoxazines. *Journal of the Chemical Society, Perkin Transactions 2* **1997**, 1499-1502.

(220) Lareginie, P.; Lokshin, V.; Samat, A.; Guglielmetti, R.; Pepe, G.: First permanent opened forms in spiro[indoline-oxazine] series: synthesis and structural elucidation. *Journal of the Chemical Society, Perkin Transactions 2* **1996**, 107-111.

(221) Maurel, F.; Aubard, J.; Rajzmann, M.; Guglielmetti, R.; Samat, A.: A quantum chemical study of the ground state ring opening/closing of photochromic 1,3,3-trimethylspiro[indoline-2,3[prime or minute]-naphtho[2,1-b][1,4]oxazine]. *Journal of the Chemical Society, Perkin Transactions 2* **2002**, 1307-1315.

(222) Yee, L. H.; Hanley, T.; Evans, R. A.; Davis, T. P.; Ball, G. E.: Photochromic Spirooxazines Functionalized with Oligomers: Investigation of Core−Oligomer Interactions and Photomerocyanine Isomer Interconversion Using NMR Spectroscopy and DFT. *The Journal of Organic Chemistry* **2010**, *75*, 2851-2860.

(223) Paquette, M. M.: Designing Optically Switchable Multifunctional Material Using Photochromic Spirooxazine Ligands. University of Victoria, 2010.

(224) Patel., D. G.: Organic Dye for Photoswitching and Photovoltaic Applications. University of Washington, 2007.

(225) Jacobsen, N. E.: *NMR data interpretation explained : understanding 1D and 2D NMR spectra of organic compounds and natural products*, 2017.

(226) Reichardt, C.: Solvatochromic Dyes as Solvent Polarity Indicators. *Chemical Reviews* **1994**, *94*, 2319-2358.

(227) Keum, S. R.; Hur, M. S.; Kazmaier, P. M.; Buncel, E.: Thermochromic and Photochromic Dyes - Indolino-Benzospiropyrans.1. UV-VIS Spectroscopic Studies of 1,3,3-Spiro(2H-1-Benzopyran-2,2'-Indolines) and the Open-Chain Merocyanine Forms - Solvatochromism and Medium Effects on Spiro Ring Formation. *Canadian Journal of Chemistry-Revue Canadienne De Chimie* **1991**, *69*, 1940-1947.

(228) Jacques, P.: On the relative contributions of nonspecific and specific interactions to the unusual solvtochromism of a typical merocyanine dye. *The Journal of Physical Chemistry* **1986**, *90*, 5535-5539.

(229) Buncel, E.; Rajagopal, S.: Solvatochromism and solvent polarity scales. *Accounts of Chemical Research* **1990**, *23*, 226-231.

(230) Hiramatsu, T.; Yoshida, H.; Sato, N.: Solvent-Dependent Structural and Electronic Behaviors of a Push−Pull Molecule: {4-[4,5-Bis(methylsulfanyl)-1,3-dithiol-2-ylidene]cyclohexa-2,5-dien-1-ylidene}malononitrile. *The Journal of Physical Chemistry A* **2009**, *113*, 9174-9179.

(231) Mustroph, H.; Reiner, K.; Mistol, J.; Ernst, S.; Keil, D.; Hennig, L.: Relationship between the Molecular Structure of Cyanine Dyes and the Vibrational Fine Structure of their Electronic Absorption Spectra. *ChemPhysChem* **2009**, *10*, 835-840.

(232) Pottier, E.; Dubest, R.; Guglielmetti, R.; Tardieu, P.; Kellmann, A.; Tfibel, F.; Levoir, P.; Aubard, J.: Substituent, Heteroatom, and Solvent Effects on the Thermal-Bleaching Kinetics and Absorption-Spectra of Photomerocyanines Issued from Spiro[Indoline-Oxazines]. *Helv Chim Acta* **1990**, *73*, 303-315.

(233) Ernsting, N. P.; Arthenengeland, T.: Photochemical Ring-Opening Reaction of Indolinospiropyrans Studied by Subpicosecond Transient Absorption. *J Phys Chem-Us* **1991**, *95*, 5502-5509.

(234) Marder, S. R.; Gorman, C. B.; Meyers, F.; Perry, J. W.; Bourhill, G.; Brédas, J.-L.; Pierce, B. M.: A Unified Description of Linear and Nonlinear Polarization in Organic Polymethine Dyes. *Science* **1994**, *265*, 632-635.

(235) Marder, S. R.; Kippelen, B.; Jen, A. K. Y.; Peyghambarian, N.: Design and synthesis of chromophores and polymers for electro-optic and photorefractive applications. *Nature* **1997**, *388*, 845-851.

(236) Allen, F. H.; Kennard, O.; Watson, D. G.; Brammer, L.; Orpen, A. G.; Taylor, R.: Tables of bond lengths determined by X-ray and neutron diffraction. Part 1. Bond lengths in organic compounds. *Journal of the Chemical Society, Perkin Transactions 2* **1987**, *0*, S1-S19.

(237) Horii, T.; Abe, Y.; Nakao, R.: Theoretical quantum chemical study of spironaphthoxazines and their merocyanines: Thermal ring-opening reaction and geometric isomerization. *Journal of Photochemistry and Photobiology A: Chemistry* **2001**, *144*, 119-129.

(238) Minkin, V. I.; Metelitsa, A. V.; Dorogan, I. V.; Lukyanov, B. S.; Besugliy, S. O.; Micheau, J.-C.: Spectroscopic and Theoretical Evidence for the Elusive Intermediate of the Photoinitiated and Thermal Rearrangements of Photochromic Spiropyrans. *The Journal of Physical Chemistry A* **2005**, *109*, 9605-9616.

(239) Perdew, J. P.; Zunger, A.: Self-Interaction Correction to Density-Functional Approximations for Many-Electron Systems. *Phys. Rev. B* **1981**, *23*, 5048-5079.

(240) Wu, Q.; Van Voorhis, T.: Direct calculation of electron transfer parameters through constrained density functional theory. *Journal of Physical Chemistry A* **2006**, *110*, 9212-9218.

(241) Peng, C. Y.; Schlegel, H. B.: Combining Synchronous Transit and Quasi-Newton Methods to Find Transition-States. *Isr. J. Chem.* **1993**, *33*, 449-454.

(242) Becke, A. D.: Density-Functional Thermochemistry.3. The Role of Exact Exchange. *J Chem Phys* **1993**, *98*, 5648-5652.

(243) Lee, C. T.; Yang, W. T.; Parr, R. G.: Development of the Colle-Salvetti Correlation-Energy Formula into a Functional of the Electron-Density. *Phys. Rev. B* **1988**, *37*, 785-789.

(244) Frisch, M. J.; Trucks, G. W.; Schlegel, H. B.; Scuseria, G. E.; Robb, M. A.; Cheeseman, J. R.; Scalmani, G.; Barone, V.; Mennucci, B.; Petersson, G. A.; Nakatsuji, H.; Caricato, M.; Li, X.; Hratchian, H. P.; Izmaylov, A. F.; Bloino, J.; Zheng, G.; Sonnenberg, J. L.; Hada, M.; Ehara, M.; Toyota, K.; Fukuda, R.; Hasegawa, J.; Ishida, M.; Nakajima, T.; Honda, Y.; Kitao, O.; Nakai, H.; Vreven, T.; Montgomery Jr., J. A.; Peralta, J. E.; Ogliaro, F.; Bearpark, M. J.; Heyd, J.; Brothers, E. N.; Kudin, K. N.; Staroverov, V. N.; Kobayashi, R.; Normand, J.; Raghavachari, K.; Rendell, A. P.; Burant, J. C.; Iyengar, S. S.; Tomasi, J.; Cossi, M.; Rega, N.; Millam, N. J.; Klene, M.; Knox, J. E.; Cross, J. B.; Bakken, V.; Adamo, C.; Jaramillo, J.; Gomperts, R.; Stratmann, R. E.; Yazyev, O.; Austin, A. J.; Cammi, R.; Pomelli, C.; Ochterski, J. W.; Martin, R. L.; Morokuma, K.; Zakrzewski, V. G.; Voth, G. A.; Salvador, P.; Dannenberg, J. J.; Dapprich, S.; Daniels, A. D.; Farkas, Ö.; Foresman, J. B.; Ortiz, J. V.; Cioslowski, J.; Fox, D. J.: Gaussian 09. Gaussian, Inc.: Wallingford, CT, USA, 2009.

(245) Peng, C. Y.; Ayala, P. Y.; Schlegel, H. B.; Frisch, M. J.: Using redundant internal coordinates to optimize equilibrium geometries and transition states. *J Comput Chem* **1996**, *17*, 49-56.

(246) SAINT. Version 7.53A ed.; Bruker AXS Inc.: Madison, Wisconsin, USA, 1997-2008.

(247) SADABS; V2008/1 ed.; Bruker AXS Inc.: Madison, Wisconsin, USA, 2008.

(248) Altomare, A. B., M. C.; Camalli, M.; Cascarano, G. L.; Giacovazzo, C.; Guagliardi, A.; Moliterni, A. G. G.; Polidori, G.; Spagna, R.: SIR97: a new tool for crystal structure determination and refinement. *J. Appl. Crystallogr.* **1999**, 115-119.

(249) Cromer, D.; Waber, J.: *International Tables for X-ray Crystallography* Kynoch Press: Birmingham, England, 1974; Vol. IV, Table 2.2A.

(250) Ibers, J. A.; Hamilton, W. C.: Dispersion corrections and crystal structure refinements. *Acta Crystallographica* **1964**, *17*, 781-782.

(251) Creagh, D. C. M., W. J.: *International Tables for Crystallography*; Kluwer Academic Publishers: Boston, 1992; Vol. C, Table 4.2.6.8.

(252) Creagh, D. C. M., W. J.: *International Tables for Crystallography*; Kluwer Academic Publishers: Boston, 1992; Vol. C, Table 4.2.4.3.

(253) SHELXTL; Version 5.1 ed.; Bruker AXS Inc.: Madison, Wisconsin, USA, 1997.

(254) Farrugia, L.: WinGX (Version 1.70). *J. Appl. Cryst* **1999**, *32*, e838.

(255) Andréasson, J.; Kodis, G.; Terazono, Y.; Liddell, P. A.; Bandyopadhyay, S.; Mitchell, R. H.; Moore, T. A.; Moore, A. L.; Gust, D.: Molecule-Based Photonically Switched Half-Adder. *Journal of the American Chemical Society* **2004**, *126*, 15926-15927.

(256) Perissinotto, S.; Carvelli, M.; Zavelani-Rossi, M.; Lanzani, G.; Bertarelli, C.; Zerbi, G.; Salerno, M.; Troisi, L.; Gigli, G.: Ultrafast optical modulation of polymer nano-structured lasers. *P Soc Photo-Opt Ins* **2008**, *7051*.

(257) Li, Z.-X.; Liao, L.-Y.; Sun, W.; Xu, C.-H.; Zhang, C.; Fang, C.-J.; Yan, C.-H.: Reconfigurable Cascade Circuit in a Photo- and Chemical-Switchable Fluorescent Diarylethene Derivative. *The Journal of Physical Chemistry C* **2008**, *112*, 5190-5196.

(258) Kopelman, R. A.; Snyder, S. M.; Frank, N. L.: Tunable Photochromism of Spirooxazines via Metal Coordination. *Journal of the American Chemical Society* **2003**, *125*, 13684-13685.

(259) Kopelman, R. A.; Paquette, M. M.; Frank, N. L.: Photoprocesses and magnetic behavior of photochromic transition metal indoline[phenanthrolinospirooxazine] complexes: Tunable photochromic materials. *Inorganica Chimica Acta* **2008**, *361*, 3570-3576.

(260) Paquette, M. M.; Plaul, D.; Kurimoto, A.; Lewarne, D. S.; Bracken, M.; Wlasenko, A.; Patrick, B. O.; Frank, N. L.: Optical Switching of Magnetic Thin Films by Ligand Photoisomerization at Room Temperature. *manuscript in preparation*.

(261) Tanaka, M.; Nakamura, M.; Salhin, M. A. A.; Ikeda, T.; Kamada, K.; Ando, H.; Shibutani, Y.; Kimura, K.: Synthesis and Photochromism of Spirobenzopyran Derivatives Bearing an Oxymethylcrown Ether Moiety: Metal Ion-Induced Switching between Positive and Negative Photochromisms. *The Journal of Organic Chemistry* **2001**, *66*, 1533-1537.

(262) Salhin, Abdussalam M. A.; Tanaka, M.; Kamada, K.; Ando, H.; Ikeda, T.; Shibutani, Y.; Yajima, S.; Nakamura, M.; Kimura, K.: Decisive Factors in the Photoisomerization Behavior of Crowned Spirobenzopyrans: Metal Ion Interaction with Crown Ether and Phenolate Anion Moieties. *European Journal of Organic Chemistry* **2002**, *2002*, 655-662.

(263) Kimura, K.; Yamashita, T.; Yokoyama, M.: Syntheses, cation complexation, isomerization and photochemical cation-binding control of spirobenzopyrans carrying a monoazacrown moiety at the 8-position. *Journal of the Chemical Society, Perkin Transactions 2* **1992**, *0*, 613-619.

(264) Mitchell, R. H.; Chen, Y. S.; Khalifa, N.; Zhou, P. Z.: The synthesis, aromaticity, and NMR properties of [14]annulene fused organometallics. Determination of the effective bond localizing ability ("relative aromaticity") and diamagnetic anisotropy of several organometallic moieties. *Journal of the American Chemical Society* **1998**, *120*, 1785-1794.

(265) Paquette, M. M.; Patrick, B. O.; Frank, N. L.: Determining the Magnitude and Direction of Photoinduced Ligand Field Switching in Photochromic Metal–Organic Complexes: Molybdenum–Tetracarbonyl Spirooxazine Complexes. *Journal of the American Chemical Society* **2011**, *133*, 10081-10093.

(266) Bellér, G.; Lente, G.; Fábián, I.: Central Role of Phenanthroline Mono-N-oxide in the Decomposition Reactions of Tris(1,10-phenanthroline)iron(II) and -iron(III) Complexes. *Inorganic Chemistry* **2010**, *49*, 3968-3970.

(267) Ferrando-Soria, J.; Vallejo, J.; Castellano, M.; Martínez-Lillo, J.; Pardo, E.; Cano, J.; Castro, I.; Lloret, F.; Ruiz-García, R.; Julve, M.: Molecular magnetism, quo vadis? A historical perspective from a coordination chemist viewpoint☆. *Coordination Chemistry Reviews* **2017**, *339*, 17-103.

(268) Sato, O.: Optically Switchable Molecular Solids: Photoinduced Spin-Crossover, Photochromism, and Photoinduced Magnetization. *Accounts of Chemical Research* **2003**, *36*, 692-700.

(269) Sato, O.; Tao, J.; Zhang, Y. Z.: Control of magnetic properties through external stimuli. *Angew. Chem.-Int. Edit.* **2007**, *46*, 2152-2187.

(270) Chorazy, S.; Podgajny, R.; Nakabayashi, K.; Stanek, J.; Rams, M.; Sieklucka, B.; Ohkoshi, S.: Fe-II Spin-Crossover Phenomenon in the Pentadecanuclear {Fe-9[Re(CN)(8)](6)} Spherical Cluster. *Angew. Chem.-Int. Edit.* **2015**, *54*, 5093-5097.

(271) Li, Z. Y.; Ohtsu, H.; Kojima, T.; Dai, J. W.; Yoshida, T.; Breedlove, B. K.; Zhang, W. X.; Iguchi, H.; Sato, O.; Kawano, M.; Yamashita, M.: Direct Observation of Ordered High-Spin-Low-Spin Intermediate States of an Iron(III) Three-Step Spin-Crossover Complex. *Angew. Chem.-Int. Edit.* **2016**, *55*, 5184-5189.

(272) Dini, D.; Hanack, M.; Ji, W.; Chen, W. Z.: Optical limiting of transition metal-phthalocyanine complexes: A photochromic effect involving the excited state of the conjugated molecule. *Mol. Cryst. Liquid Cryst.* **2005**, *431*, 559-574.

(273) Adams, D. M.; Dei, A.; Rheingold, A. L.; Hendrickson, D. N.: CONTROLLING VALENCE TAUTOMERISM OF COBALT COMPLEXES CONTAINING THE

BENZOSEMIQUINONE ANION AS LIGAND. *Angew. Chem.-Int. Edit.* **1993**, *32*, 880-882.

(274) Buchanan, R. M.; Fitzgerald, B. J.; Pierpont, C. G.: Semiquinone radical anion coordination to divalent cobalt and nickel. Structural features of the bis(3,5-di-tert-butyl-1,2-semiquinone)cobalt(II) tetramer. *Inorganic Chemistry* **1979**, *18*, 3439-3444.

(275) Telfer, S. G.; Kuroda, R.; Lefebvre, J.; Leznoff, D. B.: Boxes, helicates, and coordination polymers: A structural and magnetochemical investigation of the diverse coordination chemistry of simple pyridine-alcohol ligands. *Inorganic Chemistry* **2006**, *45*, 4592-4601.

(276) Seisenbaeva, G. A.; Kritikos, M.; Kessler, V. G.: Synthesis, X-ray single crystal and magnetic study of new heteroleptic late transition metal alkoxides with tetranuclear square planar metal core, Co4Cl2(OC2H4OEt)(6), Co-4(OMe)(2)(acac)(6)(MeOH)(2) and Zn-4(OMe)(2)(acac)(6)(C7H8). *Polyhedron* **2003**, *22*, 2581-2586.

(277) Pattacini, R.; Teo, P.; Zhang, J.; Lan, Y. H.; Powell, A. K.; Nehrkorn, J.; Waldmann, O.; Hor, T. S. A.; Braunstein, P.: Synthesis, characterization, and single-molecule metamagnetism of new Co(II) polynuclear complexes of pyridine-2-ylmethanol. *Dalton Trans.* **2011**, *40*, 10526-10534.

(278) Paramonov, S. V.; Lokshin, V.; Fedorova, O. A.: Spiropyran, chromene or spirooxazine ligands: Insights into mutual relations between complexing and photochromic properties. *Journal of Photochemistry and Photobiology C-Photochemistry Reviews* **2011**, *12*, 209-236.

(279) Ruf, M.; Noll, B. C.; Groner, M. D.; Yee, G. T.; Pierpont, C. G.: Pocket semiquinonate complexes of cobalt(II), copper(II), and zinc(II) prepared with the hydrotris(cumenylmethylpyrazolyl)borate ligand. *Inorganic Chemistry* **1997**, *36*, 4860-4865.

(280) Wang, P.; Yap, G. P. A.; Riordan, C. G.: Five-coordinate M-II-semiquinonate (M = Fe, Mn, Co) complexes: reactivity models of the catechol dioxygenases. *Chemical Communications* **2014**, *50*, 5871-5873.

(281) Overgaard, J.; Moller, L. H.; Borup, M. A.; Tricoire, M.; Walsh, J. P. S.; Diehl, M.; Rentschler, E.: Magnetism and variable temperature and pressure crystal structures of a linear oligonuclear cobalt bis-semiquinonate. *Dalton Trans.* **2016**, *45*, 12924-12932.

(282) Brown, I. D.; Altermatt, D.: Bond-Valence Parameters Obtained from a Systematic Analysis of the Inorganic Crystal-Structure Database. *Acta Crystallogr B* **1985**, *41*, 244-247.

(283) Chaudhuri, P.; Verani, C. N.; Bill, E.; Bothe, E.; Weyhermuller, T.; Wieghardt, K.: Electronic structure of bis(o-iminobenzosemiquinonato)metal complexes (Cu, Ni, Pd). The

art of establishing physical oxidation states in transition-metal complexes containing radical ligands. *Journal of the American Chemical Society* **2001**, *123*, 2213-2223.

(284) Sakiyama, H.; Powell, A. K.: Magnetic analysis of a tetranuclear octahedral high-spin cobalt(II) complex based on a newly derived magnetic susceptibility equation. *Dalton Trans.* **2014**, *43*, 14542-14545.

(285) Batsanov, S. S.: Van der Waals radii of elements. *Inorg Mater+* **2001**, *37*, 871-885.

(286) Kahn, O.: Dinuclear Complexes with Predictable Magnetic-Properties. *Angew Chem Int Edit* **1985**, *24*, 834-850.

(287) Thompson, L. K.; Matthews, C. J.; Zhao, L.; Xu, Z. Q.; Miller, D. O.; Wilson, C.; Leech, M. A.; Howard, J. A. K.; Heath, S. L.; Whittaker, A. G.; Winpenny, R. E. P.: Synthesis, structure, and magnetism of a series of self-assembled polynuclear Mn(II), Co(II), and Cu(II) cluster complexes. *J Solid State Chem* **2001**, *159*, 308-320.

(288) Thompson, L. K.; Waldmann, O.; Xu, Z.: Magnetic Properties of Self-Assembled [2 × 2] and [3 × 3] Grids. In *Magnetism: Molecules to Materials IV*; Wiley-VCH Verlag GmbH & Co. KGaA, 2003; pp 173-203.

(289) Serna, Z. E.; Urtiaga, M. K.; Barandika, M. G.; Cortes, R.; Martin, S.; Lezama, L.; Arriortua, M. I.; Rojo, T.: Dicubane-like tetrameric cobalt(II)-pseudohalide ferromagnetic clusters. *Inorganic Chemistry* **2001**, *40*, 4550-4555.

(290) King, P.; Clerac, R.; Wernsdorfer, W.; Anson, C. E.; Powell, A. K.: Synthesis and magnetism of oxygen-bridged tetranuclear defect dicubane Co(II) and Ni(II) clusters. *Dalton Trans.* **2004**, 2670-2676.

(291) Papaefstathiou, G. S.; Escuer, A.; Raptopoulou, C. P.; Terzis, A.; Perlepes, S. P.; Vicente, R.: Defective double-cubane, tetranuclear manganese(II) and cobalt(II) complexes with simultaneous mu(1,1)-Azido and mu-O bridges. *European Journal of Inorganic Chemistry* **2001**, 1567-1574.

(292) Papaefstathiou, G. S.; Escuer, A.; Font-Bardia, M.; Perlepes, S. P.; Solans, X.; Vicente, R.: Benzoate as terminal ligand in the defective double-cubane, tetranuclear cobalt(II) complex [Co-4(N-3)(2)(O2CPh)(2){(py)(2)C(OH)O}(4)]center dot 2DMF with simultaneous mu(1,1)-azido and mu-O bridges [(py)(2)C(OH)O = the monoanion of the hydrated, gem-diol form of di-2-pyridyl ketone]. *Polyhedron* **2002**, *21*, 2027-2032.

(293) Carlin, R. L.: *Magnetochemistry*; Springer-Verlag, 1986.

(294) Dolomanov, O. V.; Bourhis, L. J.; Gildea, R. J.; Howard, J. A. K.; Puschmann, H.: OLEX2: a complete structure solution, refinement and analysis program. *J Appl Crystallogr* **2009**, *42*, 339-341.

(295) Sheldrick, G. M.: A short history of SHELX. *Acta Crystallogr A* **2008**, *64*, 112-122.

(296) Sheldrick, G. M.: Crystal structure refinement with SHELXL. *Acta Crystallogr C* **2015**, *71*, 3-8.

(297) Schubert, E. M.: Utilizing the Evans Method with a Superconducting Nmr Spectrometer in the Undergraduate Laboratory. *J Chem Educ* **1992**, *69*, 62-62.

(298) Evans, D. F.: The Determination of the Paramagnetic Susceptibility of Substances in Solution by Nuclear Magnetic Resonance. *Journal of the Chemical Society* **1959**, 2003-2005.

(299) Crawford, T. H.; Swanson, J.: Temperature Dependent Magnetic Measurements and Structural Equilibria in Solution. *J Chem Educ* **1971**, *48*, 382.

(300) Ostfeld, D.; Cohen, I. A.: A cautionary note on the use of the Evans method for magnetic moments. *J Chem Educ* **1972**, *49*, 829.

(301) Yaws, C. L.: *Physical properties : a guide to the physical thermodynamic, and transport property data of industrially important chemical compounds*; Chemical engineering: New York, 1977.

(302) Grant, D. H.: Paramagnetic-Susceptibility by Nmr - the Solvent Correction Reexamined. *J Chem Educ* **1995**, *72*, 39-40.

(303) Lauffer, R. B.: Paramagnetic Metal-Complexes as Water Proton Relaxation Agents for Nmr Imaging - Theory and Design. *Chemical Reviews* **1987**, *87*, 901-927.

(304) Caravan, P.: Strategies for increasing the sensitivity of gadolinium based MRI contrast agents. *Chemical Society Reviews* **2006**, *35*, 512-523.

(305) Caravan, P.; Ellison, J. J.; McMurry, T. J.; Lauffer, R. B.: Gadolinium(III) chelates as MRI contrast agents: Structure, dynamics, and applications. *Chemical Reviews* **1999**, *99*, 2293-2352.

(306) Li, L.; Jiang, W.; Luo, K.; Song, H. M.; Lan, F.; Wu, Y.; Gu, Z. W.: Superparamagnetic Iron Oxide Nanoparticles as MRI contrast agents for Non-invasive Stem Cell Labeling and Tracking. *Theranostics* **2013**, *3*, 595-615.

(307) Terreno, E.; Delli Castelli, D.; Viale, A.; Aime, S.: Challenges for Molecular Magnetic Resonance Imaging. *Chemical Reviews* **2010**, *110*, 3019-3042.

(308) Brown, R. W.; Cheng, Y.-C. N.; Haacke, E. M.; Thompson, M. R.; Venkatesan, R.; Ebscohost E-Books - York University.: *Magnetic resonance imaging : physical principles and sequence design*; Second edition. ed.

(309) Huettel, S. A.; Song, A. W.; McCarthy, G.: *Functional magnetic resonance imaging*; 2nd ed.; Sinauer Associates: Sunderland, Mass., 2008.

(310) Na, H. B.; Song, I. C.; Hyeon, T.: Inorganic Nanoparticles for MRI Contrast Agents. *Advanced Materials* **2009**, *21*, 2133-2148.

(311) Zhou, Z. X.; Lu, Z. R.: Gadolinium-based contrast agents for magnetic resonance cancer imaging. *Wiley Interdiscip. Rev.-Nanomed. Nanobiotechnol.* **2013**, *5*, 1-18.

(312) Xiao, Y.; Wu, Y.-J.; Zhang, W.-J.; Li, X.-J.; Pei, F.-K.: Research Progress of Magnetic Resonance Imaging Contrast Agents. *Chinese Journal of Analytical Chemistry* **2011**, *39*, 757-764.

(313) Lee, N.; Yoo, D.; Ling, D.; Cho, M. H.; Hyeon, T.; Cheon, J.: Iron Oxide Based Nanoparticles for Multimodal Imaging and Magnetoresponsive Therapy. *Chemical Reviews* **2015**, *115*, 10637-10689.

(314) Rogosnitzky, M.; Branch, S.: Gadolinium-based contrast agent toxicity: a review of known and proposed mechanisms. *Biometals : an international journal on the role of metal ions in biology, biochemistry, and medicine* **2016**, *29*, 365-76.

(315) Khawaja, A. Z.; Cassidy, D. B.; Al Shakarchi, J.; McGrogan, D. G.; Inston, N. G.; Jones, R. G.: Revisiting the risks of MRI with Gadolinium based contrast agents-review of literature and guidelines. *Insights into imaging* **2015**, *6*, 553-8.

(316) Sadowski, E. A.; Bennett, L. K.; Chan, M. R.; Wentland, A. L.; Garrett, A. L.; Garrett, R. W.; Djamali, A.: Nephrogenic systemic fibrosis: risk factors and incidence estimation. *Radiology* **2007**, *243*, 148-57.

(317) Idee, J. M.; Fretellier, N.; Robic, C.; Corot, C.: The role of gadolinium chelates in the mechanism of nephrogenic systemic fibrosis: A critical update. *Crit. Rev. Toxicol.* **2014**, *44*, 895-913.

(318) Kanda, T.; Ishii, K.; Kawaguchi, H.; Kitajima, K.; Takenaka, D.: High signal intensity in the dentate nucleus and globus pallidus on unenhanced T1-weighted MR images: relationship with increasing cumulative dose of a gadolinium-based contrast material. *Radiology* **2014**, *270*, 834-41.

(319) Kanda, T.; Oba, H.; Toyoda, K.; Kitajima, K.; Furui, S.: Brain gadolinium deposition after administration of gadolinium-based contrast agents. *Jpn J Radiol* **2016**, *34*, 3-9.

(320) Kanda, T.; Fukusato, T.; Matsuda, M.; Toyoda, K.; Oba, H.; Kotoku, J.; Haruyama, T.; Kitajima, K.; Furui, S.: Gadolinium-based Contrast Agent Accumulates in the Brain Even in Subjects without Severe Renal Dysfunction: Evaluation of Autopsy Brain

Specimens with Inductively Coupled Plasma Mass Spectroscopy. *Radiology* **2015**, *276*, 228-32.

(321) Stojanov, D.; Aracki-Trenkic, A.; Benedeto-Stojanov, D.: Gadolinium deposition within the dentate nucleus and globus pallidus after repeated administrations of gadolinium-based contrast agents-current status. *Neuroradiology* **2016**, *58*, 433-441.

(322) Caravan, P.; Farrar, C. T.; Frullano, L.; Uppal, R.: Influence of molecular parameters and increasing magnetic field strength on relaxivity of gadolinium- and manganese-based T1 contrast agents. *Contrast media & molecular imaging* **2009**, *4*, 89-100.

(323) Solomon, I.: Relaxation Processes in a System of Two Spins. *Physical Review* **1955**, *99*, 559-565.

(324) Bloembergen, N.; Morgan, L. O.: Proton Relaxation Times in Paramagnetic Solutions Effects of Electron Spin Relaxation. *J Chem Phys* **1961**, *34*, 842-&.

(325) Gueron, M.: Nuclear-Relaxation in Macromolecules by Paramagnetic-Ions - Novel Mechanism. *J Magn Reson* **1975**, *19*, 58-66.

(326) Kowalewski, J.; Nordenskiold, L.; Benetis, N.; Westlund, P. O.: Theory of Nuclear-Spin Relaxation in Paramagnetic Systems in Solution. *Progress in nuclear magnetic resonance spectroscopy* **1985**, *17*, 141-185.

(327) Pan, D.; Schmieder, A. H.; Wickline, S. A.; Lanza, G. M.: Manganese-based MRI contrast agents: past, present and future. *Tetrahedron* **2011**, *67*, 8431-8444.

(328) Xu, C. J.; Sun, S. H.: New forms of superparamagnetic nanoparticles for biomedical applications. *Adv Drug Deliver Rev* **2013**, *65*, 732-743.

(329) Schutz-Sikma, E. A.; Joshi, H. M.; Ma, Q.; MacRenaris, K. W.; Eckermann, A. L.; Dravid, V. P.; Meade, T. J.: Probing the Chemical Stability of Mixed Ferrites: Implications for Magnetic Resonance Contrast Agent Design. *Chemistry of Materials* **2011**, *23*, 2657-2664.

(330) Ho, D.; Sun, X.; Sun, S.: Monodisperse magnetic nanoparticles for theranostic applications. *Acc Chem Res* **2011**, *44*, 875-82.

(331) Sharifi, I.; Shokrollahi, H.; Amiri, S.: Ferrite-based magnetic nanofluids used in hyperthermia applications. *Journal of Magnetism and Magnetic Materials* **2012**, *324*, 903-915.

(332) Meng, X. T.; Seton, H. C.; Lu, L. T.; Prior, I. A.; Thanh, N. T. K.; Song, B.: Magnetic CoPt nanoparticles as MRI contrast agent for transplanted neural stem cells detection. *Nanoscale* **2011**, *3*, 977-984.

(333) Sathya, A.; Guardia, P.; Brescia, R.; Silyestri, N.; Pugliese, G.; Nitti, S.; Manna, L.; Pellegrino, T.: CoxFe3-xO4 Nanocubes for Theranostic Applications: Effect of Cobalt Content and Particle Size. *Chemistry of Materials* **2016**, *28*, 1769-1780.

(334) Song, X. R.; Wang, X. Y.; Yu, S. X.; Cao, J. B.; Li, S. H.; Li, J.; Liu, G.; Yang, H. H.; Chen, X. Y.: Co9Se8 Nanoplates as a New Theranostic Platform for Photoacoustic/Magnetic Resonance Dual-Modal-Imaging-Guided Chemo-Photothermal Combination Therapy. *Advanced Materials* **2015**, *27*, 3285-3291.

(335) Parkes, L. M.; Hodgson, R.; Lu, L. T.; Tung, L. D.; Robinson, I.; Fernig, D. G.; Thanh, N. T. K.: Cobalt nanoparticles as a novel magnetic resonance contrast agent-relaxivities at 1.5 and 3 Tesla. *Contrast media & molecular imaging* **2008**, *3*, 150-156.

(336) Moghimi, S. M.; Hunter, A. C.; Murray, J. C.: Long-circulating and target-specific nanoparticles: Theory to practice. *Pharmacol Rev* **2001**, *53*, 283-318.

(337) Bulte, J. W. M.; Kraitchman, D. L.: Iron oxide MR contrast agents for molecular and cellular imaging. *Nmr Biomed* **2004**, *17*, 484-499.

(338) Zhang, D. W.; Yang, Z. Y.; Zhang, S. P.; Yang, R. D.: Synthesis, characterization and relaxation properties of four non-ion transition metal manganese(II), cobalt(II), nickel(II) and copper (II) complexes with derivatives from diethylene triamine pentaacetic acid and isoniazid. *Transit Metal Chem* **2006**, *31*, 333-336.

(339) Lim, T. Y.; Stafford, R. J.; Kudchadker, R. J.; Sankaranarayanapillai, M.; Ibbott, G.; Rao, A.; Martirosyan, K. S.; Frank, S. J.: MRI characterization of cobalt dichloride-N-acetyl cysteine (C4) contrast agent marker for prostate brachytherapy. *Phys Med Biol* **2014**, *59*, 2505-2516.

(340) O'Neill, E. S.; Kolanowski, J. L.; Yin, G. H.; Broadhouse, K. M.; Grieve, S. M.; Renfrew, A. K.; Bonnitcha, P. D.; New, E. J.: Reversible magnetogenic cobalt complexes. *Rsc Advances* **2016**, *6*, 30021-30027.

(341) Hao, D. P.; Ai, T.; Goerner, F.; Hu, X. M.; Runge, V. M.; Tweedle, M.: MRI contrast agents: Basic chemistry and safety. *J Magn Reson Imaging* **2012**, *36*, 1060-1071.

(342) Bertrand, J. A.; Fujita, E.; Vanderveer, D. G.: STRUCTURE OF A TETRANUCLEAR COBALT(II)-COBALT(III) COMPLEX OF BIS-(2-HYDROXYETHYL)AMINE, CO4(NH(C2H4OH)2)2(NH(C2H4O)2(4 (CLO4)2. *Inorganic Chemistry* **1979**, *18*, 230-233.

(343) Landis, C. S.; Li, X.; Telang, F. W.; Coderre, J. A.; Micca, P. L.; Rooney, W. D.; Latour, L. L.; Vetek, G.; Palyka, I.; Springer, C. S.: Determination of the MRI contrast agent concentration time course in vivo following bolus injection: Effect of equilibrium transcytolemmal water exchange. *Magn Reson Med* **2000**, *44*, 563-574.

(344) Taheri, S.; Shah, N. J.; Rosenberg, G. A.: Analysis of pharmacokinetics of Gd-DTPA for dynamic contrast-enhanced magnetic resonance imaging. *Magn Reson Imaging* **2016**, *34*, 1034-1040.

(345) Karlsson, R.: Solubility of water in benzene. *Journal of Chemical & Engineering Data* **1973**, *18*, 290-292.

(346) Markov, I. L.: Limits on fundamental limits to computation. *Nature* **2014**, *512*, 147-154.

(347) Theis, T. N.; Wong, H. S. P.: The End of Moore's Law: A New Beginning for Information Technology. *Computing in Science & Engineering* **2017**, *19*, 41-50.

(348) Geim, A. K.; Novoselov, K. S.: The rise of graphene. *Nature Materials* **2007**, *6*, 183-191.

(349) Zhang, Y. B.; Tan, Y. W.; Stormer, H. L.; Kim, P.: Experimental observation of the quantum Hall effect and Berry's phase in graphene. *Nature* **2005**, *438*, 201-204.

(350) Novoselov, K. S.; Geim, A. K.; Morozov, S. V.; Jiang, D.; Zhang, Y.; Dubonos, S. V.; Grigorieva, I. V.; Firsov, A. A.: Electric field effect in atomically thin carbon films. *Science* **2004**, *306*, 666-669.

(351) Son, Y.-W.; Cohen, M. L.; Louie, S. G.: Energy Gaps in Graphene Nanoribbons. *Physical Review Letters* **2006**, *97*, 216803.

(352) Stampfer, C.; Güttinger, J.; Hellmüller, S.; Molitor, F.; Ensslin, K.; Ihn, T.: Energy Gaps in Etched Graphene Nanoribbons. *Physical Review Letters* **2009**, *102*, 056403.

(353) Chen, Y. C.; Cao, T.; Chen, C.; Pedramrazi, Z.; Haberer, D.; de Oteyza, D. G.; Fischer, F. R.; Louie, S. G.; Crommie, M. F.: Molecular bandgap engineering of bottom-up synthesized graphene nanoribbon heterojunctions. *Nat. Nanotechnol.* **2015**, *10*, 156-160.

(354) Cai, J. M.; Pignedoli, C. A.; Talirz, L.; Ruffieux, P.; Sode, H.; Liang, L. B.; Meunier, V.; Berger, R.; Li, R. J.; Feng, X. L.; Mullen, K.; Fasel, R.: Graphene nanoribbon heterojunctions. *Nat. Nanotechnol.* **2014**, *9*, 896-900.

(355) Bai, J.; Zhong, X.; Jiang, S.; Huang, Y.; Duan, X.: Graphene nanomesh. *Nat Nano* **2010**, *5*, 190-194.

(356) Kim, M.; Safron, N. S.; Han, E.; Arnold, M. S.; Gopalan, P.: Fabrication and Characterization of Large-Area, Semiconducting Nanoperforated Graphene Materials. *Nano Lett.* **2010**, *10*, 1125-1131.

(357) Xiu, S. L.; Zheng, M. M.; Zhao, P.; Zhang, Y.; Liu, H. Y.; Li, S. J.; Chen, G.; Kawazoe, Y.: An effective method of tuning conducting properties: First-principles studies on electronic structures of graphene nanomeshes. *Carbon* **2014**, *79*, 646-653.

(358) Pereira, V. M.; Castro Neto, A. H.; Peres, N. M. R.: Tight-binding approach to uniaxial strain in graphene. *Phys. Rev. B* **2009**, *80*, 045401.

(359) Si, C.; Sun, Z. M.; Liu, F.: Strain engineering of graphene: a review. *Nanoscale* **2016**, *8*, 3207-3217.

(360) Amorim, B.; Cortijo, A.; de Juan, F.; Grushine, A. G.; Guinea, F.; Gutierrez-Rubio, A.; Ochoa, H.; Parente, V.; Roldan, R.; San-Jose, P.; Schiefele, J.; Sturla, M.; Vozmediano, M. A. H.: Novel effects of strains in graphene and other two dimensional materials. *Phys. Rep.-Rev. Sec. Phys. Lett.* **2016**, *617*, 1-54.

(361) Bissett, M. A.; Tsuji, M.; Ago, H.: Strain engineering the properties of graphene and other two-dimensional crystals. *Physical Chemistry Chemical Physics* **2014**, *16*, 11124-11138.

(362) Zhou, S. Y.; Gweon, G. H.; Fedorov, A. V.; First, P. N.; De Heer, W. A.; Lee, D. H.; Guinea, F.; Castro Neto, A. H.; Lanzara, A.: Substrate-induced bandgap opening in epitaxial graphene. *Nature Materials* **2007**, *6*, 770-775.

(363) Park, J.; Jo, S. B.; Yu, Y. J.; Kim, Y.; Yang, W.; Lee, W. H.; Kim, H. H.; Hong, B. H.; Kim, P.; Cho, K.; Kim, K. S.: Single-Gate Bandgap Opening of Bilayer Graphene by Dual Molecular Doping. *Advanced Materials* **2012**, *24*, 407-+.

(364) Oostinga, J. B.; Heersche, H. B.; Liu, X.; Morpurgo, A. F.; Vandersypen, L. M. K.: Gate-induced insulating state in bilayer graphene devices. *Nat Mater* **2008**, *7*, 151-157.

(365) Santos, E. J. G.; Kaxiras, E.: Electric-Field Dependence of the Effective Dielectric Constant in Graphene. *Nano Lett.* **2013**, *13*, 898-902.

(366) Balog, R.; Jorgensen, B.; Nilsson, L.; Andersen, M.; Rienks, E.; Bianchi, M.; Fanetti, M.; Laegsgaard, E.; Baraldi, A.; Lizzit, S.; Sljivancanin, Z.; Besenbacher, F.; Hammer, B.; Pedersen, T. G.; Hofmann, P.; Hornekaer, L.: Bandgap opening in graphene induced by patterned hydrogen adsorption. *Nat Mater* **2010**, *9*, 315-319.

(367) Chua, C. K.; Pumera, M.: Covalent chemistry on graphene. *Chemical Society Reviews* **2013**, *42*, 3222-3233.

(368) Yin, H.; Tang, H.; Wang, D.; Gao, Y.; Tang, Z.: Facile Synthesis of Surfactant-Free Au Cluster/Graphene Hybrids for High-Performance Oxygen Reduction Reaction. *ACS Nano* **2012**, *6*, 8288-8297.

(369) Tsetseris, L.; Wang, B.; Pantelides, S. T.: Substitutional doping of graphene: The role of carbon divacancies. *Phys. Rev. B* **2014**, *89*.

(370) Zhang, Y. H.; Zhou, K. G.; Xie, K. F.; Zeng, J.; Zhang, H. L.; Peng, Y.: Tuning the electronic structure and transport properties of graphene by noncovalent functionalization: effects of organic donor, acceptor and metal atoms. *Nanotechnology* **2010**, *21*.

(371) Mao, H. Y.; Lu, Y. H.; Lin, J. D.; Zhong, S.; Wee, A. T. S.; Chen, W.: Manipulating the electronic and chemical properties of graphene via molecular functionalization. *Prog. Surf. Sci.* **2013**, *88*, 132-159.

(372) Jang, A. R.; Jeon, E. K.; Kang, D.; Kim, G.; Kim, B. S.; Kang, D. J.; Shin, H. S.: Reversibly Light-Modulated Dirac Point of Graphene Functionalized with Spiropyran. *ACS Nano* **2012**, *6*, 9207-9213.

(373) Peimyoo, N.; Li, J. W.; Shang, J. Z.; Shen, X. N.; Qiu, C. Y.; Xie, L. H.; Huang, W.; Yu, T.: Photocontrolled Molecular Structural Transition and Doping in Graphene. *ACS Nano* **2012**, *6*, 8878-8886.

(374) Ferrari, A. C.: Raman spectroscopy of graphene and graphite: Disorder, electron-phonon coupling, doping and nonadiabatic effects. *Solid State Communications* **2007**, *143*, 47-57.

(375) Ferrari, A. C.; Meyer, J. C.; Scardaci, V.; Casiraghi, C.; Lazzeri, M.; Mauri, F.; Piscanec, S.; Jiang, D.; Novoselov, K. S.; Roth, S.; Geim, A. K.: Raman spectrum of graphene and graphene layers. *Physical Review Letters* **2006**, *97*.

(376) Nemes-Incze, P.; Osvath, Z.; Kamaras, K.; Biro, L. P.: Anomalies in thickness measurements of graphene and few layer graphite crystals by tapping mode atomic force microscopy. *Carbon* **2008**, *46*, 1435-1442.

(377) Ishigami, M.; Chen, J. H.; Cullen, W. G.; Fuhrer, M. S.; Williams, E. D.: Atomic structure of graphene on SiO2. *Nano Lett.* **2007**, *7*, 1643-1648.

(378) Shearer, C. J.; Slattery, A. D.; Stapleton, A. J.; Shapter, J. G.; Gibson, C. T.: Accurate thickness measurement of graphene. *Nanotechnology* **2016**, *27*.

(379) Gupta, A.; Chen, G.; Joshi, P.; Tadigadapa, S.; Eklund, P. C.: Raman scattering from high-frequency phonons in supported n-graphene layer films. *Nano Lett* **2006**, *6*, 2667-73.

(380) Bonaccorso, F.; Sun, Z.; Hasan, T.; Ferrari, A. C.: Graphene photonics and optoelectronics. *Nat Photon* **2010**, *4*, 611-622.

(381) Warner, J. H.; Schaffel, F.; Bachmatiuk, A.; Rummeli, M. H.: *Graphene: Fundamentals and Emergent Applications*; Elsevier Science Bv: Amsterdam, 2013.

(382) Graf, D.; Molitor, F.; Ensslin, K.; Stampfer, C.; Jungen, A.; Hierold, C.; Wirtz, L.: Spatially resolved raman spectroscopy of single- and few-layer graphene. *Nano Lett.* **2007**, *7*, 238-242.

(383) Dong, X. C.; Fu, D. L.; Fang, W. J.; Shi, Y. M.; Chen, P.; Li, L. J.: Doping Single-Layer Graphene with Aromatic Molecules. *Small* **2009**, *5*, 1422-1426.

(384) Bobak, J. E.; Collins, D. J.; Chan, J. K.; Frank, N. L.: Conformational Modulation of Transport in Solution-Deposited Graphene- OFETs (SD-OFETs). *manuscript in preparation*.

(385) Kruger, M.; Widmer, I.; Nussbaumer, T.; Buitelaar, M.; Schonenberger, C.: Sensitivity of single multiwalled carbon nanotubes to the environment. *New J Phys* **2003**, *5*.

(386) Mali, K. S.; Greenwood, J.; Adisoejoso, J.; Phillipson, R.; De Feyter, S.: Nanostructuring graphene for controlled and reproducible functionalization. *Nanoscale* **2015**, *7*, 1566-1585.

(387) Pinto, H.; Markevich, A.: Electronic and electrochemical doping of graphene by surface adsorbates. *Beilstein J Nanotech* **2014**, *5*, 1842-1848.

(388) Kahn, A.: Fermi level, work function and vacuum level. *Mater Horiz* **2016**, *3*, 7-10.

(389) Connelly, N. G.; Geiger, W. E.: Chemical Redox Agents for Organometallic Chemistry. *Chemical Reviews* **1996**, *96*, 877-910.

(390) Trasatti, S.: The Absolute Electrode Potential - an Explanatory Note (Recommendations 1986). *Pure Appl Chem* **1986**, *58*, 955-966.

(391) Xu, K.; Zeng, C. F.; Zhang, Q.; Yan, R. S.; Ye, P. D.; Wang, K.; Seabaugh, A. C.; Xing, H. G.; Suehle, J. S.; Richter, C. A.; Gundlach, D. J.; Nguyen, N. V.: Direct Measurement of Dirac Point Energy at the Graphene/Oxide Interface. *Nano Lett.* **2013**, *13*, 131-136.

(392) Bodnar, S. H.; Caneschi, A.; Dei, A.; Shultz, D. A.; Sorace, L.: A bis-bidentate dioxolene ligand induces thermal hysteresis in valence tautomerism interconversion processes. *Chemical Communications* **2001**, 2150-2151.

(393) Beni, A.; Dei, A.; Shultz, D. A.; Sorace, L.: Ligand design modulates photoinduced properties of cobalt-dioxolene valence tautomers. *Chemical Physics Letters* **2006**, *428*, 400-404.

(394) Carbonera, C.; Dei, A.; Letard, J. F.; Sangregorio, C.; Sorace, L.: Thermally and Light-Induced Valence Tautomeric Transition in a Dinuclear Cobalt-Tetraoxolene Complex. *Angew. Chem.-Int. Edit.* **2004**, *43*, 3136-3138.

(395) Tao, J.; Maruyama, H.; Sato, O.: Valence tautomeric transitions with thermal hysteresis around room temperature and photoinduced effects observed in a cobalt-tetraoxolene complex. *Journal of the American Chemical Society* **2006**, *128*, 1790-1791.

(396) Li, G. L.; Kanegawa, S.; Yao, Z. S.; Su, S. Q.; Wu, S. Q.; Huang, Y. G.; Kang, S.; Sato, O.: Influence of Intermolecular Interactions on Valence Tautomeric Behaviors in Two Polymorphic Dinuclear Cobalt Complexes. *Chemistry-a European Journal* **2016**, *22*, 17130-17135.

(397) Alley, K. G.; Poneti, G.; Robinson, P. S. D.; Nafady, A.; Moubaraki, B.; Aitken, J. B.; Drew, S. C.; Ritchie, C.; Abrahams, B. F.; Hocking, R. K.; Murray, K. S.; Bond, A. M.; Harris, H. H.; Sorace, L.; Boskovic, C.: Redox Activity and Two-Step Valence Tautomerism in a Family of Dinuclear Cobalt Complexes with a Spiroconjugated Bis(dioxolene) Ligand. *Journal of the American Chemical Society* **2013**, *135*, 8304-8323.

(398) Néel, L.: Théorie du traînage magnétique des ferromagnétiques en grains fins avec application aux terres cuites. *Annales de Géophysique* **1949**, *5*, 99-136.

(399) Brown, W. F.: Thermal fluctuations of a single-domain particle. *Physical Review* **1963**, *130*, 1677-1686.

(400) Lu, A. H.; Salabas, E. L.; Schuth, F.: Magnetic nanoparticles: Synthesis, protection, functionalization, and application. *Angew. Chem.-Int. Edit.* **2007**, *46*, 1222-1244.

(401) Hofmann-Amtenbrink, M.; von Rechenberg, B.; Hofmann, H.; Tan, M.: *Superparamagnetic Nanoparticles for Biomedical Applications*, 2009; Vol. 65.

(402) Mahmoodi, N. O.; Ghavidast, A.; Amirmahani, N.: A comparative study on the nanoparticles for improved drug delivery systems. *Journal of Photochemistry and Photobiology B: Biology* **2016**, *162*, 681-693.

(403) Mikami, R.; Taguchi, M.; Yamada, K.; Suzuki, K.; Sato, O.; Einaga, Y.: Reversible photo-switching of the magnetization of iron oxide nanoparticles at room temperature. *Angew. Chem.-Int. Edit.* **2004**, *43*, 6135-6139.

(404) Suda, M.; Nakagawa, M.; Iyoda, T.; Einaga, Y.: Reversible photoswitching of ferromagnetic FePt nanoparticles at room temperature. *Journal of the American Chemical Society* **2007**, *129*, 5538-5543.

(405) Al-Aqtash, N.; Sabirianov, R.: Photo-switching of magnetization in iron nanoparticles. *Journal of Materials Chemistry C* **2014**, *2*, 6873-6878.

Appendix A. NMR Spectra

Figure A1. ^{1}H NMR spectrum of **2.1** in $CDCl_3$ at 300 K recorded with a 500 MHz spectrometer.

Figure A2. ^{13}C NMR spectrum of 2.1 in CDCl3 at 300 K recorded with a 300 MHz spectrometer.

Figure A3. DEPT135 NMR spectrum of **2.1** in $CDCl_3$ at 300 K recorded with a 300 MHz spectrometer.

Figure A4. ^{1}H NMR spectrum of Mn(APSO)$(hfac)_2$ **3.1a** in toluene-d_8 at 300 K recorded with a 500 MHz spectrometer.

Figure A5. ^{1}H NMR spectrum of Co(APSO)$(hfac)_2$ **3.1b** in toluene-d_8 at 300 K recorded with a 500 MHz spectrometer.

Figure A6. ^{1}H NMR spectrum of Ni(APSO)$(hfac)_2$ **3.1c** in toluene-d_8 at 300 K recorded with a 500 MHz spectrometer.

Figure A7. ^{19}F NMR spectrum of Co(APSO)$(hfac)_2$ **3.1b** in toluene-d_8 at 300 K recorded with a 300 MHz spectrometer.

Figure A8. ^{19}F NMR spectrum of Ni(APSO)$(hfac)_2$ **3.1c** in toluene-d_8 at 300 K recorded with a 300 MHz spectrometer.

Figure A9. ^{1}H NMR spectrum of $Fe(APSO)_{3\cdot}(BPh_4)_2$ **3.2b** in THF-d_8 at 300 K recorded with a 500 MHz spectrometer.

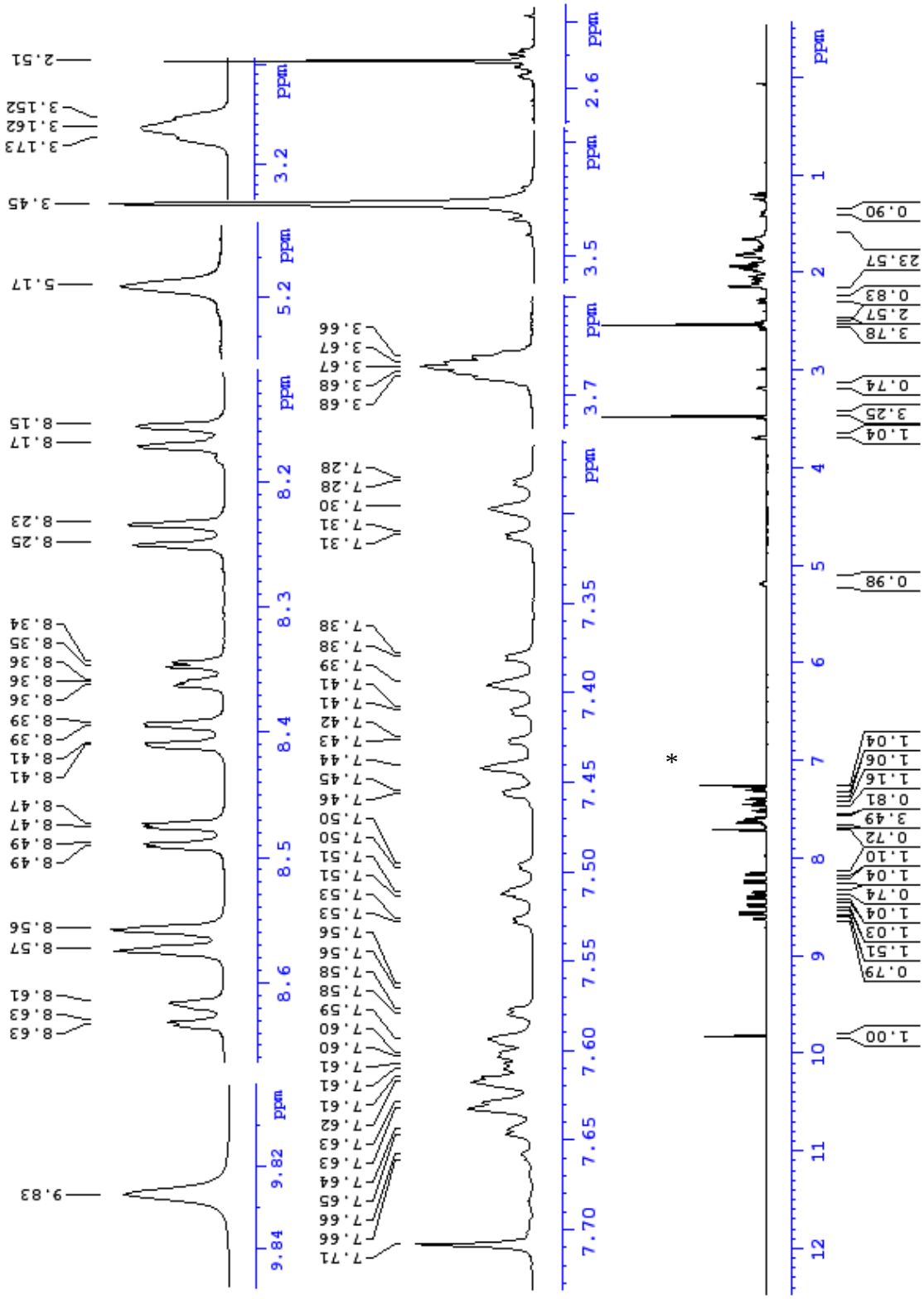

Figure A1. ^{1}H NMR spectrum of **2.1** in $CDCl_3$ at 300 K recorded with a 500 MHz spectrometer. (* $CDCl_3$ solvent)

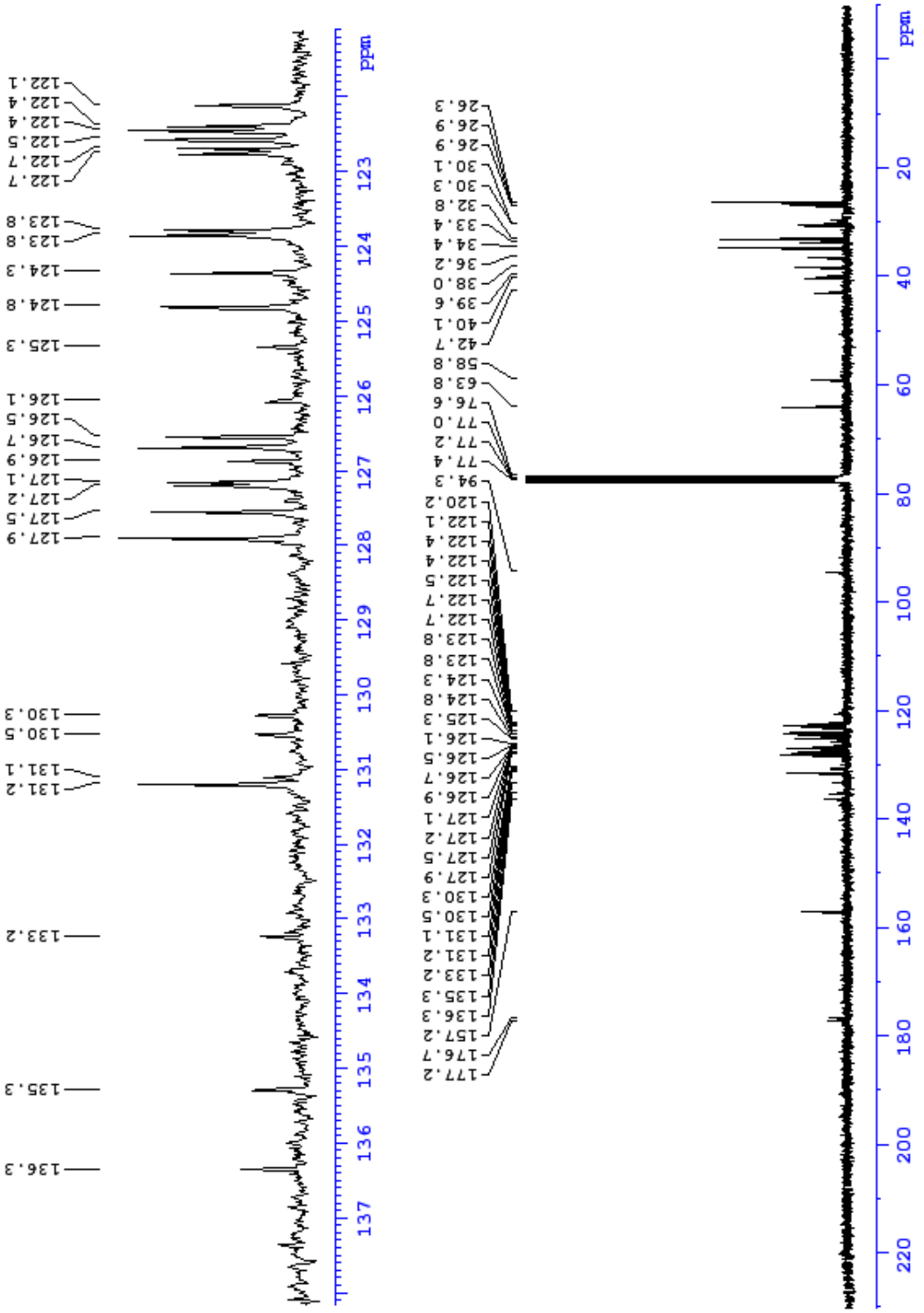

Figure A2. ^{13}C NMR spectrum of **2.1** in $CDCl_3$ at 300 K recorded with a 300 MHz spectrometer. (*$CDCl_3$ solvent)

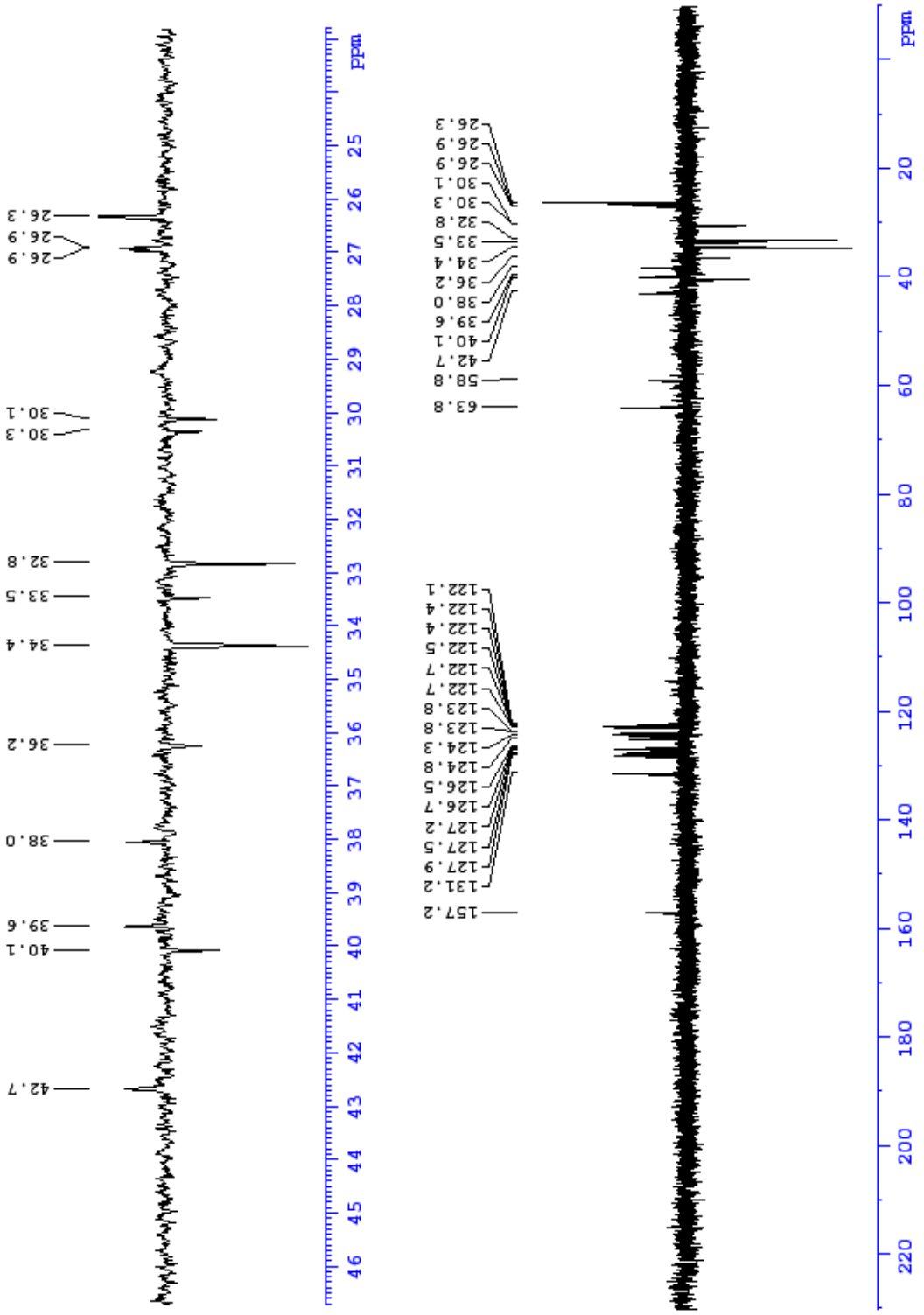

Figure A3. DEPT135 NMR spectrum of **2.1** in $CDCl_3$ at 300 K recorded with a 300 MHz spectrometer.

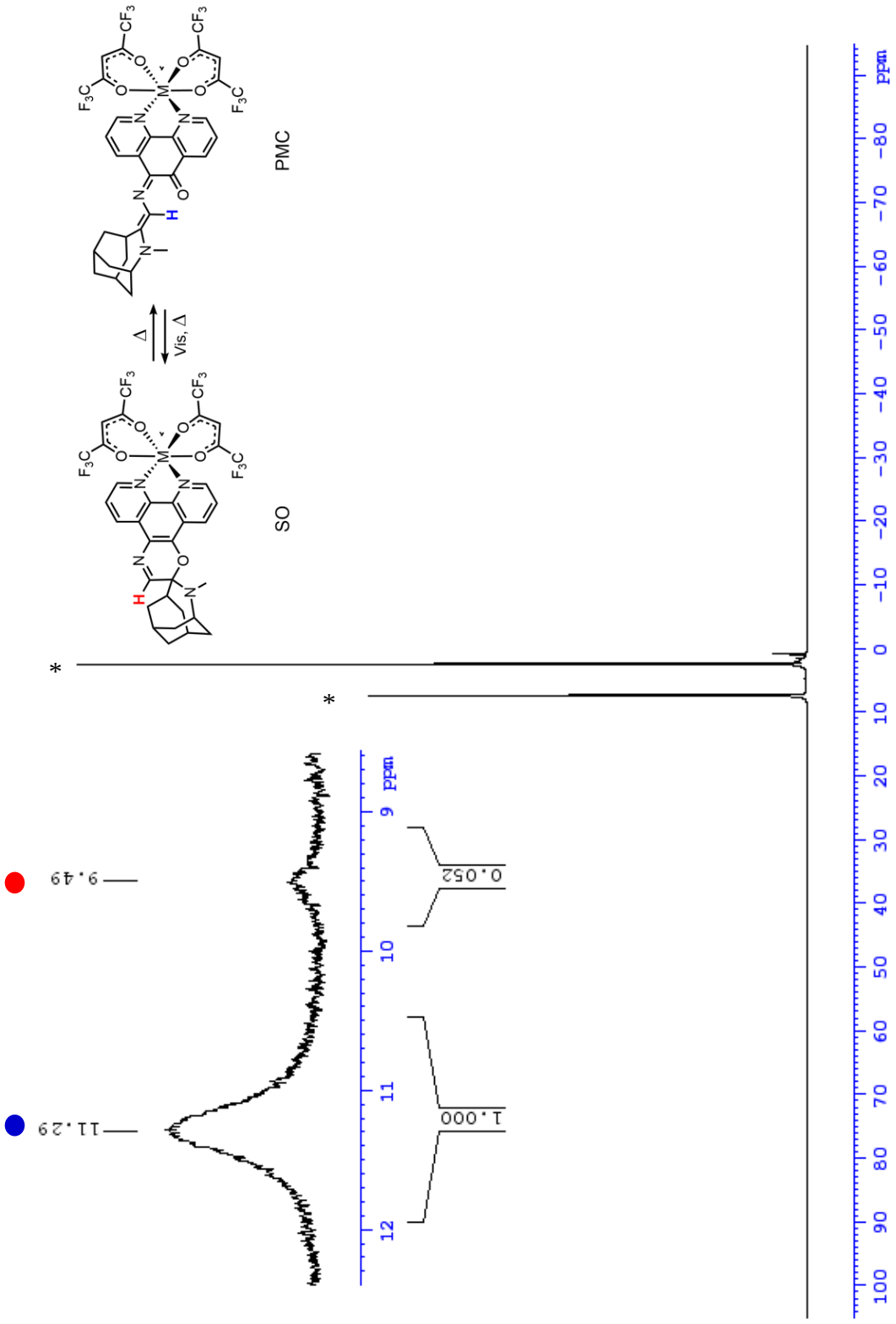

Figure A4. ^{1}H NMR spectrum of Mn(APSO)(hfac)$_2$ **3.1a** in toluene-d_8 at 300 K recorded with a 500 MHz spectrometer. (* toluene-d_8)

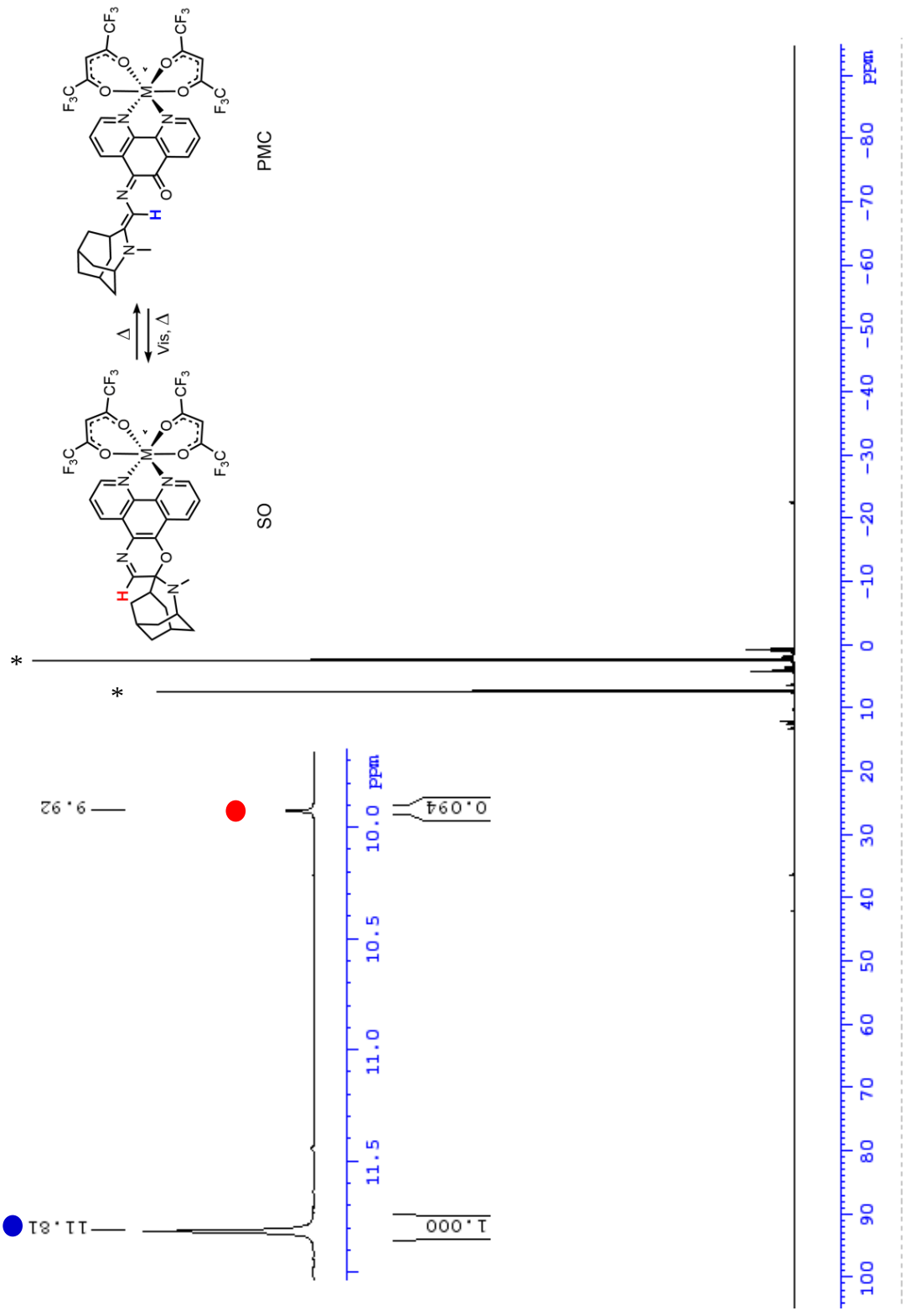

Figure A5. ^{1}H NMR spectrum of Co(APSO)(hfac)$_2$ **3.1b** in toluene-d_8 at 300 K recorded with a 500 MHz spectrometer. (* toluene-d_8)

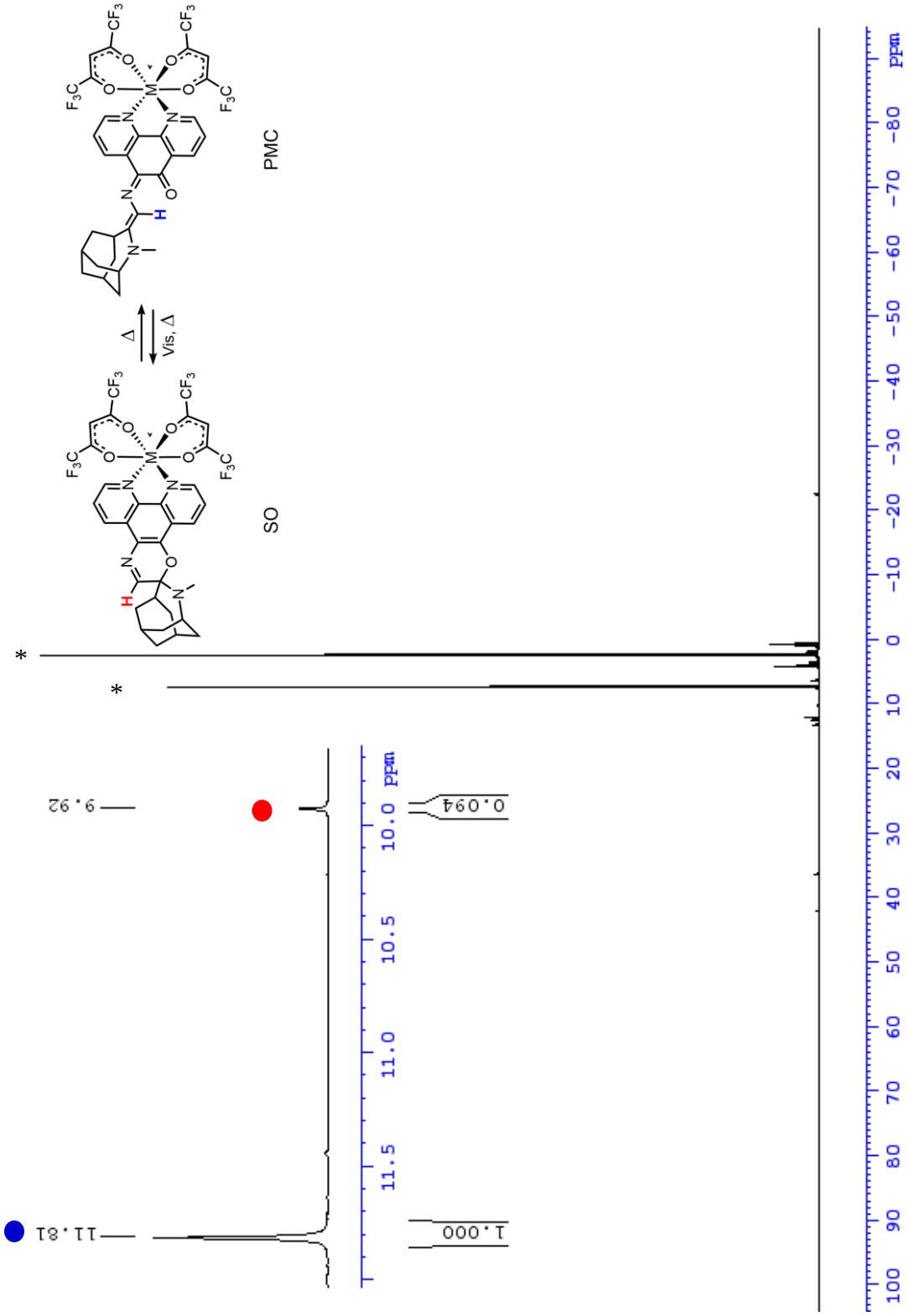

Figure A6. ^{1}H NMR spectrum of Ni(APSO)(hfac)$_2$ **3.1c** in toluene-d_8 at 300 K recorded with a 500 MHz spectrometer. (* toluene-d_8)

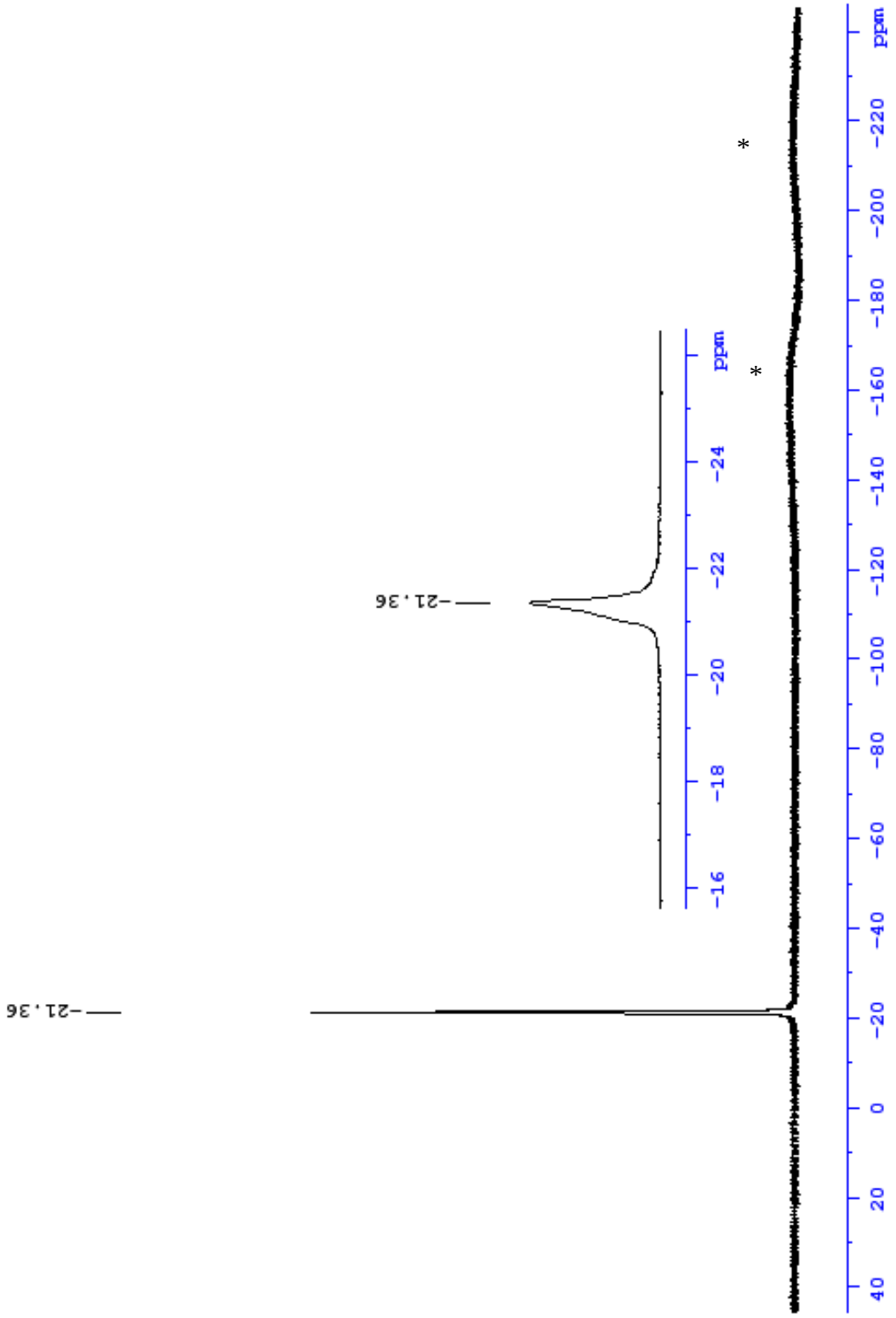

Figure A7. ^{19}F NMR spectrum of Co(APSO)(hfac)$_2$ **3.1b** in toluene-d_8 at 300 K recorded with a 300 MHz spectrometer. (* are background signals from the ^{19}F contained in the coaxial cable and ceramic part in the probe.[1]

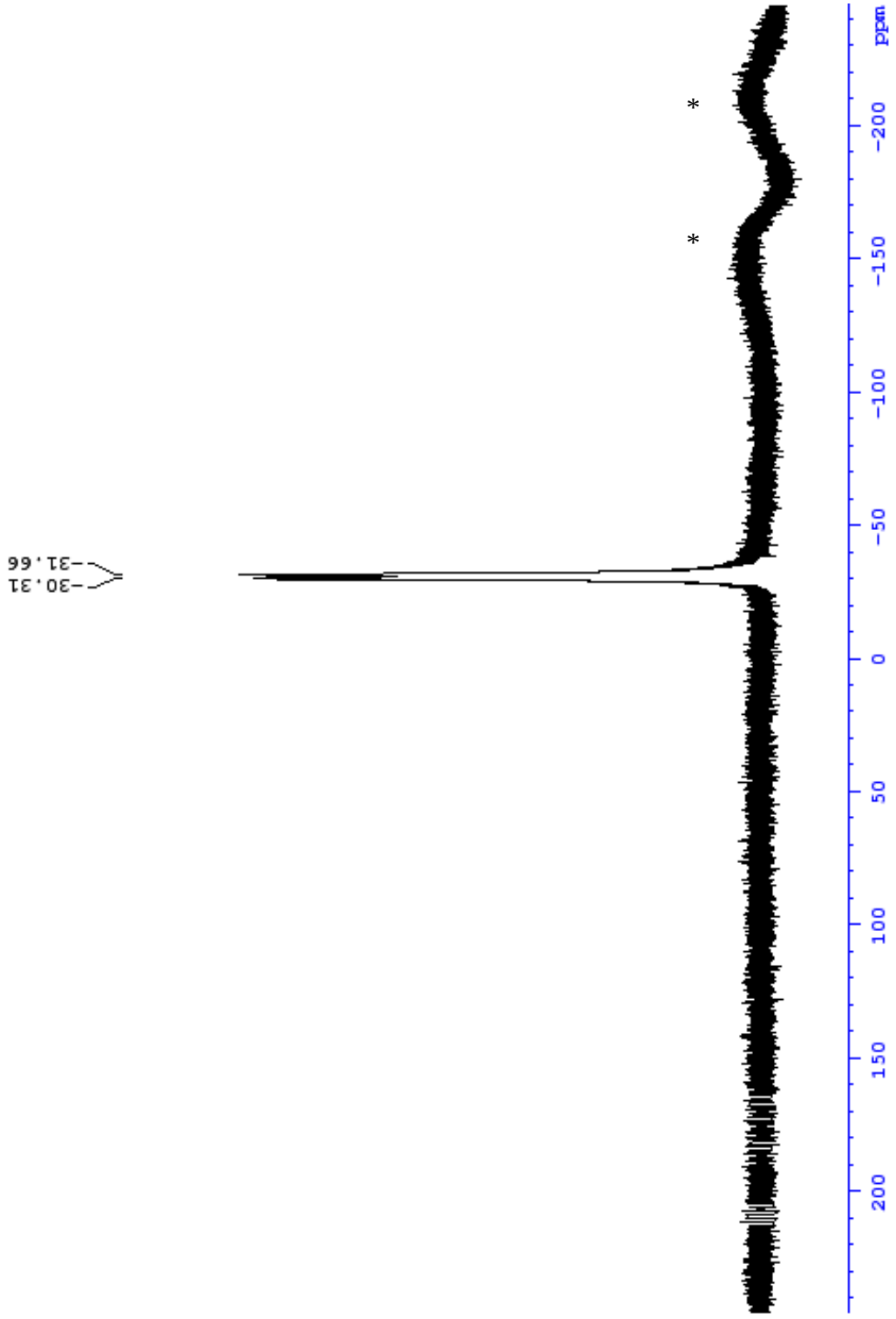

Figure A8. ^{19}F NMR spectrum of Ni(APSO)(hfac)$_2$ **3.1c** in toluene-d_8 at 300 K recorded with a 300 MHz spectrometer. (* are background signals from the ^{19}F contained in the coaxial cable and ceramic part in the probe.[1]

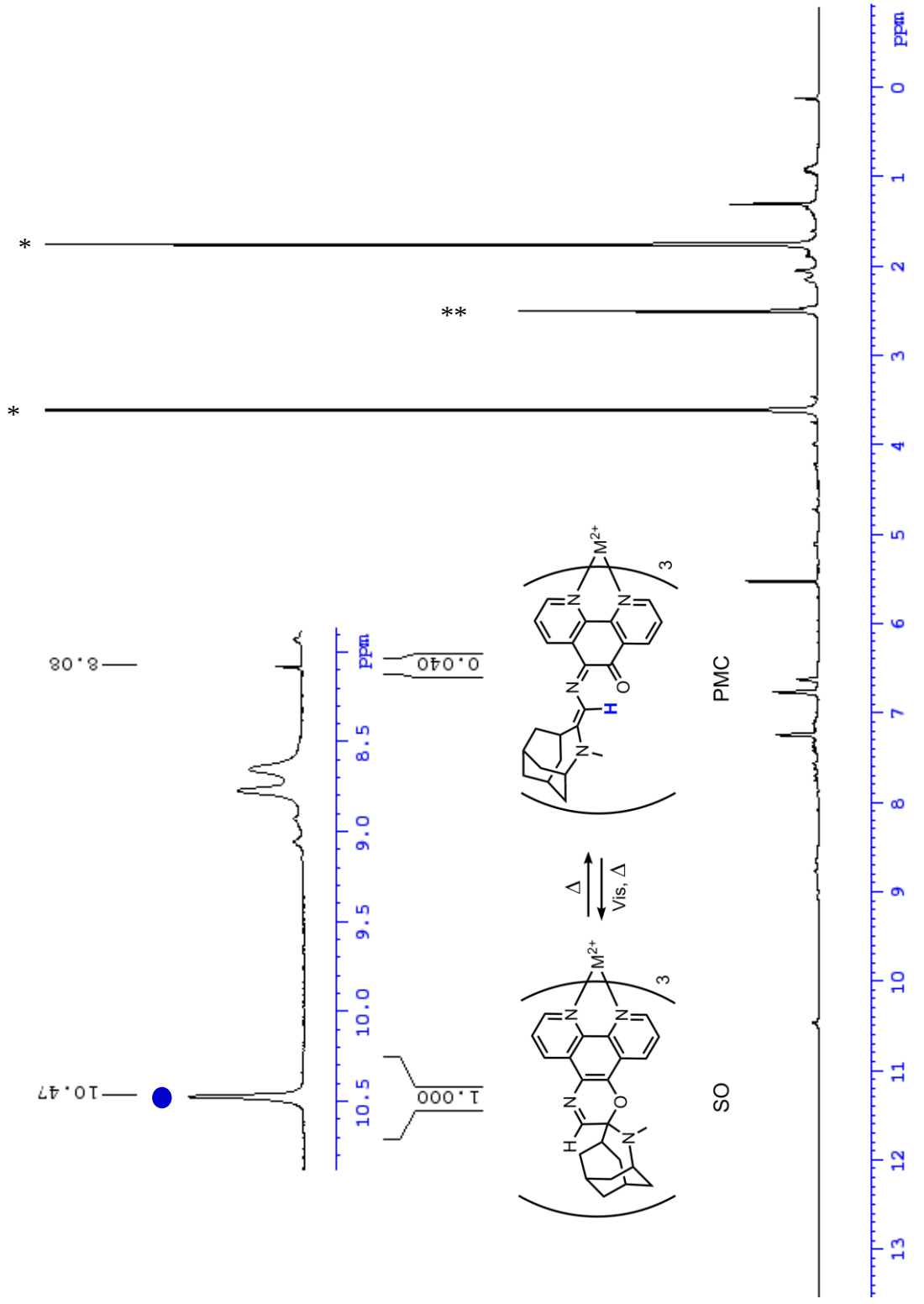

Figure A9. ^{1}H NMR spectrum of $Fe(APSO)_3 \cdot (BPh_4)_2$ **3.2b** in THF-d_8 at 300 K recorded with a 500 MHz spectrometer. (* and ** are THF-d_8 and water, respectively)

Appendix B. Crystallographic Parameters

Table B1. Crystallographic data and refinement parameters for APESO **2.1** and CoIPSO cluster **4.4**.

Figure B1. ORTEP representations of crystal structure of **2.1** for which bond lengths and angles are tabulated. Thermal ellipsoids presented at the 50 % probability level.

Table B2. Bond lengths [Å] for APESO **2.1**.

Table B3. Bond angles [°] for APESO **2.1**.

Figure B2. ORTEP representations of crystal structure of **4.4** for which bond lengths and angles are tabulated. Hydrogen atoms, t-butyl carbons and minor disordered fragments omitted for clarity. Thermal ellipsoids presented at the 25 % probability level.

Figure B3. Ball-and-stick representation of the coordination sphere around both Co1 and Co2 (major disordered fragment); hydrogen atoms, t-butyl carbons and indolyl fragment omitted for clarity.

Figure B4. Ball-and-stick representation of the coordination sphere around both Co1 and Co2 (minor disordered fragment); hydrogen atoms, t-butyl carbons and indolyl fragment omitted for clarity.

Table B4. Bond lengths [Å] for CoIPSO cluster **4.4**.

Table B5. Bond angles [°] for CoIPSO cluster **4.4**.

Table B1. Crystallographic data and refinement parameters for APESO **2.1** and CoIPSO cluster **4.4**.

	2.1	**4.4**
Empirical Formula	$C_{26}H_{26}N_2O$	$C_{136}H_{178}Co_4N_9O_{18}$
Formula Weight	382.49	2462.58
Crystal color	purple	blue
Crystal dimensions /mm	0.28 × 0.34 × 0.36	0.44×0.19×0.15
a (Å)	9.1082(3)	15.9002(9)
b (Å)	19.1136(7)	28.7289(15)
c (Å)	11.4675(4)	29.3550(16)
α (°)	90	90
β (°)	99.715(1)	90
γ (°)	90	90
V (Å^3)	1967.8(1)	13409.2(13)
Z	4	4
Space group	$P2_1/c$	*Pbca*
T (K)	90(1)	90(2)
λ (Å)	0.71073	1.54178
D_{calcd} (g cm^{-3})	1.291	1.220
μ (cm^{-1})	0.79	4.325
2θmax (°)	60.1	50.466
total reflections	34928	26880
unique reflections	5751	6893
R_{int}	0.020	0.0619
solution method	direct	dual space
R [all data] [a]	0.048	0.1925
R_w [all data] [b]	0.117	0.3733

[a] $R_1 = \Sigma\ ||F_o| - |F_c|| / \Sigma\ |F_o|$. [b] $wR_2 = [\Sigma(\ w(F_o^2 - F_c^2)^2)/\Sigma w(F_o^2)^2]^{1/2}$.

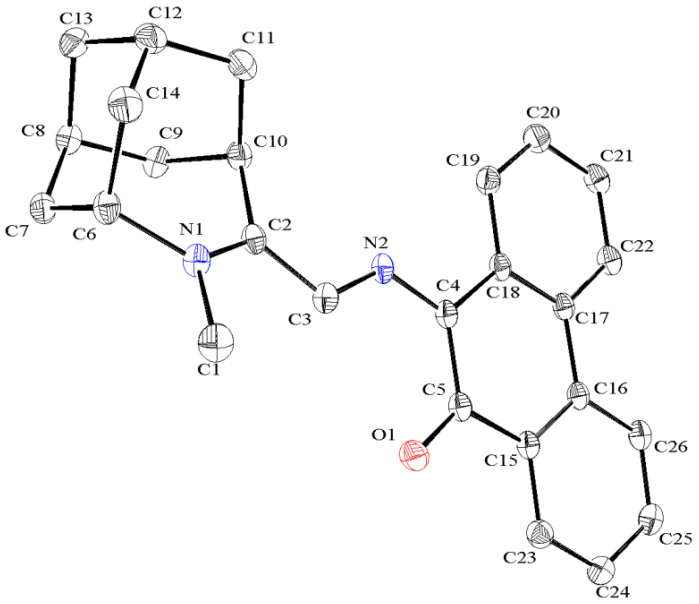

Figure B1. ORTEP representations of crystal structure of **2.1** for which bond lengths and angles are tabulated. Thermal ellipsoids presented at the 50 % probability level.

Table B2. Bond lengths [Å] for APESO **2.1**.

C(1)–N(1)	1.4696(13)	C(7)–H(7B)	0.9900
C(1)–H(1A)	0.9800	C(8)–C(9)	1.5276(13)
C(1)–H(1B)	0.9800	C(8)–C(13)	1.5368(14)
C(1)–H(1C)	0.9800	C(8)–H(8)	1.0000
C(2)–N(1)	1.3347(12)	C(9)–C(10)	1.5449(13)
C(2)–C(3)	1.4238(13)	C(9)–H(9A)	0.9900
C(2)–C(10)	1.5120(13)	C(9)–H(9B)	0.9900
C(3)–N(2)	1.3322(12)	C(10)–C(11)	1.5398(14)
C(3)–H(3)	0.9500	C(10)–H(10)	1.0000
C(4)–N(2)	1.3389(12)	C(11)–C(12)	1.5339(14)
C(4)–C(5)	1.4557(13)	C(11)–H(11A)	0.99
C(4)–C(18)	1.4691(12)	C(11)–H(11B)	0.99
C(5)–O(1)	1.2511(11)	C(12)–C(14)	1.5304(15)
C(5)–C(15)	1.4851(13)	C(12)–C(13)	1.5346(15)
C(6)–N(1)	1.4928(12)	C(12)–H(12)	1.0000

C(6)–C(7)	1.5320(13)	C(13)–H(13A)	0.9900
C(6)–C(14)	1.5340(14)	C(13)–H(13B)	0.9900
C(6)–H(6)	1.0000	C(14)–H(14A)	0.9900
C(7)–C(8)	1.5316(13)	C(14)–H(14B)	0.9900
C(7)–H(7A)	0.9900	C(15)–C(23)	1.4058(13)
C(15)–C(16)	1.4085(12)	C(21)–C(22)	1.3815(14)
C(16)–C(26)	1.4113(13)	C(21)–H(21)	0.9500
C(16)–C(17)	1.4658(13)	C(22)–H(22)	0.9500
C(17)–C(22)	1.4094(12)	C(23)–C(24)	1.3820(14)
C(17)–C(18)	1.4167(13)	C(23)–H(23)	0.9500
C(18)–C(19)	1.4101(13)	C(24)–C(25)	1.3982(14)
C(19)–C(20)	1.3842(13)	C(24)–H(24)	0.9500
C(19)–H(19)	0.9500	C(25)–C(26)	1.3831(14)
C(20)–C(21)	1.3987(14)	C(25)–H(25)	0.9500
C(20)–H(20)	0.9500	C(26)–H(26)	0.9500

Table B3. Bond angles [°] for APESO **2.1**.

N(1)–C(1)–H(1A)	109.5	C(6)–C(7)–H(7B)	108.8
N(1)–C(1)–H(1B)	109.5	H(7A)–C(7)–H(7B)	107.7
H(1A)–C(1)–H(1B)	109.5	C(9)–C(8)–C(7)	112.15(8)
N(1)–C(1)–H(1C)	109.5	C(9)–C(8)–C(13)	109.15(8)
H(1A)–C(1)–H(1C)	109.5	C(7)–C(8)–C(13)	110.03(8)
H(1B)–C(1)–H(1C)	109.5	C(9)–C(8)–H(8)	108.5
N(1)–C(2)–C(3)	120.10(9)	C(7)–C(8)–H(8)	108.5
N(1)–C(2)–C(10)	120.64(8)	C(13)–C(8)–H(8)	108.5
C(3)–C(2)–C(10)	119.24(8)	C(8)–C(9)–C(10)	113.37(8)
N(2)–C(3)–C(2)	118.16(9)	C(8)–C(9)–H(9A)	108.9
N(2)–C(3)–H(3)	120.9	C(10)–C(9)–H(9A)	108.9
C(2)–C(3)–H(3)	120.9	C(8)–C(9)–H(9B)	108.9
N(2)–C(4)–C(5)	124.53(8)	C(10)–C(9)–H(9B)	108.9
N(2)–C(4)–C(18)	115.79(8)	H(9A)–C(9)–H(9B)	107.7
C(5)–C(4)–C(18)	119.62(8)	C(2)–C(10)–C(11)	114.15(8)
O(1)–C(5)–C(4)	122.93(8)	C(2)–C(10)–C(9)	112.57(8)
O(1)–C(5)–C(15)	119.54(8)	C(11)–C(10)–C(9)	111.18(8)
C(4)–C(5)–C(15)	117.51(8)	C(2)–C(10)–H(10)	106.1
N(1)–C(6)–C(7)	112.59(7)	C(11)–C(10)–H(10)	106.1
N(1)–C(6)–C(14)	112.17(8)	C(9)–C(10)–H(10)	106.1
N(1)–C(1)–H(1A)	109.5	C(6)–C(7)–H(7B)	108.8
N(1)–C(1)–H(1B)	109.5	H(7A)–C(7)–H(7B)	107.7
H(1A)–C(1)–H(1B)	109.5	C(9)–C(8)–C(7)	112.15(8)
N(1)–C(1)–H(1C)	109.5	C(9)–C(8)–C(13)	109.15(8)
H(1A)–C(1)–H(1C)	109.5	C(7)–C(8)–C(13)	110.03(8)
H(1B)–C(1)–H(1C)	109.5	C(9)–C(8)–H(8)	108.5
N(1)–C(2)–C(3)	120.10(9)	C(7)–C(8)–H(8)	108.5
N(1)–C(2)–C(10)	120.64(8)	C(13)–C(8)–H(8)	108.5

C(11)–C(12)–C(13)	109.42(9)	C(20)–C(19)–C(18)	121.44(9)
C(14)–C(12)–H(12)	108.5	C(20)–C(19)–H(19)	119.3
C(11)–C(12)–H(12)	108.5	C(18)–C(19)–H(19)	119.3
C(13)–C(12)–H(12)	108.5	C(19)–C(20)–C(21)	120.05(9)
C(12)–C(13)–C(8)	109.24(8)	C(19)–C(20)–H(20)	120.0
C(12)–C(13)–H(13A)	109.8	C(21)–C(20)–H(20)	120.0
C(8)–C(13)–H(13A)	109.8	C(22)–C(21)–C(20)	119.59(9)
C(12)–C(13)–H(13B)	109.8	C(22)–C(21)–H(21)	120.2
C(8)–C(13)–H(13B)	109.8	C(20)–C(21)–H(21)	120.2
H(13A)–C(13)–H(13B)	108.3	C(21)–C(22)–C(17)	121.35(9)
C(12)–C(14)–C(6)	113.54(8)	C(21)–C(22)–H(22)	119.3
C(12)–C(14)–H(14A)	108.9	C(17)–C(22)–H(22)	119.3
C(6)–C(14)–H(14A)	108.9	C(24)–C(23)–C(15)	121.03(9)
C(12)–C(14)–H(14B)	108.9	C(24)–C(23)–H(23)	119.5
C(6)–C(14)–H(14B)	108.9	C(15)–C(23)–H(23)	119.5
H(14A)–C(14)–H(14B)	107.7	C(23)–C(24)–C(25)	119.30(9)
C(23)–C(15)–C(16)	119.86(9)	C(23)–C(24)–H(24)	120.3
C(23)–C(15)–C(5)	118.21(8)	C(25)–C(24)–H(24)	120.3
C(16)–C(15)–C(5)	121.93(8)	C(26)–C(25)–C(24)	120.48(9)
C(15)–C(16)–C(26)	118.20(9)	C(26)–C(25)–H(25)	119.8
C(15)–C(16)–C(17)	119.93(8)	C(24)–C(25)–H(25)	119.8
C(26)–C(16)–C(17)	121.87(8)	C(25)–C(26)–C(16)	121.03(9)
C(22)–C(17)–C(18)	119.21(9)	C(25)–C(26)–H(26)	119.5
C(22)–C(17)–C(16)	121.21(8)	C(16)–C(26)–H(26)	119.5
C(18)–C(17)–C(16)	119.58(8)	C(2)–N(1)–C(1)	121.16(8)
C(19)–C(18)–C(17)	118.35(8)	C(2)–N(1)–C(6)	124.12(8)
C(19)–C(18)–C(4)	120.28(8)	C(1)–N(1)–C(6)	114.72(8)
C(17)–C(18)–C(4)	121.35(8)	C(3)–N(2)–C(4)	125.78(8)

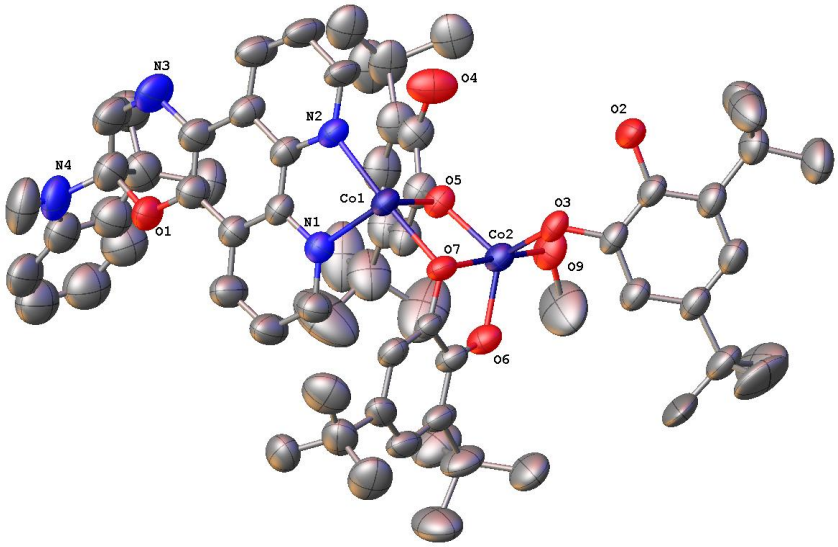

Figure B2. ORTEP representations of crystal structure of **4.4** for which bond lengths and angles are tabulated. Hydrogen atoms, t-butyl carbons and minor disordered fragments omitted for clarity. Thermal ellipsoids presented at the 25 % probability level.

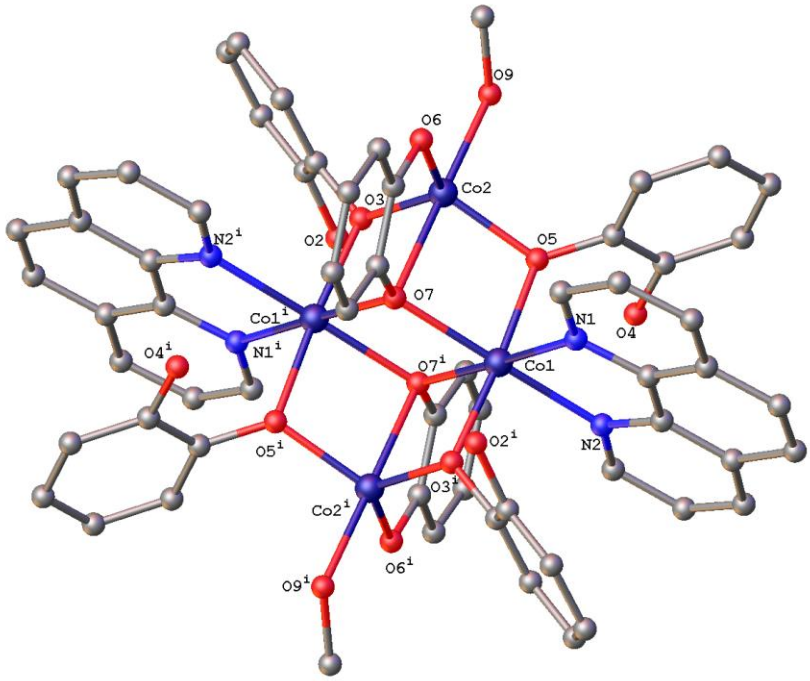

Figure B3. Ball-and-stick representation of the coordination sphere around both Co1 and Co2 (major disordered fragment); hydrogen atoms, t-butyl carbons and indolyl fragment omitted for clarity. (i) 1-X, 1-Y, 1-Z

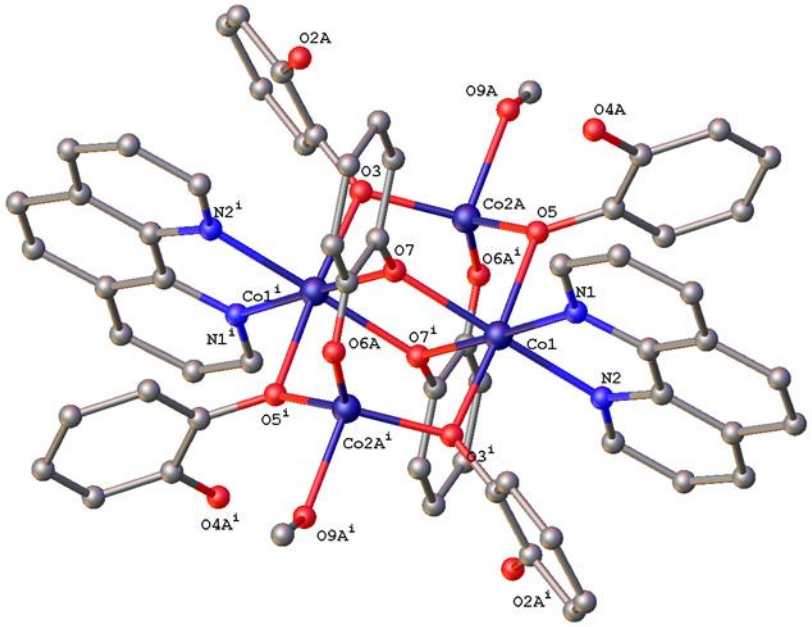

Figure B4. Ball-and-stick representation of the coordination sphere around both Co1 and Co2 (minor disordered fragment); hydrogen atoms, t-butyl carbons and indolyl fragment omitted for clarity. (i) 1-X, 1-Y, 1-Z

Table B4. Bond lengths [Å] for CoIPSO cluster **4.4**

Co(1)–O(3)’	2.069(7)	N(4)–C(23)	1.41(3)
Co(1)–O(5)	2.096(7)	N(4)–C(24)	1.28(3)
Co(1)–O(7)’	2.082(7)	C(1)–N(1)	1.3909
Co(1)–O(7)	2.114(6)	C(1)–C(2)	1.3895
Co(1)–N(1)	2.141(6)	N(1)–C(12)	1.3894
Co(1)–N(2)	2.121(5)	C(2)–C(3)	1.3897
Co(2)–O(3)	1.906(8)	C(3)–C(4)	1.392
Co(2)–O(5)	1.949(7)	C(4)–C(12)	1.3906
Co(2)–O(6)	1.913(11)	C(4)–C(5)	1.394(15)
Co(2)–O(7)	2.283(8)	C(12)–C(11)	1.344(8)
Co(2)–O(9)	2.109(10)	N(9)–C(13)	1.32(2)
Co(2A)–O(3)	1.875(9)	N(9)–C(68)	1.46(2)
Co(2A)–O(5)	1.837(10)	C(5)–C(6)	1.296(18)
Co(2A)–O(6A)’	1.70(2)	C(6)–C(7)	1.530(17)
Co(2A)–O(9A)	2.125(13)	C(7)–C(8)	1.3898

O(1)–C(5)	1.383(15)	C(25)–C(26)	1.3911
O(1)–C(14)	1.525(18)	C(25)–C(30)	1.3883
O(2)–C(25)	1.424(11)	C(26)–C(27)	1.3904
O(2A)–C(27)	1.52(4)	C(27)–C(28)	1.3909
O(3)–C(26)	1.379(8)	C(28)–C(29)	1.3887
O(4A)–C(41)	1.44(2)	C(28)–C(31)	1.508(15)
O(4)–C(39)	1.411(18)	C(29)–C(30)	1.3911
O(5)–C(40)	1.363(8)	C(30)–C(35)	1.575(17)
O(6)–C(54)	1.284(11)	C(31)–C(32)	1.478(12)
O(6A)–C(58)	1.19(3)	C(31)–C(33)	1.493(12)
O(7)–C(53)	1.354(8)	C(31)–C(34)	1.484(12)
O(9)–C(67)	1.538(17)	C(35)–C(36)	1.512(11)
O(9A)–C(67A)	1.43(6)	C(35)–C(37)	1.520(11)
N(3)–C(6)	1.431(18)	C(35)–C(38)	1.513(11)
N(3)–C(13)	1.36(2)	C(39)–C(40)	1.3903
N(4)–C(14)	1.43(2)	C(39)–C(44)	1.3925
C(7)–C(11)	1.3887	C(40)–C(41)	1.3901
N(2)–C(10)	1.3899	C(41)–C(42)	1.3918
N(2)–C(11)	1.3898	C(42)–C(43)	1.3887
C(8)–C(9)	1.3902	C(42)–C(45)	1.504(9)
C(9)–C(10)	1.3895	C(43)–C(44)	1.3886
C(13)–C(14)	1.38(2)	C(44)–C(49)	1.501(10)
C(14)–C(15)	1.80(3)	C(45)–C(46)	1.550(14)
C(15)–C(16)	1.49(2)	C(45)–C(47)	1.547(14)
C(15)–C(17)	1.486(19)	C(45)–C(48)	1.544(14)
C(15)–C(18)	1.33(3)	C(49)–C(50)	1.56(3)
C(18)–C(19)	1.3891	C(49)–C(50A)	1.487(19)
C(18)–C(23)	1.3899	C(49)–C(51)	1.52(3)
C(19)–C(20)	1.391	C(49)–C(51A)	1.490(19)
C(20)–C(21)	1.3892	C(49)–C(52)	1.553(10)
C(21)–C(22)	1.3888	C(49)–C(52A)	1.485(19)
C(22)–C(23)	1.3911	C(53)–C(54)	1.3896

C(53)–C(58)	1.3897	C(59)–C(60)	1.576(12)
C(54)–C(55)	1.3903	C(59)–C(61)	1.579(12)
C(55)–C(56)	1.3907	C(59)–C(62)	1.588(12)
C(55)–C(59)	1.545(16)	C(63)–C(64)	1.479(12)
C(56)–C(57)	1.3873	C(63)–C(65)	1.478(12)
C(57)–C(58)	1.3899	C(63)–C(66)	1.488(12)
C(57)–C(63)	1.53(2)		

Table B5. Bond angles [°] for CoIPSO cluster **4.4**.

O(3)'–Co(1)–O(5)	175.5(3)	O(5)–O(1)–C(14)	120.9(13)
O(3)'–Co(1)–O(7)'	85.7(3)	Co(2)–O(3)–Co(1)'	100.9(3)
O(3)'–Co(1)–O(7)	91.4(3)	C(26)–O(3)–Co(1)'	122.8(5)
O(3)'–Co(1)–N(1)	93.4(3)	C(26)–O(3)–Co(2)	124.1(5)
O(3)'–Co(1)–N(2)	91.3(3)	C(26)–O(3)–Co(2A)	128.3(6)
O(5)–Co(1)–O(7)	84.9(3)	Co(2)–O(5)–Co(1)	100.8(3)
O(5)–Co(1)–N(1)	90.1(3)	Co(2A)–O(5)–Co(1)	104.2(4)
O(5)–Co(1)–N(2)	92.4(3)	C(40)–O(5)–Co(1)	123.2(6)
O(7)'–Co(1)–O(5)	90.7(3)	C(40)–O(5)–Co(2)	127.6(6)
O(7)'–Co(1)–O(7)	72.0(3)	C(40)–O(5)–Co(2A)	124.9(6)
O(7)'–Co(1)–N(1)	105.1(3)	C(54)–O(6)–Co(2)	113.1(7)
O(7)'–Co(1)–N(1)	176.8(3)	C(58)–O(6A)–Co(2A)'	127.4(11)
O(7)–Co(1)–N(2)	176.3(3)	Co(1)'–O(7)–Co(1)	108.0(3)
O(7)'–Co(1)–N(2)	105.7(3)	Co(1)–O(7)–Co(2)	90.2(3)
N(2)–Co(1)–N(1)	77.4(3)	Co(1)'–O(7)–Co(2)	89.1(3)
O(3)–Co(2)–O(5)	113.9(3)	C(53)–O(7)–Co(1)'	125.8(5)
O(3)–Co(2)–O(6)	121.6(4)	C(53)–O(7)–Co(1)	123.9(5)
O(3)–Co(2)–O(7)	84.2(3)	C(53)–O(7)–Co(2)	104.1(5)
O(3)–Co(2)–O(9)	98.2(4)	C(67)–O(9)–Co(2)	113.1(13)
O(5)–Co(2)–O(7)	83.9(3)	C(67A)–O(9A)–Co(2A)	121(3)
O(5)–Co(2)–O(9)	95.9(4)	C(13)–N(3)–C(6)	112.4(15)
O(6)–Co(2)–O(5)	120.1(4)	C(23)–N(4)–C(14)	107(2)
O(6)–Co(2)–O(7)	81.0(4)	C(24)–N(4)–C(14)	116(3)
O(6)–Co(2)–O(9)	97.0(5)	C(24)–N(4)–C(23)	129(3)
O(9)–Co(2)–O(7)	177.5(4)	C(2)–C(1)–N(1)	120.0
O(3)–Co(2A)–O(9A)	100.3(8)	C(1)–N(1)–Co(1)	127.8(4)
O(5)–Co(2A)–O(3)	121.0(5)	C12–N(1)–Co(1)	112.2(4)
O(5)–Co(2A)–O(9A)	99.8(10)	C12–N(1)–C(1)	120.0
O(6A)'–Co(2A)–O(3)	112.5(11)	C(3)–C(2)–C(1)	120.0
O(6A)'–Co(2A)–O(5)	118.4(11)	C(2)–C(3)–C(4)	120.0
O(6A)'–Co(2A)–O(9A)	98.6(14)	C(3)–C(4)–C(5)	121.6(9)

C12–C(4)–C(3)	120.0	C(13)–C(14)–C(15)	110.4(19)
C12–C(4)–C(5)	118.5(9)	C(16)–C(15)–C(14)	109.1(19)
N(1)–C(12)–C(4)	120.0	C(17)–C(15)–C(14)	103(2)
C(11)–C(12)–N(1)	119.2(7)	C(17)–C(15)–C(16)	113(2)
C(11)–C(12)–C(4)	120.8(7)	C(18)–C(15)–C(14)	98(2)
C(13)–N(9)–C68	112.3(17)	C(18)–C(15)–C(16)	112(2)
O(1)–C(5)–C(4)	119.8(13)	C(18)–C(15)–C(17)	119(2)
C(6)–C(5)–O(1)	115.8(14)	C(15)–C(18)–C(19)	124(2)
C(6)–C(5)–C(4)	124.4(15)	C(15)–C(18)–C(23)	115(2)
N(3)–C(6)–C(7)	113.9(13)	C(19)–C(18)–C(23)	120.0
C(5)–C(6)–N(3)	127.8(16)	C(18)–C(19)–C(20)	120.0
C(5)–C(6)–C(7)	117.7(13)	C(21)–C(20)–C(19)	119.9
C(8)–C(7)–C(6)	123.8(8)	C(22)–C(21)–C(20)	120.1
C(11)–C(7)–C(6)	116.1(8)	C(21)–C(22)–C(23)	119.9
C(11)–C(7)–C(8)	120.1	C(18)–C(23)–N(4)	112(2)
C10–N(2)–Co(1)	126.3(4)	C(18)–C(23)–C(22)	120.0
C(11)–N(2)–Co(1)	113.7(4)	C(22)–C(23)–N(4)	128(2)
C(11)–N(2)–C(10)	120.0	C(26)–C(25)–O(2)	120.5(7)
C(7)–C(8)–C(9)	119.9	C(30)–C(25)–O(2)	119.5(7)
C(10)–C(9)–C(8)	120.1	C(30)–C(25)–C(26)	120.0
C(9)–C(10)–N(2)	120.0	O(3)–C(26)–C(25)	117.9(7)
C(12)–C(11)–C(7)	122.5(7)	O(3)–C(26)–C(27)	122.1(6)
C(12)–C(11)–N(2)	117.5(7)	C(27)–C(26)–C(25)	120.0
C(7)–C(11)–N(2)	120.0	C(26)–C(27)–O(2A)	121.2(12)
N(3)–C(13)–C(14)	127.2(19)	C(26)–C(27)–C(28)	119.9
N(9)–C(13)–N(3)	122(2)	C(28)–C(27)–O(2A)	118.5(12)
N(9)–C(13)–C(14)	110(2)	C(27)–C(28)–C(31)	124.8(6)
O(1)–C(14)–C(15)	105.3(13)	C(29)–C(28)–C(27)	120.0
N(4)–C(14)–O(1)	109.4(16)	C(29)–C(28)–C(31)	115.1(6)
N(4)–C(14)–C(15)	100.1(18)	C(28)–C(29)–C(30)	120.0

C(13)–C(14)–O(1)	110.4(17)	C(25)–C(30)–C(29)	120.0
C(13)–C(14)–N(4)	120(2)	C(25)–C(30)–C(35)	118.6(5)
C(29)–C(30)–C(35)	121.4(5)	C(47)–C(45)–C(46)	107.1(9)
C(32)–C(31)–C(28)	112.2(8)	C(48)–C(45)–C(46)	107.2(9)
C(32)–C(31)–C(33)	106.8(9)	C(48)–C(45)–C(47)	107.6(8)
C(32)–C(31)–C(34)	107.6(9)	C(44)–C(49)–C(50)	103.2(15)
C(33)–C(31)–C(28)	111.3(9)	C(44)–C(49)–C(51)	110.1(17)
C(34)–C(31)–C(28)	112.1(9)	C(44)–C(49)–C(52)	112.2(19)
C(34)–C(31)–C(33)	106.5(9)	C50A–C(49)–C(44)	110.5(15)
C(36)–C(35)–C(30)	113.4(9)	C50A–C(49)–C(51A)	103.7(12)
C(36)–C(35)–C(37)	105.8(9)	C(51)–C(49)–C(50)	110.8(13)
C(36)–C(35)–C(38)	106.0(9)	C(51)–C(49)–C(52)	111.1(14)
C(37)–C(35)–C(30)	112.7(8)	C(51A)–C(49)–C(44)	124(2)
C(38)–C(35)–C(30)	112.9(8)	C(52)–C(49)–C(50)	109.1(14)
C(38)–C(35)–C(37)	105.5(9)	C(52A)–C(49)–C(44)	109.1(19)
C(40)–C(39)–O(4)	120.5(10)	C(52A)–C(49)–C(50A)	103.9(12)
C(40)–C(39)–C(44)	119.9	C(52A)–C(49)–C(51A)	104.0(12)
C(44)–C(39)–O(4)	119.6(10)	O(7)–C(53)–C(54)	115.6(6)
O(5)–C(40)–C(39)	120.1(8)	O(7)–C(53)–C(58)	124.4(6)
O(5)–C(40)–C(41)	119.8(8)	C(54)–C(53)–C(58)	120.0
C(39)–C(40)–C(41)	120.1	O(6)–C(54)–C(53)	126.2(7)
C(40)–C(41)–O(4A)	123.2(11)	O(6)–C(54)–C(55)	113.8(7)
C(40)–C(41)–C(42)	120.0	C(53)–C(54)–C(55)	120.0
C(42)–C(41)–O(4A)	116.6(11)	C(54)–C(55)–C(56)	120.0
C(41)–C(42)–C(45)	121.9(10)	C(54)–C(55)–C(59)	127.2(6)
C(43)–C(42)–C(41)	120.0	C(56)–C(55)–C(59)	112.8(6)
C(43)–C(42)–C(45)	118.1(10)	C(57)–C(56)–C(55)	120.0
C(42)–C(43)–C(44)	120.1	C(56)–C(57)–C(58)	120.1
C(39)–C(44)–C(49)	125.3(11)	C(56)–C(57)–C(63)	123.5(6)
C(43)–C(44)–C(39)	120.0	C(58)–C(57)–C(63)	116.4(6)
C(43)–C(48)–C(49)	114.7(11)	O(6A)–C(58)–C(53)	121.0(5)
C(42)–C(45)–C(46)	112.3(15)	O(6A)–C(58)–C(57)	119.0(5)

C(42)–C(45)–C(47)	114.5(14)	C(53)–C(58)–C(57)	120.0
C(42)–C(45)–C(48)	107.8(13)	C(55)–C(59)–C(60)	109.2(8)
C(55)–C(59)–C(61)	109.4(8)	C(64)–C(63)–C(65)	119.4(14)
C(55)–C(59)–C(62)	109.8(8)	C(64)–C(63)–C(66)	94.8(15)
C(60)–C(59)–C(61)	122.4(15)	C(65)–C(63)–C(57)	111.2(10)
C(60)–C(59)–C(62)	104.8(14)	C(65)–C(63)–C(66)	105.9(16)
C(61)–C(59)–C(62)	100.3(13)	C(66)–C(63)–C(57)	112.2(10)
C(64)–C(63)–C(57)	112.0(10)		

Appendix C. Gaussian Output

Table C1. **2.1**-SO, geometry optimization, B3LYP/6-31+G(d,p)

Table C2. 2.1-TS1 (C-O bond cleavage), geometry optimization, B3LYP/6-31+G(d,p)

Table C3. 2.1-PMC-TCC, geometry optimization, B3LYP/6-31+G(d,p**)**

Table C4. 2.1-TS2 (*cis*-to-*trans* isomerization), geometry optimization, B3LYP/6-31+G(d,p)

Table C5. 2.1-PMC-TTC, geometry optimization, B3LYP/6-31+G(d,p)

Table C6. 2.2-SO, geometry optimization, B3LYP/6-31+G(d,p)

Table C7. 2.2-TS1 (C-O bond cleavage), geometry optimization, B3LYP/6-31+G(d,p)

Table C8. 2.2-PMC-TCC, geometry optimization, B3LYP/6-31+G(d,p)

Table C9. 2.2-TS2 (*cis*-to-*trans* isomerization), geometry optimization, B3LYP/6-31+G(d,p)

Table C10. 2.2-PMC-TTC, geometry optimization, B3LYP/6-31+G(d,p)

Table C11. 2.3-SO, geometry optimization, B3LYP/6-31+G(d,p)

Table C12. 2.3-TS1 (C-O bond cleavage), geometry optimization, B3LYP/6-31+G(d,p)

Table C13. 2.3-PMC-TCC, geometry optimization, B3LYP/6-31+G(d,p)

Table C14. 2.3-TS2 (*cis*-to-*trans* isomerization), geometry optimization, B3LYP/6-31+G(d,p)

Table C15. 2.3-PMC-TTC, geometry optimization, B3LYP/6-31+G(d,p)

Table C16. 2.4-SO, geometry optimization, B3LYP/6-31+G(d,p)

Table C17. 2.4-TS1 (C-O bond cleavage), geometry optimization, B3LYP/6-31+G(d,p)

Table C18. 2.4-PMC-TCC, geometry optimization, B3LYP/6-31+G(d,p)

Table C19. 2.4-TS2 (*cis*-to-*trans* isomerization), geometry optimization, B3LYP/6-31+G(d,p)

Table C20. 2.4-PMC-TTC, geometry optimization, B3LYP/6-31+G(d,p)

Table C21. 2.1-SO, geometry optimization, B3LYP/6-311+G(d,p)

Table C22. 2.1-PMC-TTC, geometry optimization, B3LYP/6-311+G(d,p)

Table C1. 2.1-SO, geometry optimization, B3LYP/6-31+G(d,p)


```
FOpt\RB3LYP\6-31+G(d,p)\C26H26N2O1\BRYNND\10-Jun
-2014\0\\# opt=tight b3lyp/6-31+g(d,p)\\APSOSO b3LYP/6-31G+(d,p)\\0,1\
N,-2.4864799399,-0.4696074592,1.4233557856\C,-0.687648511,-1.968725374
7,0.8310288205\H,-1.3186449804,-2.7894912312,1.1743360153\C,1.38064119
13,-1.0866844116,0.3414682194\C,0.8943181018,0.1971597968,0.4323341307
\N,0.5677637962,-2.1743043803,0.696662495\C,1.7479705924,1.3443460138,
0.2712648662\C,2.764369144,-1.3217206243,-0.0004562606\C,3.1212265269,
1.1423528858,-0.060015056\C,3.6357937332,-0.2146857756,-0.2200463765\C
,1.2399266584,2.655330643,0.4328267017\H,0.1931798462,2.7786703511,0.6
859223003\C,2.0625191402,3.7559132379,0.2773486224\H,1.6643227448,4.75
79500812,0.4069768844\C,3.4184701283,3.5699560097,-0.0519205205\H,4.07
00460144,4.4299047555,-0.1773739911\C,3.2639678694,-2.6401396053,-0.11
92297704\H,2.5852129122,-3.464397227,0.0675343685\C,4.5846761969,-2.86
91751539,-0.4611464803\H,4.9540196901,-3.8869798515,-0.5494300278\C,5.
4487545647,-1.7826629861,-0.6944316632\H,6.4853330893,-1.9582508977,-0
.9670451458\C,-1.4040176342,-0.6517319789,0.5173741623\C,-4.3677023898
,-0.9422916608,-1.1327645132\H,-5.1057256094,-1.627617673,-1.570450484
7\C,-4.4597201595,0.425894501,-1.8361106448\H,-5.4628303884,0.85094466
14,-1.6963906285\H,-4.3080626727,0.3151073788,-2.918121299\C,-1.782755
1402,-0.6297895688,-0.9964435012\H,-0.8924821712,-1.0353950053,-1.4918
007314\C,-4.7113783218,-0.7457250421,0.3521914632\H,-4.7036808307,-1.7
009127976,0.8896603726\H,-5.7306887318,-0.3403131813,0.421904289\C,-3.
7410996557,0.2241247932,1.05811163\H,-4.1902433688,0.48429724,2.021554
7961\C,-2.9684596407,-1.5624156411,-1.3540457744\H,-2.887063506,-2.511
7233209,-0.8114389975\H,-2.8750218641,-1.810430734,-2.4195993229\C,-3.
6024978012,1.5483570444,0.2646316464\H,-2.7965104058,2.1527195539,0.69
73346834\H,-4.5342250199,2.1120688043,0.4108385567\C,-1.9995343824,0.7
848505,-1.5747521878\H,-1.8949879595,0.7135646223,-2.6659202212\C,-3.3
853410373,1.3630719998,-1.2521416217\H,-3.4637578345,2.3493775607,-1.7
285691701\H,-1.2100942784,1.456356499,-1.2285000642\C,-2.1110607011,-0
.3511218954,2.8325781725\H,-1.7936630966,0.6652806637,3.1109140916\H,-
2.9576051436,-0.6402601891,3.4633758549\H,-1.2812671747,-1.0255305607,
3.0605976444\O,-0.4060555022,0.4359744651,0.7508791895\C,4.9792053763,
-0.4855172238,-0.5730885744\H,5.666287318,0.3330559172,-0.7548403437\C
,3.9298618006,2.2930892305,-0.2164267545\H,4.9787934181,2.1842642411,-
0.4663036352\\Version=AM64L-G09RevA.02\State=1A\HF=1191.2309625\RMSD
=3.784e-09\RMSF=3.428e-06\Dipole=-1.024704,0.5249173,-0.1737769\Quadru
pole=6.1649129,-0.6748414,-5.4900714,2.4135289,-3.4443706,0.9565518\PG
=C01 [X(C26H26N2O1)]\\@
```

Table C2. 2.1-TS1 (C-O bond cleavage), geometry optimization, B3LYP/6-31+G(d,p)

```
FTS\RB3LYP\6-31+G(d,p)\C26H26N2O1\AIKOKURI\11-Jul-2014\0
\\# opt=(tight,qst2) b3lyp/6-31+g(d,p) geom=connectivity\\APESO SO to
TCC QST2/B3LYP/6-31G+(d)\\0,1\N,-2.6943127834,-0.3240528301,1.48795211
05\C,-0.669725881,-1.5993276028,1.2641171822\H,-1.059828504,-2.3502888
35,1.9548252926\C,1.3557204435,-0.7646255409,0.3571033117\C,1.00792636
03,0.6198720691,0.4904132229\N,0.586383151,-1.726890617,0.9339193835\C
,2.0832837891,1.6158038109,0.3425257454\C,2.6878122715,-1.1511329059,-
0.091964003\C,3.3783370193,1.2413264479,-0.1052818098\C,3.6807202278,-
0.1697748726,-0.3652028\C,1.7889019675,2.9690700545,0.6086814374\H,0.7
854461128,3.2110791329,0.941685838\C,2.7509908608,3.9536965794,0.45137
40907\H,2.5158644246,4.9917735323,0.6684178809\C,4.0332736544,3.595745
3229,0.0018166394\H,4.7960938952,4.3577192921,-0.1330499881\C,3.000296
1145,-2.5152993298,-0.2917336028\H,2.2358404373,-3.2518875434,-0.07066
30222\C,4.2456475864,-2.9083036963,-0.7560682273\H,4.4624733213,-3.963
3899695,-0.8999828365\C,5.2212081902,-1.9409982619,-1.0489853698\H,6.1
95187983,-2.2384882738,-1.4266927413\C,-1.6687295768,-0.6839530166,0.7
171264096\C,-4.2664077444,-1.2049873231,-1.2213038145\H,-4.8923690157,
-1.9747191604,-1.6910051647\C,-4.4465430303,0.1313132129,-1.9674885881
\H,-5.5008677126,0.4387825354,-1.9439924886\H,-4.171541428,0.014100327
7,-3.0235029547\C,-1.7781642579,-0.6048975401,-0.8035926201\H,-0.78996
89853,-0.9049534534,-1.1590223271\C,-4.7434296047,-1.0305441286,0.2334
156197\H,-4.6277991571,-1.9627140633,0.8004058111\H,-5.8164749859,-0.7
976191311,0.2235951768\C,-4.027475642,0.1140143781,0.9811271439\H,-4.5
958615153,0.3208290295,1.8913378952\C,-2.7965644608,-1.6631258445,-1.3
17912118\H,-2.651652947,-2.6147114639,-0.7917856265\H,-2.5621890552,-1
.853791359,-2.3728595424\C,-3.9858290018,1.4146201832,0.1533952812\H,-
3.3311625077,2.1407884198,0.6484086313\H,-5.0009779288,1.8335098082,0.
1672349646\C,-2.0806396549,0.7838840769,-1.4112109532\H,-1.8047652729,
0.7320033474,-2.4729483734\C,-3.5552023872,1.2009506864,-1.3087941509\
H,-3.6779400826,2.1545165863,-1.8381783647\H,-1.4324502171,1.526980016
4,-0.9442747135\C,-2.573247772,-0.3493741331,2.9502106372\H,-2.9597670
344,0.5922675018,3.3520544724\H,-3.1469437264,-1.1781792569,3.38253199
55\H,-1.5264225405,-0.4414459751,3.233266898\O,-0.1622939885,1.0029537
567,0.8175242823\C,4.9350371839,-0.597472428,-0.8529327476\H,5.7033704
214,0.1326828533,-1.0816504876\C,4.3349134082,2.269064141,-0.271336691
2\H,5.3353975784,2.0267244534,-0.6106322264\\Version=ES64L-G09RevD.01\
State=1-A\HF=-1191.2150582\RMSD=6.291e-09\RMSF=3.471e-06\Dipole=2.903
0713,0.1173621,0.1089157\Quadrupole=9.345319,-5.0074686,-4.3378505,4.3
502177,-6.9053802,0.482354\PG=C01 [X(C26H26N2O1)]\\@
```

Table C3. 2.1-PMC-TCC, geometry optimization, B3LYP/6-31+G(d,p)

FOpt\RB3LYP\6-31+G(d,p)\C26H26N2O1\BRYNND\13-Jun
-2014\0\\# opt=tight b3lyp/6-31+g(d,p)\\tightAPESOTCC b3LYP/6-31+G(d,p
)\\0,1\O,0.1938371284,1.41733946,0.6224990369\N,0.3347869986,-1.415730
0026,1.1100845326\N,-3.0902920136,-0.1275463822,1.4610239271\C,1.26946
68333,-0.7061495423,0.4978687002\C,1.2345661088,0.7648489292,0.4244315
41\C,2.5286754547,1.4629837546,0.2107768314\C,3.7125368974,0.758616940
9,-0.1190560527\C,3.6904393993,-0.7115802259,-0.2103265758\C,2.5043415
539,-1.4159382788,0.1249100135\C,2.5388324125,2.8669304956,0.300952580
6\H,1.6056092491,3.3620565509,0.5471262371\C,3.7042808813,3.5878850845
,0.0834004705\H,3.7043672277,4.6709397555,0.1644984272\C,4.8827921112,
2.9007091317,-0.2428123153\H,5.8040194485,3.449780287,-0.4172992747\C,
2.5040669076,-2.8251832306,0.0685040944\H,1.5880064059,-3.3436880583,0
.3280053845\C,3.6371406417,-3.5337440472,-0.3060710082\H,3.6127949356,
-4.6194237527,-0.339242912\C,4.8058912603,-2.8415970805,-0.6526051973\
H,5.6954155031,-3.3829107886,-0.9616525931\C,-0.9170418733,-1.10401724
72,1.469196697\H,-1.2504525808,-1.6788662671,2.3334427802\C,-1.9385306
753,-0.3984377814,0.7962303234\C,-1.863103614,-0.1625378029,-0.7016142
295\H,-0.8114499043,-0.2903113275,-0.9516307212\C,-2.6437591597,-1.255
6017389,-1.483824195\H,-2.4281166881,-2.242454009,-1.0568498179\H,-2.2
572962752,-1.2672384424,-2.5113745058\C,-4.1602101406,-1.0011233627,-1
.5354182216\H,-4.6190631539,-1.7814613559,-2.1566321523\C,-4.813282138
5,-1.0618867097,-0.1407569262\H,-5.9030875823,-1.0054735912,-0.2641632
11\H,-4.5999335887,-2.020499104,0.3484250993\C,-4.4036423379,0.0933447
218,0.7988916159\H,-5.1189588206,0.1008087718,1.62520063\C,-4.48562162
53,1.4638343256,0.0957189137\H,-5.5487947181,1.7067795981,-0.036988652
4\H,-4.0587584516,2.2317502172,0.7514953427\C,-3.7965493337,1.47173651
33,-1.2788233296\H,-3.966225428,2.4547629485,-1.7372433396\C,-4.425099
5028,0.3796572412,-2.1662089724\H,-3.9955699199,0.4184338581,-3.175596
1583\H,-5.5052688955,0.5498549932,-2.2721685265\C,-2.2755440828,1.2552
708252,-1.1696356215\H,-1.8160417461,1.9977917482,-0.5129068848\H,-1.8
362188285,1.4051675518,-2.1649176234\C,-3.1170050439,-0.178043249,2.92
17921285\H,-3.8919564435,0.4993699678,3.2882563652\H,-2.1539326991,0.1
466523155,3.3200570745\H,-3.3331986441,-1.1878168693,3.3007854017\C,4.
8830564641,1.5144609012,-0.3430418755\H,5.8130848017,1.016051563,-0.59
02607163\C,4.8233652153,-1.4529838318,-0.6036323484\H,5.7379120699,-0.
9395063715,-0.8776121906\\Version=AM64L-G09RevA.02\State=1-A\HF=-1191.
2173488\RMSD=5.184e-09\RMSF=3.008e-06\Dipole=-2.0145965,0.0303048,-0.0
769992\Quadrupole=12.7109845,-5.9000071,-6.8109775,2.450383,-6.8207088
,0.4000959\PG=C01 [X(C26H26N2O1)]\\@

Table C4. 2.1-TS2 (*cis*-to-*trans* isomerization), geometry optimization, B3LYP/6-31+G(d,p)

FTS\RB3LYP\6-31+G(d,p)\C26H26N2O1\BRYNND\19-Jul-2
014\0\\# opt=(tight,qst2) b3lyp/6-31+g(d,p) geom=connectivity\\APESO T
CC to TTC QST2/B3LYP/6-31G+(d)\\0,1\N,-3.1128333438,0.4758153258,1.245
0805359\C,-0.8530151745,-0.3597718697,1.2261439663\H,-0.7713875982,-0.
30532025,2.3071797854\C,1.3597953125,-0.3207485927,0.2869755678\C,1.57
8208028,1.1719530133,0.4796324087\N,0.2932957387,-0.9497258838,0.62391
97334\C,2.986453141,1.615155558,0.6576041427\C,2.4933542597,-1.0950146
19,-0.283266004\C,4.0662872816,0.7719176755,0.3042468015\C,3.804077613
8,-0.5612003664,-0.288644115\C,3.2163923402,2.8987572589,1.1764016501\
H,2.3549772053,3.5128345652,1.417915867\C,4.5125866563,3.3576055198,1.
380417404\H,4.6872874358,4.3458859371,1.7944482845\C,5.5897704752,2.52
49347596,1.0537836891\H,6.6087345213,2.8644583869,1.2165560231\C,2.252
4600498,-2.3682588515,-0.8229269941\H,1.2376353721,-2.7492408804,-0.79
58501515\C,3.2854535317,-3.1174056725,-1.3762614911\H,3.0831610528,-4.
0980072562,-1.7966090749\C,4.5815988702,-2.591396752,-1.3988525645\H,5
.3956229743,-3.1586183068,-1.8407479798\C,-2.0075591945,-0.0724496496,
0.578963995\C,-4.321141154,-1.6160040176,-1.080326989\H,-4.7321411865,
-2.605874991,-1.3206068308\C,-4.86117596,-0.5810889664,-2.0862404894\H
,-5.9598584381,-0.5743489622,-2.0809423186\H,-4.548542211,-0.853277560
7,-3.1033956429\C,-2.1150574056,-0.3197460749,-0.9193040978\H,-1.08397
58639,-0.3929512034,-1.2745687653\C,-4.7769941802,-1.2502021289,0.3502
600727\H,-4.3256962243,-1.932377693,1.0818758616\H,-5.864080285,-1.398
6411387,0.4088986295\C,-4.4905803896,0.213986309,0.7713832703\H,-5.125
6857205,0.4198008709,1.6380622016\C,-2.7910302496,-1.6818498982,-1.216
6312126\H,-2.3722527571,-2.4467012296,-0.5521805736\H,-2.5459689995,-1
.9814035496,-2.2455745438\C,-4.8981298796,1.2049517285,-0.3395690983\H
,-4.5724431183,2.2101144377,-0.0484233594\H,-5.9954701049,1.2234094315
,-0.4086639127\C,-2.7816200547,0.8191224755,-1.733474556\H,-2.46076429
03,0.7034987622,-2.7780469369\C,-4.3262147534,0.8159529796,-1.71148103
66\H,-4.6749352235,1.5498074935,-2.4506118748\H,-2.3976384398,1.786830
3205,-1.3904033125\C,-2.9675920291,0.760636375,2.6604601082\H,-3.83718
91186,1.3206329416,3.012071656\H,-2.8675591142,-0.1483734893,3.2832881
619\H,-2.079410125,1.3801256631,2.8251782214\O,0.6404850416,1.95677449
48,0.5338719497\C,4.8327520486,-1.3317700382,-0.8614104288\H,5.8438460
178,-0.9433086078,-0.9029339272\C,5.3691179247,1.2563332292,0.52150962
77\H,6.2273296939,0.6372939875,0.2872966665\\Version=AM64L-G09RevA.02\
State=1-A\HF=-1191.2017368\RMSD=5.407e-09\RMSF=2.734e-06\Dipole=0.7640
124,-0.1244285,-0.0352814\Quadrupole=13.5600565,-6.1586639,-7.4013926,
2.1039791,-1.5083922,5.9269677\PG=C01 [X(C26H26N2O1)]\\@

Table C5. 2.1-PMC-TTC, geometry optimization, B3LYP/6-31+G(d,p)

FOpt\RB3LYP\6-31+G(d,p)\C26H26N2O1\BRYNND\11-Jun
-2014\0\\# opt=tight b3lyp/6-31+g(d,p) geom=connectivity\\APESOTTC b3L
YP/6-31G+(d,p)\\0,1\C,2.5570842741,-2.9963935064,-0.2181822811\H,1.981
2195038,-3.2895184325,0.6678203462\H,3.4121299336,-3.6644231601,-0.316
3095893\H,1.9137033953,-3.1229443177,-1.094930635\C,2.1310140052,-0.59
84310437,-0.0735462192\C,0.7554335156,-0.8880875021,-0.0960718338\H,0.
4079072446,-1.9105471138,-0.1192452976\C,-1.4530025177,-0.0050417583,-
0.06370391\C,-2.167844971,-1.299884662,-0.0544755817\C,4.5028439861,-1
.4115933874,-0.0063605004\H,4.9112239262,-2.423736462,-0.0268159055\C,
4.9374100193,-0.7780289182,1.3343054665\H,4.3858108322,-1.252851879,2.
1546656321\H,5.9977830162,-1.0250741825,1.4795440368\C,4.7796996847,0.
7526433479,1.3804200686\H,5.2182003791,1.1107942971,2.3209420484\C,3.3
041657967,1.1859016795,1.3384561413\H,3.2568434401,2.2753090804,1.4687
988897\H,2.7461082288,0.7475453902,2.1744561158\C,2.5971248503,0.84284
26962,0.0027220284\H,1.665892942,1.4087300766,-0.0237732725\C,3.447290
4746,1.2919325548,-1.2124450441\H,2.9915946305,0.9231349823,-2.1394542
128\H,3.4011642853,2.3882064988,-1.2578430849\C,4.9252016154,0.8713373
583,-1.1294762034\H,5.4600555709,1.3221745403,-1.9755171569\C,5.534174
0561,1.3820572964,0.1919586793\H,5.4642176284,2.4765481029,0.240403004
7\H,6.6016387229,1.1281734793,0.241092176\C,5.0998854114,-0.6550154702
,-1.2133676679\H,6.1735143342,-0.8851873151,-1.2444614417\H,4.66305446
48,-1.0494994394,-2.1386268242\C,-3.652385931,-1.271480809,0.003685097
4\C,-4.3772076809,-0.0563336914,0.0284295685\C,-3.6581242044,1.2299456
424,-0.0092544719\C,-2.2383575356,1.2459014719,-0.0527067252\C,-1.5764
97726,2.491984552,-0.0882901746\H,-0.4943749216,2.4905770606,-0.123045
9842\C,-2.2761467051,3.6896040071,-0.0812562505\H,-1.7373680246,4.6327
409815,-0.1103759079\C,-3.6769842414,3.6760966738,-0.0389019325\H,-4.2
387886858,4.6056186296,-0.0345999348\C,-4.3473702437,2.4607346448,-0.0
039313026\H,-5.4305397951,2.4728116206,0.0262538381\C,-4.3277925057,-2
.5049824075,0.0359304987\H,-3.7268730687,-3.4077273504,0.0141836387\C,
-5.7129677047,-2.5588253447,0.0946787924\H,-6.226266108,-3.5155666555,
0.1204704835\C,-6.4420077049,-1.3611331227,0.1214962043\H,-7.527341295
,-1.3840445848,0.1684222544\C,-5.7851754948,-0.1366680554,0.0887316179
\H,-6.3827668499,0.7668274288,0.1121407523\N,3.0345629561,-1.612296633
7,-0.1135192023\N,-0.1364941287,0.1195102121,-0.0765147085\O,-1.571182
0803,-2.3912261009,-0.0871001233\\Version=AM64L-G09RevA.02\State=1-A\H
F=-1191.2386393\RMSD=5.221e-09\RMSF=1.851e-06\Dipole=2.3803058,0.02148
,0.0460337\Quadrupole=15.6905551,-3.5398619,-12.1506932,-5.753102,-0.5
345946,0.0499454\PG=C01 [X(C26H26N2O1)]\\@

Table C6. 2.2-SO, geometry optimization, B3LYP/6-31+G(d,p)

FOpt\RB3LYP\6-31+G(d,p)\C24H24N4O1\BRYNND\10-Jun-
2014\0\\# opt=tight b3lyp/6-31+g(d,p)\\APSOSO b3LYP/6-31G+(d,p)\\0,1\N
,-2.4776853283,-0.4688393886,1.4214831491\C,-0.6950813363,-1.971481205
8,0.7918591878\H,-1.330519526,-2.7943970135,1.121106316\C,1.3759502746
,-1.0947738058,0.3142081704\C,0.896903887,0.1909752103,0.4179716632\N,
0.5587429231,-2.1842739217,0.6510893619\C,1.7642631924,1.3283475768,0.
2686480889\C,2.7603575182,-1.3267905017,-0.0200115289\C,3.1373513192,1
.1299200805,-0.0613589695\C,3.6454381463,-0.2307874814,-0.2271020752\C
,1.2994717238,2.6518295446,0.4316035921\H,0.2588297246,2.822681567,0.6
841080375\C,2.1848932478,3.6989162072,0.2694094477\H,1.8685341005,4.73
03988178,0.3892881964\C,3.5219265841,3.3987488395,-0.0623576614\H,4.24
20268658,4.2038567098,-0.2008324004\C,3.2870622962,-2.6311773068,-0.14
76860377\H,2.6346372941,-3.4805644208,0.0217018222\C,4.618091899,-2.78
92719805,-0.4810415506\H,5.0574639438,-3.7764344704,-0.5885316028\N,3.
9866309227,2.1687192522,-0.2241950581\N,4.9451786166,-0.4015496034,-0.
557016043\C,5.4057632292,-1.6371269205,-0.6809659402\H,6.4565015341,-1
.733258198,-0.9499518458\C,-1.4090364314,-0.6467075798,0.5021095058\C,
-4.3894243994,-0.9146201941,-1.1179325658\H,-5.1328550329,-1.594465918
9,-1.5547104891\C,-4.4885252615,0.461378515,-1.8045215088\H,-5.4895007
069,0.885482293,-1.6486757923\H,-4.3492500028,0.3626418556,-2.88926018
81\C,-1.8029044941,-0.6056335079,-1.0070919735\H,-0.9182896136,-1.0058
269345,-1.5169765798\C,-4.7151834643,-0.7355022651,0.3734071739\H,-4.7
004581429,-1.6968251184,0.8997361336\H,-5.7338693455,-0.3322147632,0.4
604435883\C,-3.7376053872,0.2273951012,1.0787449297\H,-4.1751480122,0.
4766377307,2.0502873929\C,-2.9934120102,-1.532956795,-1.3633666947\H,-
2.906772608,-2.4897034853,-0.8348982196\H,-2.9118183401,-1.7665751634,
-2.4330412052\C,-3.607708496,1.5600868824,0.2985151394\H,-2.7974203097
,2.1599389813,0.7296097881\H,-4.5377526633,2.121889401,0.4610265077\C,
-2.0253265235,0.8161644781,-1.5662159426\H,-1.9320403822,0.7573460168,
-2.6590117236\C,-3.4070932101,1.3913087075,-1.2221774262\H,-3.48995003
32,2.3826673726,-1.6870713695\H,-1.231911004,1.4834245839,-1.220616557
9\C,-2.0898043412,-0.3761447035,2.8292214271\H,-1.7708618201,0.6354353
95,3.1226379205\H,-2.9302275432,-0.6769096322,3.4625607004\H,-1.257740
3804,-1.0540162466,3.0379842439\O,-0.4000350927,0.4391094068,0.7341054
657\\Version=AM64L-G09RevA.02\State=1-A\HF=-1223.3010121\RMSD=3.648e-0
9\RMSF=3.853e-06\Dipole=-2.3861084,0.0196154,0.1387663\Quadrupole=-7.6
628506,7.7542012,-0.0913506,-5.500007,-0.087558,2.2959315\PG=C01 [X(C2
4H24N4O1)]\\@

Table C7. 2.2-TS1 (C-O bond cleavage), geometry optimization, B3LYP/6-31+G(d,p)

FTS\RB3LYP\6-31+G(d,p)\C24H24N4O1\AIKOKURI\12-Jul-2014\0
\\# opt=(tight,qst2) b3lyp/6-31+g(d,p) geom=connectivity\\APSO SO to T
CC QST2/B3LYP/6-31G+(d)\\0,1\N,-2.6726530101,-0.3385049748,1.494384200
8\C,-0.6682594859,-1.6375958918,1.2215282104\H,-1.0662122927,-2.407615
2439,1.886455359\C,1.3578199555,-0.794385778,0.327327944\C,1.019447988
6,0.588610505,0.4790359251\N,0.5844803086,-1.7658854249,0.8868571153\C
,2.098750642,1.5760505822,0.3139812858\C,2.6902377322,-1.1769977342,-0
.1183635628\C,3.3885193227,1.2087353713,-0.1512107272\C,3.6890428597,-
0.206391663,-0.4012505385\C,1.8443592442,2.9360455452,0.5691115389\H,0
.858466028,3.2216520151,0.9206851152\C,2.8506099305,3.8643511161,0.366
6183592\H,2.6963488305,4.9216694166,0.559676555\C,4.0900034634,3.40039
07235,-0.1100685221\H,4.9019451429,4.103201331,-0.2931185248\C,3.03741
80388,-2.5312598446,-0.3112410596\H,2.3008603788,-3.2965393679,-0.0917
217736\C,4.3015349296,-2.8545955111,-0.7718973466\H,4.5951581568,-3.88
88404221,-0.9268999998\N,4.3578530206,2.1253666306,-0.3641946663\N,4.9
139439697,-0.5298704652,-0.8646439833\C,5.2043476639,-1.8117747473,-1.
0464810756\H,6.2010581413,-2.030972029,-1.4262016871\C,-1.6639402915,-
0.6954514212,0.7042943319\C,-4.2931800239,-1.1474191476,-1.2064649157\
H,-4.9362980092,-1.9002353435,-1.6801021928\C,-4.4642240349,0.20373339
,-1.9276595885\H,-5.5135045077,0.5255842142,-1.8836464596\H,-4.2063283
506,0.1007316202,-2.9893998611\C,-1.7910361092,-0.5903029392,-0.813157
2881\H,-0.8118066252,-0.8987391246,-1.1861707975\C,-4.7489382497,-0.98
95301711,0.2570208028\H,-4.6419995366,-1.9324742531,0.8075624581\H,-5.
8178205057,-0.738693706,0.264487139\C,-4.0055491644,0.1311788316,1.013
4508885\H,-4.5573187439,0.3310540613,1.9353243761\C,-2.8317439184,-1.6
257084728,-1.3300130379\H,-2.6946831076,-2.5874829553,-0.8205815395\H,
-2.6137269479,-1.8031081333,-2.3906282243\C,-3.9537570293,1.4447735062
,0.2079986485\H,-3.2804692861,2.1516980945,0.7058217953\H,-4.961519865
1,1.8794533649,0.2442762834\C,-2.0814839742,0.8121564206,-1.3953865852
\H,-1.8220374213,0.7718557102,-2.4616416863\C,-3.5481618689,1.24945178
96,-1.2641375657\H,-3.6640687051,2.2133039656,-1.7758054798\H,-1.41566
35807,1.5389053,-0.9275474349\C,-2.5357410661,-0.3939079735,2.95481666
82\H,-2.8817575621,0.5548951814,3.3762726224\H,-3.1371085285,-1.207493
4057,3.3775383301\H,-1.4906195557,-0.5305461369,3.2252541814\O,-0.1420
103901,0.9802035946,0.82696799\\Version=ES64L-G09RevD.01\State=1-A\HF=
-1223.2869983\RMSD=8.689e-09\RMSF=3.391e-06\Dipole=-4.3476916,-0.22699
84,0.55871\Quadrupole=-5.6536901,4.6281839,1.0255063,-1.4230313,-2.112
8829,1.9620539\PG=C01 [X(C24H24N4O1)]\\@

Table C8. 2.2-PMC-TCC, geometry optimization, B3LYP/6-31+G(d,p)

FOpt\RB3LYP\6-31+G(d,p)\C24H24N4O1\BRYNND\13-Jun
-2014\0\\# opt=tight b3lyp/6-31+g(d,p)\\tightAPSOTCC b3LYP/6-31+G(d,p)
\\0,1\O,0.1718206834,1.3689353871,0.7271083048\N,0.3390295489,-1.49518
95076,1.0546228393\N,4.8275882572,1.4556330741,-0.3657630237\N,4.83230
90817,-1.2824463425,-0.6219276544\N,-3.0747602125,-0.2089567831,1.4498
137285\C,1.2646122215,-0.7385138935,0.4786216857\C,1.2110481087,0.7305
466532,0.4763595462\C,2.4922319766,1.4494332202,0.2592868568\C,3.68448
98717,0.7862076564,-0.1148508625\C,3.691144229,-0.6847584204,-0.230300
5925\C,2.5157487618,-1.4084594305,0.0946286139\C,2.5149848873,2.848509
2875,0.3760130302\H,1.5991067009,3.3585393989,0.6560315106\C,3.6965113
169,3.5300109105,0.1313994913\H,3.7585074855,4.6103849277,0.2186157652
\C,4.8233727843,2.7795829172,-0.2416421868\H,5.7685383676,3.2790762093
,-0.449921512\C,2.5815000617,-2.8128509453,0.0108308867\H,1.6973824813
,-3.3909280751,0.255985643\C,3.7631248834,-3.4231827826,-0.3776499402\
H,3.8413126958,-4.5041881497,-0.4468725695\C,4.8620408626,-2.609259799
9,-0.6938517937\H,5.8021816283,-3.0516725727,-1.0190235087\C,-0.916286
7741,-1.2161169567,1.4125993178\H,-1.2642895915,-1.84819085,2.23009787
01\C,-1.9311902687,-0.4603460337,0.7735050745\C,-1.853305001,-0.168246
0089,-0.7145678158\H,-0.8047531659,-0.3101153446,-0.9721505669\C,-2.65
89707982,-1.2165237937,-1.5330866707\H,-2.4635903304,-2.2226816243,-1.
1428822541\H,-2.2735846019,-1.1988778678,-2.5607710285\C,-4.1702866166
,-0.9291055372,-1.5730876348\H,-4.6443495994,-1.6754051259,-2.22373042
05\C,-4.8241388275,-1.0310370268,-0.1816213906\H,-5.9120675541,-0.9417
489603,-0.3007723316\H,-4.6352624979,-2.0138086814,0.2680203398\C,-4.3
852313685,0.0748675628,0.8020254711\H,-5.0963931386,0.0661798002,1.631
6396515\C,-4.4346296773,1.4742669004,0.1564033226\H,-5.492287207,1.747
6952639,0.0417321337\H,-3.9856859105,2.2041708164,0.8401994261\C,-3.75
44071928,1.5235650601,-1.222147229\H,-3.9074154301,2.5274478924,-1.638
9439975\C,-4.4082979361,0.4805260586,-2.1490101111\H,-3.9810593647,0.5
503792338,-3.1575897297\H,-5.4849652121,0.6764954101,-2.2444077338\C,-
2.2379553452,1.2734948802,-1.1311881769\H,-1.7600946897,1.9836370888,-
0.4524751179\H,-1.8010604303,1.4468495358,-2.1236274883\C,-3.103652944
,-0.3312951262,2.9078230513\H,-3.8555040573,0.3532172543,3.3072839335\
H,-2.1306557436,-0.0599892304,3.320463156\H,-3.3554264091,-1.350797529
4,3.2331866917\\Version=AM64L-G09RevA.02\State=1-A\HF=-1223.2888327\RM
SD=3.720e-09\RMSF=2.067e-06\Dipole=-3.6586693,-0.0056402,0.3067021\Qua
drupole=-4.1759247,5.1405358,-0.9646111,2.1390225,-2.2378693,0.4158344
\PG=C01 [X(C24H24N4O1)]\\@

Table C9. 2.2-TS2 (*cis*-to-*trans* isomerization), geometry optimization, B3LYP/6-31+G(d,p)

FTS\RB3LYP\6-31+G(d,p)\C24H24N4O1\BRYNND\07-Jul-2014\0\\# opt=(tight,qst2) b3lyp/6-31+g(d,p) geom=connectivity\\APSO TCC to TTC-2 QST2/B3LYP/+G(d)\\0,1\N,-3.1266026262,0.071081451,1.4213329009\C,-0.9690586744,-0.9938416957,1.4834016179\H,-1.0869173258,-1.2738033864,2.52463835\C,1.3272756607,-0.808450474,0.8278119421\C,1.5063834618,0.63026442,1.2982190874\N,0.244356047,-1.4853005389,0.9335735956\C,2.5961179739,1.408759078,0.654746475\C,2.5118360919,-1.4574170498,0.2070088231\C,3.6079455373,0.7806425535,-0.1048342259\C,3.6123642311,-0.7003814549,-0.2520352133\C,2.6434651048,2.7988806977,0.8258590687\H,1.876212854,3.2797059354,1.4243564133\C,3.6665038032,3.5152648251,0.2203695252\H,3.7391832226,4.5937476582,0.3164581844\C,4.6109630152,2.8022158074,-0.5312240907\H,5.4216347964,3.3282930854,-1.0322123989\C,2.551656247,-2.8486624183,0.0353967646\H,1.7082814201,-3.4398148527,0.3754361801\C,3.6632691046,-3.4274925561,-0.5609534807\H,3.732551676,-4.5015645813,-0.7016253437\N,4.5964721847,1.4778437215,-0.687623197\N,4.6846180596,-1.2628595023,-0.8337096276\C,4.7046457304,-2.5870328717,-0.9764506009\H,5.5956288583,-3.0022728285,-1.4436675418\C,-1.9584522398,-0.3805980275,0.788374429\C,-4.0496902392,-1.0584304931,-1.5986289801\H,-4.4795554335,-1.8706397203,-2.2000702209\C,-4.3263380655,0.2913214714,-2.2903211174\H,-5.4046658951,0.4309000496,-2.4469717192\H,-3.8552072334,0.3037558065,-3.2823941415\C,-1.8198705281,-0.1524026218,-0.7112349875\H,-0.7529396716,-0.2441167544,-0.9274838072\C,-4.7250127606,-1.0906988634,-0.2094562884\H,-4.4610654309,-2.0133856729,0.3227159204\H,-5.8130287535,-1.1139727118,-0.3602798106\C,-4.4146809633,0.1301406893,0.6938239448\H,-5.1760600673,0.1386070346,1.4792419252\C,-2.5290114788,-1.2680973759,-1.5210766111\H,-2.2895581824,-2.2420615396,-1.0787898845\H,-2.124828336,-1.2729426573,-2.5431749933\C,-4.5510815134,1.4522980733,-0.0896775763\H,-4.2158189101,2.2753348579,0.5517911233\H,-5.6143888966,1.6224940873,-0.3115449642\C,-2.2514061871,1.2523278612,-1.2087405503\H,-1.7600691117,1.4208357792,-2.1769572311\C,-3.7718079894,1.4320155883,-1.4136723059\H,-3.9310834655,2.3922340235,-1.9224087352\H,-1.8699481138,2.0192668165,-0.5237273114\C,-3.2165904608,-0.0941354065,2.8610825586\H,-4.0829873625,0.4543734694,3.2379871696\H,-3.3136711765,-1.1501509377,3.1760043896\H,-2.3228288641,0.3202024759,3.3385626293\O,0.8006558766,1.1125586755,2.1723749386\\Version=AM64L-G09RevA.02\State=1-A\HF=-1223.2717604\RMSD=8.791e-09\RMSF=2.292e-06\Dipole=-0.7413454,0.1307994,-0.1338433\Quadrupole=-3.5568228,9.7465651,-6.1897423,0.5216956,1.0423933,0.1258527\PG=C01 [X(C24H24N4O1)]\\@

Table C10. 2.2-PMC-TTC, geometry optimization, B3LYP/6-31+G(d,p)

FOpt\RB3LYP\6-31+G(d,p)\C24H24N4O1\BRYNND\13-Jun
-2014\0\\# opt=tight b3lyp/6-31+g(d,p) geom=connectivity\\APSOTTC-2 b3
LYP/6-31G+(d,p)\\0,1\O,-1.573881,-2.403222,-0.000012\N,-0.135094,0.121
578,-0.000017\N,-5.730192,-0.045297,0.000019\N,-4.400094,2.351454,-0.0
00001\N,3.034848,-1.607154,-0.000021\C,-1.452021,-0.013249,-0.000014\C
,-2.16373,-1.307806,-0.000009\C,-3.648767,-1.272025,0.000003\C,-4.3821
14,-0.064219,0.000007\C,-3.661967,1.224903,-0.000002\C,-2.243281,1.231
103,-0.000013\C,-4.355993,-2.484631,0.000011\H,-3.791775,-3.411451,0.0
00008\C,-5.741565,-2.460162,0.000023\H,-6.326984,-3.374395,0.000029\C,
-6.376319,-1.207733,0.000027\H,-7.463723,-1.146082,0.000037\C,-1.61366
4,2.491451,-0.000022\H,-0.531237,2.532302,-0.000031\C,-2.377073,3.6470
53,-0.00002\H,-1.911142,4.628146,-0.000028\C,-3.774667,3.52325,-0.0000
09\H,-4.409522,4.407731,-0.000008\C,0.756573,-0.884013,-0.000019\H,0.4
09,-1.906873,-0.00002\C,2.134256,-0.593107,-0.000015\C,2.598829,0.8506
83,-0.000003\H,1.666053,1.41455,-0.000011\C,3.37882,1.249103,1.278682\
H,2.871612,0.844566,2.162874\H,3.331663,2.342718,1.365645\C,4.857795,0
.825253,1.258072\H,5.345112,1.231403,2.153856\C,5.023114,-0.704725,1.2
78467\H,6.09185,-0.941344,1.368618\H,4.526533,-1.141033,2.153467\C,4.5
0785,-1.402146,0.000003\H,4.916192,-2.41424,0.000003\C,5.023151,-0.704
708,-1.278437\H,6.09189,-0.941323,-1.36856\H,4.526596,-1.141006,-2.153
457\C,4.857827,0.825269,-1.258025\H,5.345164,1.231433,-2.153791\C,5.54
1056,1.396832,0.000036\H,5.473026,2.492432,0.000042\H,6.609715,1.14373
,0.000047\C,3.378851,1.249116,-1.278665\H,2.871664,0.844586,-2.162873\
H,3.331694,2.342731,-1.365619\C,2.554978,-2.995597,-0.000047\H,3.40976
5,-3.670641,-0.000072\H,1.944981,-3.202783,-0.886123\H,1.944999,-3.202
824,0.886032\\Version=AM64L-G09RevA.02\State=1-A\HF=-1223.3102565\RMSD
=2.418e-09\RMSF=9.513e-07\Dipole=3.8412824,-0.6415995,-0.0000014\Quadr
upole=1.481931,4.104915,-5.5868459,4.9471708,-0.0000244,-0.000032\PG=C
01 [X(C24H24N4O1)]\\@

Table C11. 2.3-SO, geometry optimization, B3LYP/6-31+G(d,p)

FOpt\RB3LYP\6-31+G(d,p)\C21H23N3O1\AIKOKURI\13-Mar-2017\
0\\# opt=tight b3lyp/6-31+g(d,p) geom=connectivity\\tightAIQSOSO_opt6-
31G+dp\\0,1\N,-2.4834485139,-0.4724184983,1.4339654218\C,-0.6882544588
,-1.9631411021,0.8134823223\H,-1.3239307702,-2.7848953126,1.1452479956
\C,1.3787192453,-1.0883597097,0.3312397275\C,0.8918703385,0.2101235199
,0.4400625474\N,0.5651493746,-2.1793995214,0.672498821\C,1.7468100164,
1.3270594884,0.2712594206\C,2.7479582404,-1.2968970267,-0.0195243242\C
,3.0680040247,1.1396616777,-0.0659040367\C,3.5986394594,-0.1707856528,
-0.2341149982\C,3.3187462936,-2.5929739354,-0.1646376382\H,2.692553081
3,-3.4634935424,0.0091410124\C,5.3771041074,-1.7316242756,-0.713985613
4\H,6.4044928826,-1.9539406992,-0.9907062524\C,-1.4029100583,-0.637425
8819,0.5235855662\C,-4.3607164981,-0.922023631,-1.1358767295\H,-5.0931
181596,-1.6047634667,-1.586567579\C,-4.4649048715,0.4590306034,-1.8117
977194\H,-5.4720484125,0.8715343916,-1.6647228282\H,-4.3110796735,0.37
08129959,-2.8956136357\C,-1.7807165464,-0.5892477116,-0.9896850685\H,-
0.8855679619,-0.9751771039,-1.49207424\C,-4.7041769291,-0.7587992719,0
.3530483636\H,-4.6842670347,-1.7242347041,0.8716160664\H,-5.7284978403
,-0.3682541555,0.4315025809\C,-3.7471409927,0.2102536999,1.0783589145\
H,-4.2010685149,0.445406843,2.0459956629\C,-2.9564426246,-1.5249020507
,-1.371025337\H,-2.8664107534,-2.4869195692,-0.8524316786\H,-2.8594166
64,-1.7463866909,-2.4420379698\C,-3.6228892851,1.5507657546,0.31126362
75\H,-2.8246718475,2.1563955617,0.7565212538\H,-4.5613617804,2.1008462
774,0.4658693119\C,-2.0092046475,0.8372053539,-1.5370192837\H,-1.89864
20428,0.7910200007,-2.6289549548\C,-3.4007719503,1.3952015099,-1.20826
62681\H,-3.4878359946,2.3892967951,-1.6665612969\H,-1.2284934488,1.507
5535659,-1.1691268044\C,-2.1053507216,-0.3633935963,2.8431385632\H,-1.
8063781276,0.6556658945,3.1314075726\H,-2.9439882977,-0.6751461781,3.4
736480524\H,-1.2623430512,-1.0247260013,3.0612461754\O,-0.4050058876,0
.448964266,0.7711714458\H,1.3298094645,2.3211449358,0.3996492225\H,3.7
189727593,1.9970564309,-0.2128995424\C,4.9459138425,-0.4287365081,-0.5
940154599\H,5.6293098682,0.3973832598,-0.7710328994\N,4.5781510323,-2.
8125403584,-0.4982341896\\Version=ES64L-G09RevE.01\State=1-A\HF=-1053.
6130742\RMSD=5.774e-09\RMSF=5.699e-06\Dipole=-1.6345486,1.4048475,-0.0
436773\Quadrupole=1.1389687,-2.9858889,1.8469201,12.0686607,-1.6440422
,-0.6550057\PG=C01 [X(C21H23N3O1)]\\@

Table C12. 2.3-TS1 (C-O bond cleavage), geometry optimization, B3LYP/6-31+G(d,p)

FTS\RB3LYP\6-31+G(d,p)\C21H23N3O1\AIKOKURI\03-Apr-2017\0
\\# opt=(tight,qst3) b3lyp/6-31+g(d,p) geom=connectivity\\tightAIQSOSO
TCC_QST36-31G+dp-2\\0,1\N,-2.3339206043,0.3569688729,1.4101138896\C,-0
.1289933595,-0.5411591449,1.654095157\H,-0.4287611094,-0.9745920008,2.
610705613\C,1.8367500762,0.0770435449,0.4690833101\C,1.3787864412,1.39
96933863,0.0631135068\N,1.14627965,-0.6581995194,1.3711423483\C,2.3858
546962,2.3088423182,-0.4684554787\C,3.2004039035,-0.3245252905,0.17927
45653\C,3.6514899319,1.9027437847,-0.764665328\C,4.0954457474,0.566983
0343,-0.4693183667\C,3.6910205783,-1.6158128092,0.492958016\H,3.029170
5738,-2.3207668911,0.9883364168\C,5.7581982317,-1.1805408944,-0.405126
9401\H,6.7555955068,-1.5574979753,-0.6184999138\C,-1.2275565027,-0.096
1615572,0.8202257871\C,-3.5707649633,-1.6661988028,-0.8403005284\H,-4.
0340055857,-2.6440865533,-1.0244344397\C,-3.9268865743,-0.7032331532,-
1.989142366\H,-5.017265414,-0.5992805429,-2.0728587858\H,-3.5714226898
,-1.109612719,-2.9447204691\C,-1.2515339774,-0.5326182843,-0.637864961
3\H,-0.2085179947,-0.7521465403,-0.8728130192\C,-4.146693356,-1.111728
2308,0.4769563262\H,-3.897970095,-1.765936642,1.3218567481\H,-5.241832
8235,-1.0979440276,0.4000834444\C,-3.6939402897,0.3293913178,0.7946852
814\H,-4.3442705429,0.7105762783,1.5856743982\C,-2.0434283953,-1.86446
32805,-0.7859127234\H,-1.7680536669,-2.5575547889,0.0181602538\H,-1.72
01370376,-2.3321906704,-1.7243627685\C,-3.836436218,1.2661528438,-0.42
19604229\H,-3.3588015846,2.2270441782,-0.1993103741\H,-4.9091382062,1.
4609087771,-0.5537890976\C,-1.7441072645,0.5165604242,-1.6624721523\H,
-1.3864229131,0.1886980699,-2.6476176343\C,-3.2729918283,0.6655994642,
-1.7223119944\H,-3.5161608487,1.3524907742,-2.5429517243\H,-1.26634051
57,1.4744154708,-1.4486105292\C,-2.2822403151,0.881069816,2.7797593338
\H,-1.2625834513,1.1788544805,3.0199645482\H,-2.9271208977,1.761846645
1,2.841903513\H,-2.6303837452,0.1388030273,3.5089043498\O,0.1865516181
,1.7949513599,0.2190557899\H,2.0490592477,3.3183010653,-0.6856560376\H
,4.3526916084,2.5917437257,-1.2306347558\C,5.3948831404,0.1065337463,-
0.7645045891\H,6.1057731667,0.7611077223,-1.2622822677\N,4.9217266518,
-2.0381988094,0.2233550711\\Version=ES64L-G09RevE.01\State=1-A\HF=-105
3.594886\RMSD=4.612e-09\RMSF=2.503e-06\Dipole=-3.3689905,0.5751168,-0.
1136334\Quadrupole=3.7335951,-6.6147741,2.881179,10.4574041,-9.479681,
1.1476408\PG=C01 [X(C21H23N3O1)]\\@

Table C13. 2.3-PMC-TCC, geometry optimization, B3LYP/6-31+G(d,p)

FOpt\RB3LYP\6-31+G(d,p)\C21H23N3O1\ROOT\13-Mar-2017\0\\#
opt=tight b3lyp/6-31+g(d,p) geom=connectivity\\tightAIQSOTCC b3LYP/6-
31+G(d,p)\\0,1\O,0.049546405,1.2848237382,0.7777546206\N,0.3041093365,
-1.5809316345,1.1065313757\N,-3.0364286919,-0.1440133615,1.4430673849\
C,1.2126030624,-0.7974555377,0.5136453746\C,1.1136947112,0.6714747275,
0.5264584973\C,2.3559223723,1.4143896445,0.3104289762\C,3.5114051842,0
.8119891506,-0.0724193808\C,3.6057993559,-0.6223983577,-0.1937011042\C
,2.4761427222,-1.4167769648,0.1295795078\C,2.6252689916,-2.8195446232,
0.0293654406\H,1.776018796,-3.4543972937,0.2650976482\C,4.8118998485,-
2.6616463905,-0.6474472844\H,5.7135843804,-3.1898047072,-0.9484413648\
C,-0.9488353981,-1.2951687734,1.4283586349\H,-1.3418448421,-1.92141382
24,2.2309565425\C,-1.9285558418,-0.4904358475,0.7675596294\C,-1.862283
7109,-0.3035717278,-0.7392752867\H,-0.8281310402,-0.5292921299,-1.0000
136109\C,-2.7495218795,-1.3576047391,-1.4616635951\H,-2.6071371594,-2.
3434953987,-1.0029748144\H,-2.3869093844,-1.4387094867,-2.4943810675\C
,-4.2418181642,-0.9794665218,-1.4967854577\H,-4.7737472363,-1.73950013
32,-2.0834322936\C,-4.8743250301,-0.9389623031,-0.0916148976\H,-5.9553
801764,-0.7811800176,-0.2010205324\H,-4.7460961383,-1.8990839544,0.423
5179495\C,-4.3392868431,0.198629183,0.8036315282\H,-5.0265709005,0.296
7056918,1.6473127655\C,-4.3068549366,1.5514283229,0.0643691282\H,-5.34
61873394,1.8907286917,-0.0402541196\H,-3.7870867436,2.2915514823,0.683
6455819\C,-3.6674223446,1.4603713787,-1.331177075\H,-3.7707079955,2.44
07562343,-1.8138057255\C,-4.4071715104,0.3983257975,-2.1674118261\H,-4
.0007445896,0.3711192411,-3.1865476949\H,-5.4720563098,0.6535427202,-2
.255222957\C,-2.1678127639,1.1235227486,-1.2565637094\H,-1.6295563213,
1.8491095887,-0.643333238\H,-1.748329441,1.1908422434,-2.269245271\C,-
3.045903329,-0.1827375766,2.9081939165\H,-3.7060814039,0.6054958553,3.
2779531471\H,-2.0395361779,-0.0017727713,3.2866975228\H,-3.4067527539,
-1.1472717391,3.2901669462\C,4.7865733427,-1.2763592549,-0.5938882803\
H,5.6712934596,-0.699048121,-0.8496159506\H,2.2815533723,2.4936813813,
0.4061526158\H,4.3946321546,1.4079392394,-0.2924901115\N,3.7481790522,
-3.4331369118,-0.3362602753\\Version=ES64L-G09RevE.01\State=1-A\HF=-10
53.5949961\RMSD=4.988e-09\RMSF=1.281e-06\Dipole=-2.8196792,1.0573062,-
0.0154586\Quadrupole=10.7790399,-12.3945447,1.6155047,9.4756081,-6.179
9364,-1.1625981\PG=C01 [X(C21H23N3O1)]\\@

Table C14. 2.3-TS2 (*cis*-to-*trans* isomerization), geometry optimization, B3LYP/6-31+G(d,p)

FTS\RB3LYP\6-31+G(d,p)\C21H23N3O1\ROOT\29-Mar-2017\0\\#
opt=(tight,qst3) b3lyp/6-31+g(d,p) geom=connectivity\\tightAIQSOTCCTTC
_QST36-31G+dp\\0,1\O,-1.0005823951,2.7074530412,0.2462862266\N,-1.0309
531044,0.1495621543,-1.1874029304\N,2.5751019241,1.1042394421,-0.88565
84686\C,-1.956579248,0.5883406214,-0.4157899099\C,-1.861524818,1.85814
0499,0.4394688229\C,-2.8807456711,2.0345982827,1.4898552567\C,-3.96146
24337,1.230729764,1.5761189952\C,-4.1883910145,0.1259049919,0.65015285
41\C,-3.2258348326,-0.1828167905,-0.3342541061\C,-3.4981843374,-1.2490
167109,-1.205506578\H,-2.7711220735,-1.5019025724,-1.9707457186\C,-5.5
165768419,-1.6879090089,-0.2135751818\H,-6.4118422788,-2.3051241468,-0
.1936579683\C,0.2432198135,0.752174729,-1.3565099241\H,0.2699027628,1.
4131210185,-2.2165385124\C,1.3585145928,0.4486290816,-0.6482546362\C,1
.3092745238,-0.607664025,0.4477802404\H,0.2497858292,-0.7459282159,0.6
756888072\C,1.8308754365,-1.9784999398,-0.0541762279\H,1.4111837609,-2
.1823706059,-1.0460798318\H,1.4571460911,-2.7635672323,0.6181102723\C,
3.3656789735,-2.0507012534,-0.0826010463\H,3.6570144968,-3.0542364322,
-0.420735571\C,3.9886963854,-1.0245467307,-1.0542252781\H,5.0596575484
,-1.2512179073,-1.1489402078\H,3.5540456773,-1.133012724,-2.0559751166
\C,3.8716639837,0.4524165152,-0.5998124466\H,4.6002496837,1.0180330921
,-1.1877176518\C,4.2627600589,0.6099647616,0.8852119383\H,5.3455188276
,0.4450317636,0.9813968165\H,4.0614145067,1.6423907418,1.1932826942\C,
3.5327584683,-0.3899303621,1.7952414886\H,3.8780208405,-0.2330812438,2
.8260061852\C,3.8979504277,-1.8179343652,1.345869382\H,3.4633189376,-2
.5599363986,2.0291283002\H,4.9876232213,-1.9536848361,1.3787398169\C,1
.999146416,-0.2038113445,1.7774487135\H,1.7410289994,0.8328353385,2.02
50225541\H,1.5759643907,-0.8343993366,2.5717590628\C,2.5895912522,2.15
03832799,-1.8920706031\H,3.5421982644,2.6834496291,-1.851779752\H,1.79
16918886,2.8724550393,-1.6896288152\H,2.4520473044,1.7689591157,-2.921
2271899\C,-5.3518021885,-0.6541564131,0.7056611582\H,-6.1156992175,-0.
4543332865,1.4517405767\H,-2.7338432023,2.8775666583,2.1582307852\H,-4
.7150117736,1.4079430658,2.3404772718\N,-4.6133740769,-1.986312744,-1.
1607138871\\Version=ES64L-G09RevE.01\State=1-A\HF=-1053.5743465\RMSD=6
.257e-09\RMSF=6.790e-06\Dipole=-0.2149623,0.1365456,1.0103873\Quadrupo
le=12.4104351,-10.0831951,-2.32724,-4.4734912,-11.6107985,-2.5376828\P
G=C01 [X(C21H23N3O1)]\\@

Table C15. 2.3-PMC-TTC, geometry optimization, B3LYP/6-31+G(d,p)

FOpt\RB3LYP\6-31+G(d,p)\C21H23N3O1\AIKOKURI\14-Mar-2017\
0\\# opt=tight b3lyp/6-31+g(d,p) geom=connectivity\\tightAIQSOTTC_opt6
-31G+dp\\0,1\O,5.3931228762,-0.2259203849,3.413022883\N,3.8599117677,1
.7457509022,4.9423810382\N,1.6716710683,4.5943067784,2.8556031358\N,4.
9882224036,0.2607084975,8.0284013168\C,4.5444468751,2.8765376465,9.970
9334242\H,5.0173604539,3.725463907,10.4813508882\C,5.4991263709,1.6735
928713,10.0643201838\H,6.4466555902,1.8840244663,9.5538722271\H,5.7400
008068,1.4978539716,11.1213492893\C,4.9007866622,0.3618690386,9.510268
1099\H,5.5295932544,-0.454745757,9.8690296042\C,4.3464926098,1.0980049
321,7.1791389907\C,3.4756417514,2.2206474845,7.7085033561\H,3.10769844
24,2.7041019762,6.8032956771\C,2.2407371136,1.7201660319,8.5006645062\
H,1.50103939,2.5314289279,8.5033592868\H,1.7778249073,0.8789654982,7.9
707096133\C,2.553732651,1.3381822492,9.9584948271\H,1.6090163696,1.091
6102348,10.4600550049\C,3.2167761132,2.5316556899,10.6740882085\H,2.54
58587291,3.3999890979,10.6581772986\H,3.3984437741,2.2880343091,11.729
6048113\C,4.265159038,3.284570625,8.5133132351\H,5.2000308388,3.523531
092,7.9920920617\H,3.6666641765,4.2049504076,8.5168922629\C,3.47627223
65,0.1104008518,10.0516787132\H,3.0376897659,-0.7503084771,9.532569147
8\H,3.5773109367,-0.1734000045,11.1078336684\C,4.4932510228,0.91934392
41,5.7879943135\H,5.1102459052,0.12410368,5.3948169713\C,3.9251035732,
1.6720940479,3.6186742663\C,3.1584139602,2.6703345146,2.8633658098\C,2
.3833732793,3.6681555058,3.4959073875\H,2.3530240662,3.6986631252,4.57
98540509\C,1.691988755,4.5789188057,1.507207704\H,1.1025515006,5.34569
98749,1.0100693929\C,2.414145011,3.6503659982,0.7721828733\H,2.4007015
182,3.6765536592,-0.3142384766\C,3.166532422,2.6712937544,1.4460760302
\C,3.9407885499,1.6750932872,0.7387660739\H,3.9307956323,1.6968257028,
-0.3490473959\C,4.6614631841,0.7371726661,1.3983285694\H,5.244052351,-
0.0124588602,0.8710484666\C,4.7104406101,0.6619492124,2.8627785636\C,5
.8253554199,-0.8181599993,7.4842465544\H,5.236078944,-1.4994580066,6.8
611312664\H,6.2582166563,-1.3849557626,8.3073366462\H,6.6380906653,-0.
4160079938,6.8698981621\\Version=ES64L-G09RevE.01\State=1-A\HF=-1053.6
164358\RMSD=4.168e-09\RMSF=2.170e-06\Dipole=0.5184151,-0.6903686,2.414
2201\Quadrupole=-7.2903961,-8.7982115,16.0886076,3.0201965,3.8974107,-
5.2134472\PG=C01 [X(C21H23N3O1)]\\

Table C16. 2.4-SO, geometry optimization, B3LYP/6-31+G(d,p)

FOpt\RB3LYP\6-31+G(d,p)\C21H23N3O1\ROOT\13-Mar-2017\0\\#
 opt=tight b3lyp/6-31+g(d,p) geom=connectivity\\tightAQSOSO_opt6-31G+d
p\\0,1\N,-2.4876344526,-0.4744756082,1.4364004374\C,-0.7079278258,-1.9
864361414,0.8193174639\H,-1.3518171215,-2.8009996955,1.1528048622\C,1.
3667499127,-1.1322828306,0.3309983436\C,0.8940453303,0.1715352232,0.43
61368347\N,0.5432806663,-2.214835738,0.675416691\C,1.7591667337,1.2796
306243,0.2624579057\C,2.7339572691,-1.3601496951,-0.0165258733\C,3.077
4122096,1.0763318527,-0.0756729252\C,3.5964783781,-0.239585551,-0.2375
499885\C,3.2938465441,-2.6554184811,-0.1509586397\H,2.6666318565,-3.52
2410977,0.0260497328\C,4.6208306162,-2.7758633288,-0.5007560885\H,5.08
52274147,-3.75072178,-0.6143102269\N,4.9084381902,-0.3787529131,-0.586
4194689\C,5.3872875602,-1.6023628483,-0.7128024422\H,6.436073634,-1.68
40665148,-0.993822122\C,-1.4081176558,-0.6539498496,0.5261591188\C,-4.
3714102624,-0.9072209808,-1.1309922216\H,-5.113073414,-1.58223356,-1.5
783500546\C,-4.4572576122,0.4717985964,-1.8131638205\H,-5.4586794274,0
.8986220266,-1.667513919\H,-4.3050372901,0.3764745149,-2.8966128801\C,
-1.7869353776,-0.608667235,-0.9873282836\H,-0.8971907173,-1.0088655885
,-1.4881391148\C,-4.7123888711,-0.7325961878,0.3573070945\H,-4.7061452
904,-1.6960454172,0.8799409122\H,-5.7310388422,-0.3270717882,0.4340251
041\C,-3.7411903549,0.2255868729,1.0782812693\H,-4.1914673035,0.471858
2733,2.0448961587\C,-2.975395828,-1.5301758217,-1.3632571696\H,-2.8985
421212,-2.4905568774,-0.8394522375\H,-2.8820397579,-1.7583510526,-2.43
32634634\C,-3.5982747285,1.5609613837,0.3046109423\H,-2.7912154103,2.1
573380092,0.7463333561\H,-4.528722497,2.1250155118,0.4576932839\C,-1.9
965148854,0.8176420768,-1.5423432905\H,-1.8884430126,0.763868471,-2.63
41783198\C,-3.3799214827,1.3958622104,-1.2143409578\H,-3.4539760494,2.
3891347144,-1.6767063484\H,-1.2059883322,1.4790430599,-1.1795030447\C,
-2.10626657,-0.3609021461,2.8443668675\H,-1.7934125905,0.6559768987,3.
125439423\H,-2.9483061394,-0.6574485788,3.4777401583\H,-1.2718097839,-
1.0320374537,3.0654995815\O,-0.4006837268,0.4226869931,0.7679448292\H,
1.3524891511,2.2784118352,0.3865181356\H,3.7541704079,1.909675642,-0.2
336084649\\Version=ES64L-G09RevE.01\State=1-A\HF=-1053.6164386\RMSD=4.
342e-09\RMSF=6.529e-06\Dipole=-1.5930582,-0.0793465,-0.0352136\Quadrup
ole=-2.8010679,2.8451451,-0.0440772,-5.2410717,-1.0638778,1.4839161\PG
=C01 [X(C21H23N3O1)]\\@

Table C17. 2.4-TS1 (C-O bond cleavage), geometry optimization, B3LYP/6-31+G(d,p)

FTS\RB3LYP\6-31+G(d,p)\C21H23N3O1\AIKOKURI\28-Mar-2017\0
\\# opt=(tight,qst3) b3lyp/6-31+g(d,p) geom=connectivity\\AQSOSOTCC_QS
T36-31G+dp\\0,1\N,-2.3310152435,-0.0245713647,1.4620756702\C,-0.125807
0911,-0.9472038493,1.4392006655\H,-0.4179660711,-1.6122569551,2.254778
8188\C,1.8436725458,-0.0513617003,0.445178658\C,1.386626969,1.33235930
3,0.3632321741\N,1.1497763909,-0.9872186381,1.1282788115\C,2.391287733
9,2.3413564232,0.0543858045\C,3.2164612186,-0.3736617346,0.0923556962\
C,3.6580645552,2.0159568524,-0.3209881172\C,4.112083545,0.6493977485,-
0.3291520248\C,3.7206333857,-1.6909279873,0.1258607642\H,3.0695960281,
-2.4956056574,0.4506874003\C,5.0315958925,-1.9277859327,-0.2521184187\
H,5.4474964992,-2.9308891027,-0.2311737704\N,5.3902254475,0.4090430834
,-0.7114173437\C,5.8267510356,-0.8444952295,-0.6735470208\H,6.85603559
3,-1.0075188407,-0.9879051461\C,-1.2316979895,-0.3071977452,0.76020480
63\C,-3.601224007,-1.3981093704,-1.2187912341\H,-4.0674824059,-2.29578
87836,-1.6450830987\C,-3.973276914,-0.1699390456,-2.0722324216\H,-5.06
47070337,-0.0506504171,-2.1090212334\H,-3.6331593053,-0.3124260843,-3.
1058422827\C,-1.2767443374,-0.3507798878,-0.7615566592\H,-0.2373248765
,-0.4992223916,-1.0598865097\C,-4.158084167,-1.2071254042,0.204585925\
H,-3.8965561836,-2.0575366833,0.8466312109\H,-5.2542323538,-1.17790770
17,0.1495475756\C,-3.6994417405,0.1029814289,0.8793434531\H,-4.3387119
517,0.2637893951,1.7507900377\C,-2.0732995843,-1.600043094,-1.23719181
61\H,-1.7897164955,-2.4771834284,-0.642853331\H,-1.7636274015,-1.80982
35195,-2.2689130496\C,-3.8568138674,1.3240523296,-0.0487781986\H,-3.37
40765643,2.194157121,0.4105749156\H,-4.930702817,1.545422862,-0.110700
6746\C,-1.7836109724,0.9259716874,-1.4734819249\H,-1.4443753107,0.8623
069199,-2.5160790102\C,-3.3128665365,1.0839592509,-1.4678983676\H,-3.5
663293941,1.9600059125,-2.0783935055\H,-1.2980840475,1.7971918855,-1.0
304308911\C,-2.2612305722,0.1289572452,2.9196267966\H,-2.9042997147,0.
9624885212,3.2152870978\H,-2.6009968638,-0.7767992002,3.4375572332\H,-
1.2382000581,0.3563402537,3.216183048\O,0.1952182563,1.6769488202,0.60
92095824\H,2.0511972042,3.3726043949,0.0702698418\H,4.3737385713,2.776
1413107,-0.6210839371\\Version=ES64L-G09RevE.01\State=1-A\HF=-1053.597
6076\RMSD=8.068e-09\RMSF=6.145e-06\Dipole=-3.4127515,-0.8668157,0.2871
515\Quadrupole=-0.8707934,-0.9530089,1.8238022,-4.0650938,-3.3073997,0
.140933\PG=C01 [X(C21H23N3O1)]\\@

Table C18. 2.4-PMC-TCC, geometry optimization, B3LYP/6-31+G(d,p)

FOpt\RB3LYP\6-31+G(d,p)\C21H23N3O1\ROOT\13-Mar-2017\0\\#
opt=tight b3lyp/6-31+g(d,p) geom=connectivity\\tightAQSOTCC b3LYP/6-3
1+G(d,p)\\0,1\O,0.0332361119,1.2469175862,0.7816933569\N,0.2722537724,
-1.6214001932,1.1015174962\N,-3.0491258499,-0.1420074184,1.442177737\C
,1.1862418807,-0.8395674101,0.5164431949\C,1.0954124231,0.6311647593,0
.5275580969\C,2.3378777081,1.3681188381,0.3009897877\C,3.488822926,0.7
584857709,-0.0824068768\C,3.5830780475,-0.6785172002,-0.1886794232\C,2
.4502702234,-1.4699539607,0.1452980731\C,2.6041286078,-2.8686017653,0.
0744139226\H,1.7617440613,-3.5036542652,0.3269987624\C,4.8755740343,-2
.5268303177,-0.6388584328\H,5.8392798276,-2.9188276025,-0.958517536\C,
-0.980393497,-1.3274042055,1.4223560301\H,-1.3825433429,-1.9553972755,
2.218968228\C,-1.9480062119,-0.5063767075,0.7651266518\C,-1.8826075037
,-0.3237309053,-0.7428415441\H,-0.8535277162,-0.5705168941,-1.00513995
34\C,-2.7913778072,-1.3632613794,-1.4593964972\H,-2.6667025518,-2.3503
000534,-0.9977320827\H,-2.4333733743,-1.4537993601,-2.4929406021\C,-4.
2768776659,-0.9583593325,-1.4923905202\H,-4.823122336,-1.7102910345,-2
.0765406439\C,-4.9056221251,-0.9039869933,-0.0863738402\H,-5.983725261
6,-0.7259044035,-0.1939597376\H,-4.7941927294,-1.8652207891,0.43069393
37\C,-4.346135322,0.2249656133,0.8052244077\H,-5.0294964522,0.33837880
54,1.6502806701\C,-4.2887365698,1.575615321,0.0634153616\H,-5.32123527
18,1.9361454758,-0.0381787831\H,-3.7518557263,2.3058741037,0.679741329
5\C,-3.6565522628,1.4699975457,-1.3355474588\H,-3.7441186997,2.4511090
285,-1.8197156763\C,-4.4196957749,0.4201291912,-2.165583367\H,-4.01819
2672,0.3826760073,-3.1864494729\H,-5.4800753944,0.6946570373,-2.249841
5833\C,-2.1630306245,1.10603786,-1.2662868974\H,-1.6089000022,1.824326
5782,-0.6586679884\H,-1.746413073,1.1611026288,-2.280938137\C,-3.05607
81744,-0.1790856146,2.9071443314\H,-3.696575284,0.6248702717,3.2779636
077\H,-2.0445898923,-0.0215836503,3.282480108\H,-3.4388992577,-1.13439
70665,3.2910402989\H,2.2673462586,2.4483400192,0.387667848\H,4.3832677
619,1.3283712171,-0.3178125352\C,3.8238400618,-3.4016744456,-0.3126178
242\H,3.971911592,-4.4759586296,-0.3710298651\N,4.7684044882,-1.202972
0758,-0.5791564257\\Version=ES64L-G09RevE.01\State=1-A\HF=-1053.597707
2\RMSD=3.067e-09\RMSF=5.930e-07\Dipole=-3.2634841,-0.301973,0.102481\Q
uadrupole=-1.2828614,0.1217502,1.1611112,-3.1700571,-3.7609287,0.08151
02\PG=C01 [X(C21H23N3O1)]\\@

Table C19. 2.4-TS2 (*cis*-to-*trans* isomerization), geometry optimization, B3LYP/6-31+G(d,p)

FTS\RB3LYP\6-31+G(d,p)\C21H23N3O1\AIKOKURI\28-Mar-2017\0
\\# opt=(tight,qst3) b3lyp/6-31+g(d,p) geom=connectivity\\QST3 tightAQ
SOTCC b3LYP/6-31+G(d,p)\\0,1\O,-1.0088632707,2.6704053717,0.2086830702
\N,-1.0209608472,0.1104886969,-1.2127397229\N,2.5749016733,1.099485712
7,-0.8953225198\C,-1.9539455329,0.5480900269,-0.4497747446\C,-1.877678
9907,1.8268956527,0.3957977214\C,-2.9193191338,2.0137416171,1.41823989
19\C,-3.9953125693,1.2021467803,1.4962088816\C,-4.1978258459,0.0767190
569,0.5867106951\C,-3.215572762,-0.2395149445,-0.3773099423\C,-3.45998
23999,-1.3252248049,-1.226139504\H,-2.7153315278,-1.5883487686,-1.9696
002574\C,-5.5580840849,-1.6415438393,-0.1011491178\H,-6.495484289,-2.1
770309096,0.0325512597\C,0.2503070606,0.7210617786,-1.3791903482\H,0.2
761100386,1.3783534104,-2.2420247636\C,1.3637152907,0.4331350417,-0.66
16981039\C,1.3175381684,-0.6144064832,0.4427483029\H,0.2578649647,-0.7
625802062,0.6633922048\C,1.859396956,-1.9834121177,-0.042434201\H,1.45
09333349,-2.2007667857,-1.036336231\H,1.4892456692,-2.7668620174,0.633
8147714\C,3.3951474703,-2.0381831384,-0.0574533613\H,3.7009840731,-3.0
413163932,-0.3840076907\C,4.0142676331,-1.013590935,-1.0331926103\H,5.
088497149,-1.2287309279,-1.1171237663\H,3.5890724177,-1.1358400787,-2.
0374583335\C,3.8764541924,0.4659258606,-0.5931077259\H,4.6032823345,1.
0345593327,-1.1803022247\C,4.2534019909,0.6411587707,0.8936545207\H,5.
3371364906,0.4896008114,1.0003847708\H,4.0376251309,1.6738626176,1.190
7303584\C,3.5270465464,-0.3588233851,1.8065296656\H,3.8617079559,-0.18
87771861,2.838653257\C,3.9125638061,-1.7864174146,1.3732619021\H,3.480
797012,-2.5272557024,2.0596003449\H,5.0034128848,-1.9092794332,1.41635
12193\C,1.991591787,-0.19070855,1.7743870093\H,1.7191307438,0.84489717
48,2.0101556248\H,1.5689668695,-0.8187838266,2.5709099015\C,2.58526100
42,2.1430423038,-1.9042824825\H,3.5318245233,2.6863671945,-1.858886562
1\H,1.7782109921,2.8569372264,-1.709376504\H,2.459191831,1.7574536876,
-2.9334537526\H,-2.7938462658,2.8695146673,2.0743982408\H,-4.778338266
4,1.3667238003,2.2311720736\C,-4.6498713831,-2.0338867158,-1.092521637
4\H,-4.8761152571,-2.8761372399,-1.7386531057\N,-5.3459525684,-0.61527
77896,0.7256205256\\Version=ES64L-G09RevE.01\State=1-A\HF=-1053.578395
5\RMSD=3.693e-09\RMSF=6.736e-06\Dipole=0.1587505,-0.7613716,-0.1550522
\Quadrupole=4.1266064,-3.2002858,-0.9263205,3.8635446,1.3071655,1.8931
43\PG=C01 [X(C21H23N3O1)]\\@

Table C20. 2.4-PMC-TTC, geometry optimization, B3LYP/6-31+G(d,p)

FOpt\RB3LYP\6-31+G(d,p)\C21H23N3O1\ROOT\13-Mar-2017\0\\#
opt=tight b3lyp/6-31+g(d,p) geom=connectivity\\tightAQSOTTC_opt6-31G+
dp\\0,1\O,-1.9446008386,2.9446375475,-0.2659994873\N,-0.9220188952,0.2
090238445,-0.0580933344\N,2.4612727791,1.4660293943,-0.0958991299\C,3.
9094599415,-1.0979635773,1.3674646761\H,4.3219659707,-1.5034877999,2.3
003643587\C,4.2862078406,0.3916251266,1.2885165772\H,3.8440877427,0.95
26984847,2.120558423\H,5.3762022993,0.4833122742,1.3871274946\C,3.8914
648442,1.0617675137,-0.0460158536\H,4.4360722886,2.0056801704,-0.10431
2046\C,1.4291642057,0.5882728108,-0.0495677605\C,1.6863422538,-0.90218
64989,0.0592152918\H,0.6837392329,-1.3304225021,0.0743432467\C,2.42336
51969,-1.491363129,-1.1706845102\H,2.2255689142,-2.5713888351,-1.18754
27117\H,1.9913227553,-1.0812379815,-2.0914877499\C,3.9470492502,-1.274
6234306,-1.1418637793\H,4.3863258287,-1.8059591269,-1.9960486109\C,4.5
249654345,-1.845521809,0.1681494404\H,4.3056173712,-2.9185096396,0.240
4043424\H,5.6184075853,-1.7422274589,0.1772573853\C,2.3851420339,-1.31
17263286,1.3809334918\H,1.9267082935,-0.7775699149,2.2219199031\H,2.18
46665037,-2.379155171,1.5430096393\C,4.3244005221,0.2121255206,-1.2611
554542\H,3.9084545874,0.6501892713,-2.1763908598\H,5.4170396756,0.2913
829965,-1.3391048728\C,0.1074754626,1.0711295131,-0.1033634989\H,-0.09
09969729,2.1303314716,-0.1809073546\C,-2.2007814555,0.5565690527,-0.10
17187672\C,-3.1801004146,-0.537431194,-0.0393735206\C,-2.8028956697,-1
.8896119154,0.0614695861\H,-1.7491130236,-2.1402718799,0.0949038998\C,
-5.1301056413,-2.4914167738,0.0689700356\H,-5.9184174267,-3.2405149045
,0.1098952123\C,-4.5735078097,-0.2642786952,-0.0794782385\C,-5.0255191
886,1.1075581052,-0.182825384\H,-6.1001762094,1.264718539,-0.209988001
3\C,-4.1543556527,2.1424442833,-0.2426299869\H,-4.4923160256,3.1714745
473,-0.3201363111\C,-2.7013328249,1.9544652363,-0.2076287709\C,2.17995
40312,2.9046518249,-0.2013881793\H,1.6181803527,3.1318353287,-1.113899
4473\H,3.1209238365,3.4525413373,-0.2258521105\H,1.5916926987,3.256226
0533,0.6531437749\C,-3.7794527483,-2.873116446,0.1160765955\H,-3.51213
89461,-3.9228172374,0.1939796659\N,-5.5245179899,-1.2245609979,-0.0261
243088\\Version=ES64L-G09RevE.01\State=1-A\HF=-1053.6188901\RMSD=4.897
e-09\RMSF=2.511e-06\Dipole=3.4714724,-0.6664198,0.0989241\Quadrupole=0
.0103156,1.6486482,-1.6589638,5.7187408,-0.3775237,-0.14751\PG=C01 [X(
C21H23N3O1)]\\@

Table C21. 2.1-SO, geometry optimization, B3LYP/6-311+G(d,p)


```
FOpt\RB3LYP\6-311+G(d,p)\C26H26N2O1\BRYNND\18-No
 v-2012\0\\# opt=tight b3lyp/6-311+g(d,p)\\APeSOSO form b3LYP/6-311+G(d
,p) starting with Michelle's complex\\0,1\N,-2.4823426057,-0.463740219
8,1.4207067608\C,-0.6856246446,-1.9634440096,0.8283599536\H,-1.3164444
026,-2.7825869462,1.1713418754\C,1.3786988595,-1.0801812705,0.34161266
84\C,0.8938593252,0.2006679625,0.4316094446\N,0.5657081114,-2.16603361
03,0.6970966873\C,1.7494959768,1.3448998819,0.2750829646\C,2.759885832
3,-1.3163422991,-0.0013460004\C,3.119307897,1.142452376,-0.0560654398\
C,3.6307616952,-0.2128446815,-0.2199704493\C,1.245475467,2.6542118342,
0.4405829593\H,0.2009195191,2.779012228,0.6938028288\C,2.0683076875,3.
7504917687,0.2888924424\H,1.6734696998,4.7513792514,0.421538024\C,3.42
09556823,3.5636002147,-0.0399701146\H,4.0724137679,4.4216955253,-0.161
9985167\C,3.2572953989,-2.6326571095,-0.122872028\H,2.5794515835,-3.45
52198897,0.0638387518\C,4.5735222163,-2.8615692898,-0.4670506988\H,4.9
414722026,-3.8776371873,-0.5574648853\C,5.436444271,-1.778300149,-0.70
06590541\H,6.4700360585,-1.9553058742,-0.9759102932\C,-1.4031381112,-0
.6484534124,0.5151054546\C,-4.3643160538,-0.9462351758,-1.1285689589\H
,-5.1008452006,-1.6319808504,-1.5625478988\C,-4.4582891108,0.417996646
6,-1.835583375\H,-5.4598660995,0.8415464674,-1.6968222519\H,-4.3076365
383,0.3039973434,-2.9152604411\C,-1.7825009116,-0.630986073,-0.9969321
013\H,-0.8941192029,-1.0361734546,-1.4916520673\C,-4.7066506613,-0.745
2516758,0.354431717\H,-4.6976086912,-1.6969564875,0.8937465659\H,-5.72
46590714,-0.3418454522,0.4237773568\C,-3.7374659822,0.2269282935,1.055
2525034\H,-4.1849993046,0.4891445873,2.0165405552\C,-2.9663669713,-1.5
653385671,-1.3493958952\H,-2.8839604112,-2.5110852002,-0.8048620715\H,
-2.8744763575,-1.8171188977,-2.4121786185\C,-3.6018235171,1.5476478645
,0.2585321165\H,-2.7978480188,2.1536595189,0.6872999194\H,-4.532359444
6,2.1097329375,0.4039810076\C,-2.0009965326,0.7806542896,-1.5777596793
\H,-1.8966172638,0.7076697513,-2.6669092695\C,-3.3858870566,1.35740956
33,-1.2562017\H,-3.4660272489,2.339824481,-1.7351927519\H,-1.213905583
3,1.4528616427,-1.2342929189\C,-2.1060636928,-0.3480194699,2.828790016
7\H,-1.7785023293,0.663677405,3.1049238141\H,-2.9540304053,-0.62738951
34,3.458881886\H,-1.2844148564,-1.0297886881,3.0573053546\O,-0.4041951
606,0.4409740033,0.7452197409\C,3.9288957298,2.2898488375,-0.207674002
3\H,4.9759361157,2.179602725,-0.4568177406\C,4.9701588893,-0.484203901
9,-0.5769912596\H,5.6562393358,0.3326061359,-0.7593870181\\Version=AM6
4L-G09RevA.02\State=1-A\HF=-1191.4534062\RMSD=7.054e-09\RMSF=3.190e-06
\Dipole=-1.0470375,0.507574,-0.175338\Quadrupole=6.1254258,-0.6266792,
-5.4987467,2.4622689,-3.4524092,0.9851995\PG=C01 [X(C26H26N2O1)]\\@
```

Table C22. 2.1-PMC-TTC, geometry optimization, B3LYP/6-311+G(d,p)

FOpt\RB3LYP\6-311+G(d,p)\C26H26N2O1\BRYNND\19-No
v-2012\0\\# opt=tight b3lyp/6-311+g(d,p)\\finalAPeSOPMC form b3LYP/6-3
11+G(d,p) xtal structure\\0,1\C,2.5596047352,-2.9920431961,-0.26125746
47\H,1.9924161879,-3.3021752329,0.6224324829\H,3.4156642047,-3.6532872
549,-0.3764634831\H,1.9120867397,-3.1066040769,-1.1340126654\C,2.12853
24856,-0.5983598484,-0.0938460399\C,0.7561855111,-0.8868742464,-0.1252
022799\H,0.4135881227,-1.9089040983,-0.1558774541\C,-1.4486721338,-0.0
057406402,-0.0886045439\C,-2.1634590837,-1.3004184151,-0.0757763759\C,
4.498127812,-1.4087166342,-0.0090784362\H,4.9061812052,-2.4188183099,-
0.0331302171\C,4.914595741,-0.788457386,1.3416170321\H,4.3538784449,-1
.2700671394,2.1490298419\H,5.971141654,-1.0360495937,1.4986502418\C,4.
7547485557,0.7399880979,1.399479967\H,5.1810094952,1.0896541888,2.3462
048206\C,3.2811094108,1.171870709,1.3441304185\H,3.2307415537,2.257750
7917,1.4853912233\H,2.7143593206,0.7251171546,2.1670409054\C,2.5918643
837,0.84081074,-0.0020148828\H,1.6620597134,1.4049162899,-0.0345363126
\C,3.4546454865,1.2983390831,-1.2027910516\H,3.0118412495,0.9342449353
,-2.1355129955\H,3.4066182905,2.3927110973,-1.2436305813\C,4.930861363
7,0.8808912625,-1.1049520141\H,5.4741485564,1.3399303873,-1.9382213091
\C,5.5215405127,1.3806916625,0.2271632715\H,5.4485054083,2.4724709849,
0.2843454194\H,6.5869499155,1.1295906406,0.2871379989\C,5.1104239756,-
0.6424824308,-1.1999559723\H,6.1829287053,-0.8700020773,-1.2185851919\
H,4.6882070369,-1.0289111778,-2.1329442557\C,-3.6465412346,-1.26853886
09,0.0085568524\C,-4.36790234,-0.0556416931,0.0424812736\C,-3.64988680
8,1.2284221715,-0.0161455986\C,-2.234005113,1.2438086207,-0.0774859537
\C,-1.5745849067,2.487408346,-0.1325740067\H,-0.494854118,2.4857628303
,-0.181509133\C,-2.2727872783,3.6816707776,-0.1276137258\H,-1.73625952
1,4.6232407418,-0.172412763\C,-3.669721566,3.6684481778,-0.0681372942\
H,-4.2299788869,4.59662496,-0.0661937623\C,-4.3378732234,2.4566907293,
-0.0141505079\H,-5.4187728671,2.4686722129,0.0277864213\C,-4.321905379
7,-2.4983551835,0.0577568501\H,-3.7243858226,-3.4008753717,0.027328663
6\C,-5.7020370494,-2.5497672192,0.1438222292\H,-6.2153293753,-3.503838
0763,0.1829569425\C,-6.4273841987,-1.3539656166,0.1814735103\H,-7.5096
187454,-1.3761964436,0.2505187693\C,-5.7717788347,-0.1336189301,0.1315
826381\H,-6.3662424834,0.7693792447,0.164733741\N,3.0320751877,-1.6086
288066,-0.1379870323\N,-0.1359485063,0.1173893301,-0.1029019884\O,-1.5
726178201,-2.386016368,-0.1222101614\\Version=AM64L-G09RevA.02\State=1
-A\HF=-1191.4623254\RMSD=6.385e-09\RMSF=1.931e-06\Dipole=2.3558163,0.0
175521,0.0670959\Quadrupole=15.5983522,-3.4638335,-12.1345188,-5.71510
36,-0.7637625,-0.0525377\PG=C01 [X(C26H26N2O1)]\\@

Table C23. 2.2-SO, geometry optimization, B3LYP/6-311+G(d,p)

FOpt\RB3LYP\6-311+G(d,p)\C24H24N4O1\BRYNND\18-No
v-2012\0\\# opt=tight b3lyp/6-311+g(d,p)\\APSOSO form b3LYP/6-311+G(d,
p) starting with Michelle's complex\\0,1\N,-2.4723718877,-0.462112695,
1.417626778\C,-0.693086588,-1.9658236362,0.7859210995\H,-1.3284553639,
-2.7871581229,1.1145416922\C,1.3742769674,-1.0881706651,0.3116452061\C
,0.8968875503,0.1944911217,0.413865571\N,0.5566458215,-2.175804137,0.6
481160511\C,1.7666387836,1.3287035933,0.2699462108\C,2.7567066072,-1.3
214388894,-0.0215553961\C,3.1372738063,1.130203664,-0.0567137001\C,3.6
427093244,-0.2295759779,-0.2252880741\C,1.3050546182,2.650040275,0.436
5561691\H,0.2660835362,2.8218512101,0.6871354407\C,2.1905911735,3.6933
06887,0.2809037071\H,1.8769732053,4.7232157429,0.4041225164\C,3.524952
3366,3.393030164,-0.0478543542\H,4.2452576747,4.1968665184,-0.18088910
07\C,3.2802303232,-2.6240550934,-0.1514208787\H,2.6273516182,-3.471159
7132,0.0156633746\C,4.6077465735,-2.7834556546,-0.4832887858\H,5.04482
34786,-3.7693588474,-0.5923823121\N,3.9861666,2.1660991218,-0.21269342
91\N,4.9389397639,-0.402733922,-0.5540762061\C,5.3963118082,-1.6353286
318,-0.6800565964\H,6.4454764224,-1.733741865,-0.948253101\C,-1.408285
7539,-0.6429932442,0.4973033216\C,-4.3881005962,-0.9187796402,-1.11246
66208\H,-5.1305114853,-1.5992692887,-1.54439532\C,-4.4902394533,0.4531
261677,-1.8029518858\H,-5.4895541043,0.8756627966,-1.646996166\H,-4.35
32554327,0.3508859495,-2.88552568\C,-1.8047067145,-0.6066017198,-1.009
6431987\H,-0.9225827988,-1.0063702688,-1.5199641362\C,-4.7105311235,-0
.7349747773,0.3773643231\H,-4.693439424,-1.6927616509,0.9056810061\H,-
5.727930875,-0.3340170277,0.4653615243\C,-3.7334083273,0.2306890769,1.
076156408\H,-4.1682026898,0.4821509887,2.0460327058\C,-2.9936174572,-1
.5359392215,-1.3592443252\H,-2.9050833346,-2.4891363032,-0.828938634\H
,-2.9149300536,-1.7733078501,-2.4263010344\C,-3.6077232506,1.559713241
8,0.2921638933\H,-2.7989923991,2.1614471547,0.7181646539\H,-4.53644315
54,2.119822737,0.4549633755\C,-2.0297337358,0.8120924284,-1.5712309128
\H,-1.9379104881,0.7514055846,-2.6621281066\C,-3.4102414263,1.38559652
53,-1.2266963344\H,-3.495595743,2.3729872301,-1.6942943611\H,-1.238384
9205,1.4802252926,-1.2294031308\C,-2.0819496628,-0.3721191881,2.823688
6573\H,-1.7524717031,0.6348051771,3.1143006064\H,-2.9230581901,-0.6630
460047,3.457531003\H,-1.2578265272,-1.0574184729,3.0319478398\O,-0.397
6676077,0.4447082698,0.7241939868\\Version=AM64L-G09RevA.02\State=1-A\
HF=-1223.5338073\RMSD=2.301e-09\RMSF=3.731e-06\Dipole=-2.4040056,0.007
6966,0.1347403\Quadrupole=-7.6481225,7.7661547,-0.1180322,-5.3841769,-
0.1169203,2.3161528\PG=C01 [X(C24H24N4O1)]\\@

Table C24. 2.2-PMC-TTC, geometry optimization, B3LYP/6-311+G(d,p)

FOpt\RB3LYP\6-311+G(d,p)\C24H24N4O1\BRYNND\19-No
v-2012\0\\# opt=tight b3lyp/6-311+g(d,p)\\APSOPMC form b3LYP/6-311+G(d
,p) xtal stucture\\0,1\O,1.5732519702,-2.3999110322,-0.0705255741\N,0.
13490638,0.1182450126,-0.09008035\N,5.7162014998,-0.0483272378,0.09829
8388\N,4.3900582978,2.3448574345,-0.009184491\N,-3.0348045223,-1.59901
11921,-0.1221060846\C,1.4477483501,-0.01595419,-0.0707604525\C,2.15817
60325,-1.3105888774,-0.0458701702\C,3.6415717511,-1.2720022572,0.01894
67126\C,4.3729131656,-0.0670097671,0.0369833005\C,3.6543693989,1.22090
75075,-0.0142416548\C,2.2397081425,1.2265188754,-0.066285555\C,4.34701
09191,-2.481526743,0.0649605886\H,3.7849093964,-3.407363849,0.05016593
36\C,5.7275641646,-2.4563960883,0.1281038332\H,6.311443835,-3.36851596
52,0.1661737226\C,6.3604046161,-1.2068065034,0.1423381786\H,7.44517934
95,-1.1452400607,0.1920712807\C,1.6129160617,2.4842021775,-0.115660757
7\H,0.5331628314,2.5248716197,-0.1582331785\C,2.3748073958,3.636604774
8,-0.1103975507\H,1.9112920442,4.6159544123,-0.1487981571\C,3.76803023
09,3.5134697385,-0.0556295832\H,4.4016119935,4.3969751353,-0.050183827
9\C,-0.7582170496,-0.8827869632,-0.1038737388\H,-0.4174175516,-1.90602
20125,-0.117633696\C,-2.132210877,-0.5909384783,-0.0848060503\C,-2.592
1901813,0.8503968752,-0.0133031581\H,-1.6611780633,1.4123761185,-0.047
0385357\C,-3.4465054742,1.2946473106,-1.2252346488\H,-2.998412694,0.91
91123642,-2.1508568086\H,-3.3962155122,2.3882879197,-1.2784061771\C,-4
.9238946158,0.8806700125,-1.1315128737\H,-5.4609271115,1.3302968686,-1
.9737557945\C,-5.1050948066,-0.643529386,-1.2095673653\H,-6.1776057589
,-0.8699676376,-1.2327169448\H,-4.6774583775,-1.0419730471,-2.13499720
96\C,-4.5028887551,-1.3960128143,-0.0051634621\H,-4.911166856,-2.40606
17455,-0.0193912189\C,-4.9257180374,-0.7588606643,1.3353321322\H,-5.98
34501623,-1.0030914144,1.4887333361\H,-4.3710191107,-1.2316260659,2.15
20589064\C,-4.7638871933,0.7699320773,1.3753796366\H,-5.1953916488,1.1
316579862,2.3150322468\C,-5.5221490732,1.3974245424,0.1905444998\H,-5.
4481273477,2.4896578272,0.2349225813\H,-6.5881595275,1.148511257,0.246
7872861\C,-3.2892027322,1.198483177,1.3246187675\H,-2.7287863737,0.760
7768882,2.1566844216\H,-3.2375052968,2.2858147168,1.4528318217\C,-2.56
47373057,-2.9856755948,-0.2278168144\H,-3.4216118492,-3.6451233677,-0.
3456005181\H,-2.0081298717,-3.2886322755,0.6647850046\H,-1.9092909098,
-3.1097208789,-1.0930301869\\Version=AM64L-G09RevA.02\State=1-A\HF=-12
23.5443545\RMSD=4.847e-09\RMSF=2.173e-06\Dipole=-3.8042697,-0.640876,0
.0048098\Quadrupole=1.4919159,4.0978747,-5.5897906,-4.942481,0.1763991
,-0.2376971\PG=C01 [X(C24H24N4O1)]\\@

Table C25. 2.3-SO, geometry optimization, B3LYP/6-311G+(d,p)


```
FOpt\RB3LYP\6-311+G(d,p)\C21H23N3O1\BRYNND\12-No
v-2013\0\\# opt=tight b3lyp/6-311+g(d,p)\\Title Card Required\\0,1\N,-
2.0538825585,-0.768765691,1.2632968857\C,-0.0530565932,-1.7190810044,0
.3058552998\H,-0.5572020453,-2.6840444818,0.3377841708\C,1.853712966,-
0.4501808057,0.2223758994\C,1.1757794204,0.6643821737,0.6951202592\N,1
.2147017843,-1.6968993937,0.173346059\C,1.8524936904,1.8860494165,0.91
9225385\C,3.2375820624,-0.3417167029,-0.1058439151\C,3.1843305313,2.00
3214295,0.6099894656\C,3.9071453101,0.9019031288,0.0770708399\C,3.9981
5608,-1.4313682368,-0.6102714361\H,3.5106458223,-2.3914511948,-0.74219
70741\C,5.8993019726,-0.1587613366,-0.7649583893\H,6.9479485779,-0.135
1494099,-1.0439742936\C,-0.9615803532,-0.4885788248,0.3997805584\C,-3.
8334164891,-0.6789555394,-1.4078960482\H,-4.449920287,-1.2881231409,-2
.0784448409\C,-4.1480613188,0.8104010034,-1.6373092916\H,-5.2051559485
,1.0050808983,-1.4225745227\H,-3.9806189405,1.0823053532,-2.6858933816
\C,-1.3390054462,-0.0333965215,-1.0425069682\H,-0.3961739196,-0.110122
1565,-1.5934177716\C,-4.2002716869,-1.032625873,0.0401017178\H,-4.0323
997552,-2.0947194056,0.2414761487\H,-5.2709798448,-0.8407482979,0.1826
796479\C,-3.4067412803,-0.2042258646,1.0698332027\H,-3.8924644933,-0.3
468475741,2.0377681662\C,-2.3542426228,-0.9677884341,-1.7457662918\H,-
2.1181170127,-2.0165843995,-1.5400366432\H,-2.2229632907,-0.8340725039
,-2.8256464859\C,-3.4903967307,1.3084709171,0.7532458547\H,-2.79733887
35,1.8572796018,1.3982439433\H,-4.5009053683,1.6403045593,1.0210442593
\C,-1.7836392162,1.4412783297,-1.1402076632\H,-1.6644330975,1.75104941
26,-2.1853377003\C,-3.243940861,1.6605320192,-0.727659507\H,-3.4825453
906,2.7209816954,-0.8670357461\H,-1.1186293419,2.0712582033,-0.5482767
087\C,-1.6983020801,-1.0483800377,2.6535366195\H,-1.5487377387,-0.1381
005019,3.2500021135\H,-2.4834250039,-1.6488287507,3.1194127587\H,-0.77
09387256,-1.623138686,2.6984821167\O,-0.1414465122,0.6026888514,1.0140
538542\H,1.2901768016,2.7196337109,1.3237333029\H,3.6975101332,2.94589
60075,0.7660414952\C,5.2767185387,0.9637988601,-0.2758028107\H,5.82671
49309,1.8912382495,-0.157544408\N,5.2734212047,-1.353218917,-0.9298621
262\\Version=AM64L-G09RevA.02\State=1-A\HF=-1053.8140047\RMSD=4.082e-0
9\RMSF=4.328e-06\Dipole=-1.8460068,1.080926,0.2971189\Quadrupole=-2.63
26216,1.423575,1.2090466,11.956048,2.2823616,-0.968676\PG=C01 [X(C21H2
3N3O1)]\\@
```

Table C26. 2.3-PMC-TTC, geometry optimization, B3LYP/6-311G+(d,p)

FOpt\RB3LYP\6-311+G(d,p)\C21H23N3O1\BRYNND\12-No
v-2013\0\\# opt=tight b3lyp/6-311+g(d,p) geom=connectivity\\Title Card
Required\\0,1\O,-1.925905135,2.9959657005,-0.00008544\N,-0.926170749,
0.2496900079,-0.0000399017\N,-3.6863853004,-2.8456449945,0.0000786427\
N,2.4681097275,1.4493675824,-0.0001611967\C,3.8883938664,-1.2314923356
,1.2566908695\H,4.3053566625,-1.7084082956,2.150373642\C,4.291902045,0
.2513672336,1.277069183\H,3.872584763,0.7592152032,2.151390088\H,5.382
6604442,0.3171480501,1.3658829949\C,3.8917533237,1.0189902171,-0.00007
04463\H,4.4505048923,1.954135328,-0.0001177013\C,1.4245452477,0.590346
083,-0.0000836452\C,1.6543264129,-0.9063707691,0.000012512\H,0.6464312
053,-1.3166146967,0.0000109267\C,2.3624131632,-1.4182252586,-1.2784451
343\H,2.1430076149,-2.4879718202,-1.3703733439\H,1.9267759197,-0.93588
16822,-2.159276412\C,3.8884730612,-1.2316756642,-1.2564915153\H,4.3054
829651,-1.7087292409,-2.1500788063\C,4.4724179207,-1.9028405148,0.0001
666614\H,4.2340784832,-2.9719467592,0.0002382093\H,5.5656505773,-1.820
4988454,0.0001940617\C,2.3623355132,-1.4180546418,1.2785817429\H,1.926
6419227,-0.9355967936,2.1593224579\H,2.1429335497,-2.487790864,1.37063
78527\C,4.2919997997,0.2511744395,-1.2770635541\H,3.8727579227,0.75889
68554,-2.1514934653\H,5.3827660737,0.3169302244,-1.3657994775\C,0.1112
931231,1.095811713,-0.0000849757\H,-0.0660881379,2.1599001079,-0.00011
48489\C,-2.1999047497,0.6092313986,-0.0000222931\C,-3.1917223626,-0.47
10987045,0.0000221763\C,-2.8265654373,-1.8332776048,0.0000390731\H,-1.
7745066451,-2.0913234882,0.0000179664\C,-4.9993964995,-2.5524637697,0.
0001040875\H,-5.6796330118,-3.3988668224,0.0001362491\C,-5.4821627085,
-1.2559131068,0.0000905803\H,-6.5504087805,-1.0667859311,0.0001116667\
C,-4.5760936866,-0.1836531999,0.0000488343\C,-5.0158057657,1.192260915
5,0.0000319875\H,-6.0846386185,1.3861061762,0.000054327\C,-4.136366776
5,2.2160473653,-0.0000108323\H,-4.463342483,3.2498926155,-0.0000244057
\C,-2.6840278852,2.0139386964,-0.000043404\C,2.2139167211,2.8964270166
,-0.0002787853\H,1.6457167608,3.1971803311,-0.8847573583\H,3.163921635
1,3.4254426456,-0.0004148975\H,1.645867415,3.1973598973,0.884238048\\V
ersion=AM64L-G09RevA.02\State=1-A\HF=-1053.81867\RMSD=3.852e-09\RMSF=2
.689e-06\Dipole=2.5163628,0.3670731,-0.0000138\Quadrupole=17.4327523,-
12.4778758,-4.9548765,0.565189,-0.0005014,-0.0001158\PG=C01 [X(C21H23N
3O1)]\\@

Table C27. 2.4-SO, geometry optimization, B3LYP/6-311G+(d,p)


```
FOpt\RB3LYP\6-311+G(d,p)\C21H23N3O1\BRYNND\12-Nov
-2013\0\\# opt=tight b3lyp/6-311+g(d,p)\\AQSO SO opt 6-31G\\0,1\N,-2.0
551551491,-0.7972360957,1.2472268014\C,-0.0592151984,-1.7356344588,0.2
658145117\H,-0.5667351379,-2.699226116,0.2771686768\C,1.8508364954,-0.
4696154915,0.2044823422\C,1.1783656122,0.6376336965,0.70086305\N,1.208
4210886,-1.7132237595,0.129372395\C,1.8589531176,1.8523101161,0.949137
4585\C,3.2360990194,-0.3645728887,-0.1202013932\C,3.190436436,1.969525
319,0.6402304494\C,3.9110905068,0.8768166465,0.0865726341\C,3.99264672
17,-1.4420801935,-0.6386904892\H,3.5100685313,-2.3992984903,-0.7909978
375\C,5.3199969057,-1.2432231992,-0.9316805552\H,5.932143114,-2.043604
692,-1.3309783285\N,5.2276531076,1.054864402,-0.2133577938\C,5.8920371
293,0.0304927717,-0.7045685813\H,6.9405872471,0.2007639706,-0.93685605
03\C,-0.9623433795,-0.5037988721,0.3873972378\C,-3.8414791675,-0.64262
62036,-1.4153915906\H,-4.4637976027,-1.2352688394,-2.0954289666\C,-4.1
467081722,0.8526338834,-1.616434332\H,-5.2018432148,1.050514443,-1.394
8654674\H,-3.9803379,1.1426934251,-2.6603280248\C,-1.3415839067,-0.020
3616319,-1.0456149251\H,-0.4007161875,-0.0930724435,-1.6004079316\C,-4
.2071684782,-1.0205236811,0.026871265\H,-4.0467968935,-2.0874738152,0.
207718811\H,-5.2760212255,-0.8231357449,0.1759589856\C,-3.4039623643,-
0.2177835001,1.0694230962\H,-3.8878496144,-0.3743329975,2.0361617986\C
,-2.3650803598,-0.935106662,-1.7624198379\H,-2.1357481087,-1.989060759
2,-1.5760982704\H,-2.2361964519,-0.782658714,-2.8401722784\C,-3.477275
9898,1.3014876287,0.7807601294\H,-2.7779883266,1.8333580221,1.43312883
36\H,-4.4843683823,1.6355464148,1.0586438071\C,-1.7765599181,1.4586640
737,-1.1160506623\H,-1.6591801026,1.7859155475,-2.1560481425\C,-3.2338
428288,1.6794806254,-0.6941036479\H,-3.4660560903,2.7438865924,-0.8126
089091\H,-1.105097815,2.0736417206,-0.5158316286\C,-1.6971700492,-1.10
34142261,2.631238042\H,-1.540083549,-0.2047940799,3.2432199952\H,-2.48
47615236,-1.7072032367,3.0886815483\H,-0.7732719492,-1.6846514658,2.66
27375363\O,-0.1389900154,0.5722703586,1.0199313688\H,1.3003323937,2.68
00616516,1.3701388826\H,3.7272156259,2.896164949,0.8034619876\\Version
=AM64L-G09RevA.02\State=1-A\HF=-1053.8173494\RMSD=2.390e-09\RMSF=6.458
e-06\Dipole=-1.5802551,-0.3085408,-0.1530165\Quadrupole=-1.093553,0.23
02748,0.8632783,-5.0432897,-3.1302671,1.3679912\PG=C01 [X(C21H23N3O1)]
\\@
```

Table C28. 2.4-PMC-TTC, geometry optimization, B3LYP/6-311G+(d,p)

FOpt\RB3LYP\6-311+G(d,p)\C21H23N3O1\BRYNND\13-No
v-2013\0\\# opt=tight b3lyp/6-311+g(d,p)\\Title Card Required\\0,1\O,1
.9178955946,2.9829219598,-0.0000658764\N,0.9234561189,0.2353773771,-0.
0000115176\N,-2.4708842011,1.4461062068,-0.0000471636\C,-3.9015795316,
-1.2293648332,-1.2565097381\H,-4.320349869,-1.7047953115,-2.150174724\
C,-4.2991684077,0.2550304697,-1.2769523742\H,-3.877830088,0.7610126026
,-2.1513346087\H,-5.3896735922,0.3247433409,-1.3658955798\C,-3.8953069
803,1.0212441358,-0.0000208036\H,-4.4509251145,1.9582496577,-0.0000472
13\C,-1.4290104667,0.5827774102,-0.0000199774\C,-1.6659284235,-0.91303
01871,0.0000276494\H,-0.659339988,-1.3268187497,0.0000340939\C,-2.3761
719731,-1.422031903,1.2784354637\H,-2.1621926508,-2.4930796137,1.37097
50338\H,-1.9386539025,-0.9411246405,2.1591031569\C,-3.9015607441,-1.22
92818142,1.2566175433\H,-4.3203187497,-1.7046526197,2.1503200813\C,-4.
4881838271,-1.8983101557,0.0000802422\H,-4.2544167854,-2.968540855,0.0
001140307\H,-5.5810239997,-1.8114876996,0.0000853318\C,-2.3761905895,-
1.4221143787,-1.2783369479\H,-1.9386853641,-0.9412639028,-2.1590420297
\H,-2.1622114911,-2.4931678413,-1.3708106494\C,-4.2991464886,0.2551159
697,1.2769688171\H,-3.8777905386,0.7611547147,2.1513097851\H,-5.389649
8877,0.3248369636,1.3659276632\C,-0.1159897562,1.082798825,-0.00003290
76\H,0.0647188568,2.1461354526,-0.0000581111\C,2.1948404883,0.59738625
21,-0.0000148673\C,3.1860914183,-0.485906459,0.0000092161\C,2.82463724
88,-1.8431099769,0.0000284616\H,1.7753495103,-2.106458345,0.0000255497
\C,5.1529118918,-2.4173545121,0.0000522614\H,5.947762449,-3.1583788411
,0.0000689853\C,4.5734813317,-0.1966008595,0.000012852\C,5.0093577851,
1.1825238573,-0.0000084081\H,6.080780784,1.3515185217,-0.0000050564\C,
4.1306710866,2.2065538831,-0.0000320446\H,4.4580836864,3.2401502555,-0
.0000491379\C,2.680049134,2.0044002242,-0.0000366296\C,-2.2104890324,2
.8917252924,-0.0000944233\H,-1.6408446771,3.1904403571,0.8842591434\H,
-3.158168958,3.4249956353,-0.0001169432\H,-1.6408367818,3.1903799732,-
0.884463008\C,3.8096085191,-2.8148156905,0.0000501969\H,3.5547343482,-
3.868492883,0.0000651346\N,5.5322406082,-1.1460272653,0.0000340472\\Ve
rsion=AM64L-G09RevA.02\State=1-A\HF=-1053.8211161\RMSD=3.159e-09\RMSF=
2.848e-06\Dipole=-3.4356635,-0.6976498,0.0000149\Quadrupole=0.1367418,
1.5825267,-1.7192685,-5.6347482,0.0001334,-0.0000566\PG=C01 [X(C21H23N
3O1)]\\@

Table C29. 2.1-SO, geometry optimization, B3LYP/6-31+G(d,p)/Onsager, H_2O

FOpt\RB3LYP\6-31+G(d,p)\C26H26N2O1\AIKOKURI\11-Jul-2014\
0\\# opt=tight b3lyp/6-31+g(d,p) scrf=(solvent=water,dipole,a0=5.97) g
eom=connectivity\\APSOSO H2O b3LYP/6-31G+(d,p)\\0,1\N,-2.4876928652,-0
.4575279807,1.4159320739\C,-0.6912181371,-1.9623156876,0.8326573842\H,
-1.3243150042,-2.7815946102,1.1755232997\C,1.3805045313,-1.0856389367,
0.3476535758\C,0.8956481749,0.199806964,0.4307202431\N,0.5645996712,-2
.1709436194,0.7032448247\C,1.7534334614,1.3446622522,0.2681919876\C,2.
7650878049,-1.3237192709,0.0131994635\C,3.1275329207,1.1394157153,-0.0
562949343\C,3.6401015957,-0.2194330115,-0.2076453454\C,1.2461489052,2.
6569072795,0.4206346819\H,0.1982678209,2.7827679104,0.6673300079\C,2.0
705075336,3.7557612719,0.2625188356\H,1.6723369541,4.7587410799,0.3837
077528\C,3.4275070756,3.5665236117,-0.0603050634\H,4.0797643027,4.4254
925989,-0.1891959237\C,3.2632666231,-2.6436785642,-0.0981897193\H,2.58
11311503,-3.4652349981,0.0884275095\C,4.5847444778,-2.8770802885,-0.43
42060074\H,4.9514830409,-3.8964157197,-0.5181636268\C,5.4520960282,-1.
7932979,-0.6688200932\H,6.4892184602,-1.9717031375,-0.9384310033\C,-1.
4078573267,-0.6470710838,0.5124449829\C,-4.3690070184,-0.9451149989,-1
.1379894825\H,-5.1064119854,-1.6327402743,-1.572580761\C,-4.4613745027
,0.4195162012,-1.8479574566\H,-5.4644406191,0.8445688486,-1.7112767803
\H,-4.3092665276,0.3037108542,-2.9292762743\C,-1.7840321757,-0.6308962
878,-1.0016665158\H,-0.8929029437,-1.0382683331,-1.4944766976\C,-4.713
007633,-0.7423045105,0.3460915639\H,-4.7044655509,-1.6950194584,0.8880
683656\H,-5.7326090259,-0.3383877728,0.4139990433\C,-3.7448575788,0.23
26354675,1.047247401\H,-4.1936345975,0.4966185078,2.0096332193\C,-2.96
94562375,-1.5655599796,-1.3562552235\H,-2.8879430129,-2.5131600818,-0.
8103973224\H,-2.8749910677,-1.8168660601,-2.4209343502\C,-3.6068170775
,1.5527829443,0.2478403217\H,-2.8024516175,2.1607680791,0.6787073471\H
,-4.5391495022,2.1157361355,0.390357827\C,-2.0015292439,0.7814644547,-
1.5859815329\H,-1.895883197,0.7047985543,-2.6766491786\C,-3.3881408767
,1.3601026,-1.2676373024\H,-3.4667089276,2.3437531084,-1.7489635559\H,
-1.2128366839,1.4553775807,-1.2423845606\C,-2.1162009402,-0.3395086219
,2.8259330178\H,-1.7989342402,0.6768074232,3.1046243408\H,-2.964802594
6,-0.626907076,3.4545215398\H,-1.2876687052,-1.0148570532,3.0567957181
\O,-0.4032108572,0.4428243584,0.7404168426\C,4.9841473973,-0.494716436
2,-0.5544641972\H,5.6726333794,0.3224078384,-0.7380560565\C,3.93828848
7,2.2881996724,-0.2157371738\H,4.9879464772,2.1769334409,-0.4620680321
\\Version=ES64L-G09RevD.01\State=1-A\Dielectric=78.3553\A0=5.97\HF=-11
91.2316136\RMSD=2.448e-09\RMSF=3.486e-06\Dipole=-1.4688722,0.7046088,-
0.1773497\Quadrupole=5.6291162,-0.5005496,-5.1285667,2.9769314,-3.1569
076,0.8716341\PG=C01 [X(C26H26N2O1)]\\@

Table C30. 2.1-PMC-TTC, geometry optimization, B3LYP/6-31+G(d,p)/Onsager, H_2O

FOpt\RB3LYP\6-31+G(d,p)\C26H26N2O1\AIKOKURI\11-Jul-2014\
0\\# opt=tight b3lyp/6-31+g(d,p) scrf=(solvent=water,dipole,a0=5.88) g
eom=connectivity\\APESOTTC H2O b3LYP/6-31G+(d,p)\\0,1\C,2.5541941289,-
3.0020486002,-0.0297715317\H,1.9428182549,-3.2237934837,0.85098742\H,3
.412295972,-3.6716707083,-0.0362479366\H,1.9514278239,-3.1956035649,-0
.9230220295\C,2.1377305167,-0.6001726489,0.0063643058\C,0.7476648109,-
0.8942570993,-0.005061104\H,0.4044658725,-1.918870419,-0.0230027793\C,
-1.4628171752,-0.0190904813,-0.0018986788\C,-2.1723150991,-1.302378766
8,-0.0257263806\C,4.5111422253,-1.4086262967,0.0050579684\H,4.91306095
58,-2.4224594628,-0.0090933087\C,5.016027885,-0.7334403773,1.297760436
8\H,4.5159715932,-1.1843046751,2.1635286237\H,6.0828036807,-0.97390628
82,1.3890192991\C,4.8530919067,0.7966822119,1.2998705125\H,5.336405529
7,1.1876318182,2.2036955408\C,3.3742421491,1.2202701852,1.3211578939\H
,3.3256520961,2.312295693,1.4230914759\H,2.8625880684,0.8026208588,2.1
970872895\C,2.5994278496,0.8439147338,0.0315483896\H,1.6668352191,1.40
75370755,0.0359682942\C,3.3866825444,1.2609215785,-1.2378643057\H,2.88
36313076,0.8713833923,-2.1315491702\H,3.3389166,2.3556412268,-1.305528
7002\C,4.8653211067,0.8366435704,-1.2156686286\H,5.3573364988,1.256029
7605,-2.101879341\C,5.5425458935,1.3877240255,0.0544946771\H,5.4763701
939,2.4829727545,0.0715719159\H,6.6101686694,1.1351623868,0.0556727763
\C,5.028466048,-0.692798972,-1.2605773081\H,6.0961157687,-0.9304091576
,-1.3490538038\H,4.5369191238,-1.1158593597,-2.1450494498\C,-3.6618022
851,-1.2671365923,-0.032398297\C,-4.3850602946,-0.0503765617,-0.016585
3558\C,-3.6610352628,1.2298129423,0.0072608514\C,-2.2385703052,1.23299
06275,0.0142188347\C,-1.569661209,2.4782344299,0.0372427348\H,-0.48727
37875,2.4711201872,0.0423858072\C,-2.2615884489,3.6788679018,0.0529497
94\H,-1.7145604921,4.6174959049,0.0705123941\C,-3.6647247308,3.6766261
321,0.0461002862\H,-4.2184960193,4.6113408584,0.0582549717\C,-4.342614
4175,2.4659899099,0.0235824456\H,-5.4269204749,2.483263152,0.018590902
9\C,-4.3420228059,-2.4983037903,-0.0552535954\H,-3.7389422361,-3.40014
11363,-0.0666485462\C,-5.7285334371,-2.5504745791,-0.0628130555\H,-6.2
428771233,-3.5075598152,-0.080509993\C,-6.4568512612,-1.3508053011,-0.
0472957628\H,-7.544216556,-1.3715253972,-0.0529032413\C,-5.7964646021,
-0.128742446,-0.0246814898\H,-6.390504491,0.7780512587,-0.0131634246\N
,3.0291601492,-1.6092204824,-0.0053341551\N,-0.1360030459,0.1053889406
,0.006523598\O,-1.5872298823,-2.4038410536,-0.0403800673\\Version=ES64
L-G09RevD.01\State=1-A\Dielectric=78.3553\A0=5.88\HF=-1191.2426569\RMS
D=4.621e-09\RMSF=7.252e-07\Dipole=4.7670485,-0.0547129,0.022292\Quadru
pole=13.5682828,-3.1446737,-10.4236092,-7.2572476,0.001265,0.0803787\P
G=C01 [X(C26H26N2O1)]\\@

Table C31. 2.2-SO, geometry optimization, B3LYP/6-31+G(d,p)/Onsager, H_2O

FOpt\RB3LYP\6-31+G(d,p)\C24H24N4O1\AIKOKURI\11-Jul-2014\
0\\# opt=tight b3lyp/6-31+g(d,p) scrf=(solvent=water,dipole,a0=5.99) g
eom=connectivity\\APSOSO H2O b3LYP/6-31G+(d,p)\\0,1\N,-2.4691803386,-0
.4439280552,1.4054087789\C,-0.6958758901,-1.9559770041,0.775891953\H,-
1.3328903482,-2.7795748176,1.0998601001\C,1.3816139006,-1.0858351449,0
.3107134431\C,0.9055276784,0.2027265147,0.4030151949\N,0.5585731066,-2
.1725496095,0.6411253\C,1.7848339077,1.3343017098,0.2600258486\C,2.768
4542907,-1.3237195396,-0.0041626589\C,3.1620495288,1.1297754764,-0.047
6250122\C,3.6652803971,-0.2339973113,-0.2012809491\C,1.3211198992,2.65
94961099,0.40900609\H,0.2766863012,2.8333888501,0.6425864941\C,2.21204
13204,3.7034209427,0.2557277255\H,1.8955234828,4.7361198032,0.36387368
74\C,3.5528831919,3.3974592874,-0.0520149561\H,4.2768123282,4.20087035
41,-0.1826122503\C,3.2875269452,-2.632388265,-0.1222077038\H,2.6244309
493,-3.4750189195,0.0393357471\C,4.6216144085,-2.8018755056,-0.4375571
397\H,5.0532888397,-3.7933798008,-0.539121312\N,4.0183490499,2.1654620
678,-0.2006271024\N,4.969108333,-0.4164598464,-0.5117635775\C,5.420610
8579,-1.6564604708,-0.6274680519\H,6.4747219221,-1.7618488676,-0.88212
81971\C,-1.4155100179,-0.6351166081,0.4833596739\C,-4.4009658822,-0.92
4161512,-1.1144366682\H,-5.1436644146,-1.6104231054,-1.5407232129\C,-4
.5125341528,0.4464772712,-1.8093145282\H,-5.5141901652,0.8656730463,-1
.6501834576\H,-4.3804841857,0.3412770988,-2.8942346414\C,-1.8150601546
,-0.6009834474,-1.0233182286\H,-0.9305890964,-0.9989016124,-1.53616504
27\C,-4.7155165913,-0.7389355544,0.3787382991\H,-4.6896429776,-1.69690
09916,0.9106143851\H,-5.7364106293,-0.345071998,0.4726171281\C,-3.7417
257431,0.2374019917,1.0693833752\H,-4.1712807795,0.4891892042,2.043393
6667\C,-3.0037514589,-1.536253302,-1.3682403479\H,-2.908564801,-2.4917
301071,-0.8387860052\H,-2.9277012819,-1.7715512195,-2.4379112275\C,-3.
6262556859,1.5648907597,0.2802845875\H,-2.8189589363,2.1748881202,0.70
350723\H,-4.5596803159,2.1194968551,0.4439546386\C,-2.0494993385,0.817
7139736,-1.5872070541\H,-1.9617378959,0.7523364583,-2.6801524072\C,-3.
4331615705,1.3864465407,-1.2398882928\H,-3.5243085244,2.3738105683,-1.
7113146251\H,-1.2579321696,1.4917053228,-1.2493000522\C,-2.086038718,-
0.3741331544,2.8150610743\H,-1.7737230546,0.6347651269,3.1244296575\H,
-2.9262521537,-0.6877068373,3.4418120792\H,-1.2512980253,-1.0515326902
,3.0161094727\O,-0.3880813419,0.4600518436,0.6970210721\\Version=ES64L
-G09RevD.01\State=1-A\Dielectric=78.3553\A0=5.99\HF=-1223.3037776\RMSD
=2.287e-09\RMSF=3.864e-06\Dipole=-3.4162357,0.0439653,0.2175012\Quadru
pole=-8.6543426,7.8188822,0.8354604,-4.8214315,0.2142318,2.0040549\PG=
C01 [X(C24H24N4O1)]\\@

Table C32. 2.2-PMC-TTC, geometry optimization, B3LYP/6-31+G(d,p)/Onsager, H_2O

FOpt\RB3LYP\6-31+G(d,p)\C24H24N4O1\AIKOKURI\11-Jul-2014\
0\\# opt=tight b3lyp/6-31+g(d,p) scrf=(solvent=water,dipole,a0=5.95) g
eom=connectivity\\APSOTTC-2 H2O b3LYP/6-31G+(d,p)\\0,1\O,-1.5898188066
,-2.4099651916,-0.0000040926\N,-0.136436273,0.1198738564,-0.0000066859
\N,-5.751526064,-0.0513931457,0.0000027796\N,-4.411388011,2.3583999614
,-0.0000031156\N,3.02373617,-1.5910201813,-0.0000133337\C,-1.469510628
3,-0.0214413644,-0.0000036299\C,-2.1670989177,-1.3031136945,0.00000032
24\C,-3.6571068545,-1.2649042275,0.000001572\C,-4.3979240614,-0.059147
7977,0.0000009757\C,-3.6786337095,1.2240783738,-0.0000020429\C,-2.2552
012447,1.2181792361,-0.0000045998\C,-4.3567324155,-2.4808417018,0.0000
038661\H,-3.7799796059,-3.400331578,0.0000043589\C,-5.7430566902,-2.46
74540512,0.0000057431\H,-6.3208632845,-3.3875532651,0.0000077461\C,-6.
3854428258,-1.2192188026,0.0000051194\H,-7.4754412129,-1.1677743147,0.
0000065262\C,-1.6197947162,2.4796472525,-0.0000083586\H,-0.5374068204,
2.5141245051,-0.0000104946\C,-2.3762440747,3.6376380515,-0.0000092193\
H,-1.9019885346,4.6149236918,-0.000012063\C,-3.7761229137,3.5242305786
,-0.0000064715\H,-4.4022893192,4.4160808046,-0.0000071448\C,0.74330961
39,-0.8742305128,-0.0000066463\H,0.4016548089,-1.9000006036,-0.0000041
074\C,2.1439477355,-0.5817393234,-0.0000068817\C,2.6073850537,0.861424
1519,0.0000008916\H,1.6764552918,1.428096566,-0.0000035948\C,3.3906298
974,1.2542069653,1.2805463294\H,2.8817280323,0.8532891889,2.1660423628
\H,3.3462900968,2.3479234004,1.3636027285\C,4.8676151035,0.8239961805,
1.2579489651\H,5.3568764173,1.2267287704,2.1528864244\C,5.0230990908,-
0.7065911794,1.2802308352\H,6.0884320401,-0.9515599868,1.37011988\H,4.
526269766,-1.1423717883,2.1554927818\C,4.5128980374,-1.3992478364,0.00
000021745\H,4.9062728971,-2.4159048779,0.0000017385\C,5.0231223191,-0.7
065787505,-1.2802104678\H,6.0884573231,-0.9515447838,-1.3700826771\H,4
.5263094901,-1.1423514326,-2.1554856866\C,4.8676346703,0.8240079707,-1
.2579153142\H,5.3569083102,1.2267507912,-2.1528414135\C,5.553324055,1.
3921608677,0.0000247661\H,5.4929211471,2.4877910846,0.0000295248\H,6.6
193263669,1.1352255755,0.000031741\C,3.3906489462,1.2542164377,-1.2805
300488\H,2.881760536,0.8533047629,-2.1660366046\H,3.3463090376,2.34793
34319,-1.3635790589\C,2.5471975481,-2.9870206932,-0.0000317278\H,3.405
52106,-3.6554484346,-0.0000608697\H,1.9422933953,-3.1929301848,-0.8881
87475\H,1.9423247267,-3.1929657531,0.8881376734\\Version=ES64L-G09RevD
.01\State=1-A\Dielectric=78.3553\A0=5.95\HF=-1223.320106\RMSD=6.931e-0
9\RMSF=9.784e-07\Dipole=7.2824296,-0.9655951,0.0000003\Quadrupole=-1.0
255704,4.270619,-3.2450486,3.0702639,-0.0000262,0.000036\PG=C01 [X(C24
H24N4O1)]\\@

Table C33. 2.1-PMC-TTT, geometry optimization, B3LYP/6-31+G(d,p

FOpt\RB3LYP\6-31+G(d,p)\C26H26N2O1\AIKOKURI\19-Nov-2014\
0\\# opt b3lyp/6-31+g(d,p)\\APESO TTT DFT/B3LYP/6-31G+(dp)-2\\0,1\C,-0
.7381502008,0.7230287161,-0.0130643996\H,-0.4159633861,1.734194098,-0.
2411507255\C,1.4482793895,-0.1417725332,0.4505950802\C,2.1449349866,-1
.4627240636,0.5425651761\N,0.1521294899,-0.2416702783,0.3064753177\O,1
.5814833428,-2.4893267076,0.9179328428\C,3.5514814381,-1.4939374534,0.
0452879146\C,2.2823020313,1.0768777897,0.4835981892\C,4.2623397547,-0.
3006737408,-0.219604574\C,3.6612546924,1.0025022055,0.1365317558\C,4.1
410095469,-2.7436812902,-0.2006531374\H,3.559042849,-3.6300931634,0.02
96061419\C,5.4210380696,-2.8323985897,-0.7351394887\H,5.8675987104,-3.
8023543795,-0.9332021457\C,6.1230798359,-1.6562105221,-1.0298605989\H,
7.1181713208,-1.7091736068,-1.4628163435\C,1.7689636111,2.3095650143,0
.9373558709\H,0.7477670038,2.3587517524,1.2938287428\C,2.5592159503,3.
4534301636,0.9971423776\H,2.1365380488,4.38468163,1.3635039102\C,3.899
9922922,3.3897771571,0.6071988913\H,4.5295395534,4.2736870191,0.649544
2791\C,-2.0939023586,0.3913080131,-0.1183952707\C,-4.8311990489,-0.664
5649316,1.389063324\H,-5.3472565506,-0.7874967521,2.3502889258\C,-5.47
3957644,-1.5948350697,0.3406195162\H,-6.5461082705,-1.3763350072,0.242
2857363\H,-5.3896749584,-2.639676683,0.6662722086\C,-2.5385077459,-1.0
100618862,0.2598444463\H,-1.5994977029,-1.5334427252,0.4458649314\C,-4
.9985077354,0.8015024682,0.9446682446\H,-4.5137237758,1.4821461085,1.6
553645574\H,-6.0692284928,1.0469471914,0.9510657645\C,-4.4765940172,1.
0952234141,-0.4798728549\H,-4.8978068495,2.0580909536,-0.7775325843\C,
-3.3543464827,-1.0510410436,1.5767333197\H,-2.8753186512,-0.4104325332
,2.3269078595\H,-3.3059385742,-2.0761650502,1.9664858006\C,-4.97287943
53,0.0427512482,-1.494619189\H,-4.4792435382,0.2109670674,-2.459395624
\H,-6.0469915665,0.213124834,-1.650450652\C,-3.2744444048,-1.762932437
1,-0.8770449477\H,-3.1953247864,-2.8357717715,-0.6581750743\C,-4.76538
24666,-1.4035331927,-1.0154681811\H,-5.2140325029,-2.0759402569,-1.758
4507383\H,-2.7497935337,-1.6025006562,-1.8270078484\N,-3.0079559725,1.
3091557431,-0.5439673653\C,-2.5526872676,2.6226088471,-0.9994030089\H,
-2.1818055465,3.2396886407,-0.169064844\H,-1.7483093608,2.5213997681,-
1.7349853477\H,-3.381945712,3.1476641866,-1.4738208436\C,5.5529469841,
-0.4124624093,-0.7734017789\H,6.1201565628,0.4785041859,-1.0186533031\
C,4.4386270841,2.1728803147,0.1991120621\H,5.493867991,2.1315792038,-0
.0462703176\\Version=ES64L-G09RevD.01\State=1-A\HF=-1191.2249519\RMSD=
3.850e-09\RMSF=2.036e-06\Dipole=-1.7332436,1.7521213,-0.7873345\Quadru
pole=15.275114,-4.1564929,-11.1186212,-1.0859288,-2.5487662,2.6783962\
PG=C01 [X(C26H26N2O1)]\\@